The Modelling of Fuel Dispersion and Concentration in Direct Injection Diesel Engines

by

Christopher John Morris

A Doctoral Thesis

Submitted in Partial Fulfilment of the Requirements

for the Award of

Doctor of Philosophy of Loughborough University of Technology

September, 1975

Supervisor:- J.C. Dent, Ph.D., C.Eng.

Summary

The presented investigation develops a modelling technique, which allows measurement in a dynamically similar gas jet, to be related to the diesel engine injection process in the presence of air swirl.

Modelling experiments have been performed for direct injection processes from both the centre and the circumference of the combustion chamber. A tracer gas technique has been employed, by which, concentration of jet nozzle gas in the simulated air swirl was measured, thus yielding information on model predicted trajectory, spread and local fuel concentration. Gas concentration was measured using a specially developed hot wire anemometry technique which allowed measurement in a transient pulsed jet simulation.

The modelling theory was developed on the basis that spray droplet velocity relative to the air entrained into the spray is small after an initial jet disintegration, and droplet formation process. Consequently the fuel spray is assumed to behave as an air jet bearing a mist of liquid droplets.

Favourable comparison of model gas jet and engine fuel spray behaviour is initially made with published film data. Further comparison of engine performance and associated high speed photographic results, with the model predicted fuel dispersion and local concentration levels, is made from data obtained on a modified Petter PJ1 test engine. The results indicate that model predicted rich fuel regions, both at the combustion chamber wall and within the jet core correspond to smoke generation areas recorded on the high speed films. Similarly, experimental engine performance parameters such as exhaust emission levels, rate of pressure rise, and peak pressure are shown to directly relate to the model predicted dispersion of fuel.

The conclusions drawn are that the modelling technique has potential in optimising the fuel injection equipment specification at the design stage and effectively represents the behaviour of the modelled engine fuel spray.

Acknowledgements

The author wishes to express his gratitude to the following persons:-

Dr. J.C. Dent for his advice and assistance throughout the project.

Mr. P. Norton, and members of the technician staff of the Mechanical Engineering Department.

Mr. P.H. Clayton for his particular help in the manufacture of the hot wire probes and other experimental equipment.

Messrs. K. Topley and G. Halls for producing the photographic plates appearing in the thesis.

Mr. G. Boyden for his help and expertise in the high speed photographic work.

Finally, the author is also indebted to his wife for her patience throughout the period of study.

Publications

A paper based on a proportion of the work reported in Chapters 4, 5 has been presented to the Institution of Mechanical Engineers for future publication.

Notation

A	i) cross-sectional area of hot wire.
	ii) intercept constant in hot wire correlation law.
A_c	combustion chamber flow cross-sectional area (radius x height).
A_p	Proportion of the model gas jet weaker than 10:1 air to fuel ratio.
B	i) slope constant of hot wire correlation law.
	ii) mass transfer driving potential (Appendix A).
C_d	coefficient of discharge
C_p	specific heat at constant pressure.
d_o	diameter of jet orifice.
d_g	diameter of gas nozzle.
d_f	diameter of fuel nozzle.
d	diameter of hot wire.
E, E_o	voltage output of anemometer bridge.
f( )	denotes 'function of'
$F(\chi)$	concentration function (equation 5.1)
h	i) height of combustion chamber.
	ii) overall surface heat transfer coefficient of the hot wire.
Ho	manometer total head reading (ΔHo denotes differential head manometer reading).

I_p hot wire probe current.

J momentum flux ratio.

k thermal conductivity.

k_s hot wire material thermal conductivity at the wire support temperature.

k_w as k_s but at the mean wire operating temperature.

K1 solution variable defined by equation (4.7).

K2 solution variable defined by equation (4.8).

k_T thermal conductivity evaluated at temperature T.

l length of hot wire sensing element.

L wire material Lorenz constant.

$\dot{m}$ mass flow rate.

M molecular weight.

n i) constant exponent.

ii) molar quantity of gas.

Nu Nusselt number (h.d/k)

Pr Prandtl number. (μ.Cp/k)

p absolute pressure.

Pe Peltier coefficient.

$\dot{Q}_c$ rate of heat loss to support by conduction from the hot wire.

r	local co-ordinate of combustion chamber radius.
R	combustion chamber outer radius.
Re	Reynolds number ($\rho.U.d/\mu$)
R_l	hot wire lead resistance.
R_w	hot wire operating resistance.
R_c	hot wire room temperature resistance (at T_c).
R_t	hot wire anemometer bridge top resistance.
R_g	hot wire resistance at the local gas temperature T_g.
$\overline{R}$	universal gas constant.
s	axial curved distance along the jet centreline for jets in crossflow.
t	time.
T_m	arithmetic film temperature $(T_w + T_g)/2$).
T_w	wire temperature.
Tw'	mean wire temperature (section 4.2).
T_g	gas temperature.
T_c	reference room temperature.
T_l	$(T_w - T_g)$ (section 4.2).
U	velocity.
U_f	fuel velocity at the nozzle.
U_g	gas velocity at the nozzle.
U_s	jet velocity at centre line location 's'.
U_a	air velocity.
x	general length co-ordinate.
z	i) total length of hot wire sensing element.
	ii. general length co-ordinate.

Greek Notation

α	temperature coefficient of resistance.
β	wire material resistivity.
Δ	denotes a difference of magnitudes.
ξ	modelling scale factor.
ρ	density.
μ	dynamic viscosity.
ν	absolute viscosity.
χ	molar concentration of tracer gas.
π	ratio of circle circumference to diameter.
σ_{ab}, σ_{ba}	gas property functions defined by equation (4.26).
σ	i. swirl ratio (swirl angular velocity/engine crankshaft angular velocity).
	ii. standard deviation.
ω	angular velocity.
θ	angular displacement.

Subscripts

a	i) air or cross-flow property.
	ii) gas type reference.
b	gas type reference.
e	denotes the fuel spray effective source property.
f	i) fuel nozzle property.
	ii) hot film anemometer property.
g	gas (or jet nozzle) property.
m	denotes evaluation at the arithmetic film temperature T_m.
w	hot wire property.

Surscripts

(x')	denotes x is evaluated in the engine conditions.
($\bar{x}$)	denotes x is a mean quantity (except $\bar{R}$).

Abbreviations

TDC	Top dead centre.
ATDC	after top dead centre.
BTDC	before top dead centre.
CTDC	compression top dead centre.
BDC	bottom dead centre.
EVO	exhaust valve opens.
AVO	air valve opens.
EVC	exhaust valve closed.
AVC	air valve closed.

Index of Contents

	Page Nos.
SUMMARY	i & ii
ACKNOWLEDGEMENTS	iii
PUBLICATIONS	iv
NOTATION	v - ix
CHAPTER 1	
INTRODUCTORY DISCUSSION AND SURVEY OF PUBLISHED LITERATURE:	
General Comments	1 & 2
1.1 The Relationship of Air Swirl Intensity to Fuel Injection Variables	
1.1.1 Assessment of Air Swirl Velocity.	3 & 4
1.1.2 Evidence of Optimum Swirl Intensity.	4 - 8
1.1.3 The Effect of Nozzle Configuration.	8 - 10
1.1.4 Dependence of Exhaust Emissions on Fuel Spray and Air Swirl Intensity.	11 - 14
1.2 Discussion of the Literature Pertaining to Mathematical Analysis of Fuel Spray:	
1.2.1 General Comments.	15
1.2.2 Review of Mathematical Analysis for Fuel Sprays Injected into Still Air.	16 - 21
1.2.3 Review of Mathematical Analysises for Fuel Sprays Injected into Swirling Air.	21 - 29
1.3 Discussion of the Literature Survey	30 - 32
1.4 Definition of the Project Objective.	33

Page Nos.

CHAPTER 2

STATEMENT OF THE BASIS OF SIMILARITY BETWEEN THE DIESEL ENGINE FUEL SPRAY AND THE GAS JET MODEL

2.1 Introduction 34 - 36

2.2 Basic Concept of the Fuel Spray and Analysis in Relation to Gas Jets in Cross Flow:

2.2.1 Derivation of the Steady State Equations 37 - 39

2.2.2 Transient Analysis 39 & 40

2.2.3 Representation of the Air Cross Flow Velocity 40

2.3 Criticisms of the Modelling Concept 41

CHAPTER 3

SURVEY OF HOT WIRE CORRELATION DATA AND TECHNIQUES:

3.1 Introduction 42

3.2 Review of Salient Heat Transfer Correlations for Cylinders in Crossflow. 43 - 46

3.3 Review of Hot Wire Calibration Methods for I.C. Engine Velocity Measurement. 47 - 49

3.4 Review of Binary Gas Concentration Measurement Techniques. 50 & 51

3.5 Conclusions of the Survey of Anemometry Techniques:

3.5.1 Applicability of General Correlating Equations to Engine Velocity Measurement. 52 & 53

3.5.2 Binary Gas Concentration Measurement. 53 & 54

CHAPTER 4

DEVELOPMENT OF THE ANEMOMETRY HEAT TRANSFER CORRELATION: PRACTICAL OPERATION OF HOT WIRE ANEMOMETERS

4.1 Description of Experimental Equipment.

4.1.1 Hot Wire Anemometry Bridges: Principle of Operation. 55 & 56

		Page Nos.
4.1.2	Hot Wire Probe Construction and Manufacture	56 & 57
4.1.3	Flow Calibration Rig.	57 - 59
4.2	The Calculation of Wire Heat Transfer Coefficient with Allowance for End Conduction Loss.	60 - 63
4.3	Assessment of Wire Geometry and Thermal Properties:	
4.3.1	Wire Geometry.	64
4.3.2	Wire Material Thermal Properties.	64 & 65
4.3.3	Wire Room Temperature Resistance.	66 - 68
4.4	Anomalous Wire Surface Effects.	69 & 70
4.5	Empirical Hot Wire Heat Transfer Correlation Law:	
4.5.1	General Comments	71
4.5.2	Choice of Suitable Tracer Gas Types.	71 - 74
4.5.3	Scope of Correlation.	75
4.5.4	Representation of Gas Properties.	75 & 76
4.5.5	Aquisition and Analysis of Correlation Data	77 - 79
4.5.6	Appreciation of Typical Error: Deviation from the Correlation Law.	79 - 82

CHAPTER 5

DEVELOPMENT OF BINARY GAS CONCENTRATION MEASUREMENT TECHNIQUE:

5.1	Validation of the Concentration Sensitive Function.	83 & 84
5.2	Concentration Sensitivity Based on the Mean Correlation Law.	85 & 86
5.3	Concentration Calibration Procedure.	87 & 88
5.4	Effect of Probe Inclination to the Flow.	89
5.5	Measurement Examples in Unknown Flow Fields.	90
5.6	Error Estimate on Concentration Measurement.	91 & 92

Page Nos.

5.7 Computational Details:

5.7.1 Computation of Probe Characteristics. 93 & 94

5.7.2 Calculation Sequence for the Computation of Concentration Magnitude from a Calibrated two Wire Probe. 94 & 95

CHAPTER 6

MODELLING EXPERIMENTS BASED ON PUBLISHED DATA:

6.1 Description of the Experimental Swirl Rig. 96 & 97

6.2 Modelling Experiments Based on the Data due to Stock (86); Comparison of Model and Engine Jet Trajectories and Spread:

6.2.1 General Comments. 98

6.2.2 Steady State Model of a Radial Injection. 98 & 99

6.2.3 Transient Model of the Radial Injection. 99 - 103

6.2.4 Comparison of the Radial Gas Jet Model with the Engine Fuel Spray. 103

6.2.5 Further Modelling Tests on the Data due to Stock (86). 103 & 104

6.2.6 Comments on the Gas Jet Simulations based on the data due to Stock. 104

6.3 Modelling Experiments based on the Data Due to Rife and Heywood (36):

6.3.1 General Comments. 105

6.3.2 Data for the 80 rad/sec. Air Swirl Case. 106 & 107

6.3.3 Model based on the data of Rife and Heywood at an Air Swirl of 180 rad/sec. 107 & 108

6.3.4 Comments on the Gas Jet Simulations based on the Data of Rife and Heywood. 108

6.4 Range of Modelled Data. 109

Page Nos.

CHAPTER 7

RELATIONSHIP OF FIRED ENGINE DATA TO THE CORRESPONDING GAS JET SIMULATION:

7.1 Introductory Comments 110

7.2 Experimental Test Engine Modifications. 111 & 112

7.3 Aquisition of Fired Engine Data.

7.3.1 Fuel Injection Equipment Characteristics. 113 & 114

7.3.2 Indicated Work Done, and Fired Pressure Trace Comparisons for the Different Nozzles and Combustion Chamber Geometries. 114

7.3.3 Exhaust Emission Tests. 115

7.3.4 High Speed Photography Results 116 - 118

7.4 Air Velocity Measurements:

7.4.1 Statement of the Measurement Problem. 119

7.4.2 Experimental Equipment. 119 - 121

7.4.3 Aquisition of Data and Experimental Results. 121 - 123

7.5 Comments on Relative Performance of the Two Combustion Chambers. 124

7.6 Modelling Experiments Based on the Engine Data. 125 & 126

7.7 Relationship of Engine Data to the Gas Jet Models:

7.7.1 Qualitative Comparison of Photographic Data and Gas Jet Simulations. 127 - 132

7.7.2 Quantitative Comparison of Gas Jet Simulations and Engine Data. 132 - 134

7.7.3 Concluding Comments on the Engine Analysis. 134 & 135

CHAPTER 8

GENERAL DISCUSSION AND CLOSURE:

8.1 Gas Jet Modelling Results:

8.1.1 Model Representation of Trajectory and Spread. 136 & 137

		Page Nos.
8.1.2	Representation of Fuel Dispersion.	137 - 139
8.2	Application of the Modelling Technique to Engine Development.	140 - 142
8.3	Remarks on the Hot Wire Techniques.	143
8.4	Recommendations for Further Work.	144 & 145
8.5	Conclusion.	146

9.0 REFERENCES AND APPENDICES

REFERENCES		147 - 156
APPENDIX A	One Dimensional Single Droplet Theory.	157 - 162
APPENDIX B	General Iteration Technique.	163 & 164
APPENDIX C	Hot Wire Concentration Calibration and Heat Transfer Correlation Program.	165 - 169
APPENDIX D	Petter PJ1 test engine: Salient Details.	170

CHAPTER 1

Introductory Discussion and Survey of Published Literature

CHAPTER 1

INTRODUCTORY DISCUSSION AND SURVEY OF PUBLISHED LITERATURE

General Comments

Dispersion of fuel within the combustion chamber of large diesel engines is usually achieved by a single, centrally placed, multi-hole injector nozzle. The fuel sprays thus created, possibly up to sixteen in number, provide even angular distribution of the fuel, and air entrainment into the sprays provides the mixing process in the absence of any other air motion.

However, the introduction of air swirl becomes desirable in smaller engines, where the number of nozzle holes has to be restricted due to manufacturing difficulties associated with the drilling of small size multi-hole nozzles, and also running problems incurred by the clogging of excessively small spray holes. Hence, proportionally larger holes, usually three to five in number, are the norm in engines with cylinder capacities of one litre per bore or less. In these situations the introduction of air swirl is essentially a compensating factor for the large angular spacing of the fuel sprays and the decrease in available spray path length.

The major factors affecting power output and exhaust emission, may therefore logically be expected to be those which directly influence the distribution of fuel within the combustion chamber. Such variables are numerous and include nozzle hole size and number, injection rate, swirl intensity, injection timing, combustion chamber design etc.

By necessity therefore, the optimisation of fuel injection equipment characteristics, for any particular engine, is frequently a process of trial and error, preferably based on a large amount of experience on the part of the development engineer. Consequently ideas have been modified in light of new experience as a continuous process.

The following section of the survey is therefore intended to highlight the manner in which the fuel-air mixing process relates to engine performance, and accumulate the benefit of previous research.

1.1 The Relationship of Air Swirl Intensity to Fuel Injection Variables

1.1.1 Assessment of Air Swirl Velocity

Meaningful interpretation of engine performance data, in relation to the fuel and air mixing process, is enhanced by a pre-knowledge of variation of swirl velocity over the considered engine speed range. Such information and comparison was provided by Urlaub (1),(2), when the variation of swirl rate with engine speed was measured for a range of intake mask heights.

As may be expected, the results of Urlaub shown in Figure (1.1) indicate an increase in swirl ratio with increase in mask height. Comparison of the manner in which swirl ratio, (defined as the ratio of air and crankshaft angular velocities), varies with engine speed shows a positive gradient for the 'no-mask' data, whilst a negative gradient exists for the curves representing the swirl ratio with inlet masking. Increase in mask height or alternatively, decrease in inlet flow area, produces progressively larger rates of decrease in swirl ratio with engine speed.

The variation of swirl ratio magnitude for the different manifold geometries of Figure (1.1) is large. The results were obtained by monitoring the calibrated strain gauge output on a deflecting vane within the engine cylinder.

Methods which have been used to measure swirl velocity are varied. The early results of Lee (30) were obtained by mixing goose feathers with the intake air, and studying their motion by high speed photography. Additionally Lee used a rotating vane placed in the engine cylinder, the measurement of velocity then being achieved by instantaneously measuring the vanes angular velocity. Derham (31), and Horvatin (32) used hot wire

anemometers to measure instantaneous velocity throughout the cycle.

Measured magnitudes of swirl velocity vary greatly between the sources. The results of Urlaub (Fig. (1.1)) indicate that large relative variation is possible by minor changes to the inlet manifold geometry of an engine. Thus, apparent discrepancy in the range of recorded 'typical' swirl magnitudes, (occuring between different engines, with various port geometries and combustion chamber shapes), using different measurement techniques, is not surprising.

Measurement techniques which rely on vane rotation, or tracers in the air flow, may be open to misinterpretation over periods of high acceleration within the flow field. Hot wire anemometry techniques overcome this disadvantage due to the high response rate of the sensor. However, an area of difficulty is now presented by the calibration of the hot wire probe, since the heat transfer it detects is a function of the velocity, temperature, and density of the air. All of which are transient variables in the engine cylinder.

The following study of engine data will be seen to present a range of swirl values, and apparent discrepancy on actual 'typical' magnitudes exists. However, the trend of engine data to relative change in swirl ratio will be shown to be consistent, and it is explanation of the trend that is therefore sought.

1.1.2 Evidence of Optimum Swirl Intensity

Engine performance data corresponding to the swirl conditions of Figure (1.1) is shown in Figure (1.2). Decrease in volumetric efficiency, due to mask restriction of the intake manifold, is outweighed by improvements in both mean effective pressure and exhaust smoke level. However, the mean effective

pressure produced with the 14 mm mask becomes inferior to that of the lower swirl masks at higher engine speeds. Correspondingly, exhaust smoke emission exceeds that of the 10 mm mask. This indicates an overswirled state, direct evidence of which is found also in the work of Melton and Rogowski (3), Nagao et al (4) (5), and Watts and Scott (6).

The work of Watts and Scott compared induction swirl, as measured on a steady state blowing rig, with engine performance data. In this way, a relative measure of engine air swirl, as presented by the rig data, was related to engine performance. Figure (1.3) illustrates the result. Besides the obvious illustration of an optimum swirl rate, the curves also indicate a more marked decrease in performance for the overswirled region as compared to the underswirled state.

An indication of variation of optimum swirl speed with engine speed was also presented by Watts and Scott. Figure (1.4) indicates a decrease in swirl rate for optimum operation at higher engine speed. In this respect Figure (1.2) taken from the work of Urlaub also shows a similar trend, since it can be seen that the high swirl ratio of the 14 mm mask is beneficial at lower engine speed, but the lower swirl masks are superior at higher engine speed.

Similar illustration of optimum swirl intensity, presented by Nagao et al (4) for a deep bowl combustion chamber, is shown in Figure (1.5). The mean effective pressure curve, for maximum swirl, can be seen to represent inferior performance to that of even the no swirl data, whilst the lower swirl rate shows an improved performance. This again indicates a most severe deterioration in engine performance for the overswirled state.

The photographic work for the deep bowl chamber shown in Figure (1.5), presented by Nagao et al, clearly shows a larger jet deflection for the high swirl case, but indicates that the flame front still reaches the combustion chamber periphery. The most marked difference between the low and high swirl rate photographs occurs at the initiation of the combustion process. The low swirl film indicates impingement of the jet on the chamber wall, with ignition occuring first in the areas adjacent to the point of impingement. The film for the higher swirl rate shows that ignition occurs first in the area behind the jet within the 'wake' region, and not adjacent to the wall.

It will be of value to outline the basic viewpoints presented in explanation of the overswirled state.

Urlaub's investigation was primarily a study on the optimum conditions of air rotation and injection in engines with centrally located multi-hole nozzles. However, based on the evidence of spray deflection, observed by experimental rig simulation, impingement of the spray was shown to exist for all the test conditions, although varying proportions of deflected spray were measured. The explanation of optimum swirl rate of Pischinger and Pischinger (7), and Eisfeld (8), was cited, where the opposing centrifugal and pressure forces acting on a fuel particle in the presence of swirl, were considered.

By this concept, the solid fuel particle, under the influence of the rotating flow, may be expected to spiral radially outward. Conversely, in the presence of combustion a spiral motion towards the combustion chamber centre may be expected to occur if the density of the high temperature zone, representing the original droplet, becomes less than that of the air in the combustion chamber.

Under a similar mechanism, the denser unused air will be forced radially outward, thus enhancing the combustion process. Eisfeld postulated that optimum swirl intensity exists when this spiral mixing path, and hence air utilisation, is a maximum.

However, in considering the above concept in the event of impingement, Urlaub indicates that many other factors come to bear on the problem. Evaporation and carburation at the combustion chamber wall may be expected to depend on swirl intensity, type of fuel, thickness and spread of the fuel film, and wall temperature. Urlaub postulates that the mechanism by which auto-ignition sites are formed adjacent to the wall, is therefore highly complex, and not amenable to mathematical description.

The viewpoint of Nagao et al (4), (5), and Melton and Rogowski (3), is considerably less complex. Marked decrease in engine mean effective pressure, and increased exhaust discolouration at swirl ratios in excess of the optimum was explained in terms of the 'thermal pinch' effect.

This is considered to occur when the fuel spray does not reach the combustion chamber wall. In this event, the photographic results of Nagao et al indicate that ignition occurs within the central fuel rich core, after which point the increased temperature and reduced density of the burning fuel volume creates a resistance to outward radial motion by the reverse mechanism of that described by Eisfeld for the solitary fuel particle. Air utilisation is thereby low, and the air contained in the outer regions of the combustion chamber is prevented from reaching the fuel.

Melton and Rogowski were led to this conclusion by examination of carbon formation and deduced that 'thermal pinch' was

indicated by the restriction of carbon and combustion markings to the central regions of the combustion chamber.

1.1.3 The Effect of Nozzle Configuration

The nozzle configuration, in particular the number and size of the nozzle holes, may be expected to be as critical as the swirl ratio magnitude, because it is the inter-relationship of swirl and jet intensities, which determines the radial and angular distribution of the fuel.

The results of Nagao et al (5), obtained for sprays injected into the shallow dish type of chamber are illustrative of this effect (Figure (1.6)). In the presence of swirl both mean effective pressure and exhaust discolouration are shown to deteriorate with increase in the number of sprays, with the exception of the low swirl data where an optimum spray number is evident.

The 'no-swirl' curve shows a consistent improvement in performance as the number of sprays increase. This is explained in terms of the more even distribution of fuel, and therefore greater air utilisation throughout the chamber. Under these conditions the jet mixing, or air entrainment process, is the predominant factor in ensuring the fuel contacts the air.

Melton and Rogowski (3), also found evidence of deterioration in performance with increase in number of nozzle holes in tests conducted on the M.I.T. rapid compression machine. Figure (1.7) gives an illustration of their result, where the total pressure rise attributed to the combustion process is plotted against a pressure difference which is representative of swirl within the rig. Measured on this basis, the eight and eighteen hole nozzles can be seen to give superior performance

at low swirl intensities, whilst the four hole nozzle shows an improved performance at higher swirl rates with the optimum point clearly defined.

Increase in the number of holes at constant total area and fueling rate, will correspond to a reduction in penetration potential of the individual spray. This therefore constitutes an increased swirl influence.

The smaller angular spacing of the sprays at higher hole numbers, will produce smaller air sector separation, and danger of adjacent spray interference, or overlapping, will be increased. This may be used in part explanation of the dependence of performance on the number of spray holes, but the existence of an optimum number of sprays, as on the low swirl curve of Figure (1.6), also indicates that the matching of swirl and spray intensities is relevant.

The concept expounded by Eisfeld (8) and, Pischinger and Pischinger (7), and also the 'thermal pinch' approach, are feasible explanations of inadequate mixing processes in the presence of combustion. However, it may be postulated that the location of the first ignition site, and the proportion of previously formed near homogeneous mixture of suitable ignitable concentration is critical.

Increase in the ability of the air swirl to transport sufficient fuel from the jet periphery to the rear of the jet and hence into a 'wake' region, prior to ignition, and at radii less than the wall radius, will increase the probability of ignition far from the wall even in the event of the main jet body fully penetrating.

In creating a suitable near homogeneous mixture in the wake of the jet, the initial stages of combustion through that

fraction of the mixture may be expected to be rapid, and possibly evident by increase in combustion noise.

Comparison of sound intensity and spectrum was made by Urlaub between three and five hole nozzles. Figure (1.8) shows the measured mean effective pressure variation with number of nozzle holes, (which again shows the same trend as Figures (1.6), (1.7)), and Figure (1.9) shows corresponding sound intensities. Not only does the mean effective pressure decrease for nozzles with more than three holes, but the results also indicate a more violent, or more noisy combustion process, which will correspond to a higher rate of initial pressure rise.

Further evidence which compliments the above result may be obtained from Huber, Stock and Pischinger (9). In this context, the dispersion of fuel within the combustion chamber was represented by the fractional area it covered at the point of ignition, as recorded by Schlieren photography. The fuel spray in these cases was injected from the combustion chamber wall. Variation of mixing and fuel dispersion was achieved by changing the nozzle inclination to the combustion chamber radius, in conditions with and without air swirl. Figure (1.10) represents the data thus obtained, where the fractional area is plotted against the rate of pressure rise, and a degree of correlation can be seen to exist. The result is interesting, since the combustion produced phenomenom is represented directly in terms of fuel dispersion. Alternative representation in terms of engine variables such as nozzle hole number, swirl rate, injection rate etc., has the total effect of suggesting varying degrees of dispersion, but provides no direct comparison between equally bad mixing modes on opposite sides of the optimum.

1.1.4 Dependence of Exhaust Emissions on Fuel Spray and Air Swirl Intensity

Evidence of correlation between spray intensity, at constant swirl rate, and exhaust emission levels, was presented by Khan and Grigg (10). Figure (1.11) indicates large variation in smoke level with change in injection timing, comparison with Figure (1.12) shows a strong correlation with ignition delay. Maximum smoke emission is seen to correspond to minimum delay. The variation of ignition delay depicted by Figure (1.12) is in agreement with that presented by Lyn and Valdmanis (11).

The trend of any given curve in Figure (1.11) with injection timing is explained by reference to the Schlieren studies of Huber, Stock and Pischinger. Injection commencing at 90 degrees before top dead centre, in the presence of swirl, was seen to produce a near homogeneous mixture by the time ignition occurred. The ensuing combustion was then poor, mixing being sufficiently thorough to render a generally overweak charge. Consequently smoke level, and also mean effective pressure, were low.

Further dependence of emission levels on ignition delay, or more precisely, mixing time, is illustrated by Figure (1.13) (1.14) also taken from the work of Khan and Grigg. It can be seen on comparison with Figure (1.11), that the decrease in smoke emission, with advanced injection, is at the expense of increased nitrous oxide and carbon monoxide levels.

The figures (1.11) to (1.14) thus indicate varying degrees of the process observed by Huber Stock and Pischinger for the previously mentioned 90 degree advanced injection. The larger time available for the mixing process to occur with advanced injection is promoting correspondingly larger proportions of near homogeneous, and possibly near stoichiometric mixture. Once ignition occurs flame propagation may be expected to be rapid, and,

rate of initial pressure rise, temperature, and hence nitrous oxide formation will tend to be high. The dependence of nitrous oxide emission on charge mixedness is also inferred upon comparison of the two swirl rates in Figure (1.14), where the higher swirl intensity can be seen to provide higher nitrous oxide emissions.

The emission formation process indicated is therefore very similar to that postulated by Henein (35), and illustrated in Figure (1.15). By this concept, the increased nitrous oxide formation due to the higher swirl rate of Figure (1.14) indicates the extension of spray vapour, or fine droplet, trail depicted in Figure (1.15). Similarly extensive ignition delay, corresponding to advanced injection, is indicative of a decreased proportion of over-rich mixture as depicted by the spray core in Figure (1.15).

The inference is that the inter-relation of injection duration and ignition delay is an important parameter in determining emission formation. More exactly, the mixture formed at the point of ignition is indicated to be a major controlling factor, particularly when ignition delay exceeds injection duration. An interesting point is that this is more evident from qualitative Schlieren analysis, where the dispersion of the fuel spray is observed directly, than from the interpretation of quantitative information on engine parameters such as nozzle configuration etc.

The problems associated with interpretation of engine produced variables, such as nozzle configuration and smoke level, may be realised by again referring to Figure (1.11). Comparison of emission levels between the various nozzle configurations, at constant injection timing, presents an apparent contradiction to the above concept related to Henein's Figure (1.15).

The extension of the vapour trail has been considered to promote the emission of nitrous oxides, and inhibit carbon emission. Figure (1.11) may now seemingly suggest that decrease in single spray penetration potential, or increased swirl influence, (for higher hole number configurations), and hence jet wake extension, produces the converse effect in increasing carbon emission.

The problem is therefore one of interpretation. Figure (1.6) has already been used to illustrate the effect of spray hole number. Comparison of Figure (1.6) with Figure (1.11) shows a similar trend, which is explained by Nagao et al in terms of the 'thermal pinch' effect.

Thus a degree of balance is indicated between the heavily impinging spray with low proportions of wake homogeneous mixture, but excessive wall wetting with consequent carbon emission, and the weak jet or over intense swirl, producing excessive spray deflection, possibly under penetration, poor air utilisation, and carbon formation due to the 'thermal pinch' effect.

Interpretation of engine produced data is difficult, and ultimately the process which has to be explained is the mixture formation prior to ignition. Schlieren studies have been shown to provide direct qualitative information on the fuel dispersion. The critical manner in which air swirl and fuel spray interaction controls engine performance has been illustrated.

It is therefore proposed that any method of isolating, and hence, directly studying the fuel air mixing process divorced of the many complications of interpretation and variable interaction intrinisic to engine produced data, will be beneficial in understanding the physical processes which occur.

Analytical description of the process represents one such method of isolation. Therefore a survey of relevant published mathematical models is desirable.

1.2 Discussion of the Literature Pertaining to Mathematical Analysis of the Fuel Spray

1.2.1 General Comments

The processes which occur within a fuel spray are sufficiently complex to prevent exact analytical description. Many researchers have considered the processes occuring in single droplets subjected to high temperature air streams; Godsave (12)(13), and Henein (14) showed that such analysis provided data on single droplet heat up period and evaporation rate. However, the behaviour of single droplets is generally realised not to be indicative of the history of similar droplets contained within the fuel spray, where variation of vapour pressure, relative velocity to the entrained air, and local temperature prevent the application of results obtained for the solitary fuel particle.

The jet nature of the fuel spray was realised by Schweitzer (15)(16), who established that considerable air motion was induced by the advancing spray. The jet viewpoint has led workers such as Melton (17), Wakuri et al (18), and Thring and Newby (19) to adopt a macro-scale viewpoint of fuel sprays injected into still air: hence concepts such as source momentum and mass conservation are utilised in place of micro-scale droplet considerations. Dent (20) treated the fuel spray as a gas jet by modifying the orifice diameter used in the calculation of penetration by an adaptation of the work on co-axial gas jets performed by Forstall and Shapiro (21).

The mathematical analysis of fuel sprays injected into swirling air is complicated by the interaction of the two flow fields. Allowance for the conditions within the spray core is usually achieved either by considerable assumption or by resorting to experimental data.

1.2.2 Review of Mathematical Analysises for Fuel Sprays Injected into Still Air

The basis for rejection of the single droplet ballistic approach by both Melton and Wakuri et al was the high deceleration calculation predicts for a solitary droplet. Results of similar preliminary calculations, made by the author for single droplet histories, are shown in Figure (1.16). Calculation of the penetration was achieved by equating the droplet inertia-forces to the drag forces over small time increments, using a step-by-step iteration technique. The full derivation of these calculations is given in Appendix A.

Wakuri et al and Melton both considered the momentum of the fuel droplets to be shared with the surrounding air, hence at a short distance from the nozzle, the fuel spray was considered essentially as an air jet carrying a mist of fuel droplets (possessing negligible relative velocity to the air), and possessing a total forward momentum equal to that of the nozzle momentum.

Viewing the fuel spray as Figure (1.18), and applying the conservation of jet fluid at all axial stations, allowed Wakuri et al to derive the following penetration equation:-

$$\sqrt{\frac{\rho_f}{\rho_a}} \cdot \left(\frac{x}{d}\right)^2 \cdot \frac{1}{\sqrt{C_d}} \cdot \tan\theta = U_o \frac{t}{d} \quad \ldots\ldots \quad (1.1)$$

where ρ_a, ρ_f are the air and fuel densities respectively, x is the axial location measured from the nozzle, d the orifice size U_o the injection velocity, t the time measured from the start of injection, θ the cone half angle and C_d the nozzle discharge coefficient.

Wakuri et al, and also Sass (25), experimentally showed

that the cone half angle may be represented solely as a function of ρ_f/ρ_a.

Wakuri et al also provided a simple method of predicting the average cross-sectional air to fuel ratio at any axial station. Again referring to Figure (1.18), the mass flow rate of entrained air at an axial location x, may be defined by the product of the difference of the total volumetric flow at x and the nozzle volumetric flow, with the charge air density.

Thus:

$$\dot{m}_{ax} = \pi d^2 \rho_a \left\{ U_x \left(\frac{x}{d} \cdot \tan\theta + \frac{\sqrt{Cd}}{2} \right)^2 - \frac{Cd}{4} U_o \right\} \quad \ldots\ldots \quad (1.2)$$

The local mass flow rate of fuel $\dot{m}_{fx}$ is constant and equal to the nozzle mass flow rate which is known.

Thus the local excess air coefficient λ is defined as:

$$\lambda_x = \frac{1}{\eta_s} \cdot \frac{\dot{m}_{ax}}{\dot{m}_{fx}} \quad \ldots\ldots\ldots \quad (1.3)$$

where η_s is the stoichiometric air to fuel ratio. The variation of λ_x thus calculated is given in Figure (1.19).

Wakuri et al also investigated the nature of the fuel spray experimentally. A range of jet momentum flows were created by varying the nozzle size and injection pressure, and a range of density ratios (ρ_f/ρ_a) created by changing the air density. Resultant penetrations and cone angles were then recorded by high speed cine-photography.

Penetration was shown to be directly proportional to the square root of time, i.e.:

$$x = k\sqrt{t} \quad \ldots\ldots\ldots \quad (1.4)$$

Where k is a constant dependent on nozzle size, injection pressure, and density ratio. A non-dimensional grouping was then taken to be representative of spray penetration and shown to be

solely a function of density ratio (Figure 1.20):-

$$\left(\frac{k}{\sqrt{U_o.d}} \right) = f\left(\frac{\rho_f}{\rho_a} \right) \quad \ldots\ldots\ldots \quad (1.5)$$

Inclusion of this grouping in equation (1.1) by substitution of equation (1.4), may be shown to yield:-

$$2\theta = 2 \tan^{-1}\left(\frac{\sqrt{Cd\rho_f/\rho_a}}{(K/\sqrt{U_o.d})^2} \right) \quad \ldots\ldots\ldots \quad (1.6)$$

Comparison of the predicted cone angle (equation (1.6)) with those measured experimentally is shown in Figure (1.21).

Melton (17) proposed a comparison between the liquid fuel spray and gas jet phenonmenon. In a manner similar to that of Wakuri et al conservation of source momentum and mass were considered, but with additional provision for radial variation in forward jet velocity. Hence, by assuming a self-preserving velocity profile, and constant cone angle, Melton derived:

$$\frac{U_c}{U_o} = \sqrt{\frac{\rho_f}{\rho_a}} \cdot \frac{1}{1 + \alpha(2x/d)} \quad \ldots\ldots \quad (1.7)$$

where U_c is the local centre line velocity, and α is a constant.

The value of α is chosen to given the area of jet cross-section through which the source momentum would issue at the local centre line velocity and density in the formula:

$$\pi\left(\frac{d}{2} + \alpha x\right)^2 = \frac{\rho_f}{\rho} \left(\frac{U_o}{U_c}\right)^2 \frac{\pi d^2}{4} \quad \ldots\ldots \quad (1.8)$$

where ρ is now the local jet density.

Thus the theory now differs from that of Wakuri et al, and dependance of penetration on cone angle is replaced by its dependence on α. The value of α will therefore be a function of the assumed form of velocity profile. Melton indicated that

a value of $\propto$ = 0.085 was suitable for most diesel engine fuel spray situations, although rigourous derivation of this was not presented.

Melton provided a penetration versus time relationship as a progression from equation (1.7):-

$$\propto \frac{2x}{d} = \sqrt{\frac{4 \propto U_o}{d} \cdot \sqrt{\frac{\rho_f}{\rho_a}} \cdot t + 1} - 1 \quad \ldots\ldots \quad (1.9)$$

Axial variation of air to fuel ratio along the jet axis was shown to be a linear relationship, Melton's calculations are based on the centre line values however, and hence the point at which stoichiometric concentration is achieved is somewhat greater than that shown in Figure (1.19), where the average cross-sectional concentration due to Wakuri et al, is represented.

The point at which the centre line concentration reaches the stoichiometric value was calculated by Melton to be approximately 625 nozzle diameters. Viewing the history of a transient jet as shown in Figure (1.22), Melton postulates that dissipation of the over rich regions of the spray can only occur after the cessation of injection. On this basis he concludes that the relationship of injection period to ignition delay time is an important parameter in determining the character of the succeeding combustion process.

Successful direct application of gas jet formulae to diesel engine fuel sprays was achieved by Dent (20). The formulae for centre line velocity variation in coaxial gas jets as derived by Forstall and Shapiro (21), was applied with a correction for the large density variation between fuel and air. The correction was applied in a manner similar to that derived by Thring and Newby (19), where the actual orifice size was replaced for calculation purposes by a nozzle diameter through which the same momentum and

mass flows of fluid would occur at a density corresponding to that of the charge air. This corrected nozzle diameter is given by:-

$$d_c = d\sqrt{\frac{\rho_f}{\rho_a}} \qquad \ldots\ldots\ldots \quad (1.10)$$

The centre line velocity of the equivalent co-axial gas jet, from the formula of Forstall and Shapiro is then:

$$U_c = \frac{4}{x} \cdot d \cdot \sqrt{\frac{\rho_f}{\rho_a}} \cdot U_o \qquad \ldots\ldots\ldots \quad (1.11)$$

which upon substituting $U_c = dx/dt$ and integrating yields:

$$x = (8.C_d.U_o.d.t\sqrt{\rho_f/\rho_a})^{\frac{1}{2}} \qquad \ldots\ldots \quad (1.12)$$

Dent then showed agreement between the penetration data published in refs. (26) to (29) and the theory as by equation (1.12).

Comparison of the penetration predictions of Wakuri et al, Melton, and Dent may be made by reference to Figure (1.17). Also illustrated is the trajectory for a single 20 μm droplet injected under the same conditions and computed as in Appendix A. The calculations have been based on suitable diesel engine conditions, and the values of cone angle and constant ∝ have been taken from their respective references (18)(17).

Figure (1.17) clearly shows the single droplet penetration to be inadequate, and also indicates the predicted penetration of Wakuri et al to be somewhat less than those of Melton and Dent.

Wakuri et al assumed uniform dispersion of the jet fluid and velocity over the whole jet cross-section (Figure (1.18)), hence the source momentum was also taken to be evenly distributed over the jet area. However, dependence on radial distribution was manifested by its relationship with experimentally observed cone

angles, which were shown to be a function of density ratio, but in the absence of allowance for centre line 'amplification' of forward momentum. Melton's derivation allowed for radial velocity variation by ultimately restricting the nozzle momentum to an area less than that of the total jet cross-section, but at a velocity equal to the local centre-line velocity by equation (1.8). Most interesting in this context is the adaptation of the gas jet formulae by Dent. Radial velocity variation will now be taken intrinsically as that for the equivalent gas jet, since the centre line axial velocity variation of equation (1.11) was initially derived for pure gas jets by Forstall and Shapiro. The density correction on orifice size may thus be taken to represent a change in jet scale, at constant source velocity and momentum, to produce an equivalent gas jet of lower source density.

1.2.3 Review of Mathematical Analysises for Fuel Sprays Injected into Swirling Air

Accurate description of the air motion is a necessary prerequisite to analysis of the mixing process. Borman and Johnson (22) based their computation of swirl rate on data from the work of Lee (30), and considered a solid body air rotation to exist, hence radial variation of air swirl velocity in the combustion chamber was represented by:-

$$U = k R \quad \ldots\ldots\ldots \quad (1.13)$$

where k is a numerical constant.

Initially the equations governing the behaviour of a single droplet were derived, which predict the heat transfer to and evaporation from the droplet, together with the trajectory equation derived from Newtons first law.

In the case of fuel sprays injected into still air, Borman and

Johnson allowed for the air entrainment of the fuel spray by considering single droplets to be injected into a jet having the penetration and axial velocity variation with time as represented by mathematical curve fits to the data of Schweitzer (16). Such results, for 7.5 μm diameter droplets are reproduced in Figure (1.23). Even spacing of the penetration versus time curves for adjacent droplet trajectories may be taken to depict an established spray at that location. Thus, the results indicate a steady fuel spray exists after 0.5 msecs at 25 mm from the nozzle. Or conversely, droplets injected 0.5 msecs after the initiation of the injection process do not overtake droplets which were injected earlier, i.e. relative motion of the droplets in the spray is not significant.

In allowing for the jet protection of fuel droplets from the swirl cross-flow, Borman and Johnson again utilised the data fits of Schweitzer, which were obtained for fuel sprays injected into still air. Solitary fuel particles were designated starting times, velocities, and positions corresponding to the tip of the undeflected spray.

The trajectory then described by such a droplet may be considered similar to that of a fuel particle swept away from the jet boundary by the air crossflow, since jet protection of the droplet is no longer provided in the computation.

Results taken from the work of Borman and Johnson are reproduced in Figure (1.24). The radial and angular components of droplet motion may be presented as in Figure (1.25).

A point of considerable interest is illustrated by comparison of the radial penetration curves between the two swirl ratios in Figure (1.25). The larger radial penetration depicted for the higher swirl ratio would suggest that this component is predomin-

antly a function of the centrifugal force to which the solitary droplet is exposed.

The analysis of Hussmann, Kahoun and Taylor (23), was concerned with gasoline fuel sprays injected from the cylinder wall into swirling air, and was intended to describe the fuel stratification process in spark ignition engines. However, the principles of analysis thus derived could equally be applied to diesel engine fuel sprays.

The equations governing the droplet evaporation and trajectory were derived in a manner similar to that of Borman and Johnson. However, in applying the derived relationships for a single droplet to fuel spray situations, an entirely different approach was adopted.

Borman and Johnson overcame the lack of information and knowledge on the dynamic conditions within the spray zone by the application of Schweitzers experimental data. Hussmann, Kahoun and Taylor, however, viewed each droplet size group on a Weber number criteria. A critical ratio of shear forces to surface tension forces for each droplet size was considered to exist, beyond which value a particular droplet would be disintegrated into smaller droplets. This critical ratio was defined by the Weber number viz:-

$$We_{crit} = \frac{\rho_a U_m^2 d}{2\sigma} \qquad \ldots\ldots\ 1.14$$

where We_{crit} is the critical Weber number, ρ_a the air density, U_m the maximum survival velocity, d the droplet diameter, and σ the surface tension.

The effects of droplet interaction were thus taken to be greatest over the initial portions of the spray path where the apparent velocity of the droplet relative to the air is largest.

Hence, for a given droplet size equation (1.14) was used to define a maximum relative velocity to which it could have been exposed. Accordingly, values of drag coefficient and force were based on this maximum permissible velocity for portions of the droplets history over which the apparent relative velocity exceeded that dictated by the Weber number criteria.

This then allowed the computation of trajectory and evaporation for single droplets injected into swirling air with a form of compensation for the protection afforded by the fuel spray momentum content. However, Hussmann, Kahoun and Taylor indicated that penetrations thus calculated tended to be rather high, but stated that suitable modification of the drag relation may prove feasible in the light of more experimental data.

Fuel evaporated by a single droplet, over small time increments, was considered to be immediately swept away by the air swirl. Hence, the total mass of fuel vapour to be attributed to a particular incremental air element, could be defined from the single droplets evaporated mass during the time step, and the mass fraction the droplet possessed in the initial droplet size spectrum.

A typical set of calculated trajectories is reproduced in Figure (1.26), which corresponds to the mass distribution histogram of Figure (1.27). The derived fuel-air contour map 15 msecs after the start of injection is reproduced in Figure (1.28).

The half-logarithmic plot of Figure (1.29) is illustrative of the forces acting on the droplets. It can be seen that the velocity of the droplets referred to their injection velocity become very low (mostly less than 1%), the minimum value corresponding to the maximum percentage centrifugal or pressure force. At this point the droplet has exhausted its injection induced penetra-

tion and is being controlled predominantly by the air swirl. The consequent acceleration of the droplet then indicates its increased tendency to adopt the motion of the air. At this stage the centrifugal force acting on the droplet attains a steady and low percentage of the drag force.

These results would therefore indicate that for solitary droplets removed from the spray the centrifugal forces are of secondary importance, the predominant result being the transportation of the droplet by the air, this is well illustrated by the final, near circular, trajectories of Figure (1.26).

The work of Adler and Lyn (24), has a basically different approach to the previous droplet trajectory and evaporation techniques of refs. (22)(23). In this work the fuel spray is viewed as shown in Figure (1.30), and divided into rectangular elements of width 2b and height h.

Inspection of high speed Schlieren films of the injection process led Adler and Lyn to the conclusion that the fuel spray behaved as a quasi-solid body. That is, steps in time produced progession of the spray tip as shown in Figure (1.30), preceding envelopes then describing an established spray boundary or width. The discrete elements of the fuel spray were then considered to be under equilibrium of the inertia and drag forces of the flow field.

The unknowns to be solved were then defined as jet trajectory (centre line position), mixing zone width (2b), centre line values of velocity, concentration, and temperature, and finally the evaporation function. The latter was defined as the ratio of liquid fuel mass to total fuel mass within an individual element, and was derived independently from the experimental work of Dlauhy and Garvin (33). Relative velocity between the droplets and air

was assumed to be negligible.

The remaining unknowns were then solved by application of the equations of momentum, mass and energy conservation, a derived equation governing the width of the mixing zone (based on Prandtl's mixing length hypothesis), and finally the equilibrium equation for the spray element in the flow field. The formulation of the equilibrium equation, which governs the spray trajectory, required a deflection coefficient representing the gas forces on the spray. Adler and Lyn were forced to base this value on experimentally observed deflections from high speed spray photography.

Computations were performed for both acetone and fuel oil sprays injected into air. The presented results for fuel oil data are shown in Figure (1.31). Trajectory was matched with that observed experimentally by use of the deflection coefficient. The results correspond to an injection pressure of 125 atmospheres into air at a density of 5.7 kg/m^3. Unfortunately little information is given on the cross-flow swirl magnitude but the air rotation was assumed to behave as a forced vortex.

Figure (1.31) shows, as pointed out by Adler and Lyn, that the spray calculated width is rather narrow compared to that observed experimentally by the Schlieren film.

The results indicate a very vigorous mixing process close to the nozzle. This is highlighted by the rapid changes in density and concentration over the initial portions of the spray, the density of the spray far from the nozzle being very close to that of the charge air.

A mathematical model of particular relevance to the present project is given by Rife and Heywood in Ref. (36). The paper was

presented in October, 1974 and therefore came to the author's notice long after the major principles relating to the current project had been developed and established. It was therefore of considerable encouragement to note that others had independently derived the same basic description of the fuel spray. Namely, Rife and Heywood assumed:

1. The liquid core of the jet breaks into droplets within a few diameters of the nozzle orifice.
2. The relative velocity of fuel droplets in the jet flow is small.
3. Velocity and concentration are uniformly distributed across any section of the jet.
4. The entrainment rates are the same as those of gaseous jets.

The assumptions 1; 2; and 4 are discussed more fully later in relation to this project. (Chapter 2).

The approach of Rife and Heywood was to consider the fuel spray in a cross flow to behave as a gas jet. The assumption (1) provides the basic description of the fuel core disintegrating close to the nozzle, and the jet thereafter being composed of a mist of droplets. Assumption (2) has already been used by Wakuri et al (18), Dent (20), Adler and Lyn (24) and Melton (17).

On these basic concepts the fuel spray is viewed as an air jet bearing the droplets in its path, and assumption (4), although not theoretically founded is not unreasonable upon acceptance of (1) and (2).

Rife and Heywood then applied an analysis similar to that of Abramovich (34) for gas jets, to this idealised fuel spray model. Hence, considering the fuel spray as a gas jet, and therefore considering basically momentum and mass conservations, produced a model which is far simpler than any of the droplet based

analysises mentioned earlier.

Comparison of the calculated jet tip position, and centre line trajectory with data obtained from studies on the M.I.T. rapid compression machine (as used also by Melton and Rogowski (3)) are given in Figure (1.33) and (1.32) respectively. Agreement is good, and the total gas jet approach, when compared with single droplet analysises, is not only more readily applied but also, in the author's opinion, more realistic. However, in common with other mathematical models mixing in the presence of impingement of the jet on the combustion chamber wall cannot be described.

From the photographic evidence of the combustion process, and the theoretical analysis of the fuel spray, Rife and Heywood propose that the combustion process is controlled by the rate of mixing in the fuel jet. This is an important conclusion, since single droplet evaporation and combustion studies, (Henein (14), Godsave (12)(13)) although correct for single fuel particles, do not represent the controlling influence in diesel engine fuel sprays. A further conclusion of Rife and Heywood is also important, namely that the quasi-steady assumption of fuel spray propagation, i.e. that the fuel spray tip moves in the same path as fuel injected later, is valid.

The photographic records of Rife and Heywood led them to conclude that the fuel igniting in the initial stages of combustion, causing the first rapid pressure rise, has mixed to an average concentration near to, or less than stoichiometric. The amount of fuel mixed to this concentration will therefore depend on the relationship between mixing rate and ignition delay. This is in agreement with the results of Khan and Grigg (10) shown in Figures (1.12) and (1.14) where the increase in nitrous oxide

emissions can be attributed directly to increased 'mixedness' at the point of ignition.

1.3 Discussion of the Literature Survey

The experimental results outlined in Section 1.1 illustrate the existence of an optimum swirl intensity and its relationship with nozzle hole number and diameter. The exhaust emission levels are shown to depend on this relationship and the simplified concept of Figure (1.15) gives a reasonable explanation of the formation of nitrous oxides.

Interpretation of engine data provides some insight into the processes which occur, but ultimately the fuel-air mixing process has to be studied directly. Schlieren photographic techniques provide direct analysis on this basis, but do not provide any means of predicting the behaviour of proposed fuel nozzle specifications, with regard to the variation in fuel dispersion and hence exhaust emission levels which may be anticipated.

Ideally mathematical analysis should meet this objective, but a critical appraisal indicates that the information on predicted performance of fuel sprays is usually limited to centre-line values of trajectory and fuel concentration.

Viewing the issuing spray as a solid body projected into the cross-flow, automatically implies a complex flow structure in its wake. The existence of eddies behind the fuel 'cylinder' may be expected to form suitable mixing regions for the fractions of fuel removed by the cross-flow, from the outer, low velocity, portions of the fuel spray. Figure (1.15) has been used to illustrate that this area of the mixture is thought to be responsible for the production of nitrous oxides. In the event of near perpendicular impingement on the combustion chamber wall another vigorous mixing region is provided. However, in this region the process is highly complex due to the indeterminate ratio of fuel wetting the wall to that which rebounds and is mixed with the air.

The single droplet approaches of Borman and Johnson and also Hussmann et al, indicate that single droplet velocity, relative to the air, is not large within the established spray. Hence the successful application of simple momentum based relationships for fuel sprays into still air by Wakuri et al, Melton, and Dent have provided reasonbly proven penetration predictions. The Figures (1.16) and (1.17) further illustrate the rapid deceleration of the single droplet. Figures (1.26) (1.29) show that the droplet eventually free of the spray, (after the Weber number criteria, as used by Hussmann et al (23), allows the air relative velocity to be fully effective), follows basically the rotation of the air in absence of any allowance for eddy regions behind the jet, and the centrifugal force is seen to be a small percentage of the drag force. Similarly the results of Borman and Johnson (Figure (1.25)) show that the droplets initial radially directed momentum is quickly destroyed.

The model of Adler and Lyn is dependent upon experimentally observed trajectories for fixing a deflection coefficient to the spray. The centre line values of concentration and density indicate that the mixing of the jet, thus predicted, quickly reduces the mean density of the spray to a value which approaches that of the charge air. (Figure (1.31)) However, the predicted spread of the jet is small when compared to that of the observed fuel spray, and again indicates that the eddy 'type' mixing in the wake of the jet is important.

The mathematical analysis of Rife and Heywood is particularly relevant, since it indicates a train of thought basically similar to that used within this project. Namely that the description of the fuel spray is more effectively achieved by a gas jet approach. Under this concept the droplets are considered to move with the

air, and the fuel spray is thus reduced to an air jet bearing a mist of droplets in its path. However, in common with the previously mentioned mathematical models, the analysis of Rife and Heywood cannot describe the wake and wall impingement mixing regions.

In conclusion, therefore, engine produced data provides an insight into the mixing process but is subject to misinterpretation, and mathematical analysis, although of great benefit in predicting salient details, is not capable of describing the wake and impingement mixing processes which are relevant to the exhaust emission levels.

1.4 Definition of the Project Objective

The purpose of the project is to assess the feasibility of representing the diesel engine fuel spray by a dynamically similar gas jet model. Measurement of tracer gas concentration levels may then be used to assess the trajectory and dispersion of fuel in the engine cylinder.

Mathematical difficulties in describing the wake mixing regions and effect of wall impingement may then be bypassed and replaced by relatively straight forward measurement under laboratory conditions.

The development of the technique demands the further objective of validating the results. Therefore measurement and comparison of engine data will be made with that produced by corresponding gas jet simulations.

A measurement technique, for detecting the tracer gas concentration, capable of transient analysis, will also be developed. Hot wire anemometry will be used for this purpose.

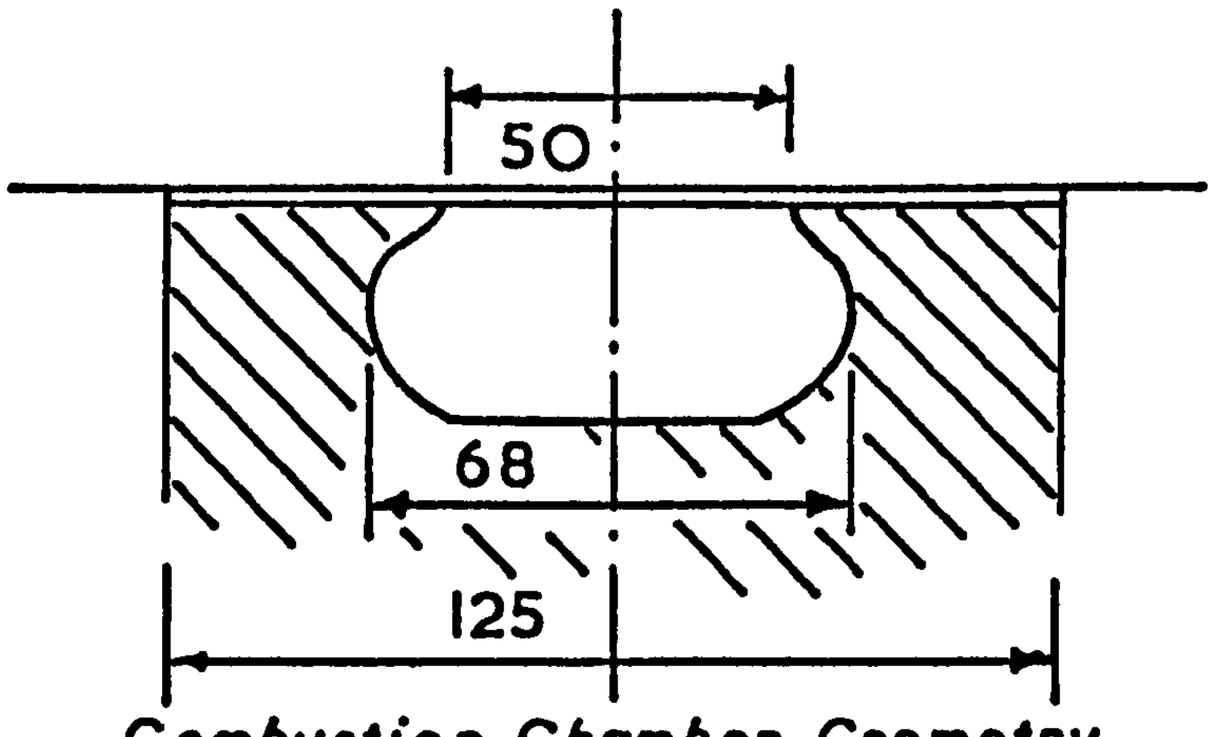

Combustion Chamber Geometry

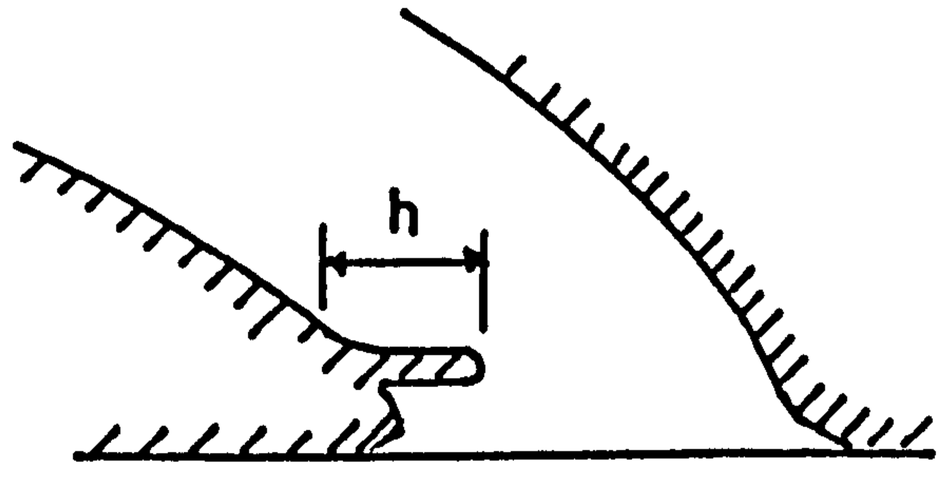

Inlet Manifold Mask Arrangement

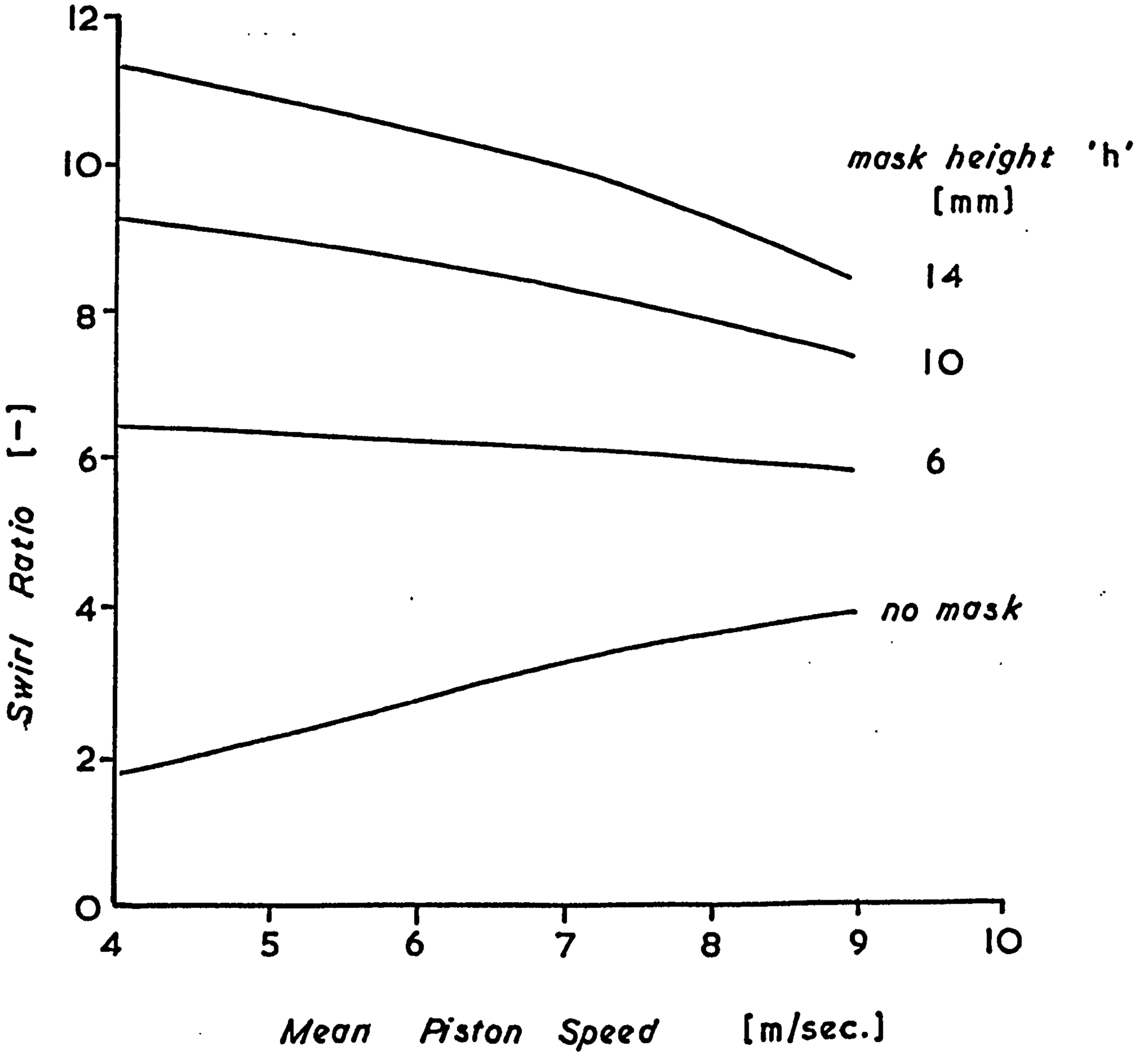

Variation of End of Compression Swirl Ratio with Mean Piston Speed.

(Results due to Urlaub (1) (2))

Fig. 1·1

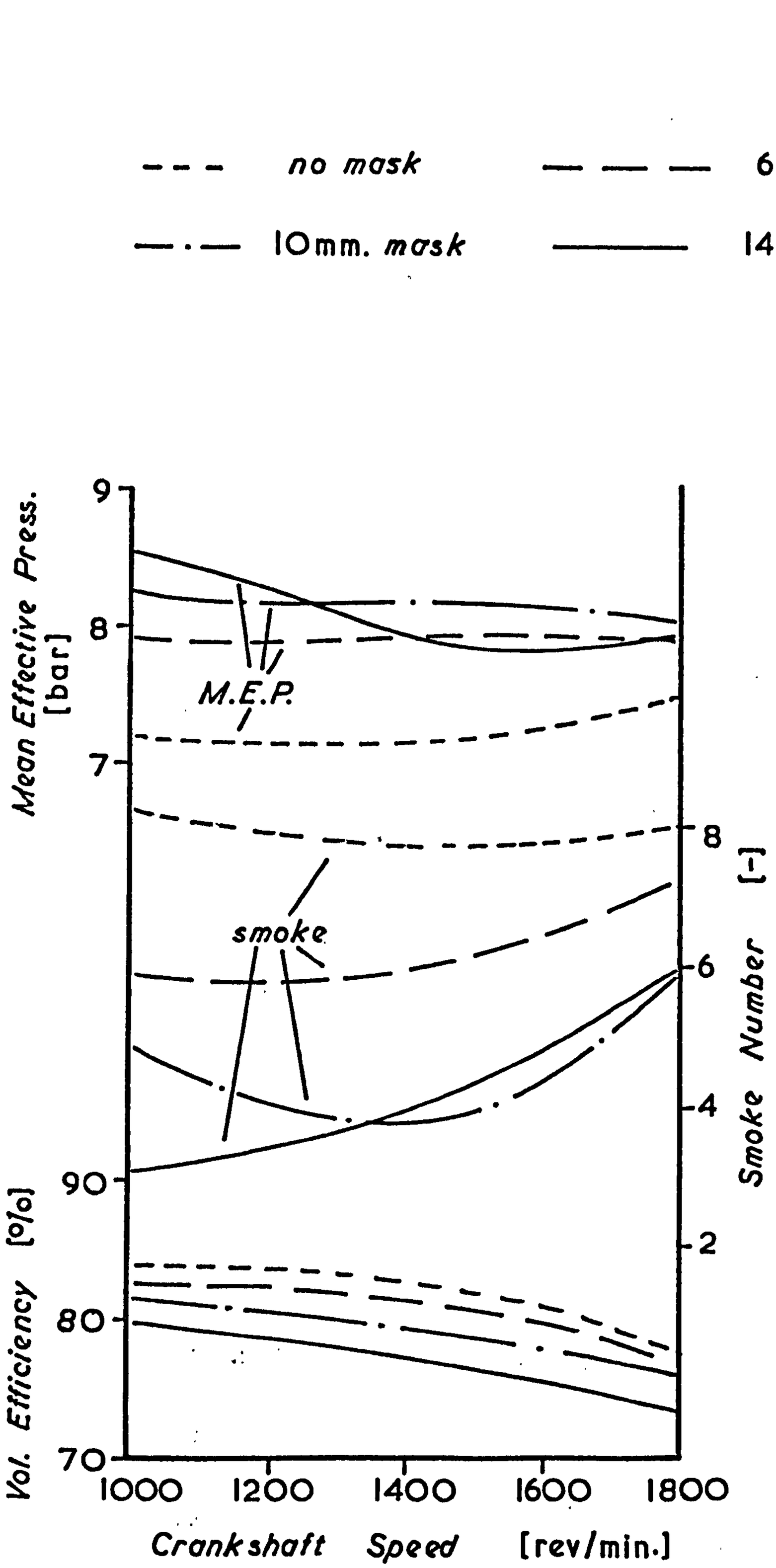

Effect of Inlet Mask Height on Engine Performance.
(Data due to Urlaub (1)(2))

Fig. 1·2

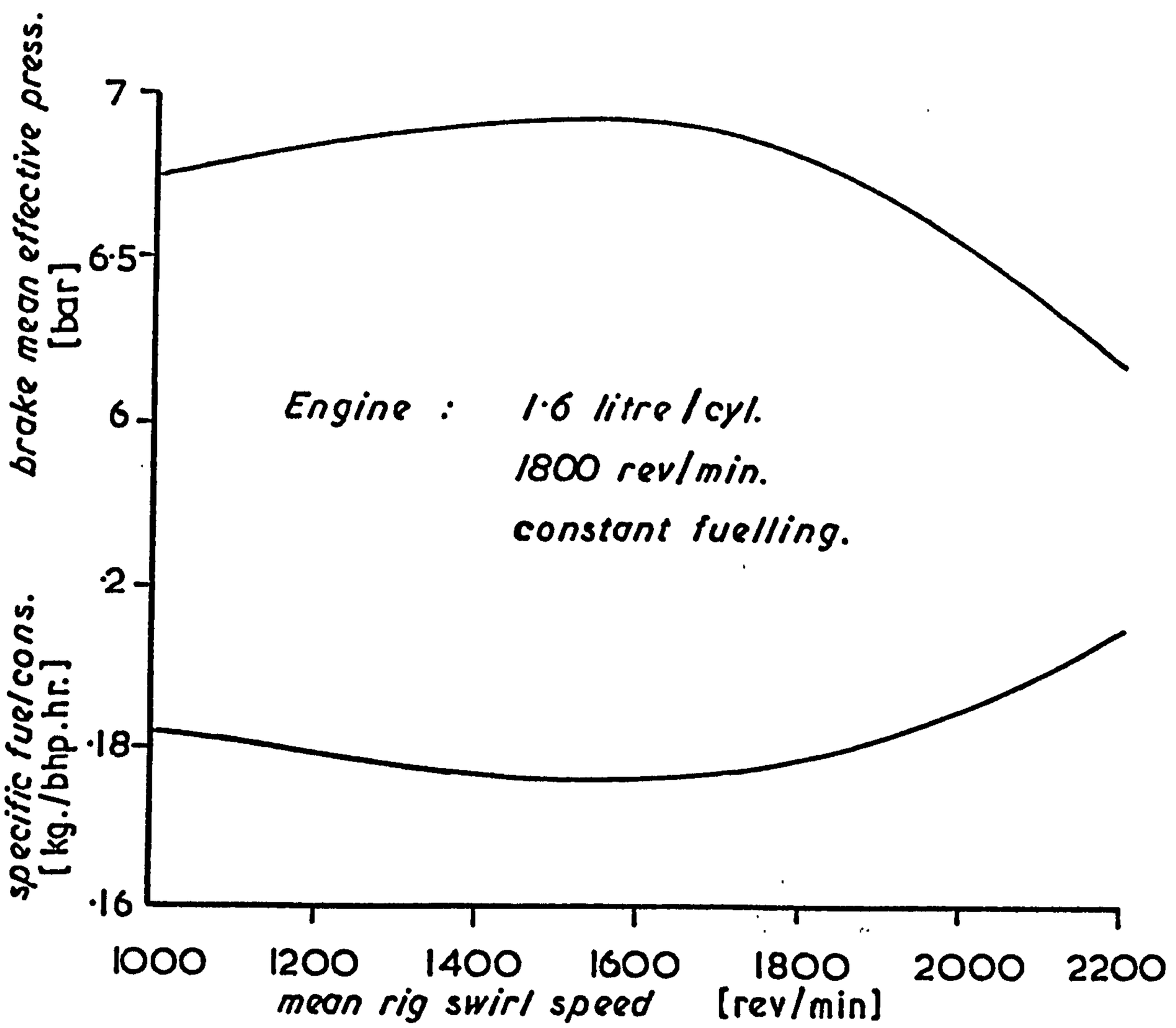

Variation of Engine Performance with Air Swirl (ref.(6))

Fig. 1·3

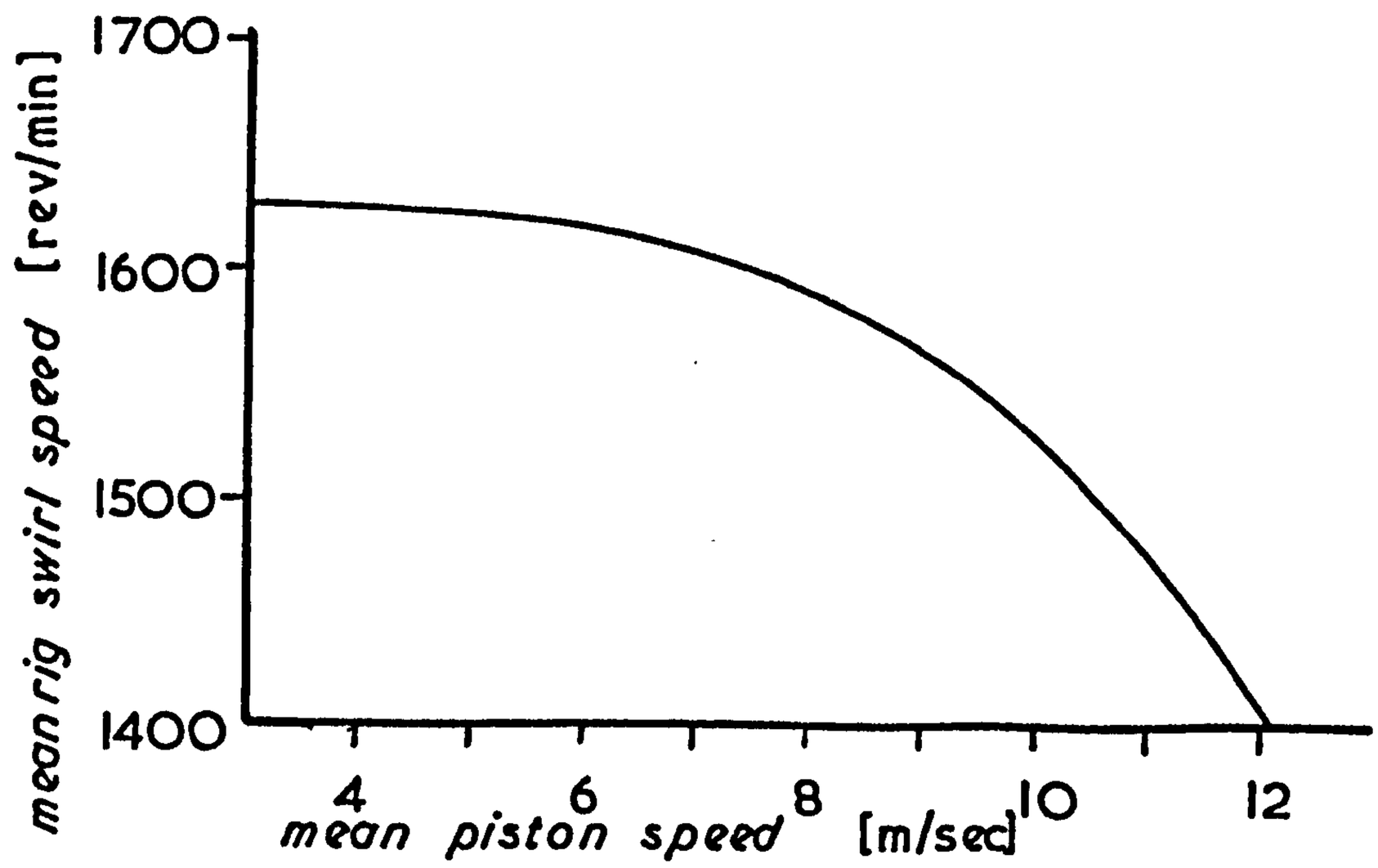

Variation of Optimum Swirl Speed with Engine Speed. (ref.(6))

Fig. 1·4

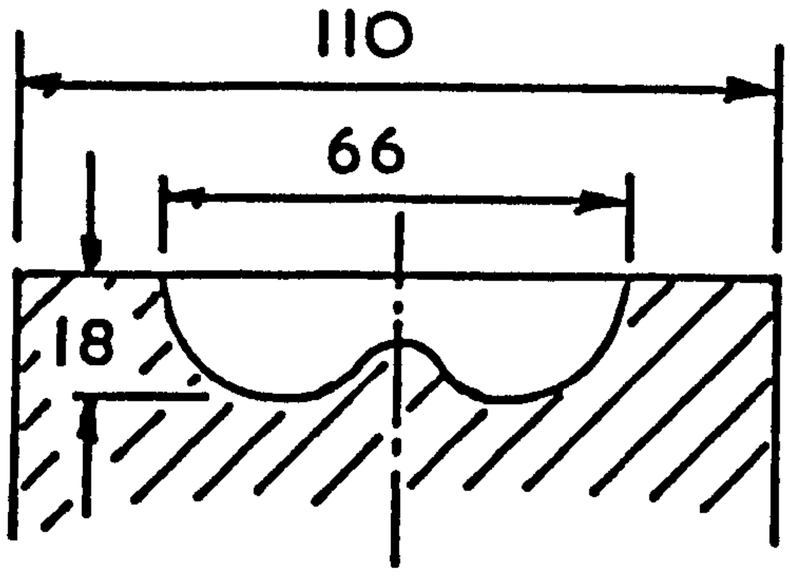

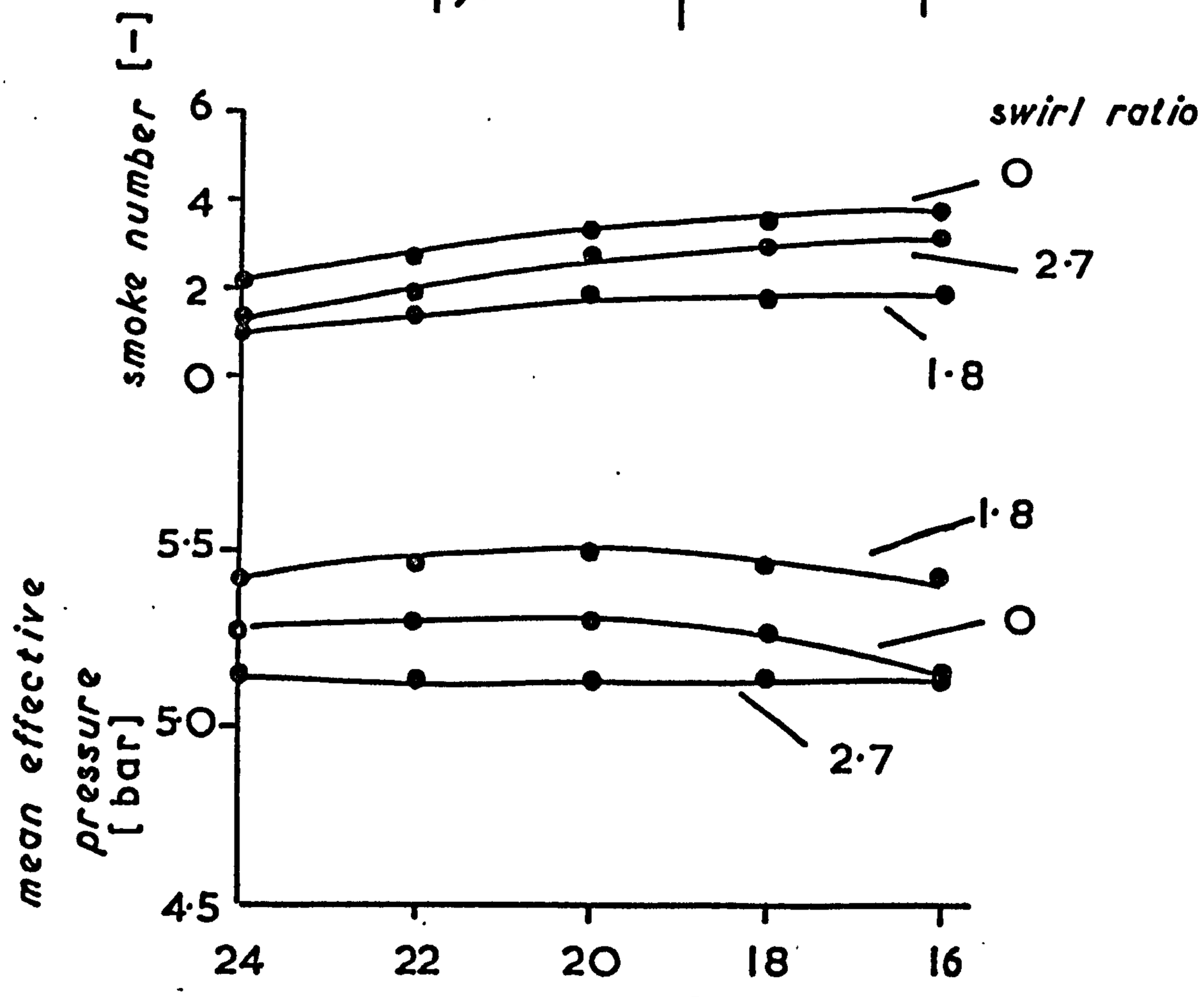

Engine Speed 1000 rev/min.

Spray Angle 140 deg.

Injected Quantity 37·2 mg./cycle

Engine Performance at Various Swirl Ratios.

(ref. (4))

Fig. 1·5

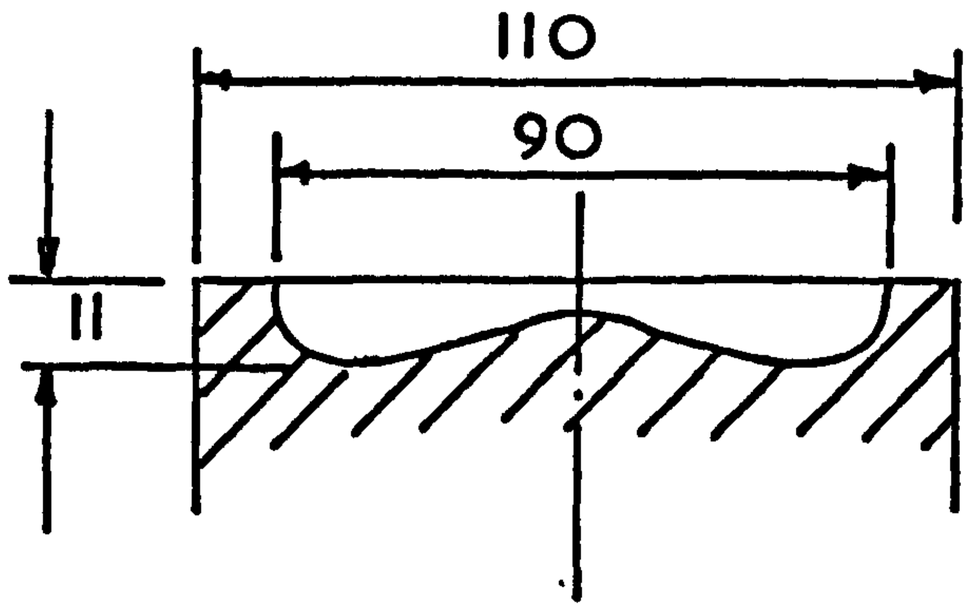

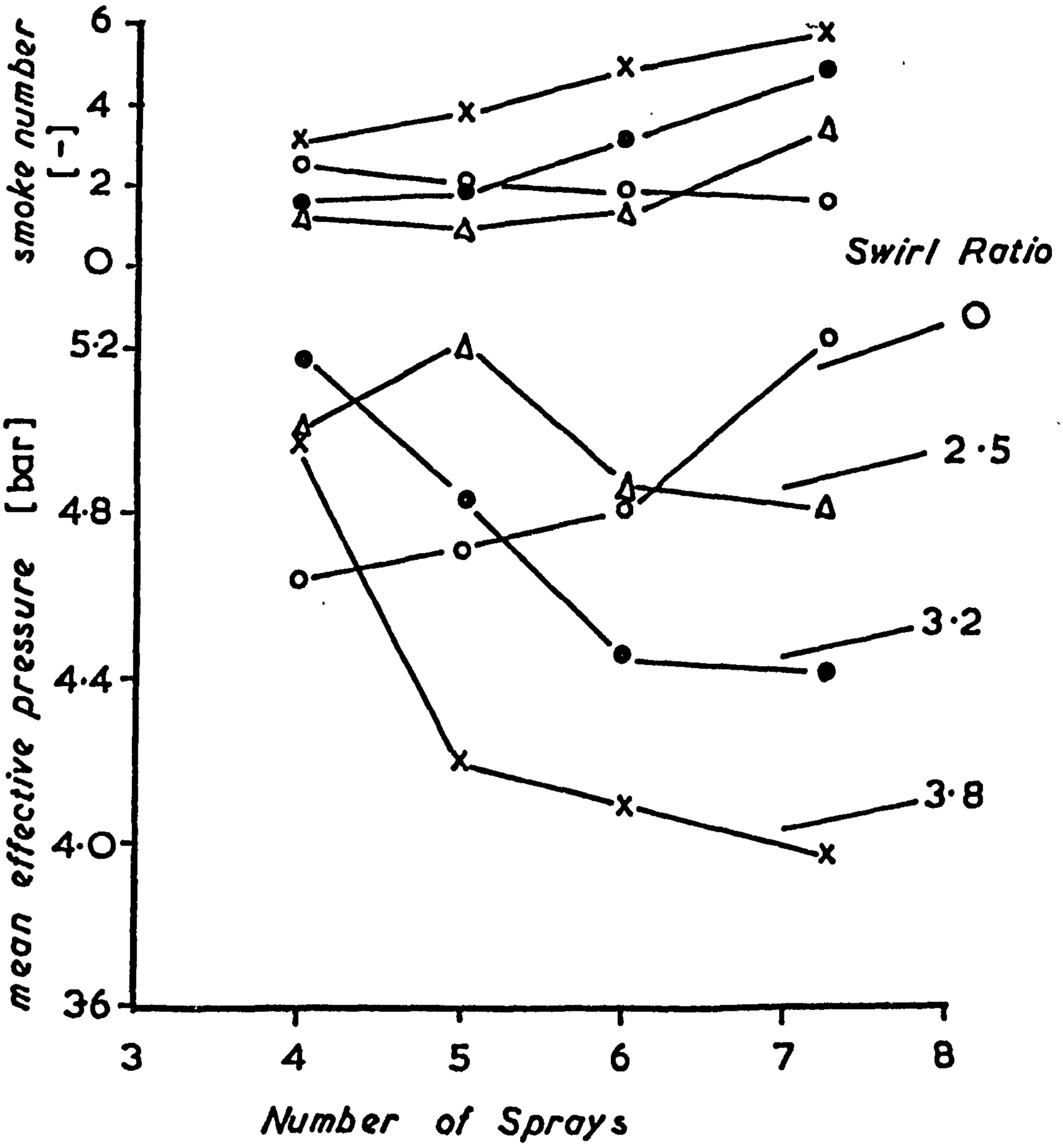

Influence of Swirl Intensity and Number of Sprays on Performance at 1000 rev/min.
(ref. (5))

Fig. 1·6

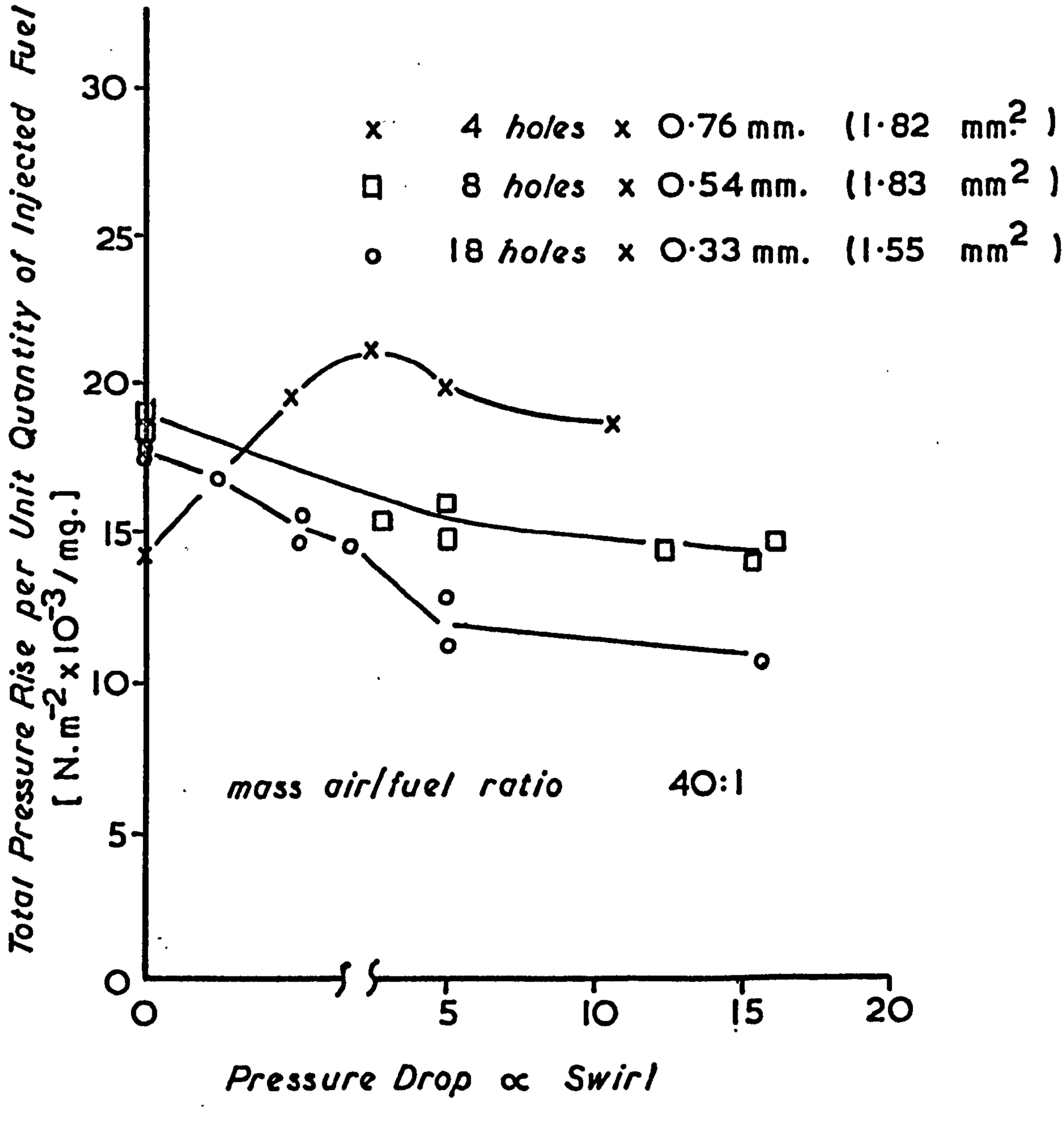

Influence of Air Swirl on Different Nozzle Configurations. (ref. (3))

Fig. 1·7

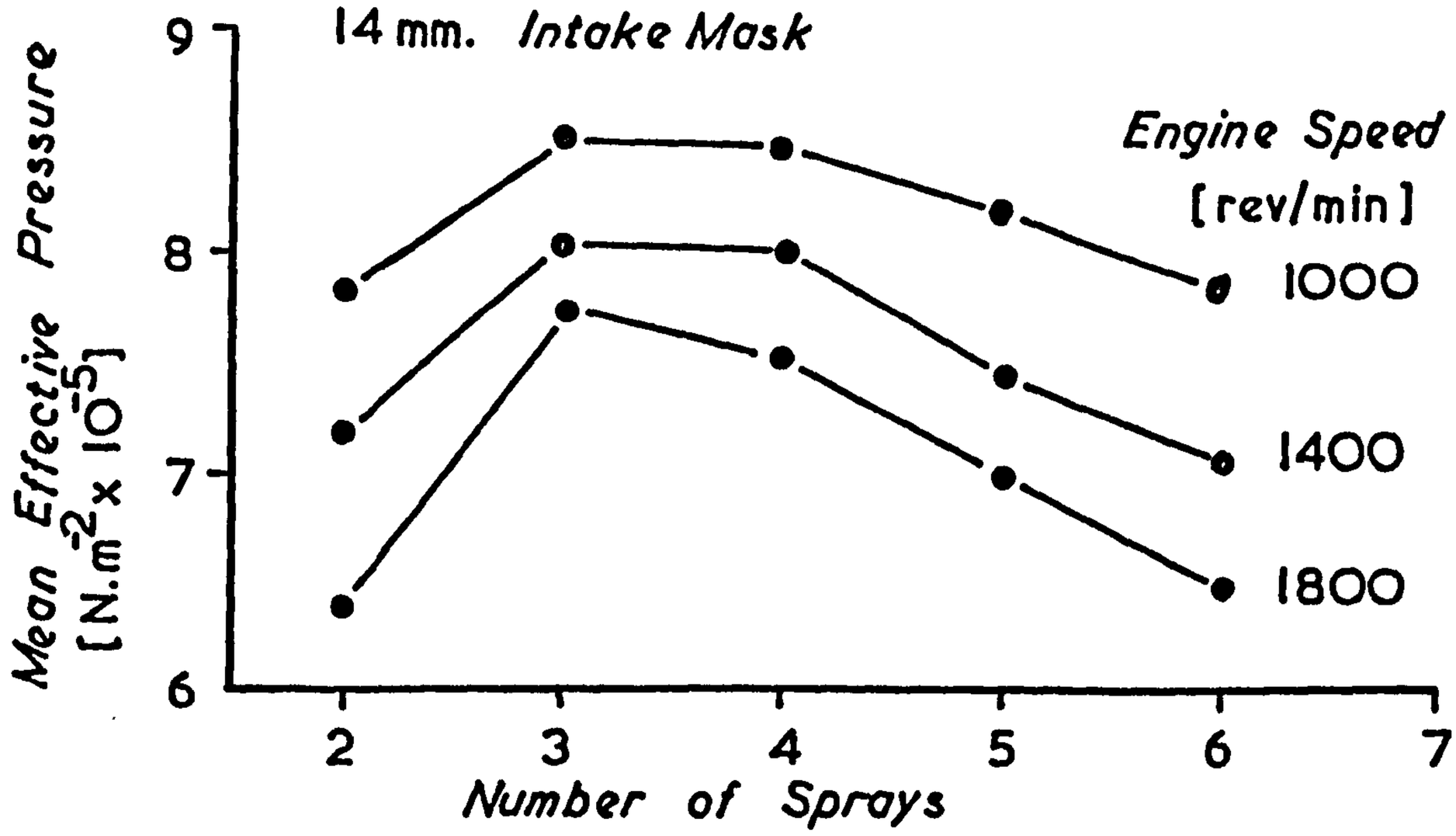

Effect of Number of Spray Holes on Mean Effective Pressure at the Smoke Limit.

(refs. (1)(2))

Fig. 1·8

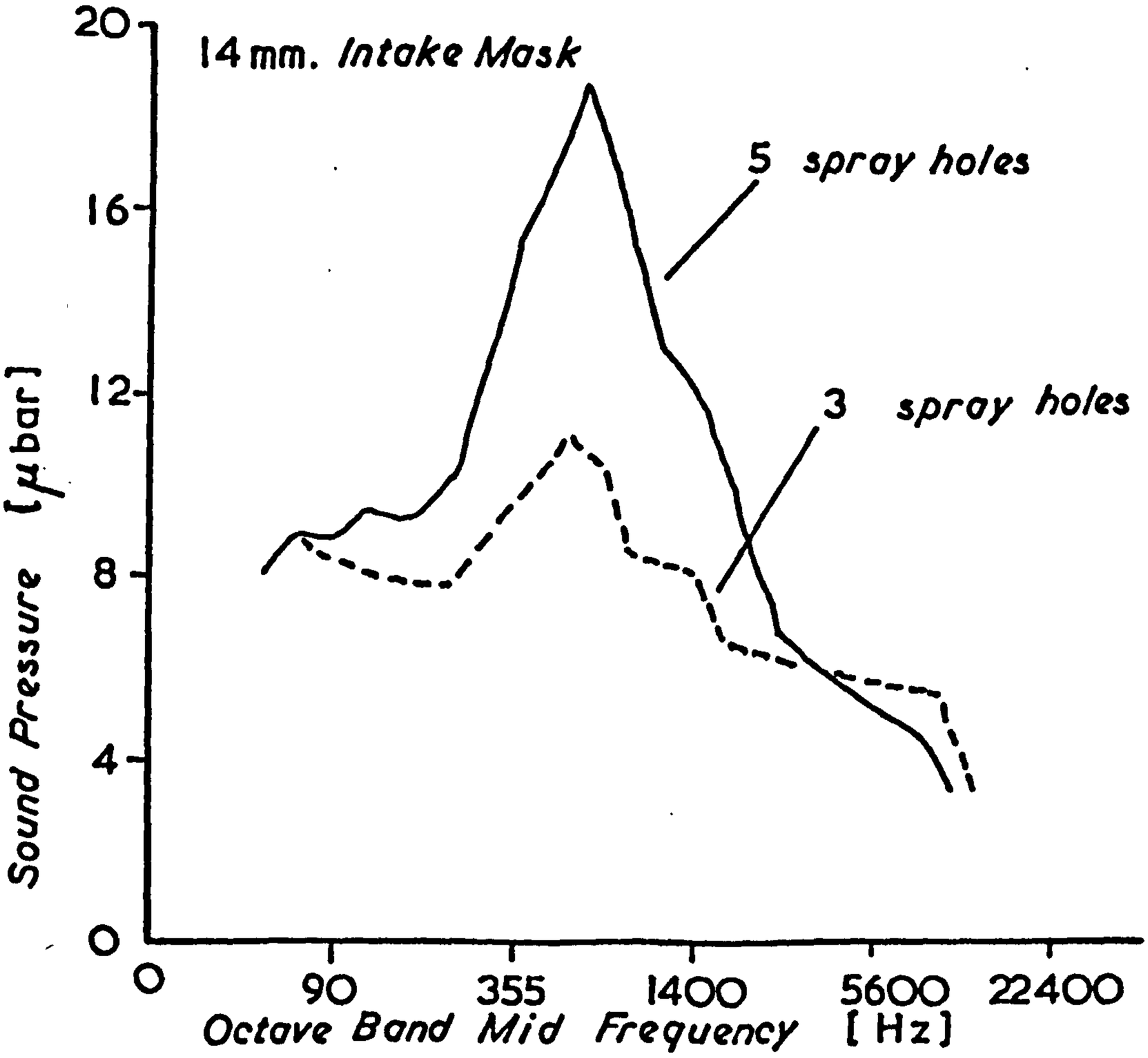

Effect of Number of Spray Holes on Sound Pressure. *(refs. (1)(2))*

Fig 1·9

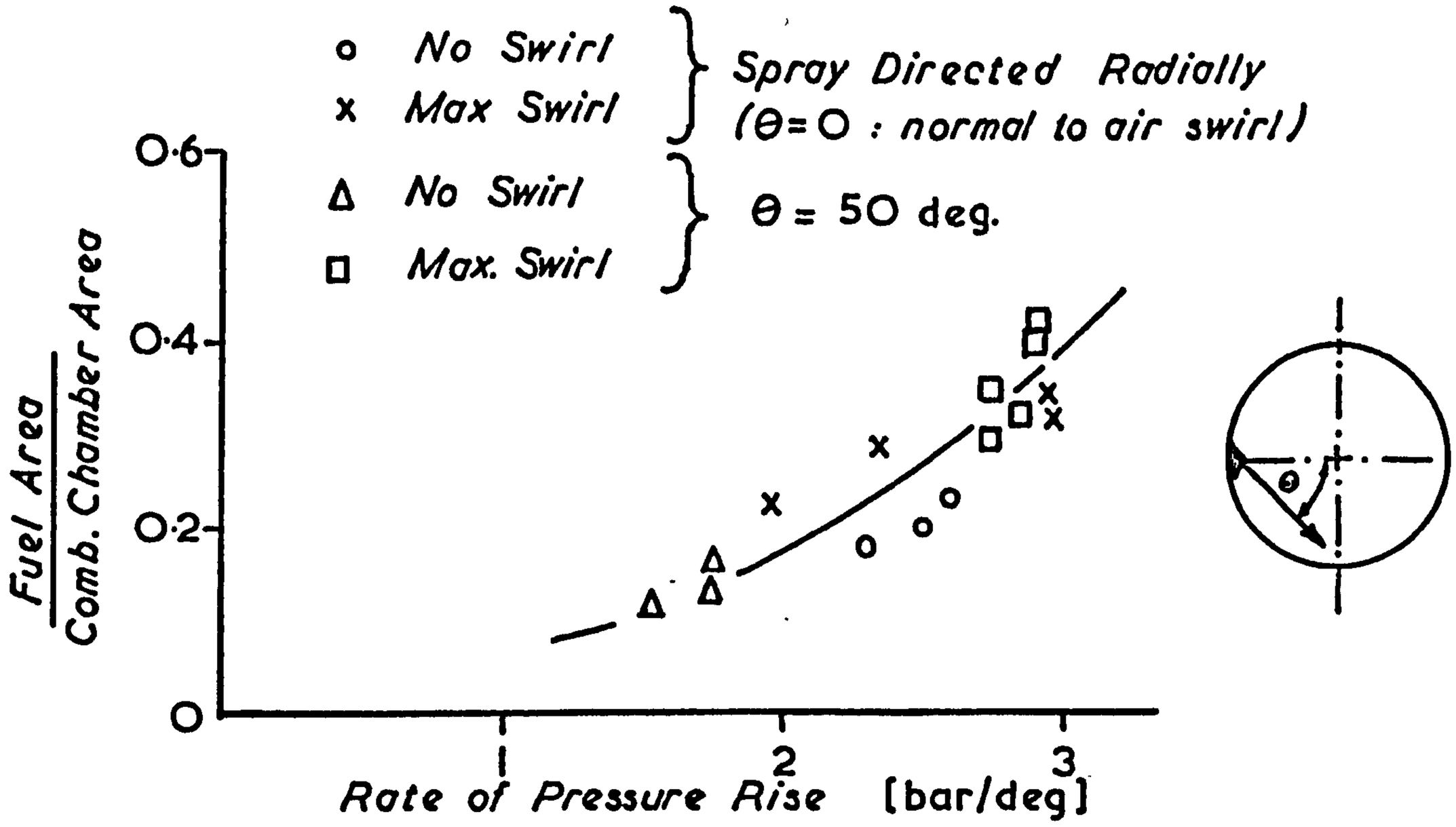

Fuel Spread vs. Maximum Rate of Pressure Rise. (ref. (9))

Fig. 1·10

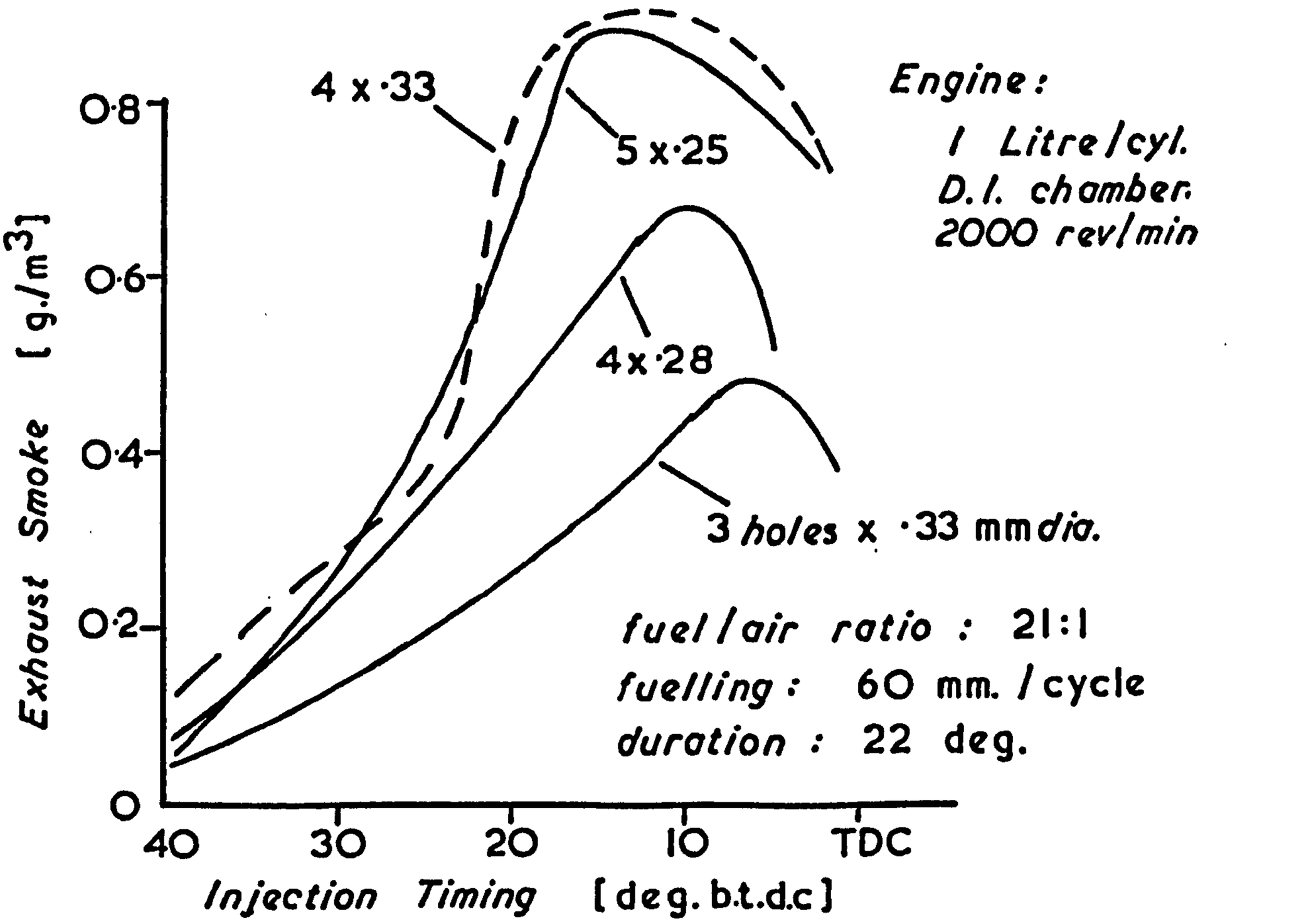

Effect of Nozzle Configuration on Exhaust Smoke (ref. (10))

Fig. 1·11

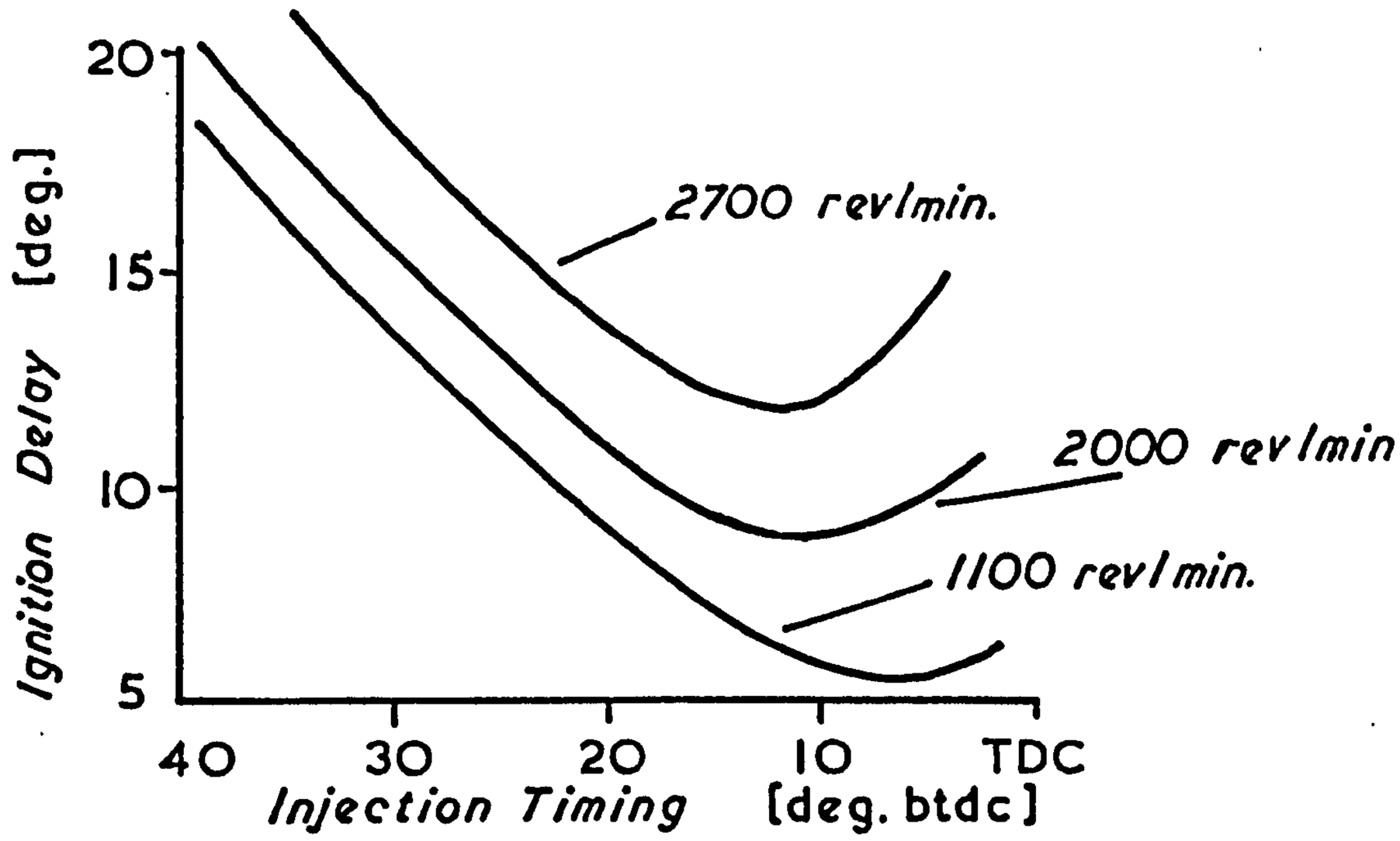

Ignition Delay vs. Injection Timing.
(ref. (10))

Fig. 1·12

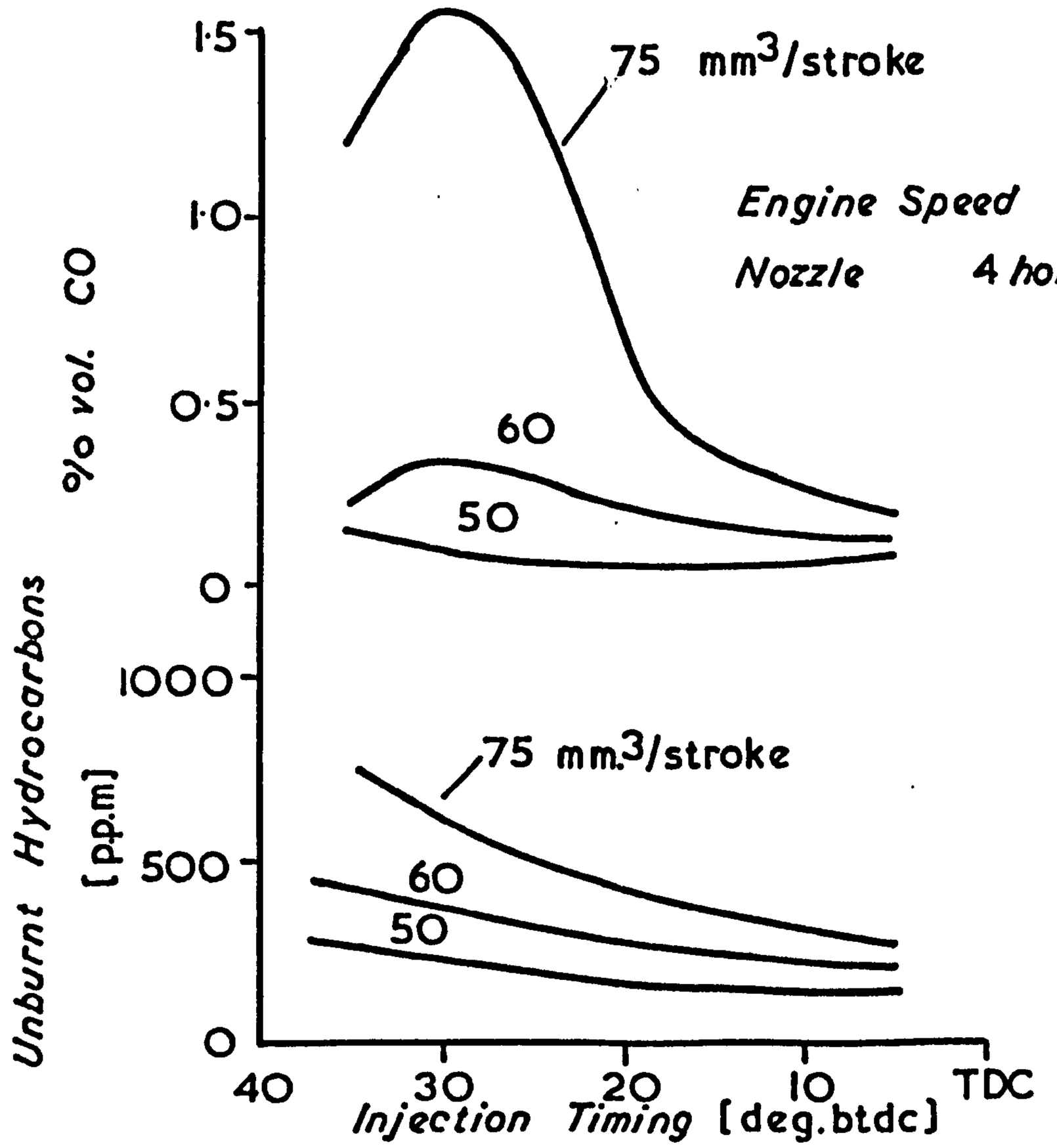

Carbon Monoxide and Unburnt Hydrocarbons Emission *(ref. (10))*

Fig. 1·13

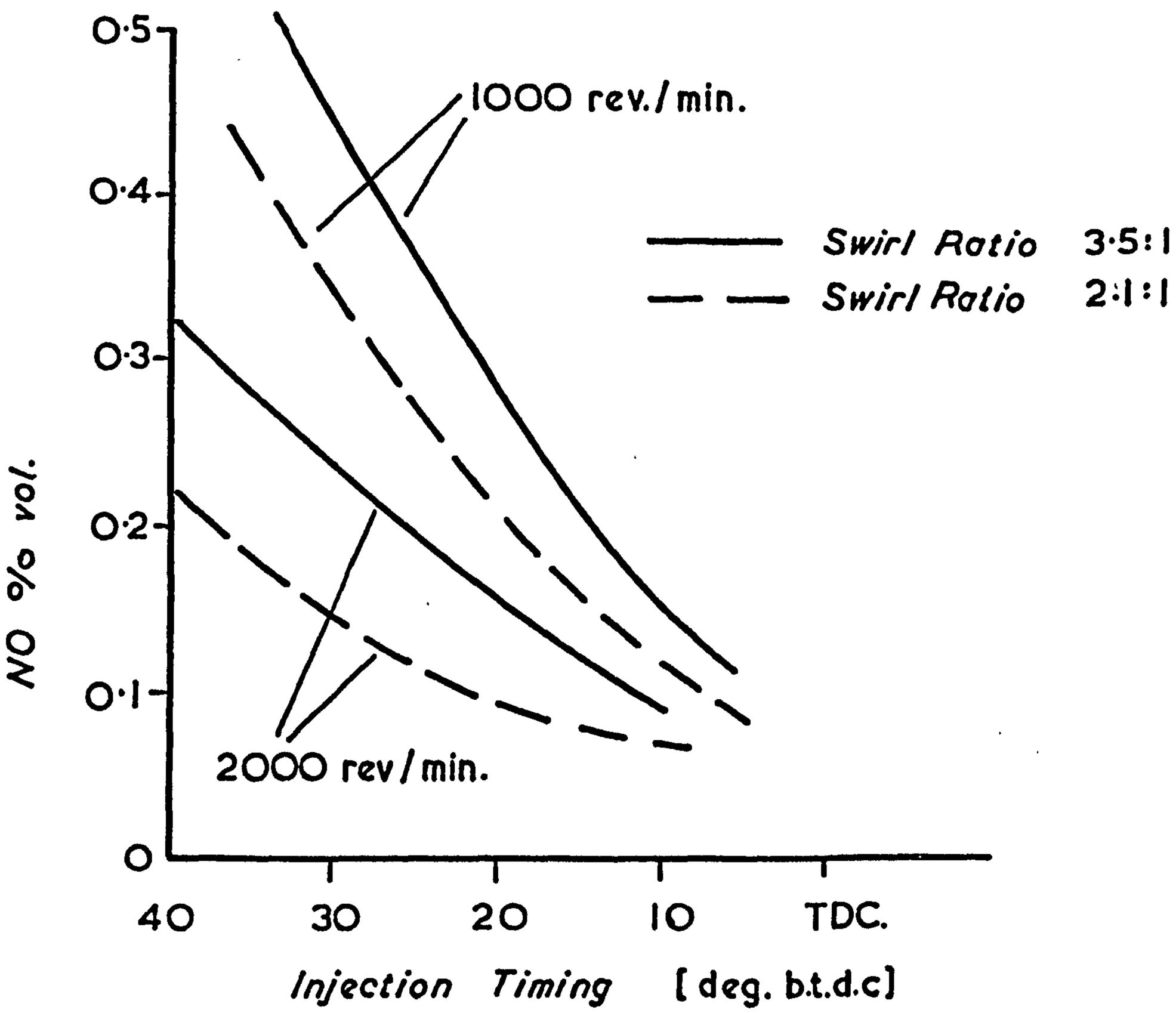

Nitric Oxide Emission for Two Swirl Rates

Fig. 1·14

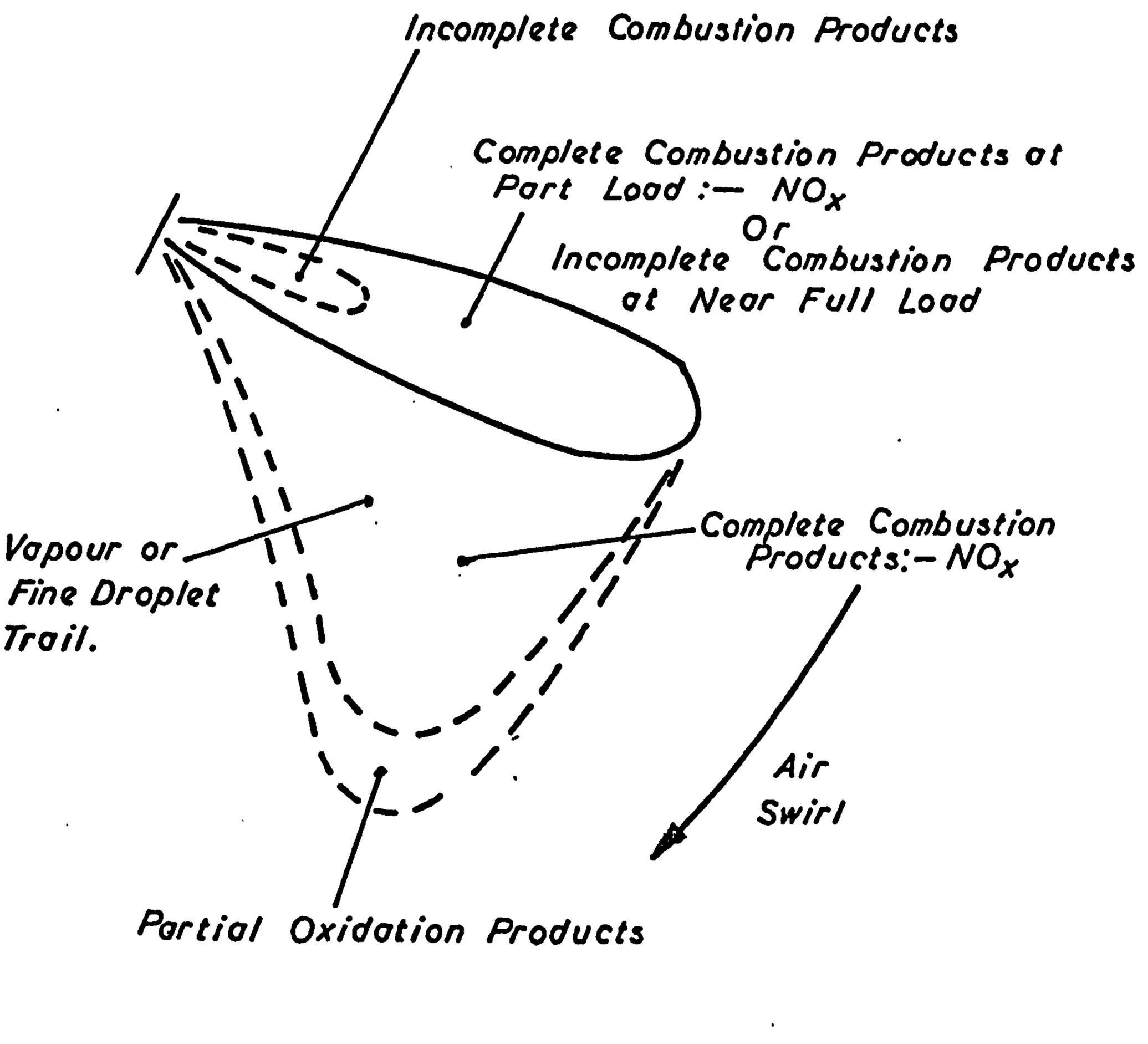

Concept of Emission Formation Sites Within the Fuel Spray as Depicted by Henein.

(Ref. (35))

Fig. 1·15

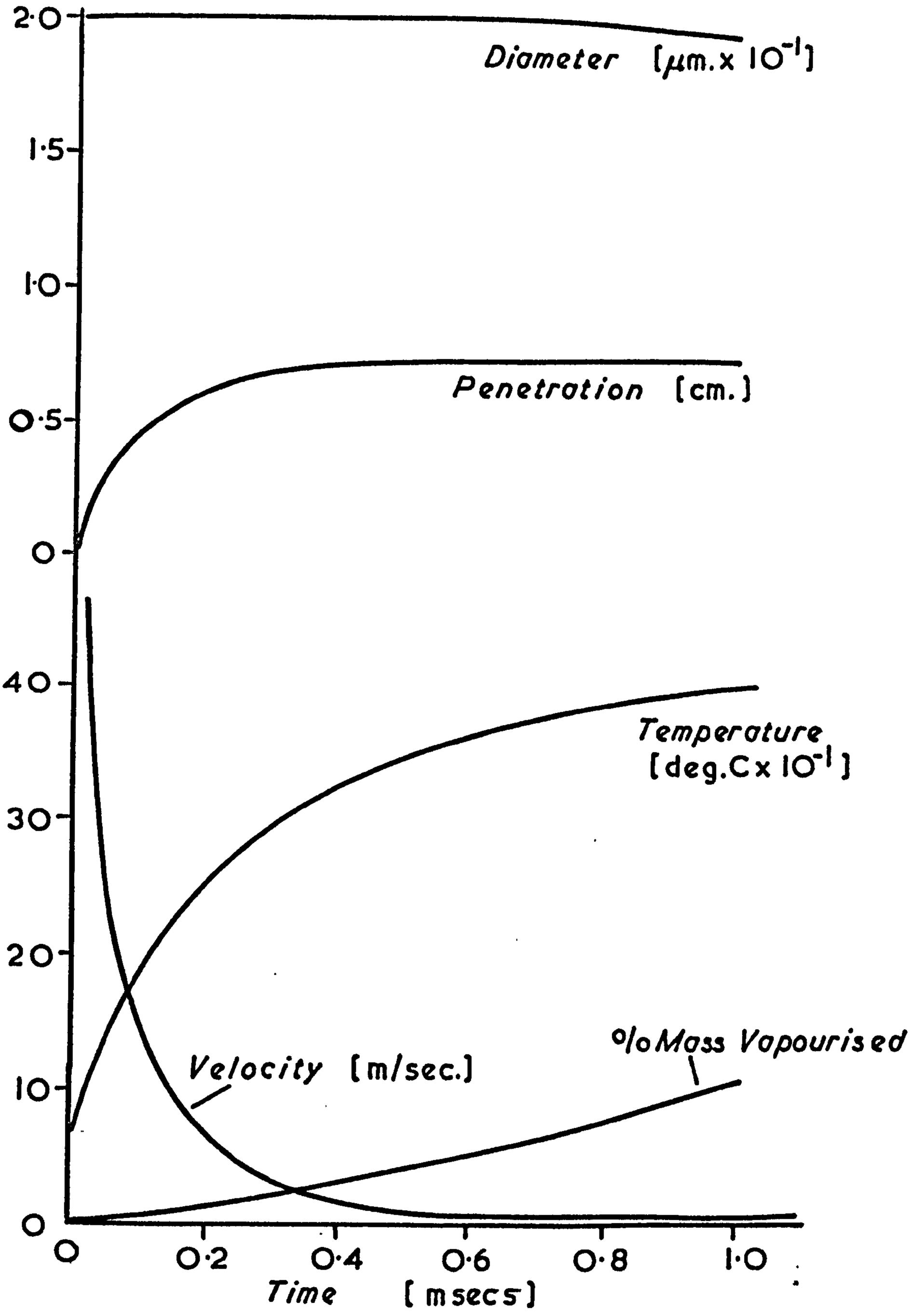

Conditions: *Injection Velocity* 110 m/sec.
Initial Dia. = 20 μm *Initial Temp.* = 60 deg.C
Liquid b.p. = 400 deg.C *Air Temp.* = 550 deg.C
Air Pressure = 55 bar.

Computed Transient History of a Single Fuel Droplet Injected into Still Air.

Fig. 1·16

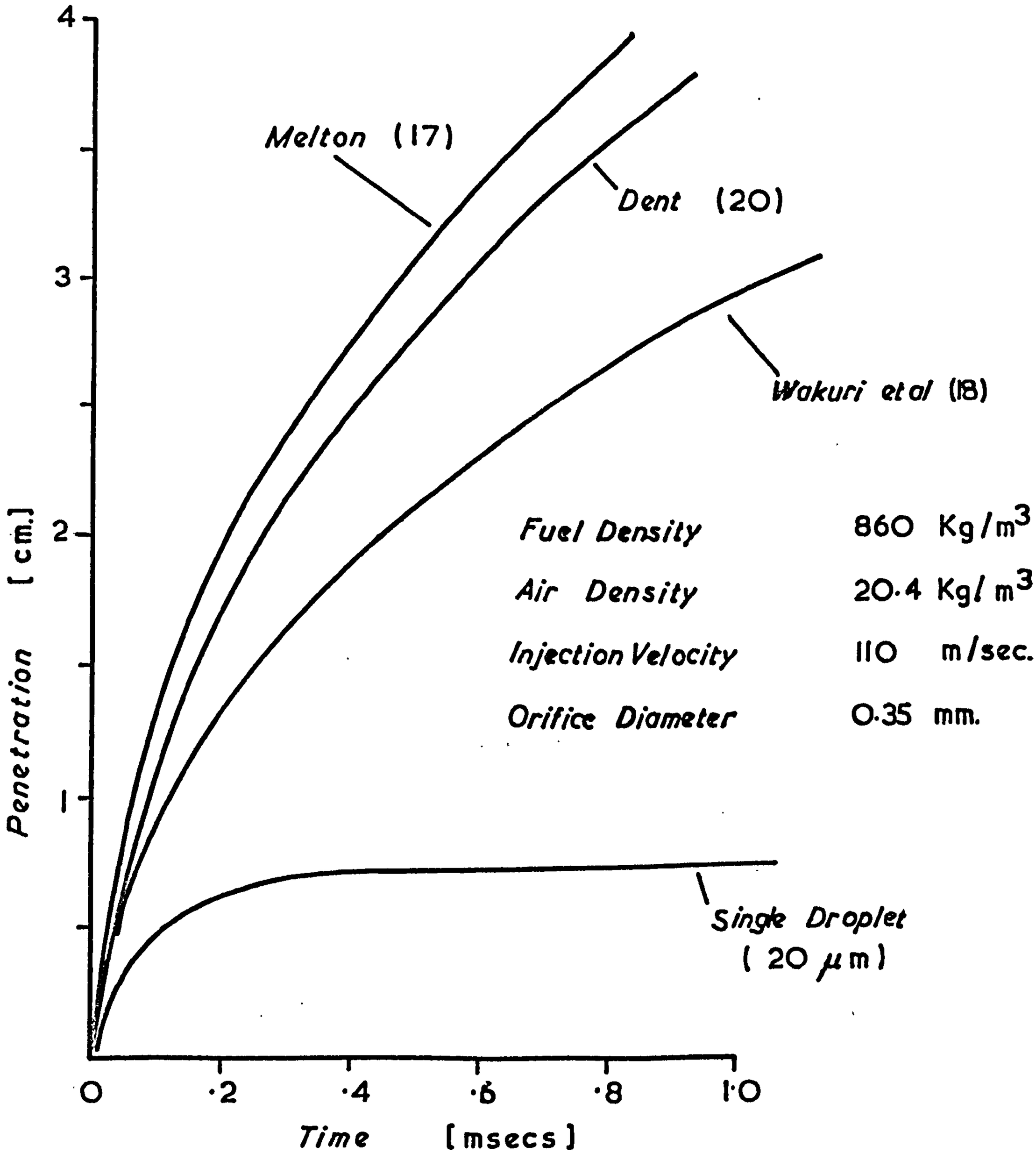

Comparison Of Spray Penetration Formulae

And Single Droplet Behaviour For Injection

Into Still Air

Fig. 1·17

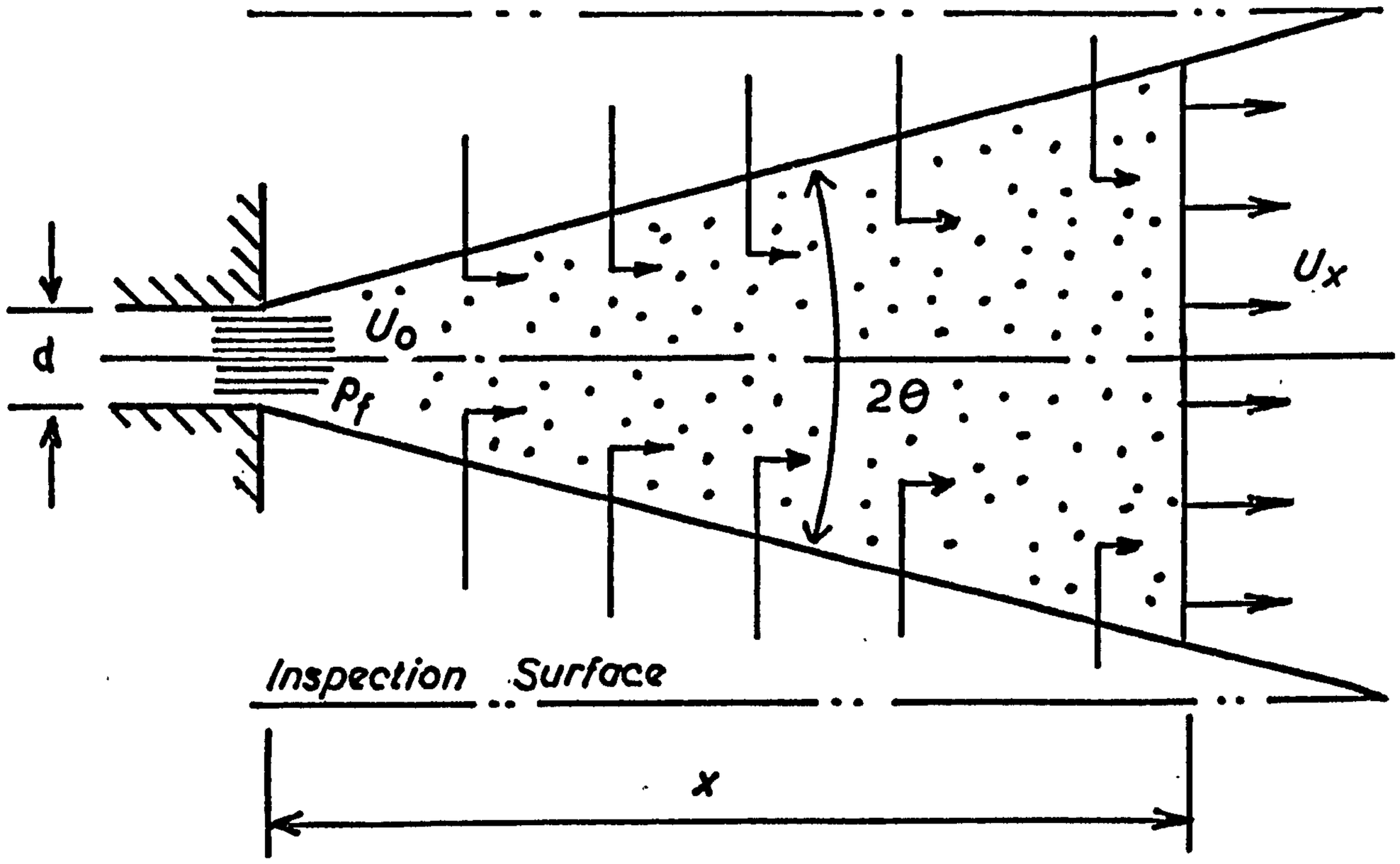

Model Of Fuel Spray Used By Wakuri et.al.

(Ref. (18))

Fig. 1·18

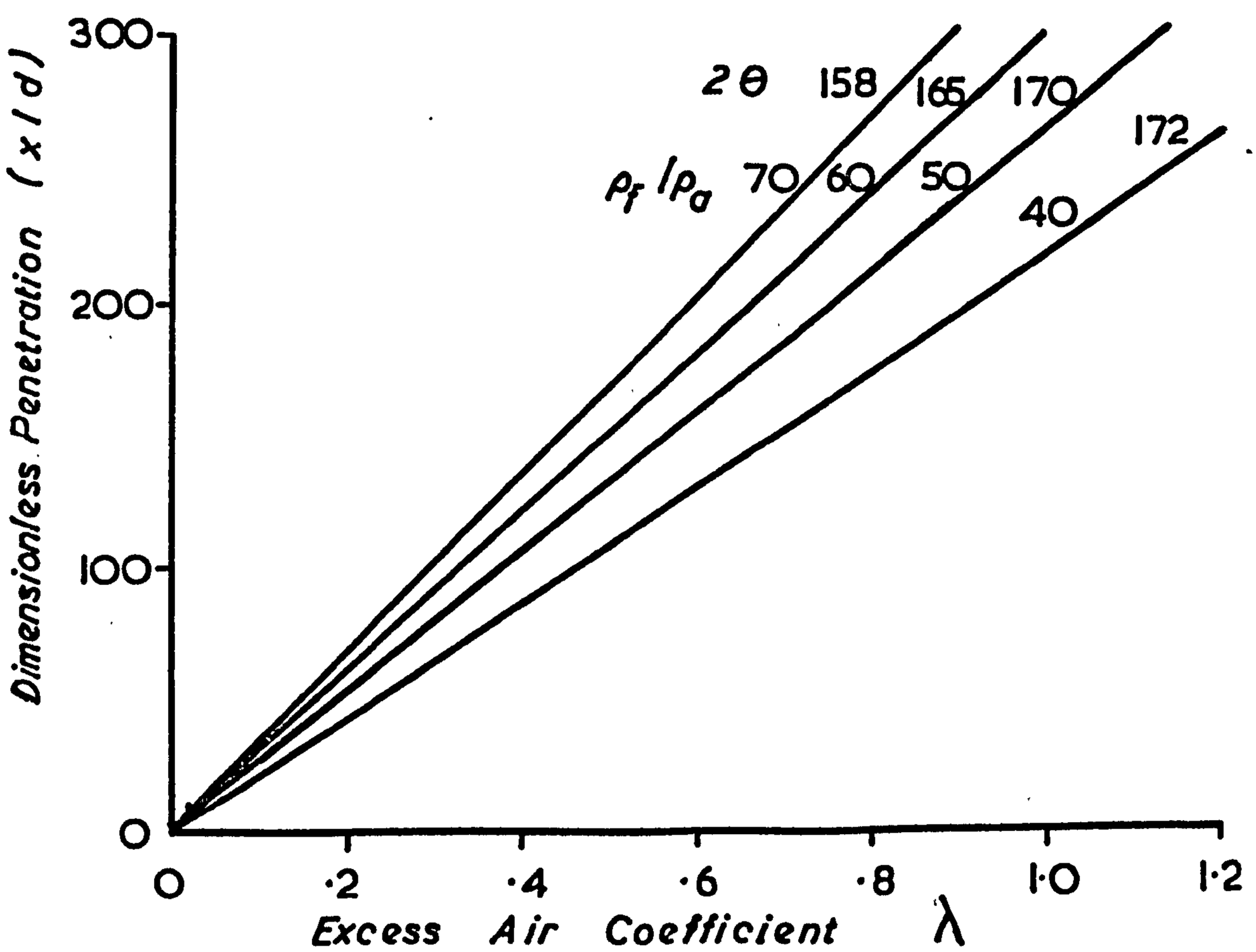

Penetration vs. Excess Air Coefficient

(Ref. (18))

Fig. 1·19

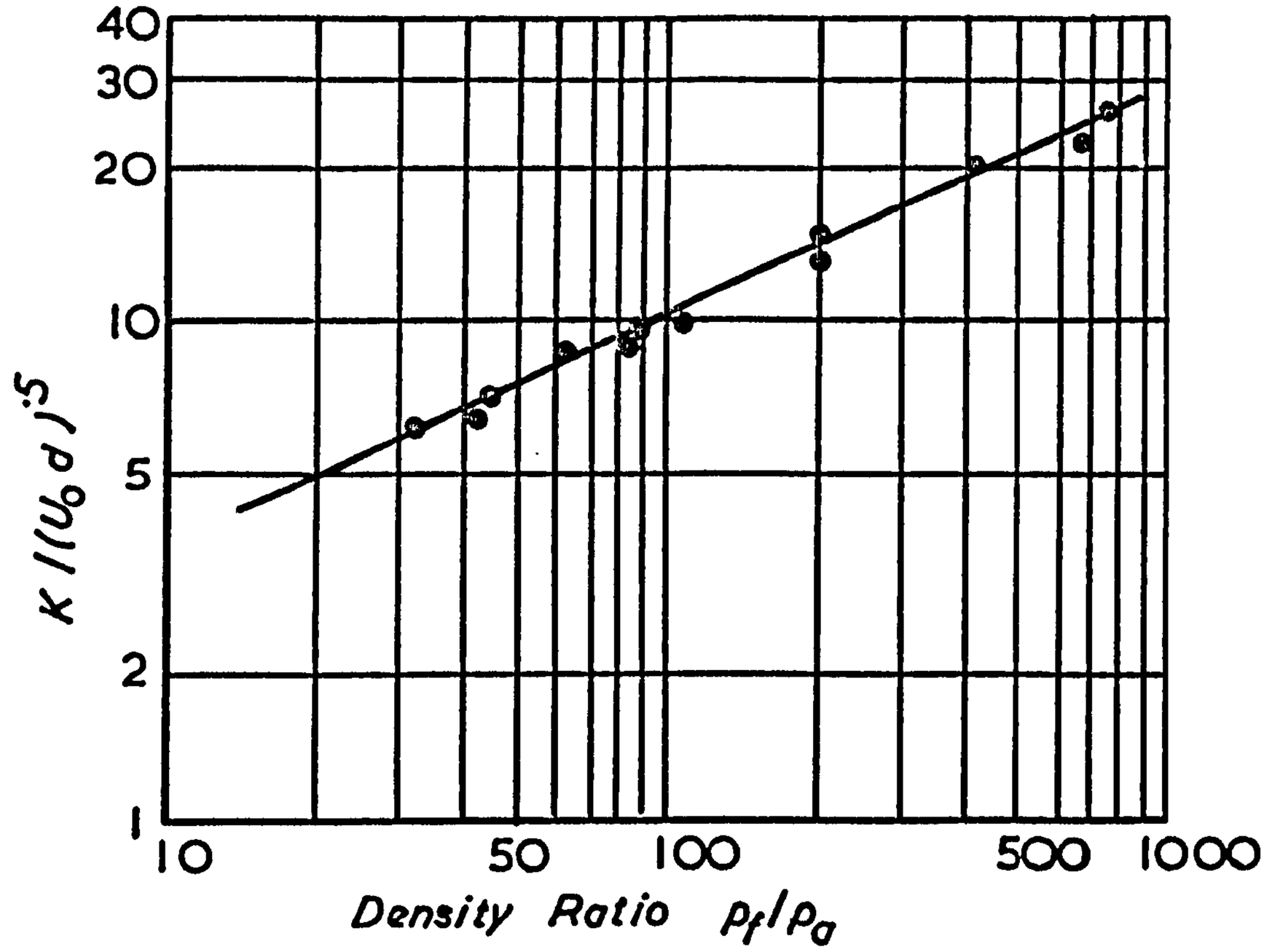

Dimensionless Spray Penetration vs. Density Ratio.

(Ref. (18))

Fig. 1·20

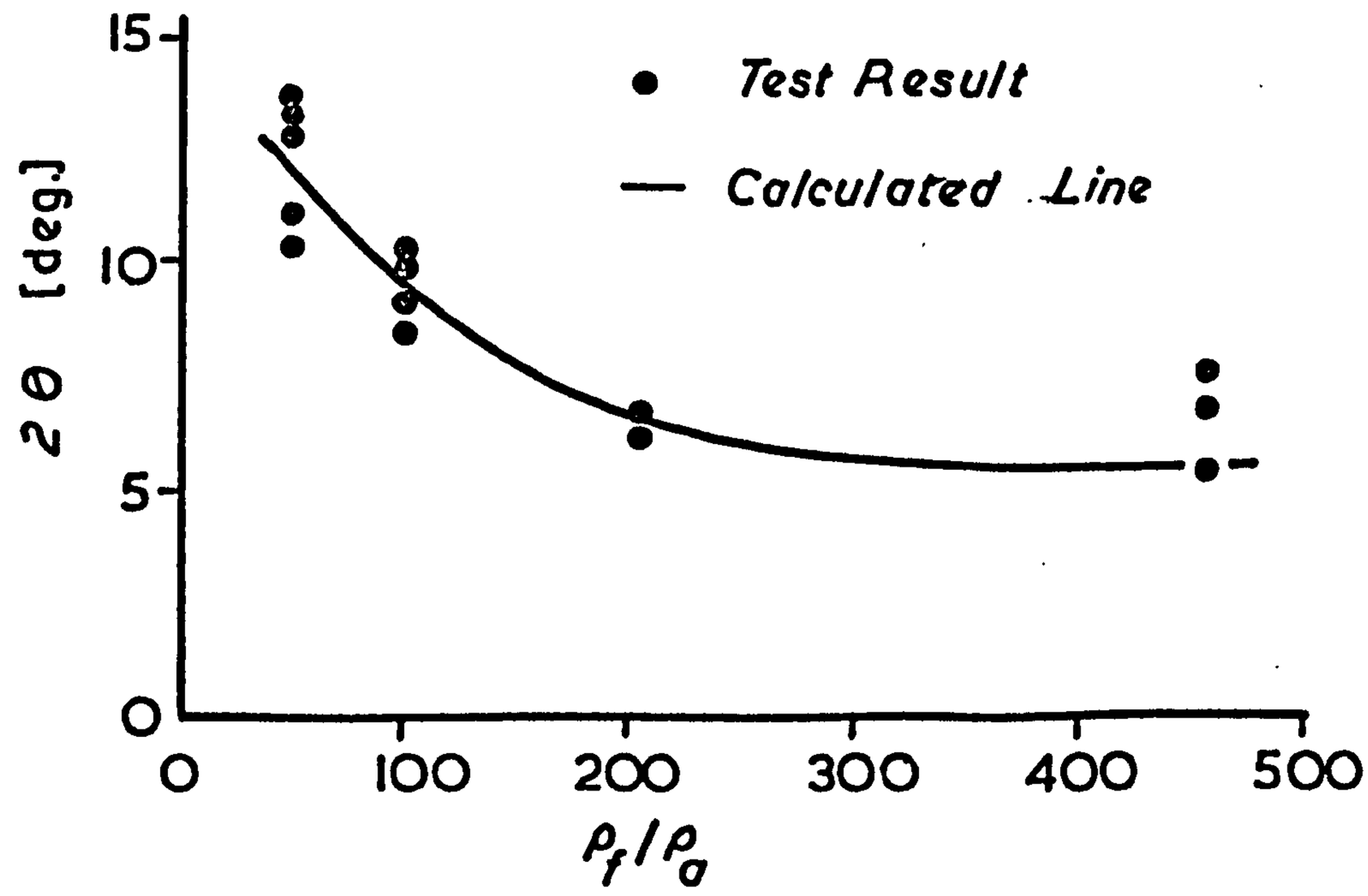

Spray Cone Angle vs. Density Ratio

(Ref. (18))

Fig. 1·21

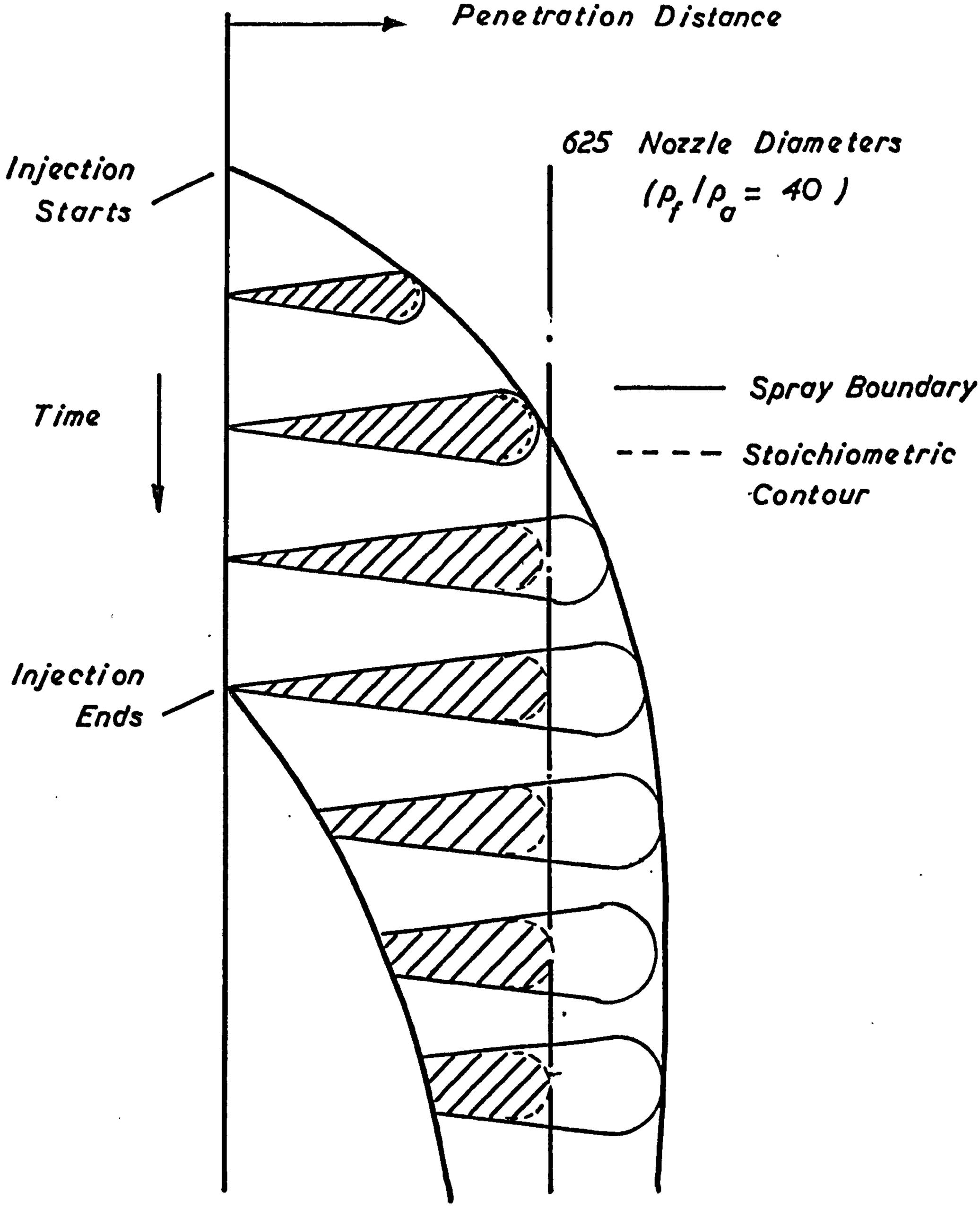

Melton's Concept of Transient Jet Behaviour. (Ref. (17))

Fig. 1·22

initial droplet dia. ≃ 7·6 μm

(fuel spray injected into still air.)

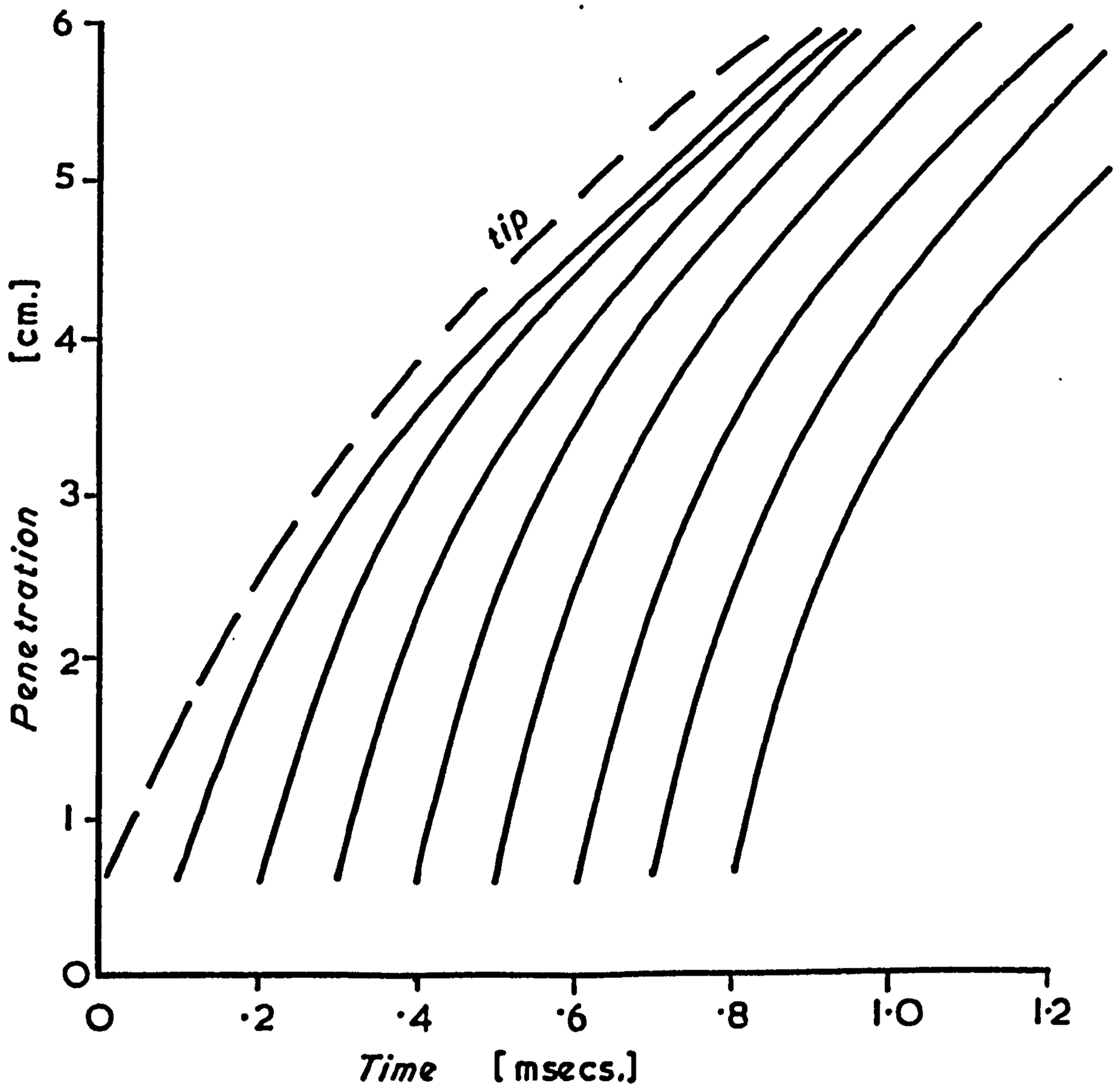

Droplet Penetration Along Spray Axis vs. Time for Droplets Started at Various Times. (Ref. (22))

Fig. 1·23

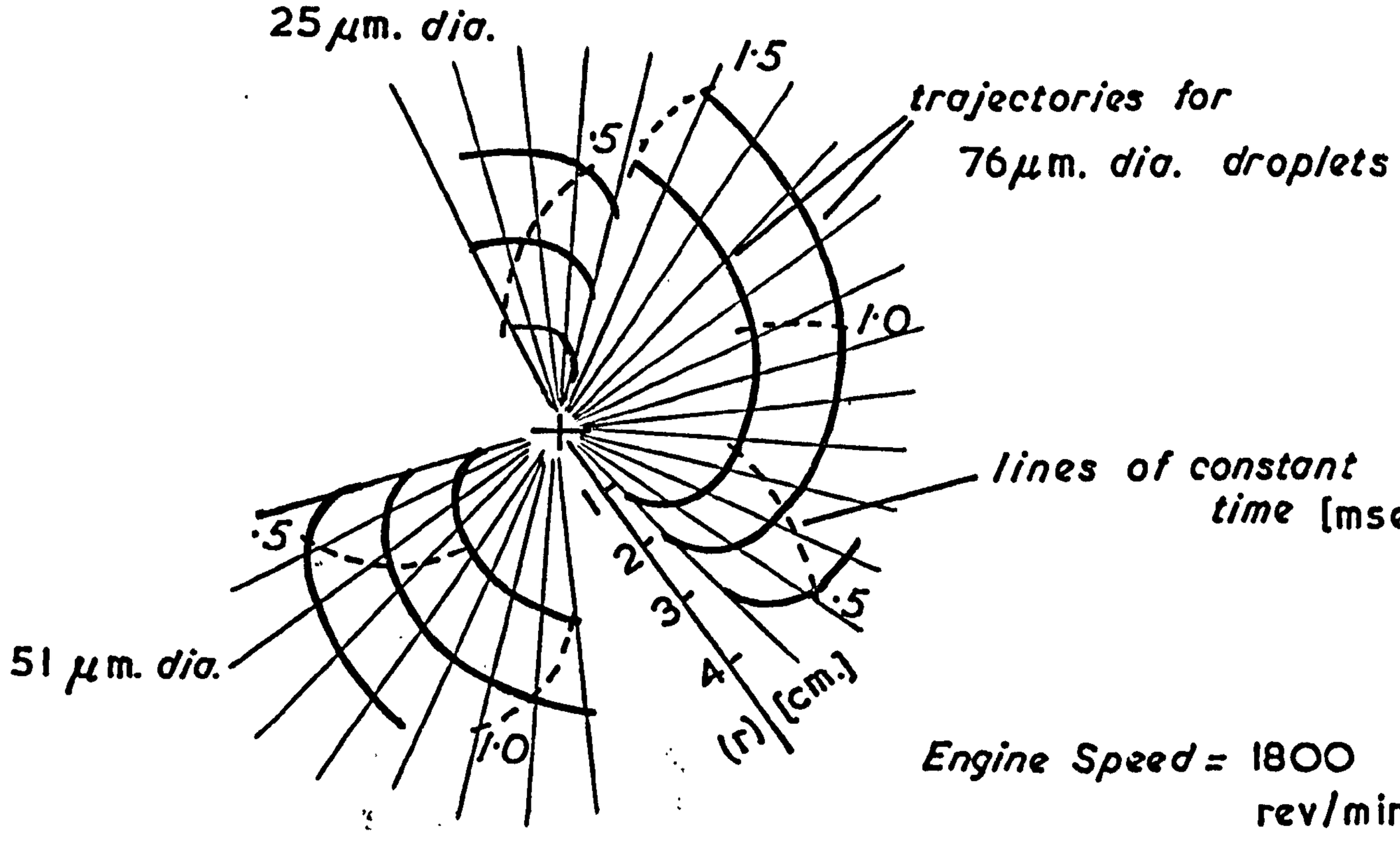

Polar Paths of 3 Different Sized Droplets.

(Ref. (22)) **Fig. 1·24**

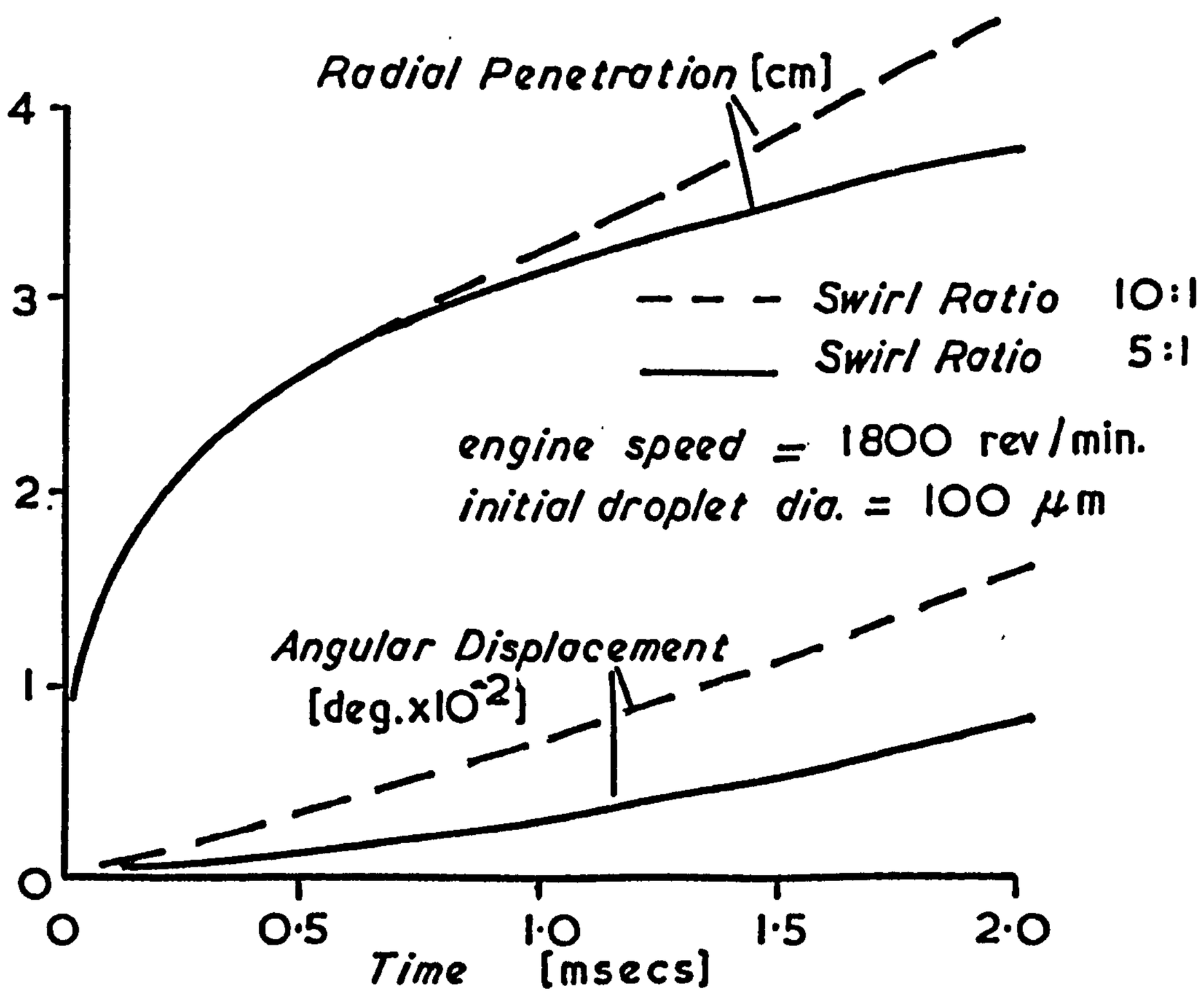

Effect of Swirl Ratio on Droplet Trajectory.

(Ref. (22)) **Fig. 1·25**

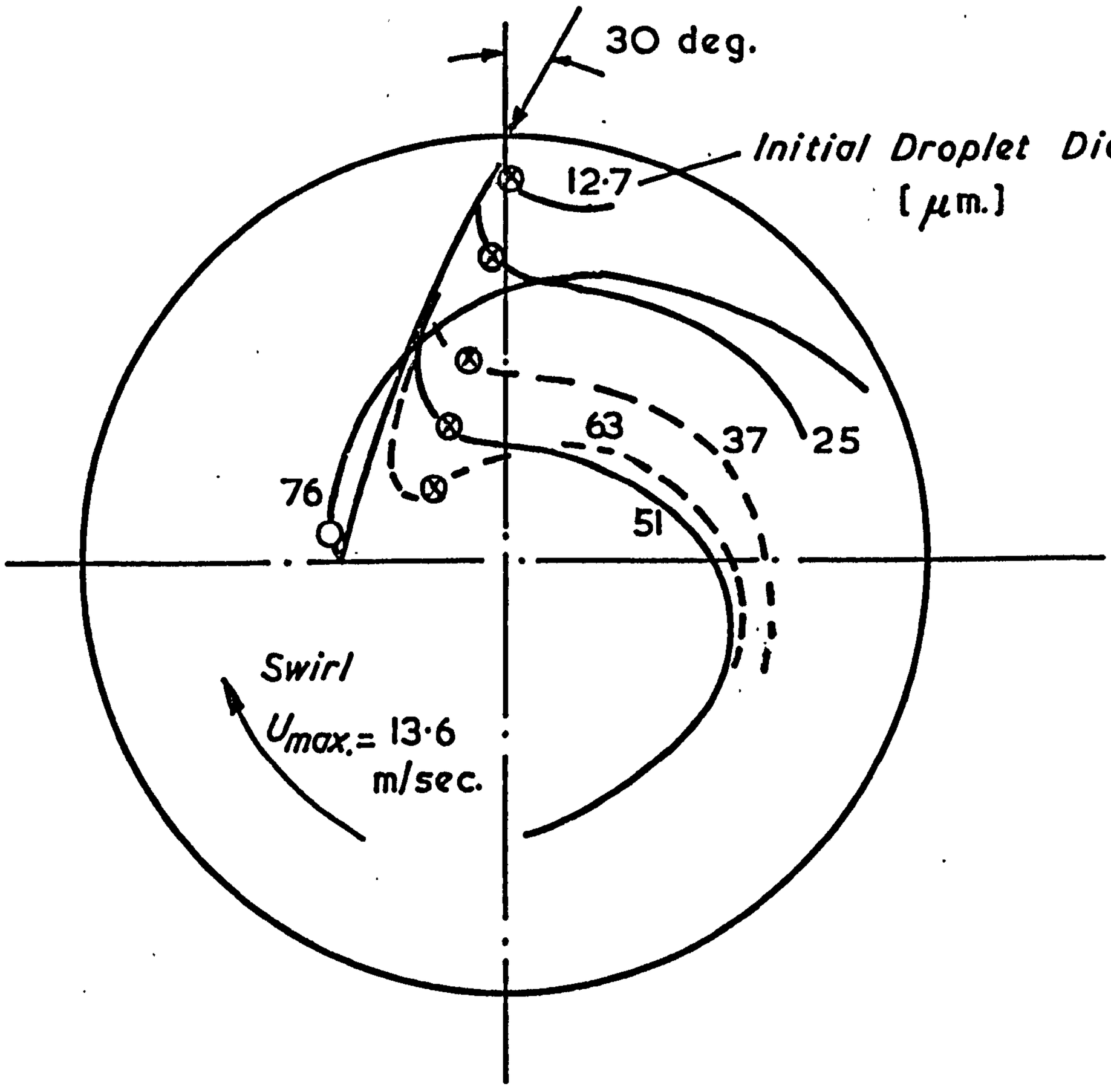

⊗ *denotes start of vapourisation*

Injection Pressure 41·6 bar

Droplet Trajectories for 30deg. Injection Angle.

(Ref. (23))

Fig. 1·26

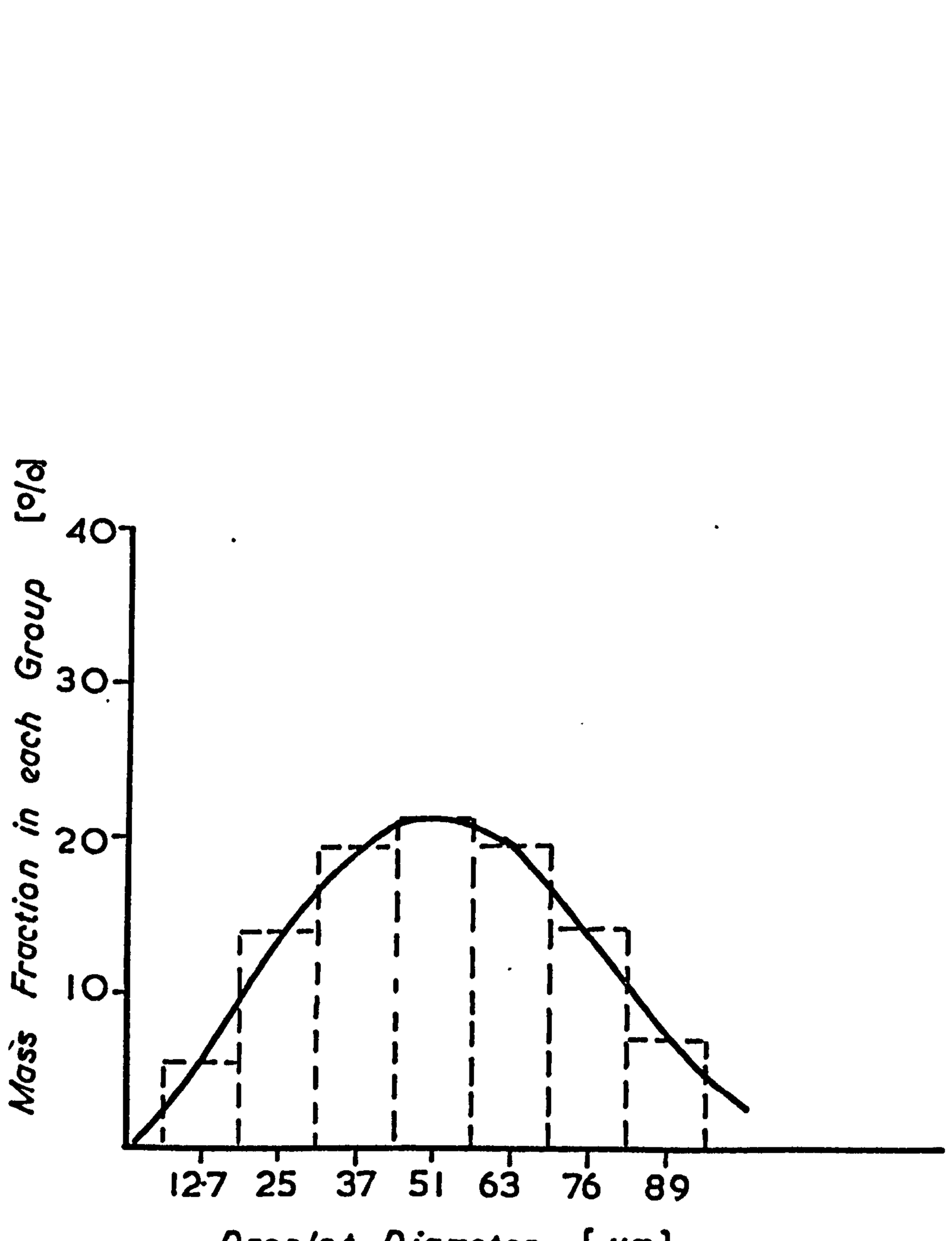

Mass Fraction Distribution used by Hussman et. al. (Ref. (23))

Fig. 1·27

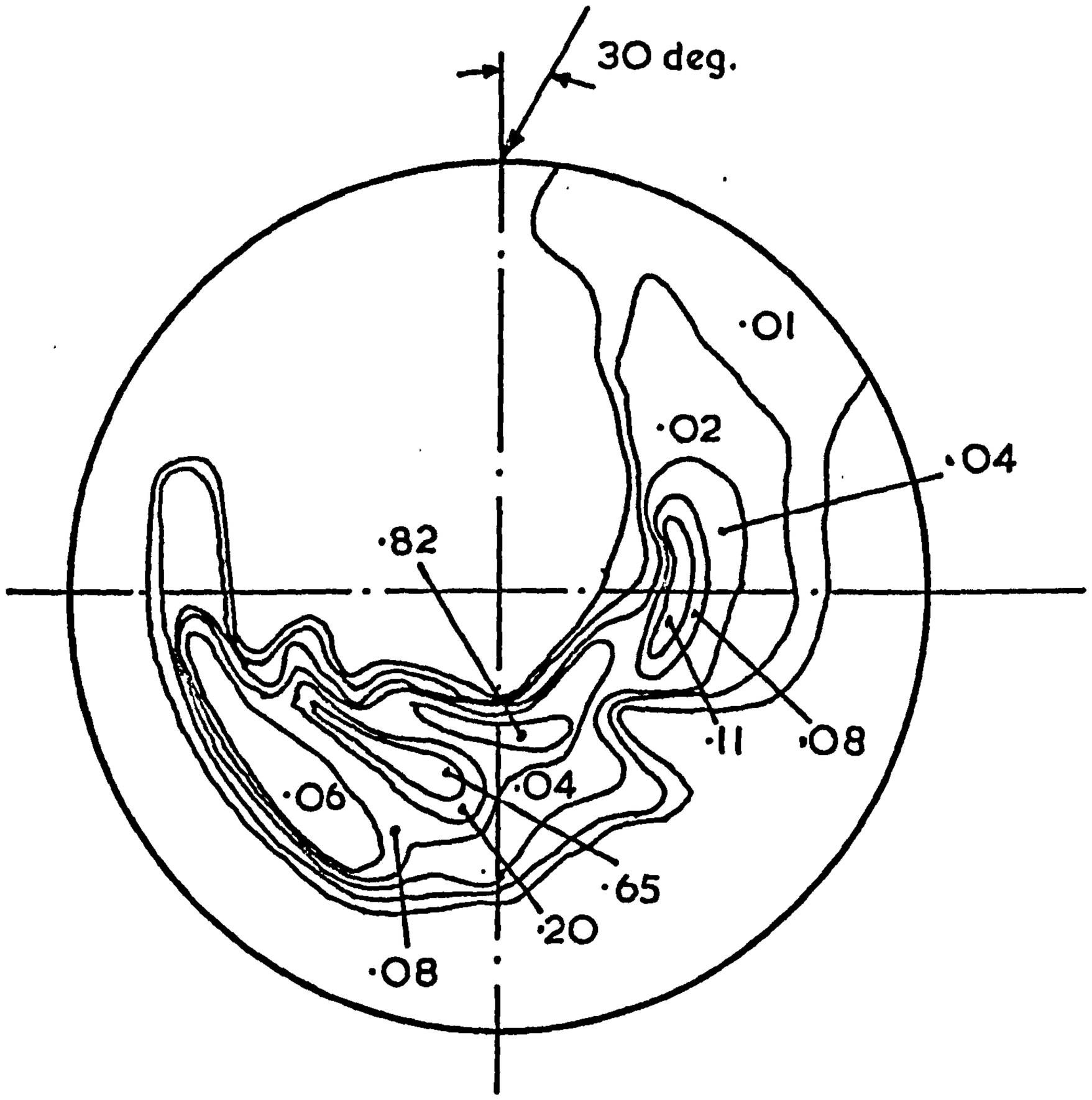

Overall fuel-air ratio = 0·02

Fuel Air Ratio Map for the Conditions of fig (1·26) (Ref. (23))

Fig. 1·28

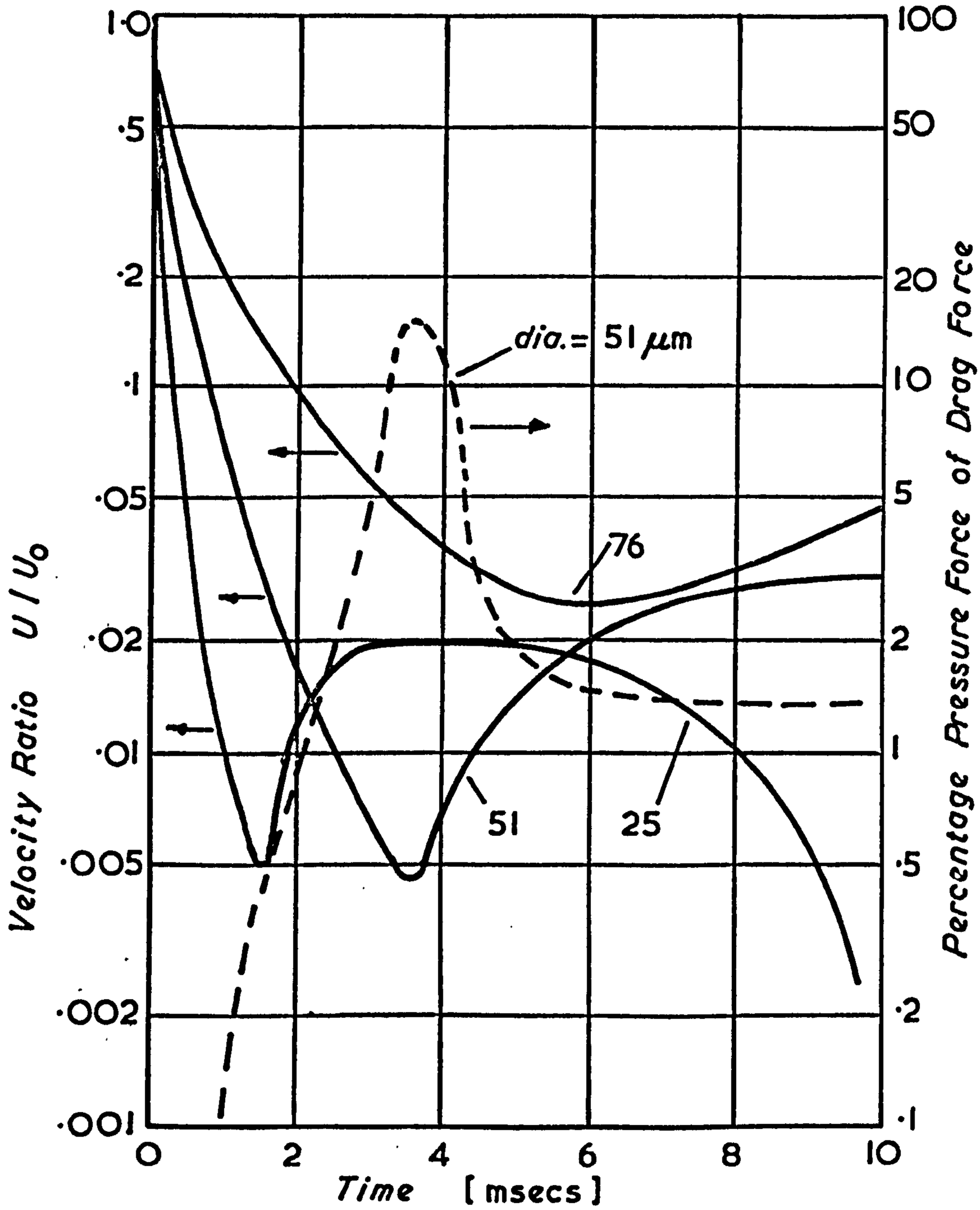

Velocity Ratio and Percentage Pressure Force for the Conditions of fig (1·26). (Ref. (23))

Fig. 1·29

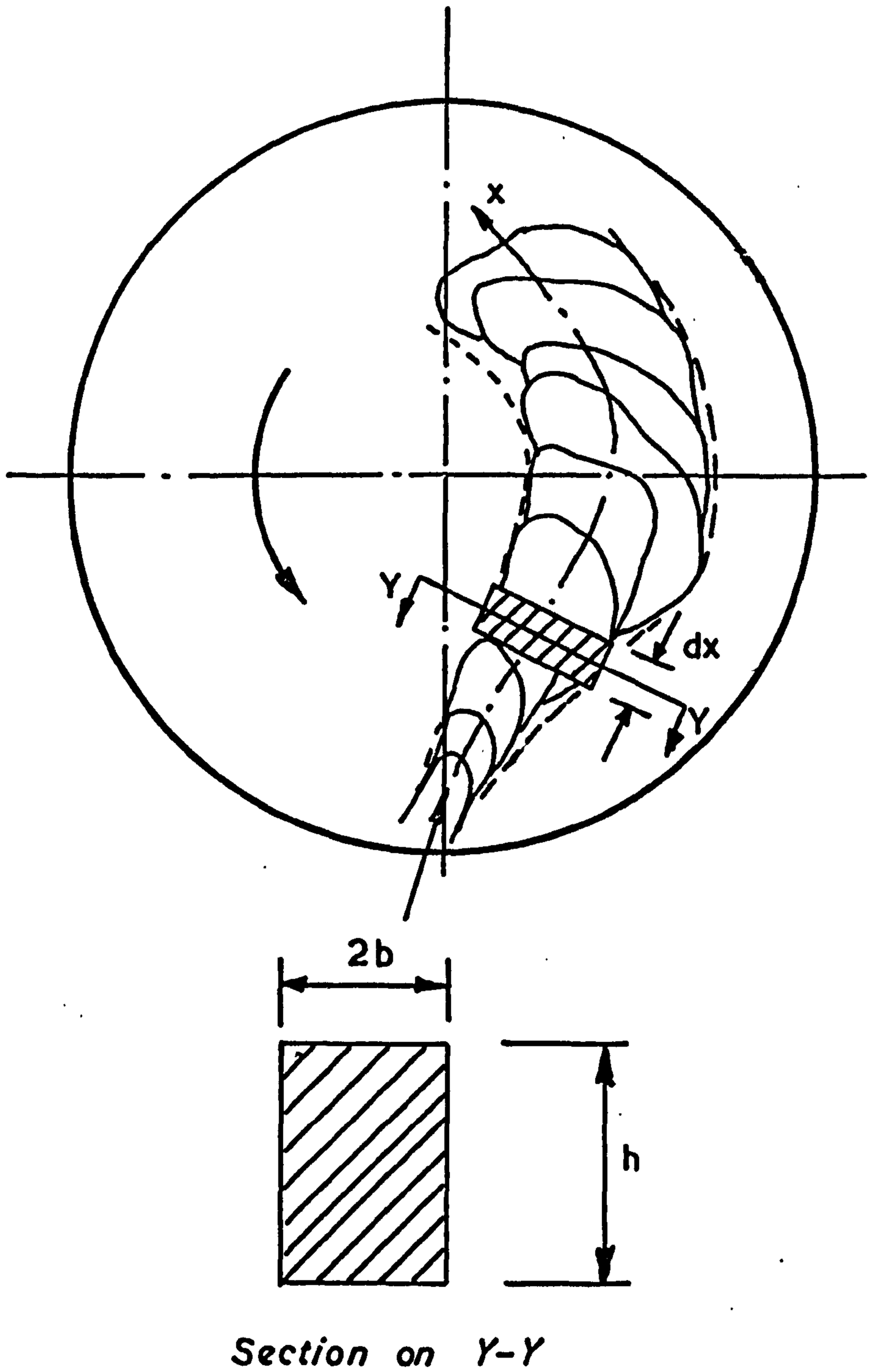

Section on Y-Y

Quasi-Solid Body Concept & Idealised Cross-Section of the Spray used by Adler and Lyn. *(Ref. (24))*

Fig. 1·30

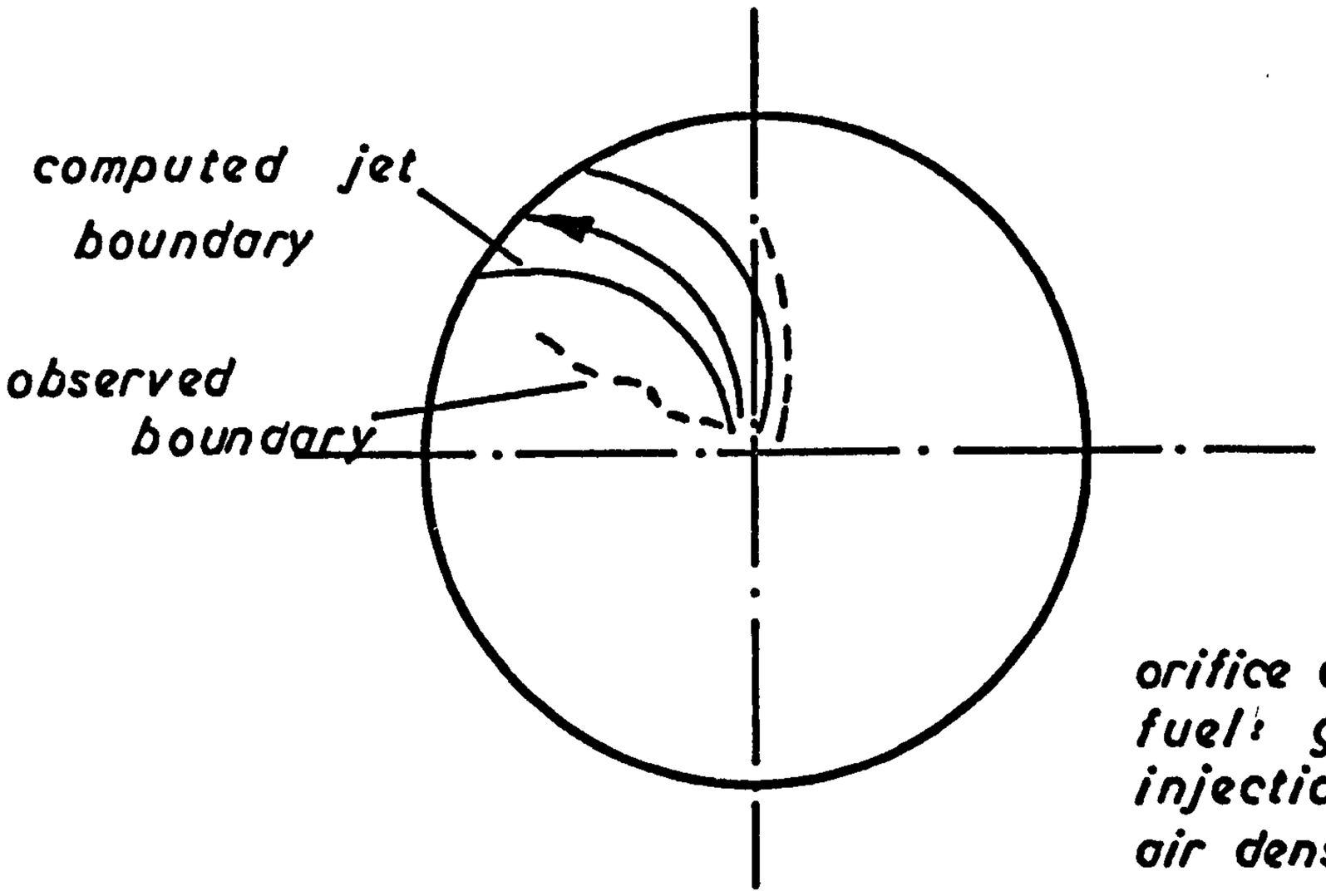

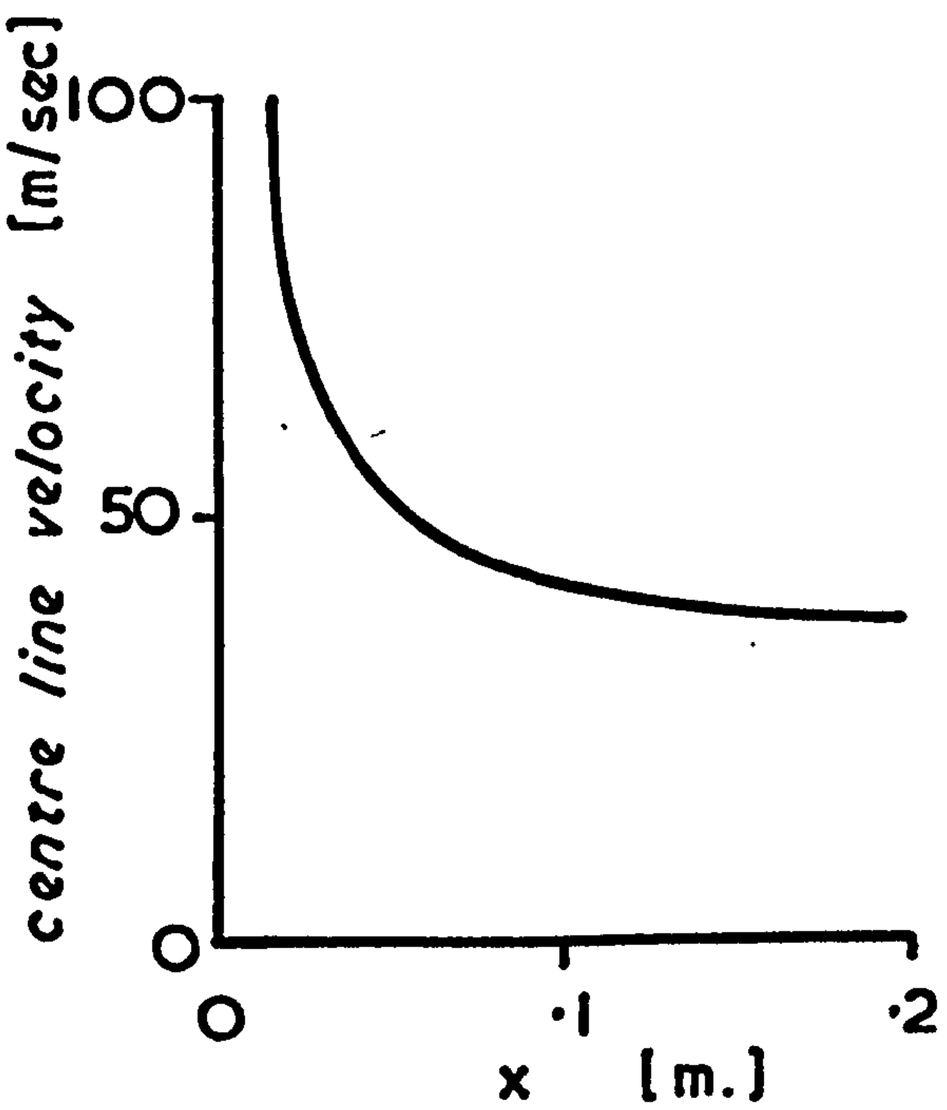

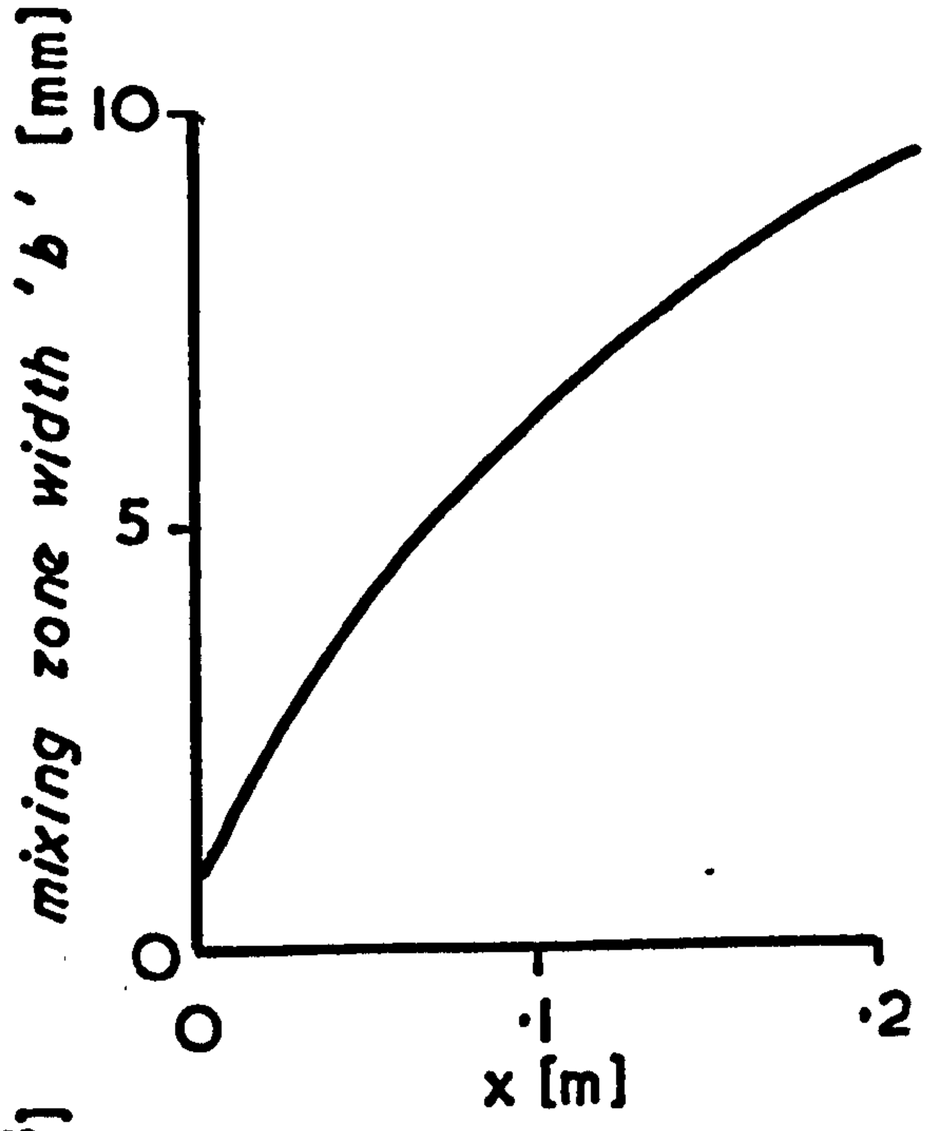

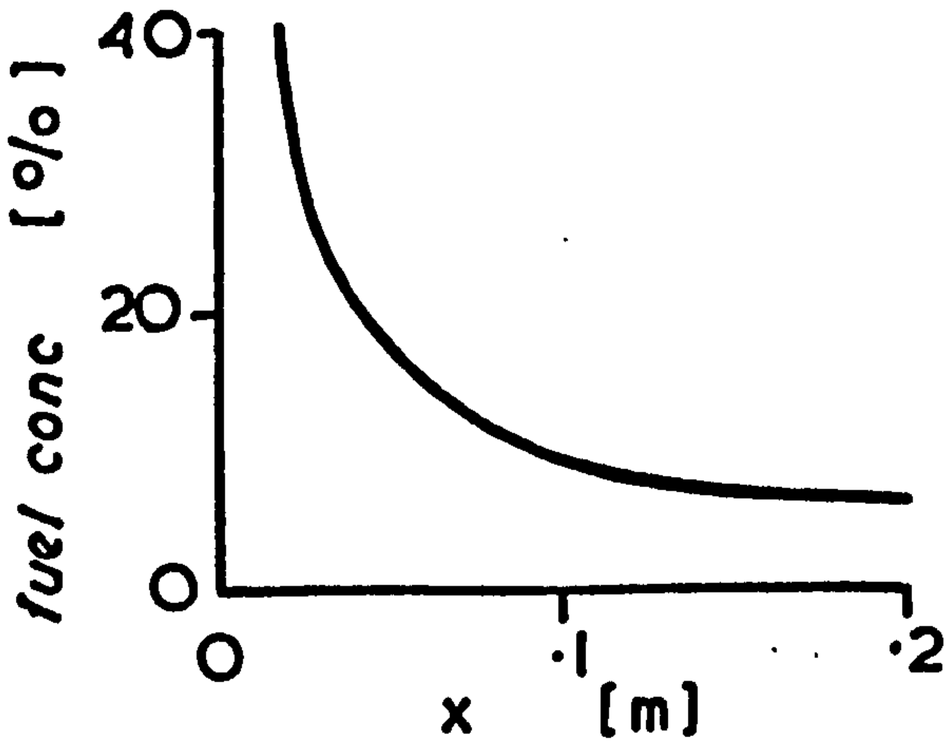

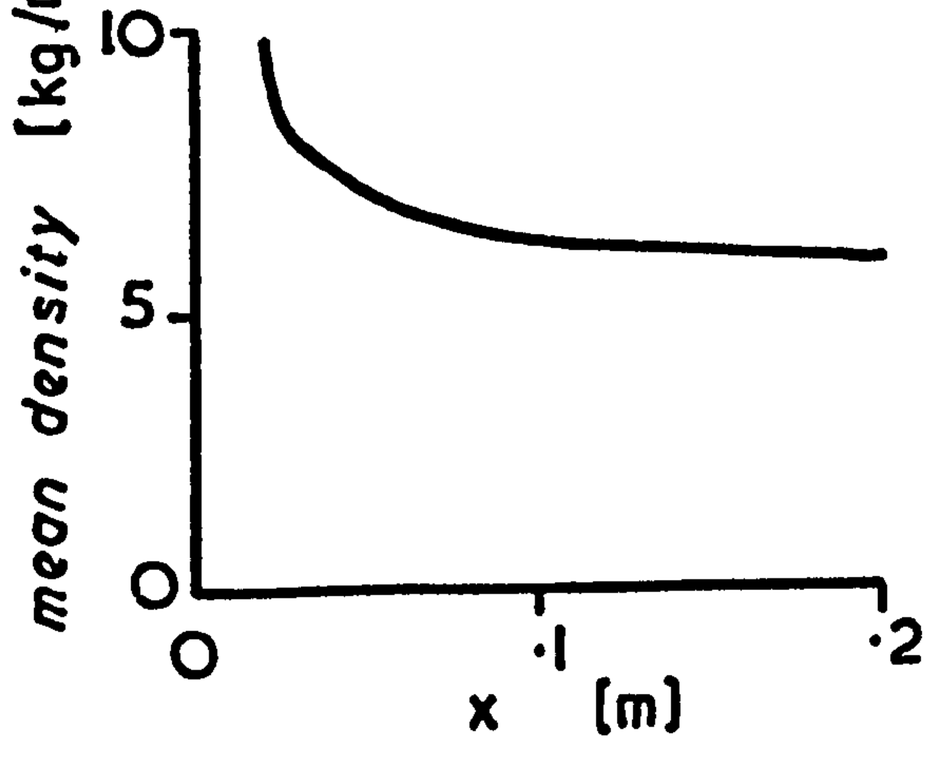

Calculated Fuel Spray Characteristics. (Ref. (24))

Fig. 1·31

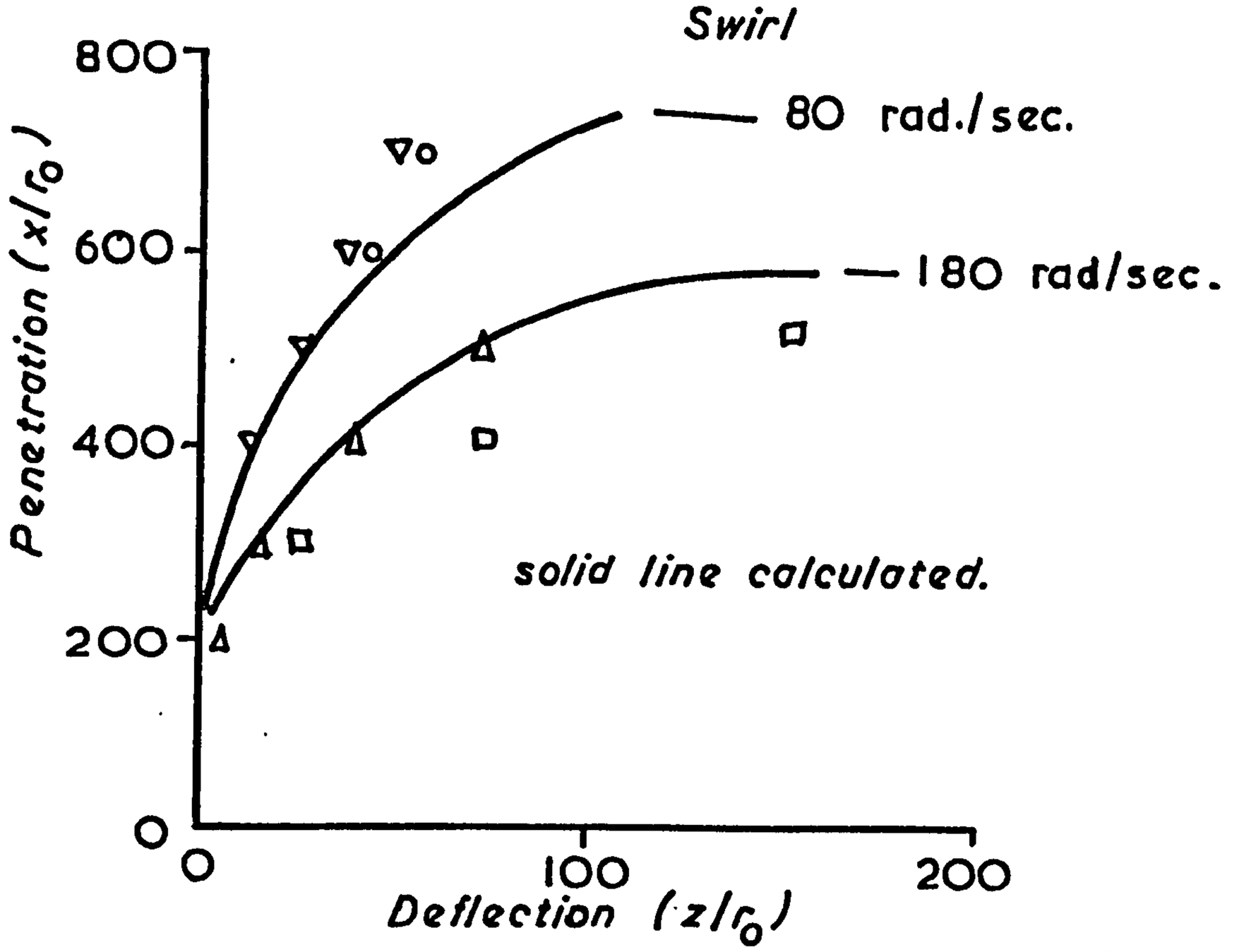

Measured and Computed Centreline Positions

(Ref. (36))

Fig. 1·32

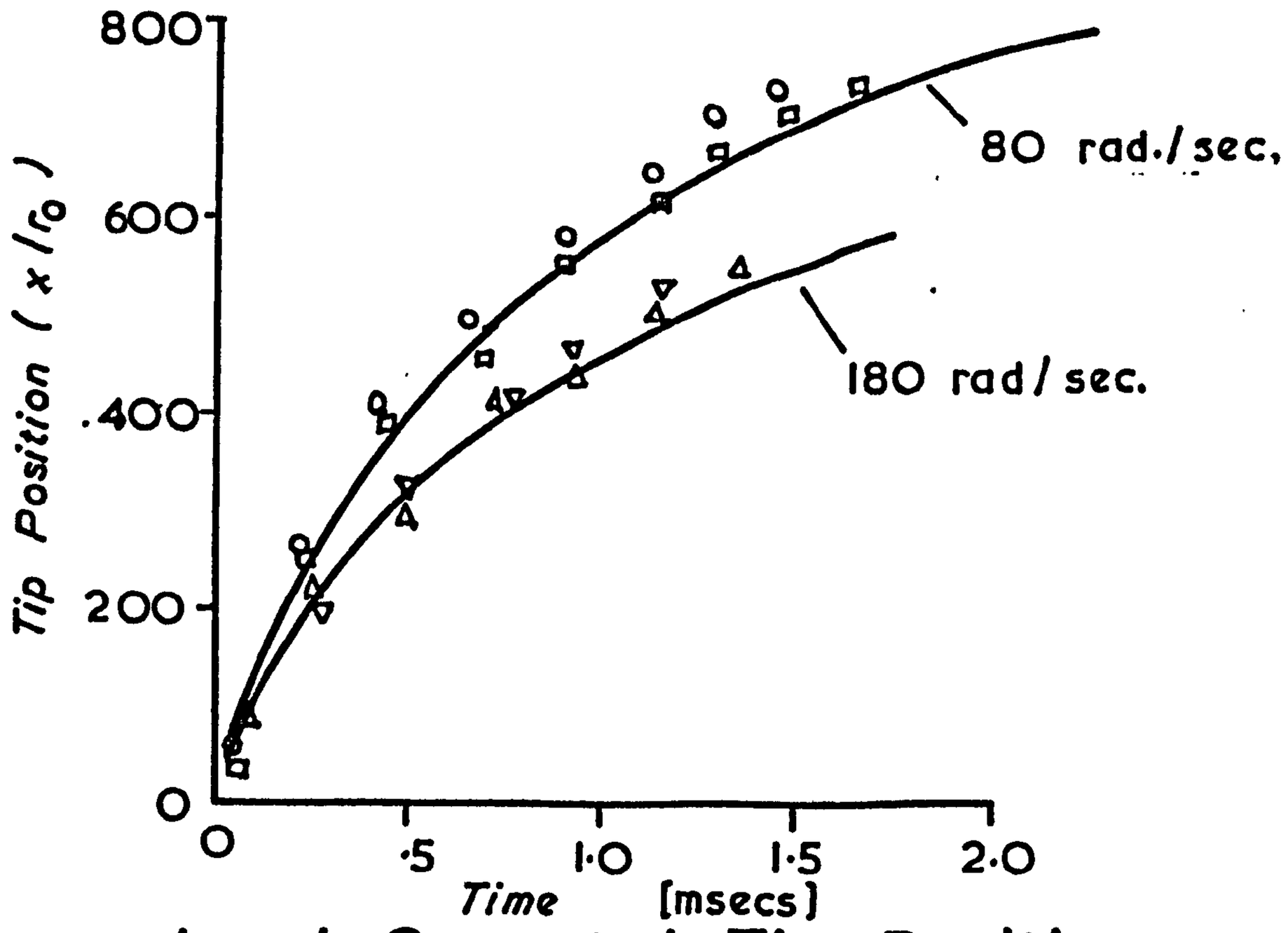

Measured and Computed Tip Positions.

(Ref. (36))

Fig. 1·33

CHAPTER 2

Statement of the Basis of Similarity between the Diesel Engine Fuel Spray and the Gas Jet Model

2.1 Introduction

Section 1.2.2 presented several theories (17) (18) (19) (20) in which the two phase diesel engine fuel spray injected into still air had been analysed using single phase gas jet principles.

In considering fuel sprays injected across an air swirl it is therefore logical to review the relevant published results for gas jets subjected to cross-flow. Separate regimes of such jets are generally accepted to be as shown in figure (2.1). In regions I and II the jet possesses a high momentum flux in relation to the transverse flow and therefore constitutes an obstacle to it. In these regions the jet acts in many ways as a solid cylinder and hence vortices and eddies are formed in its wake (regime IV). Kamotani and Greber (80) showed that the vortices thus formed acquire axial momentum from the jet and more along the jet boundary whilst increasing in strength.

Further downstream, where momentum interchange has occurred between the two flows, mixing of the two fluids is more orderly and a zone of profile similarity (III) is established. In this region the three dimensional character of the jet is relevant and a 'horse shoe' or crescent shape is created, this is illustrated together with the axes notation in Figure (2.2).

The diesel engine fuel spray may, therefore, be considered to possess all of those regions if impingement on the combustion chamber wall does not occur. However in the event of impingement it may be postulated that the regime of profile similarity (III) may not be created.

Representation of jet trajectory has been accomplished by Margason (81), Kamotani and Greber (80), Shandarov, and Ivanov, the latter two being reported by Abramovich (34).

Margason used a water vapour flow visualisation technique and determined the trajectory of isothermal jets within the momentum flux

ratio range $4 < J < 100$, where:

$$J = \frac{\rho_g \; U_g^2}{\rho_a \; U_a^2} \qquad \ldots\ldots\ldots \quad (2.1)$$

where ρ_g, ρ_a are the densities of the jet fluid and cross flow respectively.

The correlating equation thus obtained was:

$$\frac{x}{d_o} = \frac{1}{4} \left(\frac{1}{J}\right) \left(\frac{z}{d_o}\right)^3 \qquad \ldots\ldots\ldots \quad (2.2)$$

and was shown to liewithin the spread of data from the results of Jordinson (82), Keffer and Barries (83), Shandarov (34) and Ivanov (34), and other data.

Shandarov's equation was obtained for non-isothermal jets, where the free stream temperature was varied up to a maximum of three times that of the colder jet, and in the momentum flux ratio range $2 < J < 22$. The results indicated that the inclusion of momentum flux ratio in the trajectory equation automatically accommodated the effect of temperature difference between the two flows. The correlation of data for jets injected perpendicular to the cross flow was represented by:

$$\frac{x}{d_o} = \frac{1}{J} \left(\frac{z}{d_o}\right)^{2.55} \qquad \ldots\ldots\ldots \quad (2.3)$$

Of greater relevance to diesel engines applications, where values of J are high, are the results of Ivanov, which were taken over the momentum flux ratio range $12 < J < 1000$. Isothermal jets injected at various angles to the flow were investigated, the correlation when reduced to the case of a perpendicular jet is given by:

$$\frac{x}{d_o} = \left(\frac{1}{J}\right)^{1.3} \left(\frac{z}{d_o}\right)^{3} \qquad \ldots\ldots\ldots \quad (2.4)$$

Kamotani and Greber (80), considered non-isothermal jets, within the range $15 < J < 60$ and $0 < T_a - T_g < 204$ deg.C, and represented their data by:

$$\frac{x}{d_o} = a \left(\frac{z}{d_o}\right)^b \qquad \ldots\ldots \quad (2.5)$$

The constants a, b were presented graphically as a function of momentum flux ratio. The exponent b was not shown to be rigidly constant, and log a was not exactly linear with log J. In this respect their results differ from equations (2.2) (2.3) (2.4), and in contradiction to the findings of Shandarov, a slight and separate effect of temperature difference was noticed. However, this data also fell within the spread of data as summarised by Margason (equation 2.3).

Other correlations of jet centre line trajectory data are those by Callaghan and Ruggeri (83), given by:

$$\frac{x}{d_o} = \left(\frac{1}{J}\right) \left(\frac{z}{d_o}\right)^{3.3} \qquad \ldots\ldots \quad (2.6)$$

and Storms (84) given by:

$$\frac{x}{d_o} = \left(\frac{1}{J}\right) \left(\frac{z}{d_o}\right)^{3} \qquad \ldots\ldots \quad (2.7)$$

It is apparent that the majority of equations for centre-line trajectory may be represented by:

$$\frac{x}{d_o} = \left(\frac{1}{J}\right)^m \text{const.} \left(\frac{z}{d_o}\right)^n \qquad \ldots\ldots \quad (2.8)$$

The remaining problem is therefore to relate the diesel engine fuel spray to a gas jet in a realistic manner, and hence apply the form of trajectory relationships presented by equation (2.8).

2.2 Basic Concept of the Fuel Spray and Analysis in Relation to Gas Jets in Cross flow

2.2.1 Derivation of the Steady State Equations

The conclusions to the literature survey (section 1.3) indicate that the diesel engine fuel spray may be viewed basically as represented in Figure (2.3). Fuel in the nozzle may be considered as a cylinder at the density of the liquid and moving at the injection velocity U_f. If at some station further downstream the jet consists of droplets possessing negligible relative velocity to the entrained air, the transition may be considered to occur in an axial distance termed the 'break up' region. Subsequent to this initial disintegration and decceleration process, during which total momentum will be conserved and shared with the entrained air, the fuel spray may be considered to emit from an imaginary source, of larger diameter than the original fuel orifice, and to consist of fine droplets possessing little relative velocity to the entrained air.

The basic assumptions which are necessary to utilise this concept are:-

a. Momentum and liquid fuel mass are conserved between the actual fuel orifice and the effective source of the jet.

b. Deflection over the break-up region is negligible and hence the conserved momentum may be considered to act in the same direction as the original fuel orifice.

c. Liquid mass is not removed from the spray by the crossflow between the fuel orifice and effective source.

d. Relative velocities of the fuel droplets to the entrained air are small after the break-up region.

By equation (2.8), similarity of trajectory between the engine

fuel spray as depicted in Figure (2.3), and a gas jet subjected to a similar cross flow, will be achieved when:

$$J_g = J_e \quad \ldots\ldots\ldots \quad (2.9)$$

and $$d_g/R = d_e/R' \quad \ldots\ldots\ldots \quad (2.10)$$

where J_g, J_e are the respective momentum flux ratios for the gas jet and effective source, and R, R' are the respective combustion chamber radii in the model and engine, (assuming that the break-up region occupies only a few fuel nozzle diameters).

Conservation of momentum between the fuel nozzle and effective source yields:

$$\rho_f U_f^2 d_f^2 = \rho_e U_e^2 d_e^2$$

and hence: $$d_e = d_f . (U_f/U_e) . (\rho_f/\rho_e)^{0.5} \quad \ldots\ldots\ldots (2.11)$$

therefore by (2.10) $$d_g = \xi . d_f . (U_f/U_e) . (\rho_f/\rho_e)^{0.5} \quad \ldots\ldots (2.12)$$

where ξ is a scale factor defined by $\xi = R/R'$.

By eq. (2.9) $$(\rho_g . U_g^2)/(\rho_a . \bar{U}_a^2) = (\rho_e . U_e^2)/(\rho_a' . \bar{U}_a'^2) \quad \ldots\ldots (2.14)$$

where $\bar{U}_a$, $\bar{U}_a'$ are respective model and engine mass averaged air velocities, (a prime (') denotes an engine quantity).

Hence: $$\rho_e^{0.5} . U_e = (\bar{U}_a' . U_g/\bar{U}_a) . (\rho_a' . \rho_g/\rho_a)^{0.5} \quad \ldots\ldots (2.15)$$

which may be substituted in equation (2.11) to yield:

$$d_g = \xi . d_f . \frac{\rho_f . \rho_a}{\rho_g . \rho_a'} . \frac{U_f . \bar{U}_a}{U_g . \bar{U}_a'} \quad \ldots\ldots (2.16)$$

Equation (2.16) therefore maintains similarity of trajectory on the assumption that the fuel spray behaves as a gas jet after the effective source, and ensures compatability irrespective of model scale or injected gas quantity. However, if similarity of

overall mass air to fuel ratio is to be maintained, then:

$$\dot{m}_f/\dot{m}_a = \dot{m}_g/\dot{m}_a \qquad \text{OR}$$

$$(\rho_f.U_f.d_f^2)/(\rho_a'.\bar{U}_a'.A_c') = (\rho_g.U_g.d_g^2)/(\rho_a.\bar{U}_a.A_c) \quad \ldots\ldots \quad (2.17)$$

where A_c denotes the combustion chamber flow cross-sectional area (radius x height).

With compatability of engine and model geometry rearrangement of equation (2.17) yields:

$$d_g = d_f.\ \xi.((\rho_f/\rho_a)/(\rho_a'.\rho_g))^{0.5}.\ ((\bar{U}_a.U_f)/(\bar{U}_a'.U_g)) \quad \ldots\ldots \quad (2.18)$$

which may be substituted in the trajectory relationship (2.15) to yield:

$$U_g = U_f.(\bar{U}_a/\bar{U}_a') \quad \ldots\ldots \quad (2.19)$$

and hence by equation (2.16) the gas jet diameter is defined by:

$$d_g = d_f\ .\ \xi.((\rho_f.\rho_a)/(\rho_g.\rho_a'))^{0.5} \quad \ldots\ldots \quad (2.20)$$

Equations (2.19)(2.20) therefore define the gas jet velocity and nozzle diameter which is predicted to have a compatable trajectory, and overall mass air to fuel ratio, with the engine fuel spray.

2.2.2 Transient Analysis

Equation (2.19) indicates that the nozzle and air velocities present the same ratio in both the model and engine. It may be expected therefore that:

$$\frac{U_s}{U_g} = \frac{U_s'}{U_f} \qquad \ldots\ldots\ldots \quad (2.21)$$

where U_s, U_s' are the local centre line velocities in the model and engine respectively. Denoting jet axial distances by s, s' in the model and engine respectively, and corresponding times by t, t', allows equation (2.21) to be re-written:

$$\frac{ds}{dt} \cdot \frac{1}{U_g} = \frac{ds'}{dt'} \cdot \frac{1}{U_f}$$

and if initial conditions are taken as $t = t' = 0$, then integration yields:

$$t = t'. \xi. \frac{U_f}{U_g} \quad \ldots\ldots\ (2.22)$$

which relates the model and engine time scales.

2.2.3 Representation of the Air Cross Flow Velocity

Representative air velocities ($\bar{U}_a$, $\bar{U}_a'$) have been used to calculate air mass and momentum cross flows and have been taken as mass-averaged values. Therefore, for a combustion chamber of constant height h', with a velocity profile defined by $U_a' = f(r')$, (Figure (2.3)),

$$\bar{U}_a' = \frac{\rho_a' h' \int_0^{R'} f(r')\, dr'}{\rho_a'.h'.R'} = \int_0^{R'} \frac{f(r')}{R'}\, dr' \quad \ldots\ldots\ (2.23)$$

In practice $f(r')$ is unlikely to be well defined, and if the velocity profile is approximated by a forced vortex ($f(r') = \omega r'$), then $\bar{U}_a' = \omega R'/2$.

The mass averaged velocity in the model is readily defined by measuring the air mass flow rate entering the model chamber ($\dot{m}_a$). Hence, $\bar{U}_a = \dot{m}_a/(h.R.\rho_a)$. Clearly the form of air velocity profile in the model should be as similar to that existing in the engine as possible.

2.3 Criticisms of the Modelling Concept

The analysis of section (2.2) is based on similarity of trajectory, momenta ratio, and overall air to fuel ratio. The concept of a gas jet with similar trajectory may be readily appreciated, but the manner in which fuel dispersion occurs in the engine, manifested by the local air to fuel ratio contours, is not as readily appraised on a theoretical basis (section 1.2.3). Fuel dispersion and mixing rate may be reasoned to be dependent on the turbulence eddy scale and intensities generated in the jet, no attempt has been made to equate these parameters.

Hestroni and Sokolov (85) showed that the spread of a two phase co-axial gas jet, of relatively low liquid phase addition, was slightly less than its single phase equivalent. It is therefore proposed that experimental data from the model and engine injections should be assessed to establish if gas dispersion is indicative of fuel dispersion for the same overall air to fuel ratio.

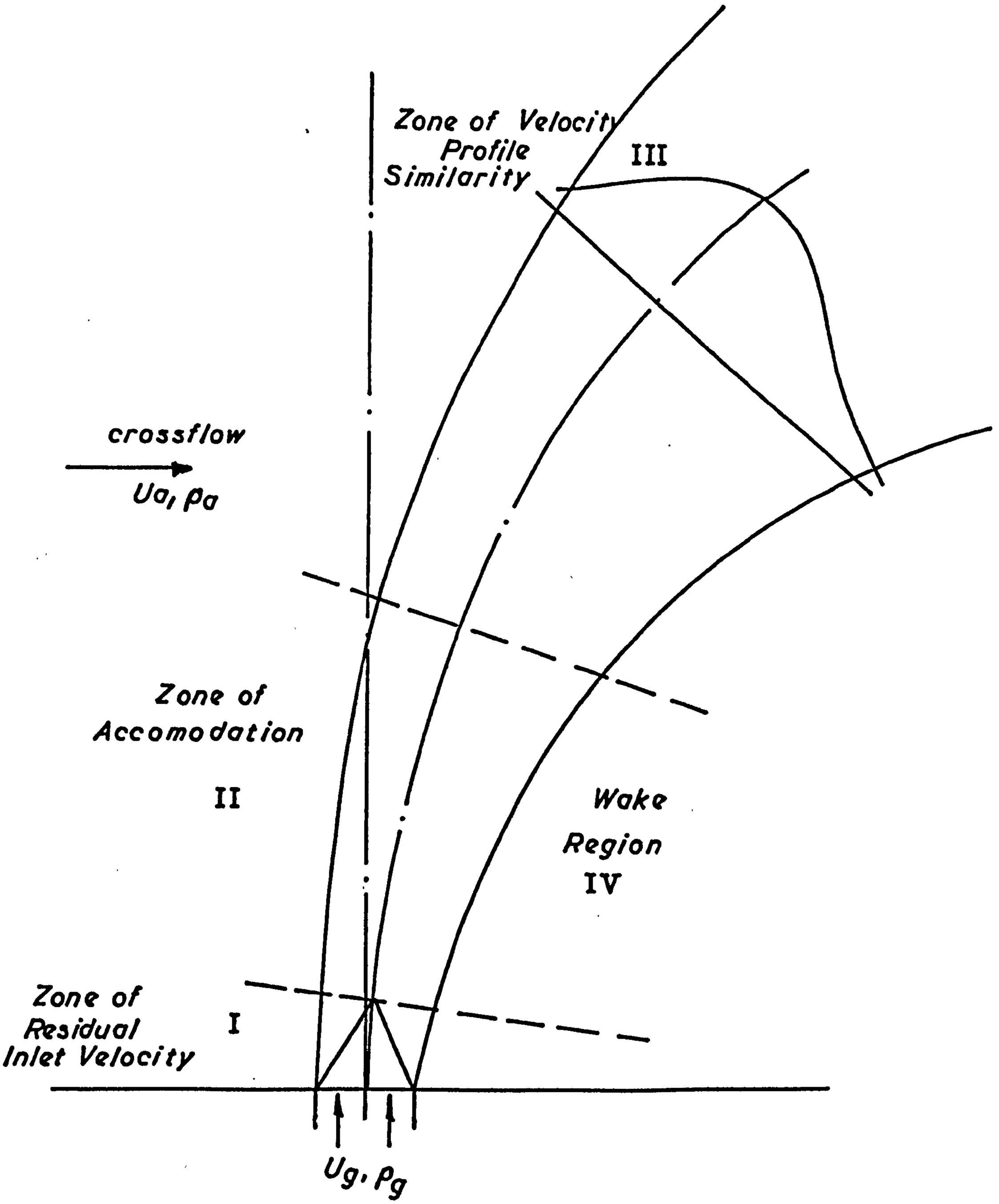

Definition of Zones for Jets in Crossflow.

Fig. 2·1

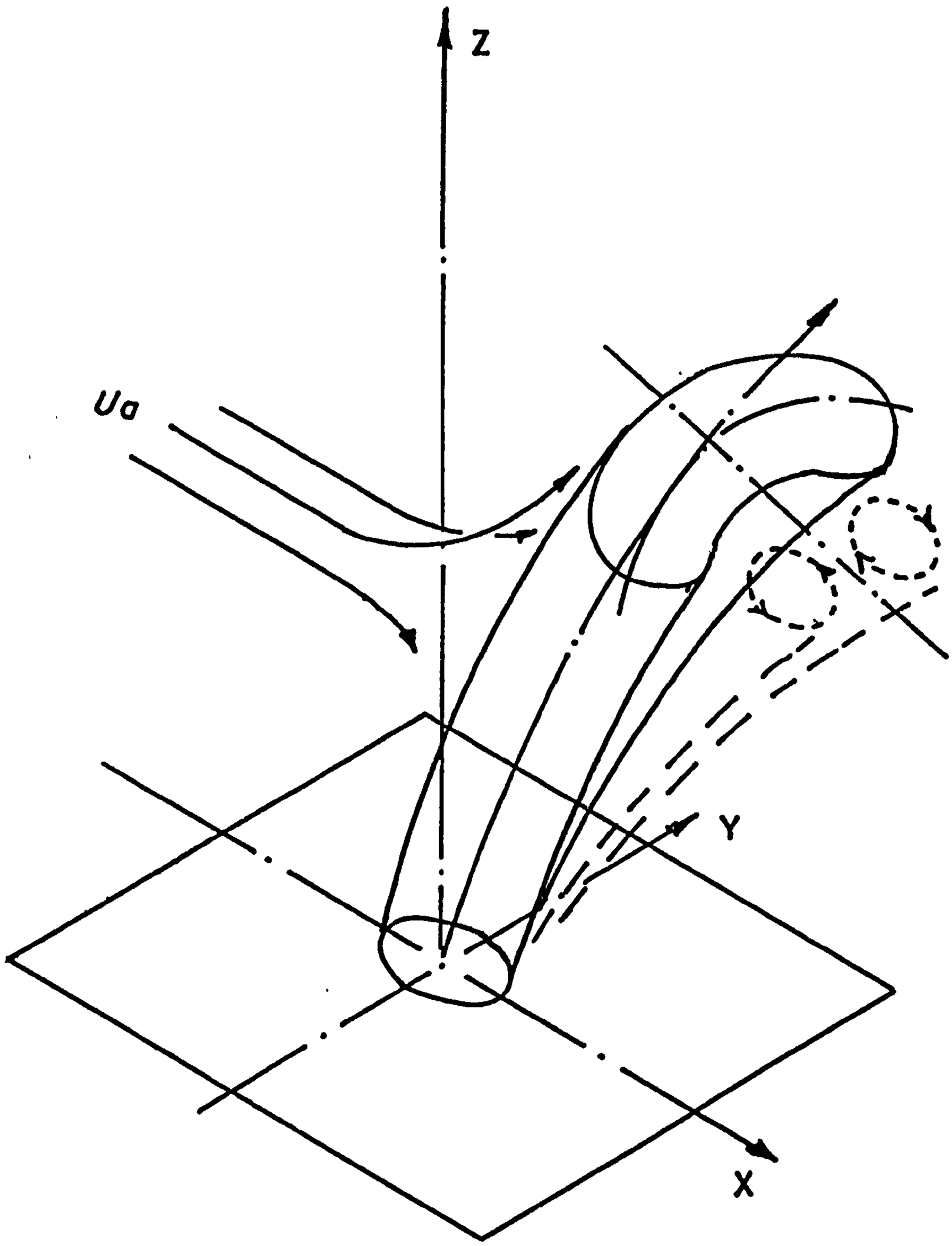

Crescent Configuration and Axes Notation

Fig. 2·2

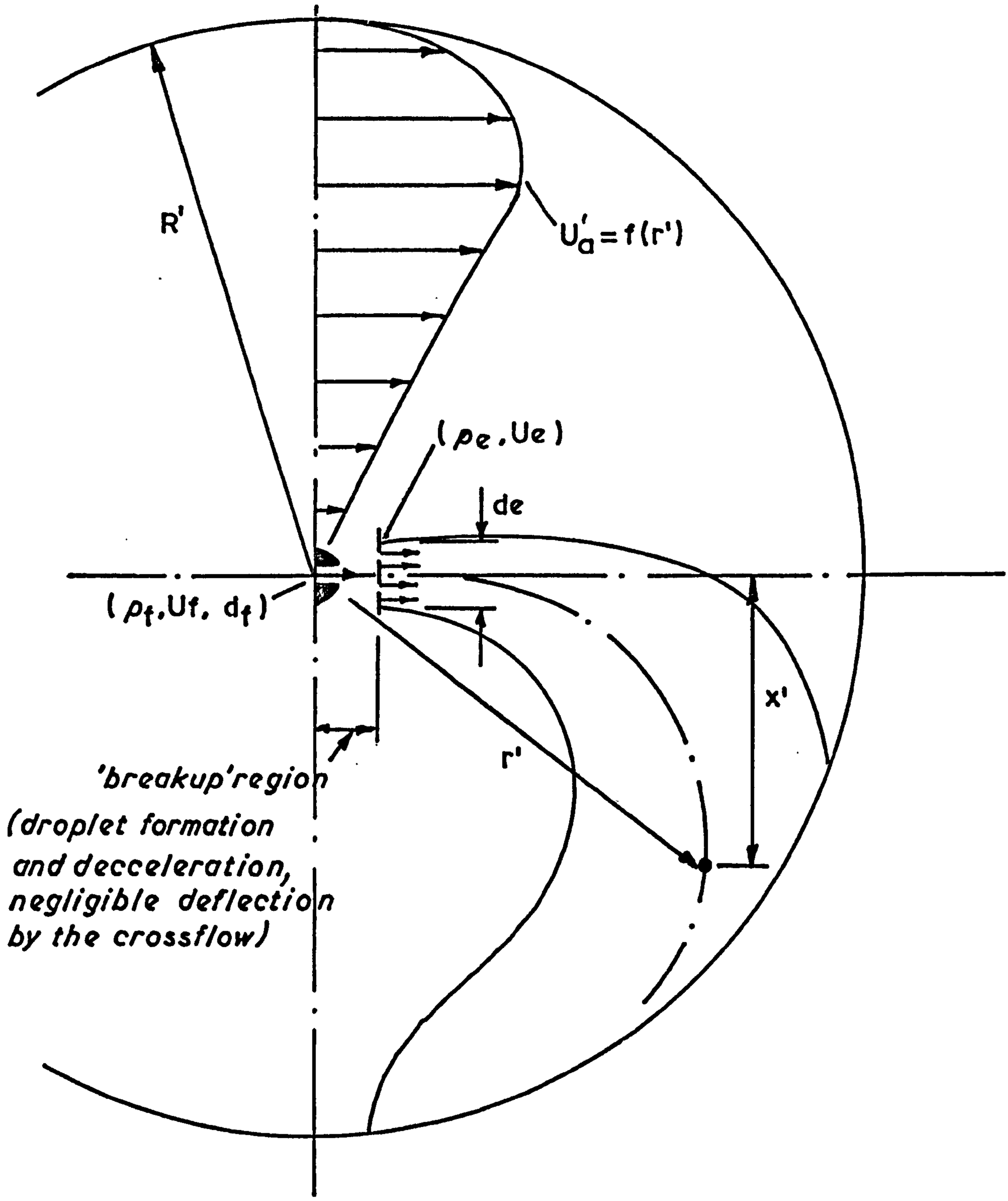

Representation of the Diesel Engine Fuel Spray.

Fig. 2·3

CHAPTER 3

Survey of Hot Wire Correlation Data and Techniques

3.1 Introduction

Reference to some methods of engine air motion measurement was made in section (1.1.1), and it was indicated that the transient nature of the process was most suitably detected by the hot wire anemometer, provided rigourous calibration of the instrument was undertaken. Successful measurements of the air velocity in motored diesel engines, using hot wire anemometers have been made by Derham (31), Horvatin (32), Khan and Grigg (10), Hassan (41) and Weidenmuller (42).

Transient analysis in dynamically similar gas jet models also poses the same requirement of response as that of air motion in an engine cylinder. Hot wire anemometers were first postulated to be capable of measuring gas concentration by Corrsin (43) in 1949 when a theoretical appraisal of the subject was published. Way and Libby (44) showed that thermal interference, between a hot wire and hot film, increased sensitivity to concentration of helium in air, and concentration level was thereby quantitatively evaluated. Devilliers and Diep (45) presented a method of measuring gas concentrations of helium and argon in supersonic flows employing the combination of a hot wire and pitot tube although this method was not capable of transient analysis. Various methods of describing the heat transfer process in flows of known binary concentration have been published, (Simpson and Wyatt (46), Baccaglini, Kassoy and Libby (47), Wassan and Baid (48) and, Wassan, Davis and Wilke (49)).

It was therefore logical to extend the hot wire anemometry technique, developed for engine air velocity measurement, to include the measurement of binary gas concentration.

Hot wire anemometers are sensitive to variables changing the rate of heat transfer from the fine sensing element. It is the accurate description of the dependance of heat transfer on fluid and wire properties which provides the method of calibration in flows of varying characteristics.

3.2 Review of Salient Heat Transfer Correlations for Cylinders in Cross flow

For forced convective heat transfer between single cylinders and incompressible cross-flows under near isothermal conditions, (or on the basis that the fluid properties are independent of temperature), dimensional analysis yields (56) (58)

$$Nu = \frac{hd}{k} = f\left(\frac{\rho U d}{\mu}, \frac{C_p \mu}{k}\right) = f(Re, Pr) \quad \ldots\ldots\ldots \quad (3.1)$$

However, for non-isothermal cases, such as will occur in this project, the relationship (3.1) must be extended to:

$$Nu = f(Re, Pr, (\text{temperature dependent term})) \ldots\ldots \quad (3.2)$$

Considerable data is available for forced convective heat transfer from heated cylinders normally orientated to the flow (refs. (46) to (60) inclusive). McAdams (58) collected and correlated data from some of these sources, together with other data. However, general correlations of this type are frequently viewed, (56) (54) (60), to be at best an engineering approximation, and not suitable for accurate instrumentation work. The details of the correlation of McAdams, together with those of other research workers, are tabulated in Tables (3.1) (3.2).

The equation of Kramer (59) (Table (3.1)) was obtained for cylinders in air, water, and various grades of oil, but by the same argument applied to the equation of McAdams, the equation may be too general for accurate measurement in gases alone. It is included in Table (3.1), however, as an illustration of the necessity for the inclusion of Prandtl number to accommodate the various fluid types.

Prandtl number for air and most gases varies only slightly with both temperature and gas type. The dependence of Nusselt number on Prandtl number as depicted by equation (3.2), is therefore masked by natural data spread, or incorporated in the temperature correction term. Consequently the remaining equations in Tables (3.1) (3.2) may

be seen to be independent of Prandtl number, and generally represented by:-

$$Nu = f(Re, (\text{temperature dependent term})) \quad ..... (3.3)$$

The equation of Ahmad (56) (57), obtained for various gas combinations, is an illustration of this point. The correlation is for a cooled sensor, and may not be directly applicable to hot wires, however the correction on Nusselt number is provided by absolute viscosity ratio.

The previously mentioned temperature correction is presented in the correlations of Hilpert (53), Collis and Williams (54), and Hassan and Dent (50), as shown in Table (3.1). The correlation of Andrews et al (60) is of interest in this context, since the corrected Nusselt number is a function of Knudsen number. The correction is shown to be relevant to fine wires, or rare gases, for which the Knudsen number is greater than 10^{-3}, and non-continium flow exists. Baccaglini et al (47), also indicate discrepancy in data correlation for flows of helium-nitrogen, and, neon-nitrogen mixtures, in which, due to poor thermal accommodation on the surface of the wire slip effects become significant.

The correlation of King (52), was based on potential flow theory for cylinders in cross-flow. Resultant discrepancy on the predicted heat transfer was reported by Collis and Williams (54), to be as high as 40%. It was observation of this deviation of King's law which promoted Collis and Williams to develop their correlation. The resultant work was meticulous in detail and the equation form as shown in Table (3.1) is generally accepted. The change at Re = 44 was reported by Collis and Williams to coincide with the onset of eddy shedding behind the cylindrical wire.

The correlation of Hilpert extends over a very large Reynolds range. However, in order to achieve close agreement to data, employing the power law shown in Table (3.1), the data is divided into four regimes. Such discontinuity, particularly at Re = 4, and Re = 40,

is the major source of discouragement against its use.

Davies and Fisher (55) evaluated the fluid properties at the free stream temperature, with the exception of thermal conductivity which was evaluated at the wire temperature. Hassan and Dent (50), showed that deviation of the predicted velocity occurred as overheat ratio was increased to that suitable for use in motored diesel engine combustion chambers. This was corrected by an empirical temperature compensation factor on the estimated velocity from the Davies and Fisher correlation:

$$U = U_{df} (Tw/Tg)^{0.3} \quad \ldots\ldots\ldots \quad (3.4)$$

where U is the corrected velocity, and U_{df} is the velocity as predicted by the Davies and Fisher equation.

Parnas (61) calibrated hot wires at various temperature loadings and compared the results between the cases for gas properties evaluated at the freestream temperature Tg, and those evaluated at the arithmetic mean film temperature Tm. A strong temperature loading effect was indicated when properties were evaluated at Tg, but when evaluated at Tm the effect was considerably reduced.

Reference to Table (3.1) (3.2) indicates that the majority of the cited correlating equations have gas property evaluation temperatures at Tm. The exception being Davies and Fisher and consequently Hassan and Dent also. The equations of King, McAdams and Kramer do not incorporate a temperature correction.

Collis and Williams indicate that loss of heat due to conduction to the wire supports is significant for length to diameter ratio (l/d) less than 1000. Consequently the majority of the cited hot wire correlations (Tables (3.1) (3.2), refs. (52) (53) (54) (60)), have been based on wires with high l/d. In practice the length of the wire for most hot wire applications in I.C. engine research has to be restricted due to vibration leading to wire breakage during measurement on the

engine (section 3.3). For this reason the analysis, and estimation, of end conduction loss due to Davies and Fisher is of relevance, and will be discussed fully in section 4.2.

3.3 Review of Hot Wire Calibration Methods for I.C. Engine Velocity Measurement

In this context the work of Hassan (41), Hassan and Dent (50) Derham (31), Dent and Derham (51), Horvatin (32), and Horvatin and Hussmann (62) are directly relevant.

Hassan established that the calibration characteristics obtained for the anemometry probes used in his project were most suitably described by the equation of Davies and Fisher provided the temperature correction of equation (3.4) was applied. Velocity prediction over all the overheat ratio range was then possible, and hence upon operation in the engine similar variation in overheat ratio due to increase in gas temperature could still be accommodated by the ambient calibration.

The work of Derham (31) continued with the same procedure. Dent and Derham (51) established that agreement of predicted and actual air velocities under ambient calibration conditions ensured agreement in the varying density flow of the engine.

The derived technique was to measure engine gas velocity at a particular wire operating temperature, Tw1, using the ambient calibration and the Davies and Fisher equation. Concurrently engine voltage traces were obtained at various other wire temperatures (and consequently overheat ratios) Tw2, Tw3 ..... The gas velocity measured at Tw1 was then used to compute the output voltages at Tw2, Tw3 ..... Comparison of voltages as predicted by the equation of Davies and Fisher, and actual engine measured voltages at Tw2, Tw3 ..... were shown to give close agreement. The conclusion drawn was that variation in gas temperature and density throughout the engine cycle was accommodated by the temperature correction of equation (3.4).

The work of Horvatin (32), as also reported in Horvatin and Hussmann (62), used the published correlation of Grigull et al (63) viz:

$$Nu = 0.43 + 0.48\ Re^{0.5} \qquad \ldots\ldots\ldots \quad (3.5)$$

The equation contains no temperature correction, but Horvatin used a heated wind tunnel to check calibration consistency at varying gas temperature (20 - 170 deg. C.).

Discrepancy of any particular wire from the calibration curve of equation (3.5) was attributed to uncertainty in wire geometry and cold (room temperature) resistance. Horvatin therefore made minor modifications to the measured, i.e. estimated, wire length in order to achieve coincidence of the actual calibration and equation (3.5).

Similarly, Derham (31) made modest changes to the estimated wire operating temperature (due to uncertainty in contact resistance' (section 4.3.3), to achieve coincidence of ambient calibration data with the equation of Davies and Fisher. Such modification was slight and incorporated as an amendment to the operating resistance at the calibration stage. Typically, a theoretical operating temperature of 750 deg. C would be increased to an "assumed" value of approximately 790 deg. C to ensure coincidence with the Davies and Fisher equation. The temperature correction of equation (3.4) then ensured validity of calibration under motored engine conditions.

Horvatin, Hassan, and Derham all included conduction end loss prediction in their calculation of heat transfer coefficient. Under conditions of varying gas temperature the wire support temperature will also fluctuate, consequently the proportionate heat loss due to end conduction may be expected to decrease with increase in gas temperature. This is particularly relevant at the low wire length to diameter (l/d) ratios necessary for mechanical strength in the engine. Derham used Pt - 20% Ir wires of diameter 10 μm, and the length to diameter ratio never exceeded 200. Horvatin found it necessary to use 15 μm Pt-Rh alloy wires, although length to diameter ratio is not stated.

Horvatin assumed a parabolic temperature profile along the wire, the integrated mean temperature of which represented the nominal wire

operating temperature. Thus on fixing the nominal mean temperature, (wire operating temperature), the temperature gradient at the wire support was expressed as a function of the assumed parabolic profile and wire length, and hence conduction end loss could be estimated.

Hassan and Derham used the end loss analysis of Davies and Fisher (section 4.2)

3.4 Review of Binary Gas Concentration Measurement Techniques

Hot wire anemometers were first postulated to be capable of simultaneous measurement of velocity and concentration by Corrsin (43). The full analysis as presented by Corrsin is involved, the basic approach was to adopt King's equation (52), and represent the simultaneous operation of two wires in close proximity by:

$$Nu_1 = A_1(\chi) + B_1(\chi)\, U^{0.5} \qquad \ldots\ldots \quad 3.6$$

$$Nu_2 = A_2(\chi) + B_2(\chi)\, U^{0.5} \qquad \ldots\ldots \quad 3.7$$

where χ is the local molar concentration fraction, and the intercept and slope parameters, A_1, A_2, B_1, B_2, are functions of χ. Corrsin proposed that the two sensors should be chosen to have different heat transfer characteristics, so that the equation (3.6) (3.7) then represent a pair of simultaneous equations with two unknowns χ, U. Dissimilarity in calibration characteristics was assumed to be achieved by using wires of different diameter. Solution of (3.6) (3.7) was then presented on a theoretical basis by assumption that the concentration function forms A_1, A_2, B_1, B_2 were known.

Little other relevant information on successful hot wire concentration measurement techniques has come to the authors notice up to the published work of Way and Libby (44) 1969. Tombach (64) is reported by Way and Libby to have attempted concentration measurement using a hot wire probe configuration, but to have abandoned the technique due to calibration shift caused by exposure to high concentrations of helium in air for long periods of time. Way and Libby, however, found that sensitivity to concentration of helium in air could be enhanced by allowing thermal interference of the hot wire onto the hot film to occur. Calibration shift problems did not occur provided the helium exposure time was limited.

The analysis was again based on King's equation which may be

represented:

$$E_w^2 = A_w(\chi) + B_w(\chi)\, U^{0.5} \quad \ldots\ldots\ldots \quad (3.8)$$

$$E_f^2 = A_f(\chi) + B_f(\chi)\, U^{0.5} \quad \ldots\ldots\ldots \quad (3.9)$$

where E represents the wire output voltage and the subscripts w,f, refer to the hot wire and hot film respectively.

Re-arrangement of (3.8) and (3.9) yields:

$$E_w^2 = A_w\{1 - (B_w/B_f)(A_f/A_w)\} + (B_w/B_f)\, E_f^2 \quad \ldots\ldots\ldots \quad (3.10)$$

which may be more easily represented by:

$$E_w^2 = f_1(\chi) + f_2(\chi)\, E_f^2 \quad \ldots\ldots\ldots\ldots \quad (3.11)$$

where $f_1(\chi)$, $f_2(\chi)$ are the respective intercept and slope functions of equation (3.10).

Calibration data for operation in known concentrations, at high film temperature (275 deg. C), and low wire temperature (50 deg.C), with the wire downstream to the film is represented in Fig. (3.3). The dependence of $f_1(\chi)$ and $f_2(\chi)$ on concentration level is not great. Similar data for the wire upstream of the film (0.05 mm), T_w = 100 deg.C, T_f = 275 deg.C, and therefore creating thermal interference of the wire onto the film, is shown in figure (3.4). Separation of the calibration curves is greatly enhanced, and hence voltage readings, E_f, E_w, provide explicit definition of both gas concentration and velocity.

3.5 Conclusions of the Survey of Anemometry Techniques

3.5.1 Applicability of General Correlating Equations to Engine Velocity Measurement

The correlating relationships of McAdams and Kramer are based on a wide range of data and may prove too general for accurate velocity prediction. The equation due to King has been criticised on its potential flow basis of derivation and reported to give large systematic errors on heat transfer prediction (54). The equations of Collis and Williams have been meticulously derived, but are not directly applicable to I.C. engine research due to limitation on the overheat ratios employed and the low length to diameter ratio necessary for mechanical strength in the engine. Similar arguments apply to the correlation of Andrews et al, where additionally the correction on Nusselt number is difficult to apply due to the necessity to indirectly include the accommodation coefficient for the wire material and gas type.

Incompatability of the equation due to Davies and Fisher to the I.C. engine measurement problem has caused workers such as Hassan and Derham to develop the original relationship beyond its initial range. In particular the extensive range of overheat ratios presented by operation in the engine cylinder promoted the application of the empirical temperature correction of equation (3.4) to the velocity predicted by the original Davies and Fisher equation, (for which $T_w/T_g < 2.0$). The inclusion of a temperature correction terms is in itself a predictable requirement for operation over a wide temperature range (equation 3.3).

However, mechanical strength requirements in the engine limit the wire length to diameter ratio to a typical maximum value of 200. Wire weld contact resistance then becomes a

significant proportion of the wires measured room temperature resistance, and consequently both Horvatin and Derham were forced to make minor modifications to the estimated wire operating details, in order to ensure coincidence with the respective original equations. Horvatin made allowance for data deviation from equation (3.5) by modifying the estimate of wire length and measured room temperature resistance, and Derham effectively modified the operating temperature estimate in order to compensate for the contact resistance deviation. The correction used by Derham increased the estimated wire temperature and therefore implied a room temperature resistance slightly less than that which was directly measured, usually corresponding to an effective contact resistance value of approximately 0.2 Ω.

In light of the above mentioned difficulties encountered upon direct application of published hot wire equations, it is to be concluded that a heat transfer correlation of data, based on typical probe configurations as used in the engine, would be a desirable extension to the previously developed techniques. Such a correlation should therefore extend over a sufficiently wide overheat ratio range, and incorporate consideration of the weld 'contact' resistance error which is relevant at the low length to diameter ratios employed.

Additionally, the heat transfer relationship of the sensor will be a critical consideration in developing the binary gas concentration measurement technique, hence, additional correlation of data for various gas types is desirable.

3.5.2 Binary Gas Concentration Measurement

The analysis of Corrsin (43) is of interest, but up to the present has received little attention and development.

The method of Way and Libby indicates that concentration

sensitivity of hot wire configurations may be achieved, but is heavily dependent on the interference of the two sensors. Measurement in the recirculating wake of the dynamically similar gas jet model may be expected to present uncertainty in flow direction and hence interference characteristics. The technique is also limited to operation at the calibration gas temperatures.

During the initial stages of this project, gas jet modelling in the engine was contemplated, and a technique was therefore sought which provided the facility to measure gas concentration under non-isothermal flow conditions.

Consequently it was concluded that a technique should be developed, possibly similar to that of Corrsin, which does not rely on sensor thermal interference, and has the facility to operate in non-isothermal flow fields. Such a technique will be related to the heat transfer correlation proposed in section 3.5.1.

Table 3.1

Author	Ref.	Gases	Gas Temp. (deg C)	$\frac{T_w}{T_g}$	$\frac{l}{d}$	No. of Wires.	Prop. Temp.	Re	Equation
King	52	Air	~20	1.50 to 4.50	>1000	10	Tm	0.055 to 55.0	$Nu = \cdot 318 + \cdot 690\, Re^{0.5}$
Hilpert	53	Air	~20	1.14 to 4.47	539 to 5130	12	Tm	1 → 4	c = ·89, m = ·33
								4 → 40	c = ·82, m = ·39
								40 → 4,000	c = ·62, m = ·47
								4,000 → 40,000	c = ·17, m = ·62
									$Nu = c\left(Re\left[\frac{T_w}{T_g}\right]^{1/4}\right)^m$
Collis and Williams	54	Air	~20	1.1 to 2.0	2070 to 8660	4	Tm	·02 → 44	$Nu\left[\frac{T_m}{T_g}\right]^{-\cdot 17} = \cdot 24 + \cdot 56\, Re^{\cdot 45}$
								44 → 140	$Nu\left[\frac{T_m}{T_g}\right]^{-\cdot 17} = \cdot 48\, Re^{\cdot 56}$
Davies and Fisher	55	Air	~20	< 2·0	400 to 1200	—	Tg (kat Tw)	< 50	$Nu = \left[\frac{2.6}{\gamma\pi}\right] Re^{\cdot 33}$
Hassan and Dent	50	Air	~20	1.29 to 3·58	< 200	1	Tg (kat Tw)	< 50	as above but $U = U_{df}(T_w/T_g)^{0.3}$
Mc. Adams	58	Air	—	—	—	various sources	Tm (ρ at Tg)	0.1 → 1000	$Nu = \cdot 32 + \cdot 42\, Re^{\cdot 52}$
Kramer	59	Oil Water Air	—	—	—	—	Tm	0.01 → 10,000	$Nu = \cdot 42 Pr^{\cdot 2} + \cdot 57 Pr^{\cdot 33} Re^{\cdot 5}$

Author	Ref.	Gases	Gas Temp. (deg. C)	$\frac{Tw}{Tg}$	$\frac{l}{d}$	No. of Wires	Prop. 'Temp'	Re	Equation
Ahmad	56 57	$He-N_2$ N_2-CO_2 $He-CO_2$	427 to 1227	0.25 to 0.75 (cooled sensor)	—	1	Tm	4 → 40	$Nu[\frac{\nu_g}{\nu_m}]^{.15} = .207 + .497\,Re^{.45}$
Baccaglini et.al.	47	$He-N_2$ $Ne-N_2$	~20	1.1	116	1	—	—	direct calibration of sensor
Way and Libby	44	He-Air	~20	1.17 to 2.7	150	1	—	—	direct calibration of sensor
Andrews, Bradley, and Hundy.	60	Air N_2-CH_4	~20	1.05 to 3.5	24 to 1300	>100	Tm	0.015 → 20	$Nuc = .34 + .65\,Re^{.45}$ where $Nuc = \frac{Nu}{1 - 2.Kn.Nu}$

Table 3.2

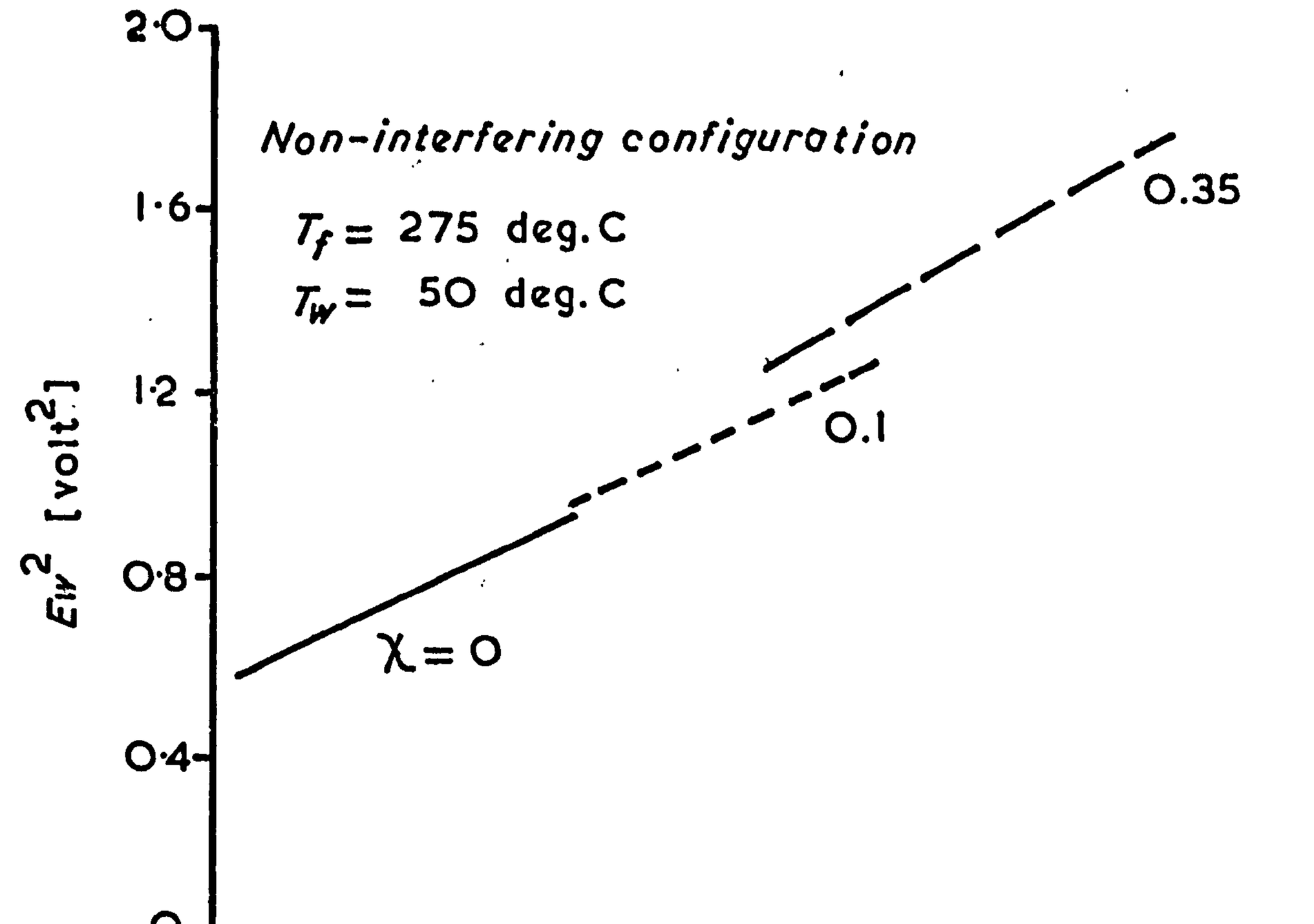

Fig. 3·3

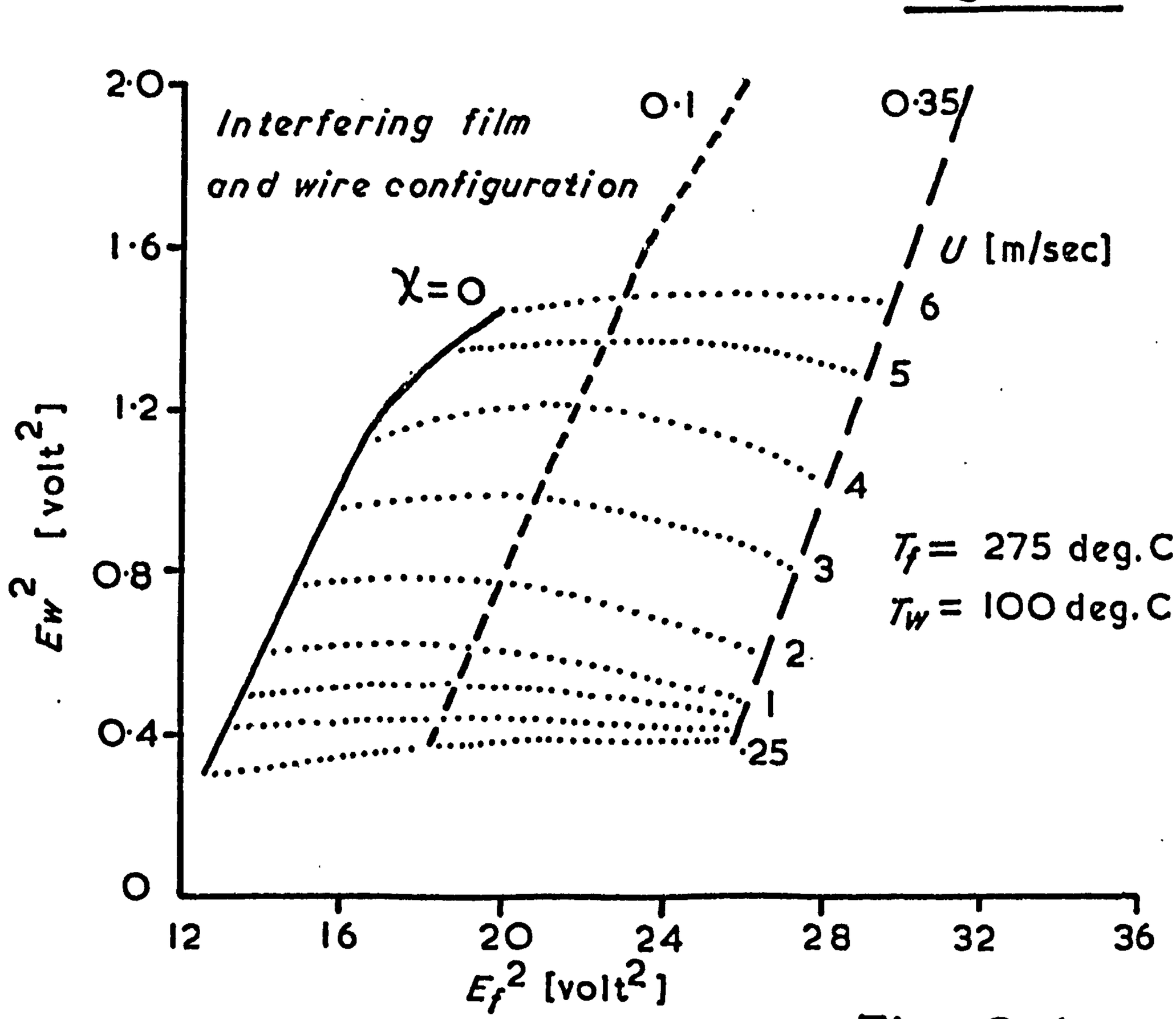

Fig. 3·4

Concentration Technique due to Way & Libby [44]

CHAPTER 4

Development of the Anemometry Heat Transfer Correlation: Practical Operation of Hot Wire Anemometers

4.1 Description of Experimental Equipment

4.1.1 Hot Wire Anemometry Bridges: Principle of Operation

The general principle of operation of constant temperature bridges may be explained by reference to the simplified circuit of figure (4.1).

The probe system, comprising lead and wire resistive loads (R_l, R_w) form one arm of a wheatstone bridge, the remaining current path in the active side being formed by the bridge top resistance R_t. The passive arms of the bridge comprise resistances R_t', variable resistance R_{lc}, and decade resistance R_d.

The servo-amplifier maintains balance of the bridge by control of the voltage E_0, and hence probe current I_p, Thus E_0 is indicative of the power dissipation in the wire necessary to maintain its resistance, and hence temperature, constant. Therefore the probe current is given by:

$$I_p = E_0/(R_t + R_l + R_w) \quad \ldots\ldots\ (4.1)$$

and for fixed probe operating details is a function of the velocity and thermal properties of the flow encountered by the wire.

Initial setting of the bridge is achieved by adjusting R_{lc} to correspond to the probe lead resistance, and R_d to correspond to the required wire operating resistance. Servo-amplifier balance then ensures that:

$$\frac{R_t}{R_l + R_w} = \frac{R_t'}{R_{lc} + R_d}$$

In practice $R_t' > R_t$ so that only a small proportion of the available bridge current is used in the passive arm. In the DISA 55M10 and 55M11 bridges used in this project $R_t' = 20\ R_t$. Thus passive arm contact resistances become negligible.

The 55M10 plug in unit has a 50 Ω bridge top resistance and

maximum probe current of 0.55A. The 55M11 unit has a 5 Ω bridge top resistance and maximum probe current of 2A when operated in conjunction with the DISA 55D22 power booster adaptor.

Steady state output voltages were monitored by the DISA 55D31 and Solartron A220 digital voltmeters.

4.1.2 Hot Wire Probe Construction and Manufacture

The salient design details of all probes used in this project are shown in figure (4.2). The nichrome steel pins were mounted in glazing flux in order to give the necessary strength at the high steady state gas temperatures encountered during high temperature calibration in the flow rig (section 4.1.3).

The connecting plug at the rear of the probe was manufactured from individual gold plated pins and sockets (commercially available), mounted in bakelite, in a manner which allowed only one position of connection. The jack connections on the flying leads were of the BNC type.

This combination of connections was found to give highly repeatable contact resistance, such that successive disconnections produced negligible change in the measured lead resistance (<< 0.01Ω).

The choice of conducting material within the probe body was of importance since variation in probe body temperature produces change in the lead resistance and subsequent error in probe current (equation 4.1) may be introduced.

Magnesium oxide insulated, twin conductor, 'Nichrome' sheathed cabling ('Pyrotenax').of outside diameter 1.6 mm, was used for this purpose.

Copper was chosen for the 'Pyrotenax' conducting material since its low resistance matched the cable compensation capacity of DISA anemometry equipment.

The table below indicates the magnitude of error, per $100^{o}C$ change in probe body temperature, to be anticipated for a probe body length of 300 mm, with R_w = 10 Ω, R_t = 5 Ω, and R_1 = 0.5 Ω. It should be noted however that the probe length thus represented is greater than that normally employed, and heating of the probe body is unlikely to be over its entire length.

Conductor Material	Temp. Coef. % C	Probe Lead Resis. Ω	Change Per $100^{o}C$ Ω	% change in $R_L + R_w + R_t$
NICHROME	0.00018	4.0	0.072	0.37
COPPER	0.00393	0.144	0.056	0.36

The magnitude of error thus represented was not thought to be significant. However, it is worthy of note that Horvatin and Hussmann (62) water cooled the probe body in order to eliminate change in lead resistance.

Development of the gas concentration measurement technique required the simultaneous operation of two wires for isothermal flows and three wires for non-isothermal flows. Figures (4.3) (4.4) illustrate a typical concentration probe.

The fine sensing wire (usually 10 μm diameter) was welded to the Nichrome support pins using a DISA 55A11 micro manipulator and a capacitor discharge unit in conjunction with a binocular microscope.

4.1.3 Flow Calibration Rig

The design of the calibration rig allowed the simultaneous metering, mixing and heating of two gas types. Hence calibration in air and air/gas mixtures at various temperatures was possible.

A schematic arrangement of the rig is shown in figure (4.5) and a photograph with associated anemometry equipment is shown in figure (4.6).

The metering orifices were designed with a length to diameter ratio of 4, with reference to the experimental work of Lichtarowitcz, Duggins and Markland (67), and constructed as shown in figure (4.7). The variation in coefficient of discharge according to Lichtarowitcz et al as also shown in figure (4.7) may be represented by:

$$\frac{1}{C_d} = \frac{1}{C_{du}} + \frac{20}{Re}\ (1 + 2.25\ 1/d) - \frac{0.005\ 1/d}{1 + 7.5\ (\log 0.00015\ Re)^2} \quad \ldots\ (4.2)$$

where C_{du} is the ultimate value of C_d when $Re > 5 \times 10^3$, and Reynolds number (Re) is based on the orifice diameter and differential head predicted velocity through the orifice.

Tests were conducted to check the suitability of equation (4.2) to the orifices constructed in this project. The equation of continuity may be applied between the orifice in question and the measuring section (figure (4.5)) due allowance being made for the temperature and pressure differentials in the rig as measured by thermocouples T_1, T_2, T_3, and manometer tappings Ho1, Ho2. The computed test section velocity was then compared with that measured directly by the pitot tube in the test section, and a further check made by comparison with a hot wire anemometer which had been previously calibrated in a DISA 55D41 wind tunnel.

Figure (4.8) shows the comparison of pitot and hot wire measured velocities, and indicates that pitot velocity is indicative of wire velocity. Figure (4.9) shows the orifice predicted velocity versus pitot measured velocity for the two orifice sizes used in the project. Two 4 mm diameter orifices provided meter-

ing of flows for the gas concentration technique, whilst the 10 mm diameter orifice was used to obtain extended Reynolds number range in air calibrations.

The conclusion drawn from the rig commissioning tests was that the computed orifice C_d values were satisfactory and that test section velocities thus computed were correct.

4.2 The Calculation of Wire Heat Transfer Coefficient with Allowance for End Conduction Loss

In the absence of end conduction loss the average heat transfer coefficient of the wire may be represented by:

$$h = \frac{I_p^2 R_w}{\pi d z (T_w' - T_g)} \qquad \ldots\ldots\ldots (4.3)$$

However, if heat is lost by conduction to the supports a fraction of the total power dissipation ($I_p^2 R_w$), should not be attributed to convective cooling. The magnitude of conduction loss will then be a function of the temperature profile along the length of the wire, manifested by the temperature gradient at the probe support:

$$\dot{Q}_c = - k_s . A . \left\{\frac{dT_1}{dx}\right\}_{z/2} \qquad \ldots\ldots\ldots (4.4)$$

where $A = \pi d^2/4$ and $T_1 = T_w - T_g = f(x)$

Hence neglecting radiant heat transfer:

$$I_p^2 R_w = h.\pi.d.z. (T_w' - T_g) + 2k_s A \left\{\frac{dT_1}{dx}\right\}_{z/2} \qquad \ldots\ldots\ldots (4.5)$$

where T_w' is the representative mean wire temperature.

The basis for calculation of wire temperature profile has been taken from the work of Davies and Fisher (55). Davies and Fisher considered the heat balance acting on a small element of wire as shown in figure (4.10), and established the following differential equation:

$$\frac{d^2 T_1}{dx^2} + K_1 T_1 + K_2 = 0 \qquad \ldots\ldots\ldots (4.6)$$

where $$K_1 = \frac{I_p^2 \beta_g \alpha}{k_w A^2} - \frac{\pi dh}{k_w A} \qquad \ldots\ldots\ldots (4.7)$$

$$K_2 = \frac{I_p^2 \beta_g}{k_w A^2} \qquad \ldots\ldots\ldots (4.8)$$

K_1 for most wire materials is known to be negative, and solution of

(4.6), giving the variation of T_1 with x, is then:

$$T_1 = \frac{K_2}{K_1} \left\{ \frac{\cosh\ (\sqrt{|K_1|}\ .\ x)}{\cosh\ (\sqrt{|K_1|}\ .z/2)} - 1 \right\} \qquad \ldots\ldots\ (4.9)$$

Differentiation of (4.9) yields the required temperature gradient at the wire support:-

$$\left|\frac{dT_1}{dx}\right|_{z/2} = \frac{K_2}{\sqrt{|K_1|}}\ .\ \tanh\ (\sqrt{|K_1|}\ .\ z/2) \qquad \ldots\ldots\ (4.10)$$

In unusual circumstances K_1 may be positive, and the solution of (4.6) then becomes:

$$T_1 = \frac{K_2}{K_1} \left\{ \frac{\cos\ (\sqrt{|K_1|}\ .\ x)}{\cos\ (\sqrt{|K_1|}\ .\ z/2)} - 1 \right\} \qquad \ldots\ldots\ (4.11)$$

The criterion on which K_1 is positive or negative may be easily established from (4.7).

Since if $K_1 < 0$ $\quad \frac{\pi dh}{k_w A} > \frac{I_p^2 R_g \alpha}{k_w . z . A}$

and considering: $\quad h = \frac{I_p^2 R_w - 2\dot{Q}_c}{\pi dz\ (T_w' - T_g)}$

it may be readily shown that:

if $K_1 < 0$ then $\quad \frac{2\dot{Q}_c}{I_p^2 R_w} < \frac{R_g}{R_w} \qquad \ldots\ldots\ (4.12)$

and if $K_1 > 0$ then $\quad \frac{2\dot{Q}_c}{I_p^2 R_w} > \frac{R_g}{R_w} \qquad \ldots\ldots\ (4.13)$

Wire materials considered in this project have been Pt - 10 % Rh, Pt - 20% Ir, Pt - 30% Ir alloys and pure Iridium. The latter material gave positive values of K_1 due to the high wire thermal conductivity promoting high conduction end loss, and a high temperature coefficient of resistance (0.0042 $1/^{o}C$) providing a low magnitude of the ratio

R_g/R_w. However, work was discontinued on this material due to its low resistivity creating difficulty in accurate room temperature resistance measurement.

Hence, for the remaining materials which exhibit a negative value of K_1, equation (4.7) may be re-arranged after substitution of

$R_g = \frac{\beta_{g.z}}{A}$ to give:

$$h = \frac{k_w.A}{\pi d} \{|K_1| + \frac{Ip^2 R_g \alpha}{k_w.z.A}\} \quad \ldots\ldots (4.14)$$

and substitution of (4.10) and (4.14) in the overall heat balance (4.5) yields, upon re-arrangement:-

$$0 = \frac{Ip^2 R_w}{A.k_w.z.(T'_w - T_g)} \{1 - \frac{2}{z}.\frac{k_s}{k_w}.\frac{R_g}{R_w} . \frac{\tanh (\sqrt{|K_1|}. z/2)}{\sqrt{|K_1|}} - \frac{(R_w - R_g)}{R_w}\} - |K_1|$$

$\ldots\ldots (4.15)$

Solution of (4.15), yielding the value of $|K_1|$, then allows solution of (4.14) to calculate the average heat transfer coefficient directly.

Data required for the solution of average heat transfer coefficient is therefore:

a. Probe Current Ip, defined by equation (4.1)

b. Probe resistance values (R_w, R_g)

c. Wire geometry (z, d)

d. Temperature coefficient of resistance (equation (4.14))

e. Wire material thermal conductivities at the support temperature, k_s, and mean wire temperature, k_w. The support temperature, or temperature of the wire element adjacent to the weld, which dictates the value of k_s, is itself unknown. The assumption that the wire adjacent to the weld is at the ambient gas temperature, has therefore been made.

The representation of wire material properties is therefore essential to the solution of (4.15), and is discussed in section (4.3.2).

The variable K_1 is not explicitly defined by equation (4.15) and has therefore to be solved by a computational iteration technique, details of which are given in Appendix (B), and the computational solution of equation (4.15) may be studied by reference to Appendix (C), (subroutine 'HTRANS').

4.3 Assessment of Wire Geometry and Thermal Properties

4.3.1 Wire Geometry

The length of each calibrated wire was measured by a travelling vernier microscope. Error in length measurement is greater than generally realised due to uncertainty in the origin of the wire adjacent to the support weld, and 'bowing' of the wire between the supports. Estimated error in wire length measurement by this method is ±0.05 mm, which for a 2 mm wire represents 2.5%.

Wire diameter for the platinum alloy wires has been taken as that nominally stated by the manufacturers. The fine wire is produced by a precision drawing process for these materials and significant error on diameter is unlikely.

4.3.2 Wire Material Thermal Properties

Wire material thermal conductivity at temperature T, may be related to the resistivity at the same temperature by the Lorenz constant L:

$$k = \frac{LT}{\beta} \qquad \ldots\ldots \quad (4.16)$$

Powell et al (70) showed that the Lorenz constant of platinum metals remains sensibly constant for temperatures above 0 deg.C, and may be approximated in most cases by $L \simeq 2.43$. Exact values of Lorenz constant used in this project have been close to this value, but have beeh chosen to give agreement between published values of resistivity and thermal conductivity at 20 deg.C, (68) (69), variation with temperature then being given by:

$$\beta_g = \beta_{20} \, (1 + \alpha(Tg - 20)) \qquad \ldots\ldots \quad (4.17)$$

and equation (4.16).

Published values of wire material temperature coefficient α, (68, 69, 71), have not been used directly since slight discrepancy frequently exists between published values and that exhibited by individual batches of wire. The accuracy of temperature coefficient is critical since error in its assumed value will be reflected as an error in mean wire operating temperature. Use of the hot wire probe as a resistance thermometer in the engine cylinder also demands an accurate value of temperature coefficient.

Wire material resistance-temperature characteristics were obtained by welding large sample lengths of the wire to the steel supports of two asbestos bodied mountings. Resistances of the samples were then measured under steady state conditions at various temperatures, in a muffle oven, to an accuracy better than 0.01Ω by the DISA-M system resistance measurement facility, and temperature was monitored by an iron-constanton thermocouple and the Solartron A220 digital voltmeter.

Wire sample lengths were greater than 2 cm, (ten times normal anemometer probe wire length), in order to minimise the effects of 'contact' resistance on the total measured value, (section 4.3.3). Prior to the actual test the wire was heated in the oven to a temperature > 400 deg.C for a period of up to four hours. Subsequent cooling then revealed a lower room temperature resistance, and indicated an annealing process had occurred. This is in keeping with the findings of Hassan (41).

Results for the wire batches used in this project are shown in figure (4.11).

4.3.3 Wire Room Temperature Resistance

Wire mean operating temperature is defined from the measured wire material temperature coefficient, bridge decade resistance setting, and room temperature resistance (R_c), by

$$T_w = \frac{1}{\alpha} \{\frac{R_w}{R_c} - 1\} + T_c \quad \ldots\ldots (4.18)$$

Hence error in the measured value of R_c produces error in operating temperature estimate.

Davies and Fisher showed that error in cold resistance measurement is created by the Peltier effect at junctions of dissimilar metals in the probe lead system, whereby small power dissipation is considered to occur at such junctions, but unlike resistance power dissipation, is proportional to current. Thus the total power dissipation due to an applied voltage (E_o) may be represented by:

$$Ip\ E_o = Ip^2 (R_w + R_L) + \Sigma I\ P_e \quad \ldots\ldots (4.19)$$

where P_e is the Peltier coefficient for the metal pair comprising the junction. Equation (4.19) shows that Peltier power dissipation is most significant at low current values. The DISA M system uses less than 2 mA probe current when operating in the resistance measurement mode.

As probe current increases so R_w increases due to heating of the sensing element. Therefore power dissipation due to wire resistance will increase in proportion to the product of the current squared and R_w, until at normal operating currents Peltier power dissipation is insignificant. It is also worthy of note that decrease in wire length (and hence R_c), will produce a proportionate increase in the significance of the Peltier effect under resistance measurement conditions at ambient air temperature.

Hence for anemometer probes suitable for engine applications the effect cannot be ignored.

Davies and Fisher (55) overcame the error due to Peltier effect by calculating the room temperature resistance from the measured wire length and published material resistivity. However, it has been shown (section 4.3.1) that length measurement may be in error by ±.05 mm. Considering a nominal probe of 2mm, and resistance 10 Ω, this represents a possible resistance error of ±0.25 Ω.

Derham (31), recognised resistance estimate error existed, and considered it to be a contact resistance existing at the wire support weld. Thus on computation of the velocity by the equation of Davies and Fisher, empirical modification of the wire operating temperature was incorporated to allow for this effect as previously discussed in sections (3.3) (3.5.1). None of the other previously reviewed correlations (Tables (3.1) (3.2)) indicate any compensation for error in cold resistance, however, in keeping with the high l/d ratio employed in many of the correlations contact resistance may have been of little significance in relation to the total measured cold resistance magnitude.

In this project a simple but effective method of determining the actual wire cold resistance has been developed.

Figure (4.12) shows the effect of operating the wire at resistancesclose to the measured cold resistance value in constant velocity flows. The measured voltage can be seen to become assymtopic to zero at an operating resistance below the measured cold resistance value. Further, the separation of the different velocity curves indicates the sensor is still acting as an anemometer at the nominal cold resistance value. Where the

difference between the velocity curves becomes zero represents the point at which the sensor no longer behaves as an anemometer, and the resistance value corresponding to this point may be reasoned to be close to the actual wire cold resistance.

Plotting the difference in output voltage between the two velocity curves produces the second curve of figure (4.13), and provides a clearly defined cold resistance value.

Variation between the cold resistance value thus obtained and the measured cold resistance was found to be constant with wire material type. Typically, errors in measured cold resistance were found to be as tabulated below:

Wire Material	Wire dia. (μ m)	'Contact' resistance error (Ω)
Pt - 10% Rh	10	0.16
Pt - 20% Ir	10	0.12
Pt - 30% Ir	15	0.08
Ir	12.7	0.04

4.4 Anomalous Wire Surface Effects

During the early stages of development of an overall wire correlation equation, difficulty was encountered due to shift in the wires operating characteristics. It has been indicated in section (4.3.2) that an initial change in wire cold resistance is to be expected due to the relieving of stresses developed in the drawing and coiling processes during manufacture. Therefore prior to calibration a preliminary annealing process was carried out in which the wires measured cold resistance would have decreased by typically 0.04 Ω. Ideally stability of wire calibration characteristics should exist after this process.

However, it was found that subsequent prolonged operation of the wires, particularly in high temperature air flows, at high wire temperatures, produced a continuing increase in wire cold resistance and corresponding decrease in output voltage levels.

Bradley and Entwistle (72) reported similar effects on Platinum and Platinum-Rhodium resistance thermometers. Figure (4.13) shows some of their results and indicates that increase in resistance still occurs with immersion in non-oxidising gases. Tests were also undertaken on wires heated in vacuo, and a small change in resistance was again reported. This finding was attributed to adsorption and desorption of the gas into the wire surface, whilst the more marked change obtained with immersion in air and oxygen was attributed to sublimation and oxidation of the wires surface at high temperatures.

The upper illustration of figure (4.14) shows a scanning electron micro-photograph of a Pt - 10% Rh wire which was operated for one hour in the flow calibration rig (figure 4.6).in high temperature air (240 deg.C) at a wire temperature of 750 deg.C. Surface deterioration is evident and therefore indicated that the sublimation and oxidation processes encountered by Bradley and Entwistle were occuring at the

operating conditions used in this project. This result also explains calibration drift problems which are frequently encountered with hot wire operation in engine cylinders, and have often been attributed to oil contamination of the wire surface.

In light of the above results, and the possibility of adsorption induced variation in resistance with exposure to differing gas types in the binary concentration technique, it was concluded that the surface of wires used in this project should be quartz coated.

This was achieved by passing the wires through the flame produced by a 10% mixture of Hexamethyldisiloxane in methylated spirits. Calibration drift was then effectively prevented. The lower photograph of figure (4.14) shows a wire operated under the same conditions as the previous illustration and shows no deterioration of the coated surface. The results of Bradley and Entwistle (figure 4.13) also shows considerably reduced variation in cold resistance for the quartz coated wires.

It is of interest to note that the variation in resistance due to adsorption and desorption of differing gas types explains the limitation on helium exposure time for uncoated wires reported by Way and Libby (44) (section 3.4).

Wire diameter must increase modestly due to the quartz coating but from measurements made on the electron scanning microscope photographs no marked increase was detected. It has therefore been assumed that wire diameter remains close to that stated by the manufacturers.

4.5 Empirical Hot Wire Heat Transfer Correlation Law

4.5.1 General Comments

The fluctuation of gas temperature within the combustion chamber throughout the engine cycle makes it a necessary condition that the derived correlation should be applicable to all relevant over-heat ratios. The work of Parnas (61) (section 3.2) indicated least temperature loading dependence with the gas properties evaluated at the arithmetic mean film temperature:-

$T_m = (T_w + T_g)/2.$

The description of heat transfer in binary gas mixtures requires that the derived correlation should be applicable to suitable tracer gas types. However, the inclusion of Prandtl number for gases considered in this project is likely to be an unnecessary complication from the preceding review of correlations (52, 53, 54, 55, 56, 60), because it is sensibly constant for all gases.

A general correlation of the form:

$$\text{Nu (temp. loading factor)} = A + B\,Re^{n} \quad \ldots\ldots \quad (4.20)$$

is therefore, sought, where:

$$Re = \frac{\rho_m U d}{\mu_m}$$

and $$Nu = \frac{hd}{k_m}$$

where subscript m denotes the arithmetic mean property evaluation temperature.

4.5.2 Choice of Suitable Tracer Gas Types

The correlation of heat transfer data is necessary for tracer gases presenting suitable sensitivity characteristics in the binary gas concentration technique to be developed. Assuming

that the heat transfer characteristics of the sensor may be represented by an equation of the form of equation (4.20) allows application of theory basically similar to that proposed by Corrsin (43) (section 3.4).

For two wires operating simultaneously, in close proximity, and at different wire temperatures, the simultaneous equations:

$$f(Tm_1)\ Nu_1 - A_1 = B_1\ Re_1^n \qquad \ldots\ldots\ (4.21)$$

$$f(Tm_2)\ Nu_2 - A_2 = B_2\ Re_2^n \qquad \ldots\ldots\ (4.22)$$

may be obtained.

Division of (4.21) by (4.22) yields the third equation:

$$\frac{f(Tm_1)\ h_1\ d_1 / \overline{k}m_1 - A_1}{f(Tm_2)\ h_2\ d_2 / \overline{k}m_2 - A_2} - \frac{B_1}{B_2}\left\{\frac{\overline{\rho}_{m1}}{\rho_{m_2}} \cdot \frac{d_1}{d_2} \cdot \frac{\overline{\mu}_{m1}}{\mu_{m2}}\right\}^n = 0 \qquad \ldots\ldots\ (4.23)$$

which is independent of gas velocity.

The measured sensor currents will yield the respective heat transfer coefficients (h_1, h_2) (section 4.2) whilst the remaining unknowns $\overline{\rho}_{m1}$, $\overline{\rho}_{m2}$, $\overline{k}_{m1}$, $\overline{k}_{m2}$, $\overline{\mu}_{m1}$, $\overline{\mu}_{m2}$, are functions of gas concentration.

Sensitivity to concentration is limited to the properties $\overline{k}_{m1}$, $\overline{k}_{m2}$, $\overline{\mu}_{m2}/\overline{\mu}_{m1}$, since the ratio of gas densities may readily be shown to be equal to the inverse ratio of the corresponding film temperatures, by application of the characteristic gas equation.

Variation of mean thermal conductivity $\overline{k}$ and mean dynamic viscosity $\overline{\mu}$, with molar concentration χ may be calculated by:

$$\bar{\mu} = \frac{\chi . \mu_b}{\chi + (1 - \chi)\sigma_{ba}} + \frac{(1 - \chi)\mu_a}{\chi\sigma_{ab} + (1 - \chi)} \quad \ldots\ldots (4.24)$$

$$\bar{k} = \frac{\chi . k_b}{\chi + (1 - \chi)\sigma_{ba}} + \frac{(1 - \chi)k_a}{\chi\sigma_{ab} + (1 - \chi)} \quad \ldots\ldots (4.25)$$

where the subscripts a, b denote the property evaluated for the pure component, and χ represents the molar concentration of component b, i.e.

$$\chi = \frac{n_b}{n_a + n_b}$$

and $$\sigma_{ab} = \{1 + (\mu_a/\mu_b)^{0.5}(M_b/M_a)^{0.25}\}^2 / \{8(1 + M_a/M_b)\}^{0.5} \quad .... (4.26)$$

and σ_{ba} is as (4.26) with the subscripts a, b interchanged.

Equation (4.24) is due to Wilke and cited in Reid and Sherwood (65), and the equation (4.25) is due to Mason and Saxena (66).

Iterative solution of (4.23) is therefore possible. Suitable estimates of molar concentration χ may be used to evaluate $\bar{\mu}$, $\bar{k}$ in equations (4.24) (4.25) at the respective film temperatures until satisfactory convergence in equation (4.23) is achieved for the experimental values of h_1, h_2.

The ability to converge to an accurate solution of (4.23) is dependent on the inequality of the two terms at concentration estimates other than the correct root. That is, given experimental values of h_1, h_2, equation (4.23) becomes a concentration dependent function of the form:

$$\underbrace{\frac{\text{const.}/\bar{k}_{m1} - A_1}{\text{const.}/\bar{k}_{m2} - A_2}}_{\text{GROUP 1}} - \underbrace{\text{const.}\left\{\frac{\bar{\mu}_{m2}}{\bar{\mu}_{m1}}\right\}^n}_{\text{GROUP 2}} = 0 \quad \ldots\ldots (4.27)$$

Varying estimates of χ now change the values of groups 1 and 2 via the thermal properties k_m, μ_m. Gases with thermal properties close to air may be immediately reasoned to be unsuitable tracer agents. Exact sensitivity considerations are presented in section (5.2), however on a preliminary basis the following method was adopted.

If constants A_1, A_2 are assumed to be approximately equal, then neglecting their influence on the value of group 1 will only have the effect of increasing its magnitude. The equation (4.27) may therefore be further simplified to give:

$$\text{const.} \frac{\bar{k}_{m2}}{\bar{k}_{m1}} - \text{const.} \left\{ \frac{\bar{\mu}_{m2}}{\bar{\mu}_{m1}} \right\}^n = 0 \quad \ldots\ldots\ldots (4.28)$$

In this approximate form relative variation of the ratios $\bar{k}_{m2}/\bar{k}_{m1}$, and $\bar{\mu}_{m2}/\bar{\mu}_{m1}$ with molar concentration χ provides the degree of inbalance about the solution root.

Evaluation of thermal property ratios at different concentration levels may be made by equations (4.24) (4.25). Variation in ratio magnitude therefore provides a relative comparison of suitability of gas type.

Figures (4.15) (4.16) shows the percentage change in k_2/k_1 and μ_2/μ_1 for various gas types. The ratio μ_2/μ_1 shows little change with χ, and hence sensitivity is mainly provided by the k_2/k_1 ratio.

A result of considerable interest is shown by the helium (k_2/k_1) curve. Large difference in gas thermal conductivities between helium and air is illustrated not to be indicative of high sensitivity (cf. figure 3.3). The hydrocarbon gases indicate a more satisfactory variation in ratio k_2/k_1 with χ and therefore, on this preliminary basis, are more satisfactory tracer agents.

4.5.3 Scope of the Correlation

The range of overheat ratios presented by the engine gas temperature variation for a wire operating at 750 deg.C is approximately 1.32 to 3.50 for typical diesel engine compression ratios. Similar range should therefore be represented in the flow calibration rig by varying both gas and wire operating temperatures.

The available rig air velocity accurate metering range (imposed by the extremes of minimum measurable orifice head drop), and the onset of compressibility effects in the orifice throat) extends from 2.0 m/s to 100 m/s in the test section. This represents a maximum Re = 50 for a 10 μm wire operating at 200 deg.C. Similar calculation at high wire temperature and minimum air velocity describes a minimum Re = 0.5.

Thus data will be represented in the range:

$$0.5 < Re < 50 \quad ,$$

This corresponds favourably to the range represented by the equation of Davies and Fisher (55)(figure 3.1) as used by Hassan (41) and Derham (31), for measurement of mean gas velocity.

4.5.4 Representation of Gas Properties

The computation of gas properties has been designed to incorporate their temperature dependence. This is necessary to represent property values with continual variation in engine charge air temperature, and at differing rig calibration temperatures. Hence published data has been represented by polynomials of the form:

$$\mu_T = \sum_{i=1}^{a} a_{i-1} \cdot T_m^{(i-1)} \qquad \ldots\ldots\ (4.29)$$

$$k_T = \sum_{i=1}^{a} a_{i-1} \cdot T_m^{(i-1)} \qquad \ldots\ldots\ldots \quad (4.30)$$

for each gas type considered. The gas properties thus represented are shown in figure (4.17).

Published values were compared prior to the selection of data (73) (74) (75) (76)(77) (78) and only modest discrepancy found between the sources with the exception of ref. (78) for propane. Hence in the interests of compatability data was drawn from the single source of ref. (77).

The mean properties of mixtures at the required arithmetic mean film temperature may then be obtained from the pure component values by equations (4.24) (4.25) (4.26).

The mean density of the gas mixture may be calculated from the apparent molecular weight,

$$\overline{M} = \chi M_b + (1 - \chi) M_a \qquad \ldots\ldots\ldots \quad (4.31)$$

where subscripts a, b denote the separate constituents and X is molar concentration of (b) in (a + b), hence by the gas equation of state:

$$\overline{\rho}_m = \frac{\overline{M}.p}{\overline{R}\ T_m} \qquad \ldots\ldots\ldots \quad (4.32)$$

Computation of the gas properties is programmable and input data required is limited to the current wire and gas temperatures, together with the relevant polynomial coefficients a_0 .....a_8 as required by equations (4.29) (4.30).

Variation in mean thermal conductivity thus computed for propane-air mixtures areshown in figure (4.18).

4.5.5 Aquisition and Analysis of Correlation Data

More than thirty wires were tested in various gases at different overheat ratios and the characteristic Nusselt-Reynold co-ordinates computed. Gas temperature was varied between 18 deg.C and 300 deg.C, and wire temperature between 180 deg.C and 750 deg.C. A total of approximately 585 data points were therefore obtained.

The method of determining the final equation form is best explained by reference to the process performed on each individual wire.

Figure (4.19) shows the Nusselt number versus Reynolds number data for a single wire operating at the illustrated overheat ratios. Considering the data for T_w = 548 deg.C and T_g = 20 deg.C, the data may be replotted as:

$$Nu = f(Re^n)$$

as in figure (4.20). The various Reynold exponents produce the obvious effect of linearising the data. The plot for n = 0.4 is shown to be most suitable, although in practice little variation in linearity was obtained by modest variation of n in the range $0.38 < n < 0.42$. Repetitive analysis of the data from many wires showed the value n = 0.4 to be the most suitable.

Figure (4.21) shows the data of figure (4.19) replotted on this basis for all the considered overheat ratios in air. Systematic deviation of the data at differing overheat ratios is apparent. Similar to the correction employed by Collis and Williams (54) the inverse ratio of film and absolute gas temperatures was found to be an effective temperature loading factor. Further repetitive analysis for the initial wires correlated*

showed that the relationship:

$$Nu \cdot \left\{\frac{T_m}{T_g}\right\}^{-0.12} = f(Re^{0.4}) \qquad \ldots\ldots \quad (4.33)$$

produced coincidence of data for individual wires irrespective of temperature loading. Figure (4.22) shows the result for the air data of figure (4.21).

Figure (4.23) shows ethane and 25% ethane data obtained with the same wire compared to the line of figure (4.22), and illustrates the important result derived for the gas considered in this project, namely that variation in gas type is accommodated by the Nusselt-Reynold number property groupings, no further property grouping is necessary, (cf. the correlations of Ahmad Table 3.2 (ref (56) (57)).

All the data correlated are represented in figures (4.24) (4.25) where in the interests of clarity the data have been plotted on separate axes.

Figures (4.26) (4.27) show the respective ambient and high temperature data for air replotted about the least squared error line to all the data represented in figures (4.24) (4.25). Figures (4.28) (4.29) (4.30) show similar plots about the same least squared error line for propane, ethane and argon.

The general correlation law obtained from the presented data is thus:

$$Nu \left\{\frac{T_m}{T_g}\right\}^{-0.12} = 0.253 + 0.582\, Re^{0.4} \qquad \ldots\ldots \quad (4.34)$$

The data has a coefficient of correlation of 0.994 and standard deviation of $\sigma = \pm 0.042$.

Comparison of the form of the correlation law presented is most easily made with that of Collis and Williams (54) (Table 3.1) applicable to pure air at room temperatures. The derived Reynold

exponent and temperature loading correction are both less than those presented by Collis and Williams, but the differences may be attributed to disparities in wire length to diameter ratios, wire surface quality (due to the quartz coating), and methods of calculating the heat transfer coefficients.

The effect of allowance for conduction end loss on the overall heat balance (equation 4.5), is not marked, figure (4.31) shows the typical effect of neglecting end loss, and is seen to produce a shift in intercept and slope. Calculated end loss seldom exceeded ten per cent of the total heat dissipation.

Figure (4.32) shows typical computed temperature profiles by equation (4.9) for a Pt - 10% Rh wire operating in ambient air, and figure (4.33) compares the profiles for the ambient and high temperature air cases.

4.5.6 Appreciation of Typical Error: Deviation from the Correlation Law

Data scatter about the least squared error line in figures (4.26) to (4.30) is indicative of the deviation of individual wire correlations, since typically the degree of self correlation for any particular wire produced the modest data scatter about the least squared error line as shown in figures (4.22) (4.23). The band within which 95% of individual wire correlations should fall is therefore represented by the lines at $\pm 2\sigma = \pm 0.082$ on figures (4.26) to (4.30). Explanation of this deviation may be achieved by considering the error incurred in the calibration process of individual sensors.

The sources of error have been considered to arise from the following parameters:

a. Operating wire temperature

b. Gas temperature estimation

c. Recorded bridge voltage

d. Measured wire length

e. Room temperature resistance

f. Wire material temperature coefficient.

For a function value Y, dependent on may variables $V_1, V_2, V_3 \ldots\ldots V_n$, with associated individual errors, $v_1, v_2, v_3 \ldots\ldots v_n$, and related by $Y = f(V_1, V_2, V_3 \ldots V_n)$, the cumulative percentage error on Y incurred by the individual errors $v_1, v_2, v_3 \ldots\ldots v_n$ may be estimated by (79).

$$\% \text{ error } Y = \frac{100}{Y} \left\{ \left(\frac{\partial f}{\partial V_1}\right)^2 \cdot v_1^2 + \left(\frac{\partial f}{\partial V_2}\right)^2 v_2^2 + \left(\frac{\partial f}{\partial V_3}\right)^2 v_3^2 + \ldots \left(\frac{\partial f}{\partial V_n}\right)^2 v_n^2 \right\}^{\frac{1}{2}} \quad \ldots\ldots\ldots (4.35)$$

For the purposes of error computation it has been assumed that error on items e) f) are manifested only by a resultant error in a). Hence by equation (4.18):

$$\frac{\partial T_w}{\partial \alpha} = -\frac{1}{\alpha^2} \left\{ \frac{R_w}{R_g} - 1 \right\} \quad \text{and} \quad \frac{\partial T_w}{\partial R_g} = -\frac{R_w}{\alpha R_g^2}$$

Allowing an estimated error on α of 6% and 3% error on R_g. (representative of temperature coefficeint wire batch deviation and intercept error on figure 4.12 respectively), provides the typical cumulative error on T_w of ±2.2%. Hence for a wire operating at nominally 700 deg.C a possible error of approximately ±15.5 deg.C is indicated. In a similar manner the same percentage error will be present on gas temperature estimate when measured using the wire as a resistance thermometer.

Similarly computation of typical error for actual data points may be performed on heat transfer coefficient and the

necessary differentials may be obtained from equation (4.3) using the experimental value of heat transfer coefficient as reference in the final percentage analysis (equation 4.35).

The inclusion of allowance for end loss on the error analysis, (hence using equations (4.14) (4.15)) was thought to be an unnecessary complication in light of the results of figure (4.31). Thus the calculated errors are not inclusive of error on end loss estimate, but deviation about the true mean line will still be effectively represented.

Error on heat transfer coefficeint will be greatest for small differences of wire and gas temperature, since error in either will then provide relatively large proportionate change in the denominator of equation (4.3). Error computation has therefore been undertaken for the cases of high and low over-heat ratio at high and low gas temperatures.

For an individual wire, calibrated at ambient gas temperature, data scatter about its own correlation line will be mainly a result of voltage reading error. Error on wire length estimate and wire temperature estimate, although present, may be reasoned not to materially affect the self-correlation of the individual sensor. The comparison of many individual wire correlations to their mean correlation line (equation 4.34) should however allow for the error contributions incurred by individual wire temperature and length misrepresentation. Similarly the data for correlation in gases at room temperature may be expected to be free of any significant error contribution from the gas temperature estimation, but this effect should be included for high gas temperature correlations.

Error on Nusselt number is also created by erroneous values

of thermal conductivity being computed as a result of the previously mentioned wire and gas temperature errors. This may be readily calculated by differentiation of the polynomials of section (4.5.4).

The table in figure (4.34) shows typical values of such computation for two overheat ratios. In both cases data scatter about an individual wire correlation line is shown to be low, but clearly increases at high gas temperatures. Inclusion of error contributions from wire length and temperature estimates to give the scatter of data around the mean correlation line shows respective large increases in error.

Error on wire temperature is related to cold resistance and temperature coefficient errors and this strong dependence of error is therefore indicative of the importance of accuracy on wire temperature estimate.

It is therefore to be concluded that calibration of individual wires is desirable, and the correlation work reported in this chapter should be used to predict the equation form:

$$Nu \left\{\frac{T_m}{T_g}\right\}^{-.12} = A + B\, R_e^{0.4} \qquad \ldots\ldots (4.36)$$

Calibration data will then yield the individual wire characteristics by providing the numerical constants A, B in the likely range as depicted by the $\pm 2\sigma$ lines of figures (4.26) to (4.30).

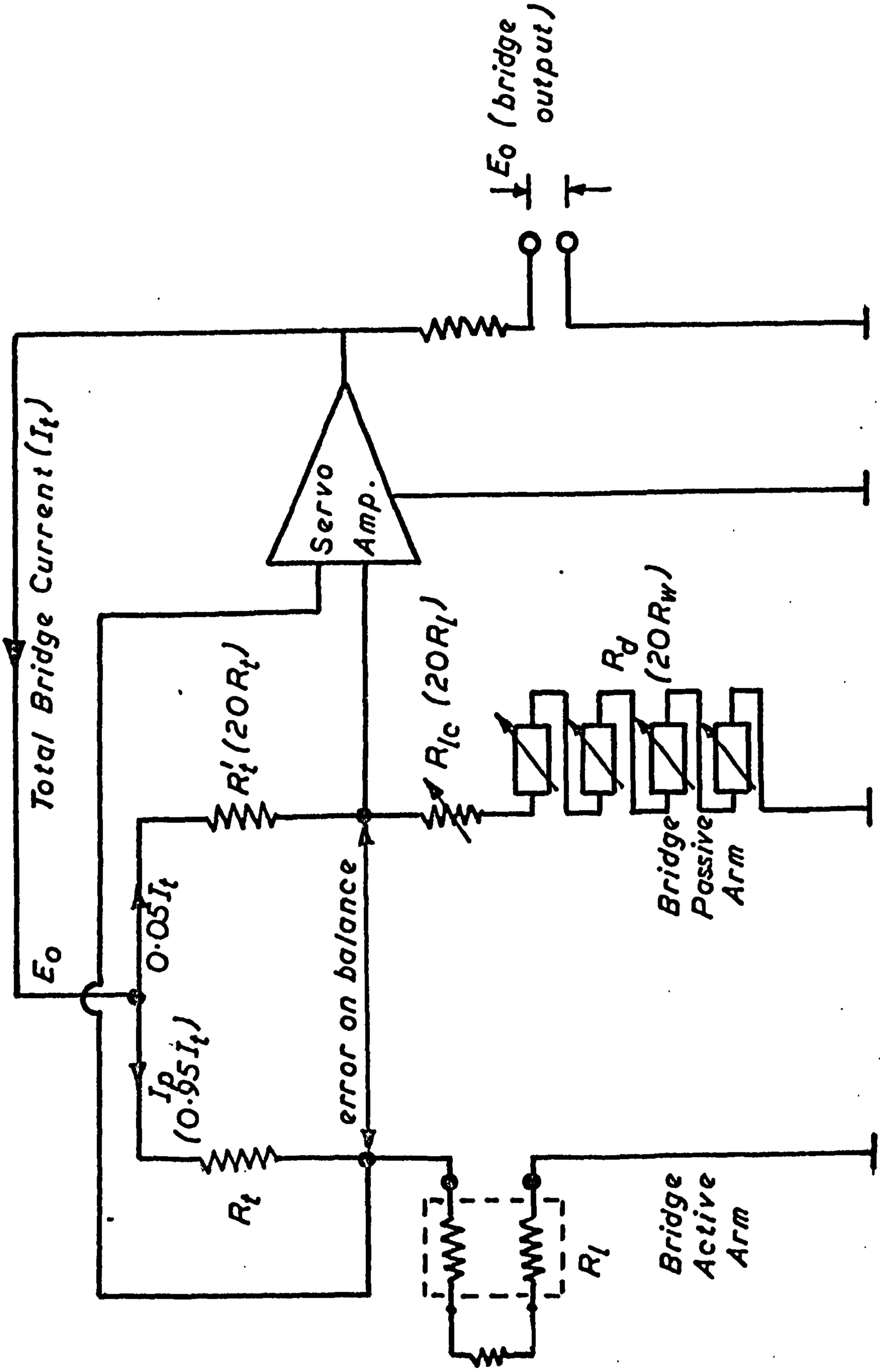

Schematic Circuit of a Constant Temperature Anemometer Bridge

Fig. 4·1

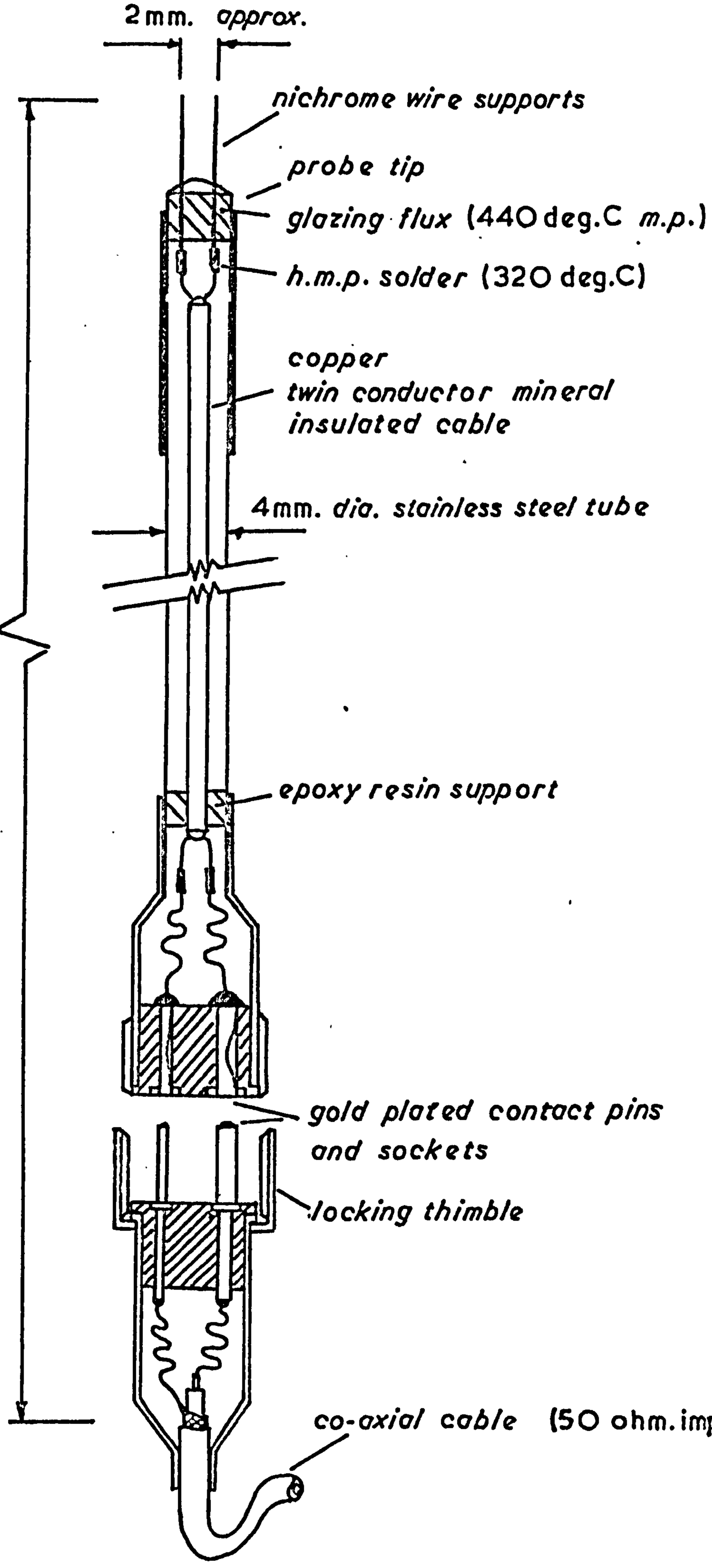

Probe Body Salient Details

Fig. 4·2

Three Wire Concentration Probe Body and Lead Assembly.

Fig. 4·3

Three Wire Concentration Probe Tip.

Fig 4·4

Schematic Arrangement of Hot Wire Calibration Rig

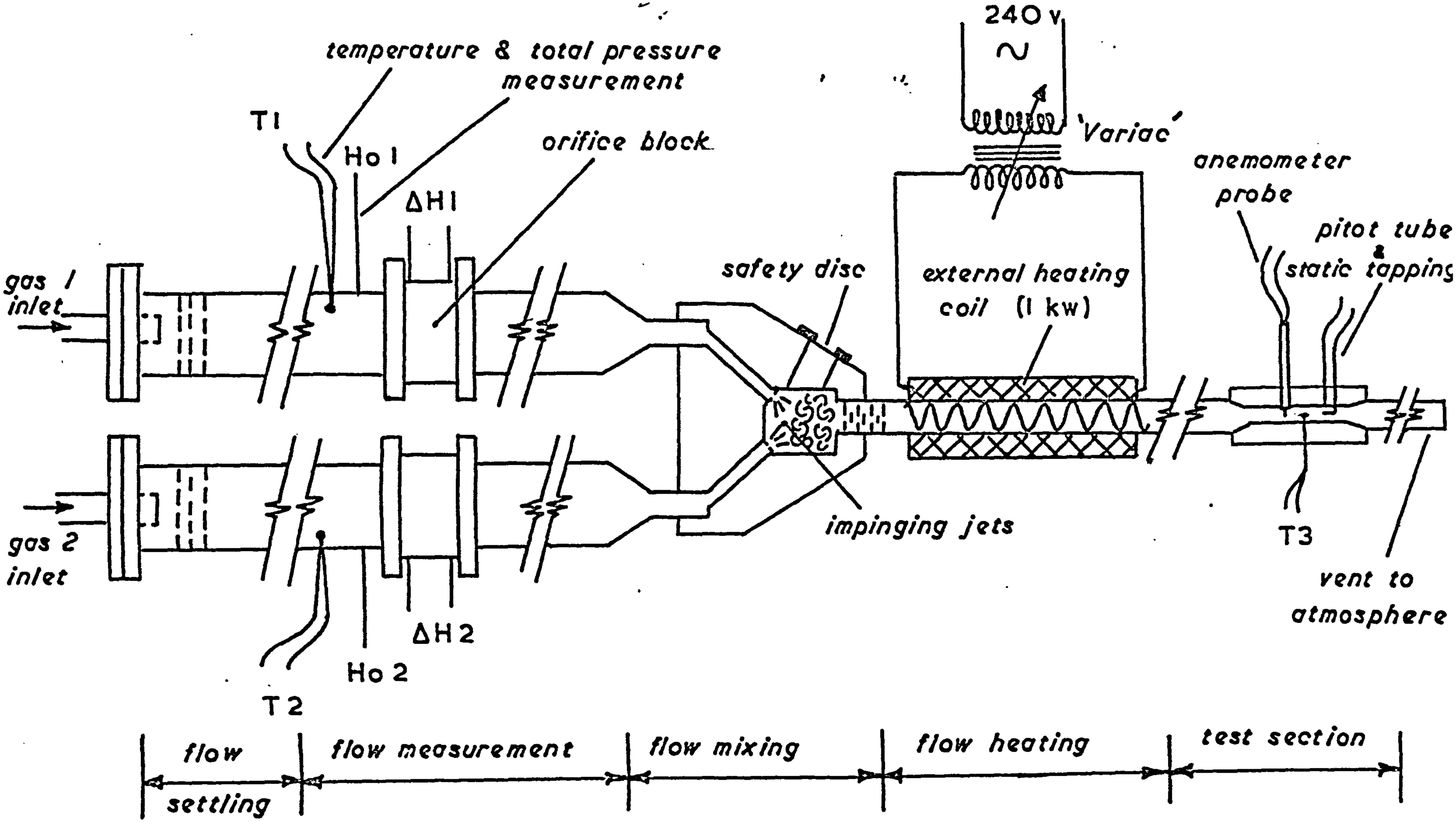

Fig. 4.5

Flow Calibration Rig.

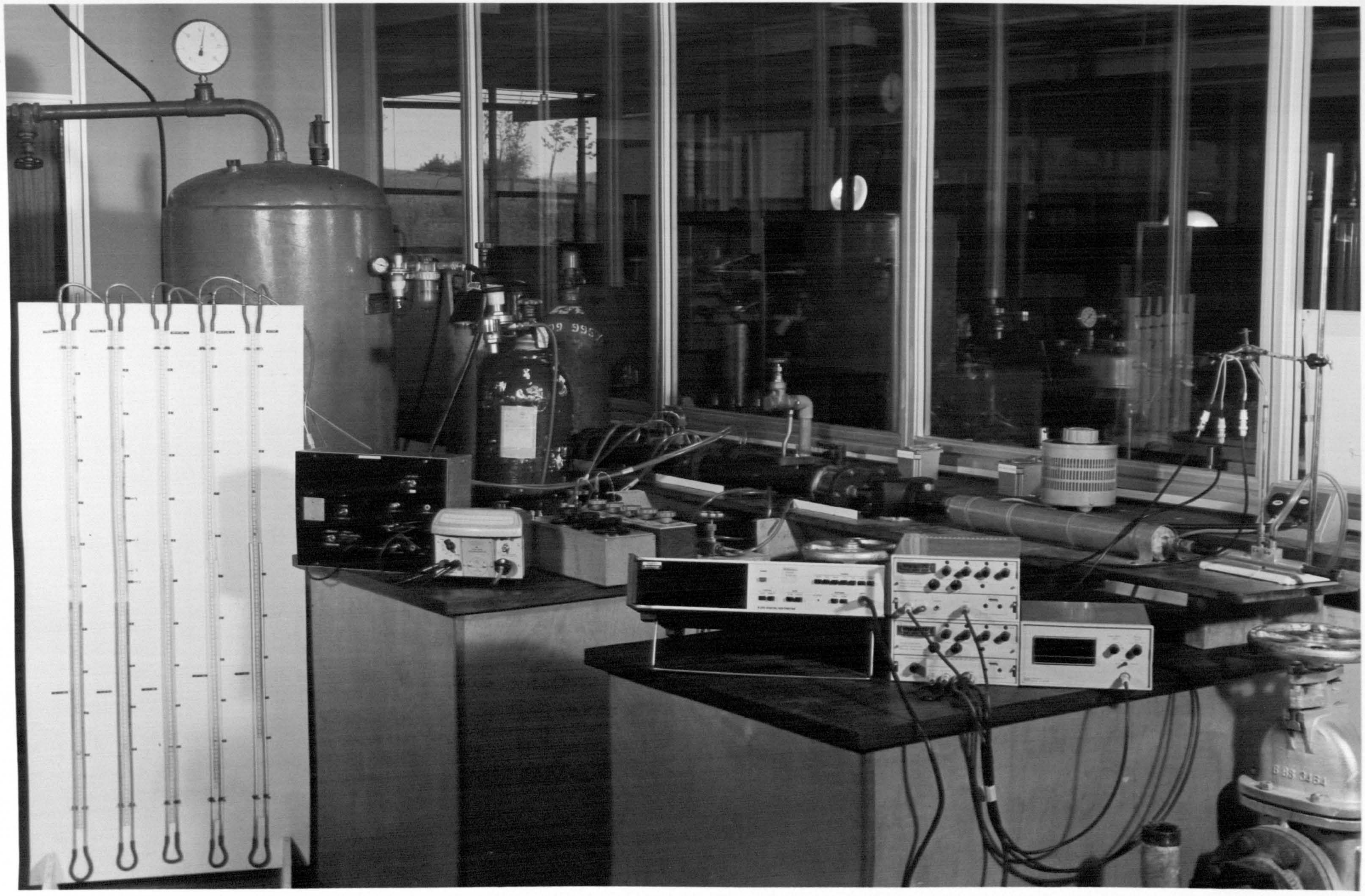

Fig. 4.6

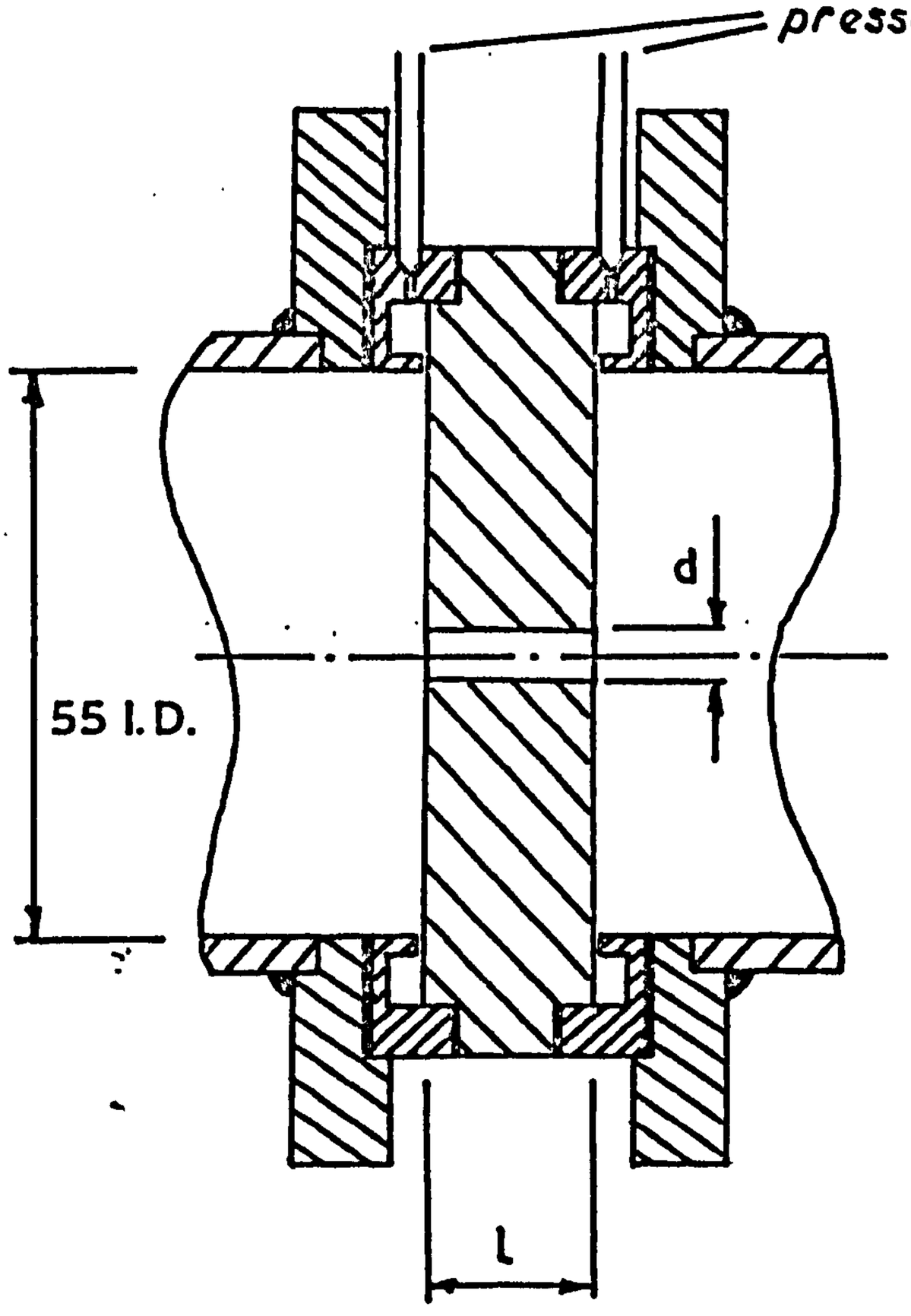

Orifice	Dimensions
d	l
4	16
10	40

dimensions in mm.

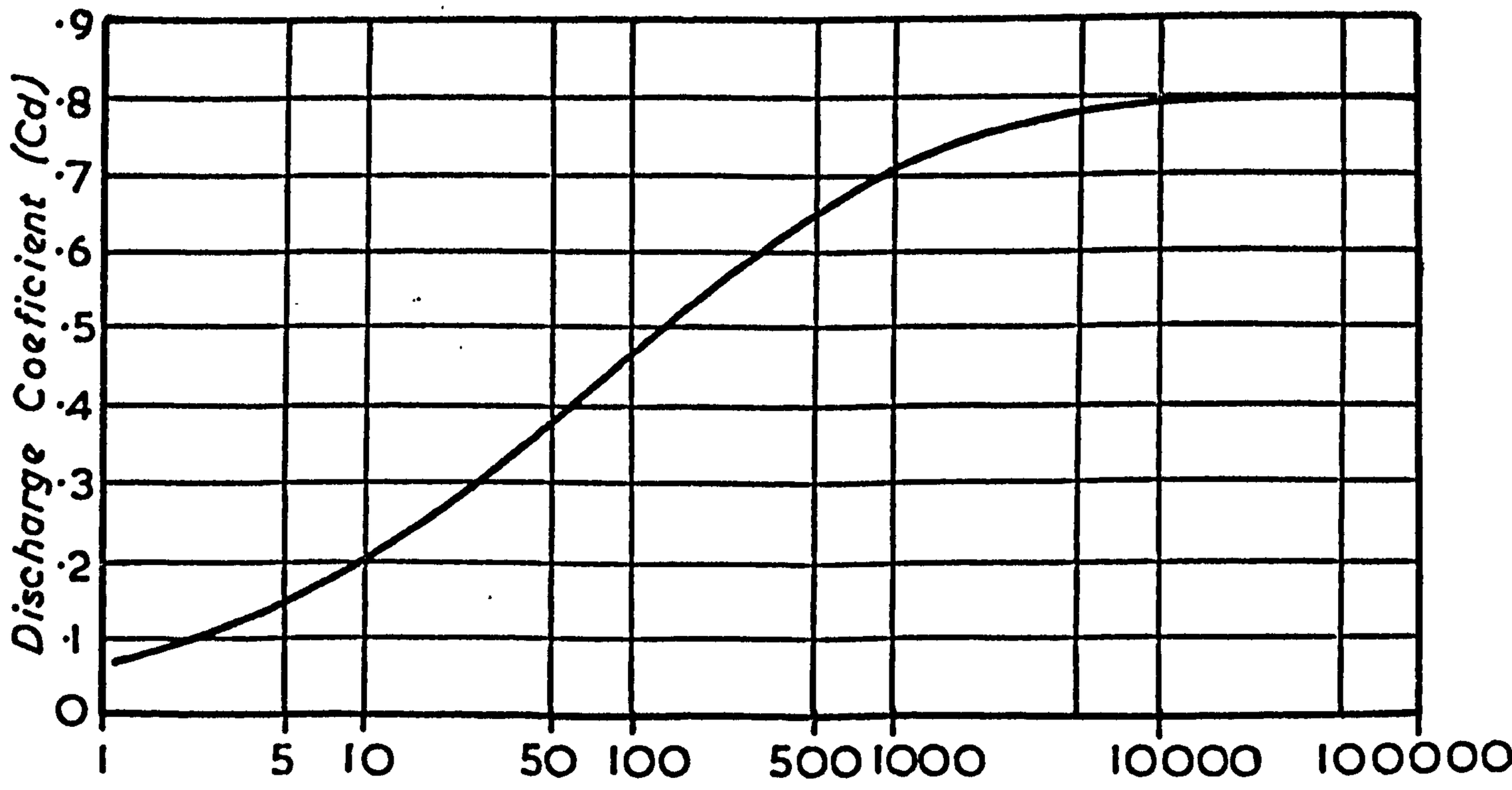

Details of Orifice Block Geometry and Flow Characteristics

Fig. 4·7

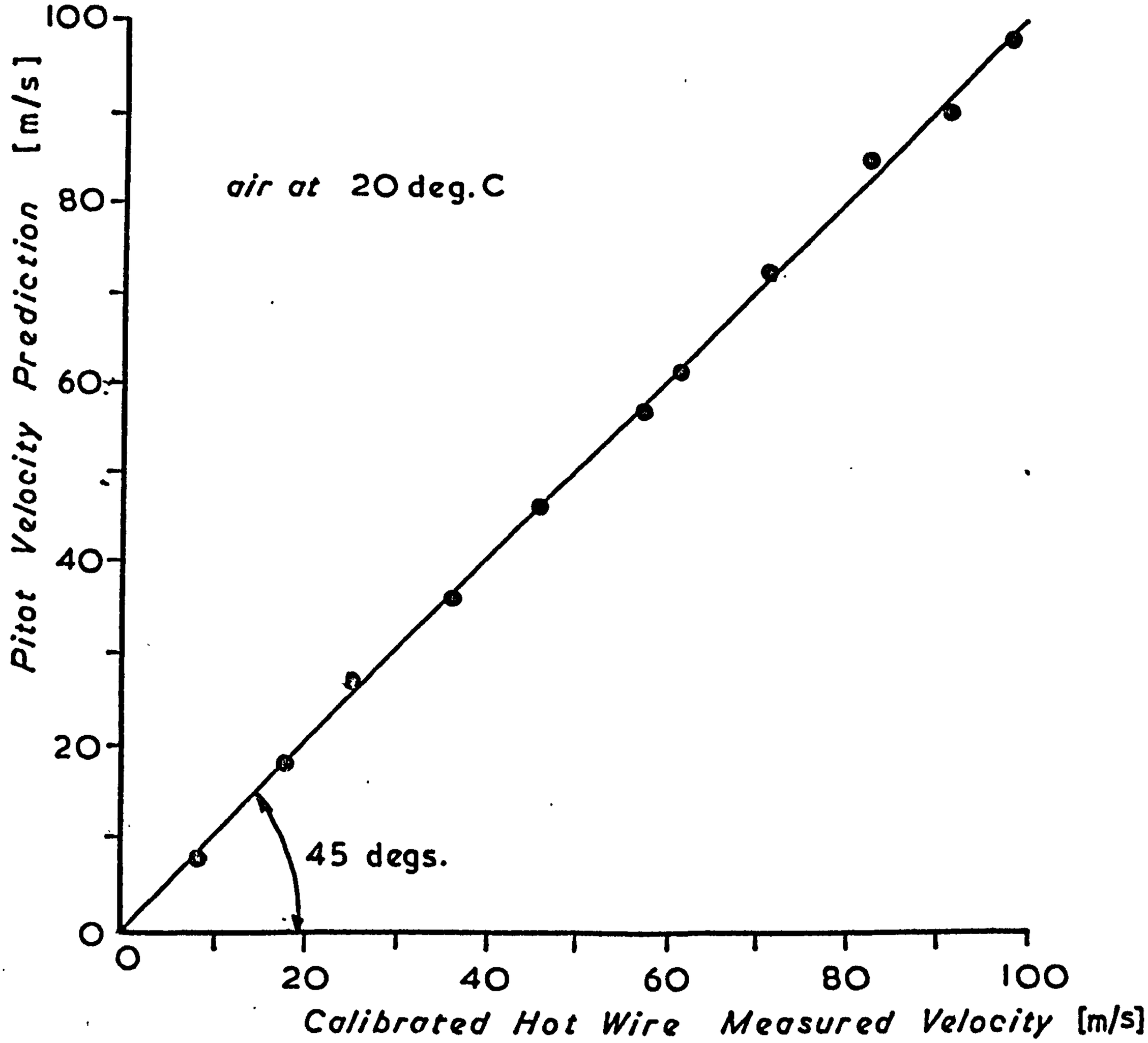

Comparison of Pitot Tube Test Section Velocity Measurement with an Independantly Calibrated Hot Wire Anemometer.

Fig. 4·8

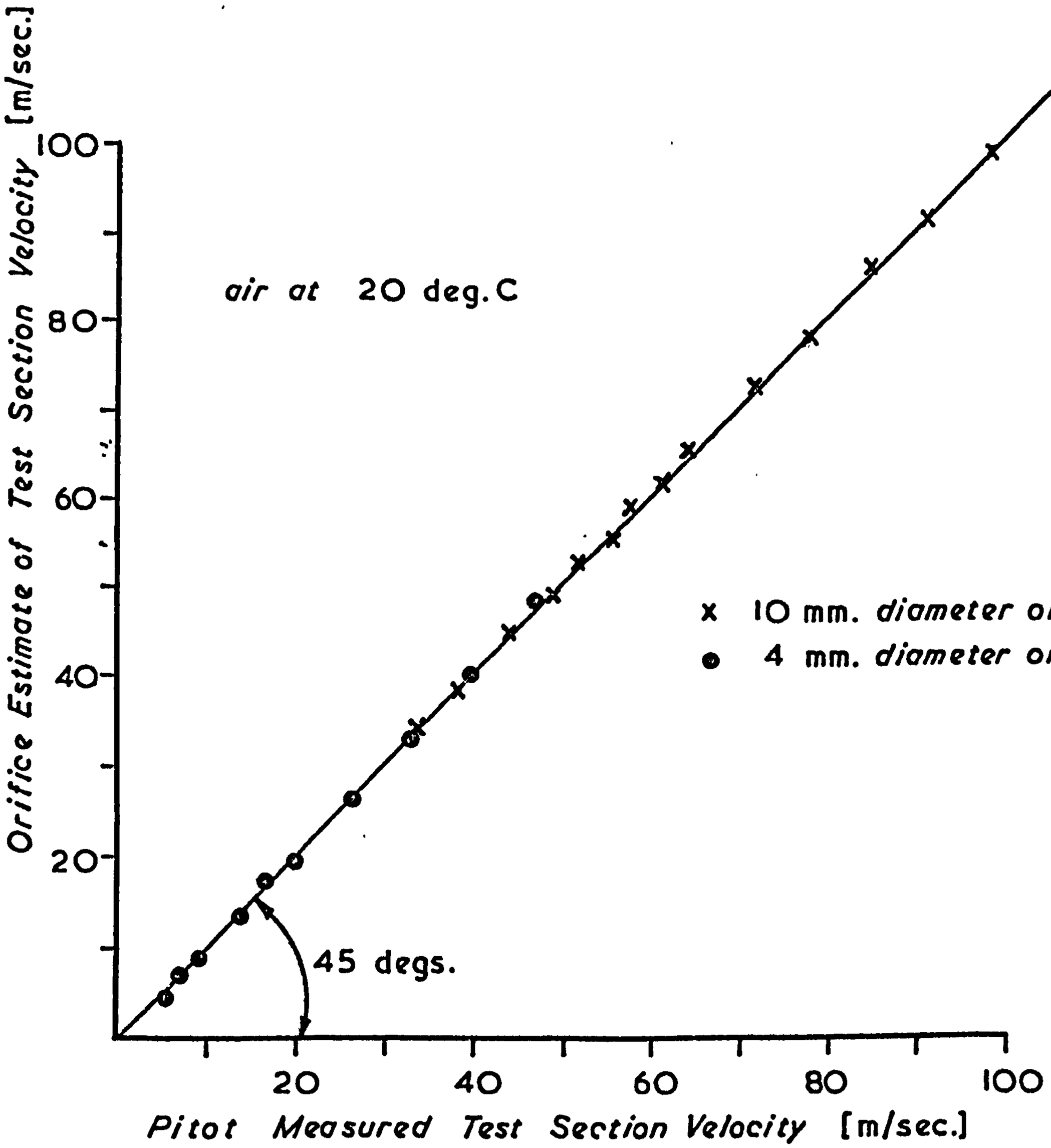

Comparison of the Pitot-Measured & Orifice-Predicted Test Section Velocity

Fig. 4.9

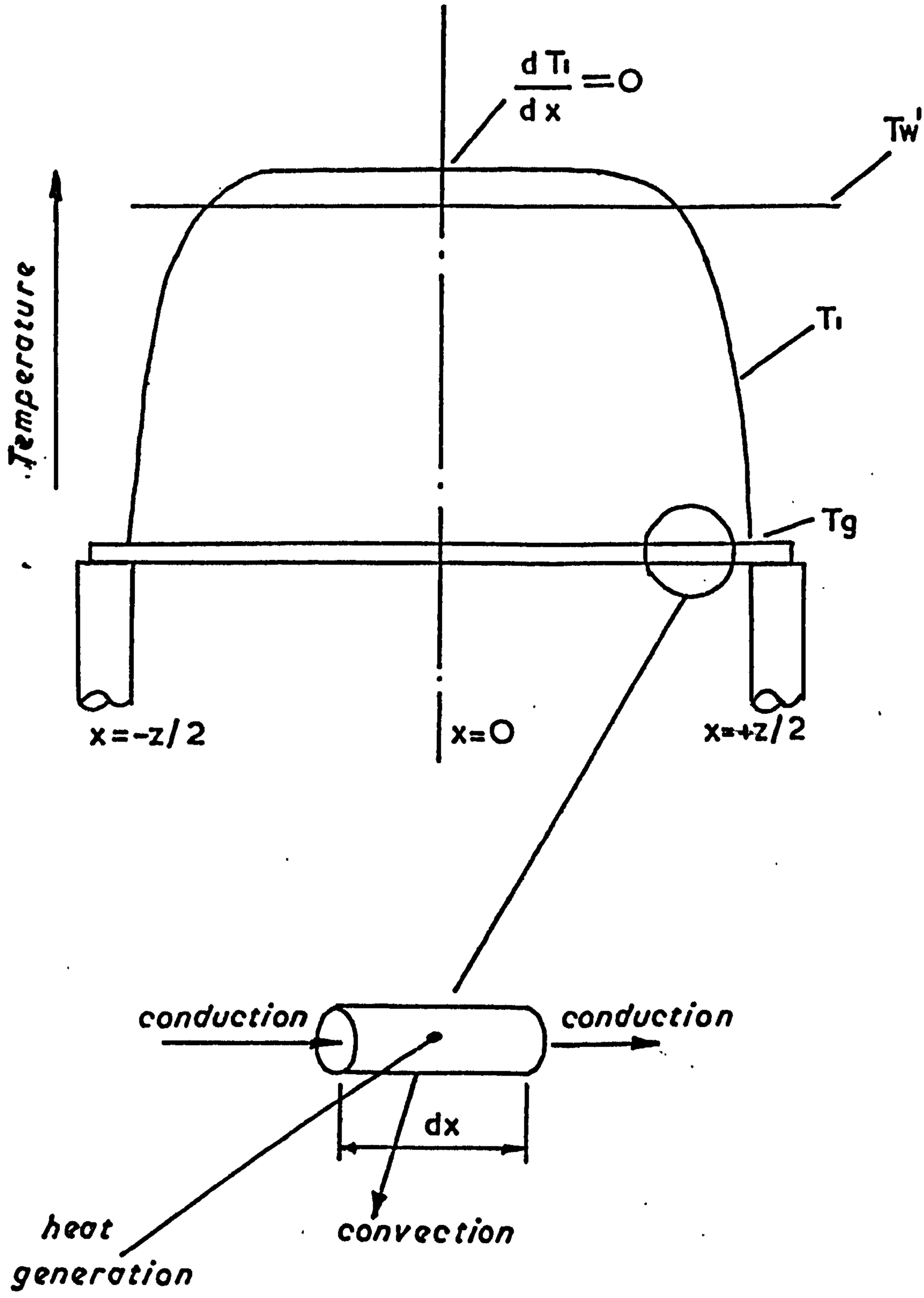

Geometry for the Calculation of
Wire Heat Transfer Coefficient

Fig. 4.10

Material	Temperature Coeficient [(deg.C)$^{-1}$]
Ir	0·00422
Pt-10% Rh	0·00158
Pt-20%Ir	0·000825
Pt-30%Ir	0·000680

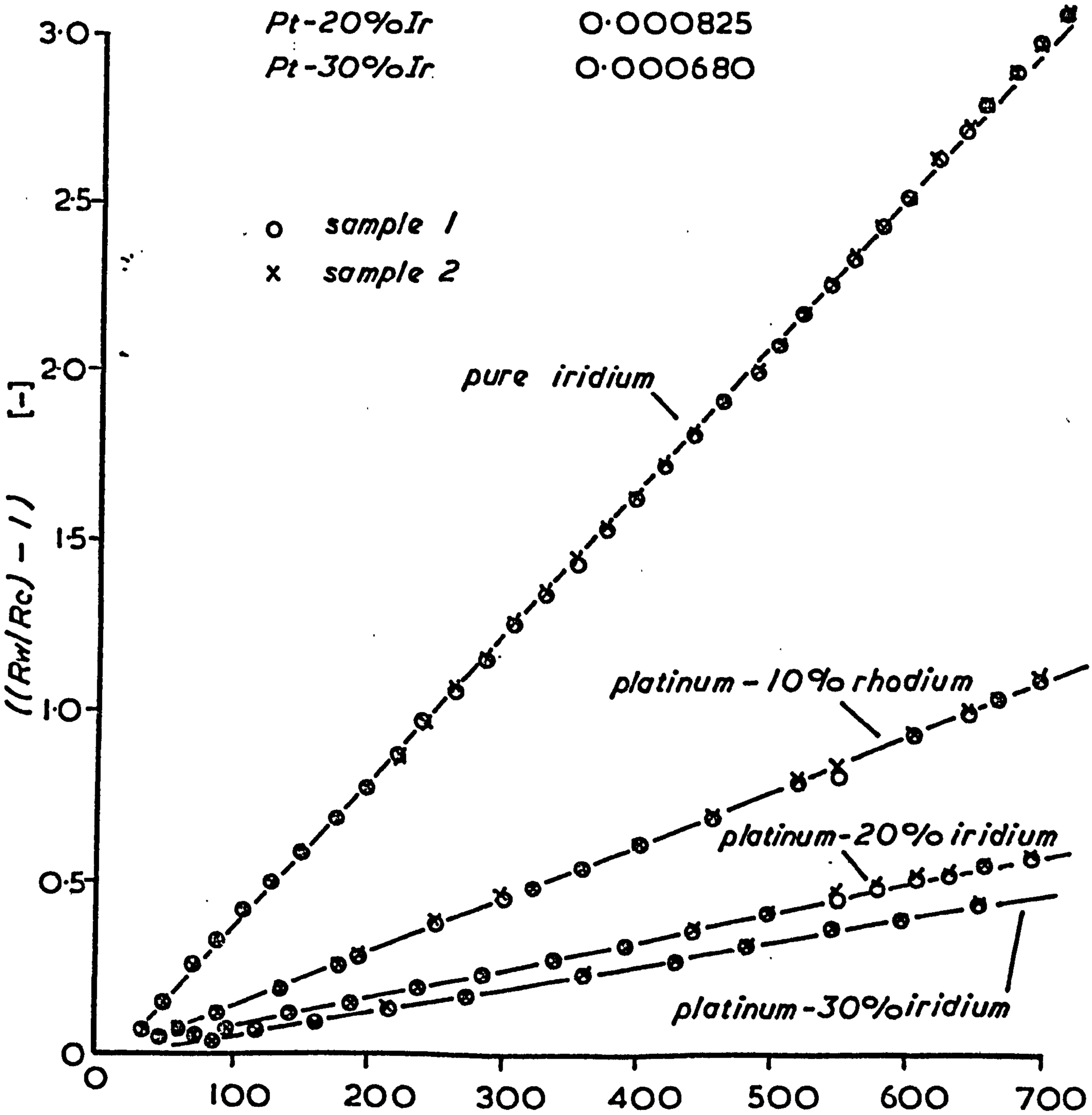

Experimental Resistance - Temperature Characteristics for various Wire Materials

Fig. 4·11

Effect of Operating and Hot Wire at Room Temperature Resistance

Resistance Values close to the Nominal Resistance

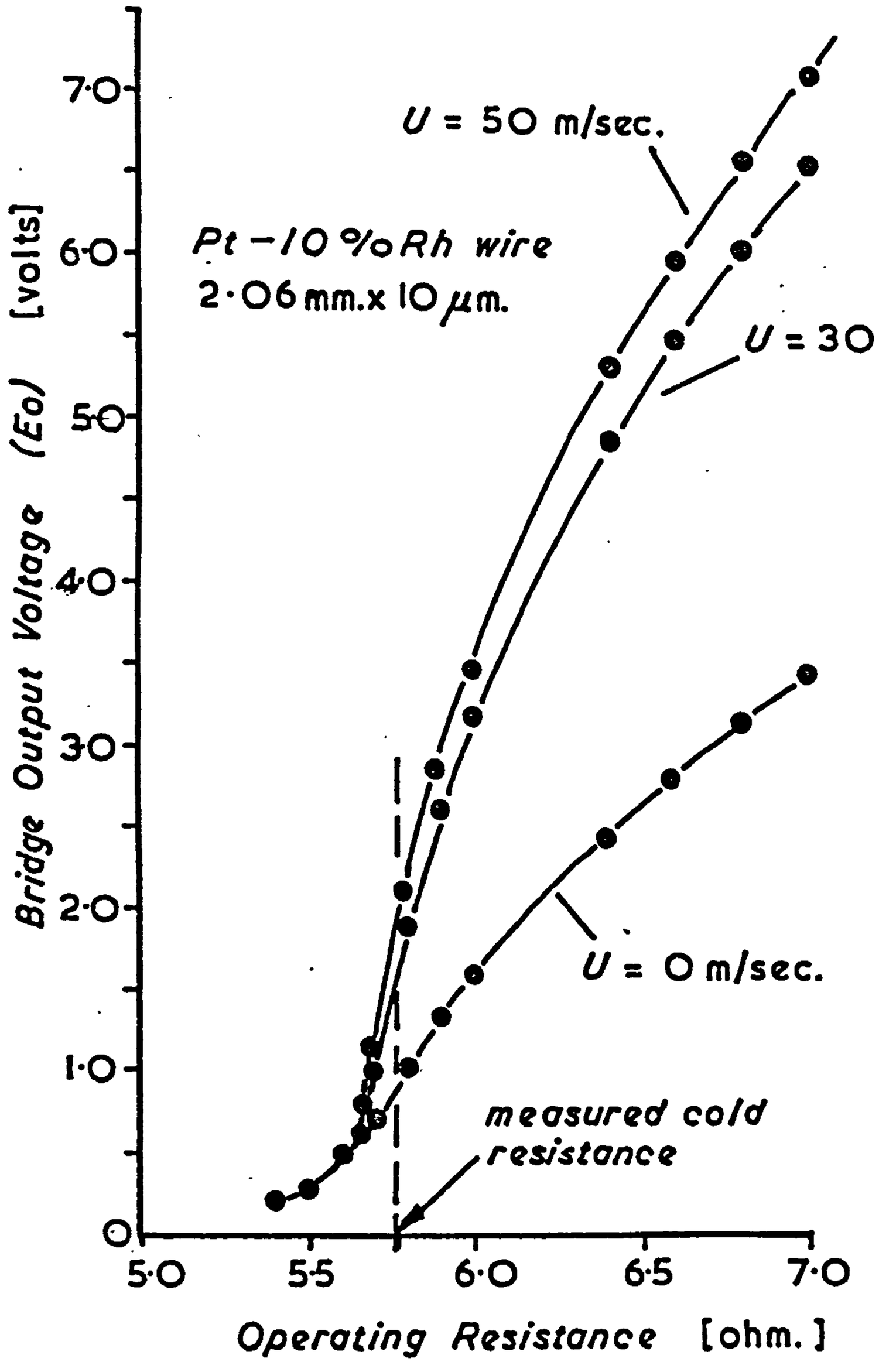

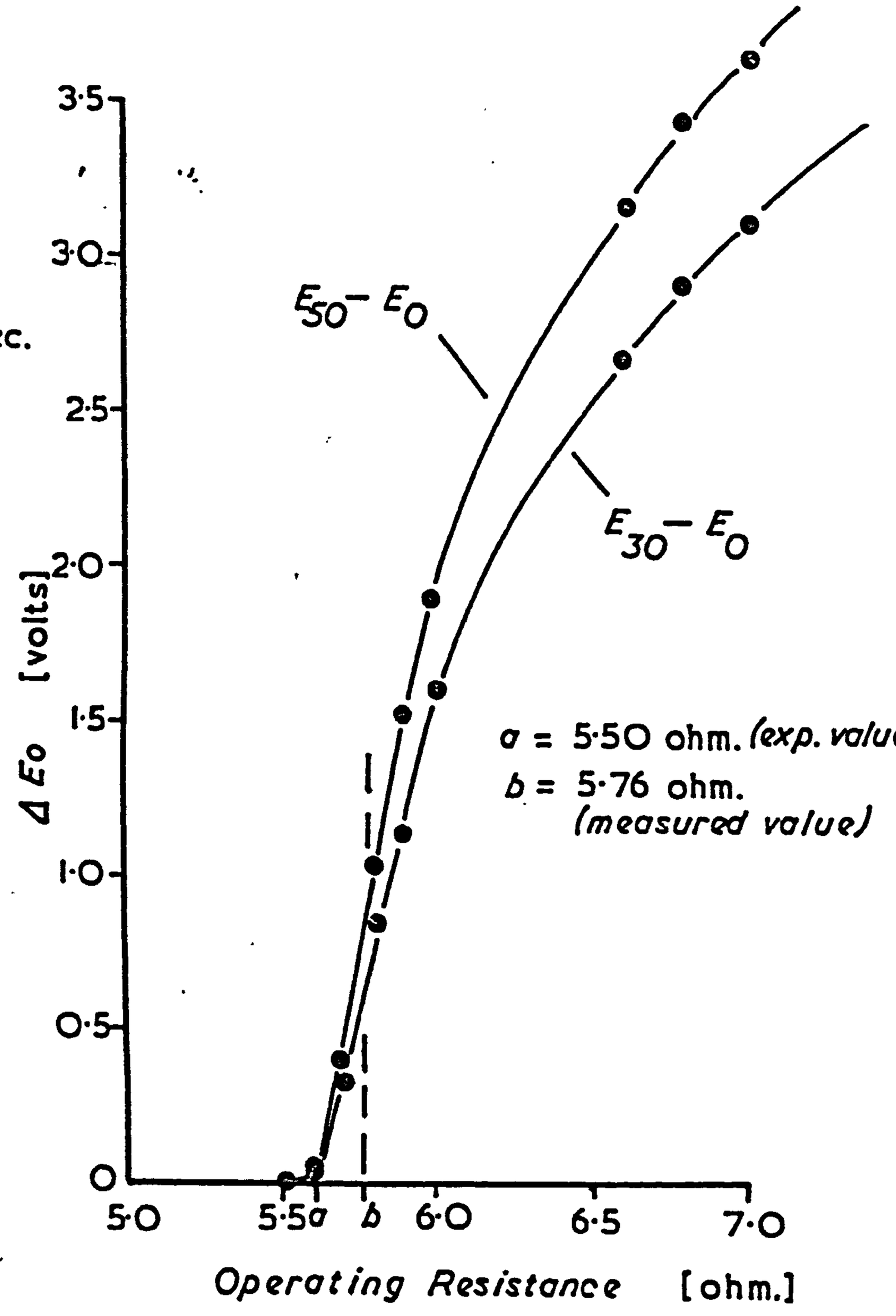

Fig. 4·12

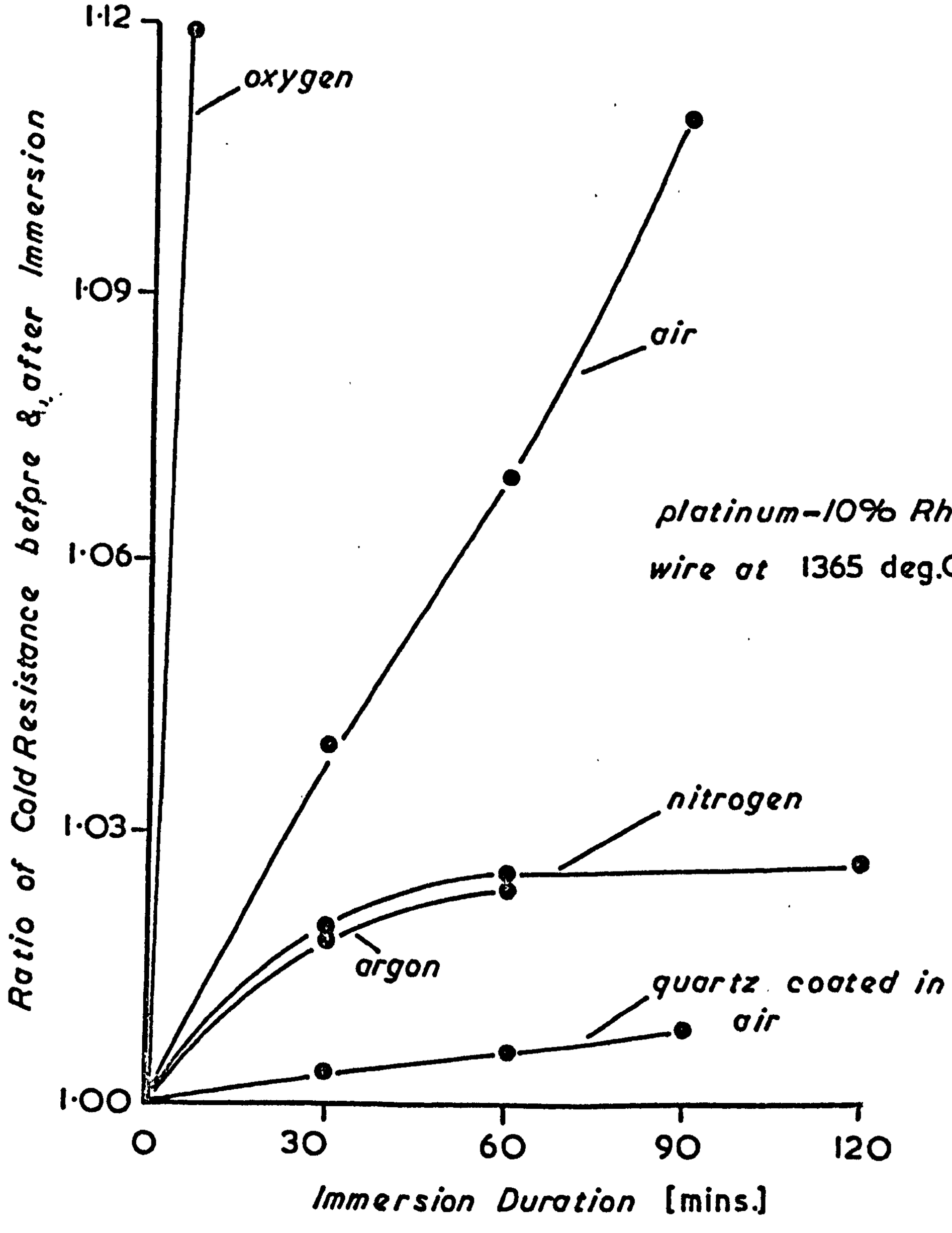

Change in Cold Resistance after Immersion in Various Gases at High Temperature

(Results due to Bradley & Entwistle [72])

Fig. 4·13

Surface Deterioration on an Uncoated Wire (X 2000)

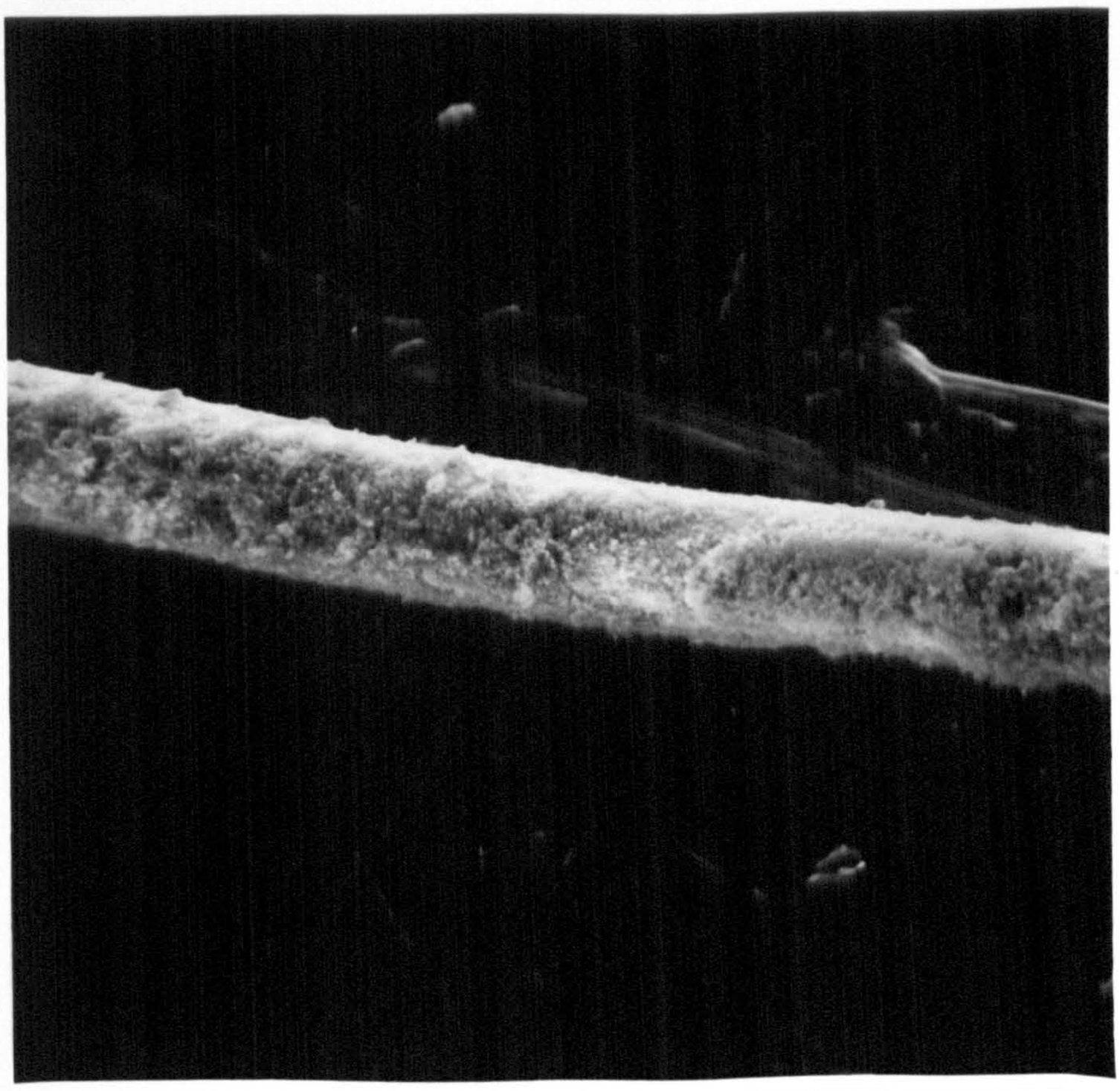

Quartz Coated Wire (X 2000 magnification.)

Fig. 4·14

Approximate Relative Suitability of Tracer Gases

K_2 evaluated at 500 deg. C

K_1 evaluated at 200 deg. C

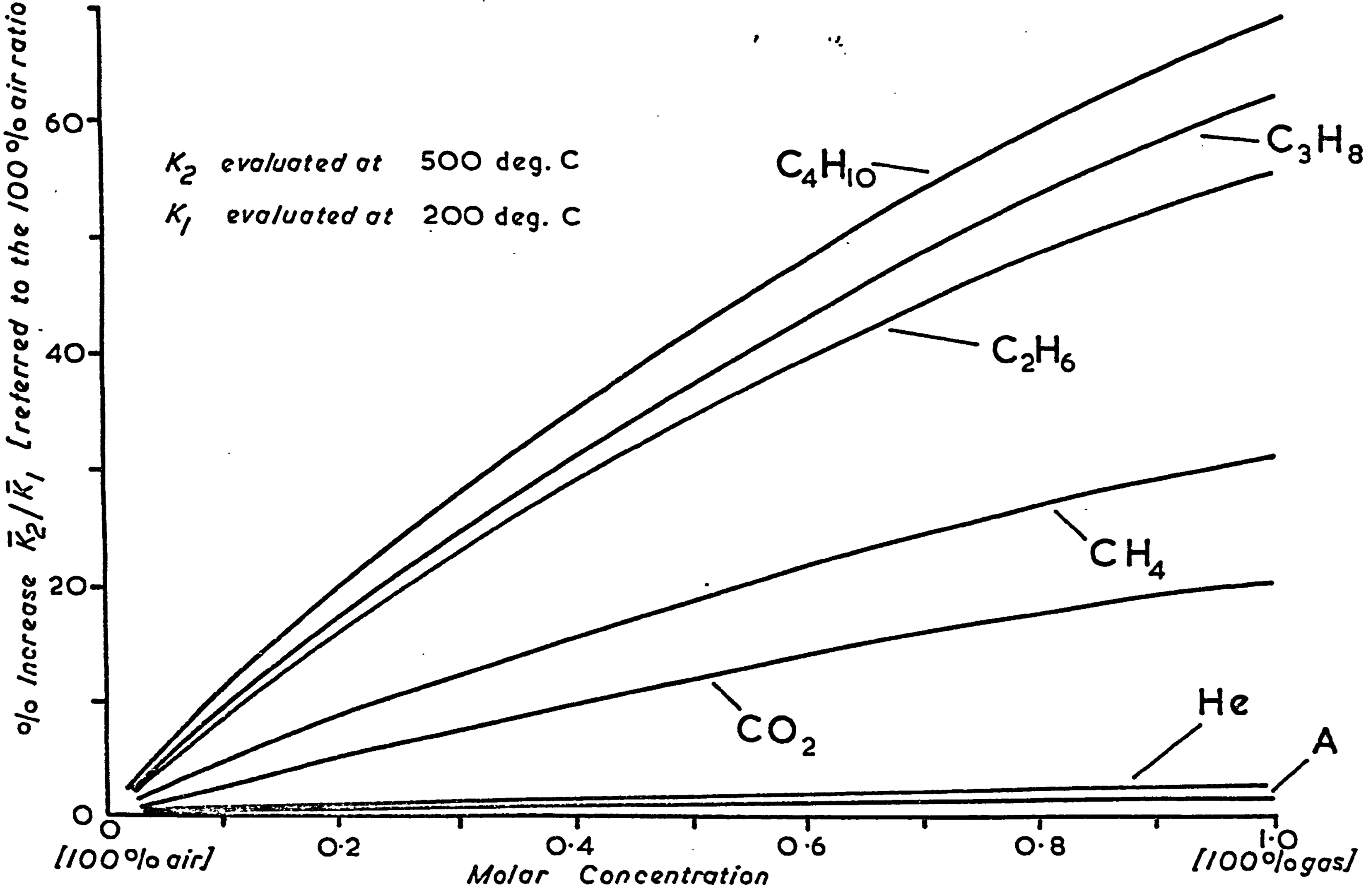

Fig. 4·15

Gases — Approximate Relative Suitability of Tracer

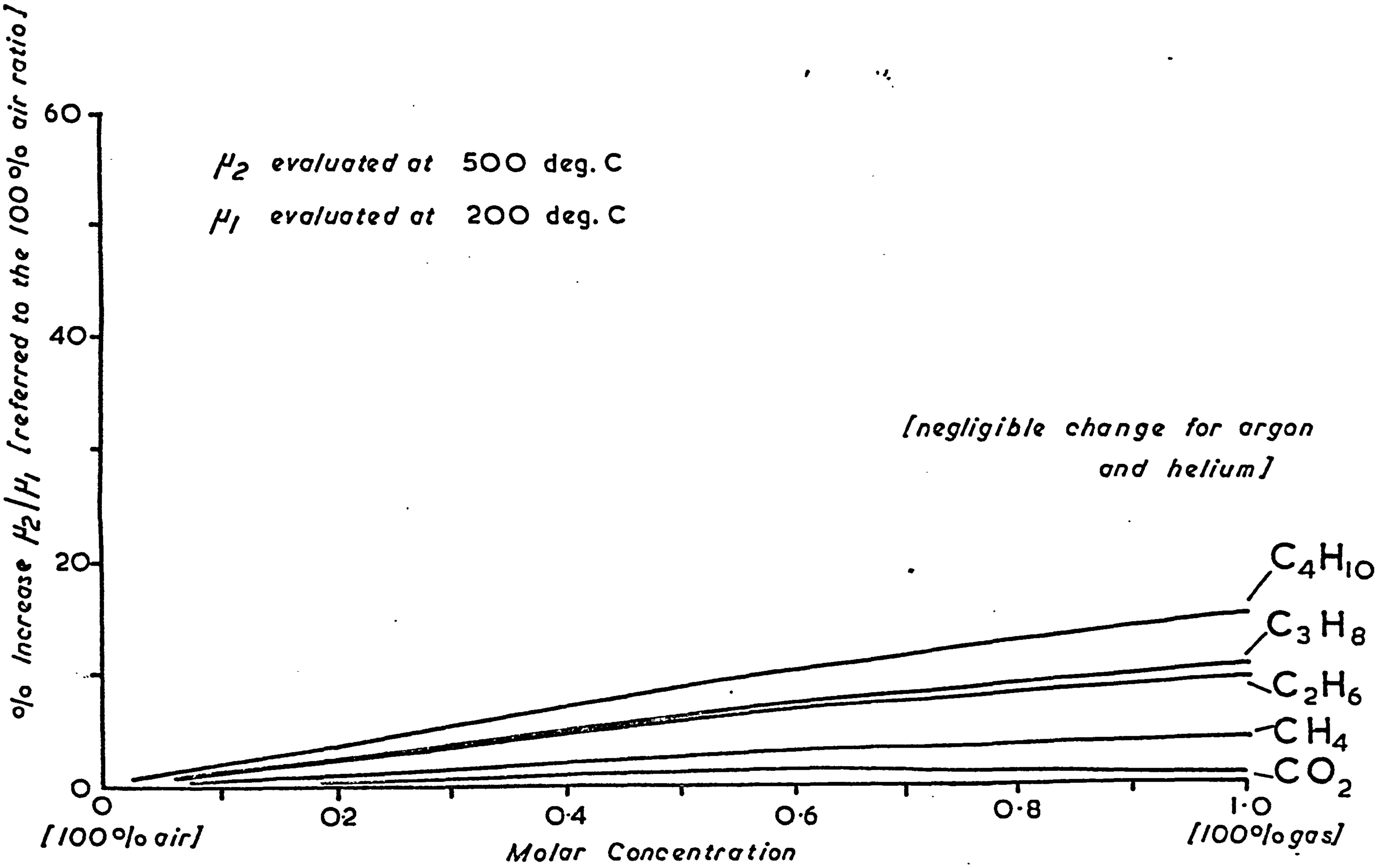

Fig. 4.16

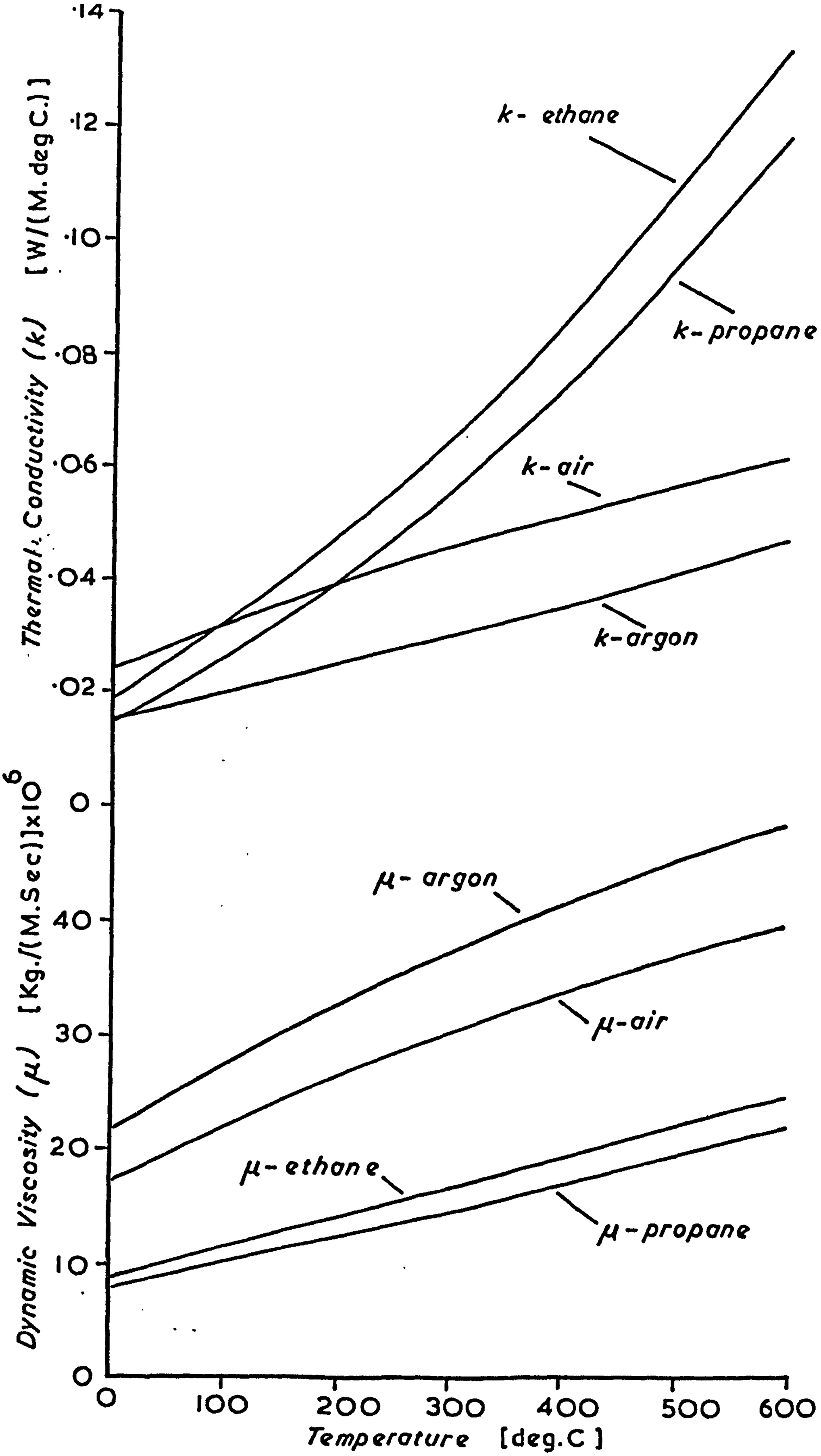

Gas Property Variation with Temperature

Fig. 4·17

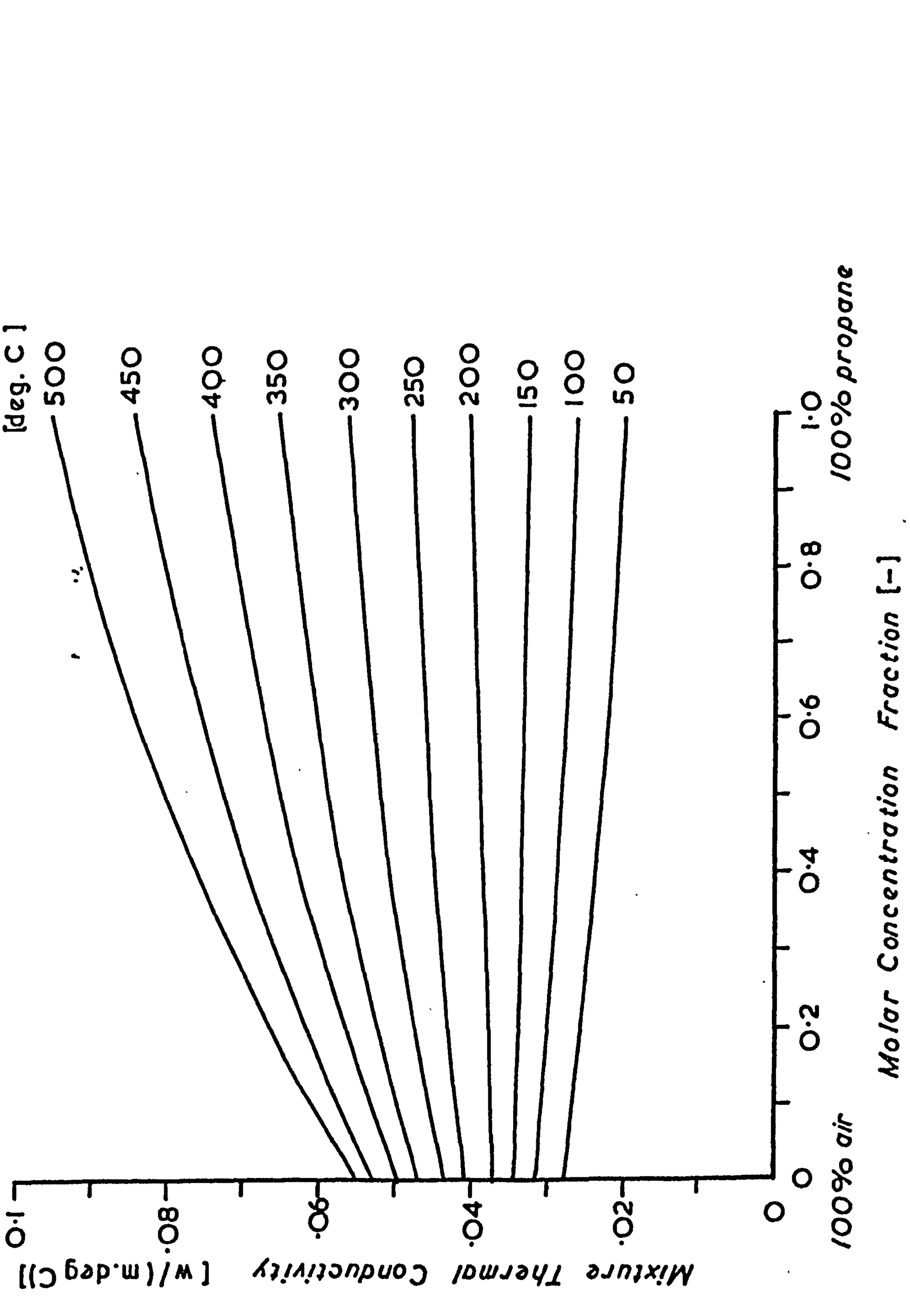

Variation of Mixture Thermal Conductivity for Propane - Air Mixtures.

Fig. 4·18

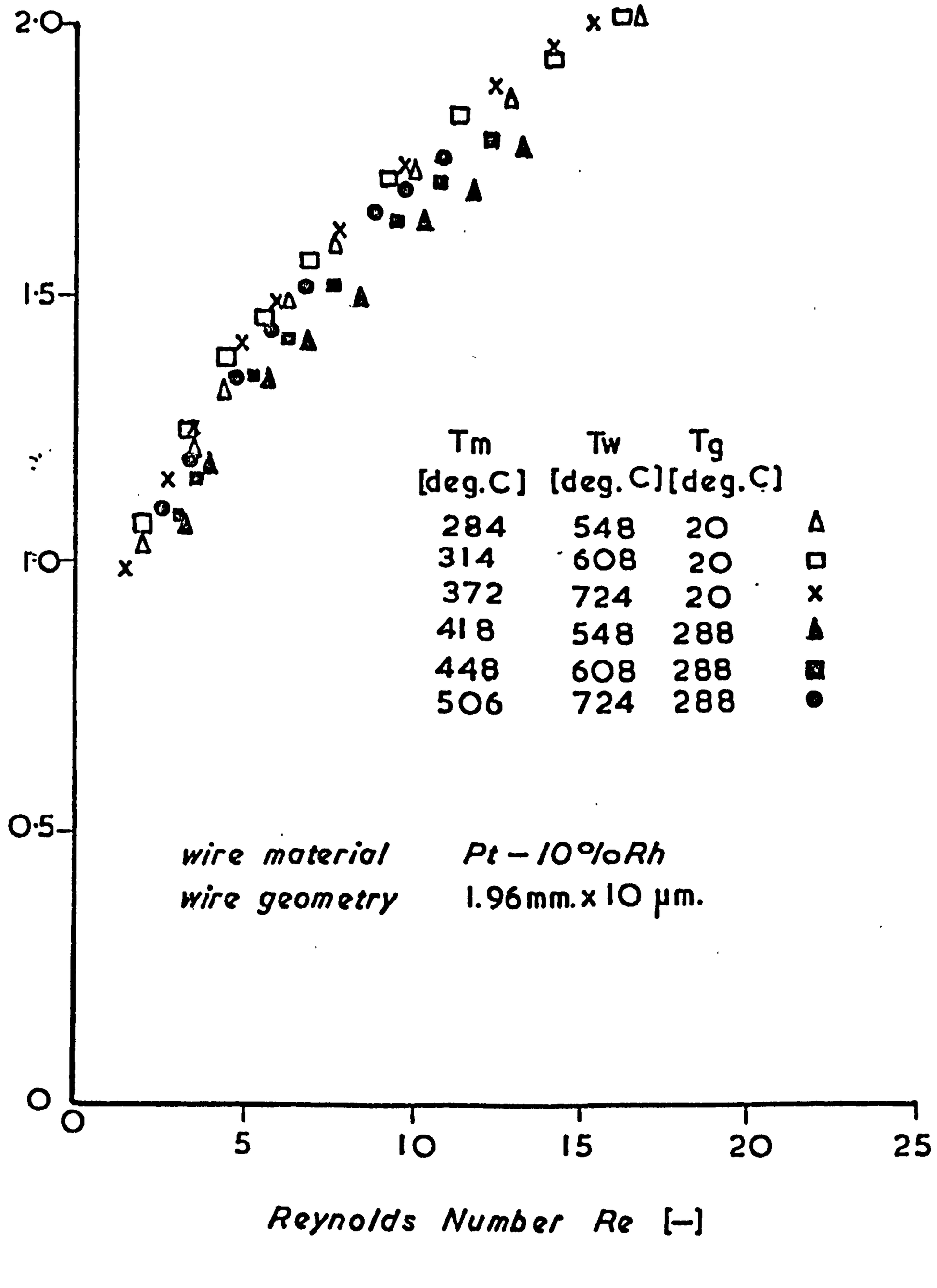

Data for a Single Wire Operating in Air

Fig. 4·19

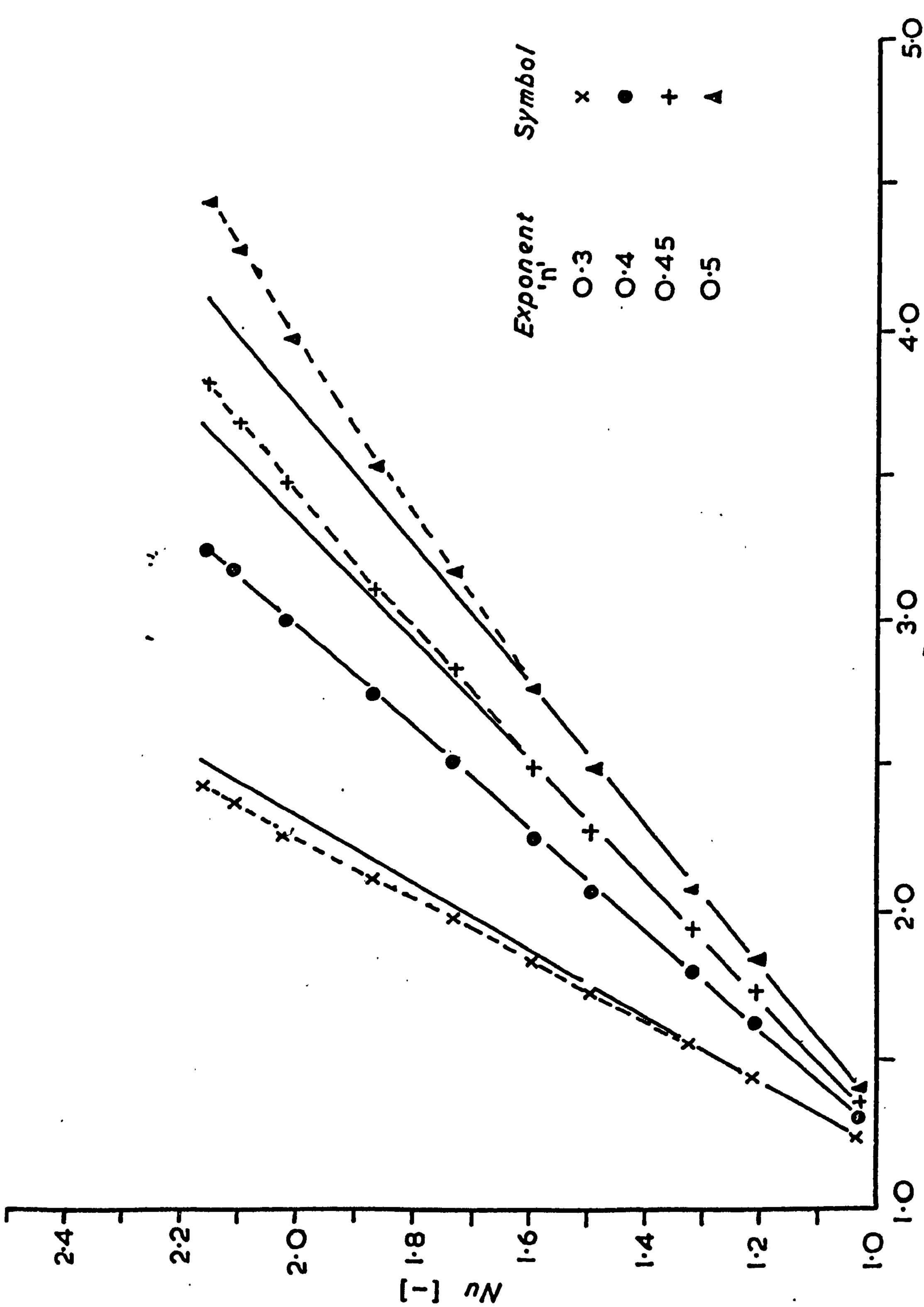

Linearising Effect of Various Reynold Number Exponents

Fig. 4·20

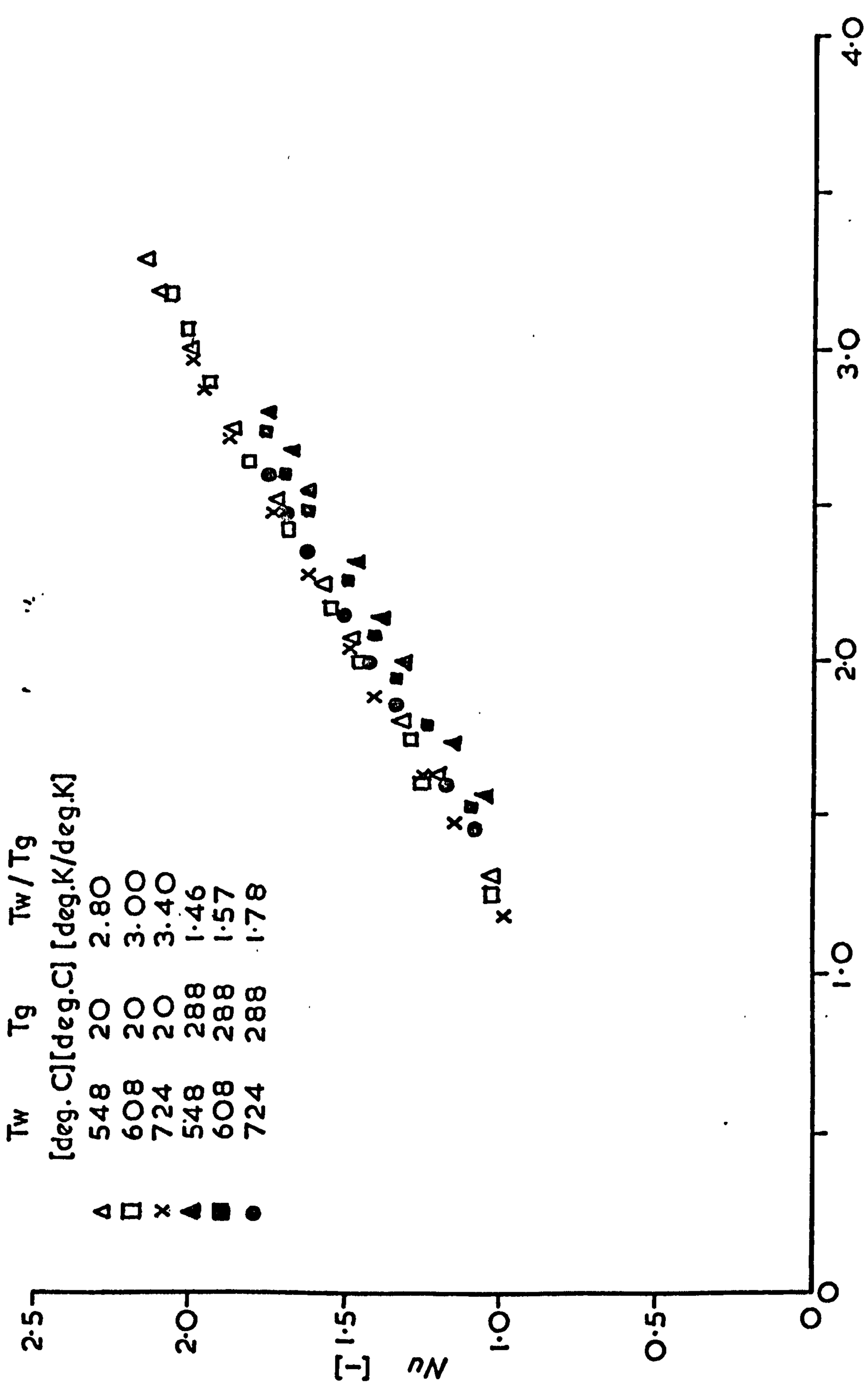

Illustration of the Systematic Deviation with Overheat Ratio

Fig. 4·21

Fig. 4.22

Typical Correlation of Data for a Single Wire Operating in Air

	Tw [deg.C]	Tg [deg.C]	Tm [deg.C]	$(Tm/Tg)^{-.12}$ [deg.K/deg.K]
△	548	20	284	·93
□	608	20	314	·92
x	724	20	372	·91
▲	548	288	418	·98
■	608	288	448	·97
●	724	288	506	·96

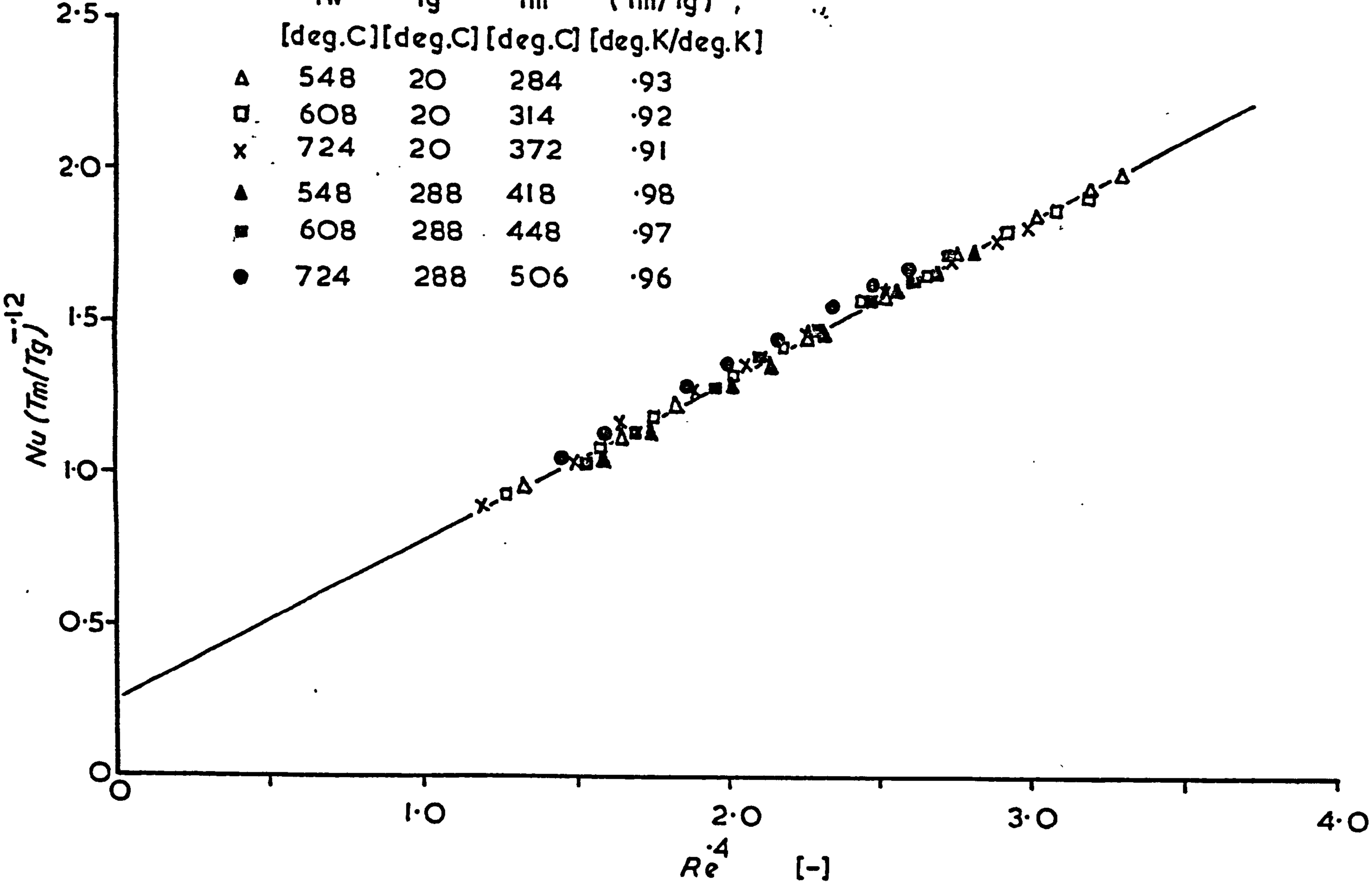

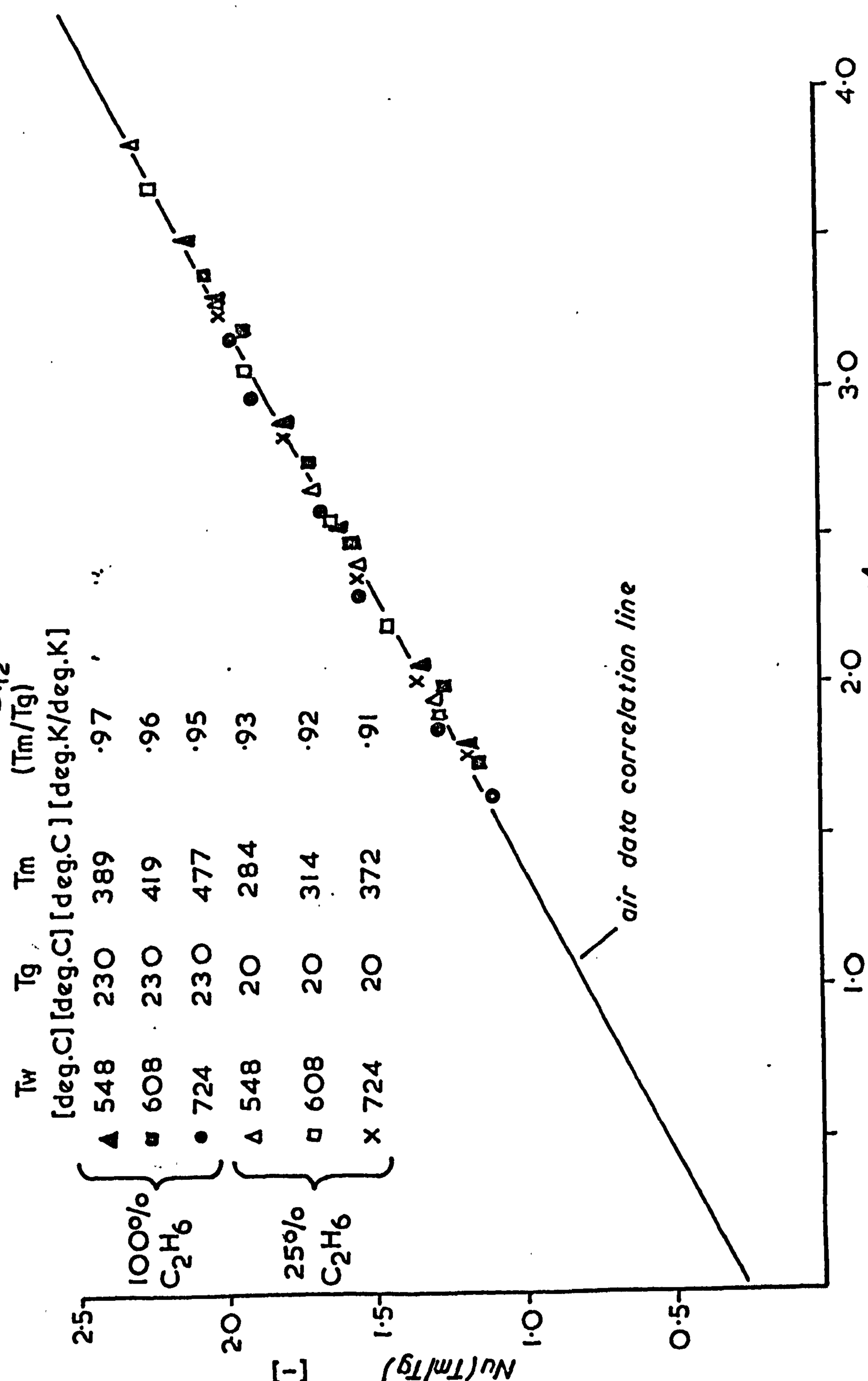

Typical Grouping of Ethane & 25% Ethane Data about the Corresponding Air Correlation Line

Fig. 4·23

Data for Hot Wires Operating in Air

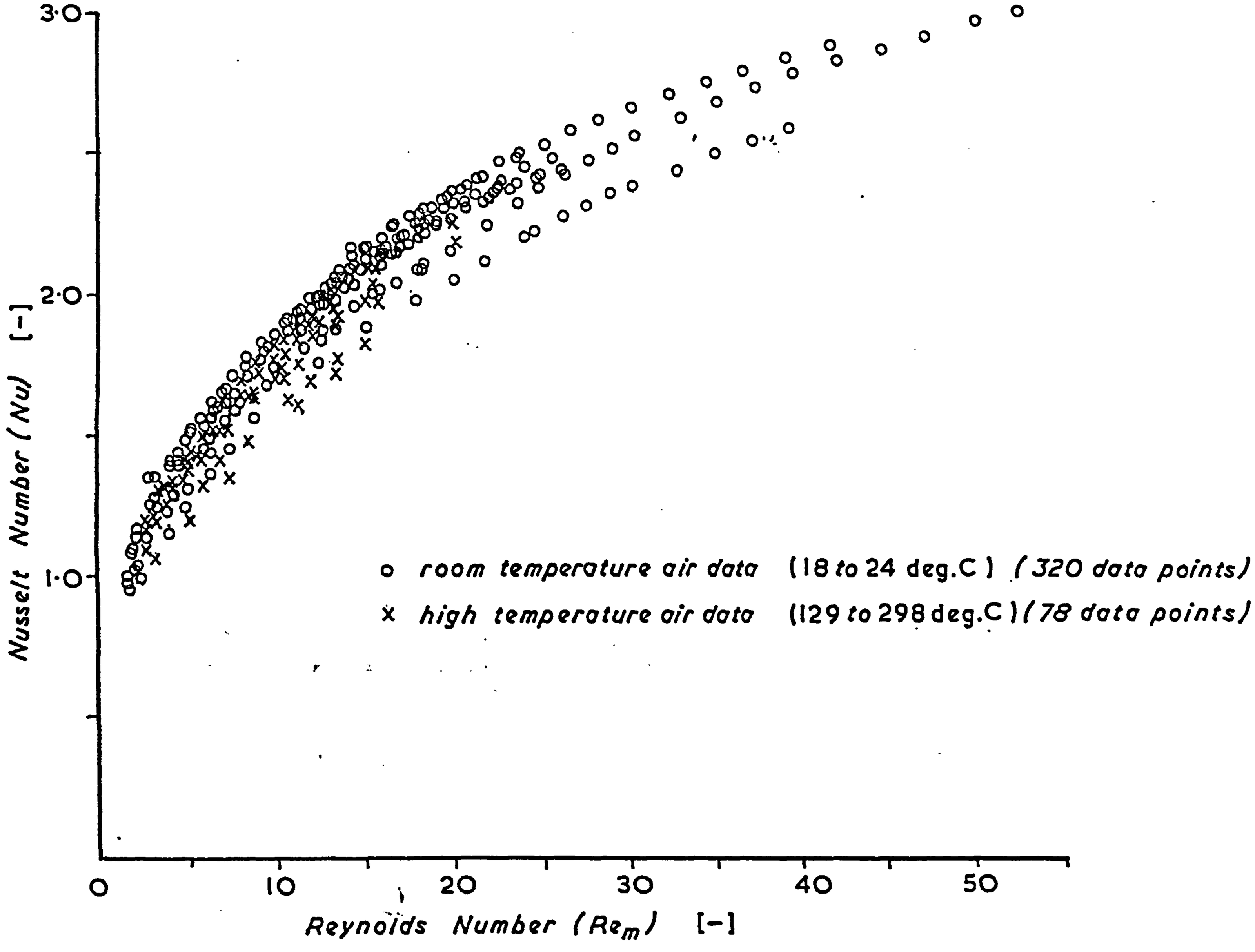

Fig. 4·24

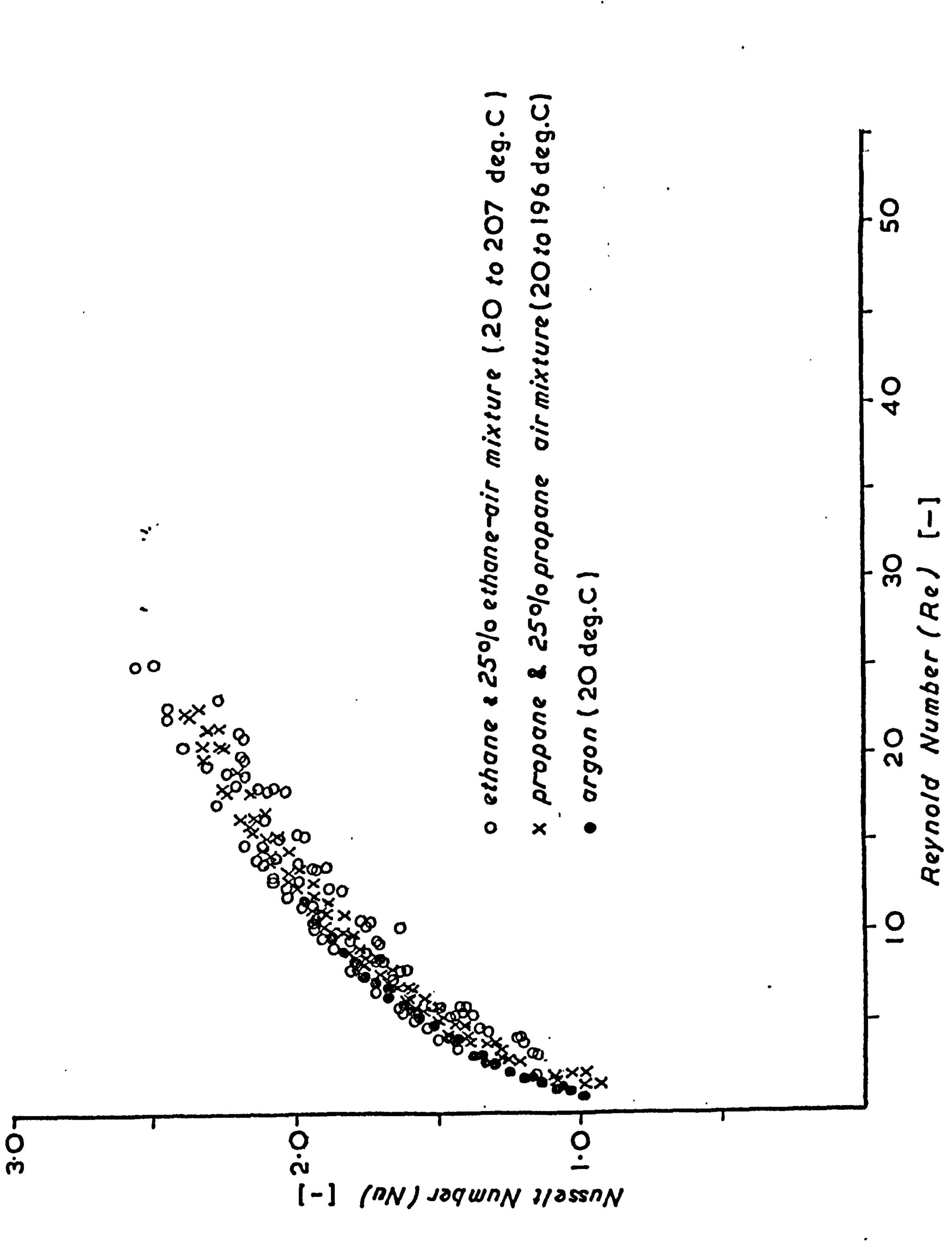

Data for Hot Wires Operating in Ethane Propane & Argon

Fig. 4·25

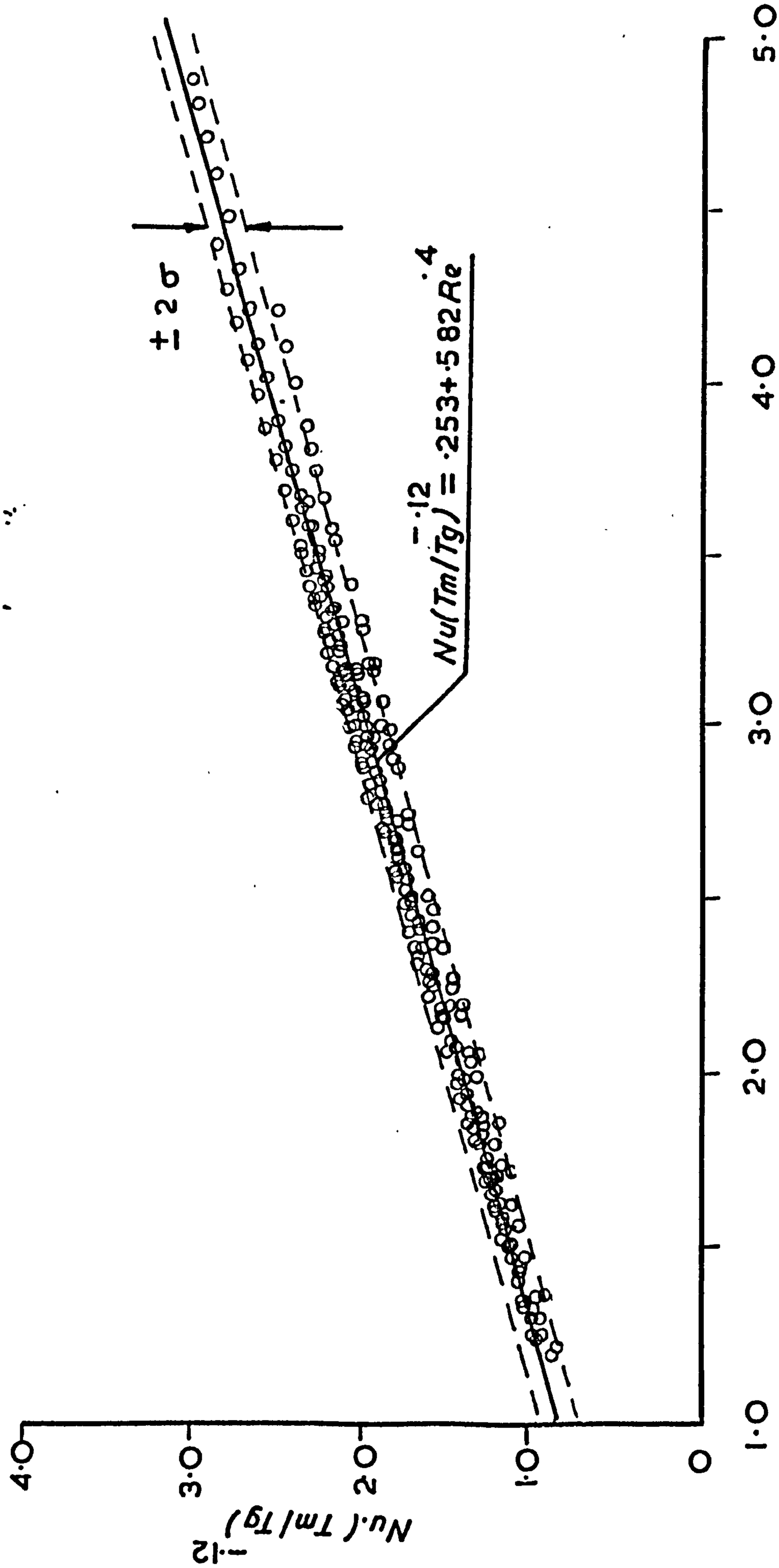

Ambient Air Data about the Mean Correlation Line for all the Data

Fig. 4·26

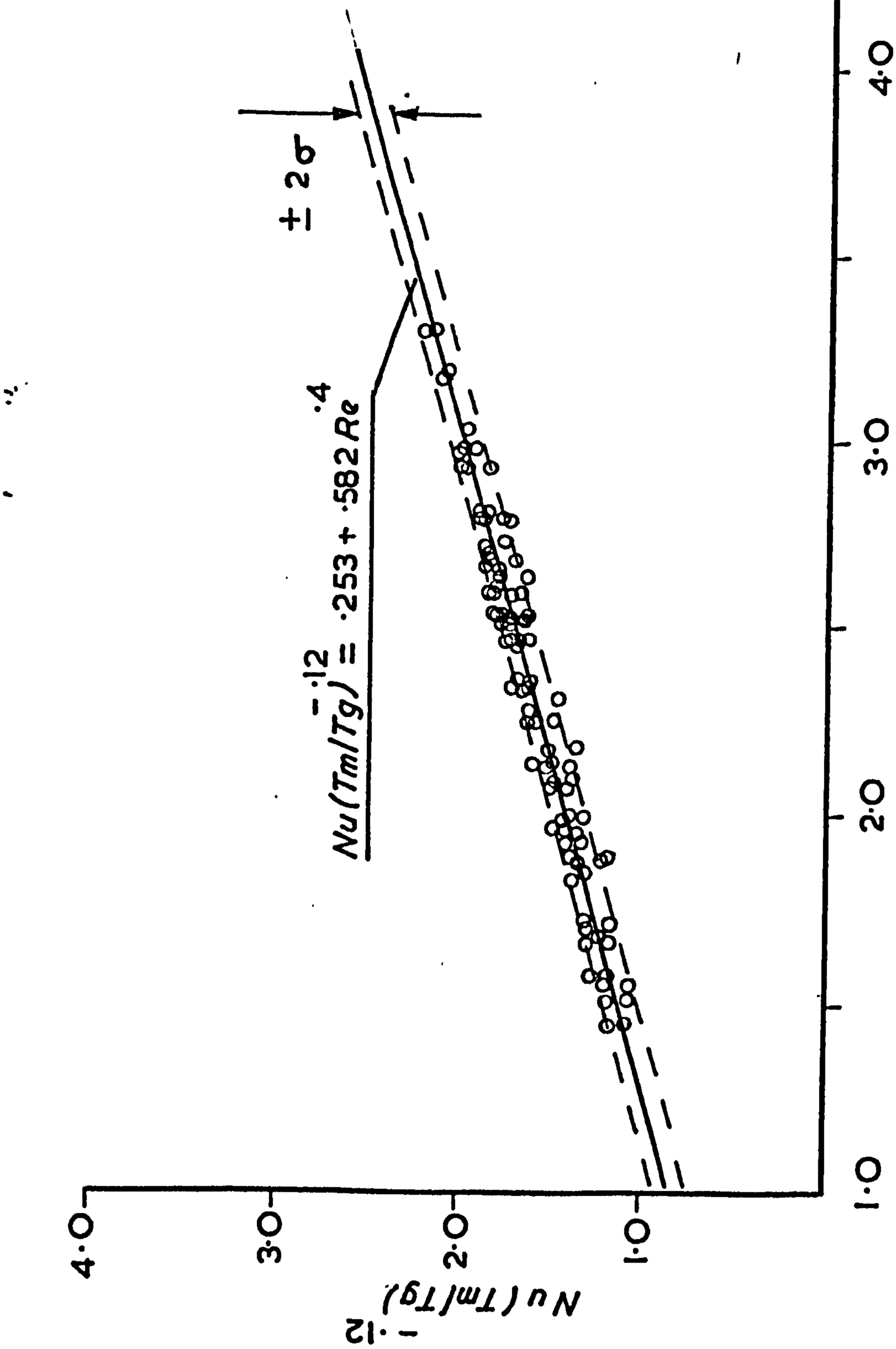

High Temperature Air Data about the Mean Correlation Line for all the Data

Fig. 4·27

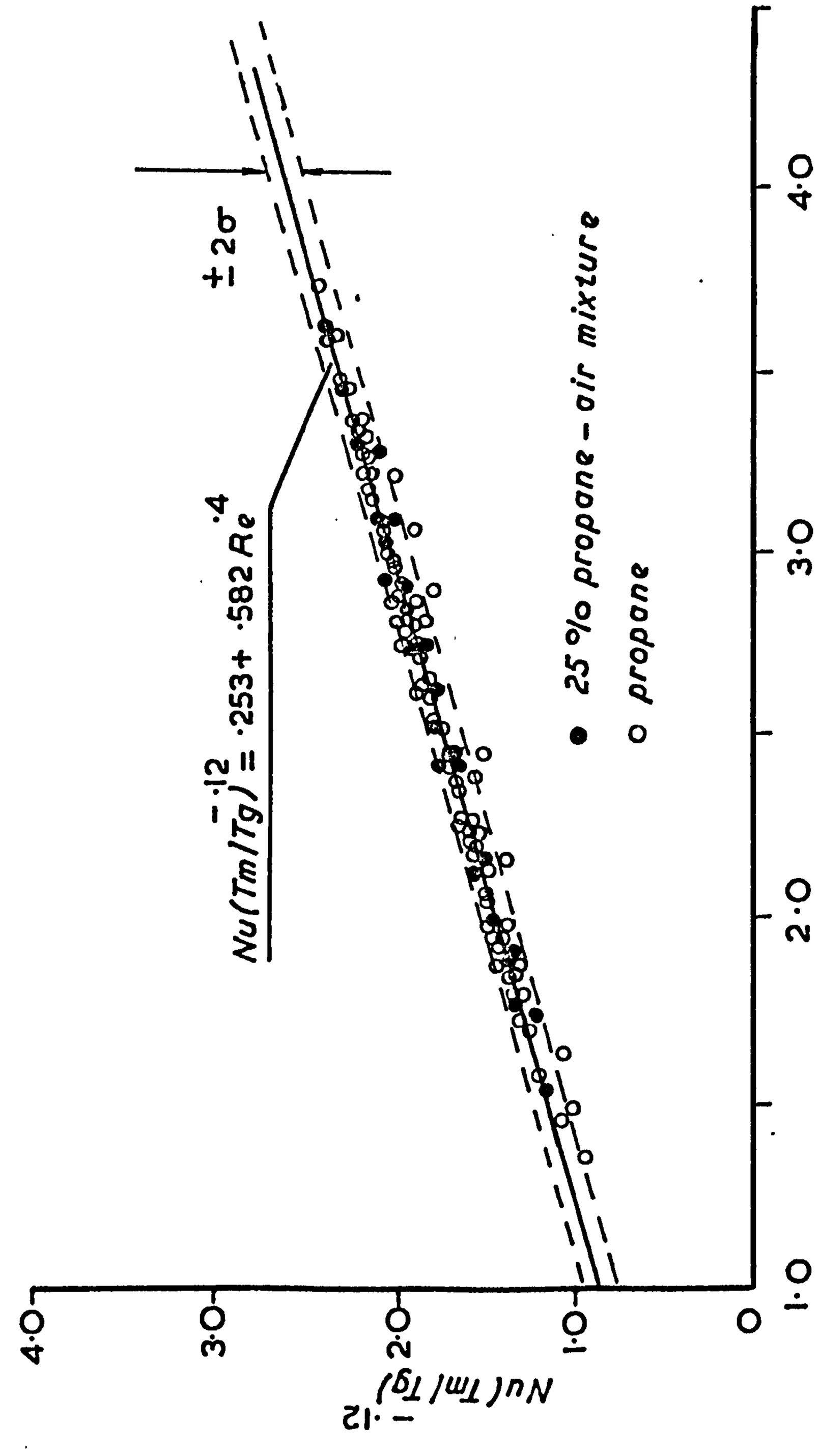

Propane & 25% Propane – air Mixture Data about the Mean Correlation Line for all Data

Fig. 4·28

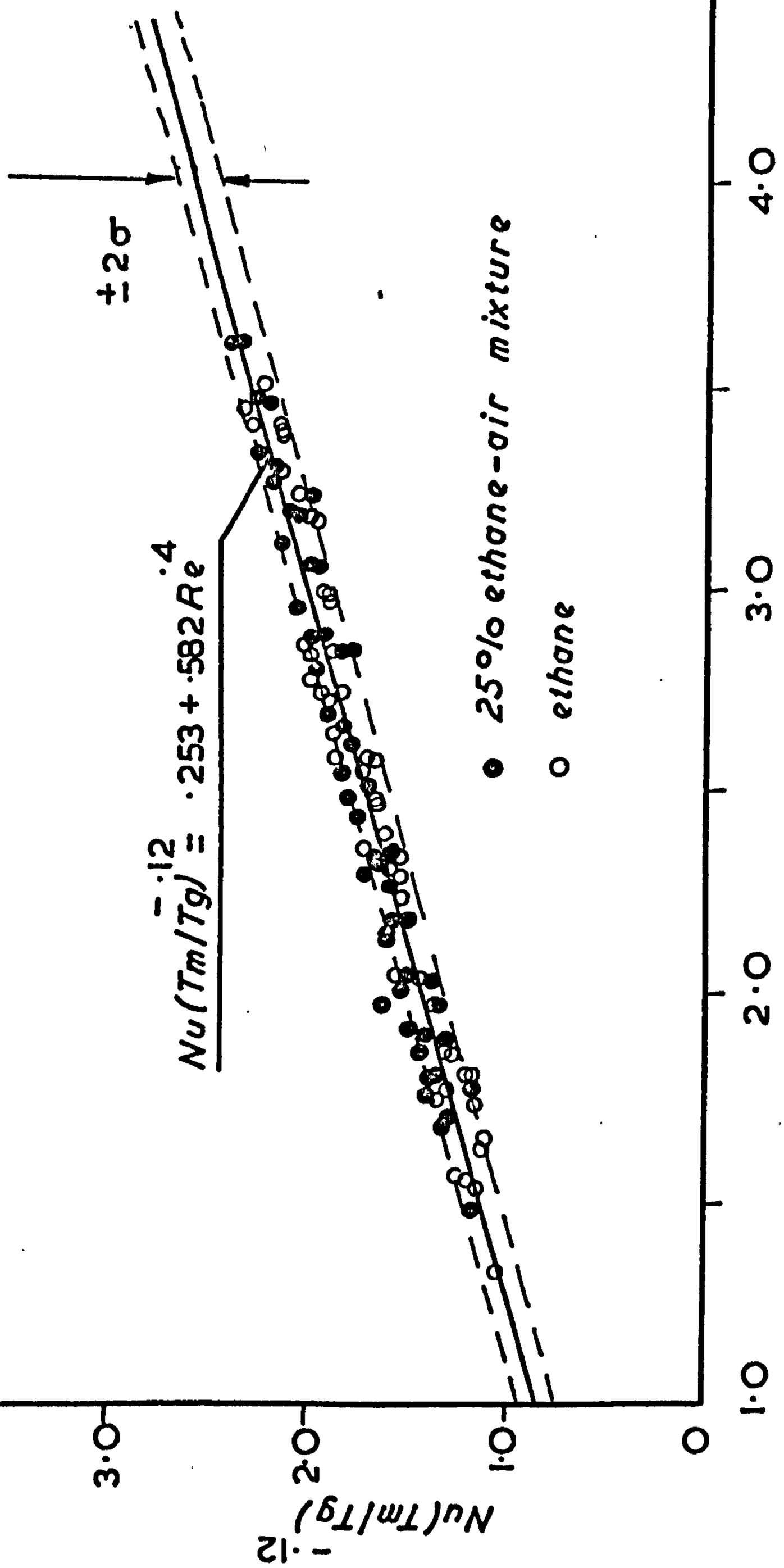

Ethane & 25% Ethane Air Mixture Data about the Mean Correlation Line for all Data

Fig. 4·29

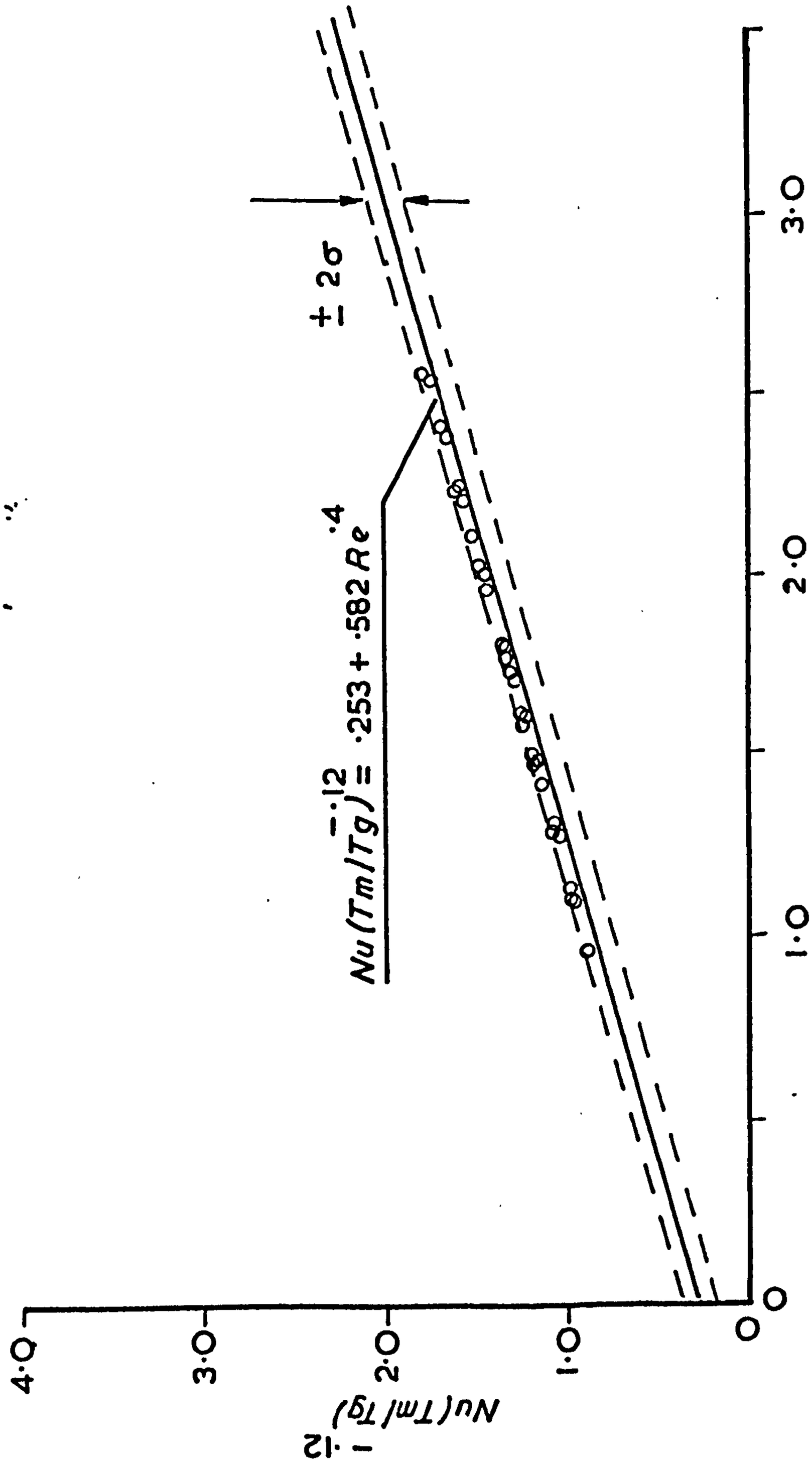

Argon Data (ambient temperature) about the Mean Correlation Line for all the Data

Fig. 4·30

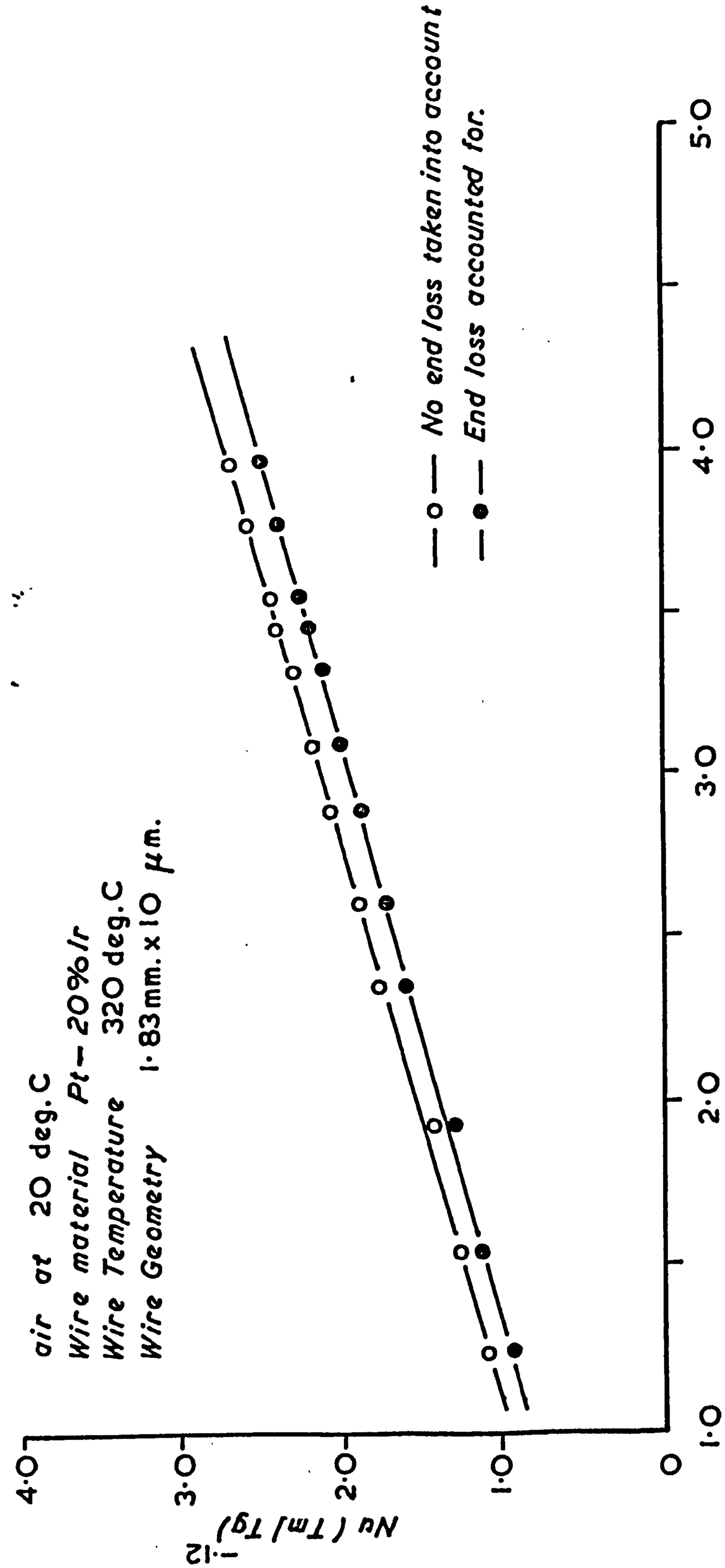

Comparison of Wire Heat Transfer Data with & without Calculated Conduction End Loss.

Fig. 4·31

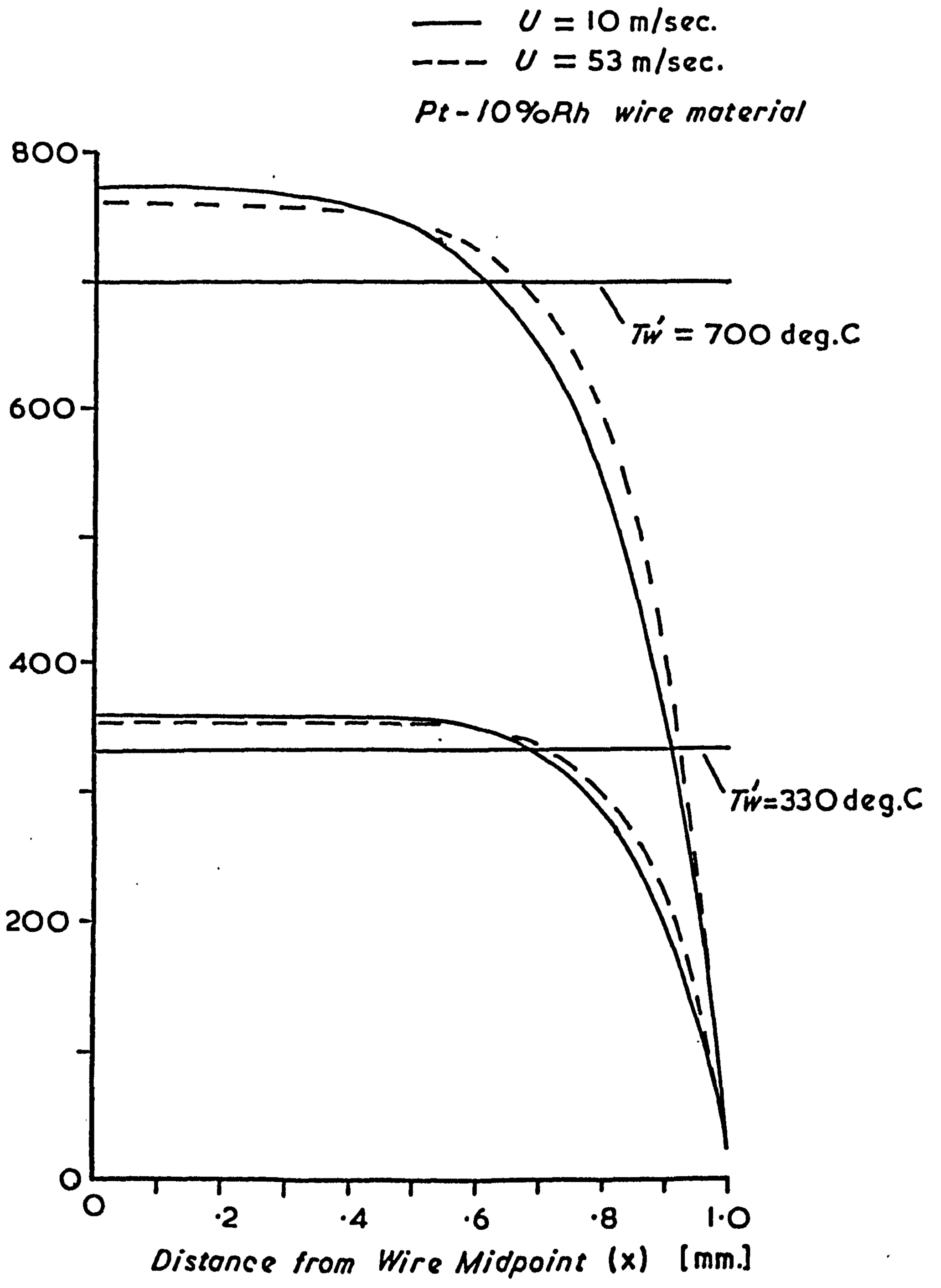

Typical Wire Temperature Profiles at Ambient Gas Temperature

Fig. 4·32

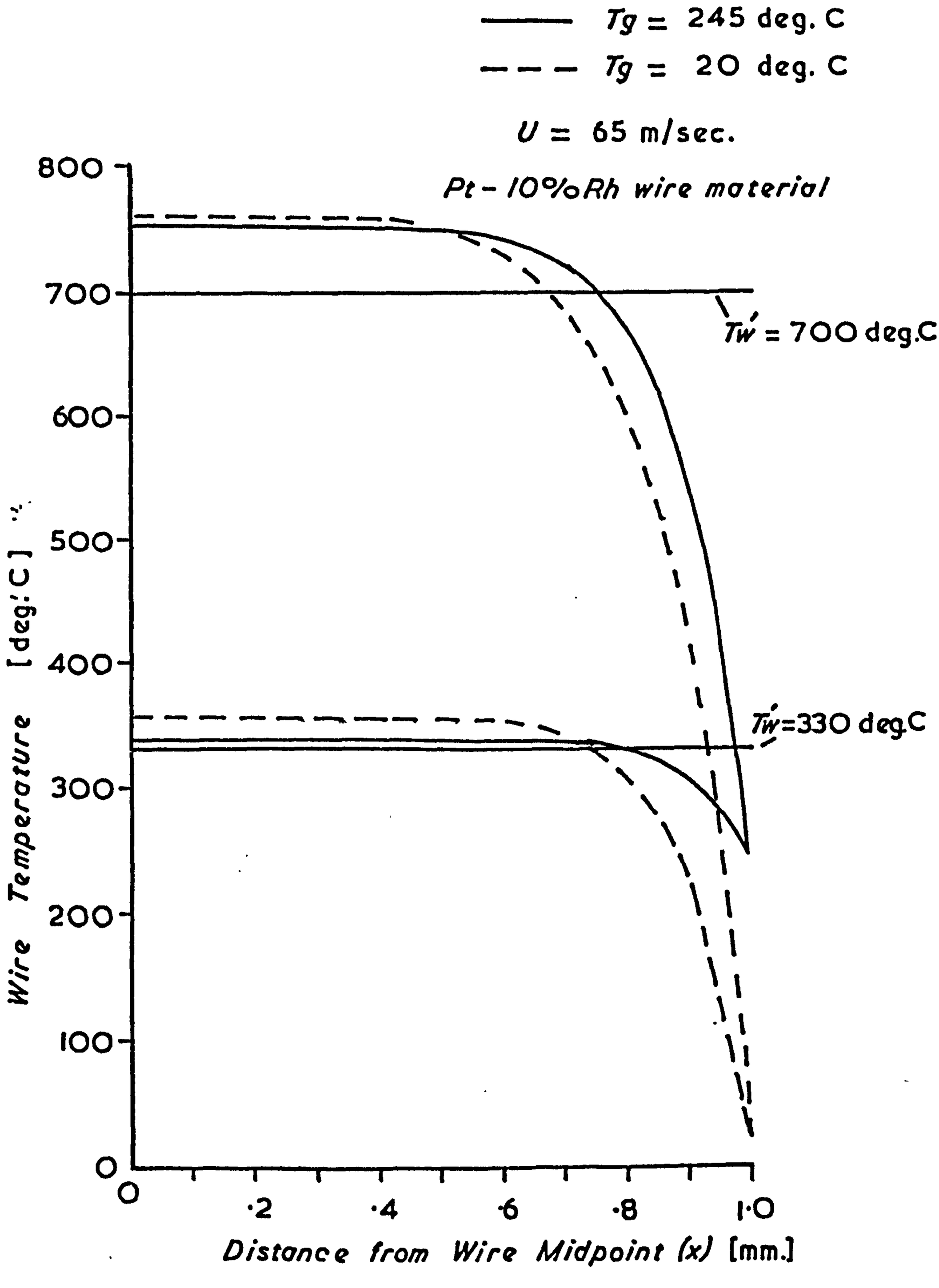

Comparison of Wire Temperature Profiles at High and Low Gas Temperatures

Fig. 4·33

Tw/Tg	Individual Wire Data Scatter(%)		General Correlation: Seperate Wire Correlation Deviation from the mean Correlation Law(%)	
	Room Temp. Data	High Temp. Data	Room Temp. Data	High Temp. Data
1·23	± 0·42	± 6·79	± 10·46	± 12·47
2·68	± 0·31	± 1·8	± 4·8	± 5·2

Component Errors :-

Output Voltage ± 0·5 % Wire Length ± 0·05 mm.

Temperature Coefficient ± 6·25 % Cold Resistance ± 3·0 %

High Gas Temperature ± 2·2 %

Typical Error Magnitudes on Nusselt Number

Fig. 4·34

CHAPTER 5

Development of the Binary Gas Concentration Measurement Technique

5.1 Validation of the Concentration Sensitive Function

The empirical correlation of heat transfer data, or the ability to describe the characteristics of a single wire in the form of equation (4.36) regardless of gas type, allows application of the concentration dependent function of equation (4.23). The form of the correlation equation indicates that re-arrangement results in the following function which is independent of velocity (section 4.5.2):-

$$F(\chi) = 0 = \{Nu_1 (\frac{Tm_1}{Tg})^{-.12} - A_1\} - \{Nu_2 (\frac{Tm_2}{Tg})^{-.12} - A_2\} \cdot \frac{B_1}{B_2} \{\frac{\bar{\rho}m_1 d_1}{\bar{\rho}m_2 d_2} \frac{\bar{\mu}m_2}{\bar{\mu}m_1}\}^{0.4}$$

..... (5.1)

Figure (5.1) shows data plotted on this basis, for a probe having two parallel non-interferring wires, operating in the flow calibration rig of figure (4.5) where concentration level is known and hence the gas properties may be computed by equations (4.29) (4.30) (4.24)(4.25) at the respective film temperatures. The data represented extends over the velocity range 10 m/s to 82 m/s and the function is therefore shown to be independent of velocity.

Computation of concentration level from two bridge outputs for a probe placed in an unknown concentration flow field therefore requires the reverse process. Namely, from the two heat transfer correlating equations, and recorded voltage levels, the concentration magnitude to obtain zero value of the function (equation 5.1) has to be determined. This has been achieved by computational methods using the iteration subroutine as developed for the calculation of wire heat transfer coefficient from equation (4.15). The actual iteration techniques for the two ceses are therefore identical although the external function form and solution variable are different (Appendix B). Computational details are involved and in order to avoid distraction from the main points of the technique are described later in section (5.7).

Of prime importance is the manner in which the function of equation (5.1) provides sensitivity to concentration.

Figure (5.2) shows the function $F(\chi)$ plotted against concentration estimate for a single data point extracted from Figure (5.1), and indicates the manner in which variation in the magnitude of $F(\chi)$ about the correct concentration estimate occurs. For any iteration process equality about the root should be high, hence convergence will be most readily defined when:

$$\left|\frac{\partial F(\chi)}{\partial \chi}\right|_{F=0} \quad \text{is large.}$$

Differentiation of $F(\chi)$ with respect to concentration χ is in itself not analytically possible. However, numerical differentiation may be achieved by suitable programming techniques, and the above parameter has therefore been used to provide a measure of concentration sensitivity for two hot wire sensors.

5-2 Concentration Sensitivity based on the Mean Correlation Law

The general correlation of heat transfer data (section 4.5) indicates that a typical wire has a characteristic calibration with A = 0.253 and B = 0.582 in equation (4.36). Hence the concentration function F(X) may be represented for a typical wire pair by:

$$F(X) = Nu_1\{\frac{Tm_1}{Tg}\}^{-.12} - Nu_2\{\frac{Tm_2}{Tg}\}^{-.12}\{\frac{Re_1}{Re_2}\}^{0.4} + 0.253\{\frac{Re_1}{Re_2}\}^{.4} - 1\} \quad \ldots\ldots (5.2)$$

and similarly for either wire operating in a known flow at known concentration levels:

$$h = \frac{\bar{k}_m}{d}\{.253 + .582\{\frac{\bar{\rho}_m.U.d}{\bar{\mu}_m}\}^{0.4}\}\{\frac{Tm}{Tg}\}^{0.12} \quad \ldots\ldots (5.3)$$

where the mean properties $\bar{k}_m$, $\bar{\rho}_m$, $\bar{\mu}_m$ may be evaluated by equations (4.25) (4.24) (4.32) at the respective film temperatures.

Variation of $F(\chi)$ with χ may thus be computed for any gas type, wire temperature pair, velocity and concentration.

Figure (5.3) shows the result of such computation for the gases propane, ethane, argon and helium at a concentration of $\chi = 0.5$ in air, and velocity of U = 20 m/s. Definition of the root F(X) = 0 at $\chi = 0.5$ as defined by the slope of the function, can be seen to be poor for helium and argon. This is in keeping with the approximate sensitivity predictions of section (4.5.2).

Of particular interest is the manner in which sensitivity changes with the variables of gas velocity, gas concentration, and the two wire probe operating temperature pair.

Figure (5.4) shows variation of $F(\chi)$ with χ for ethane at the temperature pair 150/650 deg.C and various velocities. The numerically computed differential $\{\partial F(\chi)/\partial\chi\}$ at F(X) = 0 illustrates more effectively the variation in sensitivity with gas velocity for the four considered gases at $\chi = 0.5$ (figure 5.5).

Figures (5.6) (5.7) similarly show variation of the sensitivity parameter with concentration at different constant velocities for the temperature pair 150/650 deg.C. Variation in sensitivity parameter with operating temperature pair at all concentration levels is shown in figures (5.8) (5.9). The figures may be seen to indicate the summise, that increased sensitivity occurs with increased difference in film temperatures, is approximately correct.

The sensitivity relationships for propane and ethane have favourable characteristics for the gas jet modelling process. High concentration at the jet source is associated with high velocity and hence the inherent decrease in sensitivity due to the former is likely to be offset by the latter. Similarly as velocity decreases and jet mixing occurs at stations distant from the jet source, so sensitivity is enhanced at low concentration levels, and therefore compensates for the decrease in sensitivity with decrease in velocity.

The above sensitivity analysis confirms the findings of section (4.5.2) and indicates the hydrocarbon gases are the most suitable tracer agents.

5.3 Concentration Calibration Procedure

Theoretically the wire characteristic constants A, B of equation (4.36) may be obtained by calibration in either pure gas. However in the interests of caution calibration has always been performed in both gas types and additional random mixture data recorded in order to verify the concentration computation after calibration.

Calculation of the Nusselt - Reynold number relationship follows basically the same procedure as that for the overall correlation data and this, together with the concentration iteration technique has been combined in a single computer programme, since many of the required subroutines are common to both procedures. Details of this are given in section (5.7).

Concentration measurement in an isothermal flow only requires verification of the coincidence of calibration data for the two considered gas types, and figure (5.1) is indicative of the degree of coincidence to be anticipated on the concentration function for isothermal data. Figure (5.10) shows the typical agreement obtained between concentration and velocity measurement from a calibrated probe and the actual rig metered concentrations and velocities.

Extension of the technique to measurement in non-isothermal flows requires the simultaneous measurement of gas temperature, and the calibrated wires should then also produce coincidence of data on the concentration function (equation 5.1) for all gas temperatures.

Gas temperature for non-isothermal concentration measurement was monitored by a third wire on the probe used as a resistance thermometer (figures (4.3, 4.4)).

Figure (5.11) shows the coincidence of data obtained on the concentration function for a typical non-isothermal flow test in the calibration rig and indicates a rather more scattered grouping around the 45 degree line than that hitherto obtained for isothermal tests

ɑ typically shown in Figure (5.1).

For the data represented in Figure (5.11) increase in gas temperature from 20 deg.C to 200 deg.C fixes the minimum suitable wire operating temperature at approximately 400 deg.C. The upper wire temperature is limited by flammibility of the hydro-carbon tracer gases. Experience indicates that 'flickering' combustion of the gas adjacent to the wire occurs at wire temperatures in excess of 650 deg.C in near stoichiometric mixtures. Therefore the safe maximum attainable difference in wire film temperature is reduced from 450 deg.C for the isothermal case to 125 deg.C in these non-isothermal flow tests. The work of section (5.2) indicates a considerable reduction in sensitivity may therefore be anticipated (figures 5.8, 5.9). Simultaneously the number of error sources has also increased to include error on gas temperature (approximately 2.2% (section 4.5.6)), and the worst error on computed Nusselt number may then be considered to be approximately 6.8% by figure (4.34).

Figure (5.12) shows the measured concentration and velocity values compared with the rig metered values for non-isothermal flow and again indicates a rather scattered nature of the data.

It is to be concluded that since this degree of error is present on non-isothermal flows produced in the calibration rig, where fluctuations in velocity and temperature are low, considerably worse error may be anticipated for non-isothermal measurements in typical turbulent flows such as the jet mixing phenomenom.

5.4 Effect of Probe Inclination to the Flow

The variation of concentration estimate with change in probe inclination to the flow is of interest when measuring in complex flow fields such as that occurring with the gas jet normal to the air flow. Recirculation in the jet wake in such situations will create uncertainty in flow direction, although maximum bridge output voltage may be taken to indicate approximate normality.

Tests have been conducted in the flow calibration rig to determine the error on computed concentration and velocity at various inclination angles. Figure (5.13) shows comparison of actual and computed velocities and concentrations, where the computed values are based on the wire characteristics when normally orientated.

Marked error on concentration estimate is seen to only occur with angles of inclination greater than 30 degs. and at 45 degs. error has increased to measurable proportions. Corresponding error on velocity estimate tends to follow a sine relationship while the computed concentration on which the velocity prediction is based is substantially correct. However, error on computed concentration creates deviation from the sine relationship once inclination becomes severe.

It is to be concluded that in cases of uncertain flow direction maximum bridge output on the leading wire will ensure correct concentration computation since actual inclination to the flow is then unlikely to be greater than 30 degs.

5.5 Measurement Examples in Unknown Flow Fields

Illustration of the potential of the technique and experience in its application was obtained by preliminary tests.

Isothermal concentration measurement was made in a steady state gas jet. Figure (5.14) illustrates the measured axial concentration and compares it with the formula due to Thring and Newby (19).

Similarly radial concentration distribution was measured at axial locations of 5, 10, 25 jet diameters. The results are shown plotted in Figure (5.15). The data may be normalised.and compared with the formula of Forstall and Shapiro (21) indicating a self-preserving mass concentration profile exists, as in figure (5.16).

Measurements were also made in a non-isothermal co-axial gas jet. The inner jet fluid emerged at 60 deg.C with the outer co-axial flow at 145 deg.C. The inner and outer jet fluids were respectively ethane and air.

Typical measured radial distributions of temperature and concentration are shown in figure (5.17). The total data thus generated may be used to draw the concentration and temperature contours as shown in figure (5.18)

Figure (5.19) shows the cross-sectional concentration profiles for an isothermal propane jet issuing perpendicularly to a uniform air cross-flow and arranged as illustrated, in a rectangular wind tunnel. The data may be translated into a contour map (figure 5.20) and jet trajectory and the presence of re-circulation zones are then evident. A strong 'wake' re-circulation zone is shown and a weaker upstream zone is created by the jet fluid deflected upstream by the impingement process.

5.6 Error Estimate on Concentration Measurement

With correct calibration procedure, and well defined bridge output voltages possessing low fluctuations due to fluid turbulence, isothermal concentration measurement may be achieved to the accuracy shown in figure (5.10). However in practical measurement situations such as those illustrated in section (5.5), error on concentration estimate will be increased due to error in interpretation of the fluctuation in digital voltmeter outputs due to fluid turbulence.

Such error incurred by the recording of erroneous voltage values may be considered as a misrepresentation of $F(\chi)$ as depicted in figure (5.21). Non-zero at the correct root of $F(\chi)$ may be represented by an error ΔF. Consequent error on concentration estimate will then be related to the sensitivity parameter by:

$$\Delta\chi = \Delta F \cdot \left.\frac{1}{|\partial F/\partial\chi|}\right|_{F=0} \qquad \ldots\ldots 5.4$$

In a manner similar to the error analysis of section 4.5.6, the change in function value of $F(X)$ due to the errors on the individual bridge output voltages E_{01}, E_{02} represented by ΔE_{01}, ΔE_{02}, may be represented by:

$$|\Delta F| = \left\{\left(\frac{\partial F}{\partial E_{01}}\right)^2 \Delta E_{01}^2 + \left(\frac{\partial F}{\partial E_{02}}\right)^2 \Delta E_{02}^2\right\}^{\frac{1}{2}} \quad \ldots\ldots (5.5)$$

Subsequent error in concentration magnitude may then be computed by equation (5.4).

The results of such computations, (requiring numerical differentiation of equation (5.1)), are given in figure (5.22) where nominal values of error on recorded mean voltage level have been taken as those found to be typical from observed voltage fluctuations in the conducted experiments of section (5.5). Error in recorded mean voltage has been taken as ±0.5% representing for an actual bridge output of

10.00 volts a possible recorded mean value in the range 9.95 to 10.05 volts.

The error on argon data is seen to be high for all concentration levels and similarly the error for helium is excessive at low gas concentrations.

Ethane and propane display very modest errors on concentration estimate particularly in the low concentration range which is of greatest interest in the proposed fuel spray modelling experiments.

5.7 Computational Details

The two basic requirements of the technique are:-

a. To establish from calibration data the constants A, B as presented in equation (4.36).

b. To calculate, from experimental bridge output voltage and gas temperature, the flow concentration and velocity by the iteration process using the established two wire calibration characteristics.

Both requirements have been developed in a single computer program which therefore presents a choice of calculation sequences. A third alternative is presented for the case where calibration velocities over the wires have been established by other means such as the DISA 55D41 wind tunnel.

The purpose of the following section is not to provide intricate detail on the computing procedure but mainly to outline the calculation paths required. Calculation paths are depicted in the flow chart of figure (5.23) and the actual program listing and segment descriptions are presented in Appendix (C), to which subroutine names in this section directly relate.

5.7.1 Computation of Probe Characteristics

The recorded bridge voltage outputs from the calibration tests have to be related to the flow characteristics as metered by the orifices and subsequently Nusselt and Reynolds number calculated.

Test section velocity and concentration are computed from the two orifice mass flow rates, their stagnation temperatures and pressures, and the test section temperature, by the equations of continuity and mass conservation. The subroutine 'ORIFLOW' calculates the separate orifice mass flow rates using equation (4.2). Test section velocity and concentration is then calculated

from the combined orifice flows in subroutine 'ODATA'.

Corresponding bridge voltage outputs are used to calculate the heat transfer coefficients of the two wires as in section (4.2) using the iteration procedure of Appendix (B) in subroutine 'HTRANS'.

A further subroutine 'NDATA' then combines the wire and orifice data to present Nusselt-Reynold co-ordinates using the function segments 'CPT', 'KM', 'VM' to calculate mixture property values for the concentration levels calculated in 'ODATA', at the twin wire respective film temperatures. 'NDATA' is also designed to least squared error fit the total data for each wire and hence provide the constants A, B for equation (4.36). From these calibration constants the concentration function of equation (5.1) is computed and the necessary data groupings required to plot the twin wire relationship as typically illustrated in figure (5.1) are evaluated and output.

Thus when using the program in this calibration mode input data comprises the total rig flow data readings $\Delta H1$, $\Delta H2$, H01, H02, T1, T2, T3 as depicted in figure (4.5), and for the purpose of checking, the test section pitot-static head also. Additionally the wire operating temperatures, bridge voltage outputs, and wire properties etc. are required.

Program output then presents the raw data as Nusselt-Reynold co-ordinates, with constants A, B evaluated in equation (4.36) for each wire, the test section velocities and concentration levels, calculated mean gas mixture property levels, and the concentration function plot similar to that of figure (5.1).

5.7.2 Calculation Sequence for the Computation of Concentration Magnitude from a Calibrated two wire Probe

The subroutine 'CONX2' is used to calculate mixture concentration levels from recorded bridge voltage outputs. Twin wire heat

transfer coefficients are firstly computed in subroutine 'HTRANS'. The wire operating temperatures and experimental gas temperatures are used to calculate the 100% gas property values km_1, km_2, μm_1, μm_2 at the respective film temperatures by the polynomials of equations (4.29) (4.30) in function segment 'CPT'.

Iteration within 'CONX2' is achieved by using the iteration subroutine 'CJMIT' (Appendix B) and the external concentration function 'FCX', as based on equation (5.1). The iteration variable is molar gas concentration X and successive estimates of the root are used to calculate the mean gas properties in the function segments KM, VM (based on equations (4.24)(4.25), until the value of F(X) (equation (5.1)) is less than 10^{-8}.

Iteration error is then substantially less than any real experimental error and may be calculated from equation (5.4) for typical sensitivity as depicted in figures (5.3) to (5.9) for the considered operating conditions and tracer gas employed.

Corresponding velocity calculation is achieved in subroutine 'VELX2', where the derived concentration value is used to calculate the mixture properties and velocity by the wire characteristics A, B, in equation (4.36) for each of the two wires.

Data input for this mode of program use is therefore limited to the experimental bridge voltage values, and the two wire characteristics as presented by the calibration program procedure. Wire geometries and material details are also required.

Output is presented as concentration estimate and the two wire velocity estimates based on the concentration value.

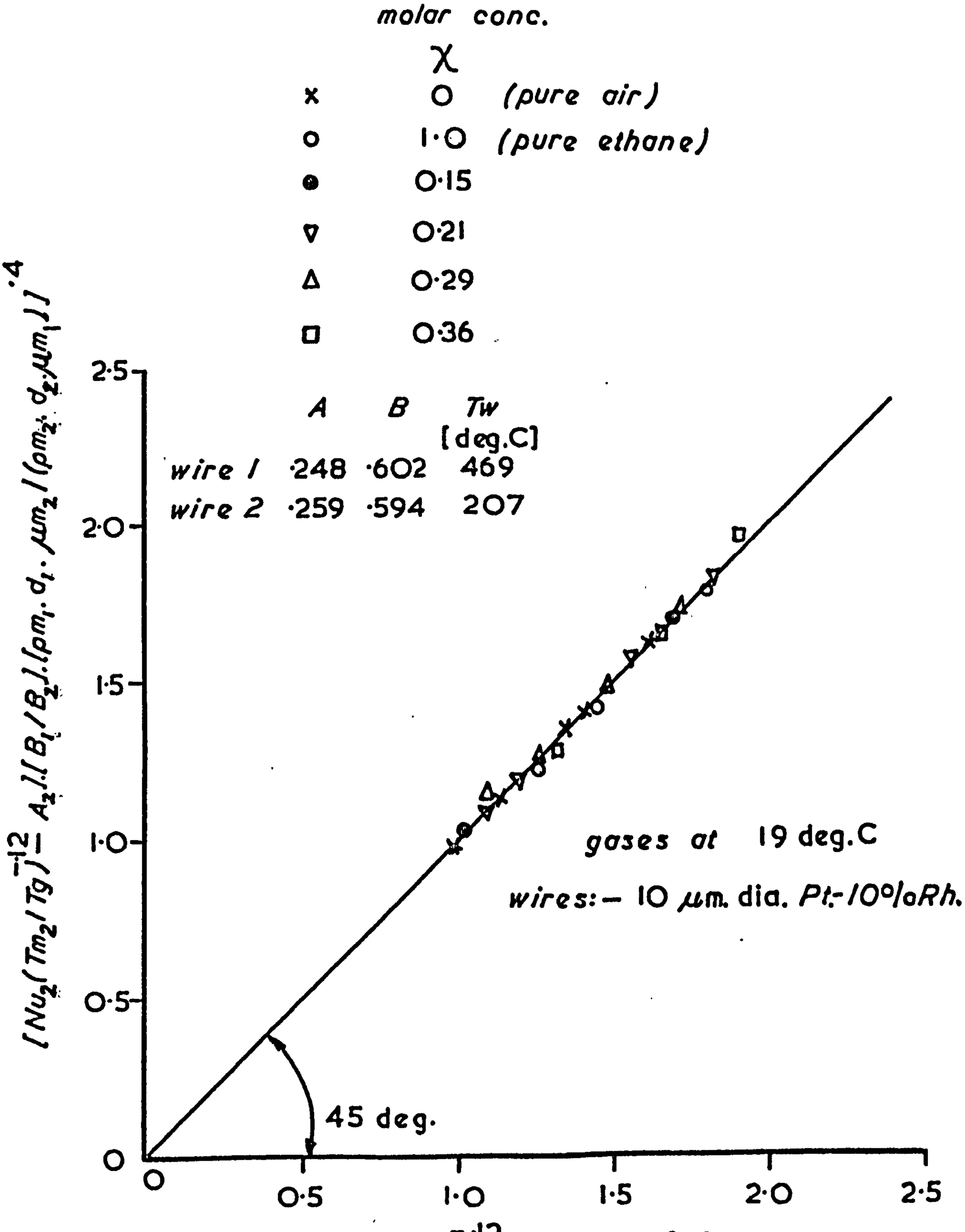

Typical Concentration Function Coincidence of Data for Ambient Temperature Probe Calibrations.

Fig. 5·1

metered conc. - 0·29

metered velocity - 15 m/sec.

Tw_1 - 469 deg. C

Tw_2 - 207 deg.C

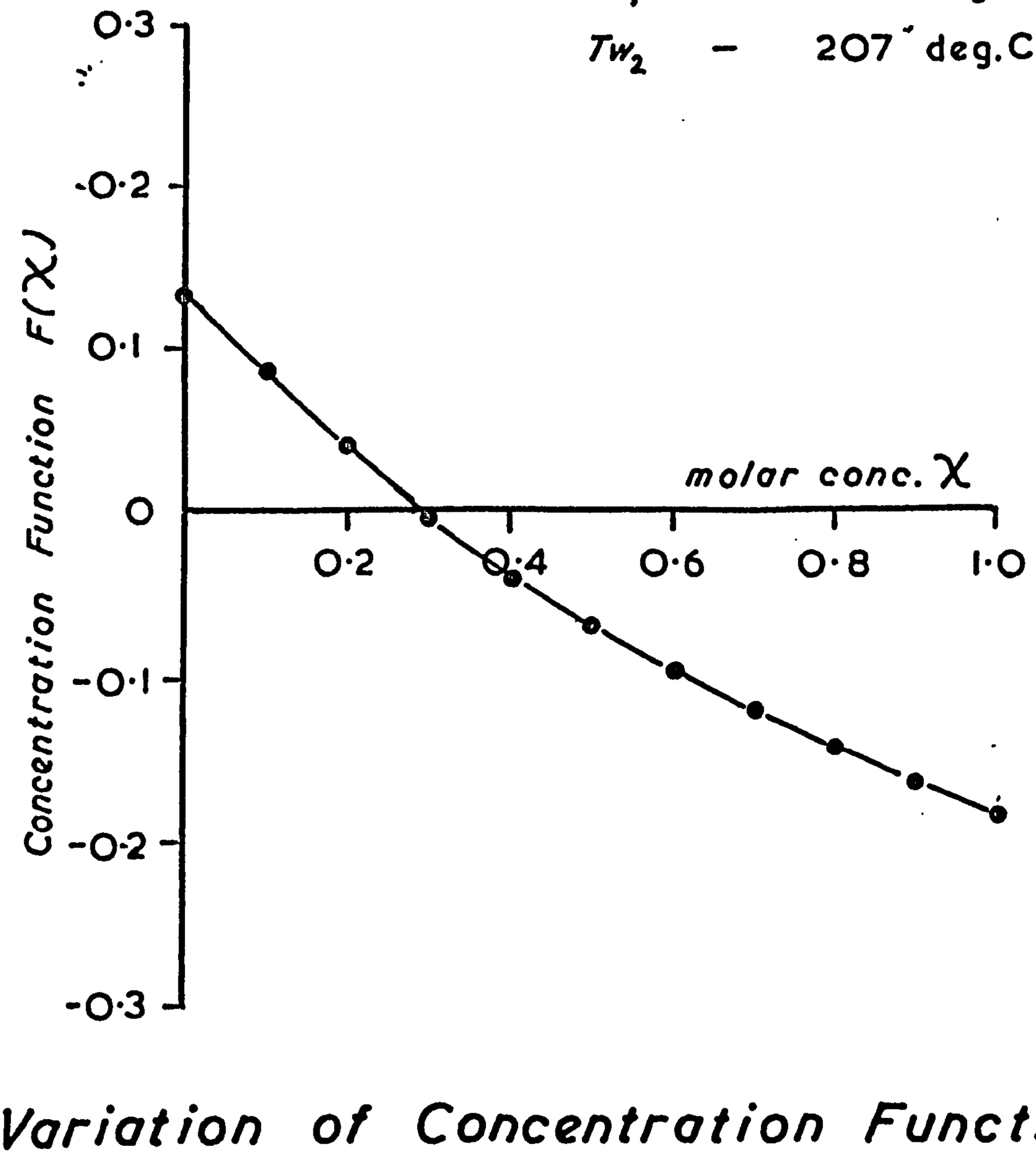

Variation of Concentration Function F(χ) with Concentration Estimate χ

Fig. 5·2

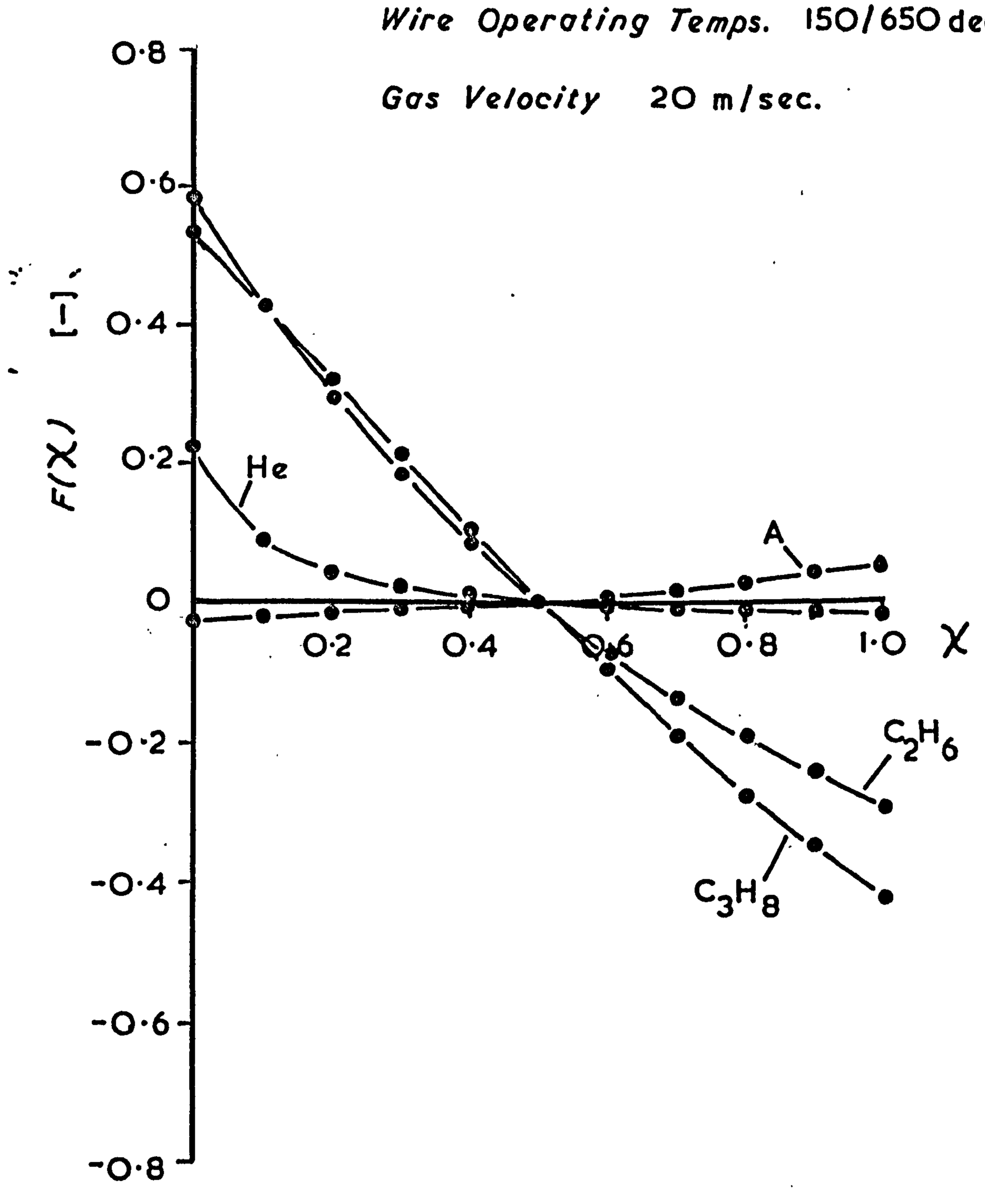

Computed Variation of $F(\chi)$ about the Correct Concentration ($\chi = 0.5$) for Various Gases in Air.

Fig. 5·3

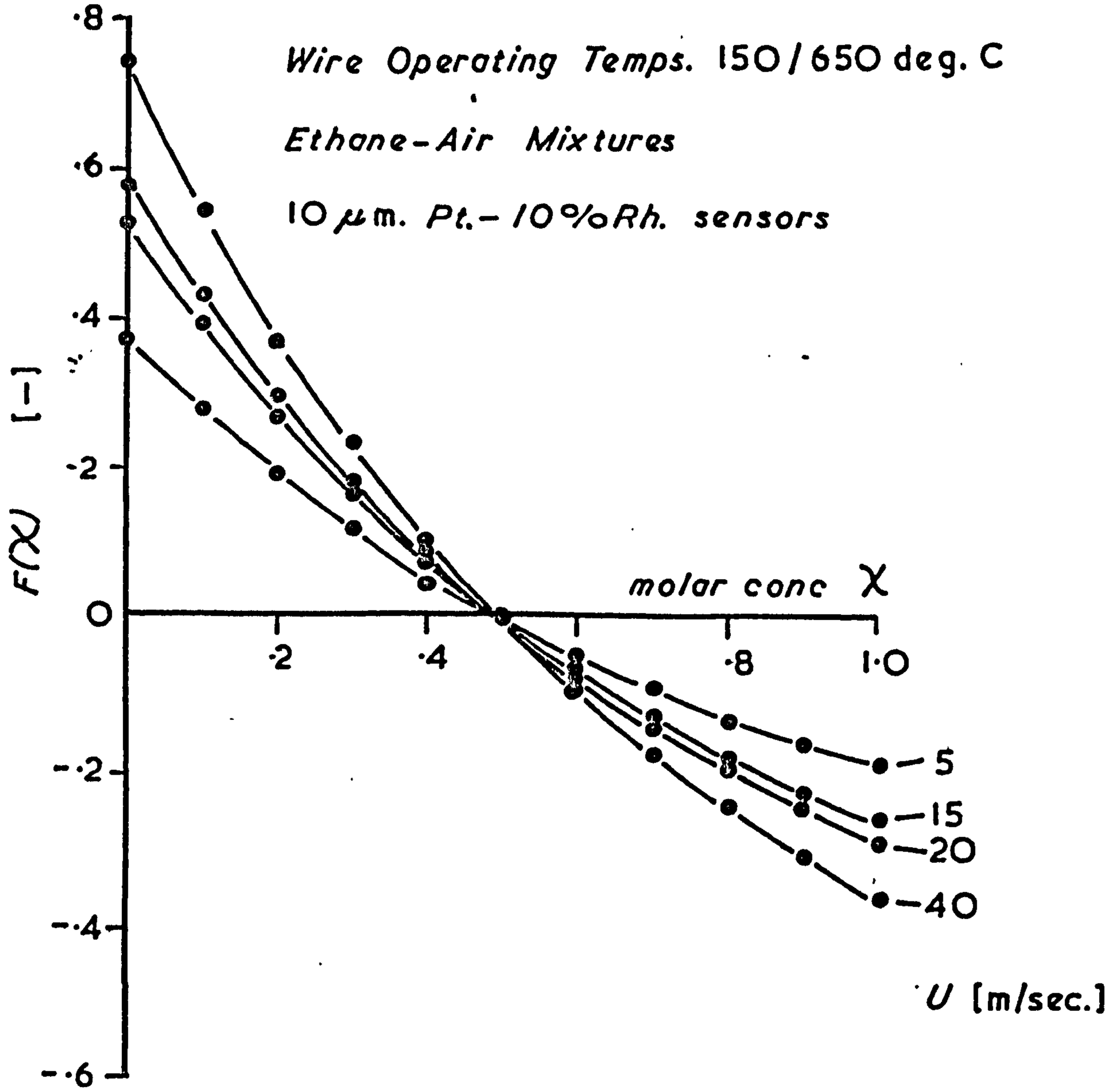

Computed Variation of $F(\chi)$ about the Correct Concentration ($\chi = .5$) for Various Mixture Velocities.

Fig. 5·4

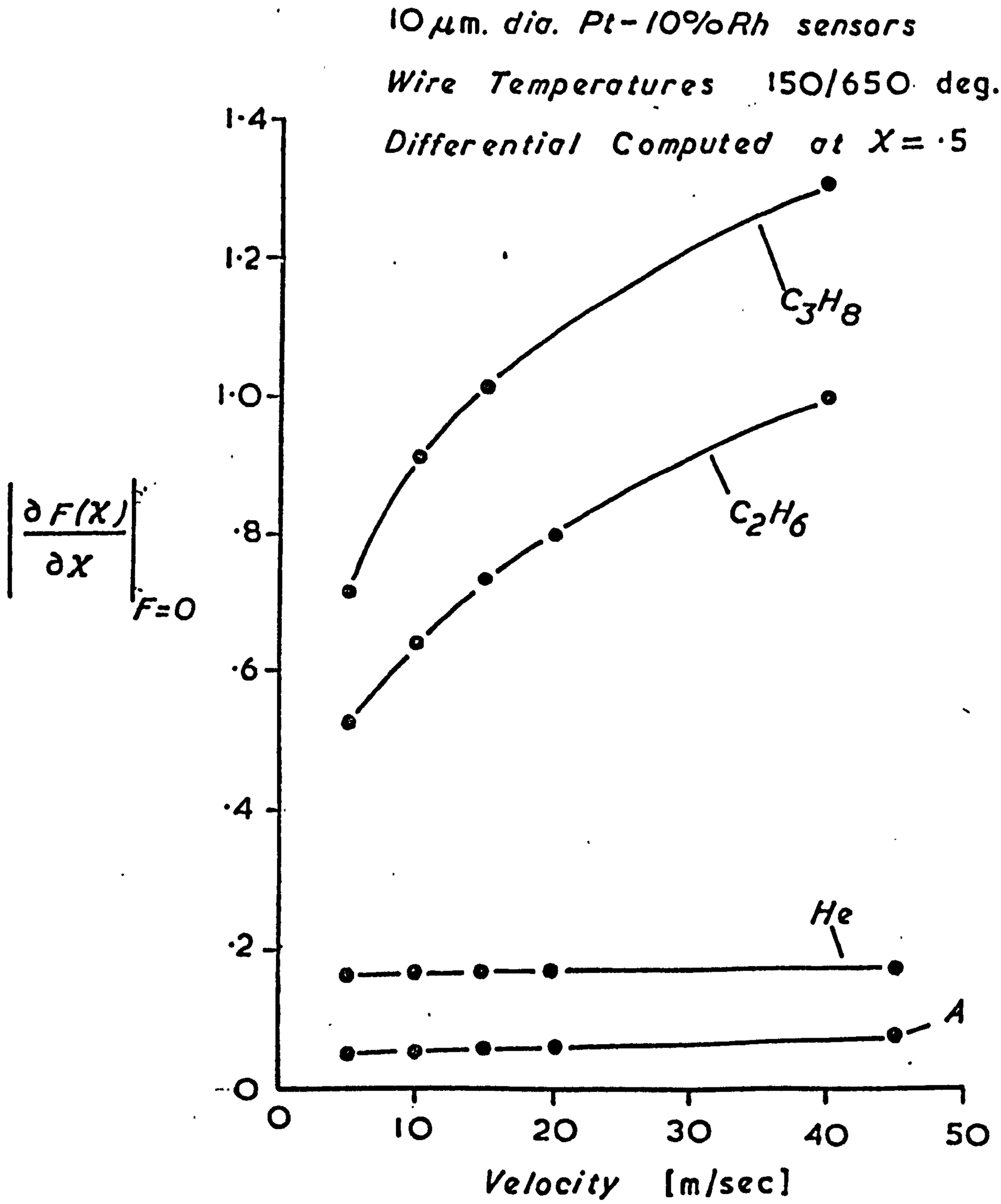

Variation in Sensitivity Parameter with Velocity for Various Gases in Air.

Fig. 5·5

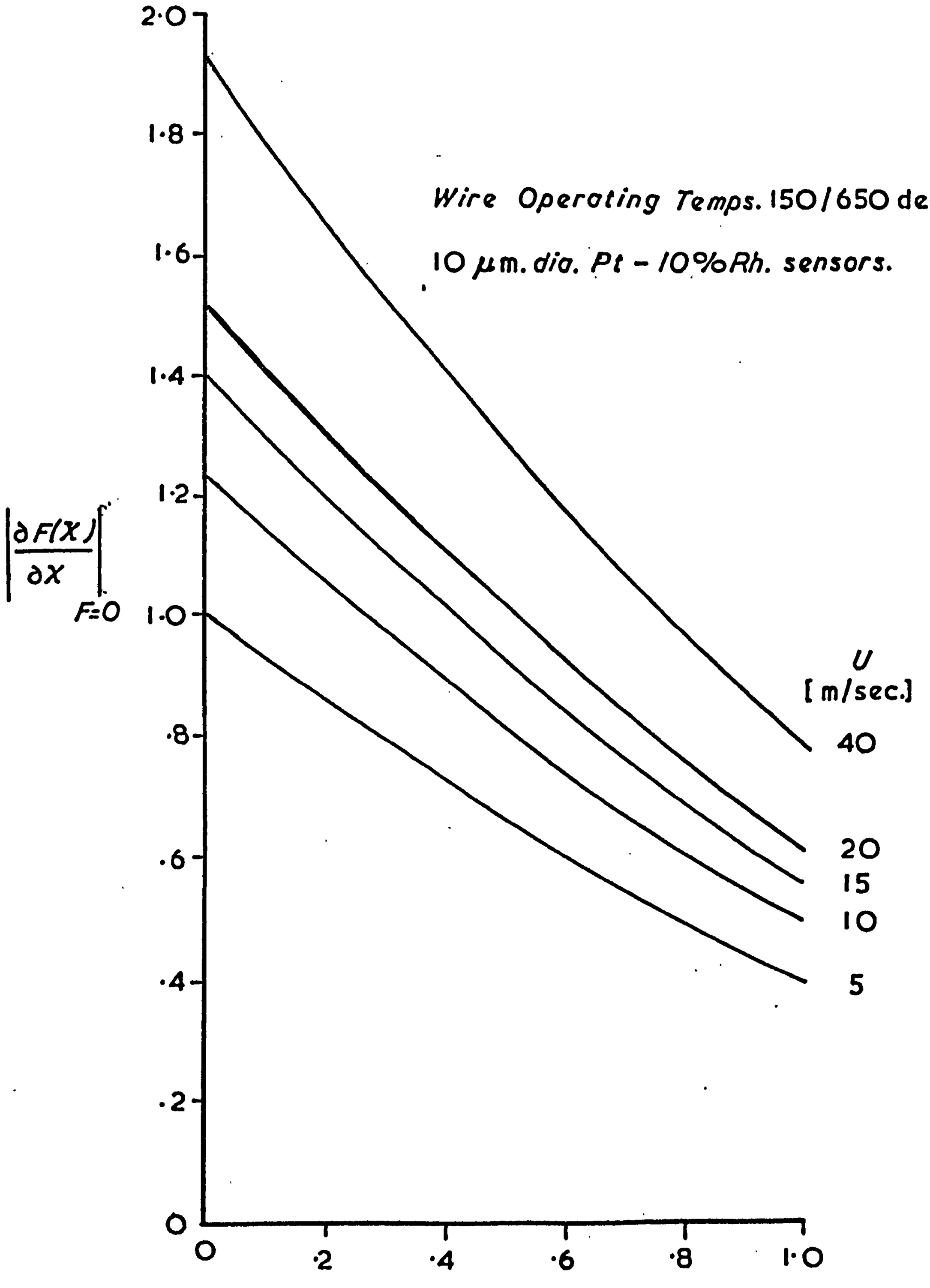

Sensitivity Variation with Concentration of Propane (C_3H_8) in Air at Constant Velocity.

Fig. 5·6

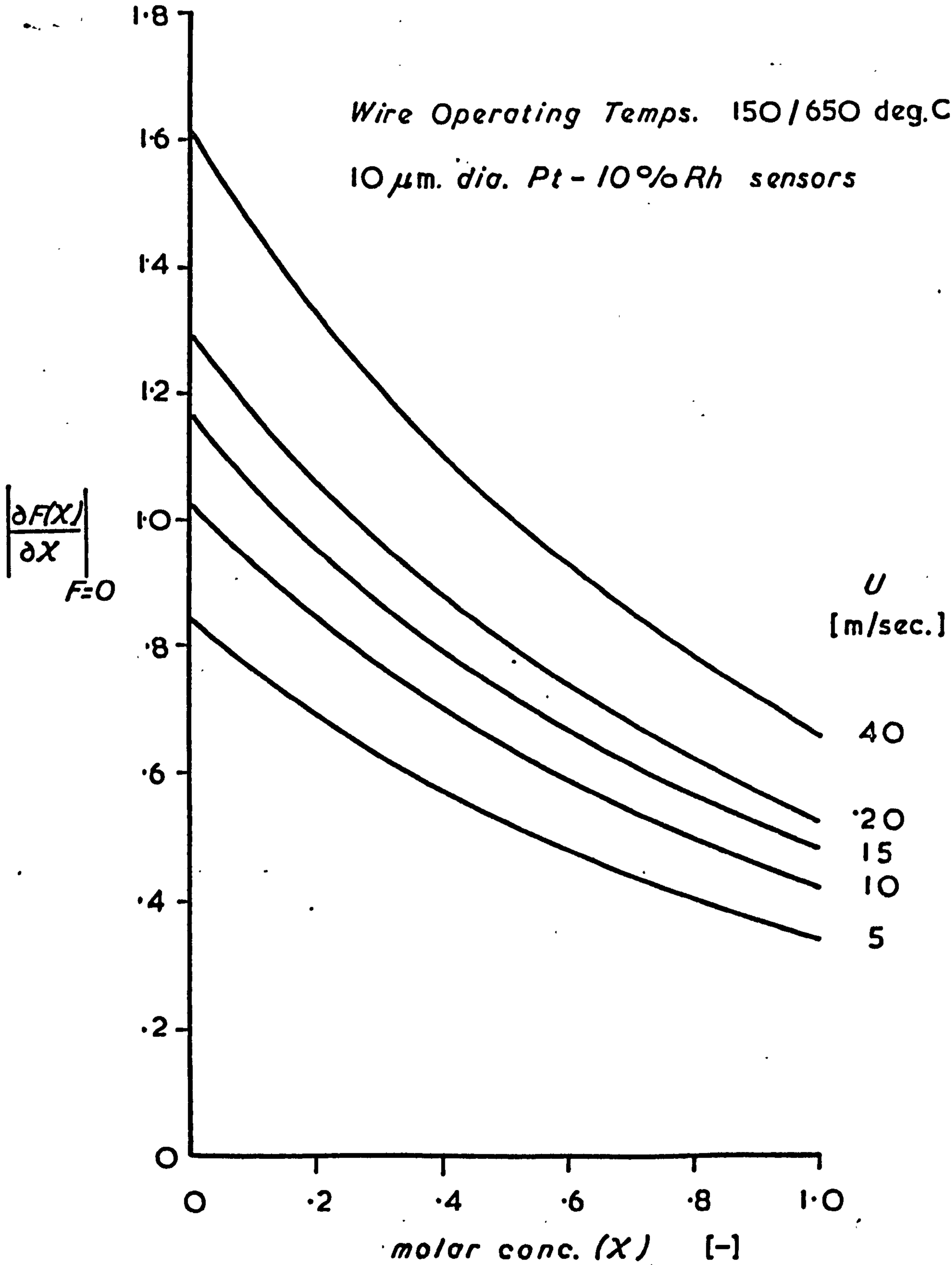

Computed Sensitivity Variation with Concentration of Ethane (C_2H_6) in Air at Constant Velocity.

Fig. 5·7

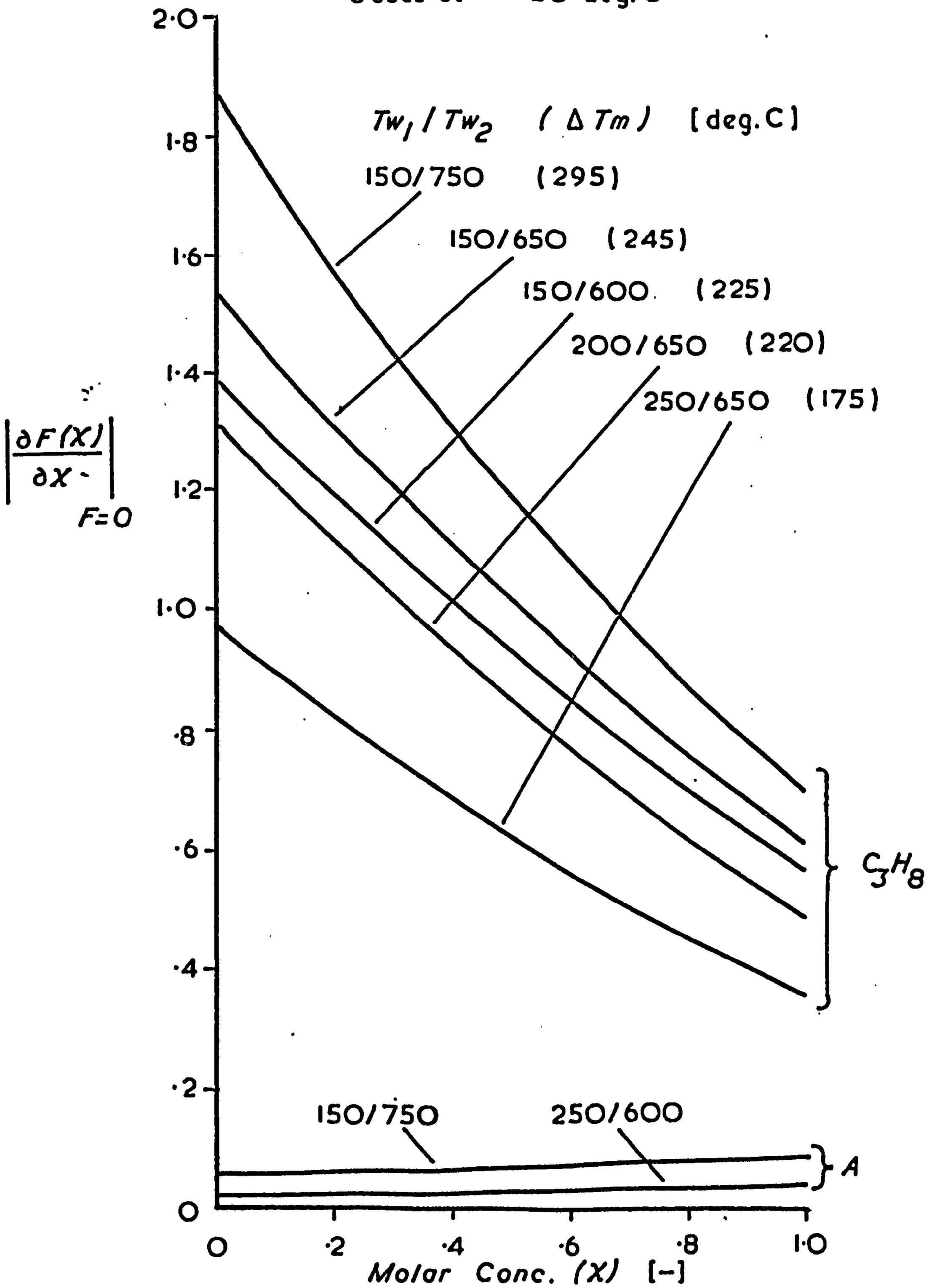

Computed Sensitivity Parameter Variation with Operating Temperature Pair.

Fig. 5·8

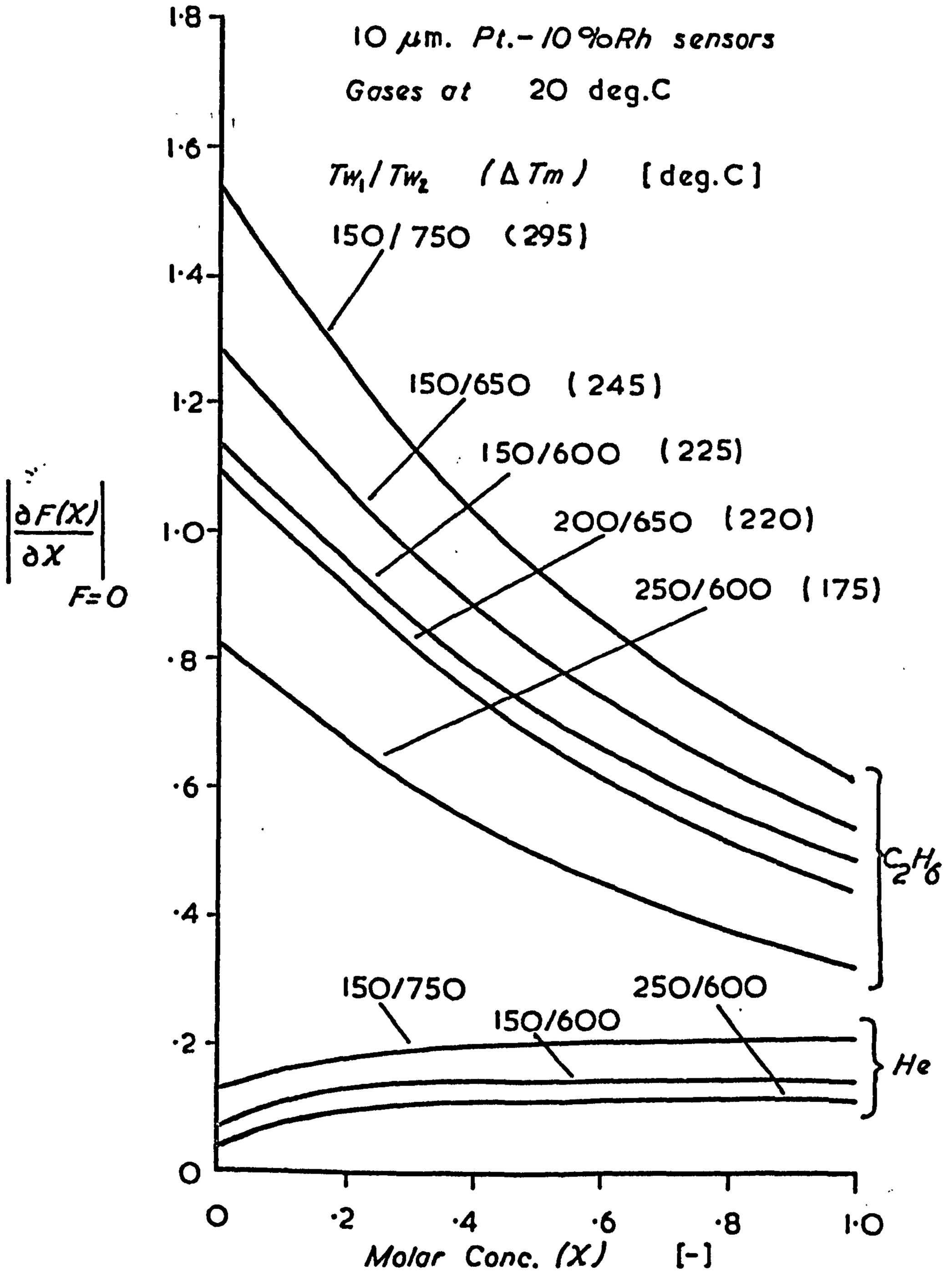

Computed Sensitivity Parameter Variation with Operating Temperature Pair.

Fig. 5·9

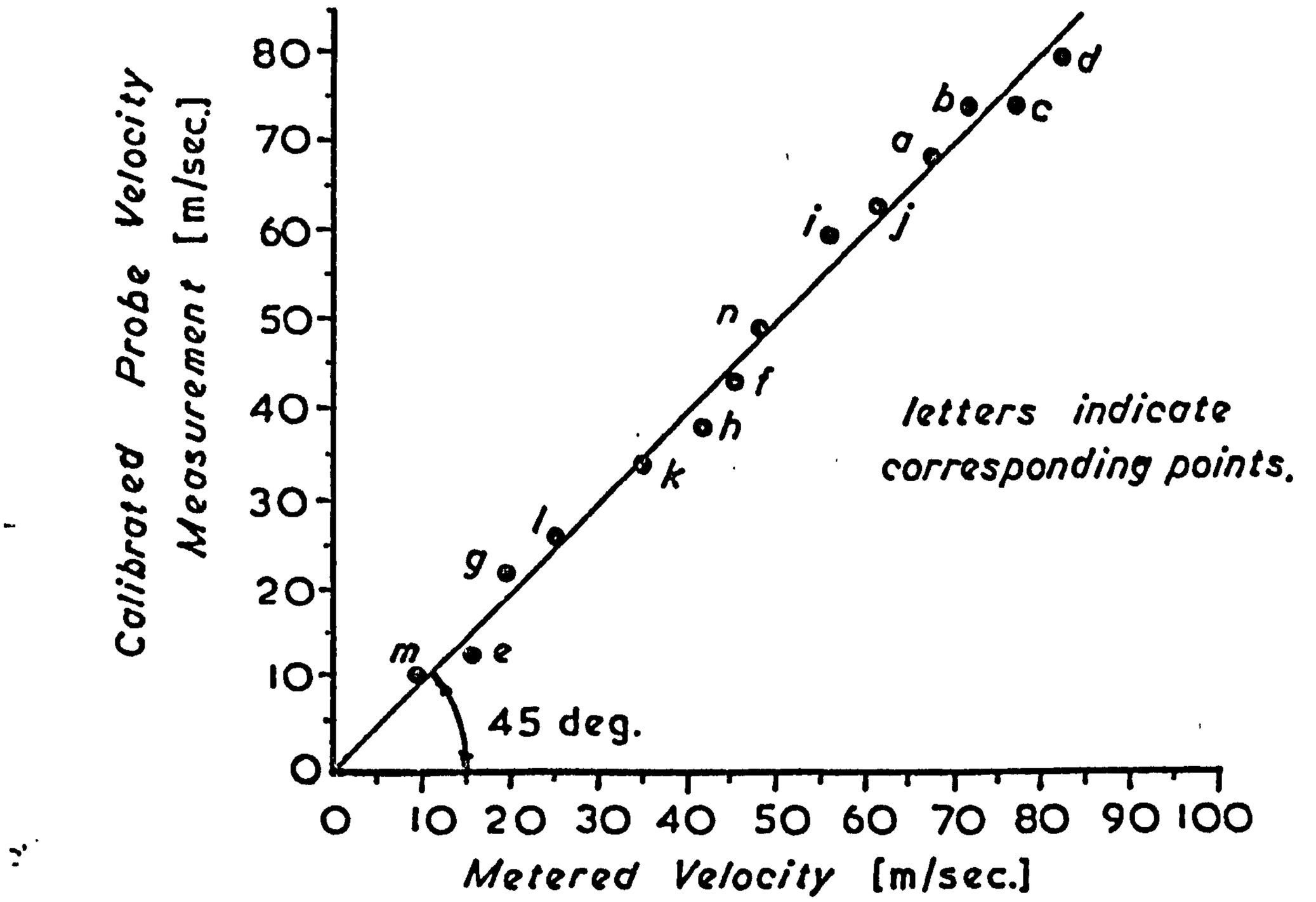

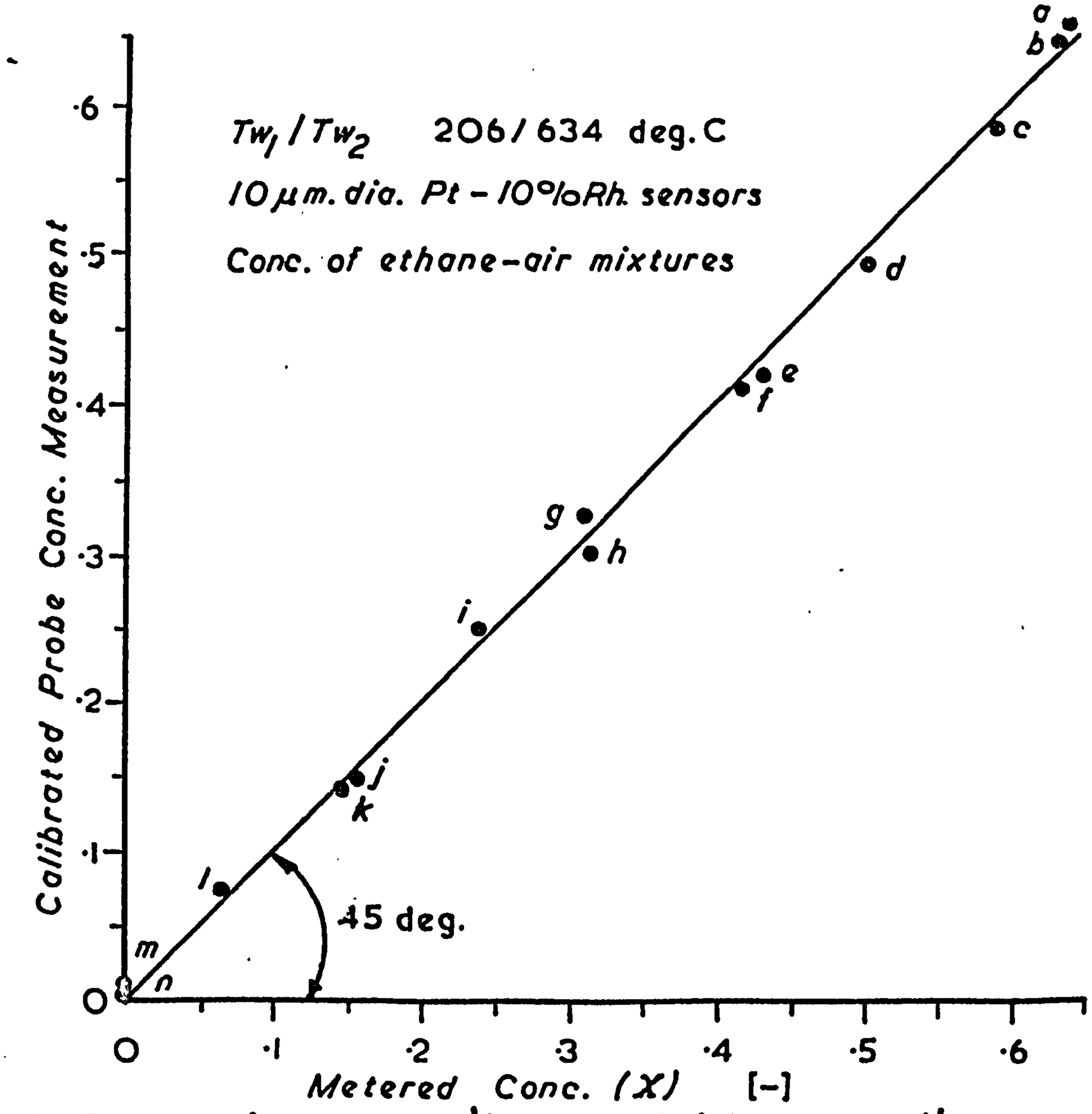

Typical Comparison of 'Actual & Measured' Concentrations & Velocities at 20 deg. C

Fig. 5·10

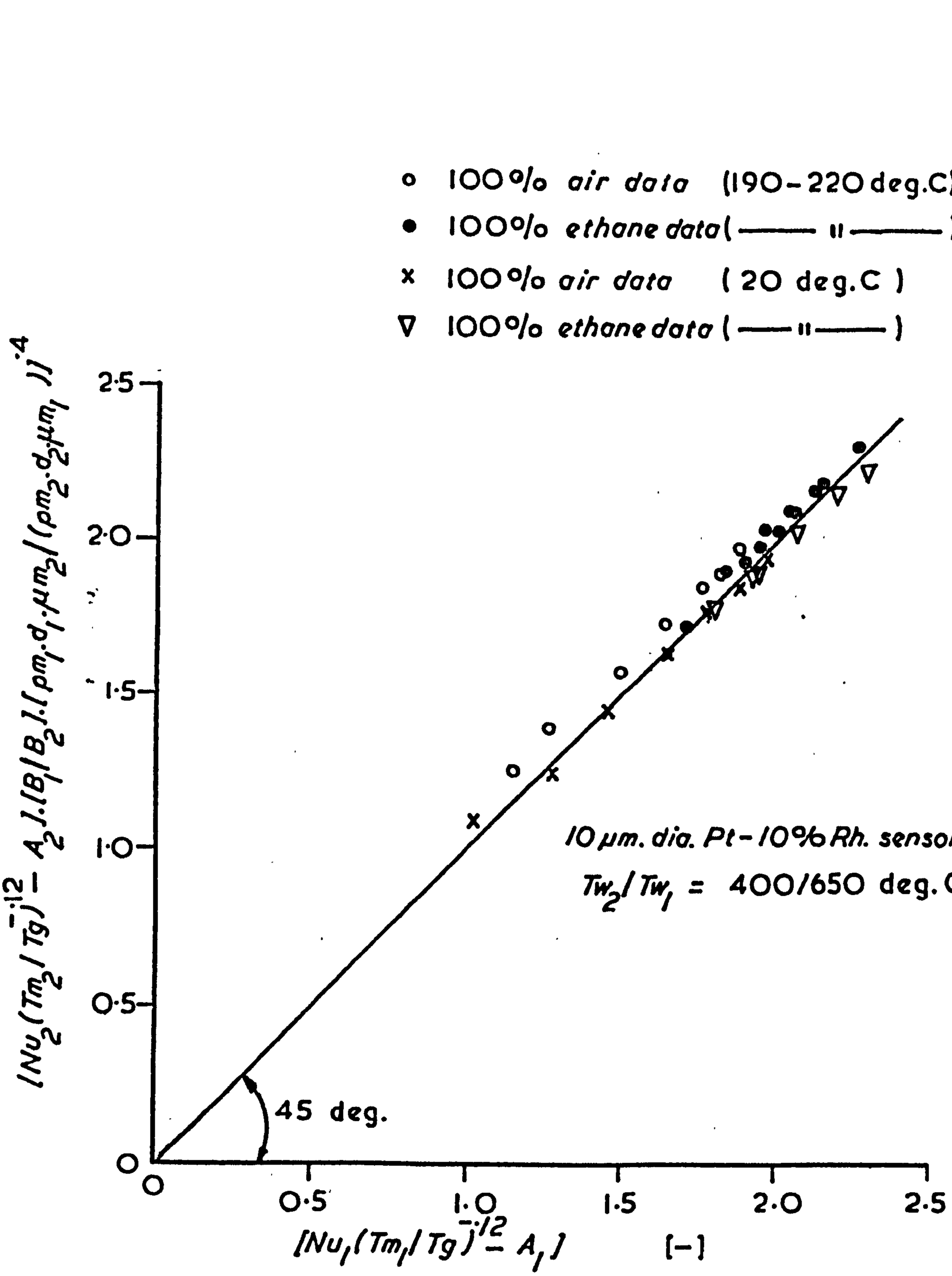

Typical Concentration Function Coincidence of Data for Non-Isothermal Probe Calibrations

Fig. 5.11

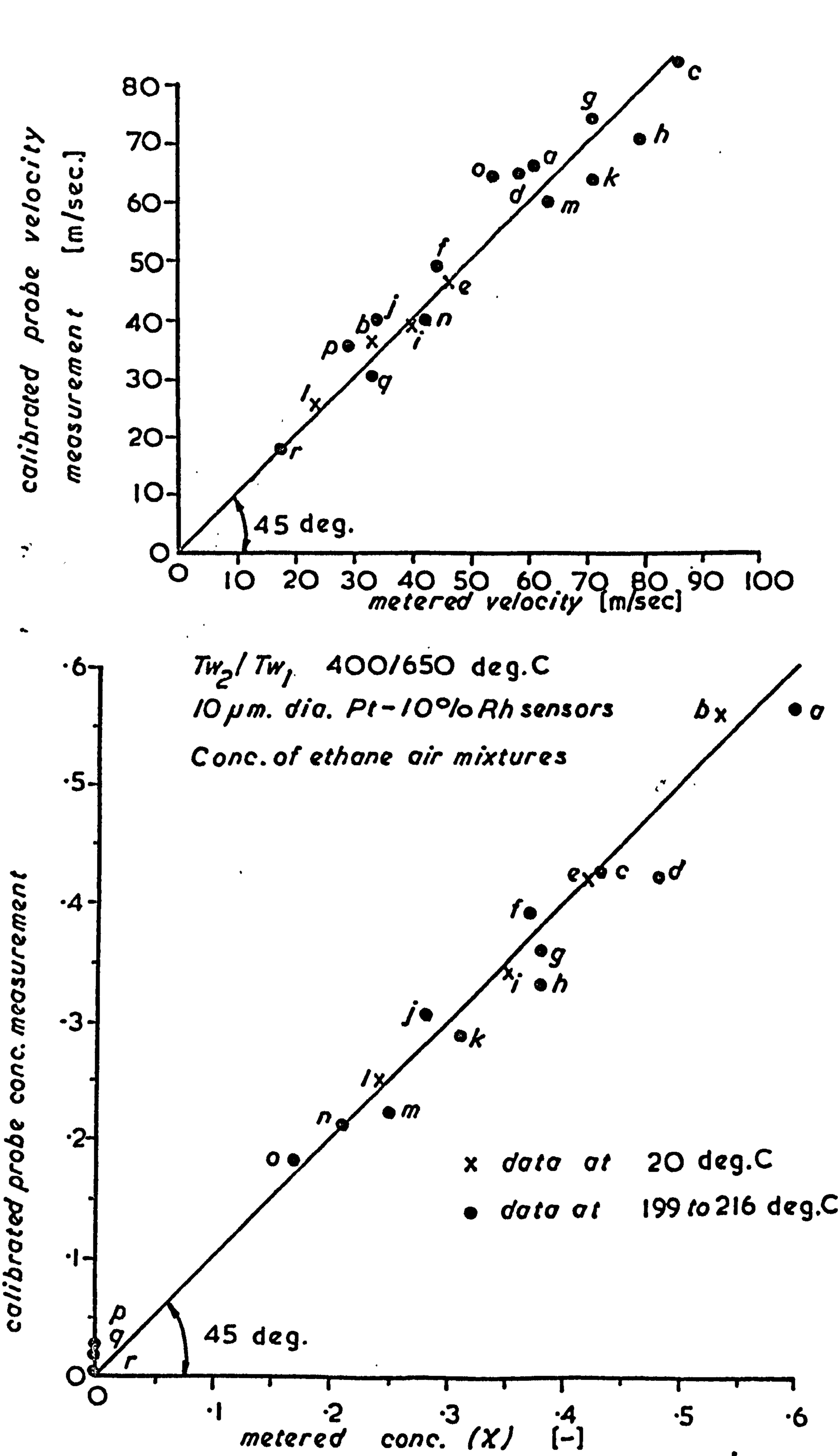

Typical Comparison of 'Actual & Measured' Non-Isothermal Concentration & Velocity Data.

Fig. 5·12

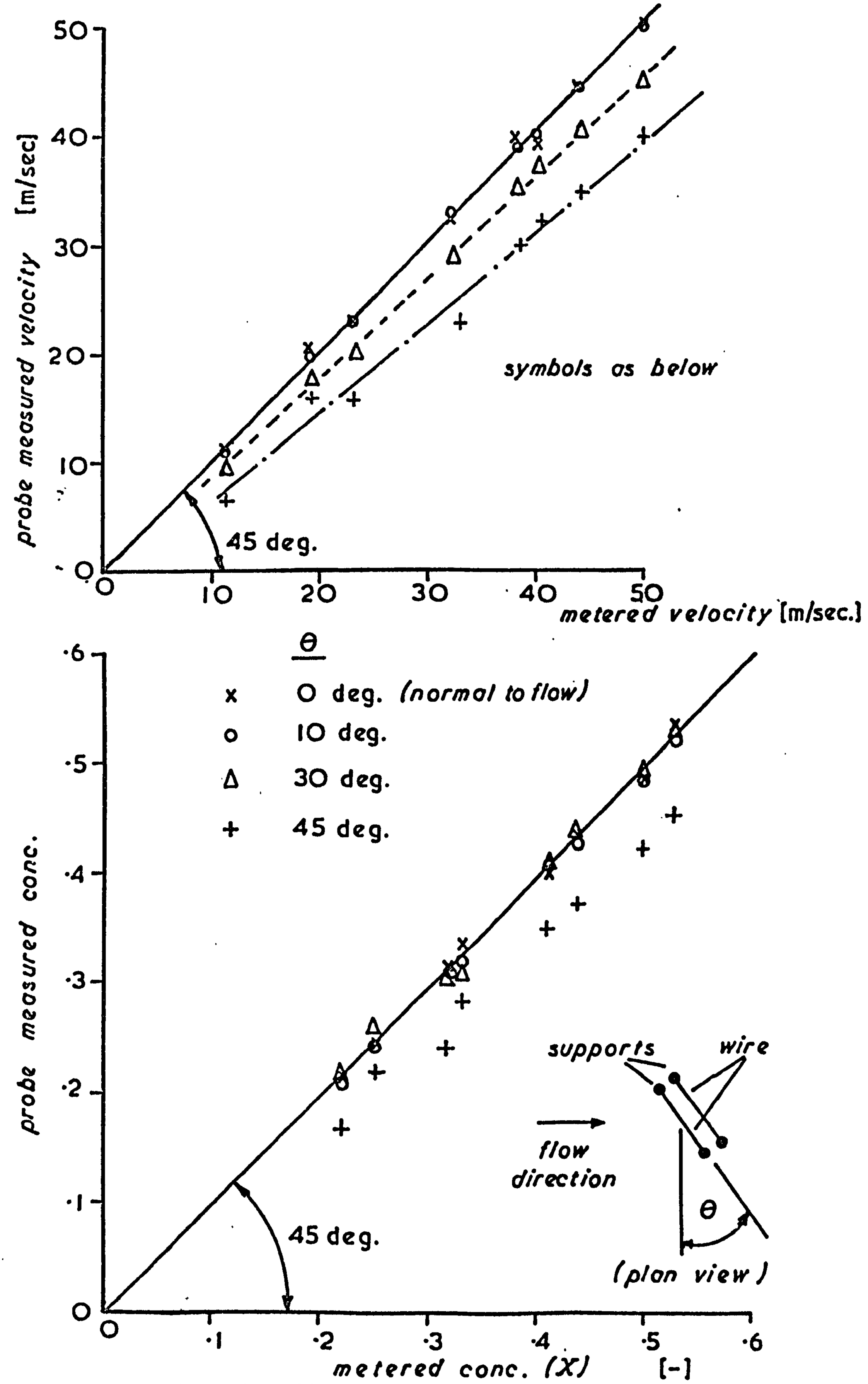

Effect of Probe Inclination to Flow Direction

Fig. 5·13

Axial Concentration Distribution for a Free, Isothermal, Steady State, Propane Jet in Air.

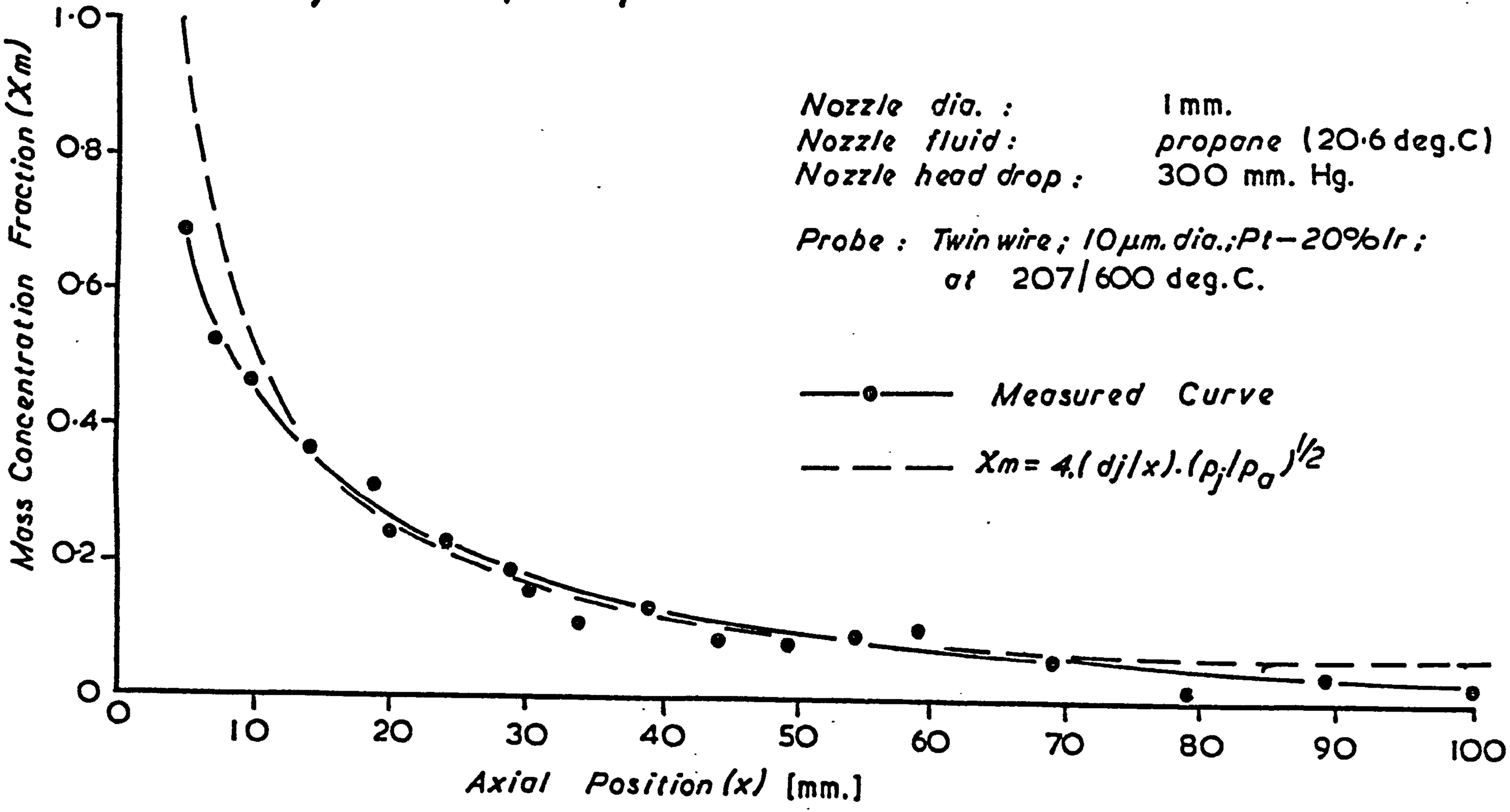

Nozzle dia. : 1 mm.
Nozzle fluid : propane (20·6 deg.C)
Nozzle head drop : 300 mm. Hg.

Probe : Twin wire ; 10 µm. dia. ; Pt – 20% Ir ;
at 207/600 deg.C.

Fig. 5.14

Radial Concentration Distributions for the Steady State Propane Jet in Air.

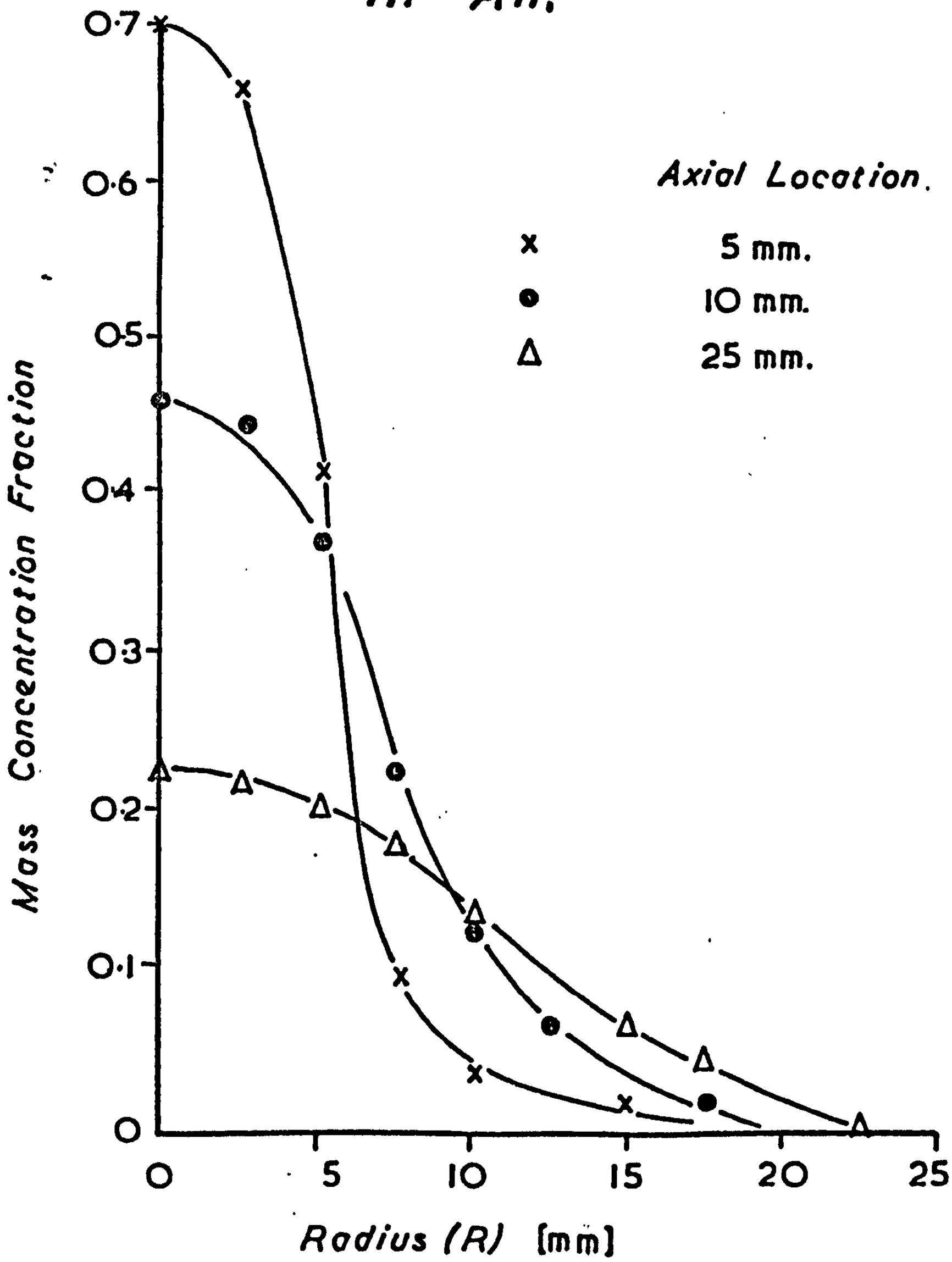

Fig. 5·15

Normalised Radial Concentration Distribution for the Steady State Propane Jet in Air.

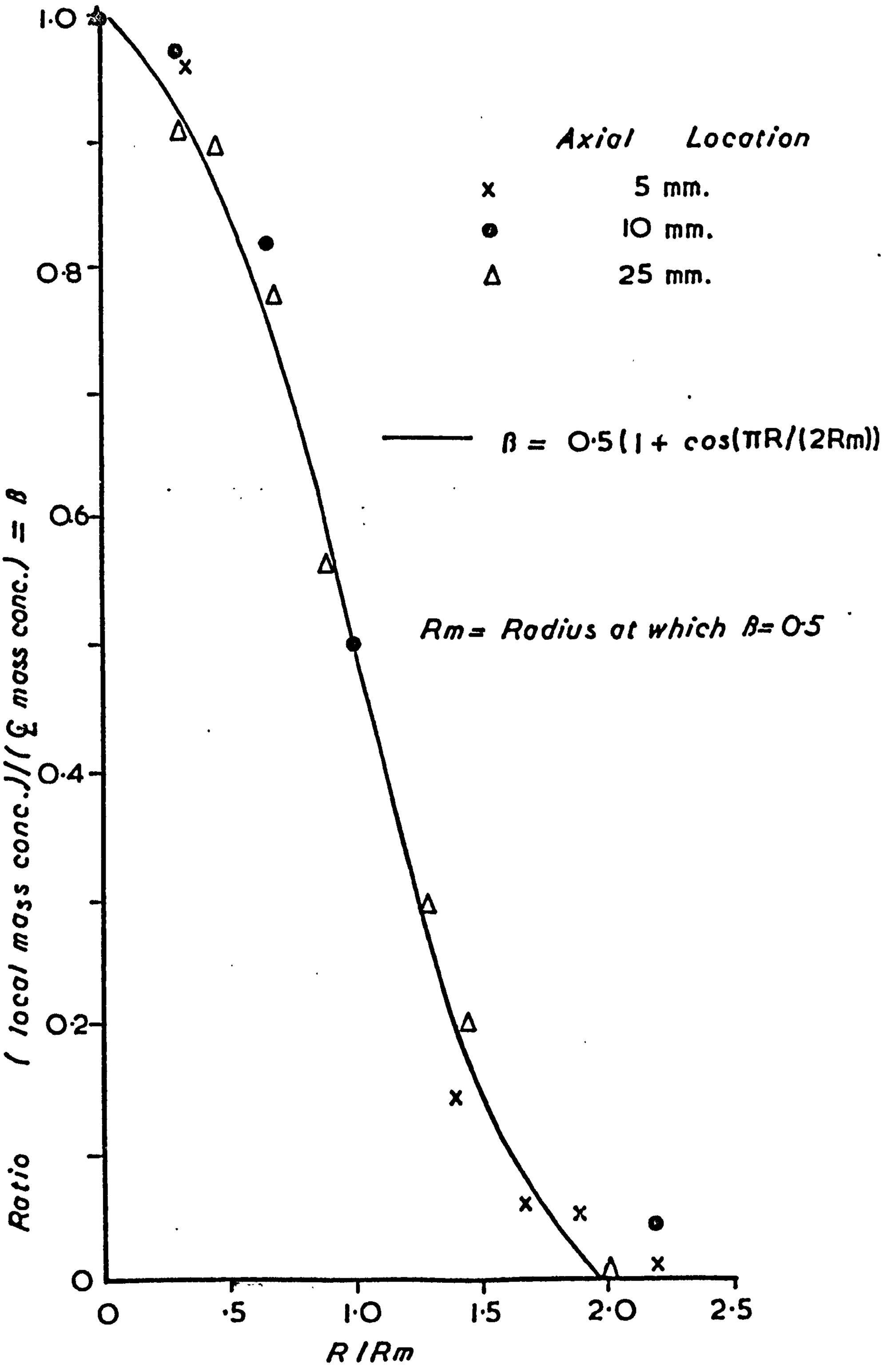

Fig. 5·16

Typical Radial Profiles for the Non Isothermal Co-Axial Jet.

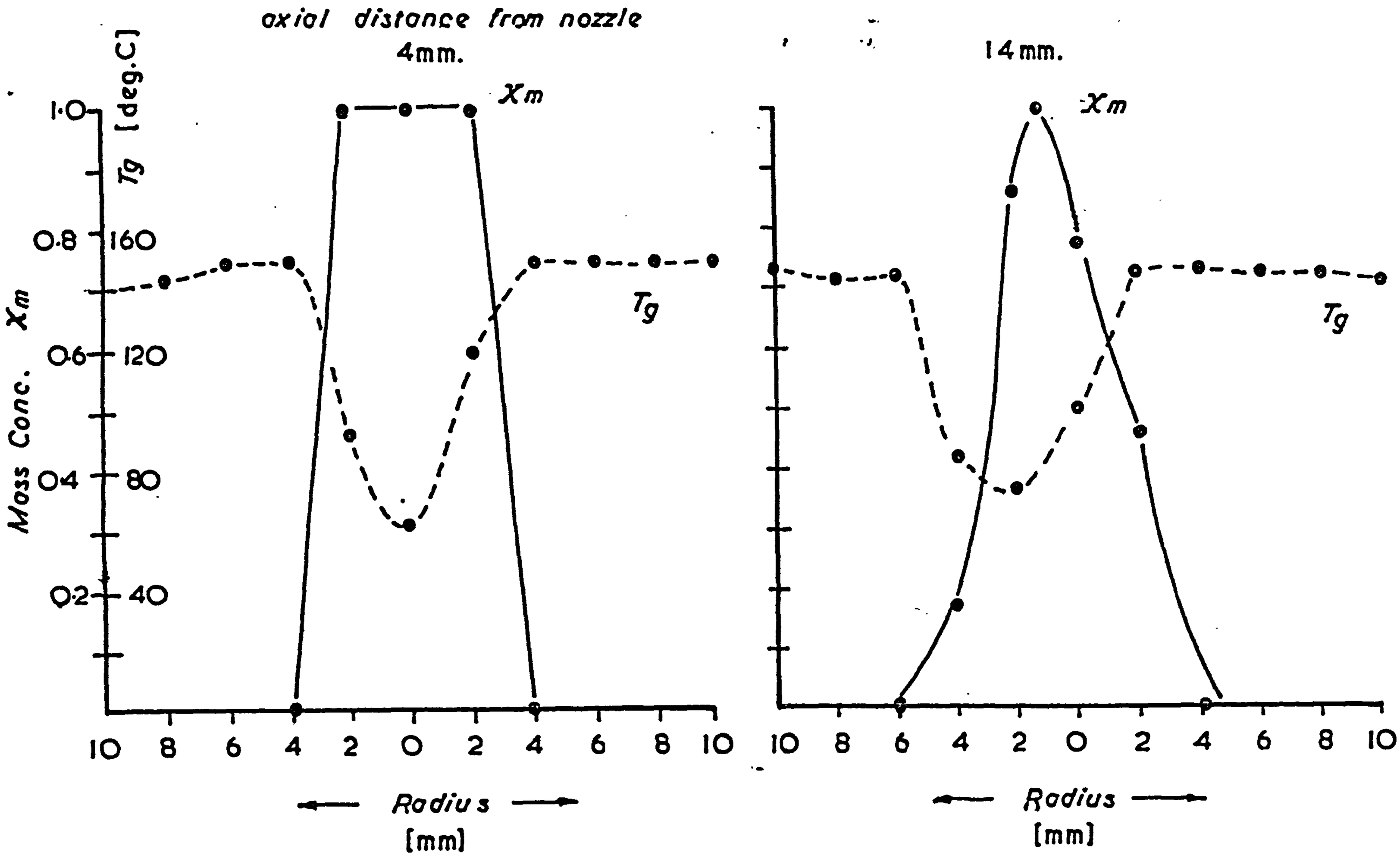

Fig. 5.17

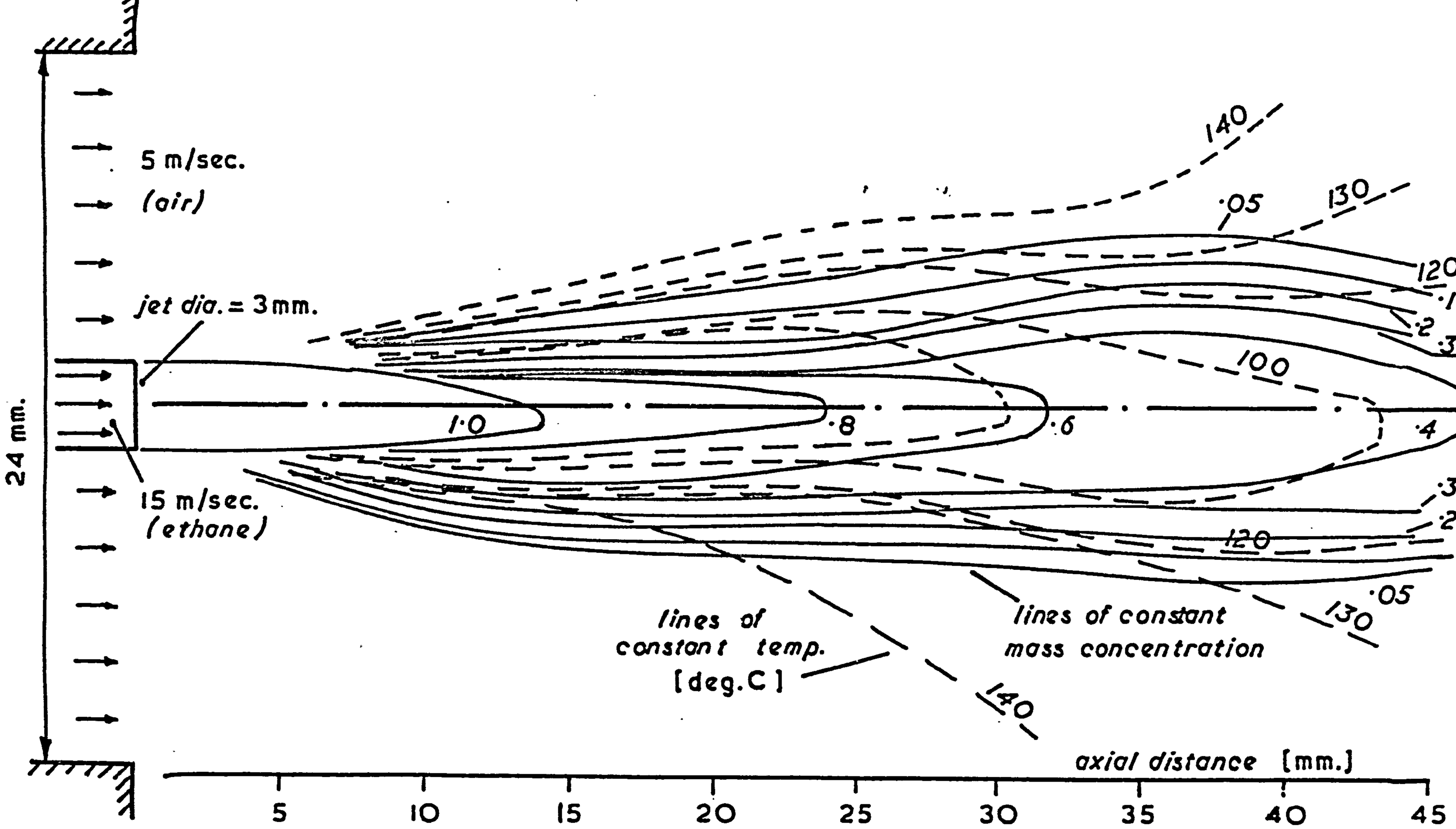

Fig. 5.18

Contours of Constant Temperature & Concentration for the Non Isothermal Coaxial Ethane Jet.

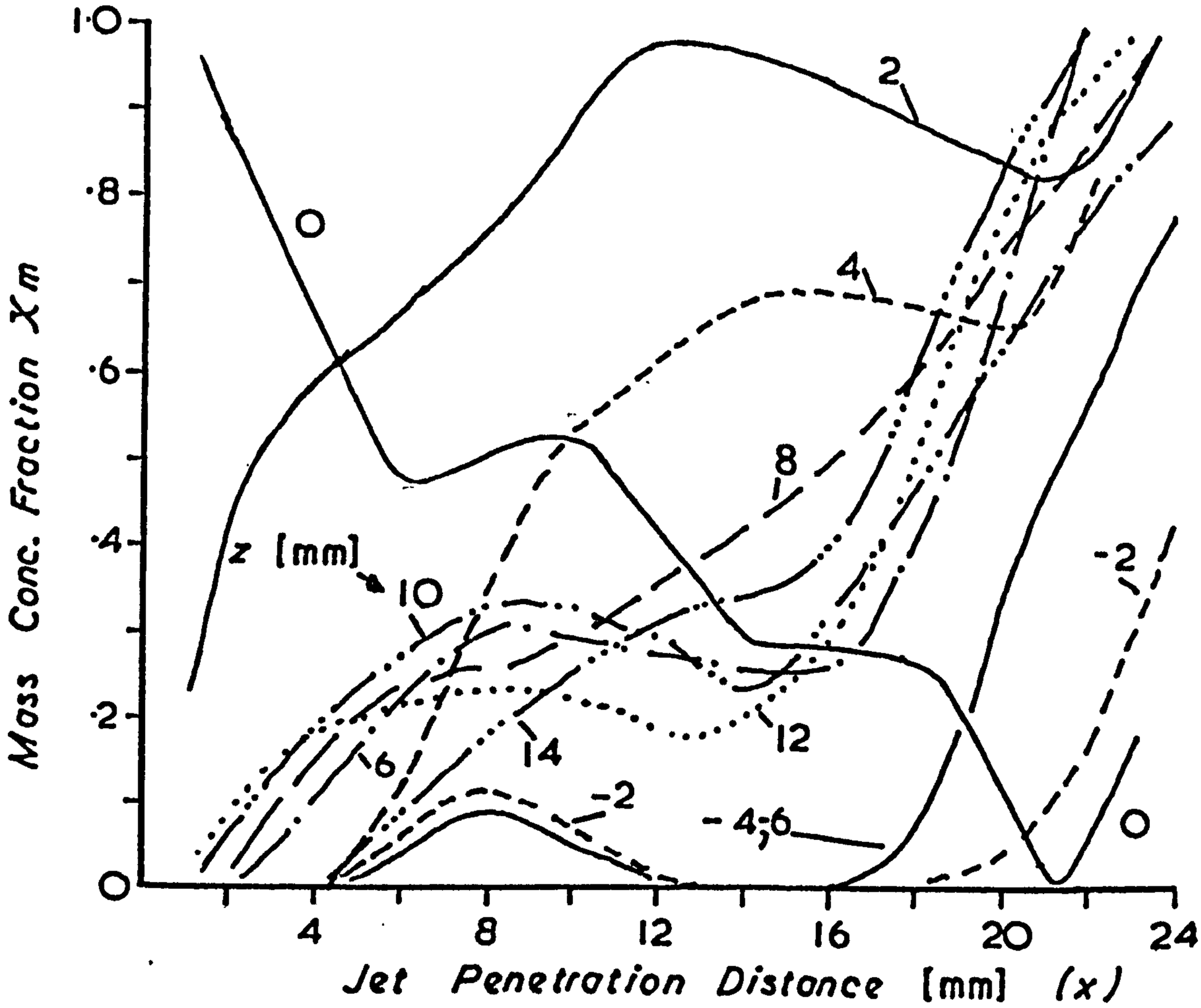

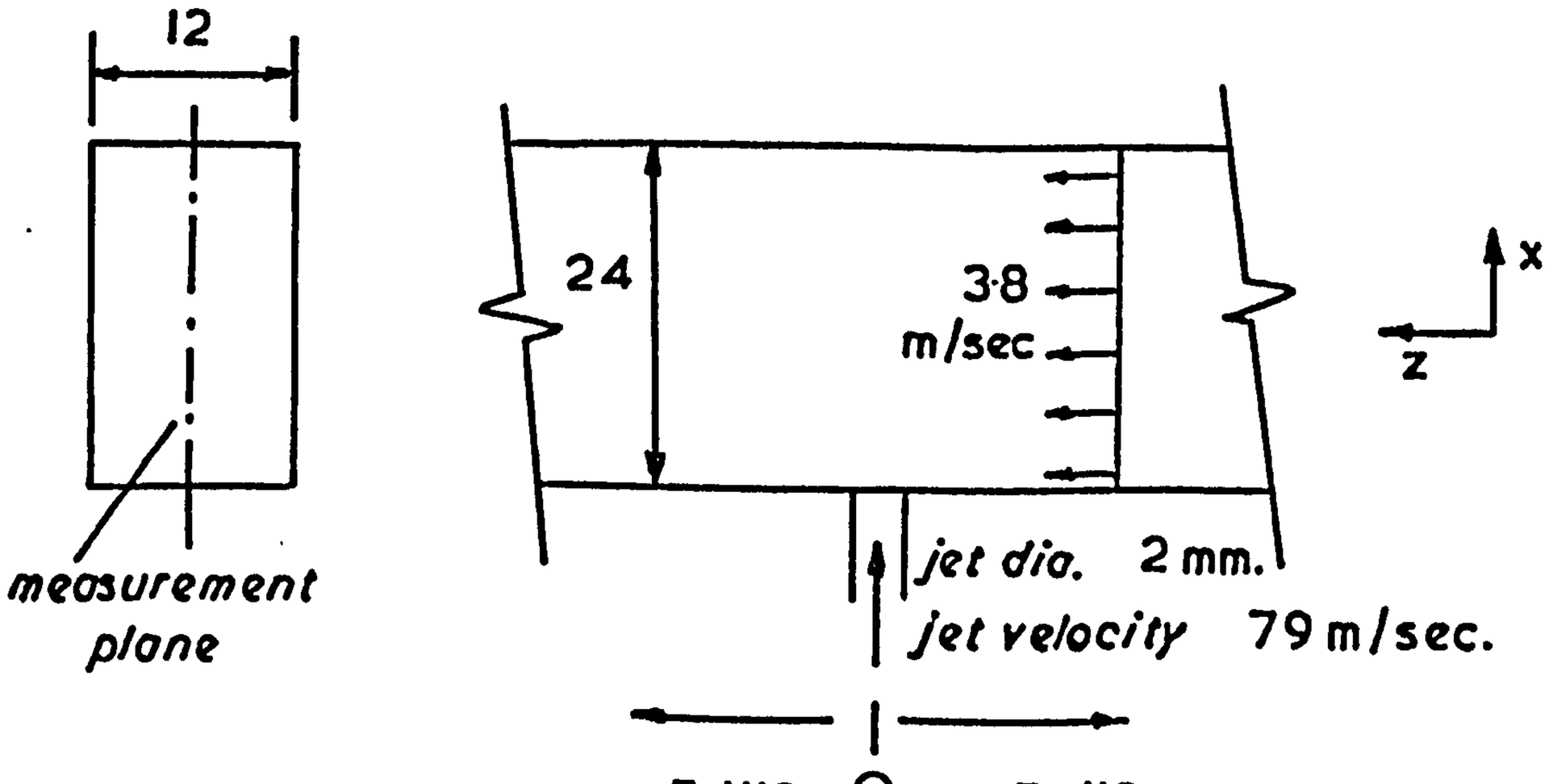

Cross Sectional Concentration Distributions for an Enclosed Jet in a Crossflow.

Fig. 5·19

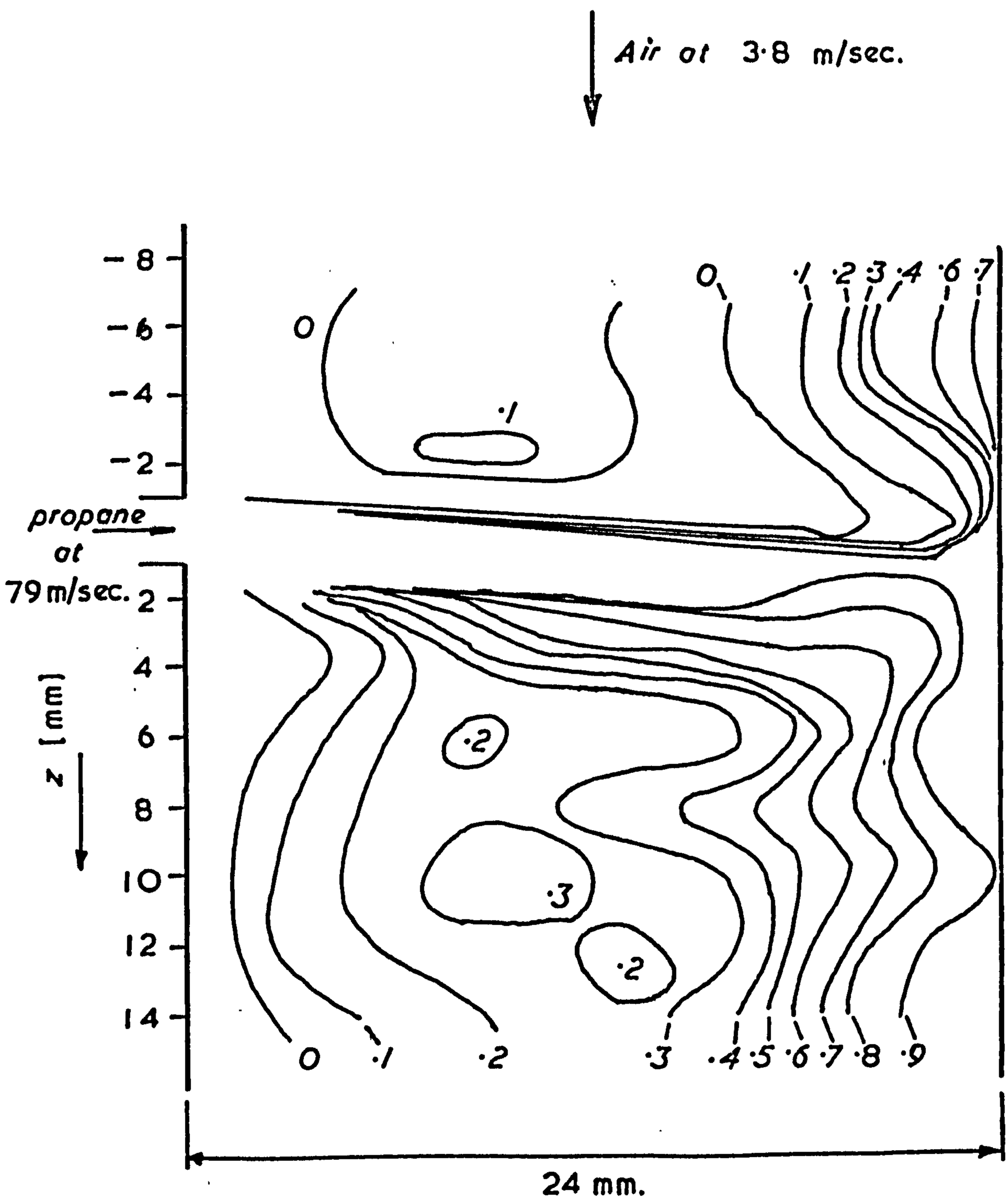

Contours of Constant Mass Concentration for the Enclosed Jet in a Crossflow.

Fig. 5·20

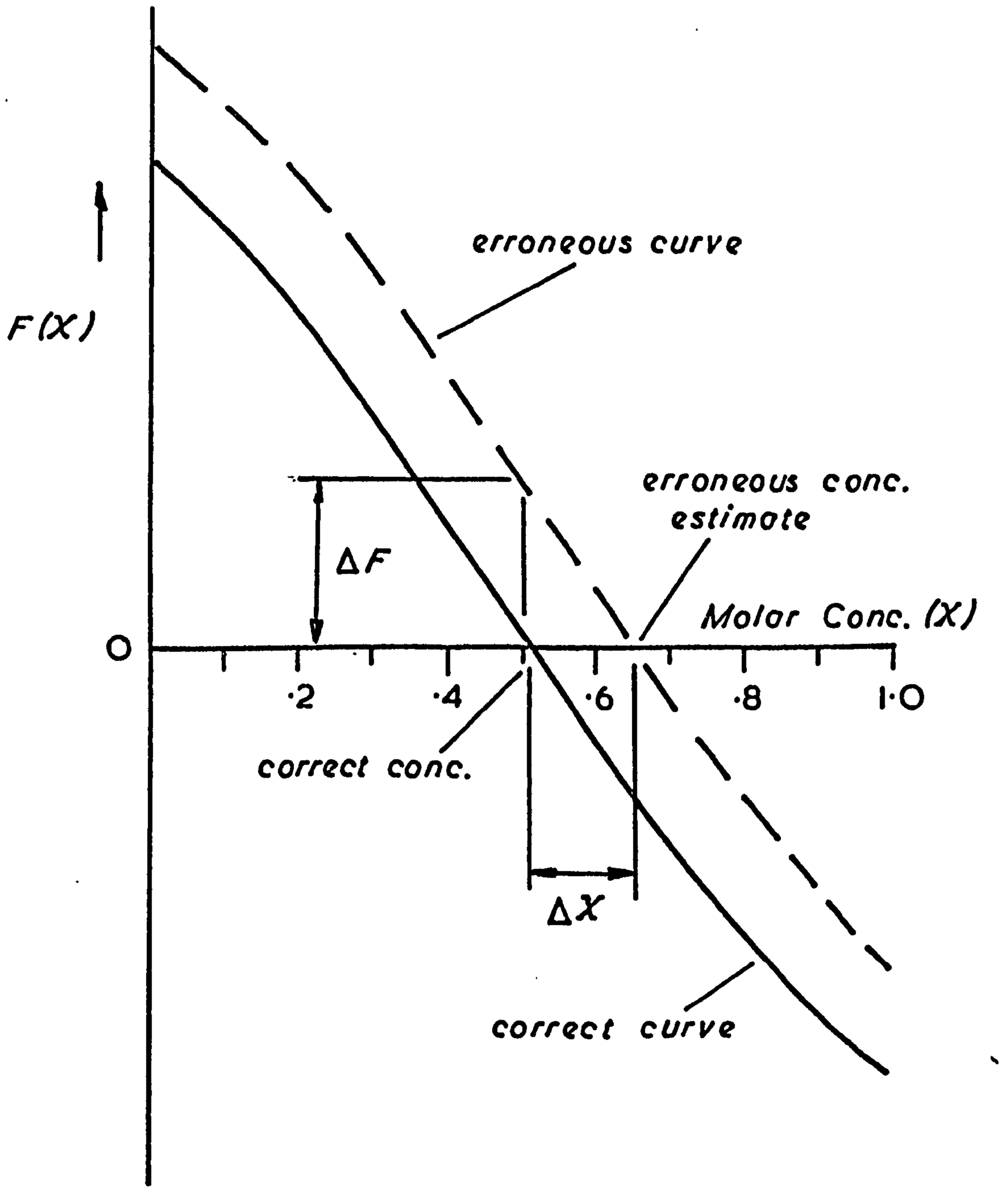

Illustration of the Erroneous Computation of Concentration Magnitude.

Fig. 5·21

wire temps.	150/650 deg.C
wire geometries	10 μm.x 2·0 mm.
wire material	*Pt – 10%Rh.*
gas temp.	20 deg.C
gas velocity	10 m/sec.
voltage fluctuation error:	± 0·5%

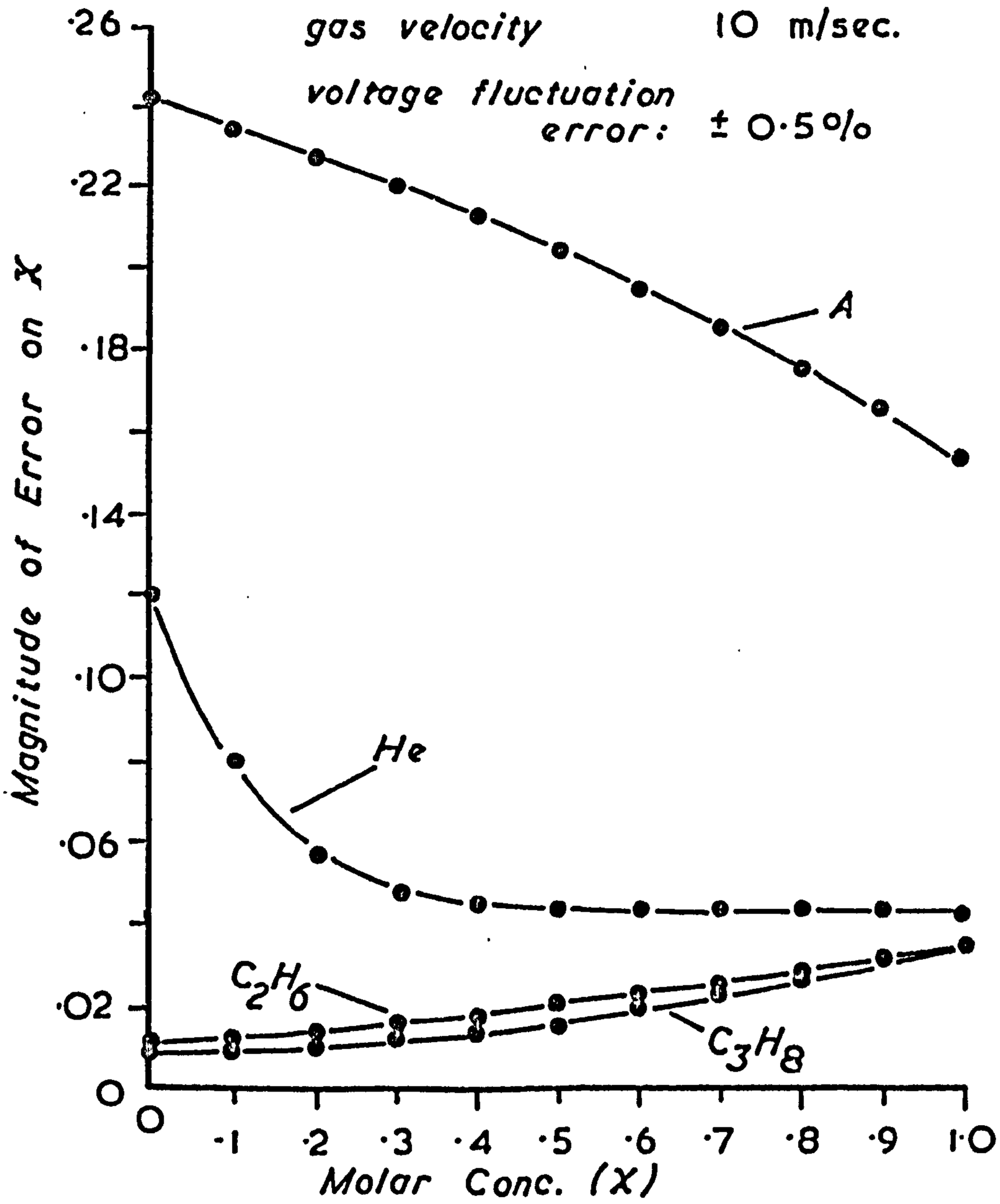

Computed Error on Concentration Magnitude.

Fig. 5·22

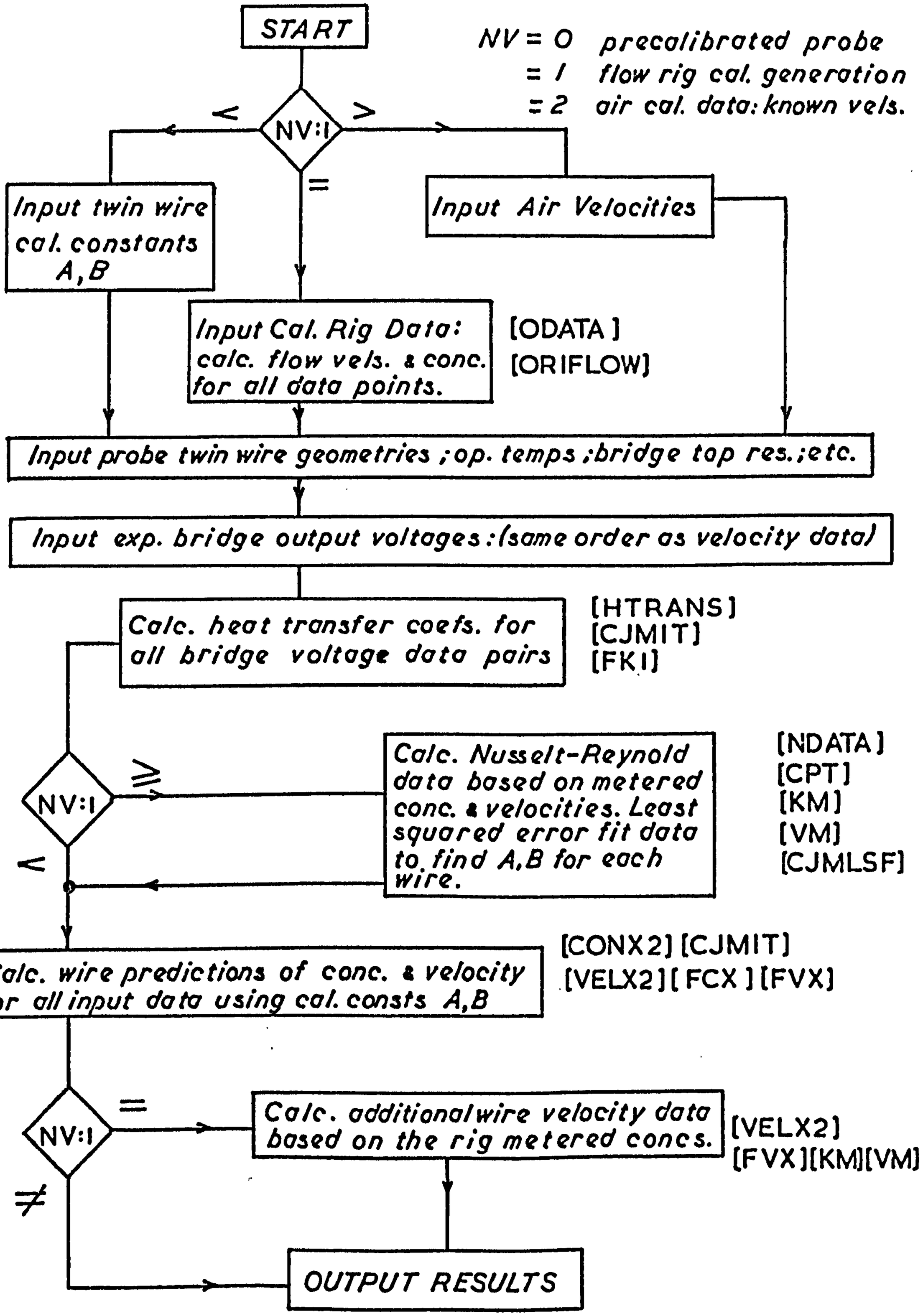

Symbols in [ ] denote subroutine and function segment names (see full program listing)

Calculation Sequence for the Concentration Calibration & Computation Procedure.

Fig. 5·23

CHAPTER 6

Modelling Experiments Based on Published Data

6.1 Description of the Experimental Swirl Rig

A steady state flow rig of fixed geometry was designed and manufactured to allow a non-uniform velocity profile to be created. The salient details are shown in figure (6.1). Air mass flow rate, yielding the mass meaned velocity, (section (2.2.3)), was externally metered by the 10 mm. air orifice mounted within the flow calibration rig (section (4.1.3.)).

On entering the modelling rig the air is deflected by a vane which may be rotated to provide variation in air velocity profile. Optimum vane geometry, and the positioning of air passages through the vane, were determined experimentally to produce suitable velocity profiles across the measurement zone. The measurement zone (figure 6.1) represents a 150 deg. sector of a circular combustion chamber.

Exchangeable brass 'screw-in' gas jets could be placed at three locations within the rig. Two locations were provided on the centre column orientated parallel or at 20 deg. to the model top surface, thus allowing for suitable jet inclination in the engine.

The third location was at the circumference of the model combustion chamber as shown in figure (6.1). Minor variation in geometry was achieved with modelling clay and forming templates to create any necessary radii etc. in the combustion chamber design.

Probe traversing facility was provided by a rotating protractor disc, and a radial slider mechanism, thus allowing complete flexibility of probe position within the chamber. The traversing arrangement may be more effectively illustrated by reference to figure (6.2).

Variation in velocity profile with vane opening (defined in figure (6.1)) is shown in figure (6.3). At constant mass meaned model velocity, a variety of rig profiles may therefore be created. The manner in which the initial profile compares to profiles at subsequent

angular radii throughout the measurement zone, is also illustrated in figure (6.3) for a constant vane opening of 15 mm. Modest variation is indicated, but this amount of change was considered to be within a normally accepted experimental error band.

6.2 Modelling Experiments based on the Data due to Stock (86); Comparison of Model and Engine Jet Trajectories and Spread

6.2.1 General Comments

The work of Stock (86) has already been discussed in Section (1.1) where the published paper (9) based on the thesis of ref. (86) was reviewed. The work reported in the thesis is of greater detail and provides the necessary data for the modelling experiments. Additionally, a copy of the Schlieren film data has been made available and direct comparison of model and engine trajectory and spread is therefore possible.

Three different nozzle configurations have been modelled and represent an interesting range in injector inclination to the air swirl.

6.2.2 Steady State Model of a Radial Injection

Prints of the injection process are shown in figure (6.4). Injection is from the circumference of the combustion chamber, and the nozzle is directed radially to the centre of the chamber, air swirl is in an anti-clockwise direction.

Injection commenced 15 deg. b.t.d.c. and had a duration of 4 degs. crankshaft rotation. Nozzle diameter was 0.7 mm., injection rate 5 mm^3/crank deg., engine speed 1000 rev/min., and compression pressure was 32.95 bar.

At compression top dead centre the combustion chamber was effectively a cylindrical disc of 29 mm. radius. The radial velocity profile across the combustion chamber, as measured by Stock, is shown in figure (6.5), and may be represented in non-dimensional form as illustrated. A rig vane opening of 17 mm was found to produce the most suitable comparison of profile (figure 6.5).

Calculation of the fuel nozzle exit velocity (based on the injection rate, nozzle area, and a value of C_d = 0.83 from ref. (87)), yielded U_f = 94 m/sec.

Modelling tests were conducted at two rig mean air velocities, of 3.25 m/sec, and 5.6 m/sec. The gas jet nozzle diameter by equation (2.20) was calculated to be 5.22 mm for propane and 6.60 mm for ethane.

Figures (6.6)(6.7)(6.8) compare the model measured steady state concentration profiles, obtained with the hot wire anemometry technique, for three different conditions of similarity. The profiles are represented along radii of the model combustion chamber at values of 'θ' denoting angular displacement from the nozzle in the direction of the airs rotation. Measurement was made on the horizontal plane containing the nozzle centre line.

Agreement of the three different modelling conditions, based on the similarity theory of section (2.2.1), indicates conformity of trajectory and spread irrespective of tracer gas type and air velocity. The data scatter on each of the cross-sectional jet profiles was thought to be indicative of natural data spread, and not due to modelling discrepancies. Jet trajectory and spread is seen to be consistent.

The data obtained for the propane model at $\bar{U}_a$ = 3.25 m/sec. is reproduced in figure (6.9) as a mass air to fuel ratio contour map, and more effectively illustrates trajectory and spread of the steady state model.

6.2.3 Transient Modelling of the Radial Injection

The engine injection duration of four crankshaft degrees rotation, corresponds to 0.67 msecs. in real time. Applying

equation (2.22) therefore indicates that the corresponding duration on the model is 10.5 msecs. at a mean rig air velocity of 3.25 m/sec. Alternatively, an engine crankshaft rotation of one degree corresponds to 2.62 msecs. on the model time scale.

A pulsed gas jet was created by a specially designed and manufactured rotary valve, driven by a 'Servomex' variable speed D.C. motor and control unit. Pulse length of the gas jet could then be varied by control of the valve rotor angular velocity. The ratio of 'on' time to 'off' time was 0.045, hence ample duration existed for the scavenging of gas between successive injections in the model simulation. The experimental equipment associated with this set of tests is shown in figure (6.10).

Gas nozzle exit velocity variation with time was measured by the calibrated concentration probe positioned on the exit plane of the nozzle. The pulse was found not to be perfectly square, but its rise time was short and a substantial percentage of its duration represented a constant injection velocity. Pulse length and character at the nozzle plane was highly repeatable (figure 6.11). Further downstream from the nozzle the pulse appeared typically as shown in the second oscillogram of figure (6.11), and some variation in pulse width and location of peaks existed between successive injection processes. Therefore, representative voltage-time traces were obtained at each measurement location within the model combustion chamber, by a data processing technique which has also been employed for the transient engine analysis to be discussed in chapter (7).

In the case of the transient jet analysis the time dependent variables to be simultaneously recorded were the two output voltages from the concentration hot wire probe and a

timing pulse. The timing pulse was produced by a photo-cell viewing a slotted disc mounted on the valve rotor. The positive rising edge of the pulse, (corresponding to light transmission through the disc's slot), was set to correspond to the initiation of the injection process at the nozzle exit plane (cf the voltage traces of figure (6.11)).

Figure (6.12) shows the data processing sequence for a single voltage trace and associated timing pulse channel. The signal was modified by a d.c. voltage bias and attenuation stage such that the maximum and minimum voltages of the trace lay within the acceptance band of the 'Racal Store 4' frequency modulating tape recorder. On completion of the data recording process,known calibration voltages were also recorded and hence modified by the same circuitry.

The recorded signal was then replayed to the input channel of a high speed A/D converter on a Hewlett Packard 5451A computer. A small computer program was used to average any required number of input traces. Origin of the time scale on individual sample traces was maintained constant by using the photo-cell timing pulse as a triggering voltage on the A/D converter unit. Hence a typical, or mean, voltage time trace was generated and stored in the computer data core, with sampling ordinates at intervals as defined by the A/D converter setting. The averaged trace was then output via a high speed paper tape punch.

In the case of the transient jet analysis two paper tapes, corresponding to the voltage time traces averaged over twenty injection processes, of the hot wires of the concentration probe, were therefore created for each measurement location.

Voltage levels on the paper tape did not represent actual test voltages due to the bias and attenuation process, and discrepancy between input and output levels of the tape recorder. Therefore, the similarly recorded calibration voltages were also digitised onto paper tape. Signal paper tapes and associated calibration level paper tapes, were then processed by an I.C.L. 1904 digital computer using a simple conversion program to relate the 'punched' voltages on the paper tapes to 'actual' voltages from the calibration levels. 'Actual' voltage-time traces thus generated were output on punched card and therefore formed data for the relevant processing program.

For the purposes of the transient jet analysis the analogue signal was digitised at a sampling period of one ordinate (sample) every 100 μsecs. Thus the 10.5 msec. injection pulse was represented by approximately 100 ordinates.

Concentration magnitude, at any measurement location, at appropriate points in time, could then be extracted. Hence, at a single point in time, concentration magnitude at every measurement location could be accumulated and processed in the same manner as the steady state analysis, to produce the gas jet envelope at that instant.

The resultant concentration maps, (at successive time intervals after the start of the injection process, corresponding to engine steps of 1 deg. crankshaft rotation), are shown in figure (6.13). Comparison of the envelopes thus produced with the steady state jet envelope and trajectory may be made as in figure (6.14).

The comparison of figure (6.14) illustrates an important result, namely, that the steady state trajectory and spread is sensibly identical to the transient jet. i.e. Successive

envelopes of the transient jet propagate along the path defined by the steady state analysis.

6.2.4 Comparison of the Radial Gas Jet Model with the Engine Fuel Spray

The engine fuel spray envelopes illustrated in figure (6.4) are represented in figure (6.15) to the same scale as the gas jet model diagrams. The light yellow are adjacent to the dark 'fuel' boundary of figure (6.4) represents a fine droplet or vapour trail. The figure (6.15) illustrates both boundaries. Figure (6.16) compares the outer boundary at each film frame interval (1 deg. crankshaft steps) with those produced by the gas jet model. Substantial agreement may be seen to exist. The minor discrepancies which are evident on comparison of the envelope were thought to be acceptable by the author in relationship to the modelling concept and the amount of variation which may be expected to occur between successive injections in both the model and the engine.

6.2.5 Further Modelling Tests on the Data due to Stock (86)

Two further modelling tests based on the data of Stock were also executed. In these cases injector inclination was again horizontal but at an angle of 50 deg to the combustion chamber radius. Propane tracer gas was used and the models were based on the same parameters as those for figure (6.13). On the basis of the above favourable comparison between transient and steady state models the tests were conducted only for the steady state case.

Figure (6.17) shows the results obtained with a gas jet inclination 50 degs. against the air swirl rotation. Figure (6.18) shows the corresponding film sequence. Basic similarity

is apparent and the trajectory and spread of the engine spray and model gas jet are compared in figure (6.19).

Similarly, figure (6.20) shows the mass air-fuel ratio profile map obtained for the same nozzle inclined 50 deg. with the air swirl, and figure (6.21) shows the corresponding film sequence copied from the thesis of Stock. Figure (6.22) shows a representative engine fuel envelope (at 356 deg.) compared with the gas jet model envelope. Impingement onto the combustion chamber wall is seen to occur at 70 - 90 deg. from the injector nozzle, the gas jet model shows similar impingement characteristics.

6.2.6 Comments on the Gas Jet Simulations Based on the Data due to Stock

Overall spread and trajectory of the gas jet models have been shown to be similar to those of the engine. An interesting result has been illustrated on comparison of the steady state and transient analysis which confirmed that the steady state jet is basically similar to the transient model. Hence, the complications of transient data analysis are unlikely to be necessary for most typical diesel engine injection processes.

However, the above modelled situations, although allowing comparison of jet behaviour, have not allowed comparison of engine auto-ignition sites and corresponding model predicted local air to fuel ratio. This is because the large fuel nozzle diameter used in Stock's tests created a richer than average fuel spray, and auto-ignition sites observed on the film were located outside the model measurement zone.

6.3 Modelling Experiments based on the Data due to Rife and Heywood (Reference 36)

6.3.1 General Comments

Two injection conditions have been modelled from this reference. Spray trajectory was observed by direct high speed cine-photography, dense regions of the spray prior to ignition were made visible by illumination from flash bulbs. The tests were conducted on the M.I.T. rapid compression machine and provide information on trajectory, and auto-ignition sites within the established spray. Low density, vapour regions were not visible by this direct photographic technique. The filmed data is of injection at a fuel nozzle velocity of 91.2 m/sec. from a single hole centrally placed nozzle of diameter 0.152 mm., into a circular combustion chamber of 50.8 mm (2 inches) radius. Modelling experiments have been performed for filmed data at the two swirl rates of angular velocities 80 and 180 rad/sec.

The velocity profile of the rapid compression machine was found to be most effectively modelled with a modelling rig vane opening of 15 mm (figure 6.3). Modelling was performed at a mean rig air velocity of 3.25 m/sec., and gas jet orifice velocities of 146 m/sec., and 65 m/sec., providing predicted similarity by equation (2.19) at the 80 and 180 rad/sec. air swirls respectively. The requisite gas jet diameter was calculated by equation (2.20) to be 0.75 mm.

Gas concentration measurements were made in the plane of the jet centre line and represented as projected onto a plane normal to the camera viewing angle. Hence, direct comparison may be made of the film and model trajectories.

6.3.2 Data for the 80 rad/sec. Air Swirl Case

Measurement by the hot wire concentration technique, for the model as described in (6.3.1) provided data to produce the mass air to fuel ratio contour map as shown in figure (6.23). The relevant sector of the circular combustion chamber is shown and scaled to correspond to the actual dimensions.

Impingement of the jet is seen to occur, and the super-imposed centre line points as extracted from ref. (36) display a high degree of coincidence with the line of maximum jet concentration.

An interesting region of low mixture concentration is indicated in the 'wake' region of the jet, centred at a radius of 0.75 inches, and indicates accumulation of jet fluid in a low pressure wake region.

Reproduction of the relevant combustion photographs are shown in figure (6.24) which illustrates the spontaneous ignition and flame progression sequence through the jet. These may be represented as in figure (6.25), where the boundary of the gas jet model is also illustrated. Comparison of the primary ignition source, and the corresponding area of figure (6.23), indicates that 'actual' ignition occurs in a 'predicted' air to fuel ratio of approximately 10:1 to 15:1, i.e. in a region predicted to be slightly richer than stoichiometric. Subsequent flame propagation (figure 6.25) is seen to proceed approximately parallel to the combustion chamber wall, and against the air's rotation. The figure (6.23) indicates that the flame front therefore travels through regions predicted to be mixed close stoichiometric concentration. Envelope (3) (cf. with figure 6.24)) indicates a considerably brighter combustion, indicative of a 'richer' burning process. This corresponds to the model impinge-

ment point and mixtures in the range 10:1 to 8:1 mass air to fuel ratio.

The flame envelope (4) of figure (6.25), (cf. figures (6.24)(6.23)) is of particular interest because a bright ignition nucleus is indicated and represented as a secondary auto-ignition point in figure (6.25). The high luminosity of this source would suggest that if ignition had not occurred in envelope (1) then the first auto-ignition centre may have occurred in this region. Further, the flame propagation from this source is rapid and spreads outwards from the nucleus, in a manner represented in figure (6.25) by envelopes (5) and (6).

Envelopes (5), (6) (cf. figure 6.24) would suggest that the rapid combustion during these stages, and the expansion of the high temperature gases, has destroyed the initial jet profile, transport and mixing of fuel may then be reasoned to be controlled, at least in part, by the combustion induced turbulence.

6.3.3 Model based on the data of Rife and Heywood at an Air Swirl of 180 rad/sec.

Combustion photography of this injection process was not presented in reference (36) and therefore detailed comparison of the model mass air to fuel ratio contours with the ignition nuclei and subsequent flame propagation may not be made.

The mass air to fuel ratio contour map, obtained by concentration measurement in the model, is shown in figure (6.26). Impingement of the fuel spray on the combustion chamber wall is predicted not to occur and comparison of the depicted fuel spray with the previous 80 rad/sec result of figure (6.23) shows a marked difference in fuel concentration levels.

Data points extracted from reference (36) are superimposed

on the figure (6.26) and again indicate a close agreement of jet model and fuel spray trajectories. Personal communication with Professor Heywood revealed that the twin centre line trajectories represented are resultant of data scatter from separate film sequences.

6.3.4 Comments on the Gas Jet Simulations based on the Data of Rife and Heywood

As in the results of section (6.2), trajectory is seen to be accurately represented by the gas jet simulations. Further evidence is also presented which indicates that auto-ignition site location and subsequent flame propagation, during the initial combustion stages, relate closely to the model mass air to fuel ratio predictions.

Further analysis of data, with more detailed information on the auto-ignition characteristics of the spray, is desirable. The work reported in chapter 7 is of relevance in this context.

6.4 Range of Modelled Data

The five model similarities examined within this chapter represent a wide range in engine conditions (particularly for momentum flux ratio J), and may be summarised as below:

SOURCE	U_f (m/sec)	$\overline{U}a'$ (m/sec)	d_f (mm)	$d_g(C_3H_8)$ (mm)	J (-)
STOCK (86)	94	42.5	0.7	5.22	7.8
R.and H. (36)	91.2	2.04	0.152	0.75	2830
R.and H. (36)	91.2	4.56	0.152	0.75	590

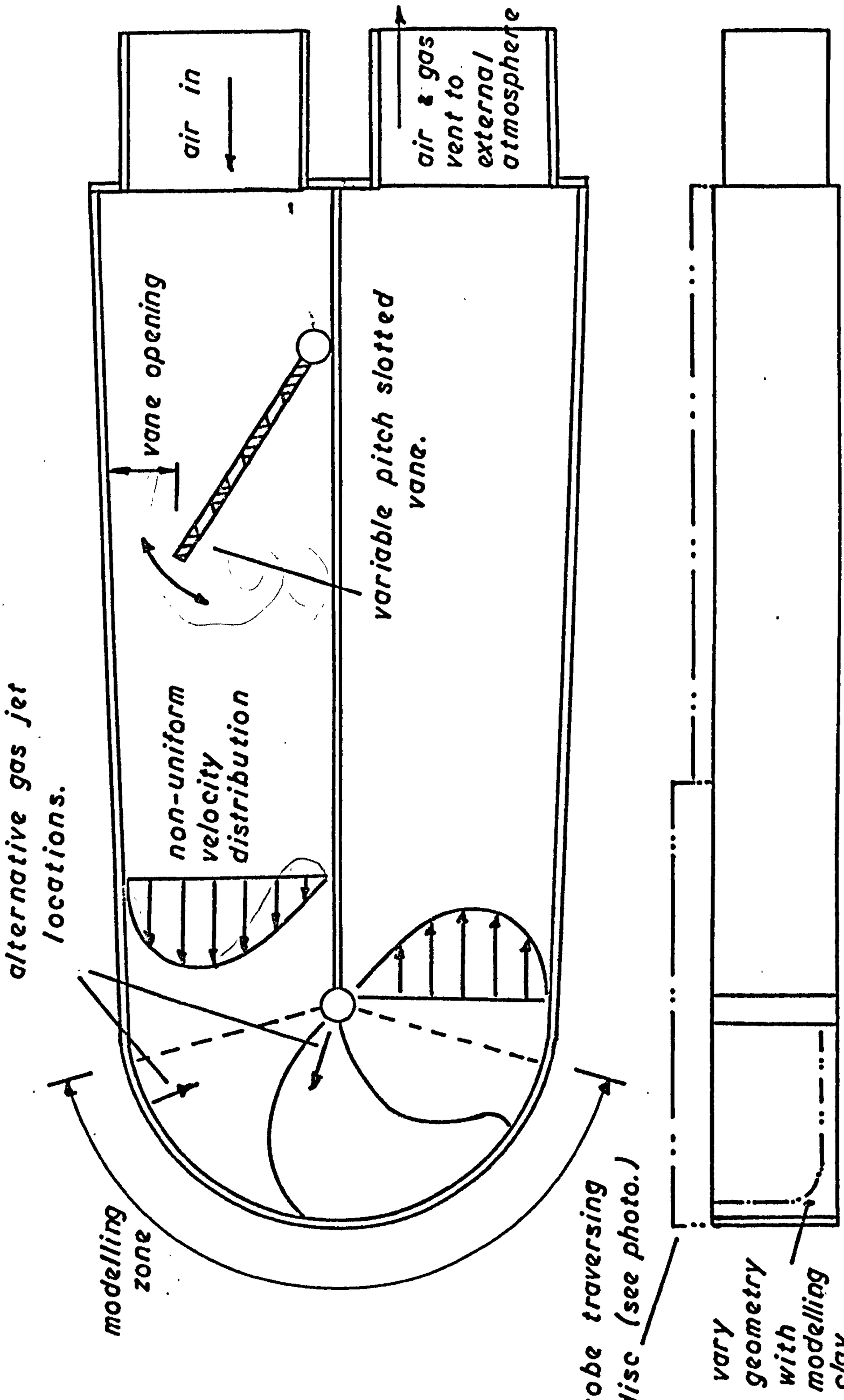

Modelling Rig Salient Details.

Fig. 6.1

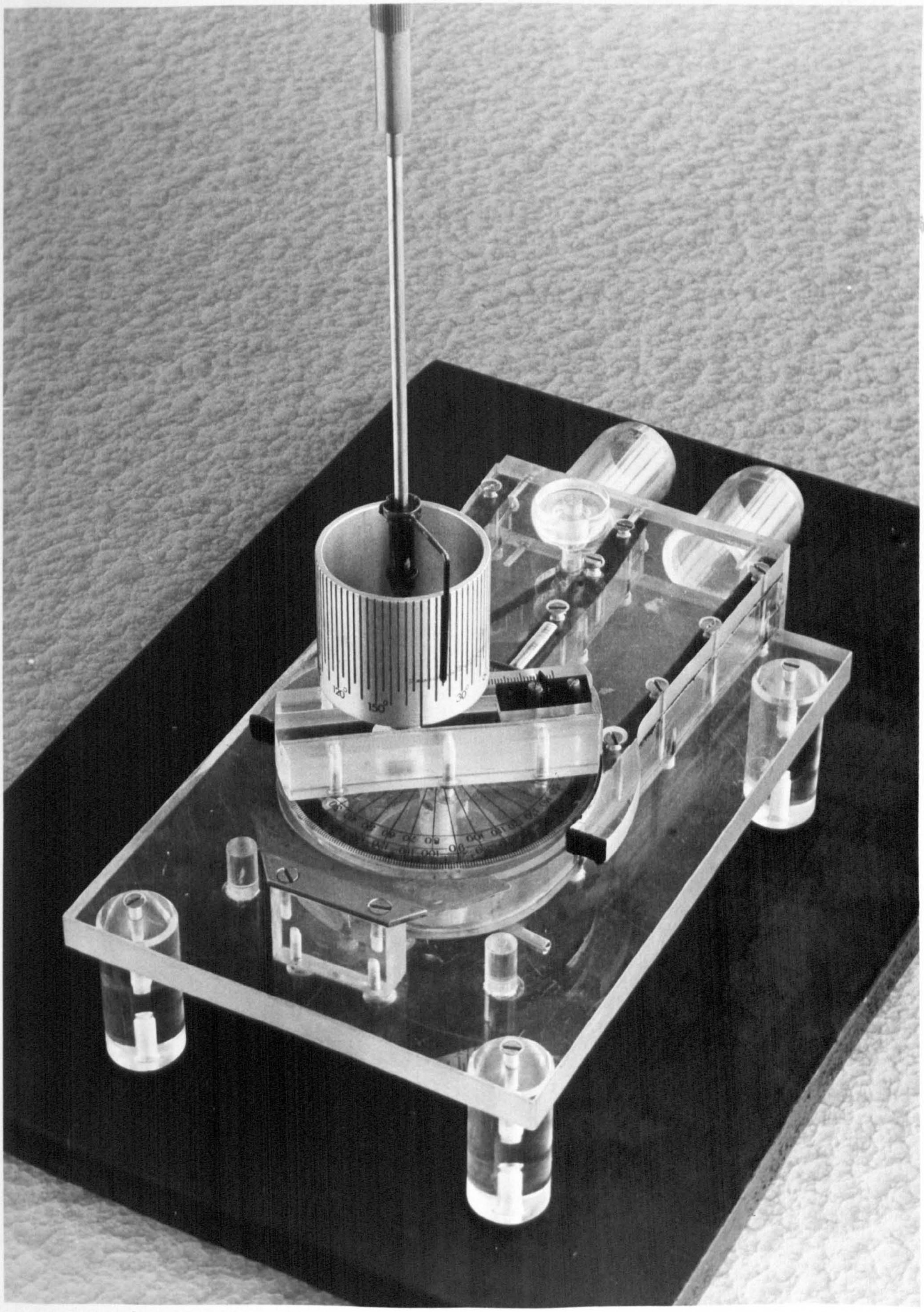

Gas Jet Modelling Rig

Fig. 6·2

Rig Air Velocity Profiles.

Fig. 6.3

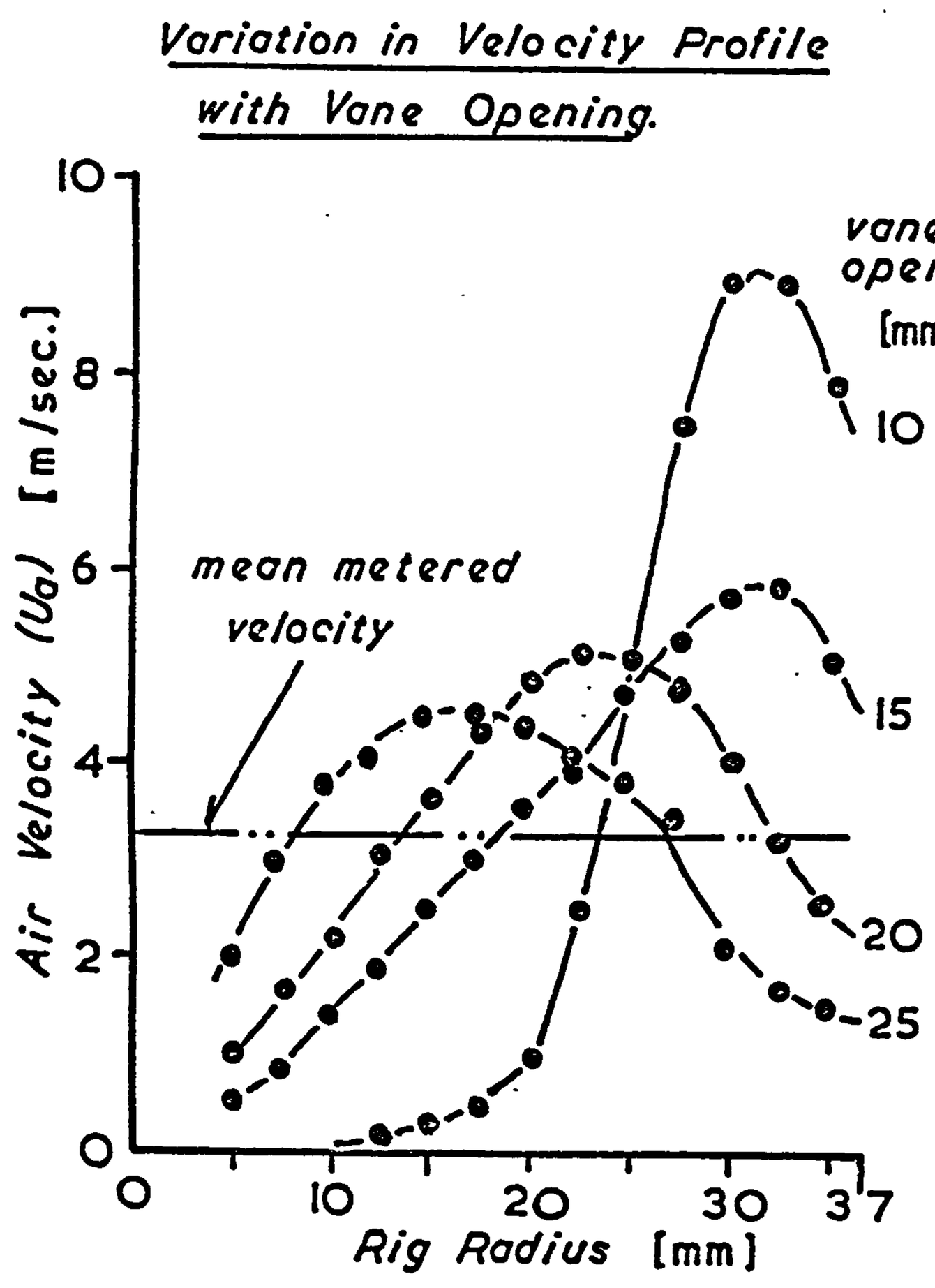

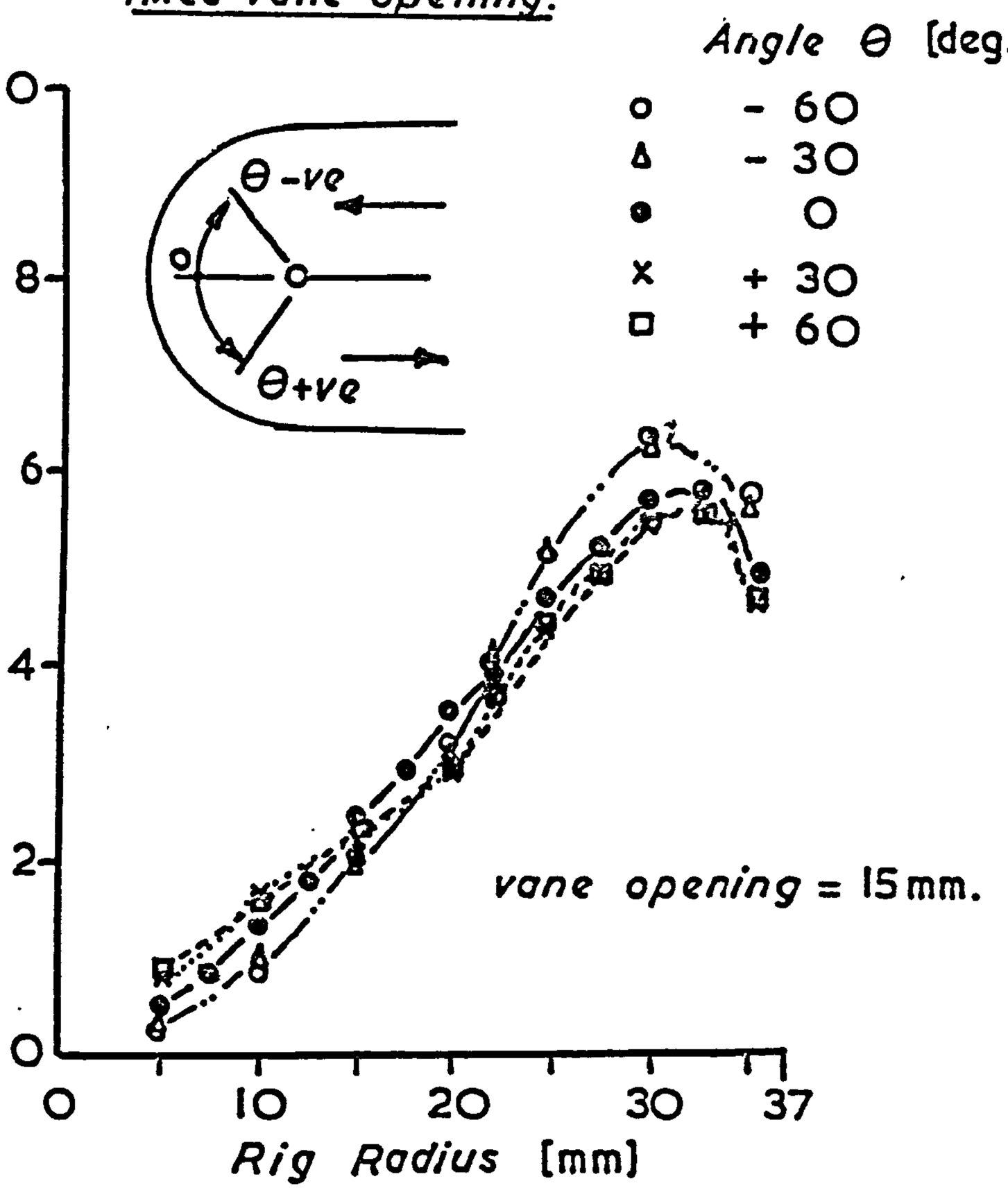

1 frame = 1 crankshaft deg. rotation

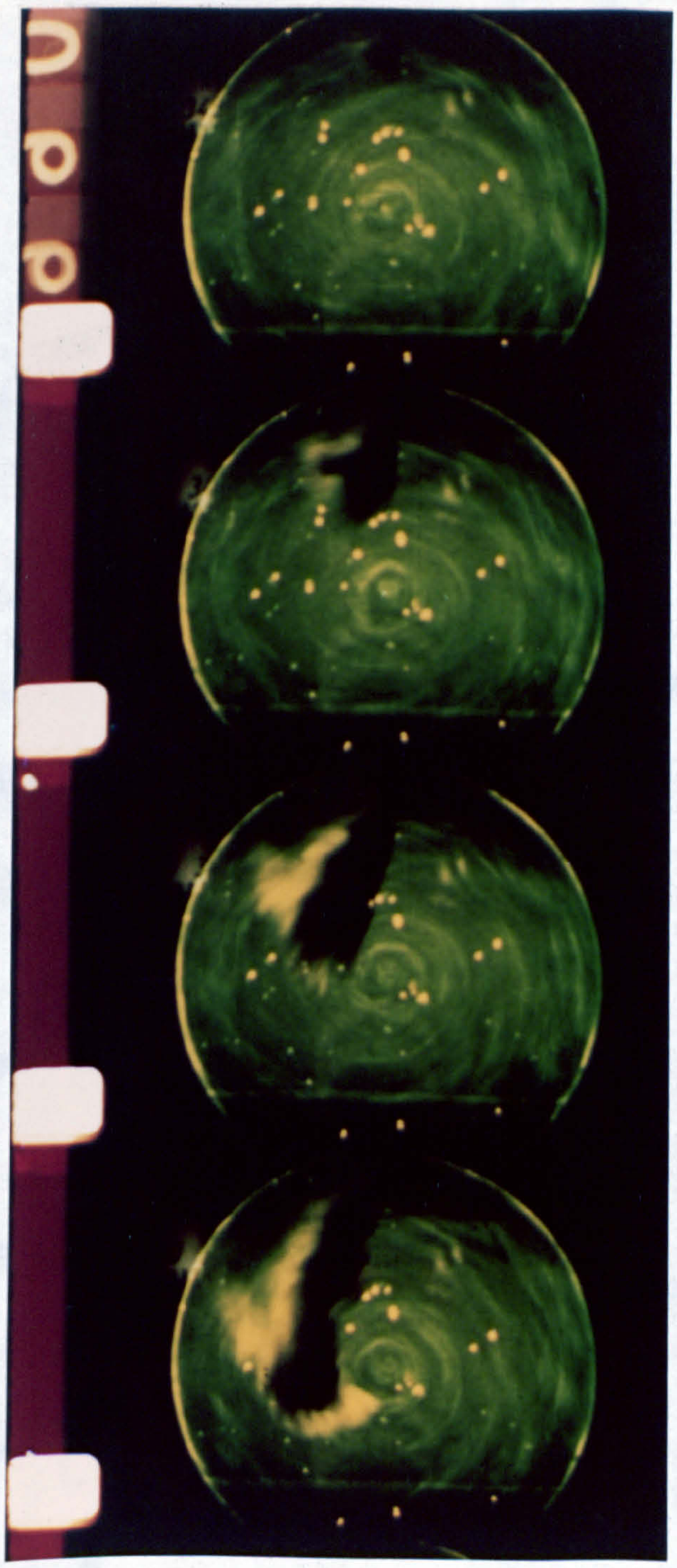

Swirl Anticlockwise. Inj. commences 15 deg. btdc.

Radial Injection Sequence Copied from the Film due to Stock (86)

Fig. 6·4

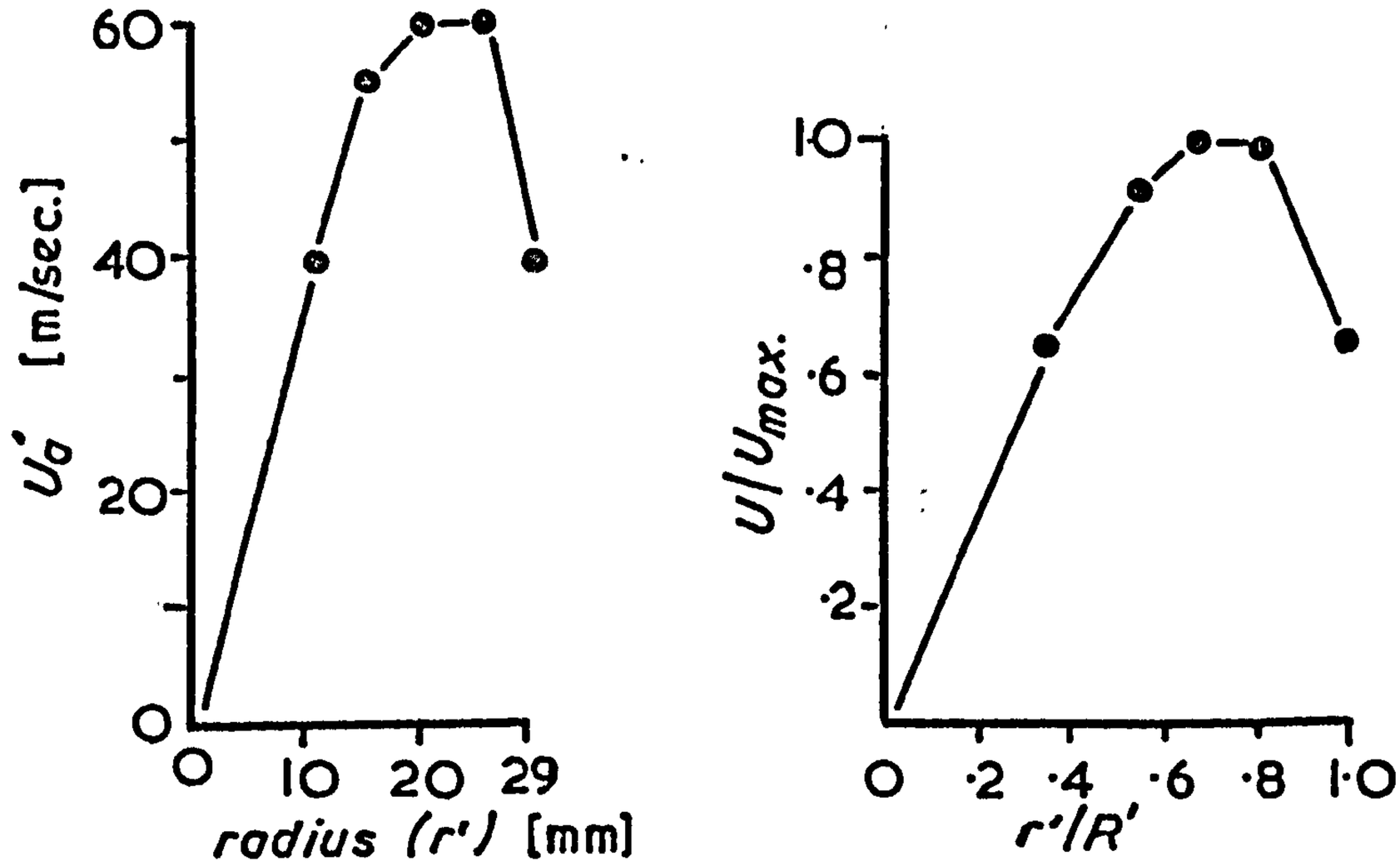

Stock's Velocity Profile for 15 deg. b.t.d.c. (ref. (86))

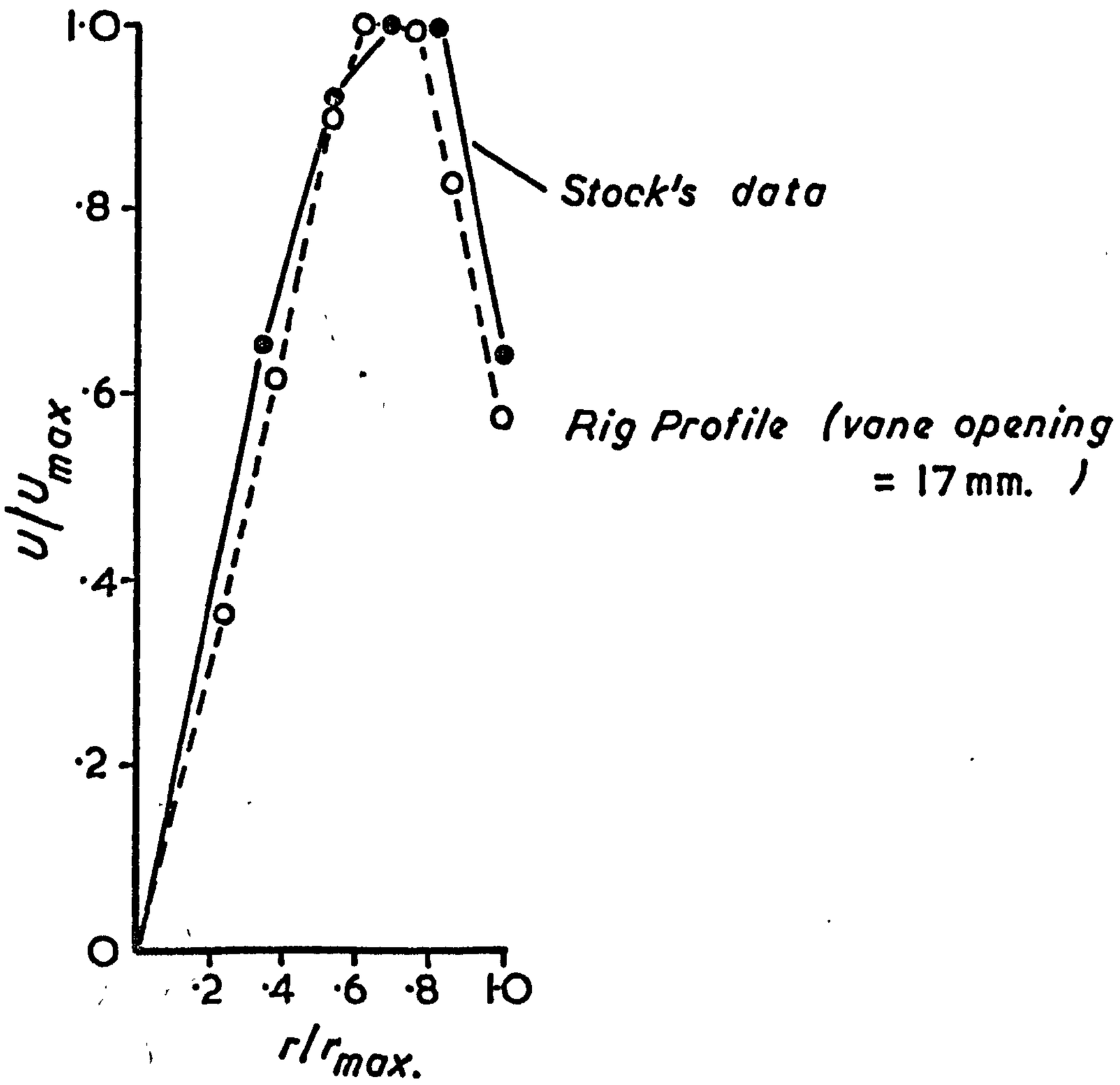

Comparison of Engine and Rig Velocity Profiles.

Fig. 6·5

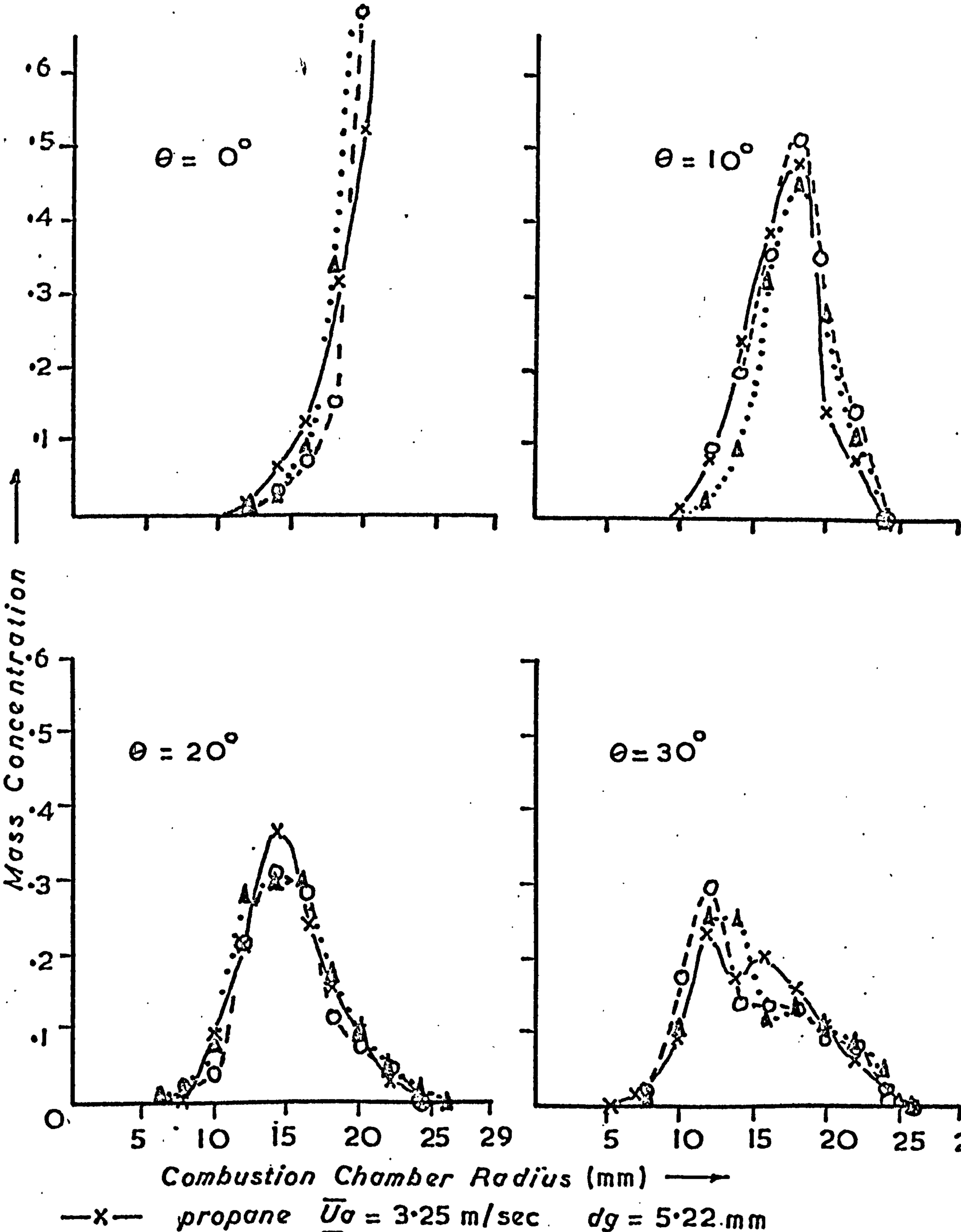

Comparison of Various Model Similarities
(data of Stock (86); jet normal to air swirl)

Fig. 6·6

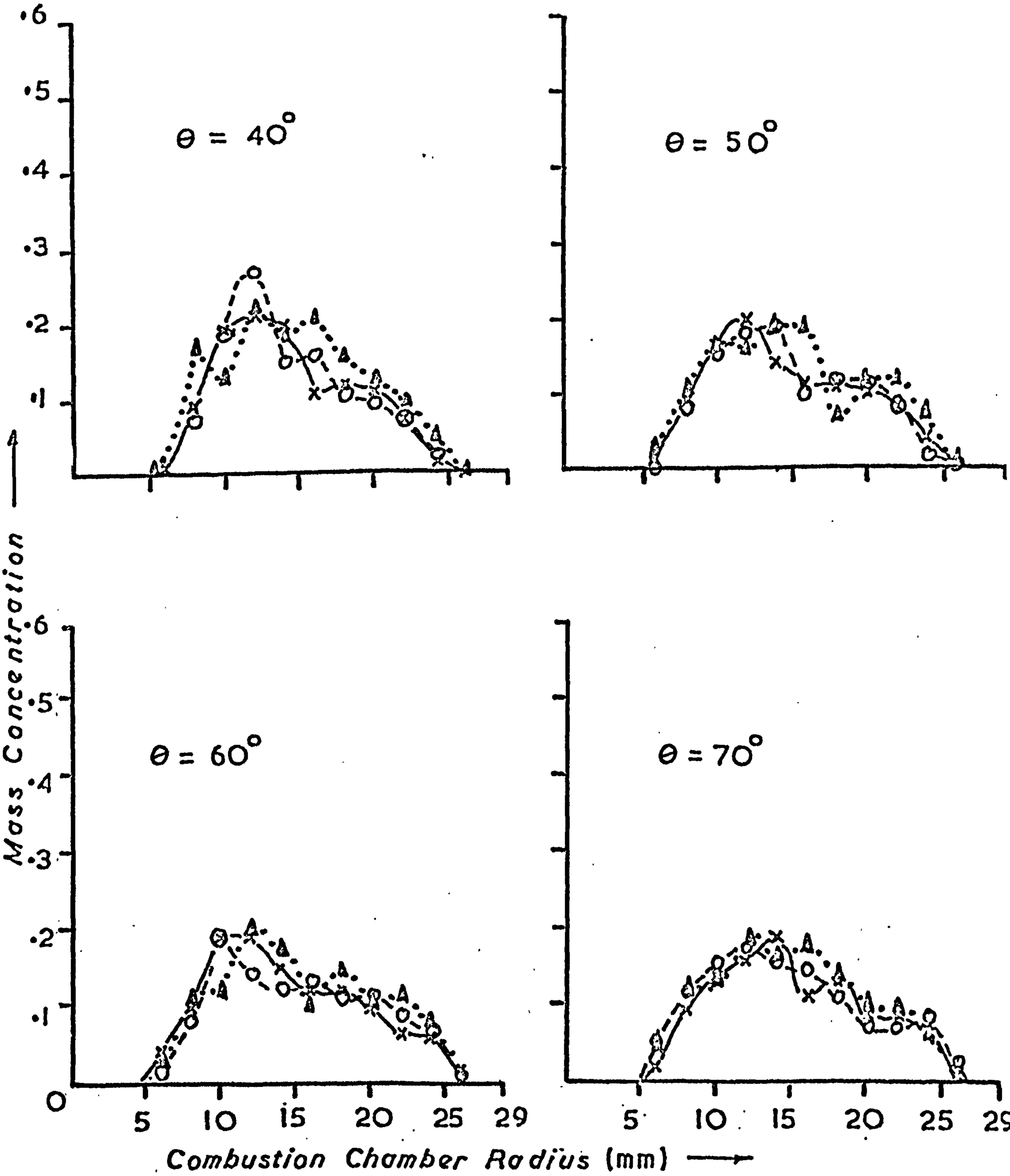

Comparison of Various Model Similarities
(data of Stock (86); jet normal to air swirl)

Fig. 6·7

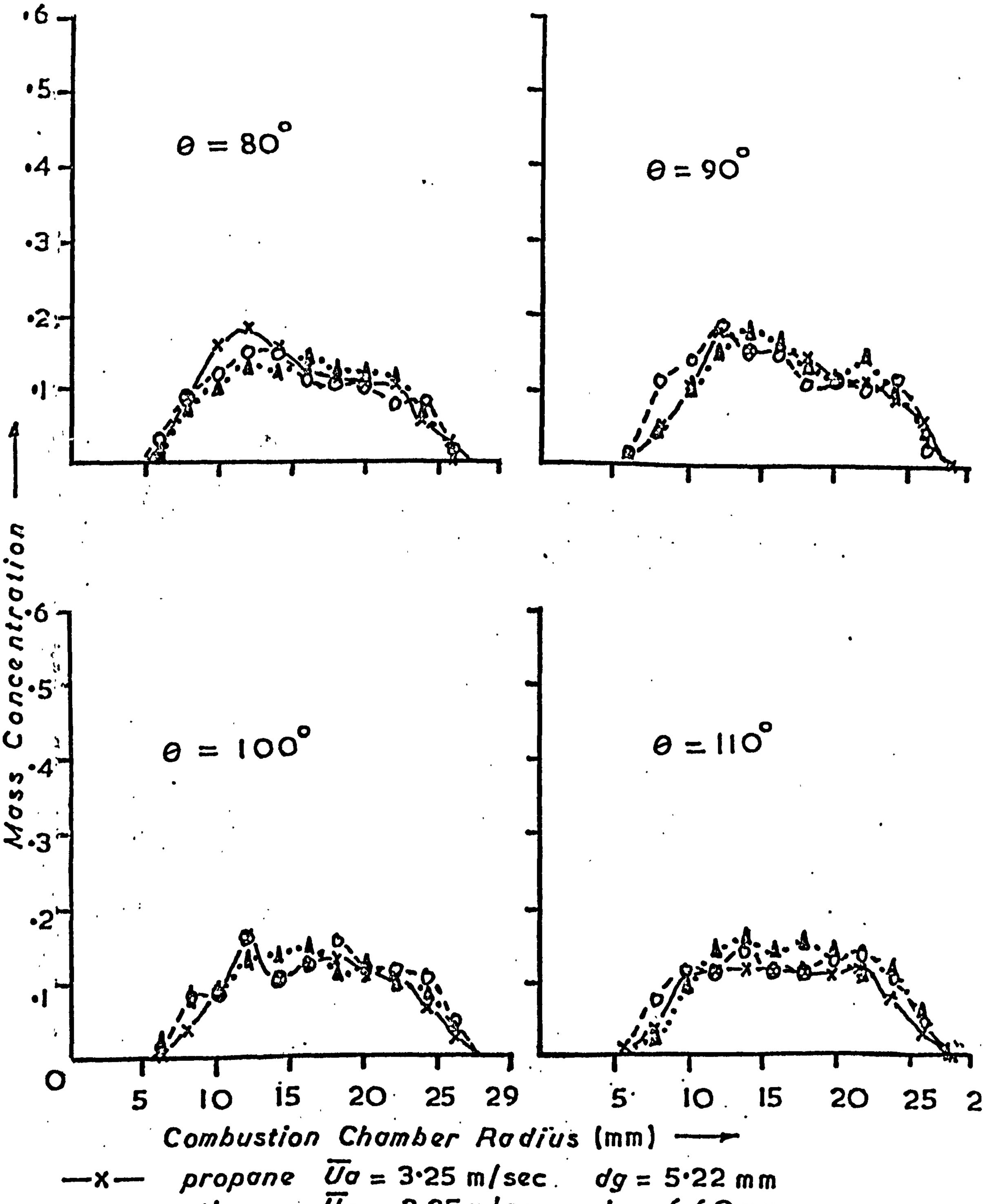

Comparison of Various Model Similarities (data of Stock (86); jet normal to air swirl)

Fig. 6·8

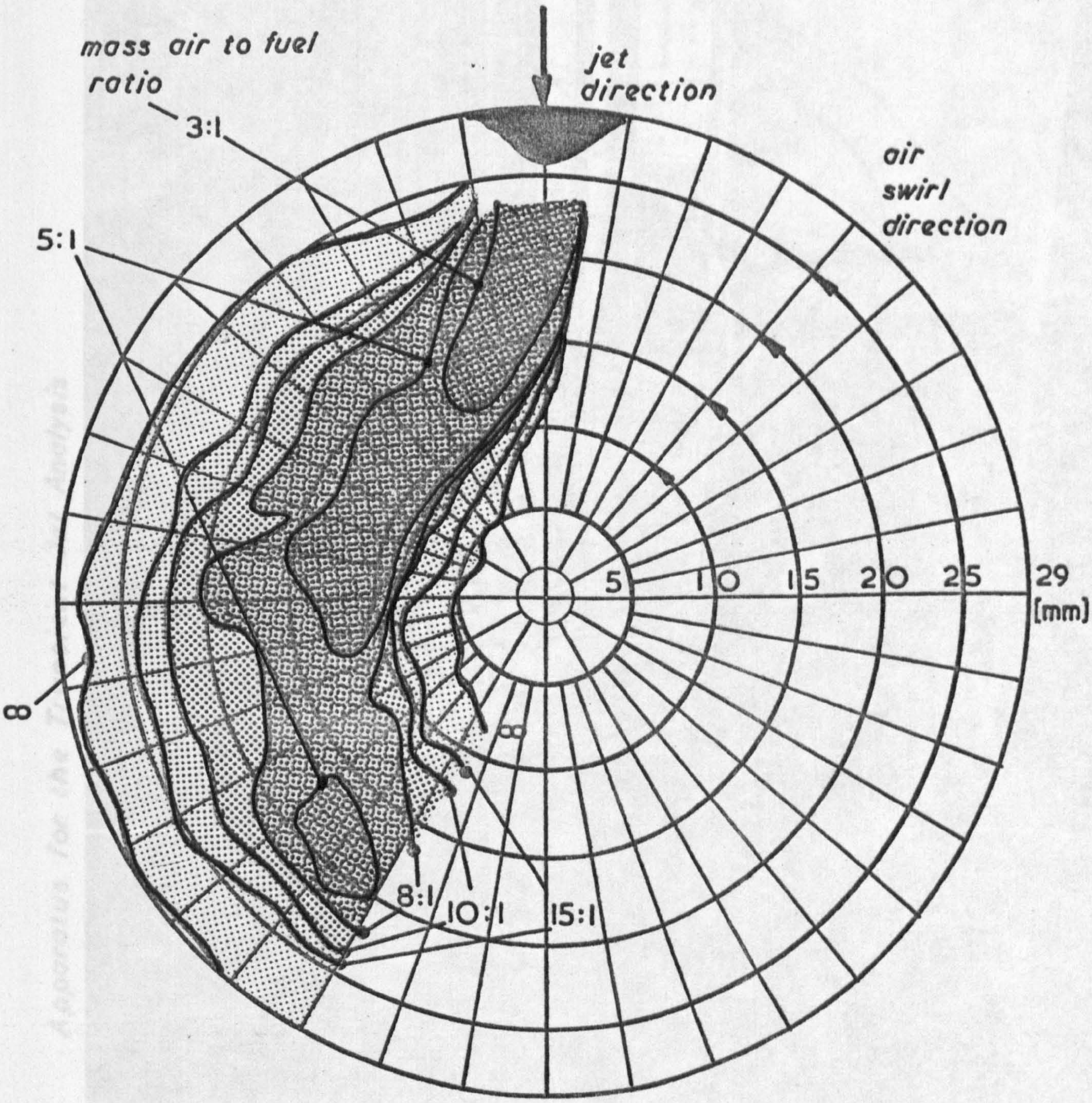

Gas Jet Simulation for the Fuel Spray Injected Radially : Modelled on the Data due to Stock, (ref. (86)) (Steady State Model)

Fig. 6·9

Apparatus for the Transient Jet Analysis

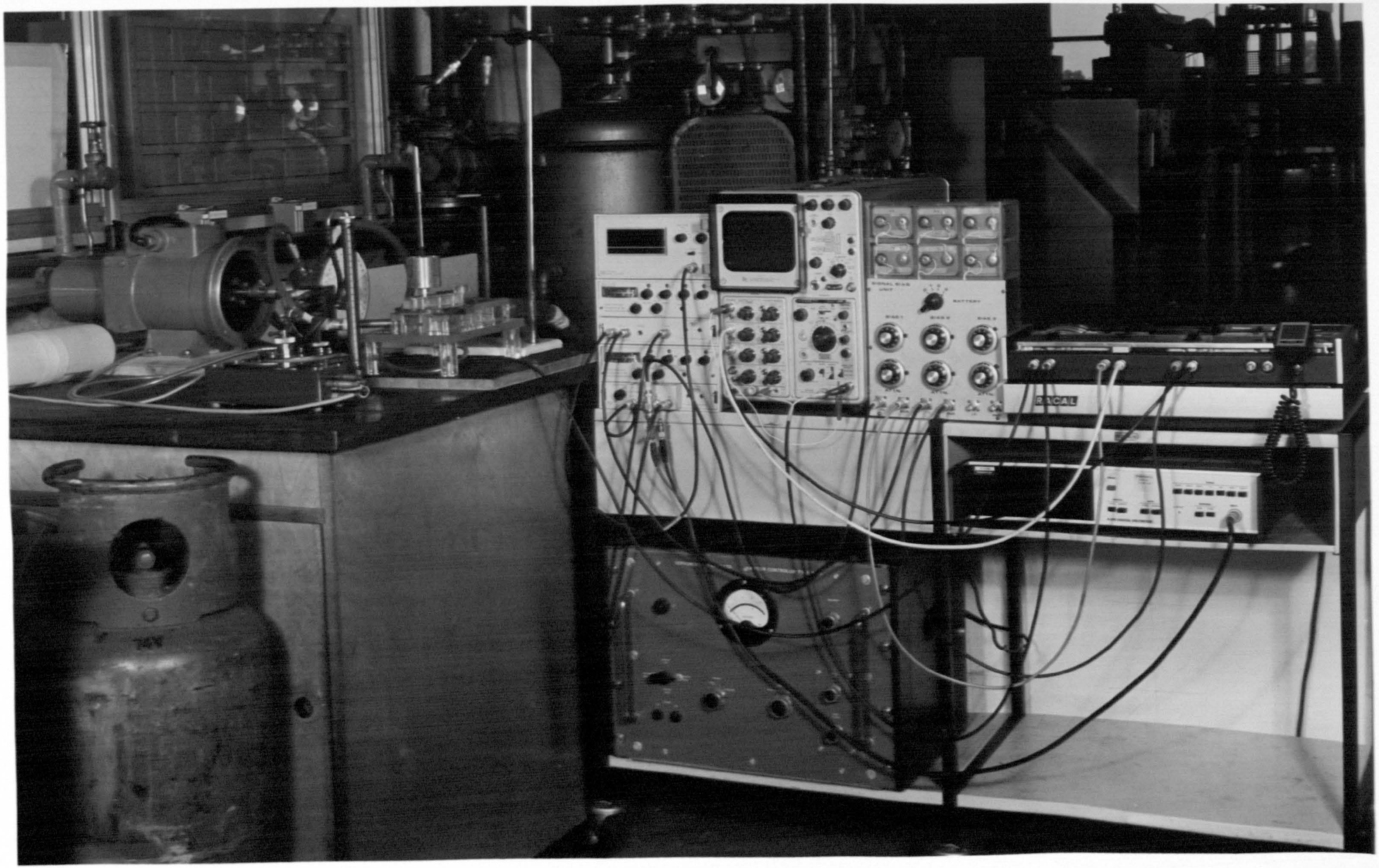

Fig. 6·10

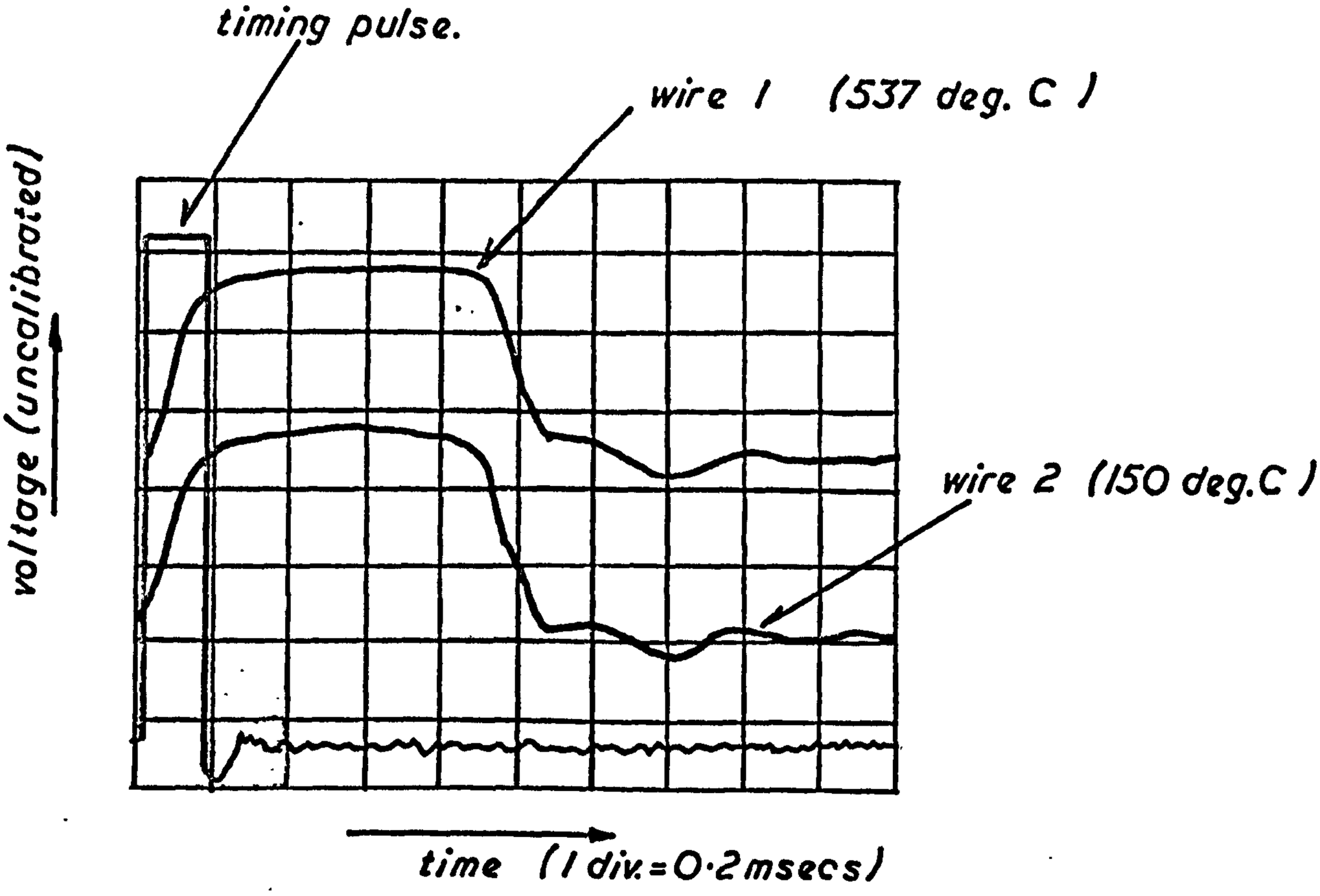

Transient Voltage Traces at the Nozzle Outlet Plane

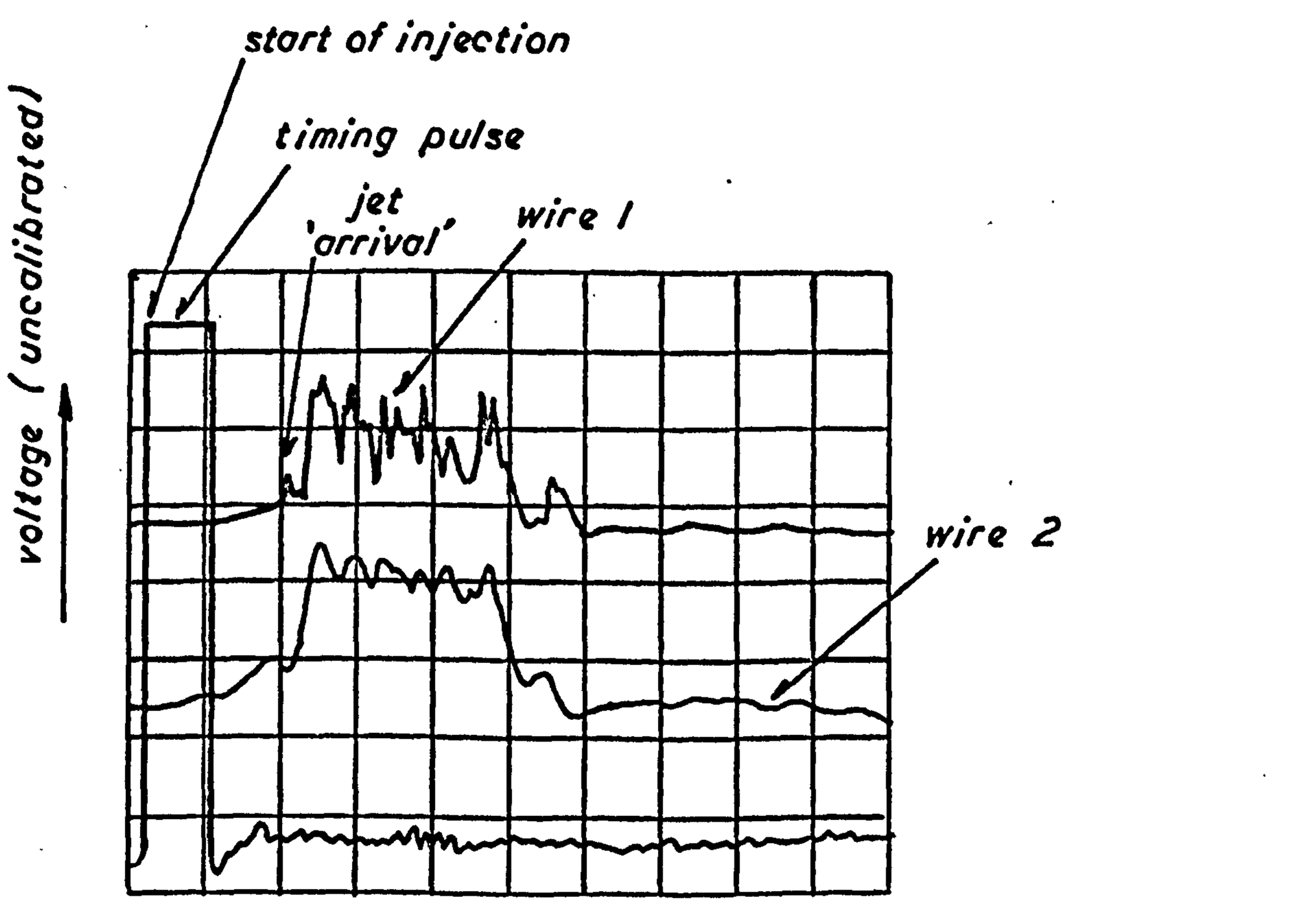

Typical Voltage Trace at a Location 'Downstream' of the Nozzle.

(traces copied from 'Polaroid' photographs)

Fig. 6·11

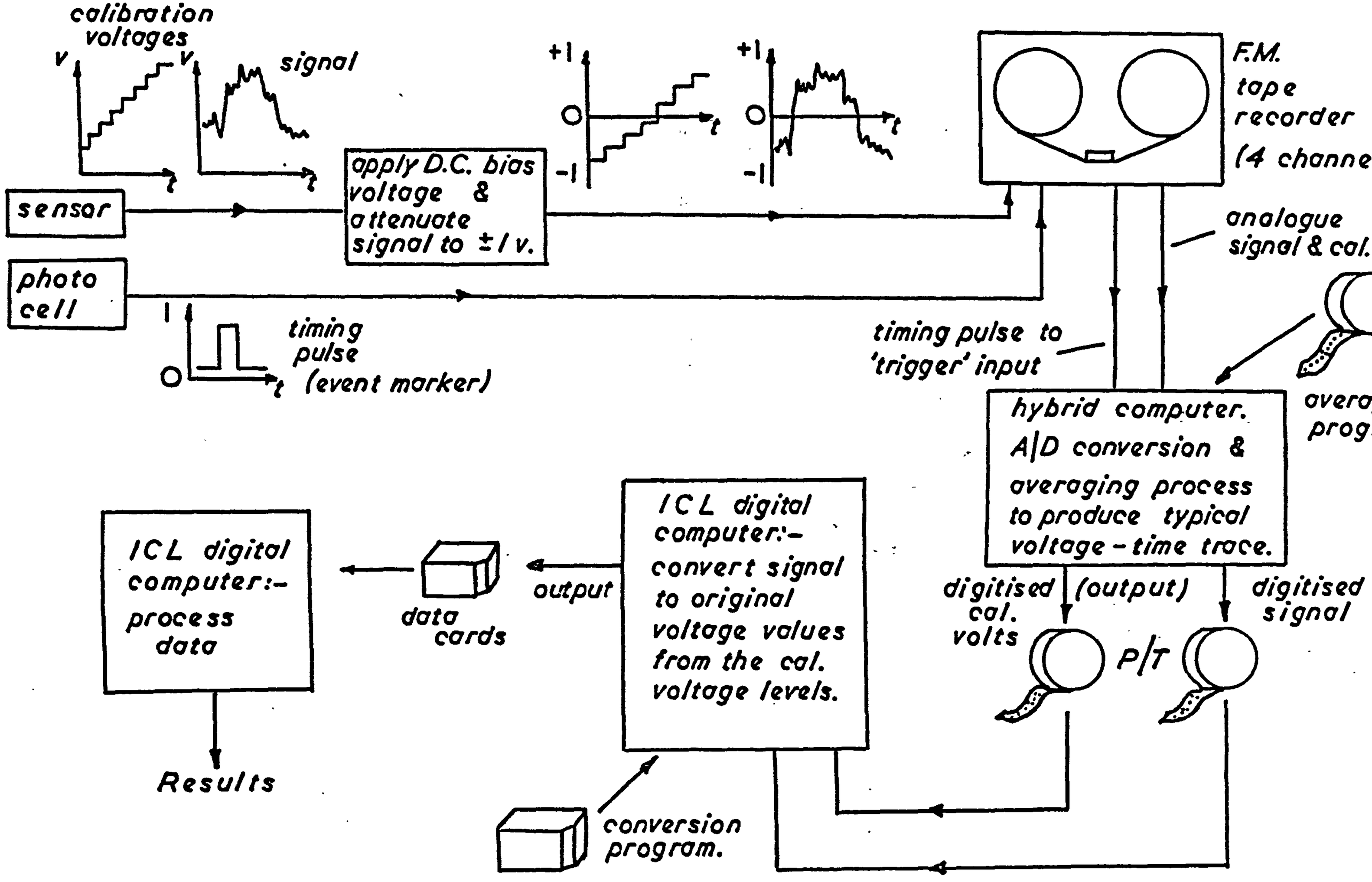

Fig. 6.12

Data Processing Sequence for Transient Events.

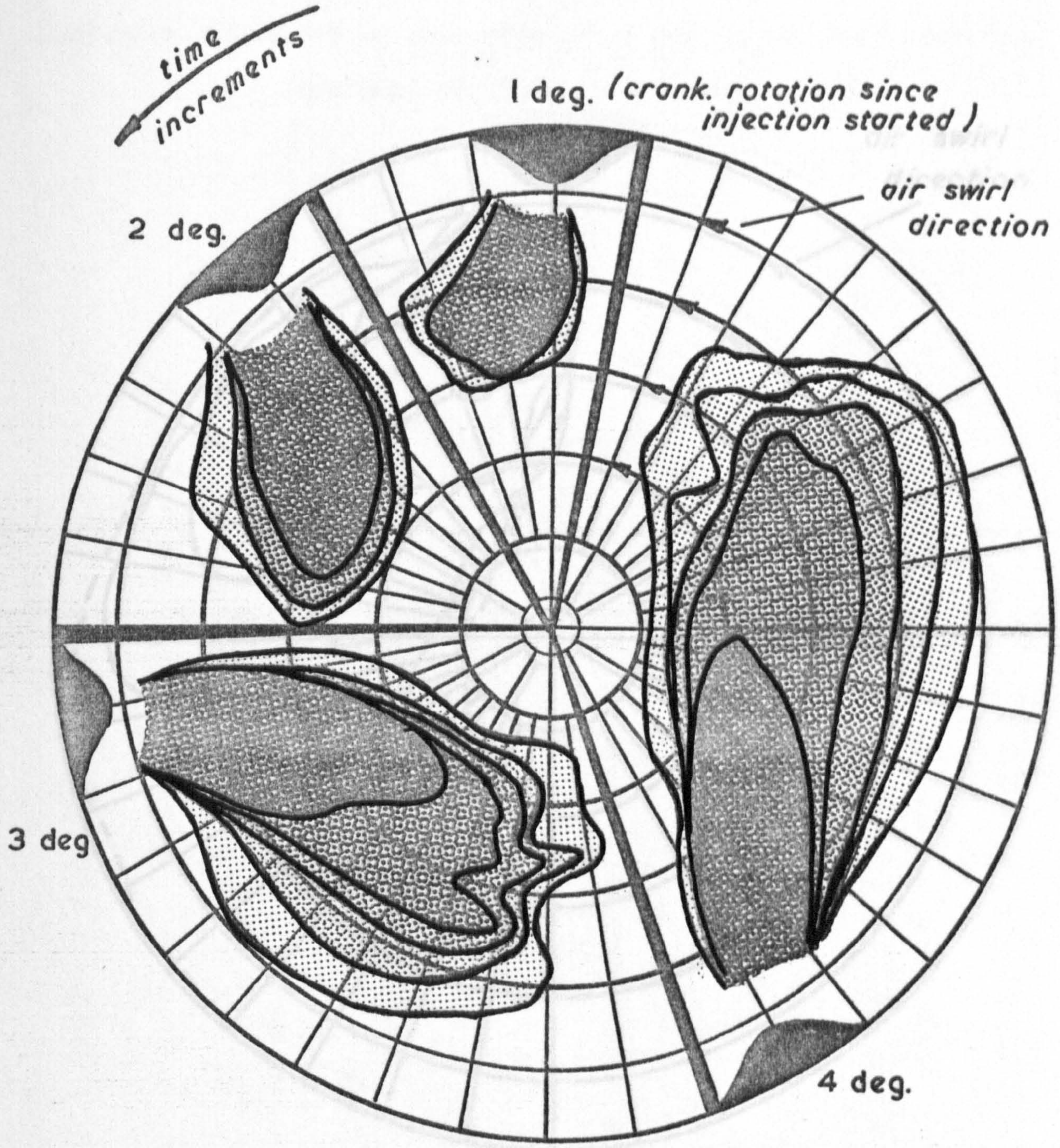

Mass air to fuel ratio contours: (in order outer to inner) :—

1 deg. map : (∞ , 3:1) . 2 deg. map: (∞ , 15:1, 3:1) .

3 deg. map : (∞, 15:1, 10:1, 5:1, 3:1) . 4 deg.map: (∞,15:1,10:1, 5:1,3:1)

Transient Gas Jet Simulation : Radial Injection: Modelled on the Data due to Stock. (ref.(86)).

Fig. 6·13

——————— Transient gas jet model boundaries (1 deg. steps)

– – – – – Steady state gas jet model boundary.

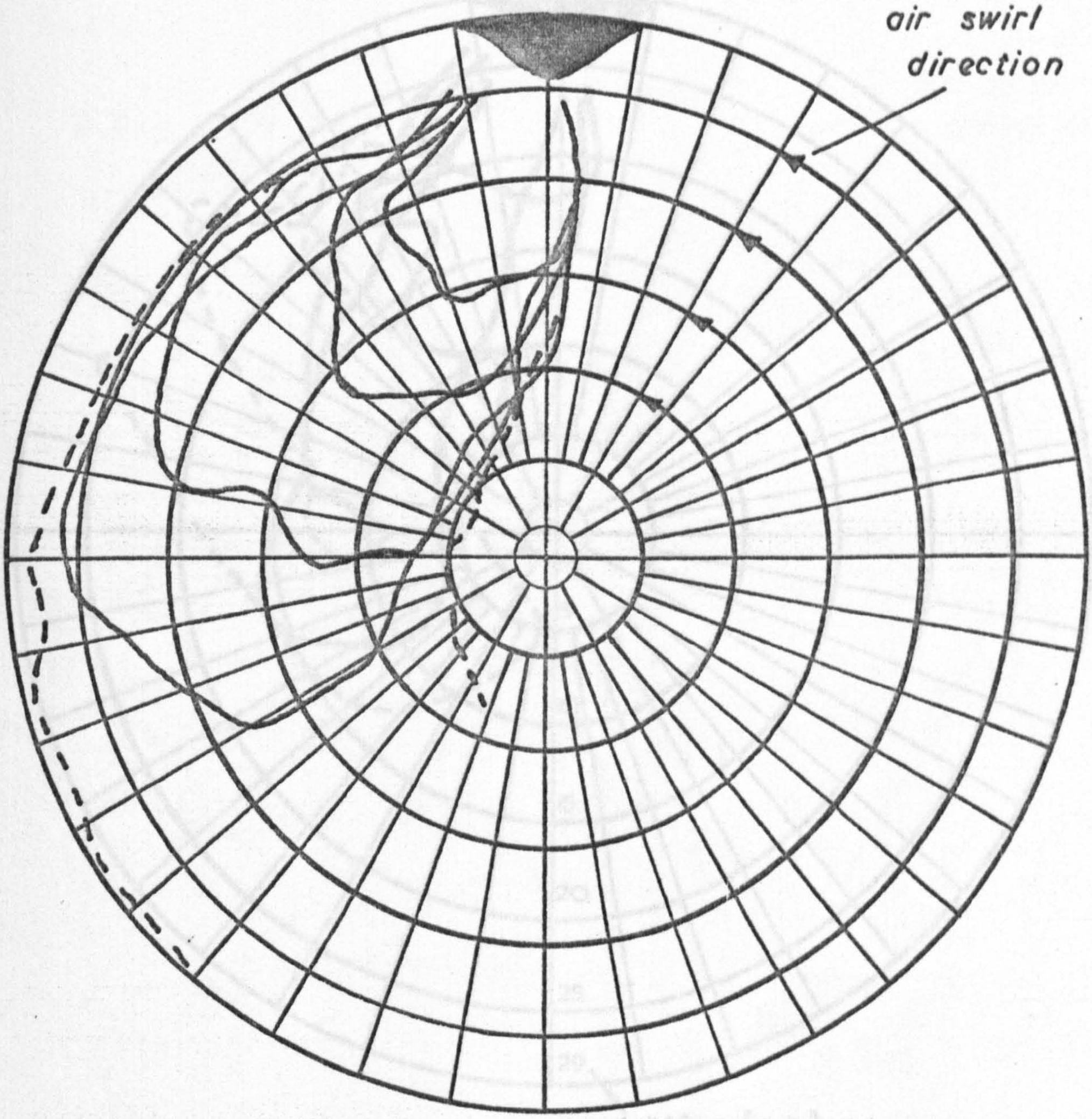

Comparison of Transient and Steady State Gas Jet Model Spread and Trajectory.

Fig. 6·14

——— 'Fuel' Boundary

— — — 'Vapour' Boundary

Succesive envelopes at intervals of 1 deg. crankshaft rotation.

(Injection duration = 4 crank. deg.)

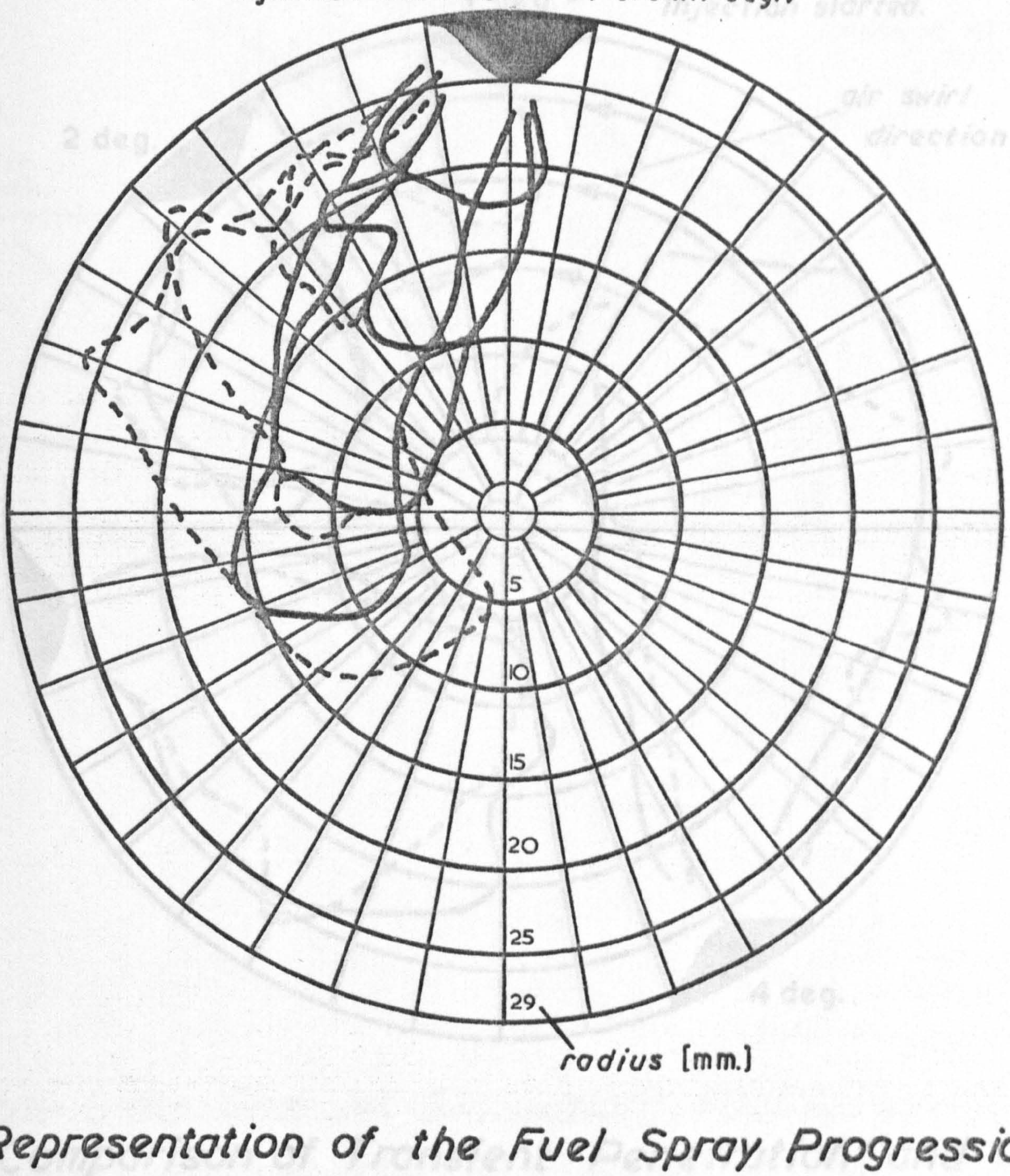

Representation of the Fuel Spray Progression taken from the Film Sequence. (Ref. (86))

Fig. 6·15

– – – – – Engine fuel spray envelope (ref. (86))

——————— Gas jet simulation envelope

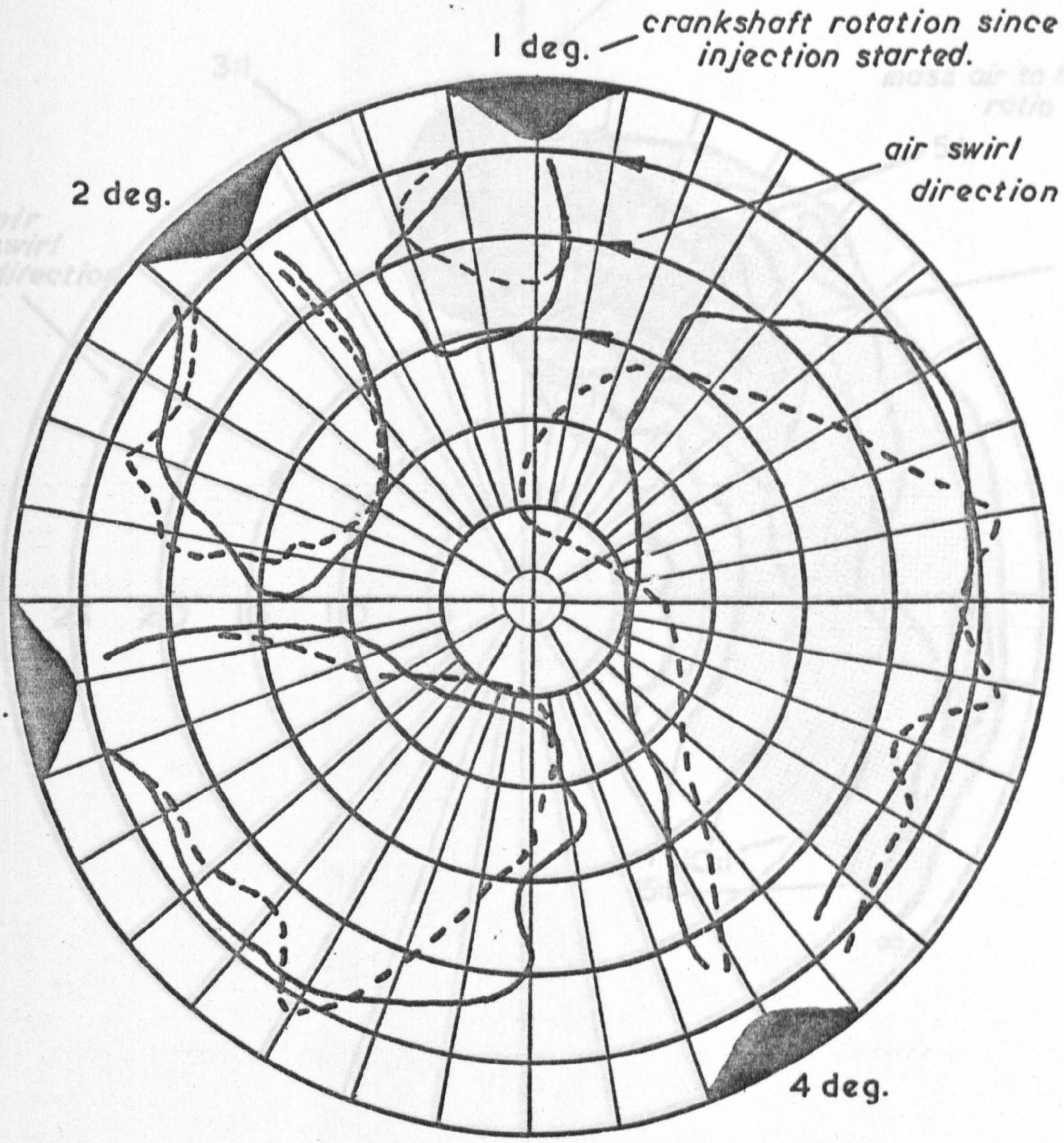

Steady State Gas Jet Simulation: Fuel Spray Comparison of Transient Penetration and Spread between the Gas Jet Simulation and Engine Fuel Spray.

Fig. 6·16

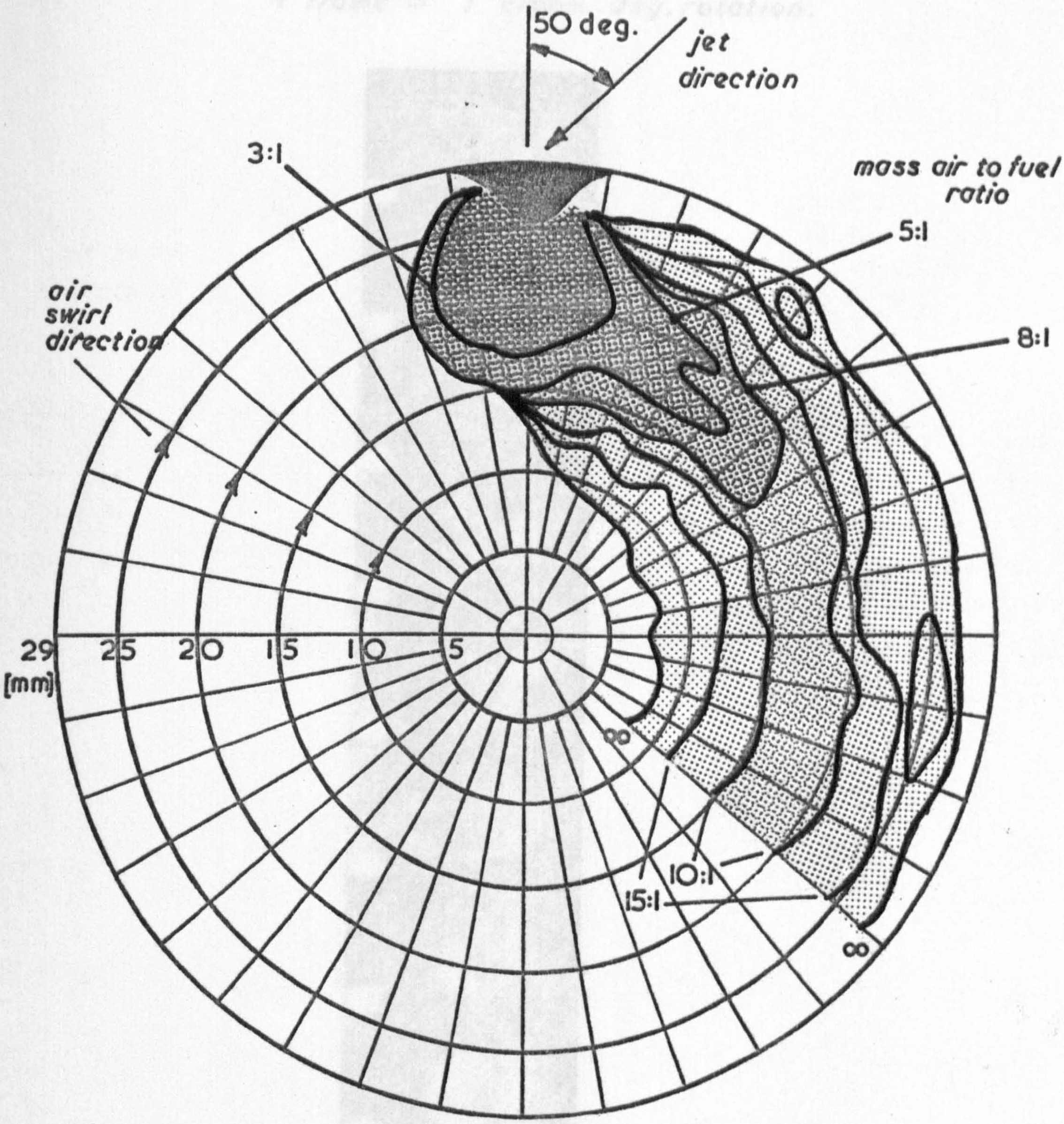

Steady State Gas Jet Simulation: Fuel Spray Injected Against the Swirl Rotation; Modelled on the Data due to Stock. (ref. (86))

Fig. 6·17

1 frame ≙ 1 crank. deg. rotation.

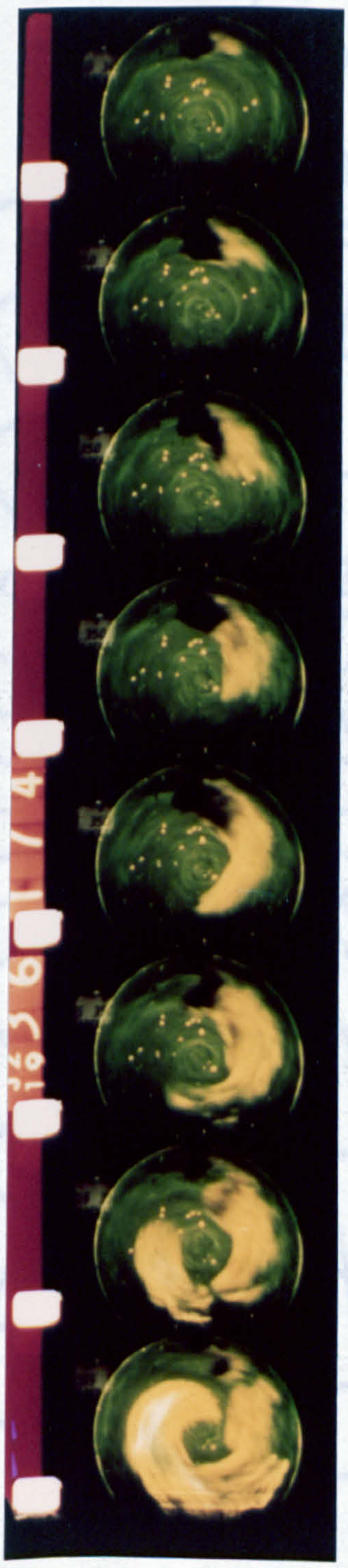

Swirl Clockwise

Film Sequence for Injection 50 deg.
against the Swirl Rotation (ref. 86)

Fig. 6·18

— — — — Engine fuel spray envelope (ref. (86))

——————— Gas jet simulation envelope.

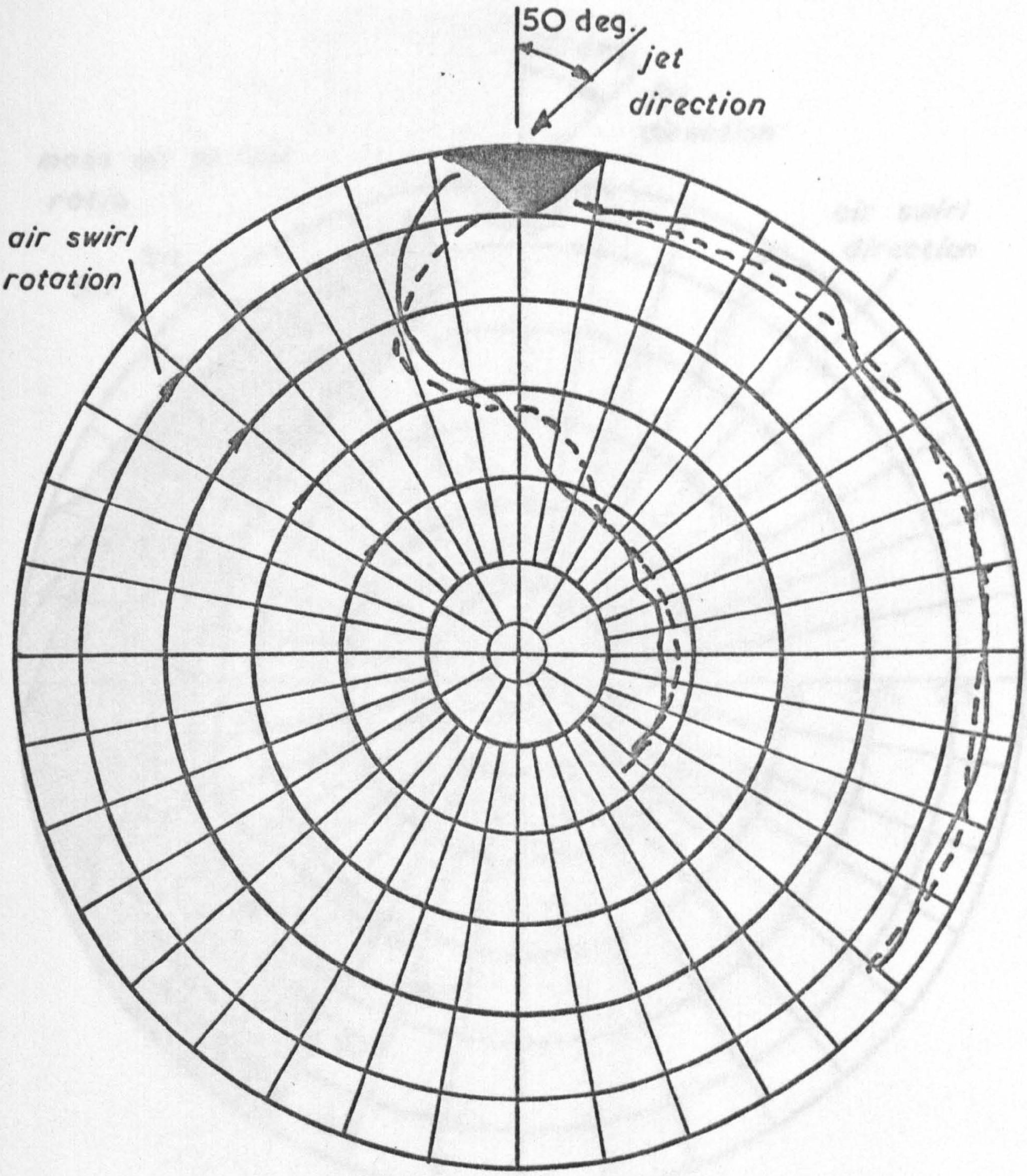

Comparison of Trajectory and Spread between the Engine Fuel Spray and Steady State Gas Jet Simulation. (Injection Against the Air Swirl.)

Fig. 6·19

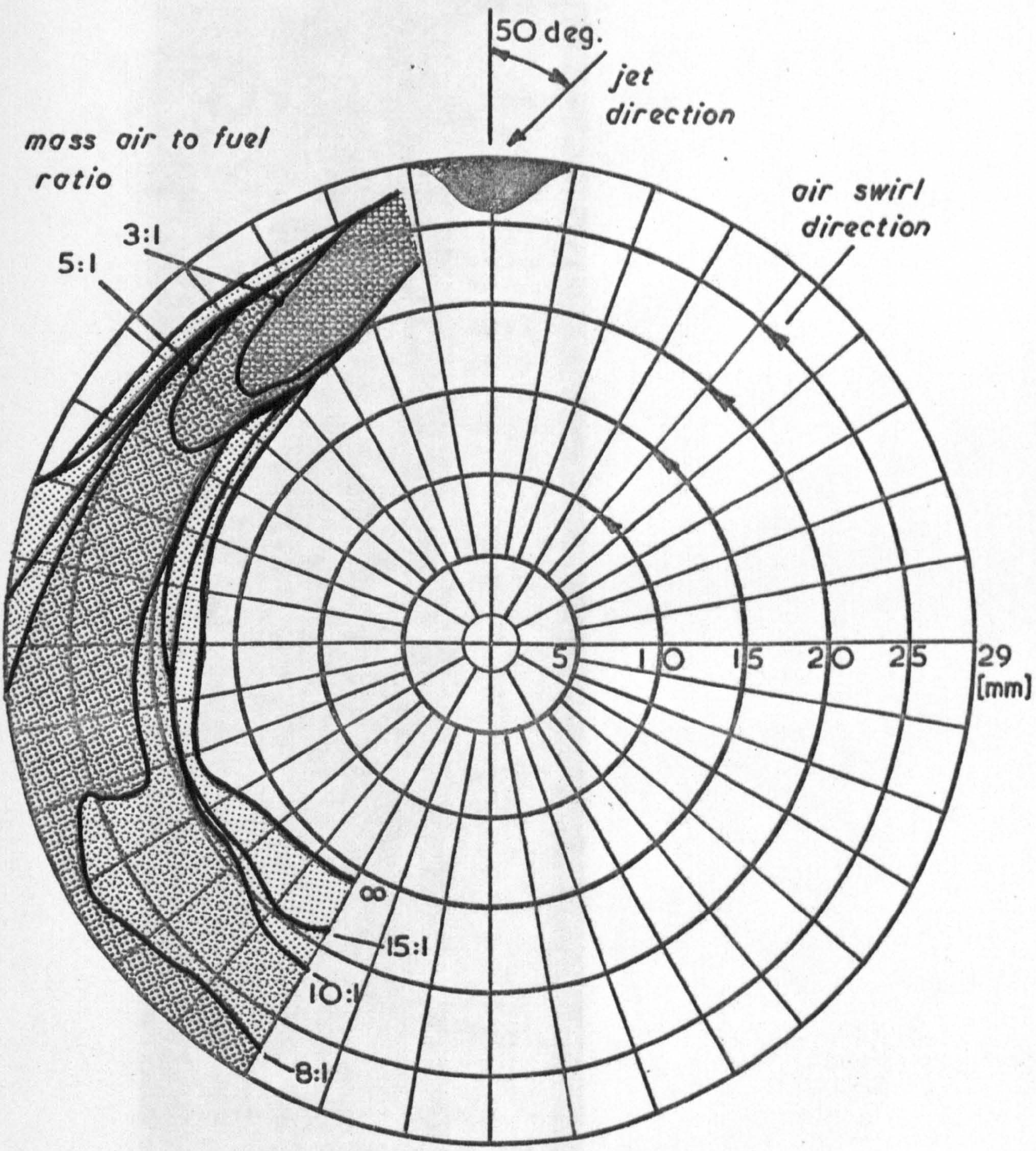

Steady State Gas Jet Simulation: Fuel Spray Injected with the Swirl Rotation ; Modelled on the Data due to Stock. (ref.(86))

Fig. 6·20

swirl anticlockwise

Film Sequence for Injection 50 deg. with the Swirl Rotation. (ref. 86)

Fig. 6·21

— — — — Engine fuel spray envelope (ref. (86))

———— Gas jet simulation envelope.

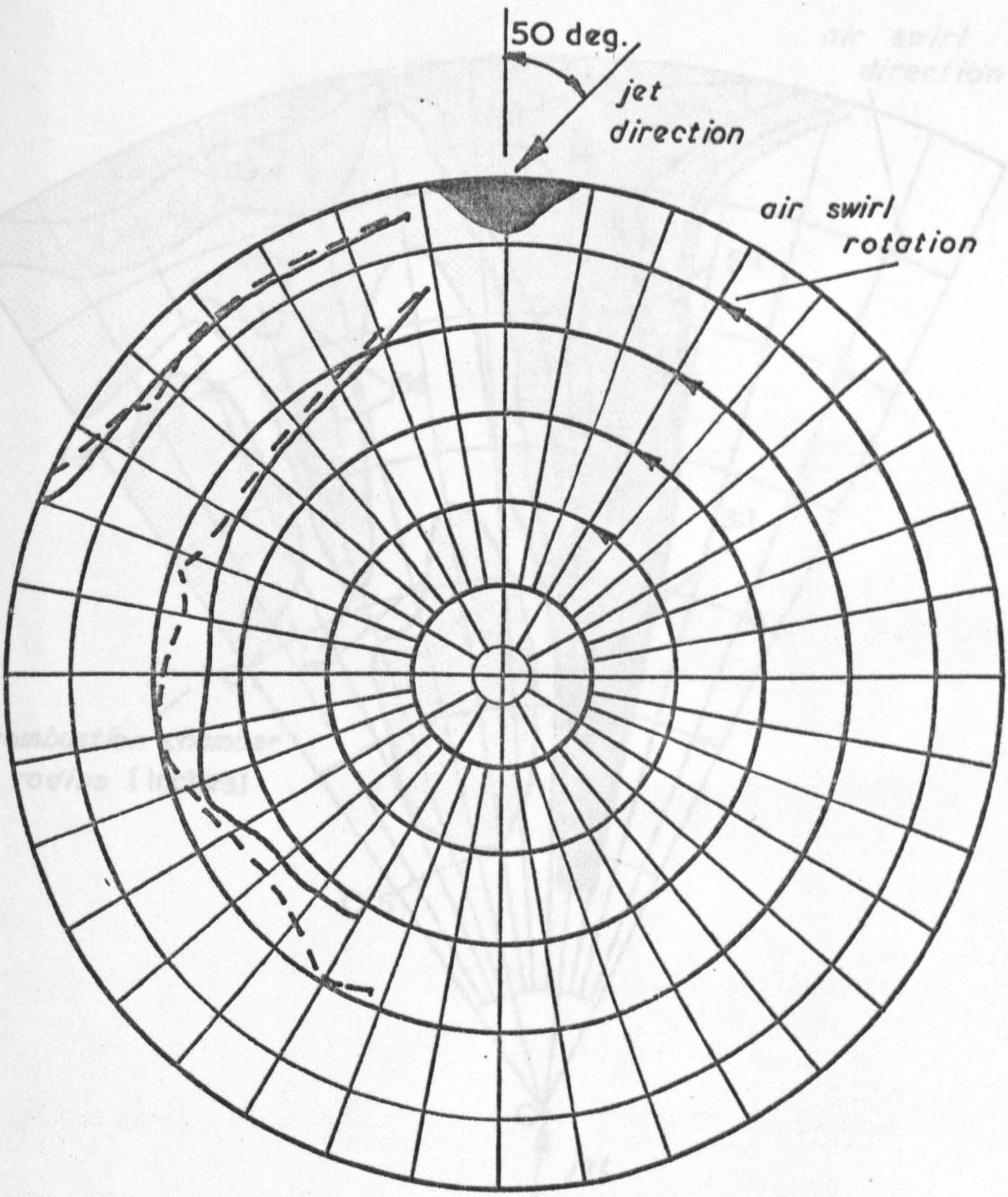

Comparison of Trajectory and Spread between the Engine Fuel Spray and Steady State Gas Jet Simulation. (Injection with the Air Swirl.)

Fig. 6·22

● *Fuel spray centre line co-ordinates (ref. (36))*

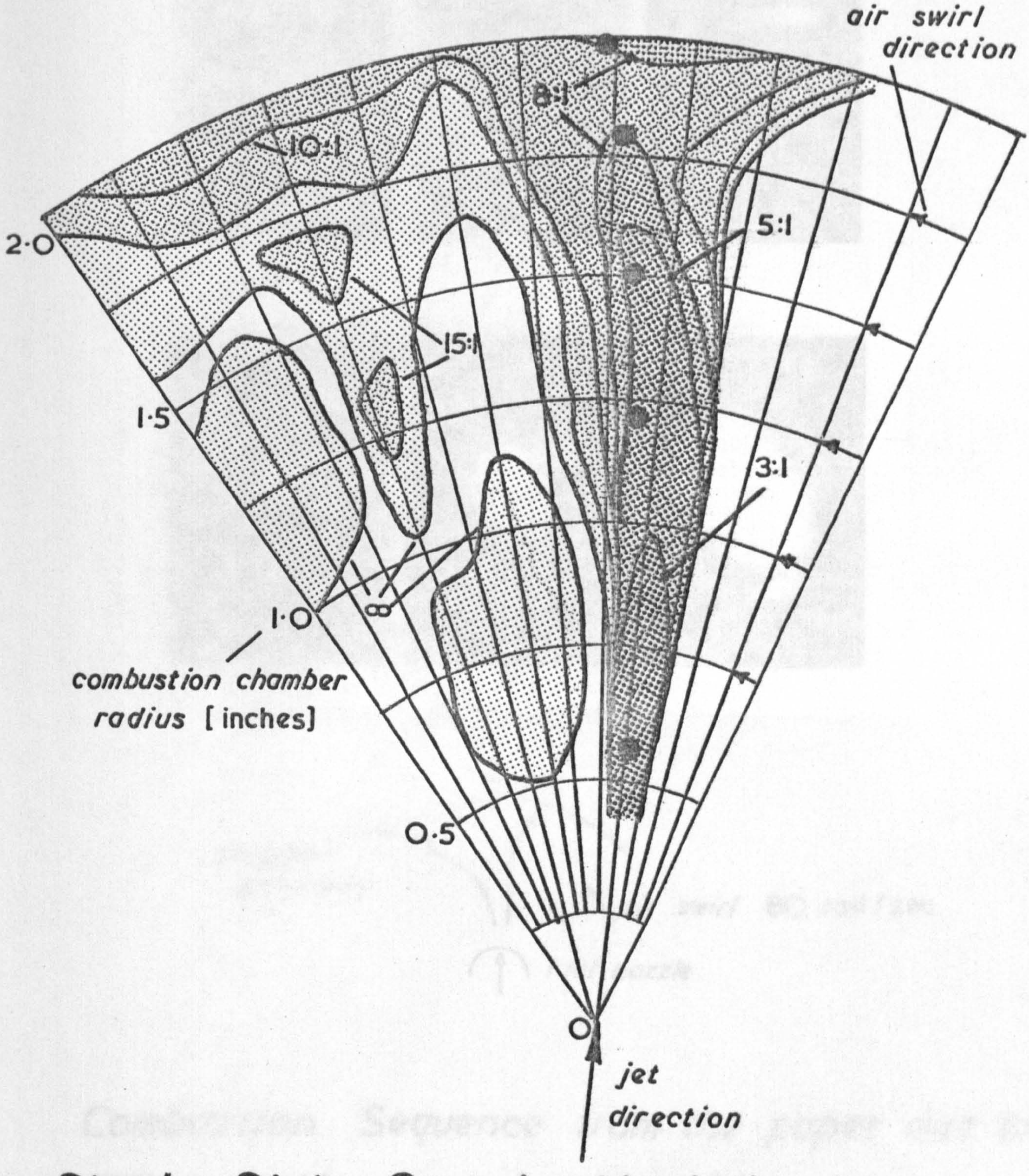

Steady State Gas Jet Simulation based on the Data due to Rife and Heywood (ref. (36)) for an Air Swirl of 80 rad./sec.

Fig. 6·23

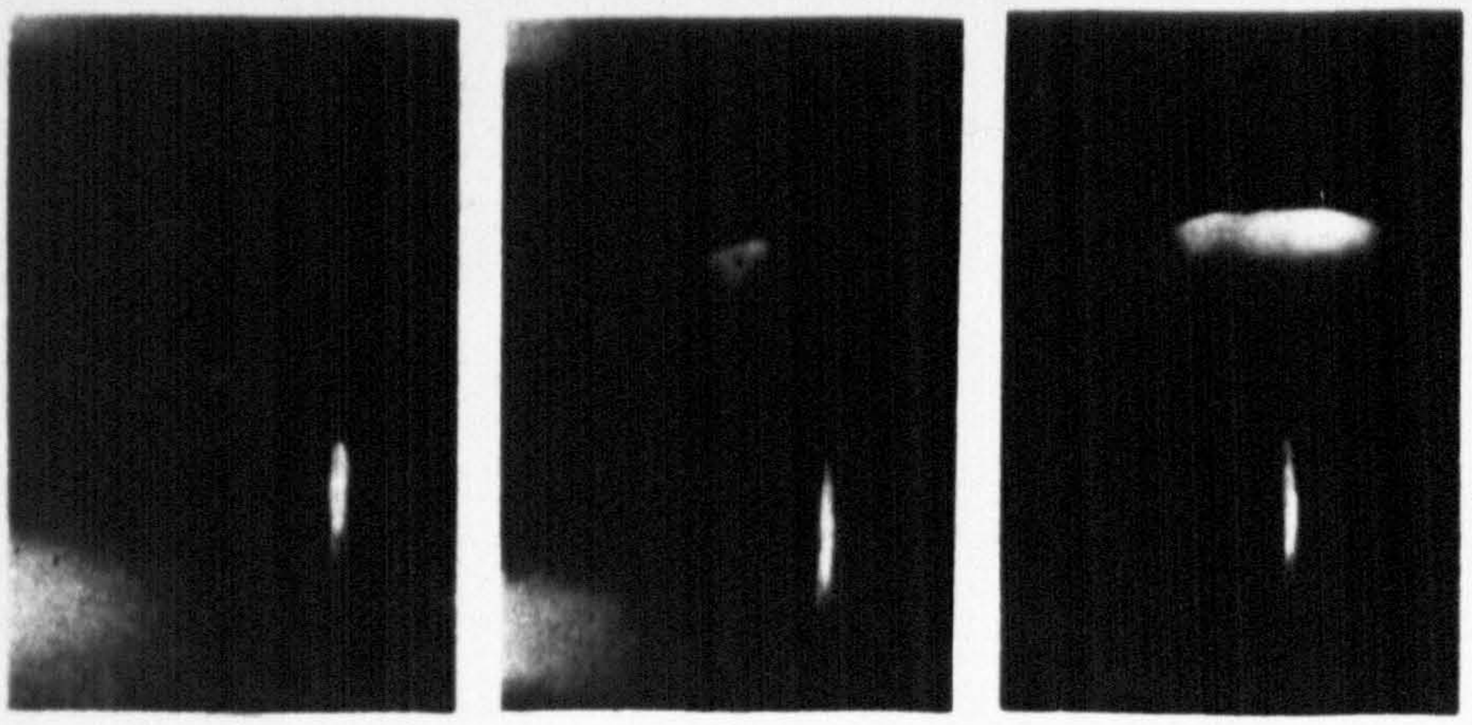

A B C

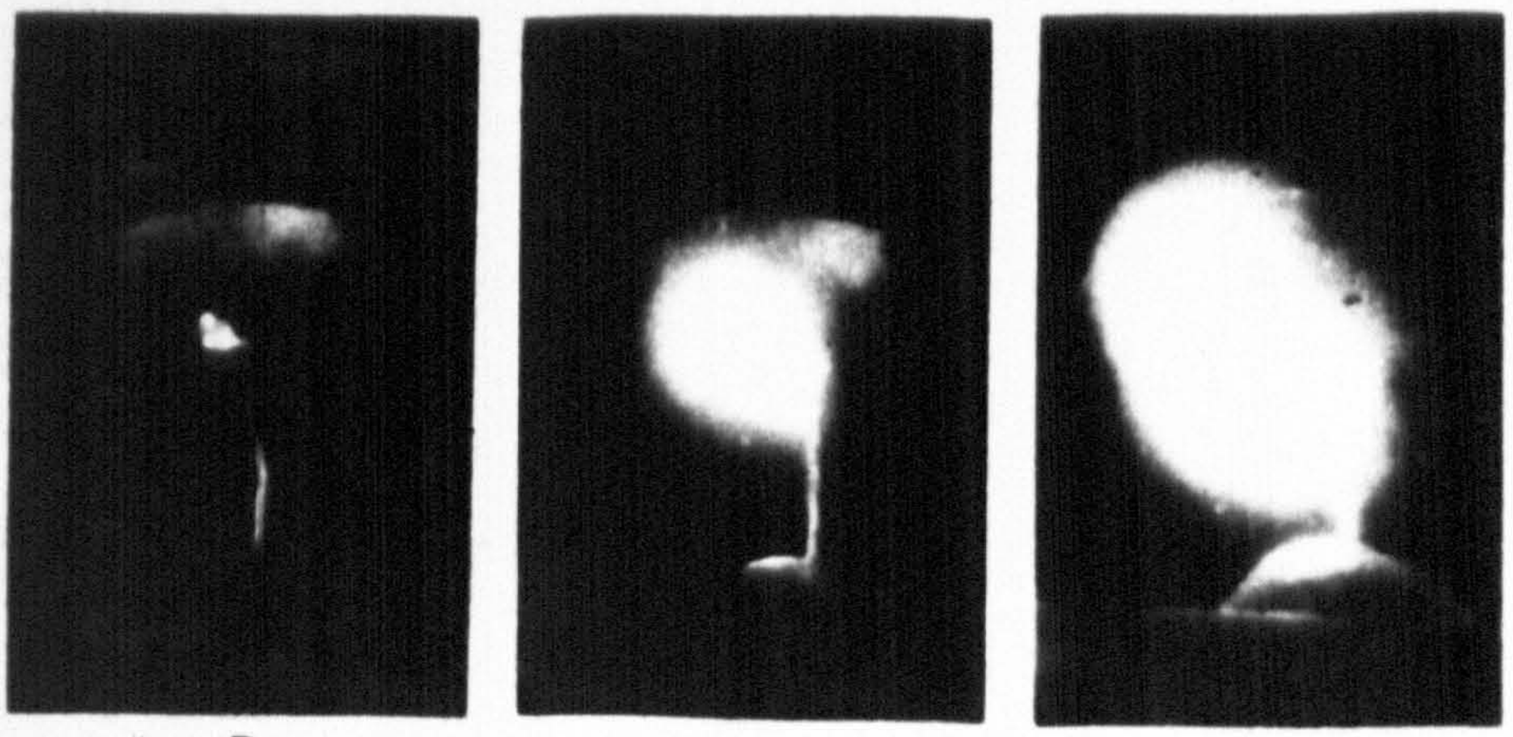

D E F

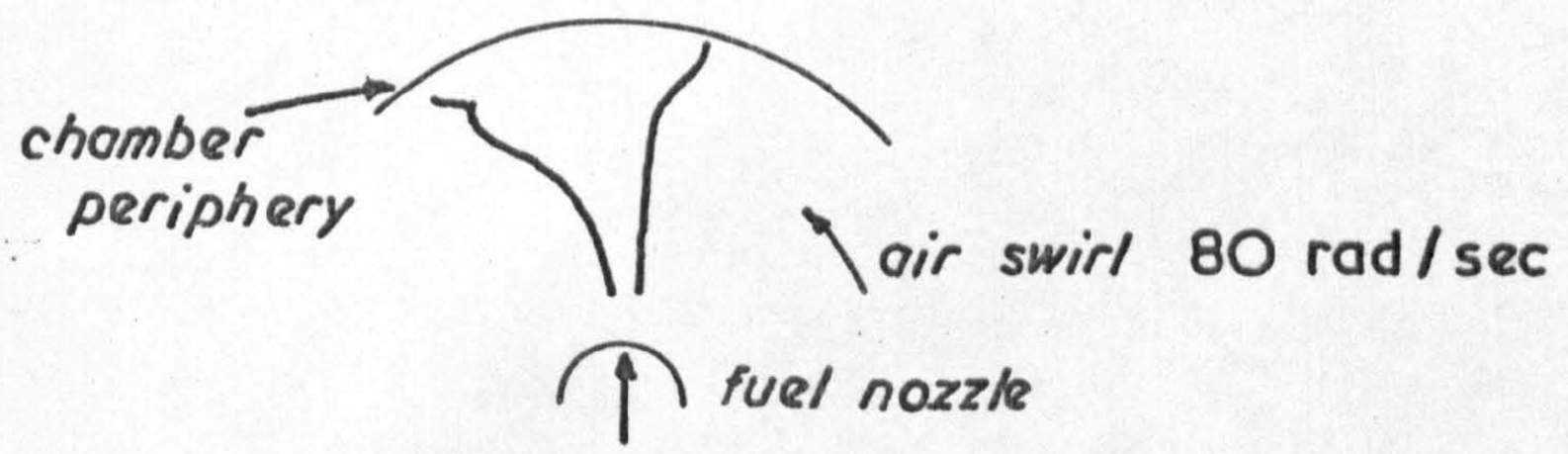

Combustion Sequence from the paper due to Rife and Heywood (ref. (36)).

Fig. 6·24

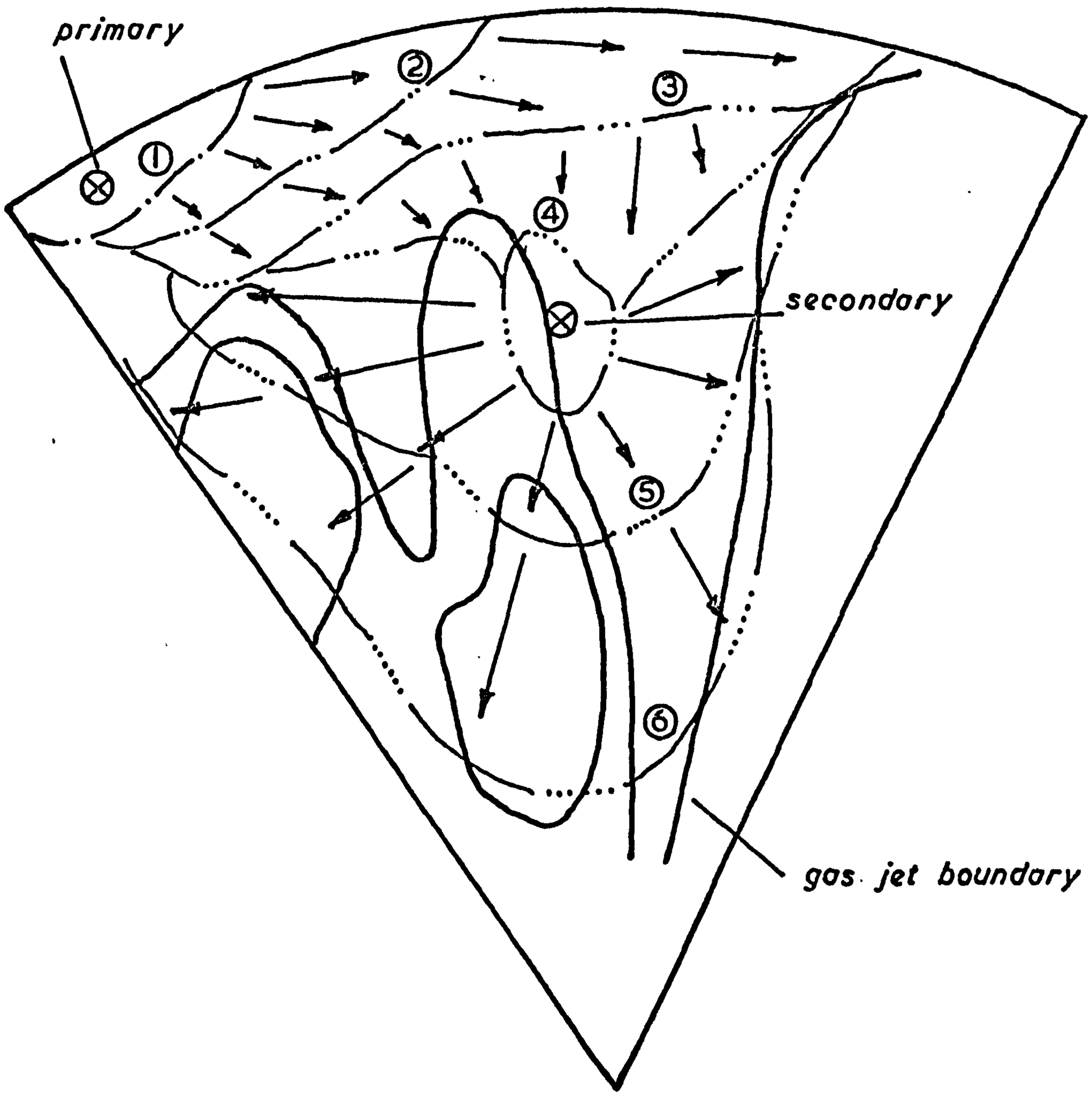

Analysis of Flame Propagation through the Fuel Spray. (Data obtained from the film of Rife and Heywood ref.(36))

Fig. 6·25

● *Fuel spray centre line co-ordinates (ref. (36))*

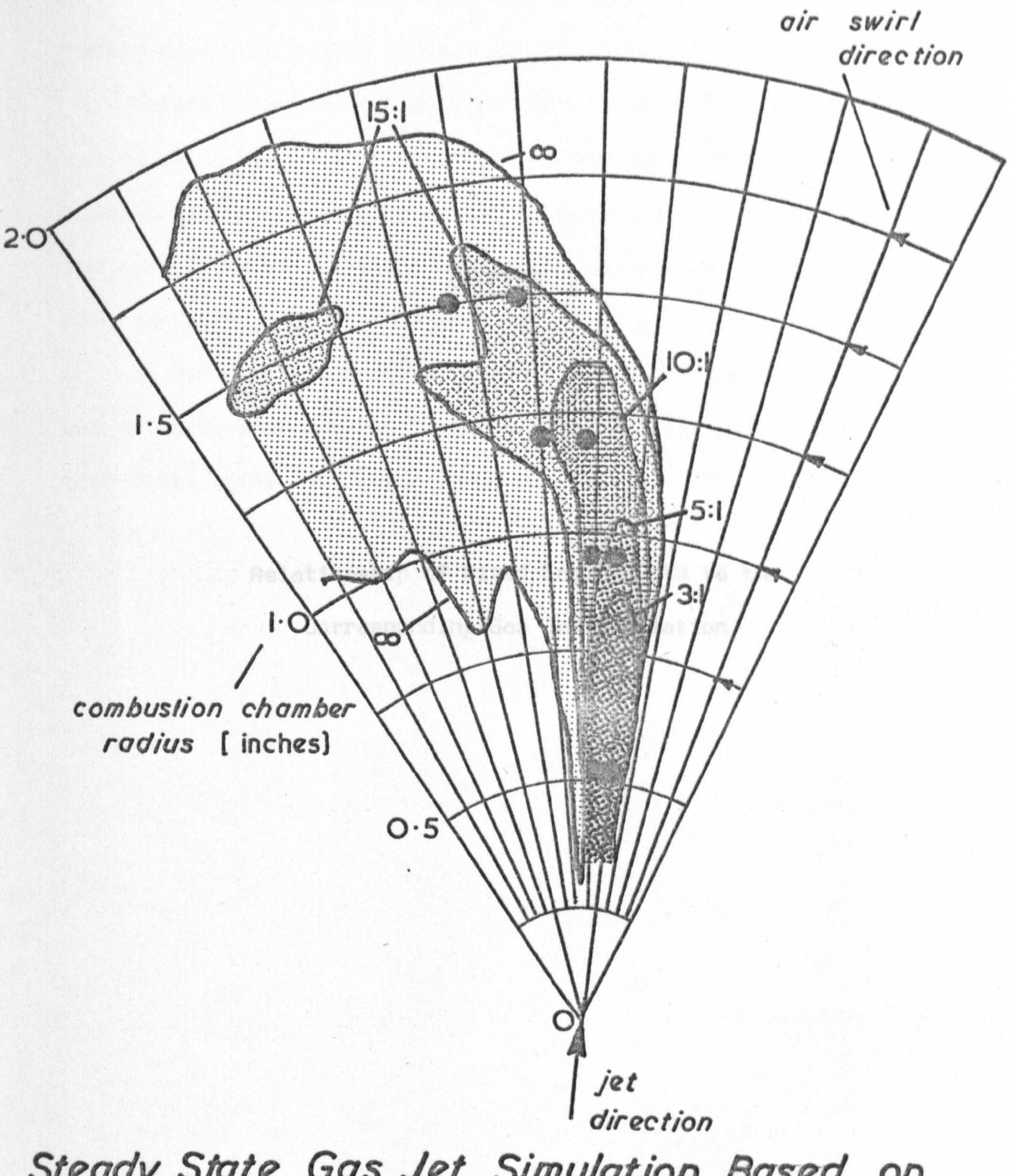

Steady State Gas Jet Simulation Based on the Data of Rife and Heywood. (ref. (36))
for an Air Swirl of 180 rad/sec.

Fig. 6·26

CHAPTER 7

Relationship of Fired Engine Data to the Corresponding Gas Jet Simulation

7.1 Introductory Comments

The work reported in this chapter attempts to directly relate engine data with the gas jet simulated mixing of the fuel spray.

Engine data has been obtained for three fuel injector nozzles to define cycle mean effective pressure, maximum rate of pressure rise, exhaust emission levels, and fuel injection equipment characteristics. Additionally a study of the combustion process using high speed direct cine-photography has been undertaken.

In order to allow accurate gas jet modelling of the fuel spray, air velocity measurements in the motored engine cylinder have also been made, using hot wire anemometry techniques.

7.2 Experimental Test Engine Modifications

The tests have been conducted on a considerably modified Petter PJ1 engine. (Salient specification details as in Appendix D).

It was found necessary to replace the existing cylinder head with a specially designed, and manufactured, fabricated head. Many of the original features were maintained however. Existing inlet and exhaust valves were used, but relocated in the replacement head design, and the original valve rocker gear and injector body were also utilised. However, in order to provide the necessary viewing area for filming the combustion process, a 'two level' design was employed. Injector body inclination and nozzle central position were maintained as in the original engine, but the valve rocker gear was located on a second platform above the injector body. Figure (7.1) shows the arrangement of the head on the engine, where it may be seen that the design then allows the location of the viewing window aperture in the area previously occupied by the valve gear.

Air swirl was generated by a near tangential inlet port and a 180 deg. inlet valve mask.

Figure (7.2) shows an assembly drawing of the cylinder head and illustrates the salient details.

The original Petter PJ1 combustion chamber was of the deep bowl toroidal type, and the orifice (throat) on the piston crown was of insufficient diameter to allow adequate viewing of the combustion process. The original piston was therefore machined to allow the insertion of 'false' piston crowns with self contained combustion chambers. Figure (7.3) shows the two chamber shapes used in this project. The volumes of both chambers were measured, and the bump clearances correspondingly modified to ensure that similar compression ratios existed. For both chambers the volumetric compression ratio was 16.9:1.

The facility to mount a 'Kistler' pressure transducer was also provided, and replacement of the viewing window with a drilled brass plug allowed the insertion of a hot wire anemometer probe at various radii in the combustion chamber. For measurement at small radii the probe was inserted through the injector passage by a similar brass plug mounting system.

Rotating disc and photo-cell assemblies, similar to that described in section (6.2.3), were mounted on external extensions of the engine cam and crankshafts. Six equi-spaced slots in the crankshaft disc created voltage pulses at a frequency proportional to engine rotational speed. A 'Racal' computing counter was used to sample the pulses and display the engine speed in rev/min. A single slot in the camshaft disc provided one pulse per engine cycle set to coincide with induction top dead centre, and was used as the timing pulse for the data processing sequence as illustrated in figure (6.12) (Section 6.2.3).

When required, the engine was driven by an A.C. motor, and a variable transformer provided speed control of the motored engine. Under fired engine conditions an unconventional method of applying load was employed. The fired engine was allowed to drive the motor armature against the field winding flux induced by the mains supply. Various transformer 'speed' settings, below the fired engine speed, then provided various degrees of flux loading on the engine. Hence, at a given fuelling rate, engine speed could be maintained constant by adjustment of transformer speed setting.

A micrometer type screw adjustment allowed repeatability of fuel pump rack setting. The original 'Bryce' (8mm diameter plunger), fuel pump was used for all the tests.

7.3 Aquisition of Fired Engine Data

7.3.1 Fuel Injection Equipment Characteristics

Calibration of the nominal fuel pump rack setting, measured on the micrometer screw adjustment, was achieved by timing the fired engine consumption of a known volume of fuel at constant engine speed. Hence, the number of fuel pump plunger strokes could be calculated for the timed period and the quantity of fuel delivered per stroke readily determined for a range of nominal fuel rack settings at a constant engine speed of 1000 rev/min.

Injection duration for a given injected fuel quantity was found to be dependent on fuel nozzle hole area and nozzle opening pressure. Fuel line pressure was measured by a 'Kistler' fuel line transducer located 25 cm. from the injector nozzle (measured along the fuel line path). Simultaneously, needle lift was measured by a 'DISTEC 915', non-contacting, inductive displacement transducer which was calibrated prior to the tests. Upper frequency limit of the displacement transducer was 20 kHz., and hence the short rise time at the opening of the injector nozzle could be effectively monitored. Figure (7.4) shows a set of injector characteristics, at 1000 rev/min., for a single hole nozzle of diameter 0.35 mm. Figure (7.5) summarises the results for the three nozzles used in this project at a constant engine speed of 1000 rev/min. Spill port closure was set at 23 degrees before top dead centre, however at a nozzle opening pressure of 150 bar, (maintained constant for all the fired data tests), elasticity of the fuel line, and delay in pressure pulse arrival at the injector needle, can be seen from the results of figure (7.4) to produce a dynamic injection timing of 15 degrees before top dead centre at 1000 rev/min.

Satisfactory injection duration for all three nozzles was considered to occur for an injected fuel quantity of 40 mm^3 per pump stroke. Therefore all fired engine data aquisition has been based on the fuel injection characteristics at 1000 rev/min and the above injected quantity.

7.3.2 Indicated Work done, and Fired Pressure Trace Comparisons for the different Nozzles and Combustion Chamber Geometries

Fired cylinder pressure traces were measured using a Kistler type 628B capacitive pressure transducer and associated charge amplifier, type 5001. The data was recorded and processed as depicted in figure (6.12), averaging was performed over ten engine cycles. Approximately 1200 ordinates were generated onto punched data card for each meaned engine cycle trace. The tests were conducted for all three nozzles and the two combustion chambers at the previously mentioned conditions of 1000 rev/min engine speed, and 40 mm^3/cycle injected quantity.

Subsequent processing of the data was achieved on the I.C.L. 1904 computer using a specially written computer program. Numerical integration of each trace allowed computation of the indicated mean effective pressure. Numerical differentiation of each trace, provided data on the maximum rate of pressure rise after the initiation of combustion.

Figures (7.6) (7.7) show the respective pressure traces for the two combustion chambers as referenced in figure (7.3).

A point of considerable interest, to be noted at this stage, is the similarity for the data of identical nozzles in the two chambers. Little effect of chamber geometry is apparent.

7.3.3 Exhaust Emission Tests

Exhaust gas was sampled as a continuous flow from a tapping 2m. from the engine manifold, and presented to the infra-red gas analysising equipment manufactured by "The Analytical Development Co. Limited". Direct measurement of carbon monoxide, unburnt hydrocarbons, and nitrous oxide emissions were thereby obtained. Concurrently a fixed volume of exhaust gas was drawn through standard, special purpose, filter papers. The detection of reflected light from a standard source then provided a measure of exhaust smoke emission measured on the 'Dunedin' smoke analyser. A scale reading of 'zero' corresponds to the unsoiled filter paper, and a scale reading of 'ten' corresponds to a totally black surface. Calibration of the infra-red gas detection equipment was achieved by sampling known gas mixtures (supplied by 'Rank Precision Industries') prior to the test run, after a suitable equipment 'warm' up period of three hours. However, subsequent drift of calibration was found to occur and frequent re-calibration was necessary.

Emission levels were measured for all three fuel nozzles in both combustion chambers at an engine speed of 1000 rev/min. and a range of fuel pump rack settings from 20 mm^3/cycle to 50 mm^3/cycle injected fuel quantity. The results are shown in figures (7.8) (7.9).

Marked similarity for the two combustion chambers is seen to exist, particularly in view of the limitation on measurement accuracy imposed by the previously mentioned calibration drift problems. This is consistent with the similarity in pressure trace data presented in figures (7.6) (7.7).

7.3.4 High Speed Photography Results

A 'Hycam' high speed cine camera was used to obtain the filmed data. Time scale, or crankshaft rotational position, was recorded on the film by using the photocell sensor and a slotted disc mounted on the engine camshaft extension. Slots were machined in the disc to a known'pattern' (i.e. at irregular angular spacings) and the disc adjusted so that a fixed point in the pattern corresponded to a known point in the engine cycle. Suitable electronic circuitry was used to present a high voltage to a neon-light mounted within the camera body on receiving any of the triggering pulses created by the photocell unit and slotted disc combination. Thus, the neon light was caused to flash with the disc slot pattern, and was located such that the light exposed the edge of the cine film (adjacent to the sprocket holes). Consequently the position in the cycle of any frame on the film could be easily determined by its position relative to the exposed portions of the film edge.

Trial tests were performed using monochromatic film which allowed 'on-site' processing, and a rapid feed-back of data. Optimum filming conditions, and camera settings could then be predicted for the subsequent colour film tests.

The viewing window was machined from 'perspex' acrylic sheet, thus providing the maximum possible viewing area. Mounting of a quartz window in the same sized aperture considerably reduced the viewing area because of the additional separate brass mounting rings required. Prior to each film sequence the perspex window was polished flat with rubbing compound on a plate glass surface. Final 'finish' was achieved by soft polishing with paper tissue. Before inserting the perspex window, the engine was run to allow normal operating temperatures to stabilise.

with the quartz window in position. Rapid replacement of the quartz window with the larger window, then allowed ample running time to obtain the filmed data, before any sooting or deterioration of the perspex surface occurred.

An important finding of the monochrome film preliminary tests was that the two combustion chambers produced not noticeable variation in combustion characteristics for constant fuel nozzle configuration. This is also upheld by the results of figures (7.6) (7.7) (7.8) (7.9). Consequently colour film was only used on the combustion chamber 1 as depicted in figure (7.3).

Filmed data was obtained at an engine speed of 1000 rev/min. and fuelling rate of 40 mm^3/cycle. Film speed was a nominal 6000 frames/sec. 'Tungsten' colour film (Ektachrome EF 7242) was found to most effectively represent the combustion process colour spectrum. 'Daylight' colour film was found to produce an overall red bias on the colours.

The camera direction is shown in figure (7.10), and the viewed spray was arranged to have the original, i.e. undeflected, path as also illustrated.

The colour film results are shown for the three nozzles (for combustion chamber I) in figures (7.11) to (7.16)). The results will receive more discussion in section (7.7). Figure (7.17) shows prints from the monochromatic film for the 1 x 0.35 mm nozzle at the same engine conditions but for combustion chamber II (figure 7.3), and may be compared with the combustion chamber I results of figures (7.11) (7.12). Initial character of the spray, i.e. before combustion is totally established, may be seen to be almost identical. Auto-ignition occurs in similar regions of the spray and any apparent

difference may be attributed to the different film development and printing processes. Prints of the 'reversal' colour film were obtained from copies made on 35 mm 'negative' colour film. Hence a degree of fine detail is lost. The fine streaks, due to burning droplets appearing on the monochromatic film are an example of this effect.

7.4 Air Velocity Measurements

7.4.1 Statement of the Measurement Problem

The work of Chapter 4 showed that the heat transfer from the sensing element of a hot wire anemometer is defined by equation (4.36) irrespective of wire overheat ratio, where the constants, A, B may be anticipated to vary slightly between individual sensors. Re-arrangement of equation (4.36) yields:

$$U = \frac{\mu_m}{d.\rho_m} \left\{ \left(\frac{h.d}{k_m} \cdot \left\{ \frac{T_m}{T_g} \right\}^{-0.12} - A \right) \cdot \frac{1}{B} \right\}^{2.5} \quad \ldots\ldots (7.1)$$

The overall surface heat transfer coefficient (h) may be calculated as in section (4.2) and is a function only of bridge output voltage, probe details, and gas temperature. For operation in the motored engine cylinder the air properties μ_m, k_m, may be sensibly expressed as functions of instantaneous wire film temperature as in section (4.5.4) and the remaining property, ρ_m, may be calculated from the characteristic gas equation at the instantaneous air pressure and temperature.

Hence, the measurements required to allow computation of air velocity throughout the engine cycle are the time dependent variables of air temperature and pressure, and anemometer probe bridge voltage output. Instantaneous values of velocity may then be computed by equation (7.1) for a calibrated probe for which the constants A, B have been determined from the flow calibration rig.

7.4.2 Experimental Equipment

A single wire probe, manufactured as shown in figure (4.2), was used to measure the air velocity in the engine cylinder. Derham (31) showed that the rotation of the air was essentially

two dimensional at piston positions close to compression top dead centre. Therefore the wire axis was mounted horizontally, i.e. parallel to the piston face, so that probe rotation allowed the separation of swirl and squish velocity components.

The DISA M-system anemometry bridge, (50 Ω bridge top resistance, see section (4.11)), was used for engine air velocity measurement. The 'Racal Store 4' F.M. tape recorder was used to record the various sensor signals after appropriate biasing and attenuation together with the timing pulse, (section 6.2.3) as generally represented in figure (6.12). A tape speed of 15 inches per second was used, and represented an upper frequency limit of 5 kHz.

A 'Kistler' capacitive pressure transducer, (as introduced in section (7.3.2)), was used to provide the motored engine cylinder pressure trace. Cyclic temperature variation was measured using the hot wire probe as a resistance thermometer, (based on the experimentally determined value of resistance temperature coefficient for the Pt - 10% Rh. wire employed (figure 4.11)). Probe location for temperature measurement was at a combustion chamber radius of 24mm. and depth of 10 mm. from the cylinder head flame face, with the wire orientated normal to the direction of the air swirl.

Engine rotational speed was monitored as described in section (7.2).

The test engine and associated equipment required for the air velocity tests is shown in figure (7.18).

Data for the anemometer probe heat transfer calibration was obtained in the flow calibration rig (section 4.1.3), for a range of overheat ratios presented by operation of the wire at 750 deg.C and 540 deg. C, over the air temperature range of

19 deg. C to 230 deg. C, and a velocity range of 4 m/sec to 96 m/sec. The data was seen to be correlated in the form of equation (4.36), and the constant A, B were computed to be 0.249 and 0.591 respectively, after processing by the calibration program described in section (5.7.1). The probe was operated at a wire temperature of 750 deg. C in the engine tests. Wire material was Pt. - 10% Rh., (quartz coated), and wire geometry was 1.96 mm. x 10 μm diameter.

7.4.3 Aquisition of Data and Experimental Results

Velocity measurements have been made in both combustion chambers at engine speeds of 600, 800, 1000, 1200 rev./min. Due to limitation on time, measurement in combustion chamber II (figure 7.3) was restricted to that necessary to establish a comparison of air motion with combustion chamber I.

Cylinder pressure and temperature traces were obtained for all the engine speeds as described in section (7.4.2) and processed as depicted in figure (6.12). Air temperature at compression top dead centre (CTDC) was measured to be approximately 20 deg. C higher at 1200 rev/min than at 600 rev/min. Motored engine cylinder pressure and temperature traces at 1000 rev/min are illustrated in figure (7.19).

Air velocity measurements in combustion chamber I were made at five combustion chamber radii at each engine speed. Probe insertion at the radii 10, 17, 21, 27 mm., was through the brass plug mounted in the window aperture, to a depth of 10 mm. below the cylinder head flame face (see figure 7.3). For the 5 mm radius probe location, the probe was inserted down the injector body hole, and therefore the axis of the wire was not maintained parallel to the piston face for this location. Swirl velocity component was measured by positioning the probe so that the wire

axis was radial to the combustion chamber, i.e. normal to the tangent. Squish velocity component was measured by rotating the probe so that the wire axis was normal to the combustion chamber radius.

Squish component was measured only at the 27 mm radius, i.e. adjacent to the combustion chamber lip, where its magnitude may be expected to be greatest.

The recorded voltage traces were averaged over ten engine cycles and digitised to approximately 750 ordinates per cycle (approximately 1 crank deg. interval). The above data was used in conjunction with a specially written computer program for the calculation of the air velocity. The flow chart for the computer program is shown in figure (7.20).

Air velocities as a function of engine crankshaft rotation were then generated. Figure (7.21) to figure (7.25) inclusive show the computed swirl velocity traces at the four engine speeds and five radii for combustion chamber I, and figure (7.26) shows the squish velocity component at a radius of 27 mm for the four engine speeds.

The general form of the traces show three velocity peaks corresponding to induction air motion, compression swirl motion, and exhaust air motion. The relevant portions of the traces are adjacent to CTDC, when fuel injection and mixing occurs.

Velocity magnitudes at the respective radii may be replotted as combustion chamber swirl velocity profiles. Figure (7.27) shows the variation of swirl velocity profile for 30 degrees either side of CTDC at 1000 rev/min. Figure (7.28) shows similar profiles at the four engine speeds at CTDC. The profiles so generated may be approximated by a forced vortex representation as shown, and hence, on the basis of a solid body rotation a mean

swirl ratio $\bar{\sigma}$ may be calculated. Figure (7.29) shows the variation of mean swirl ratio at CTDC with engine speed. Similar to the results of Urlaub (1) (2), (figure (1.1)), swirl ratio decreases with engine speed, and the magnitudes of the results of figure (7.29) approximately correspond to the 10 mm mask curve of figure (1.1).

Measured squish velocity component at CTDC and 27 mm radius (figure 7.26) is low compared to the corresponding swirl velocity (figure 7.25). It is worthy of note that the hot wire probe will sense heat transfer from its surface even when the flow is parallel to the wire axis. Tests conducted on the flow calibration rig showed that a wire with its axis parallel to the flow may indicate a velocity up to 15% of the actual longitudinal component. Hence, part of the illustrated compression squish (figure 7.26) must be attributed to the heat transfer induced by the predominant swirl motion.

Figures (7.30) (7.31) show velocity traces for the combustion chamber II at a radius of 23 mm. The squish component is again seen to be low compared to the swirl component at CTDC. The figure (7.28) shows the measured swirl velocity plotted in relation to the profiles of combustion chamber I, and indicates a substantial compatability in swirl magnitudes between the two combustion chamber shapes.

7.5 Comments on Relative Performance of the Two Combustion Chambers

As previously indicated, figures (7.6) (7.7) show a marked similarity of pressure trace data for both combustion chambers, figures (7.8) (7.9) show similarity in exhaust emission levels, and essentially the same spray formation was found to exist from the high speed cine-film data. Figure (7.28) indicates that substantially the same air motion is generated in both cases.

The 'squish' lip of combustion chamber II is therefore seen to have little effect. Actual shape of the two chambers differ, but both were designed to allow viewing of the combustion process through the window, at similar compression ratios, and are therefore of similar diameter and depth. Air motion may be expected to be consistent unless a substantial decrease in 'throat' diameter forces the air to adopt a radial (squish) motion as the charge air is transferred to the inner bowl when the piston approaches CTDC. Such an air motion may be expected to redirect tangential angular momentum. The mathematical model, due to Derham (31), which was developed to predict the air swirl motion, was based on the conservation of angular momentum on transfer of the charge air from the larger cylinder bore diameter, to the smaller combustion chamber diameter. It is logical therefore that bowls of similar radii may be anticipated to produce similar swirl ratios unless the path of the air is caused to substantially deviate from the induced tangential motion.

The comparison of data between combustion chambers I and II therefore illustrates that exhaust emission levels and power output are predominantly a function of the air-fuel mixing process. Change in chamber shape will only affect either of these parameters by influencing the air motion and, logically, the spray path length. As resolved in section (1.1) it is therefore the air-fuel mixing process which has to be described.

7.6 Modelling Experiments Based on the Engine Data

Motored engine, compression data, for the engine speed of 1000 rev/min may be summarised as below:-

Peak compression pressure	31.8 bar
Peak compression temperature	456 deg. C
Peak compression air density	15.2 kg/m^3
Representative air velocity (10 deg. BTDC)	10.8 m/sec

The latter item being obtained by manual integration of the profile represented in figure (7.27).

Similarly the fuel injection characteristics for each nozzle may be analysed and combined with the above data to yield the gas jet diameter and velocity by equation (2.20) (2.19) for a model air velocity of 3.25 m/sec., yielding:-

Fuel Nozzle Spec. (No. x size)	Fuel Nozzle Velocity (m/sec)	Gas Jet* diameter (mm)	Gas Jet Velocity (m/sec)
1 x .35 mm	198	2.67	58.5
4 x .30 mm	108	2.29	32.0
4 x .24 mm	165	1.83	48.5

* Propane tracer gas

For the modelling experiments a vane opening of 14 mm was found to most effectively simulate the air velocity profile (figure 6.3).

Measurement of model gas concentration was again made in the plane containing the jet axis using the hot wire anemometry technique. Steady state tests were performed since ignition always occurred in the established fuel spray (figures 7.11 to 7.16). The resultant concentra-

tion maps for the combustion chamber I are shown in figures (7.32), (7.33), (7.34).

Due to the extreme similarity between the engine performance obtained for the two combustion chamber shapes modelling experiments were not performed for combustion chamber II.

7.7 Relationship of Engine Data to the Gas Jet Models

7.7.1 Qualitative Comparison of Photographic Data and Gas Jet Simulations

With the direct photographic technique employed comparison of trajectory of the fuel spray and gas jet may be made when the combustion process illuminates the established spray (cf. figure (7.11), frame 3 at 2.5 deg BTDC). Further information on the auto-ignition sites, 'combustion' evident distribution of fuel, and occurence of smoke generation is provided. The gas jet models provide information on fuel distribution over the surface containing the jet centre line and a point worthy of note is that the engine fuel distribution and photographed combustion are three dimensional.

Comparison will initially be made between the photographic results of figures (7.11) (7.12) and the corresponding gas jet model of figure (7.32). (1 x 0.35 mm. dia. nozzle).

Both model and engine display an essentially straight jet with heavy wall impingement. Fuel concentration at the combustion chamber wall is predicted to be high in the model, and wall wetting would therefore be anticipated in the engine. Suitable ignition sites within the model are presented along the 10:1 to 15:1 regions parallel to the wall and behind the spray body, which corresponds closely to the photographed behaviour, (figure 7.11, frame 2, at 5 deg. BTDC.), where auto-ignition is seen to occur simultaneously in two separate regions; adjacent to the wall downstream of the impingement point, and adjacent to the spray body in the 'lee' of the air swirl.

An area of interest is presented in the wake of the gas jet model, close to the nozzle, where an accumulation of fuel is apparent (figure 7.32). A low pressure wake region may be

formed due to the reasons outlined in section (2.1) and fuel thereby trapped. Concentration of gas in this area is seen to be low, but no evidence of such an accumulation is apparent from the engine photographs. The flame front reaches these regions by the end of injection (figure (7.11) from TDC to 2.5 deg. ATDC), but is indicative of combustion expansion and mixing rather than flame propagation through a preformed mixture.

The engine spray is most effectively represented in frame 3 (figure 7.11) at 2.5 deg. btdc, and marked similarity with the gas jet model is apparent (figure 7.32). The most intense combustion at this point occurs in the jet wake, immediately behind the jet core, and in the mixture band predicted by the model to be between 15:1 to 5:1.

Heavy smoke generation becomes evident from 15 deg. ATDC to 30 deg. ATDC with dense smoke nuclei being formed in the area approximately corresponding to the combustion chamber edge and the impingement point (see frames at 20, 22.5 and 25 deg. ATDC, figure 7.11). The implication is that the combustion process is then sufficiently intense to cause ignition, and partial burning of the deposited wall fuel layer, corresponding in the gas jet model to the narrow 3:1 contour at the wall.

Earlier in the combustion process the jet body does not become fully ignited until 2.5 to 5 deg. ATDC. Model predicted air to fuel ratio in the spray body is less than 3:1, therefore, similar to ignition at the wall sufficient heating of the fuel-rich portions only occurs when combustion has become well established. This is also in accordance with the postulation of Melton (17), in relation to figure (1.22), namely, that the dissipation and combustion of the fuel rich regions in the spray core could only occur after cessation of injection. In relation

to figure (7.11) this can be seen to be so, since intense combustion of the jet body corresponds to the end of injection when the air swirl rotates and destroys the original spray.

The total combustion process is prolonged, and still visible at 70 deg. ATDC, (figure 7.12), although piston motion has then exceeded the camera focus depth of field.

Dissipation of the model predicted rich wall regions is therefore seen to be a slow process requiring heating and subsequent combustion of the colder fuel layer. Combustion efficiency may then be expected to be additionally controlled by the rate at which air contacts the wall fuel layer. Figure (7.6) indicates a low peak pressure for this nozzle and low rate of initial pressure rise, accordingly figure (7.8) shows high smoke and unburnt hydrocarbon emissions, and low NO_x emission.

Figures (7.13) (7.14) and the corresponding gas jet model of figure (7.33), for the 4 x 0.3 mm diameter nozzle, present a different mode of combustion.

The viewed spray ignites close to the nozzle, and simultaneously, close to the combustion chamber wall (frame 1, figure 7.13). Flame propagation through the pre-mixed fuel is rapid (frame 2), and a wide combustion band is established by approximately 4.5 deg. BTDC (frame 3). On frame 3 a darker brown 'smoke' area at the combustion chamber edge, slightly to the left of centre, becomes visible. This suggests the spray impingement point and jet deflection and considerable spread is therefore inferred by the sequence up to frame 4 (3 deg. BTDC), although the spray body is hidden by the combustion process. By CTDC (frame 6) flame has filled the viewing window. Comparison with the previous 1 x 0.35 mm nozzle (figure 7.11) effectively illustrates the difference in the initial combustion rate of the

two sprays and is clearly evident from the pressure trace data of figure (7.6).

Subsequent to the injection process the brown 'smoke' area rotates with the air swirl and by 3 deg. ATDC the air 'gap' separating the viewed spray combustion from the 'upstream' spray becomes visible. From 3 deg. ATDC to 8.7 deg. ATDC the 'smoke' area rotates out of view. By 36 deg. ATDC decay of the combustion process is evident, comparison with the same point in the cycle for the 1 x .35 mm nozzle (figure 7.12)) again indicates the difference in combustion rates.

The gas jet simulation of figure (7.33) predicts considerable jet deflection and in this respect agrees with the photographic results. Additionally, spread of the jet is large, and a wide trail, starting at approximately 10 mm radius is produced, and therefore corresponds to the early ignition and rapid combustion areas of frames 1 and 2, figure (7.13). Gas concentration on impingement represents an air to fuel ratio between 5:1 and 3:1 and clearly corresponds with the above mentioned smoke generation. The model therefore predicts a fuel spray with both a wide lean trail in its wake, and a high fuel concentration at the combustion chamber wall and along the jet centre line. In the latter respect the model prediction is similar to figure (7.32) for the 1 x 0.35 mm diameter nozzle, but due to the lower injection velocity for figure (7.33), (see section 7.6), increased deflection and a wide lean trail are also produced. The results of figure (7.8) indicate both high nitrous oxide and smoke emission levels for the 4 x 0.3 mm diameter nozzle. The explanation is therefore related to the concept of Henein (35), figure (1.15), where the high nitrous oxide emissions were attributed to the lean 'trail' regions of the model and the incomplete combustion products were

attributed to the fuel rich core, and logically, the fuel rich wall regions also.

Figures (7.15) (7.16) illustrate the photographic results for the 4 x 0.24 mm diameter nozzle, and figure (7.34) illustrates the corresponding gas jet simulation. The left hand spray, in view through the window aperture, is discussed below.

Auto-ignition occurs simultaneously in three separate locations, subsequent flame propagation to the spray body is rapid, as depicted in frame 2 of figure (7.15), (approximately 8.6 deg. BTDC). Wall impingement is evident and negligible deflection of the spray body occurs. No smoke generation is indicated and large areas of fuel free space persist throughout the combustion process. Combustion later in the sequence (5 deg. ATDC onwards) is restricted to burning at the outer combustion chamber radii.

Comparison of auto-ignition sites with the gas jet model again indicate location along the 15:1 to 10:1 contour. The ignition nucleus near to the nozzle (figure 7.15, frame 1) is indicative of combustion in the wake generated region behind the gas jet (cf. figure 7.34). Such a wake 'collection' of jet fluid has already been illustrated in figures (6.23) (7.32) although evidence of ignition in this area has not been previously observed. The ignition nucleus close to the combustion chamber edge (figure 7.15, frame 1), corresponds to the area downstream of the gas jet model impingement point where the concentration near to the wall is in the region 10:1 to 15:1.

Generally gas jet predicted air to fuel ratio at the combustion chamber wall is in the region of 10:1, and therefore considably weaker than the previous results of figures (7.32) (7.33). This therefore coincides with the absence of smoke generation in figures (7.15) (7.16).

The combustion process for this nozzle is rapid and is decaying by 25 deg. ATDC (figure 7.16). The appearance is 'cleaner', with flames distinctly brighter and less red than the previously discussed film sequences. Jet body 'core' concentration in the model (figure 7.34) is also seen to be less rich and extent of the 3:1 boundary is reduced. The fuel spray form is most effectively illustrated early in the combustion process in frame 2 (figure 7.15) where substantial comparison with the gas jet simulation of figure (7.34) may be made.

7.7.2 Quantitative Comparison of Gas Jet Simulations and Engine Data

Quantitative comparison of trajectory and spread, and auto-ignition site location, between various gas jet models and corresponding engine fuel sprays, has already been made in chapter 6. The purpose here is to show a degree of correlation between exhaust emission levels, pressure trace data and the simulated fuel spray mixedness.

Section 1.1 presented evidence that the interaction of fuel spray and air swirl intensities was related to the engine performance. Figures (1.9) (1.10) illustrated that increased 'mixedness' promoted higher rate of initial pressure rise and figure (1.14) was used to indicate that increased swirl influence promoted increased Nitrous oxide emission. The concept of Henein (35), figure (1.15), was thereby supported, and indicates that extension of the relatively weak regions may promote increase in nitrous oxide emissions, initial rate of pressure rise, peak pressure, and hence combustion noise. Conversely, increase in the proportion of rich spray regions may be anticipated to promote increased emission of smoke, unburnt hydrocarbons, and due to partial carbon oxidations, increased

carbon monoxide emission also. The concept of Melton (17), figure (1.22), may also be anticipated to be relevant since as indicated for the 1 x 0.35 mm. diameter nozzle, dissipation of over rich fuel regions, within the spray core, may only occur after the cessation of injection.

The air-fuel contour maps of figures (7.32) (7.33) (7.34) therefore provide a direct means of quantifying the spray mixedness, and the experimental engine data of figures (7.6) (7.8), provide the necessary performance comparison.

The area of each spray model covered by a predicted air to fuel ratio weaker than 10:1, expressed as a fraction of the total jet area, has been used as a parameter of model predicted mixedness. (The respective areas were measured using a planimeter)

The lower histogram of figure (7.35) shows the result for the three considered nozzles. Consequently, the 1 x 0.35 mm. diameter nozzle spray is predicted to be less than 40% mixed to an air to fuel ratio weaker than 10:1, measured on the 'area' basis.

The upper histograms of figure (7.35) show engine data for each nozzle which may logically be expected to increase with increased spray mixedness. Model 'mixedness' parameter, and engine data, are therefore shown to follow a similar trend.

The lower histogram of figure (7.36) shows the converse area parameter for the three nozzles, i.e. the fractional area of each gas jet model covered by air to fuel ratio regions richer than 10:1 are represented. Consequently, the 1 x 0.35 mm diameter nozzle spray is predicted to be more than 60% mixed to an air to fuel ratio richer than 10:1, on the 'area' basis.

The upper histograms of figures (7.36) show the engine data for each nozzle which may be expected to increase with proportion

of rich spray mixture. A degree of correlation between model 'mixedness' and engine data is again indicated.

7.7.3 Concluding Comments on the Engine Analysis

The set of engine data, has been shown to be complimentary to the gas jet models.

High values of nitrous oxide emission, rate of initial pressure rise, maximum cycle pressure, and a rapid combustion process occur for the 4 x 0.24 mm. diameter nozzle, and have been explained by reference to the mixture presented by the corresponding simulation. (figure (7.34) (7.35))

Conversely, high values of unburnt hydrocarbon emission, smoke number, carbon monoxide emission, and a prolonged combustion process, occur for the 1 x 0.35 mm. diameter nozzle, and have been attributed to the high jet core and wall fuel concentrations presented in the model. (figure (7.32) (7.36))

The 4 x 0.3 mm diameter nozzle produces both relatively high smoke and nitrous oxide emissions and combines the worst characteristics of the above mentioned cases. The model indicates that the large jet diameter promotes fuel rich regions in the jet core and at the impingement point despite the low injection velocity (section 7.6). However, jet deflection occurs and the low velocity portions at the outer spray body are transported by the air swirl to form a generally 'weak' mixture in a jet trail, where the photographic data indicates auto-ignition and rapid initial combustion originate. The generally weak trail, and associated rapid combustion have been postulated to be responsible for the nitrous oxide emission (section 7.7.2), whilst the rich jet core and wall impingement zone have been proposed as responsible for the smoke emission in conjunction with the photographic evidence.

The carbon promoting, slow and late dissipation of the rich fuel core within the spray as proposed by Melton (figure 1.22) and the emission formation concept of Henein (figure 1.15) are therefore seen to be upheld.

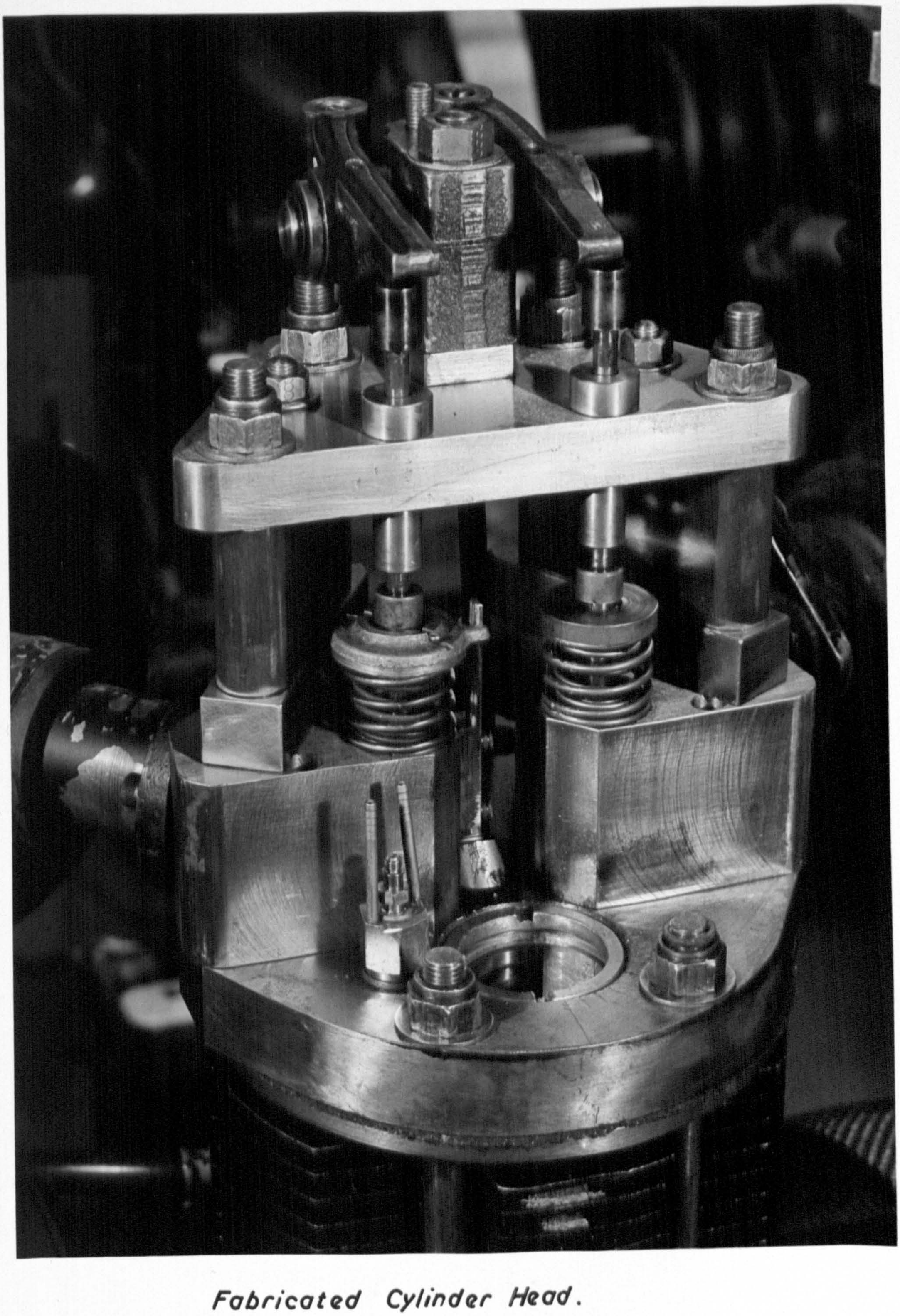

Fabricated Cylinder Head.

Fig. 7·1

Details of Fabricated Cylinder Head

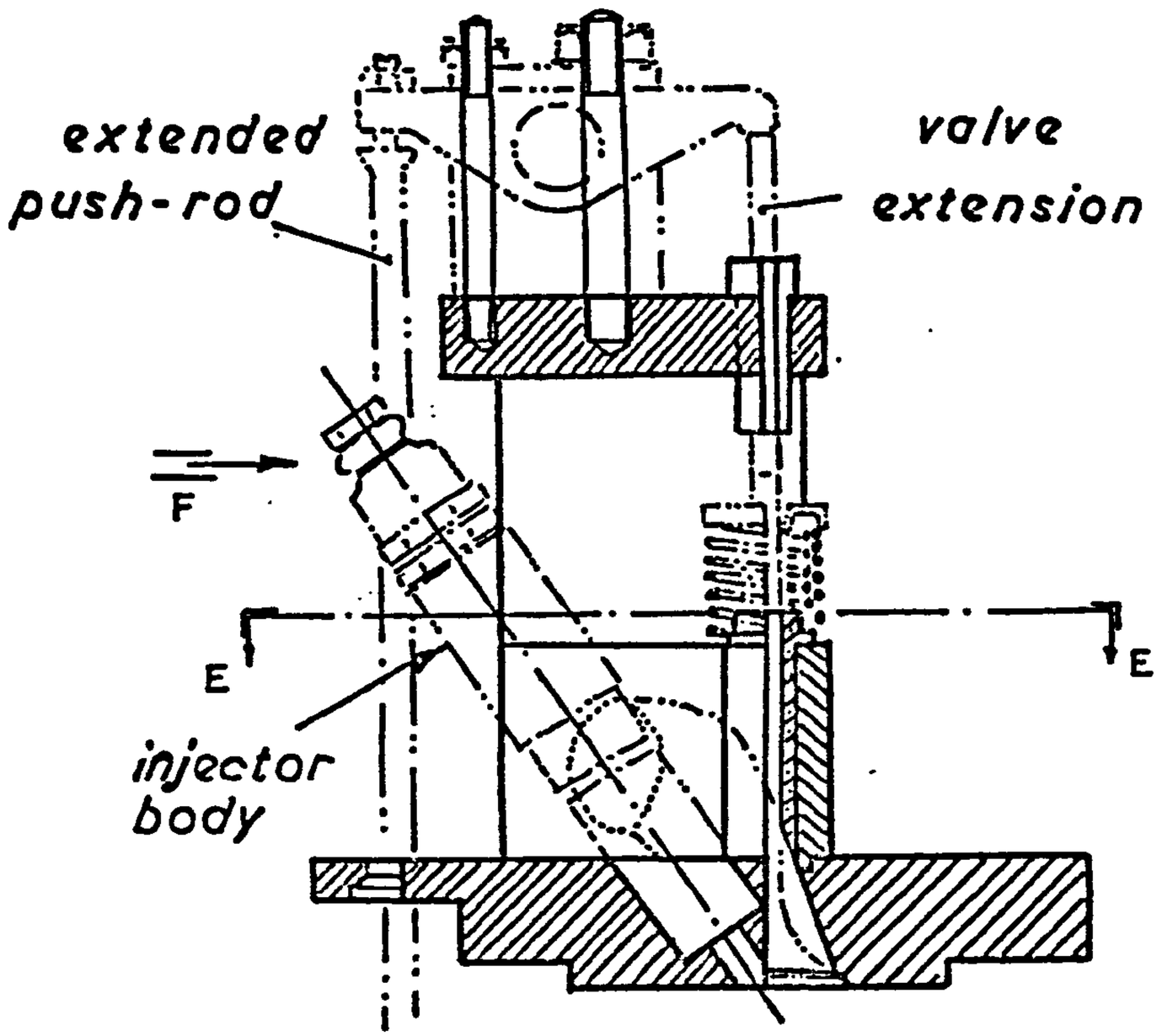

SECTION ALONG A-A

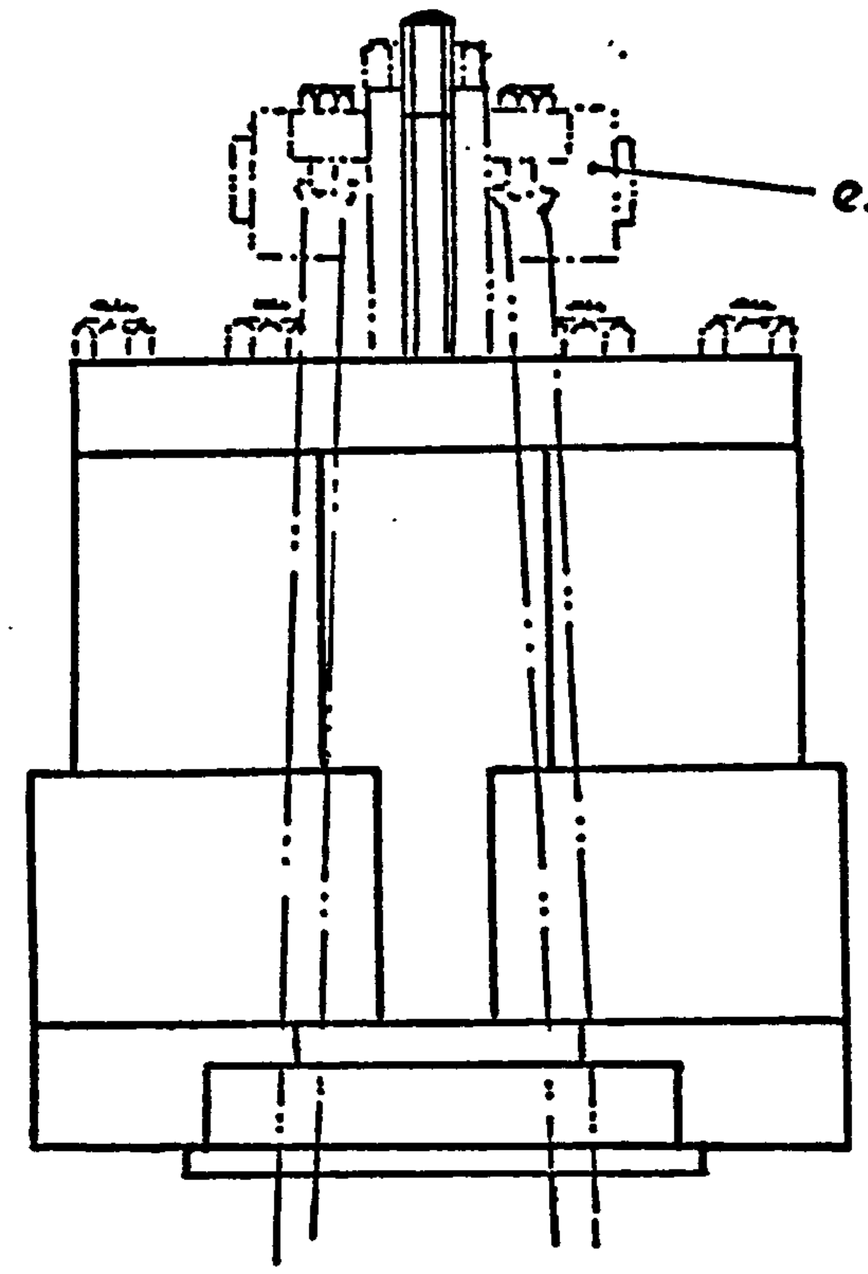

VIEW ON F

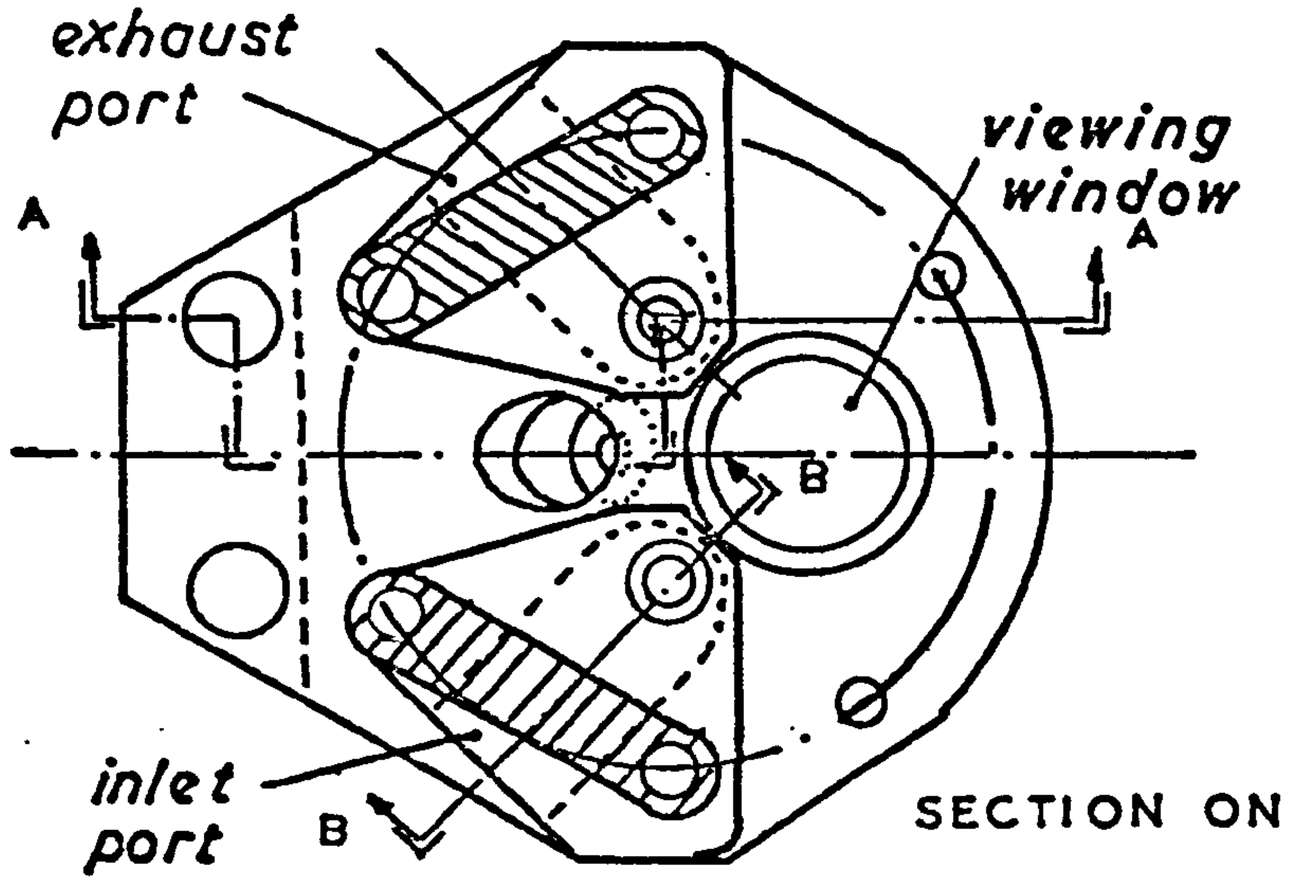

SECTION ON E-E

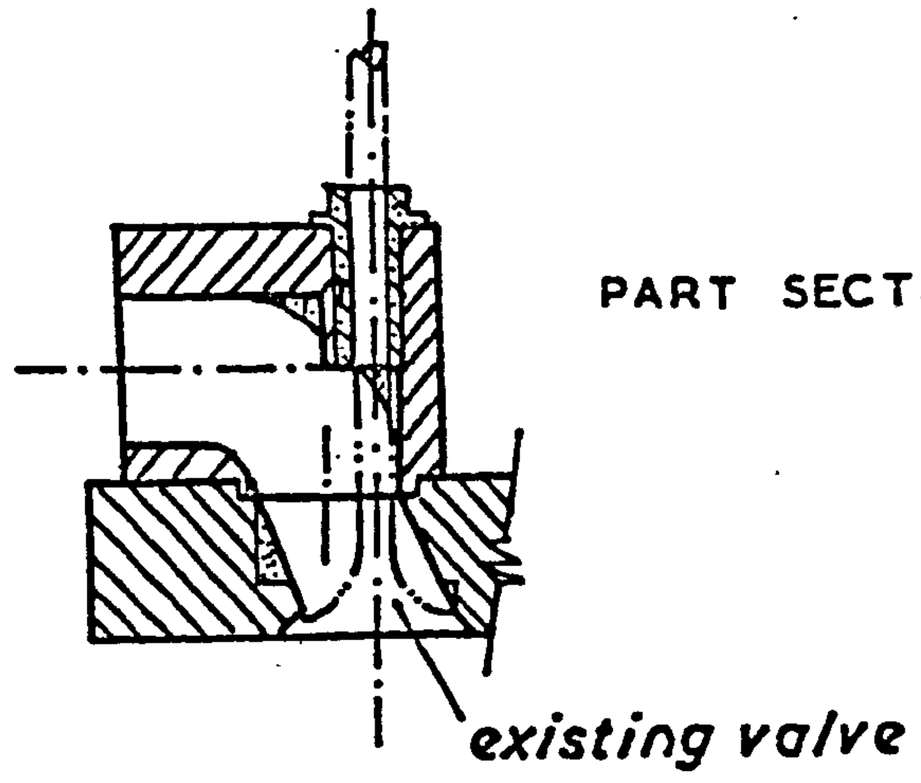

PART SECTION ON B-B

Fig. 7.2

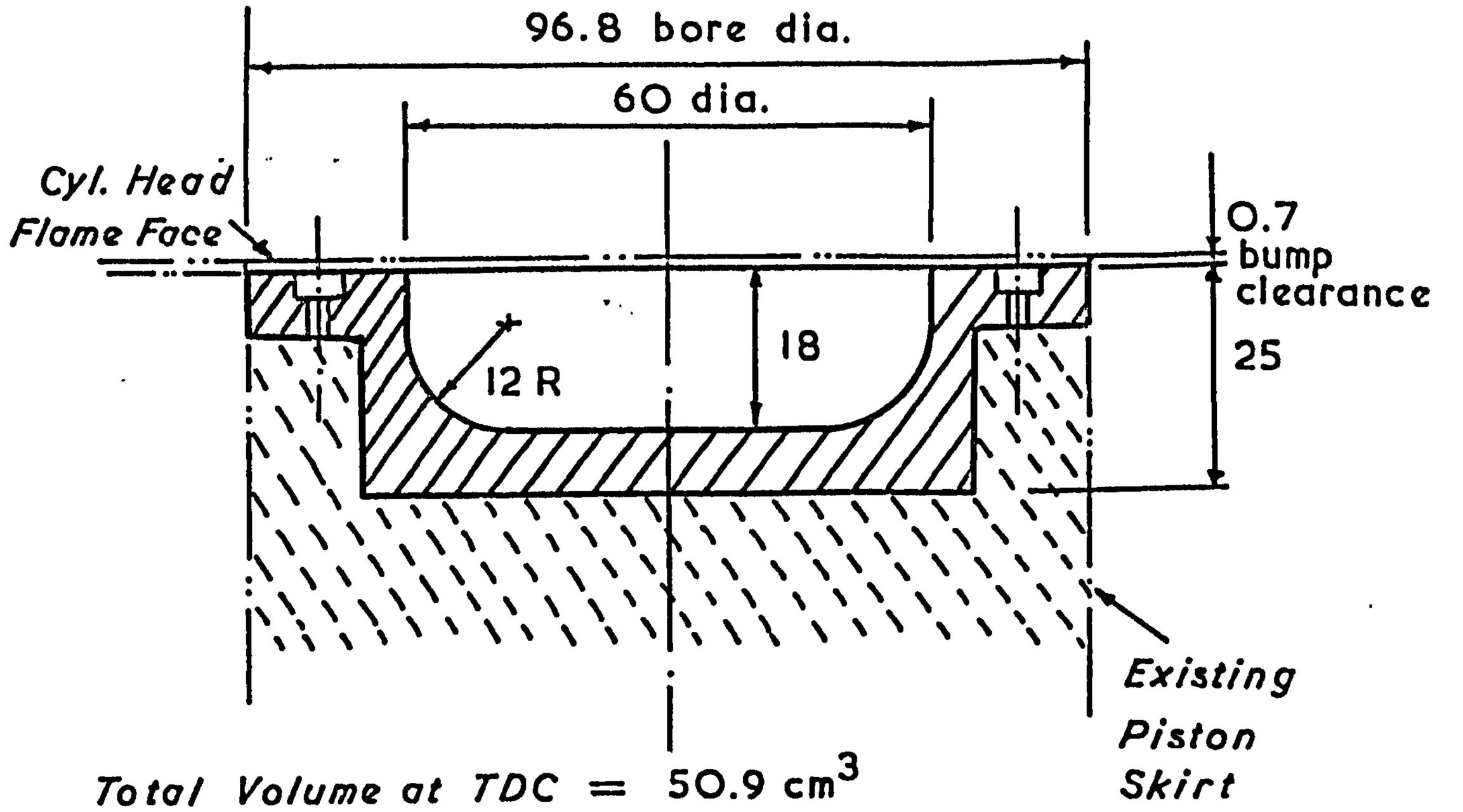

Details of Combustion Chamber I

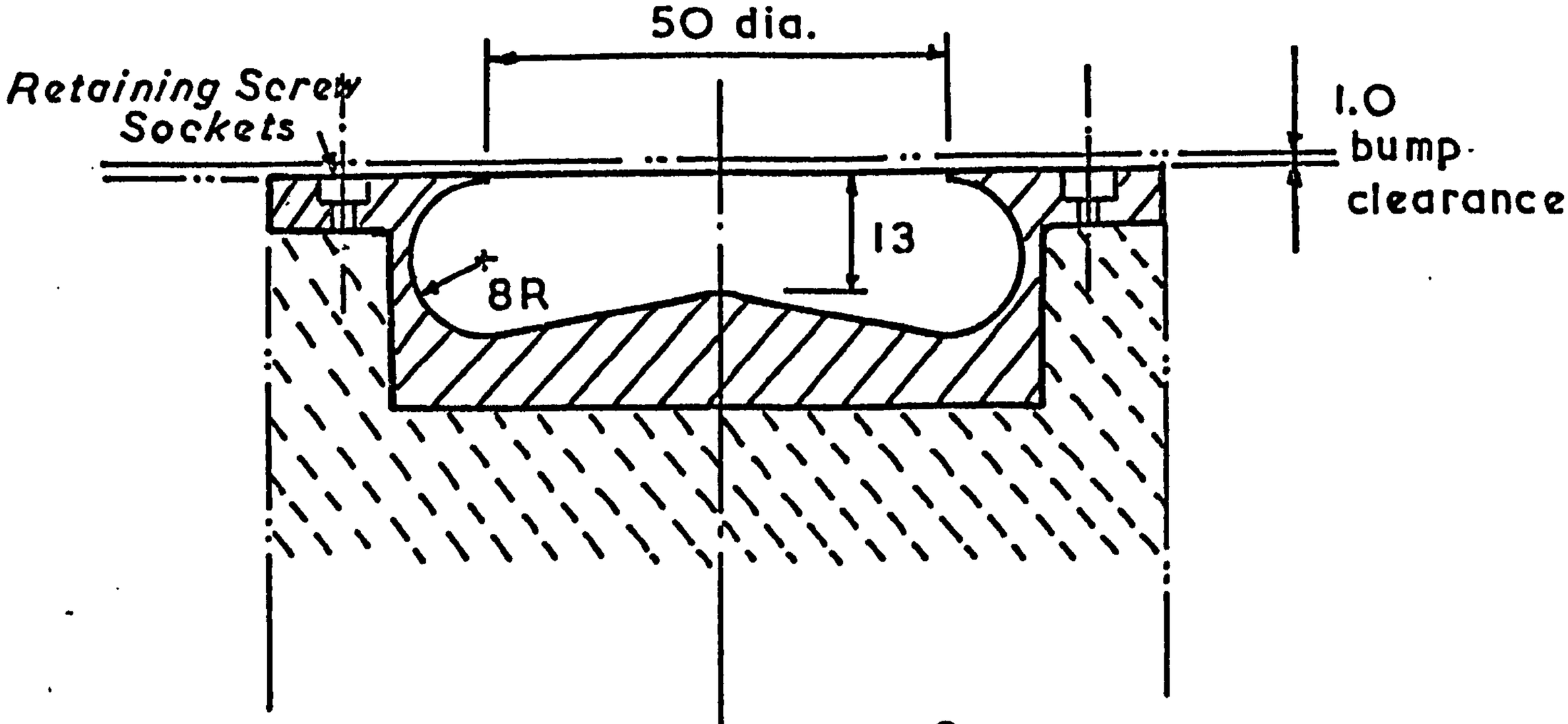

(Dimensions in mm)

Details of Combustion Chamber II

Fig. 7·3

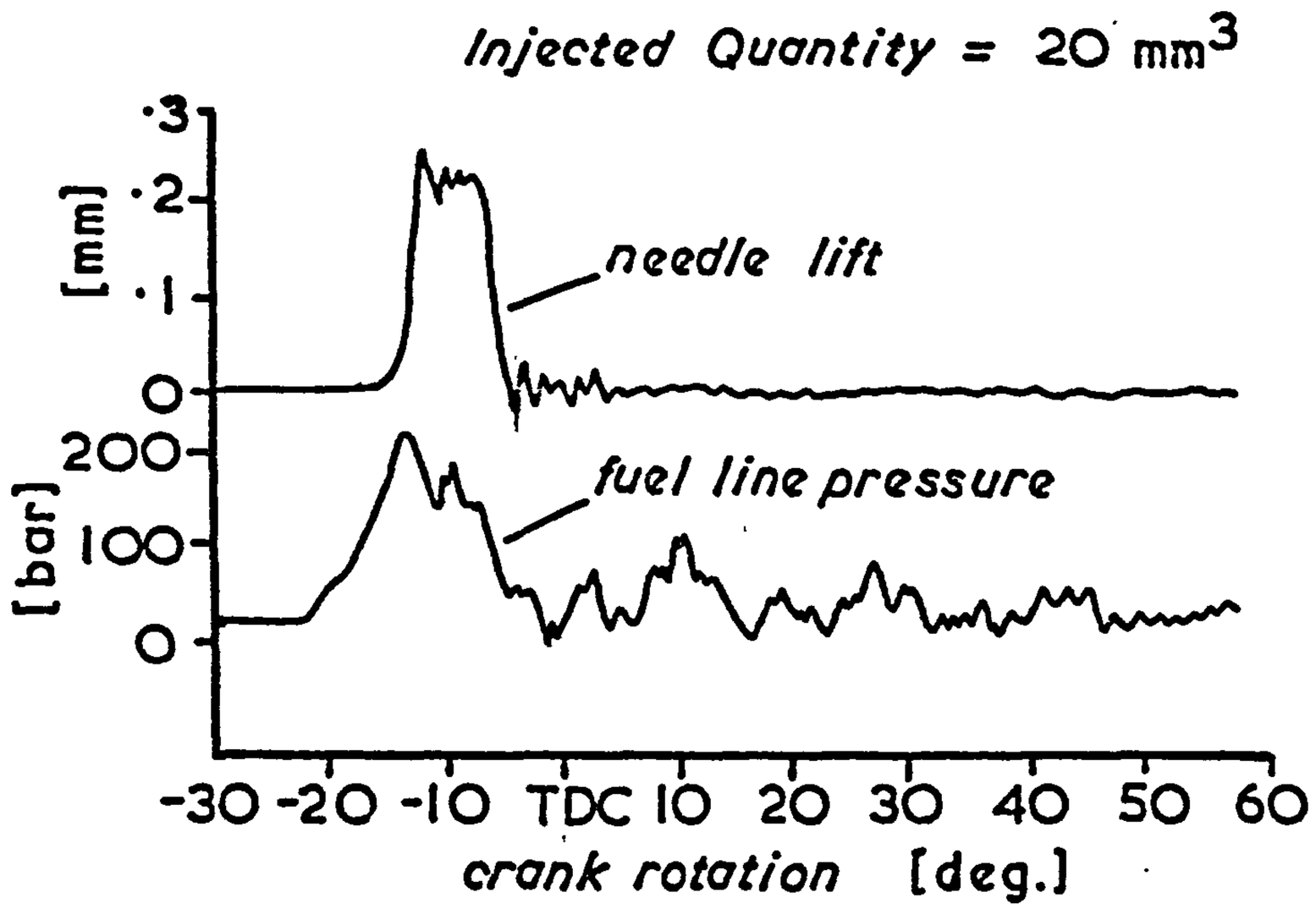

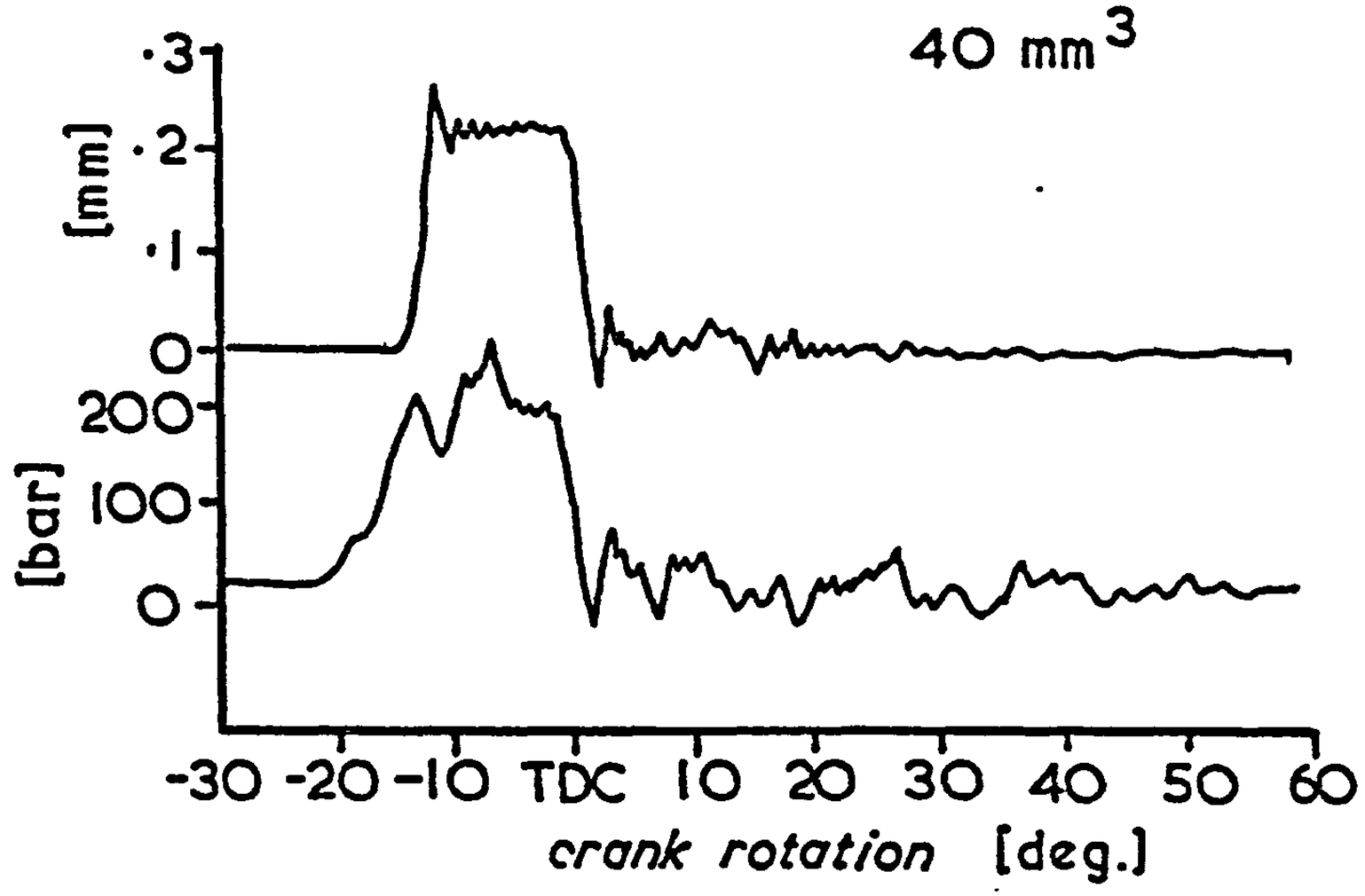

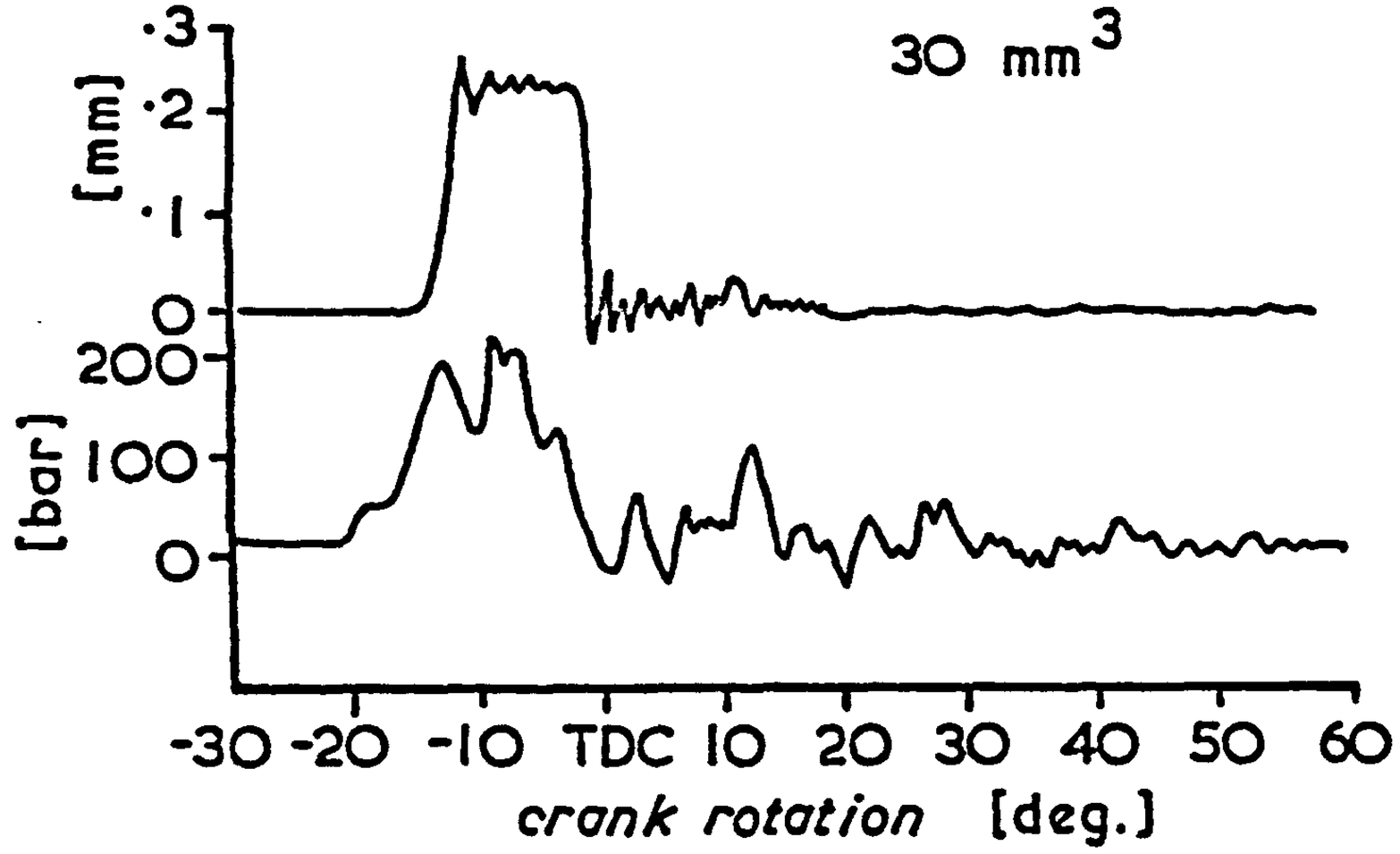

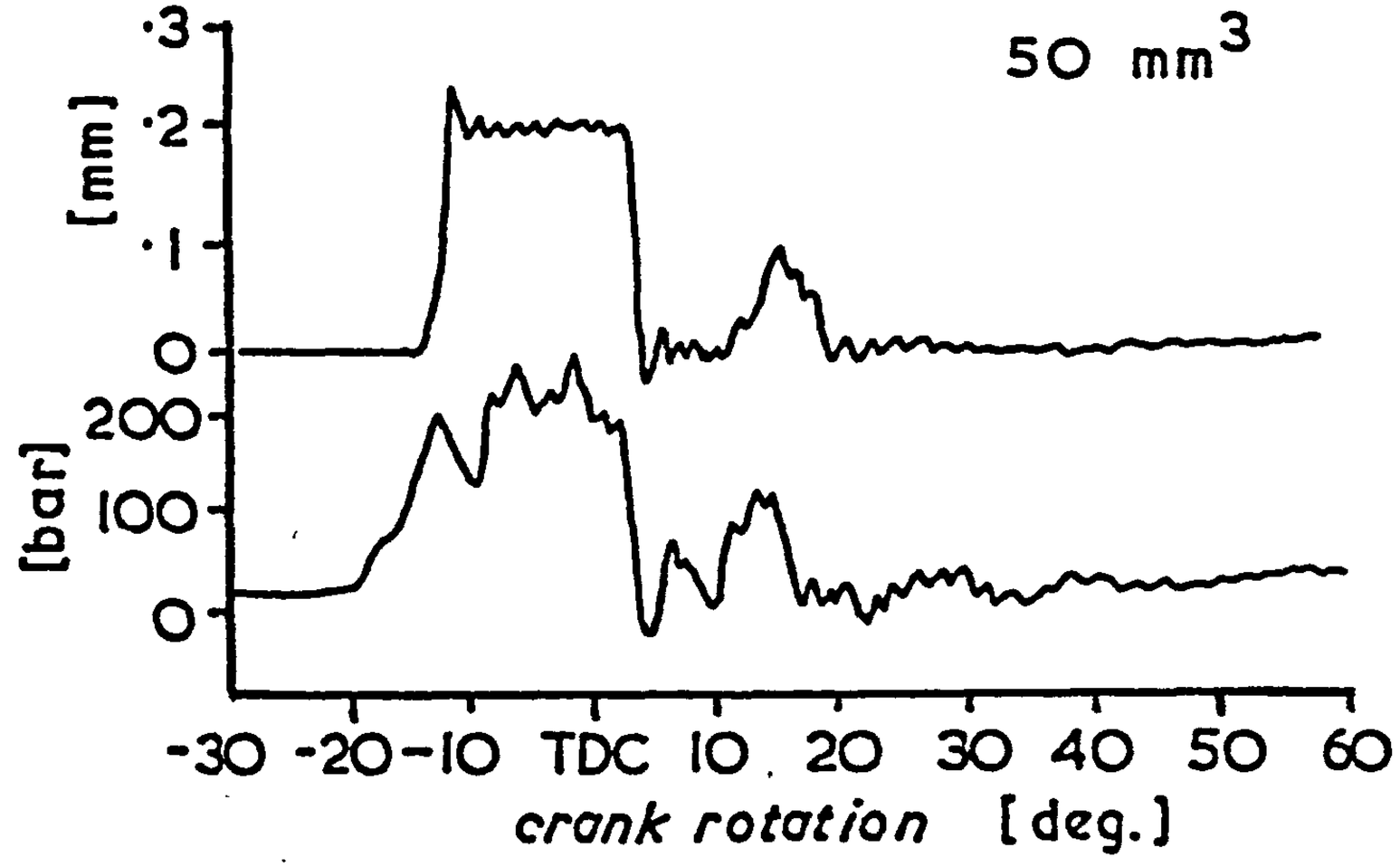

Fig. 7.4

Engine Speed :- 1000 rev/min. *N.O.P :-* 150 bar. *Nozzle :-* 1 *hole* x ·35 mm. *dia.*

Typical Fuel Injection Characteristics

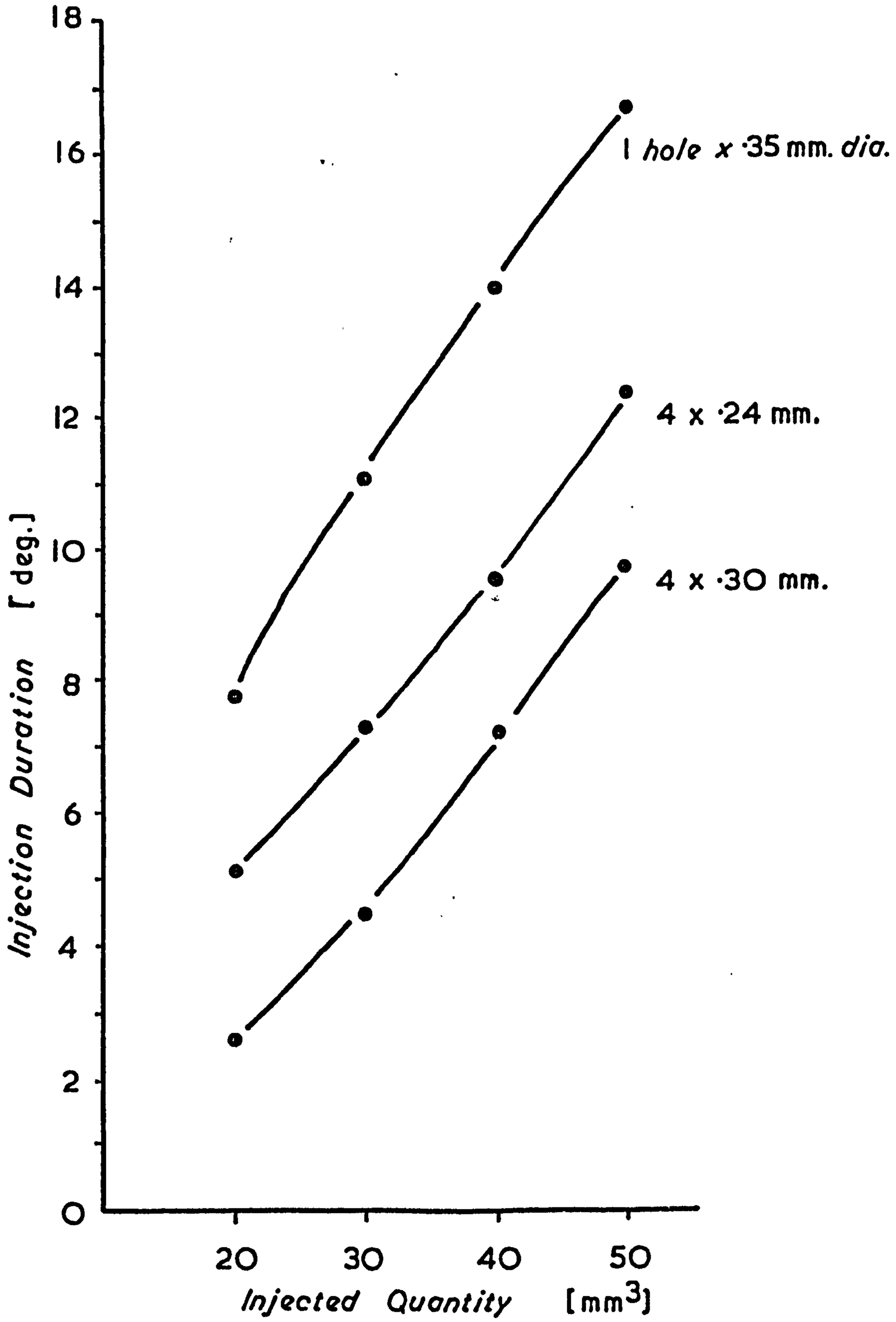

Injection Duration at 1000 rev./min.

Fig. 7·5

nozzle	IMEP [bar]	ΔP^{*} [bar]	$\theta P_{max.}$ [deg]	$\left[\frac{dP}{d\theta}\right]_{max.}$ [bar/deg]
1x·35	5·33	17·2	366	6·16
4x·3	6·48	34·2	367	11·66
4x·24	6·24	38·2	363	17·56

$^{*}\Delta P = P_{fired} - P_{comp.}$

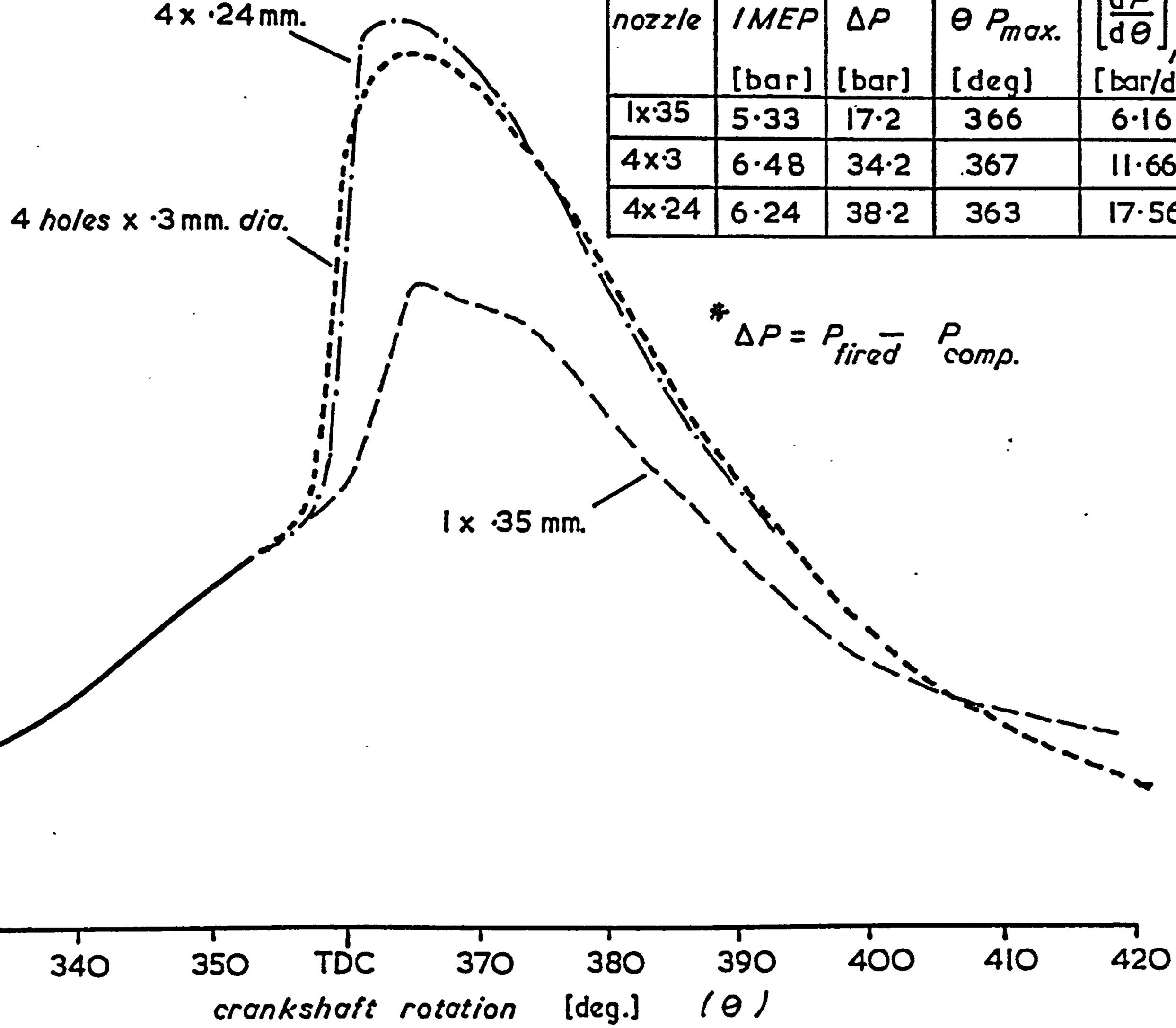

Fig. 7.6 Fired Pressure Traces for Chamber I

nozzle	IMEP [bar]	ΔP^{*} [bar]	$\theta P_{max.}$ [deg]	$\left[\frac{dP}{d\theta}\right]_{max.}$ [bar/deg.]
1 x·35	5·27	18·3	366	5·63
4x ·3	6·51	35·7	364	12·76
4x·24	6·30	37·9	365	17·21

$^{*}\Delta P = P_{fired} - P_{comp.}$

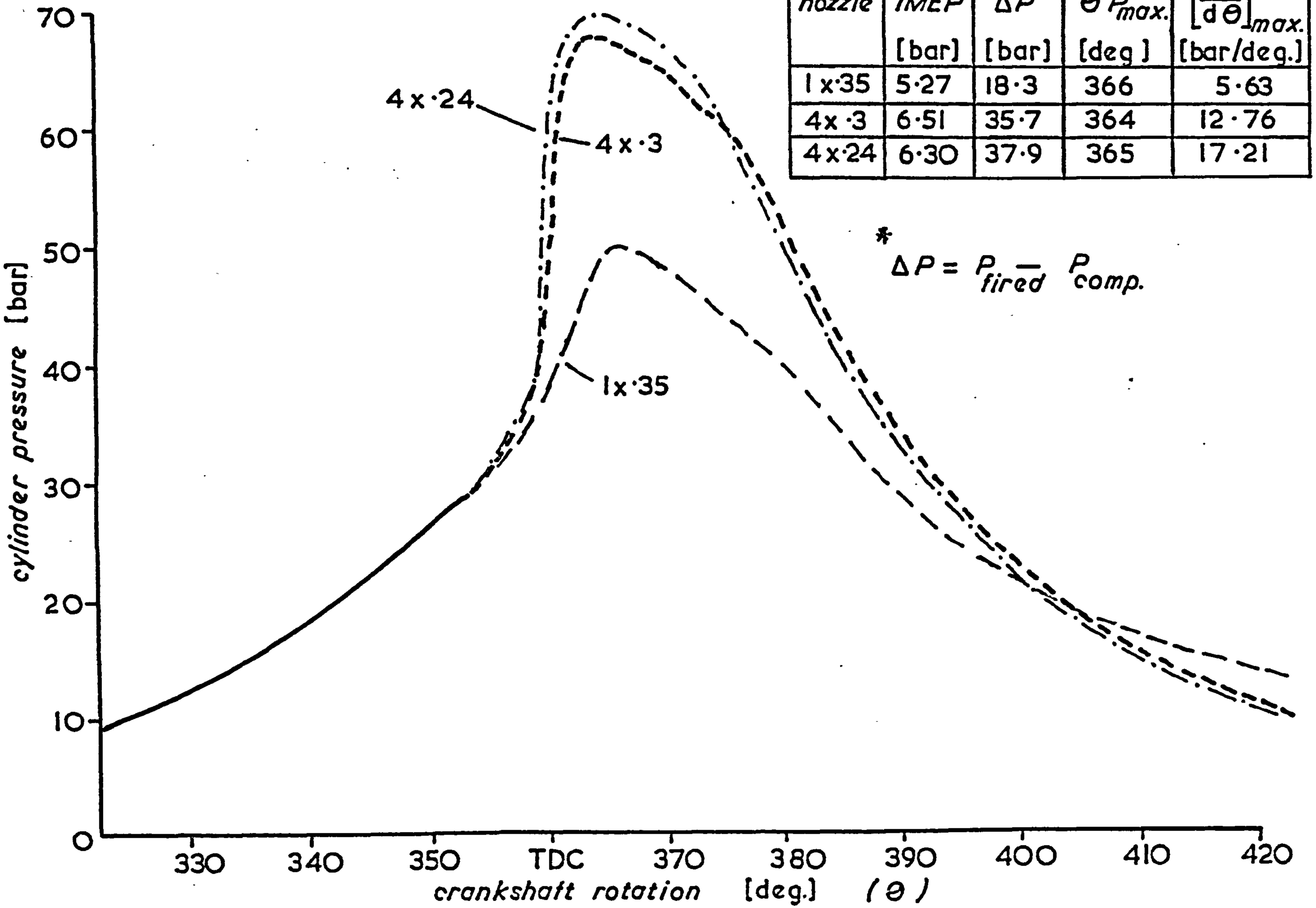

Fig. 7.7 Fired Pressure Traces for Chamber II

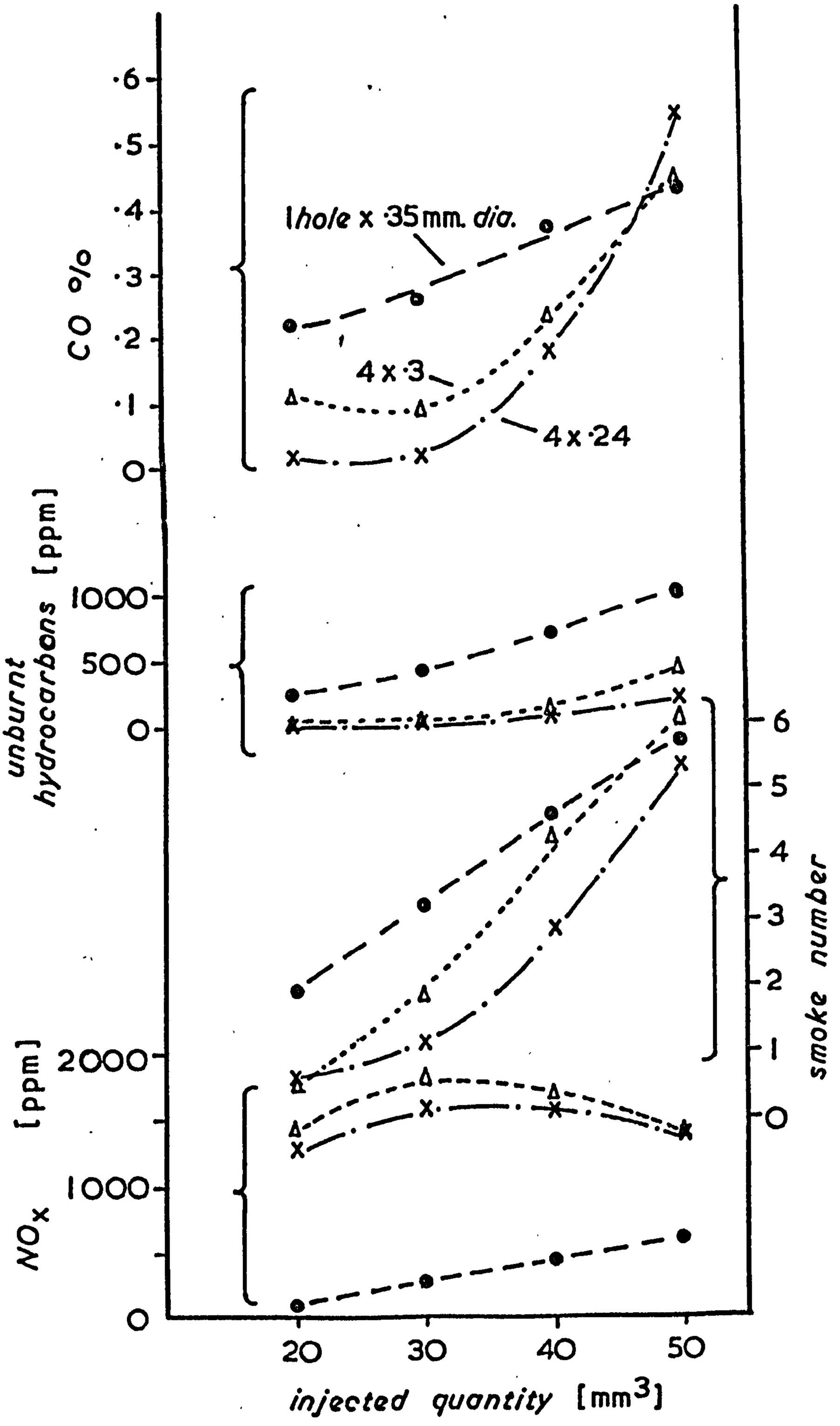

Exhaust Emissions for Chamber I

Fig. 7·8

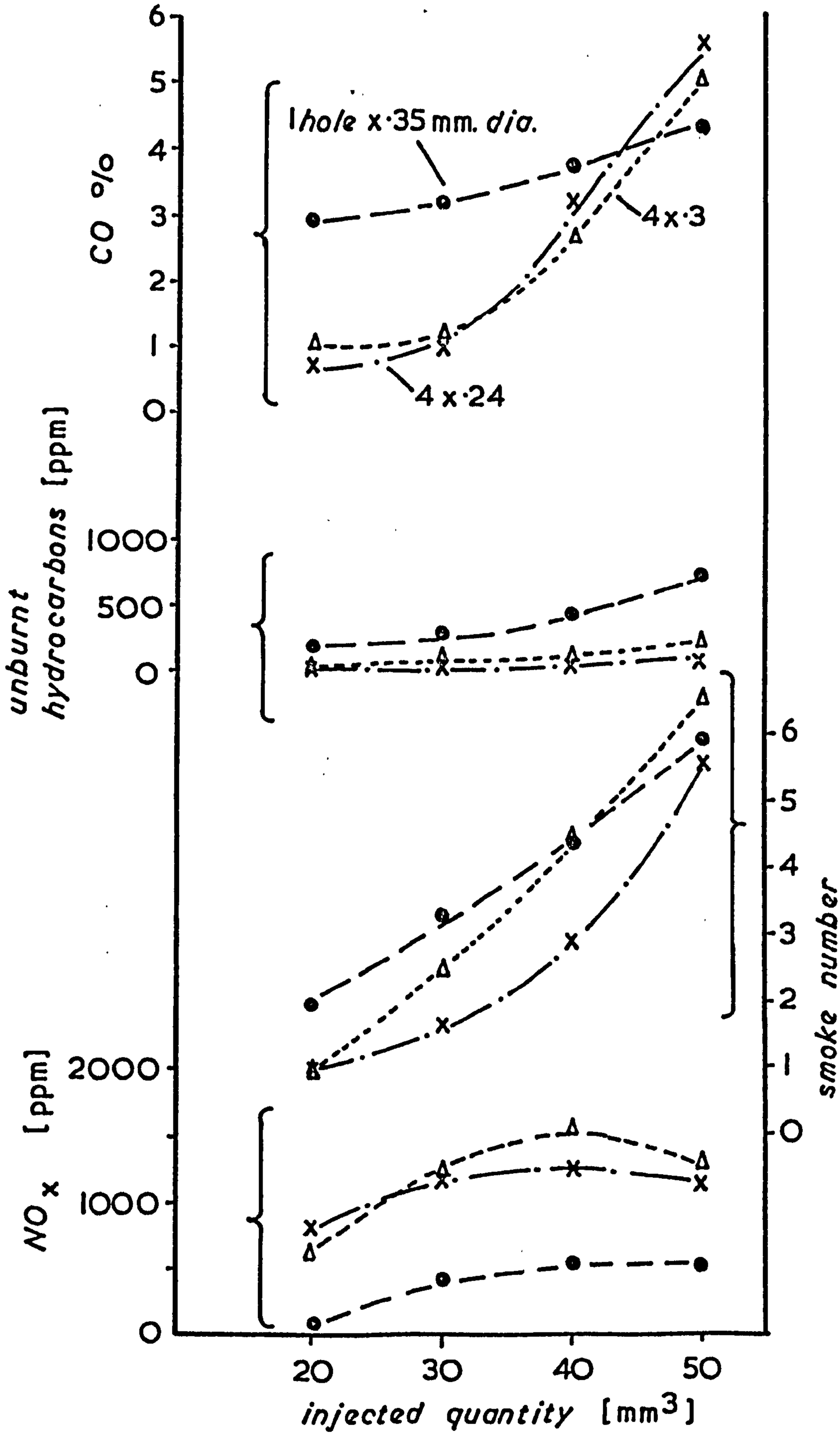

Exhaust Emissions for Chamber II

Fig. 7·9

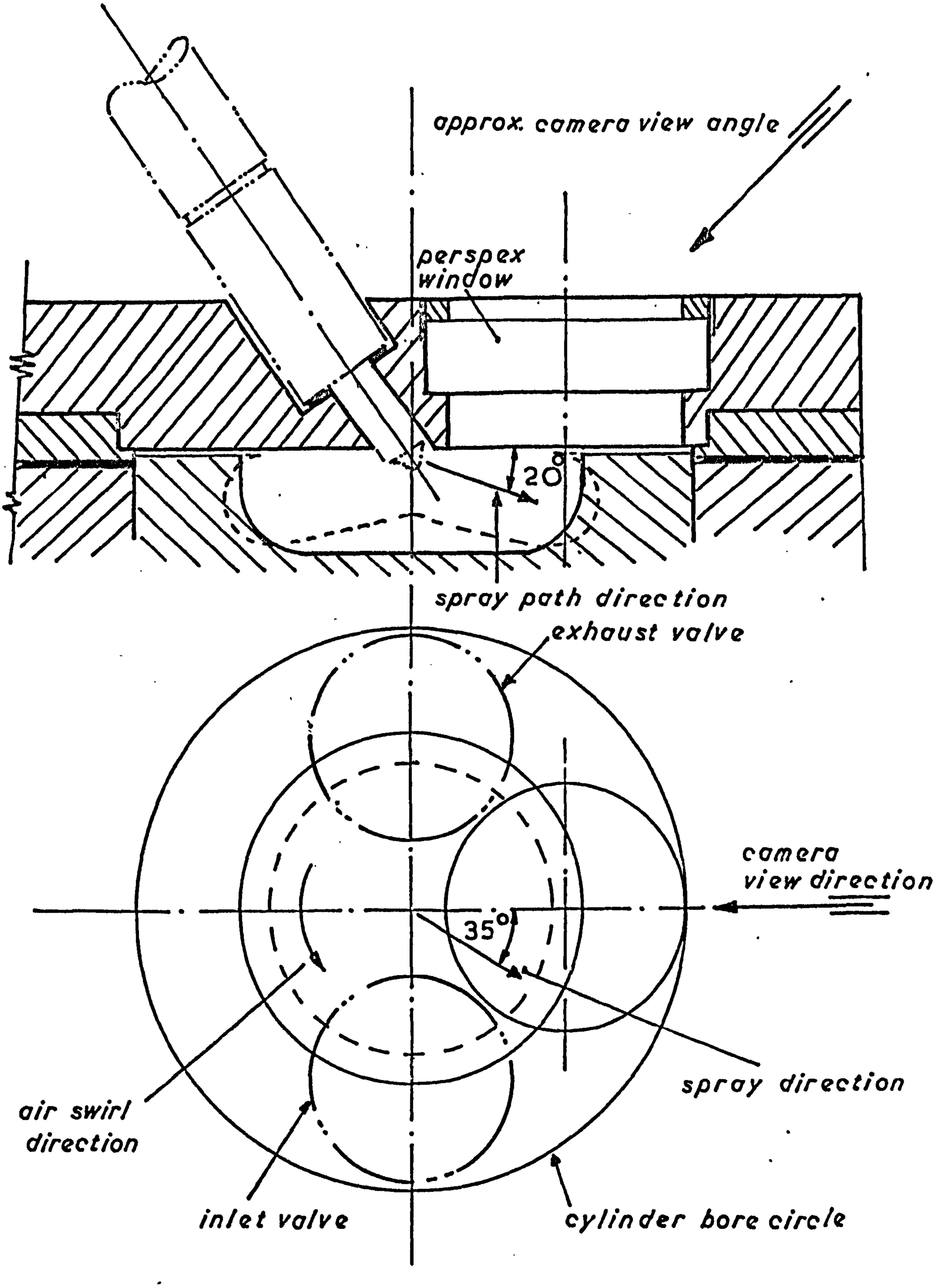

Diagram Showing the Camera Viewing Angle

Fig. 7.10

(comb. chamber I)

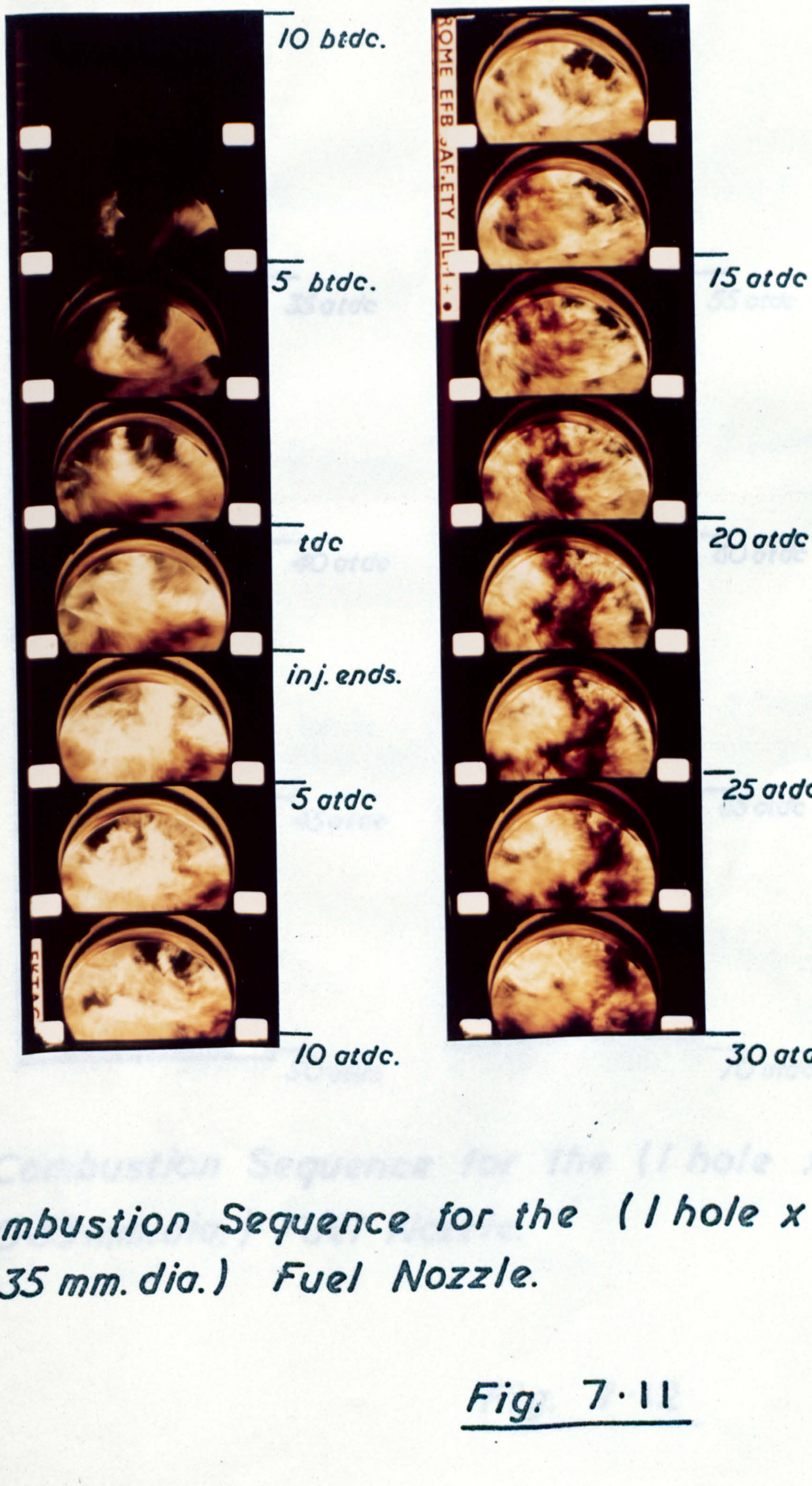

Combustion Sequence for the (1 hole x 0·35 mm. dia.) Fuel Nozzle.

Fig. 7·11

(comb. chamber I)

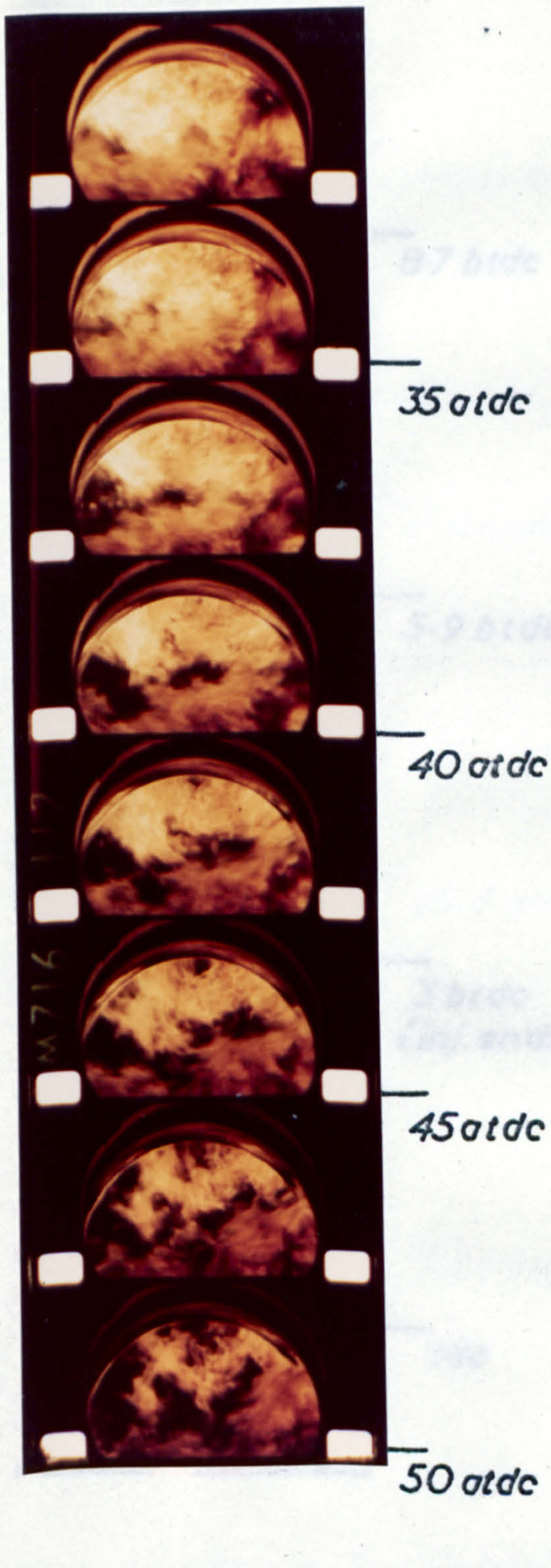

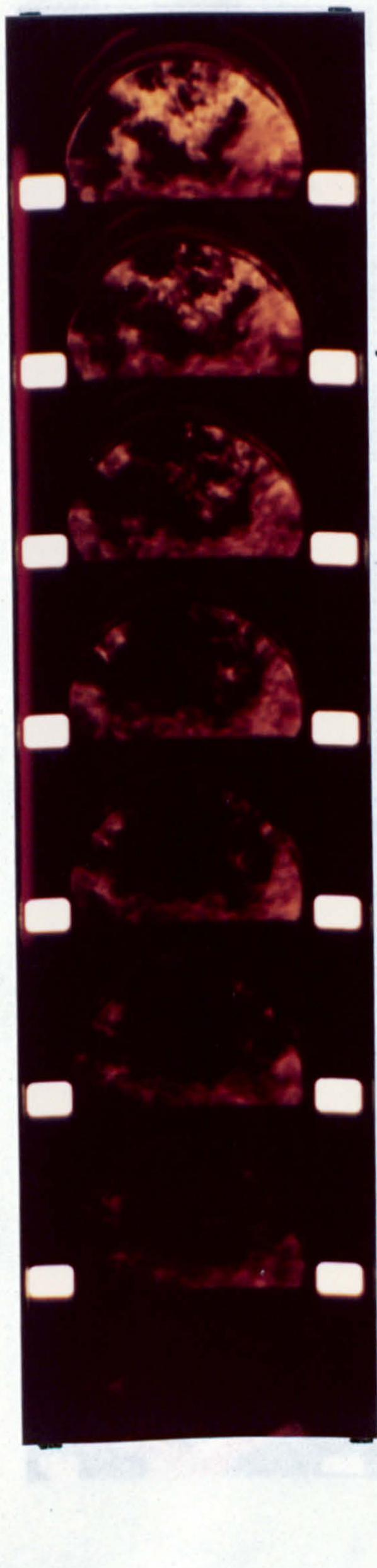

Combustion Sequence for the (1 hole x 0·35 mm. dia.) Fuel Nozzle.

Fig. 7·12

(comb. chamber I)

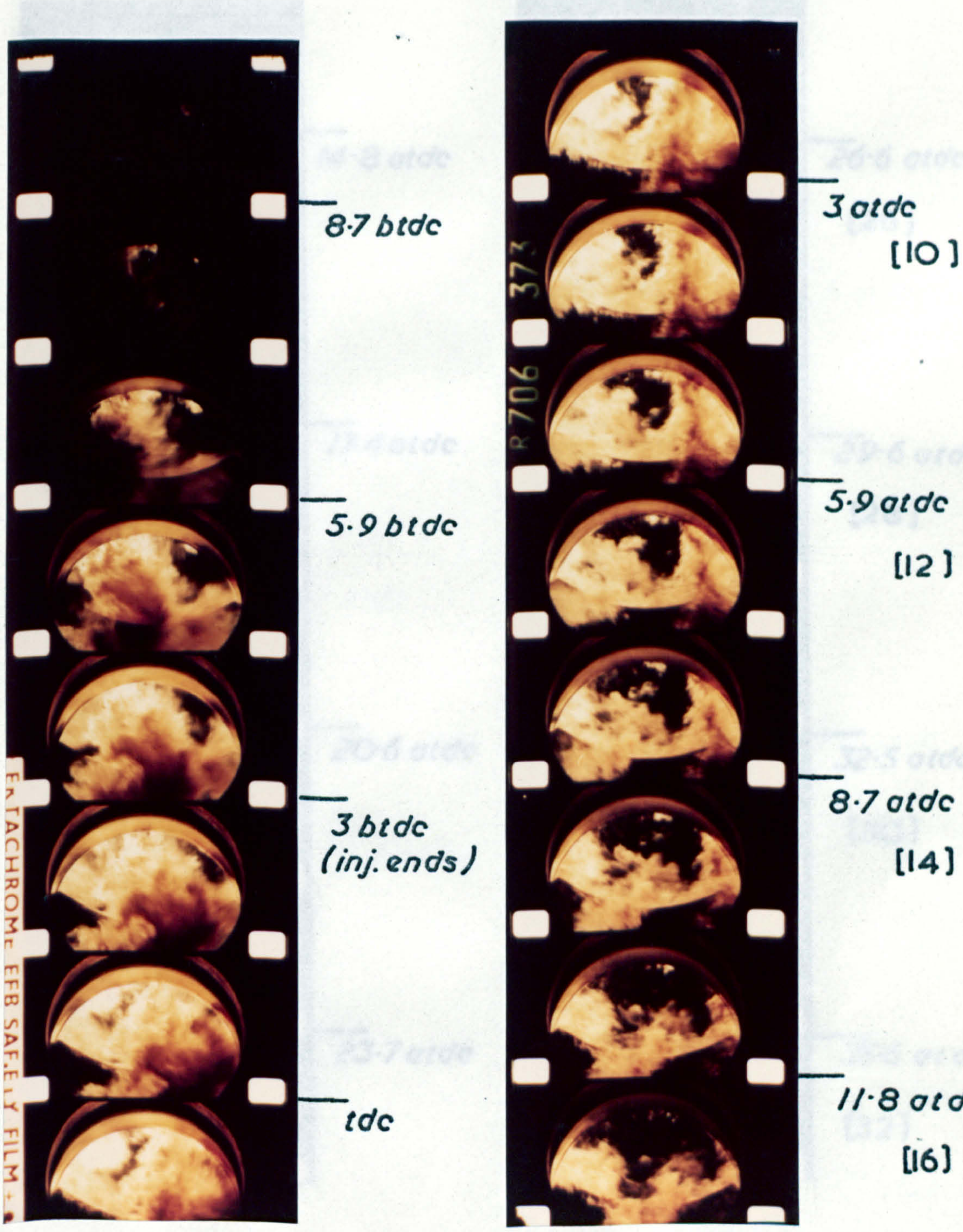

Combustion Sequence for the (4 hole x 0·30 mm. dia.) Fuel Nozzle.

Fig. 7·13

(comb. chamber I)

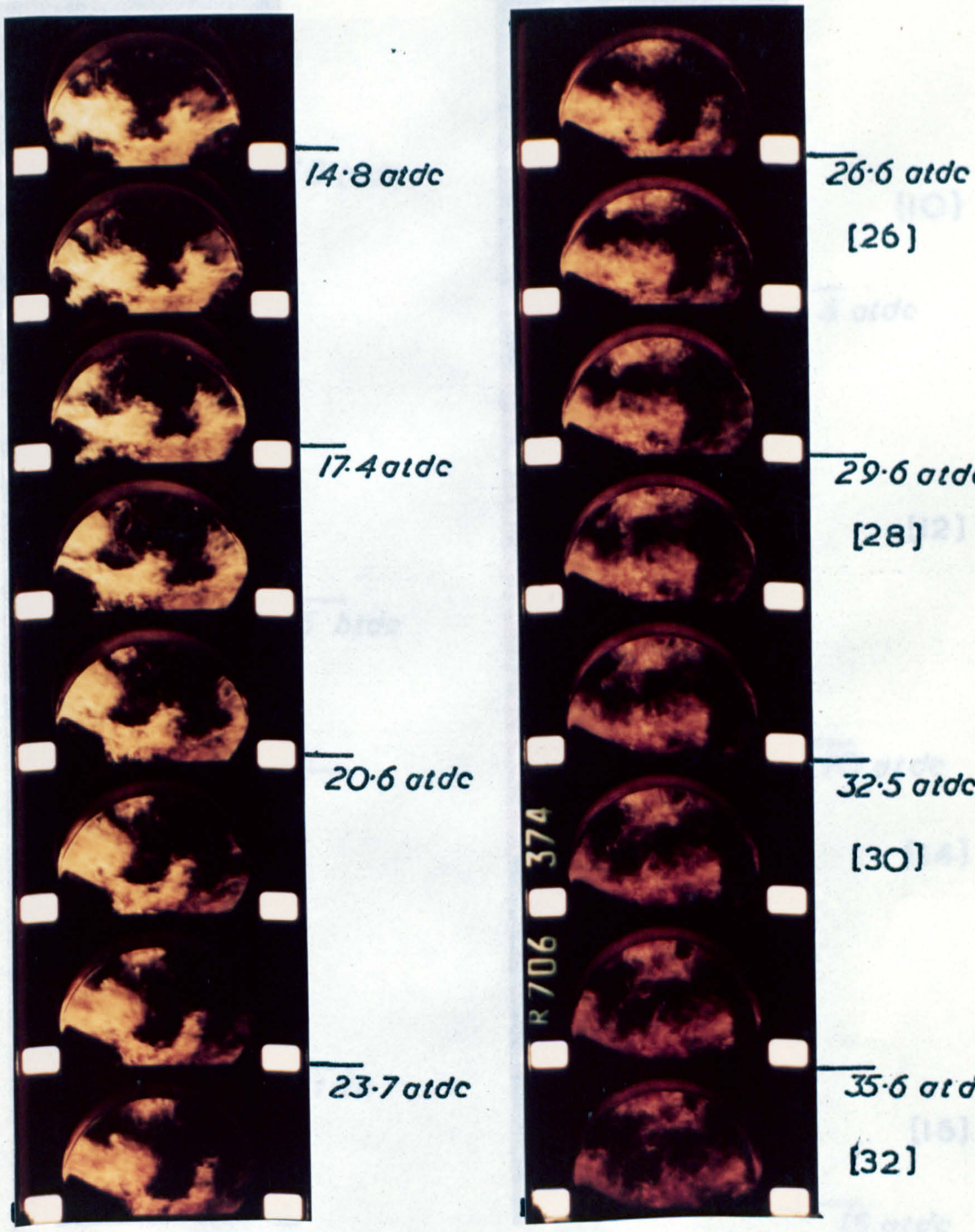

Combustion Sequence for the (4 hole x 0·30 mm. dia.) Fuel Nozzle.

Fig. 7·14

(comb. chamber I)

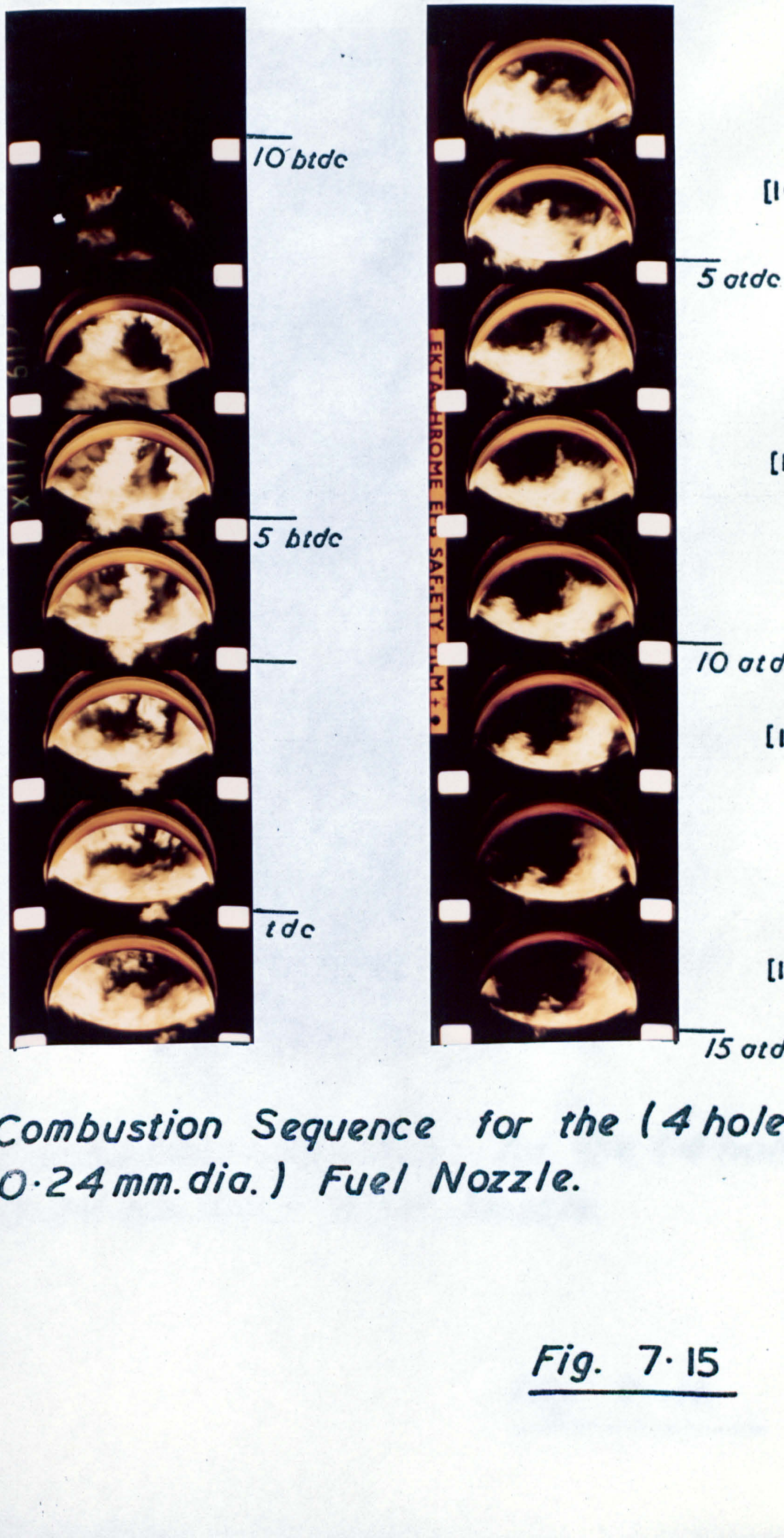

Combustion Sequence for the (4 hole x 0·24 mm. dia.) Fuel Nozzle.

Fig. 7·15

(comb. chamber I)

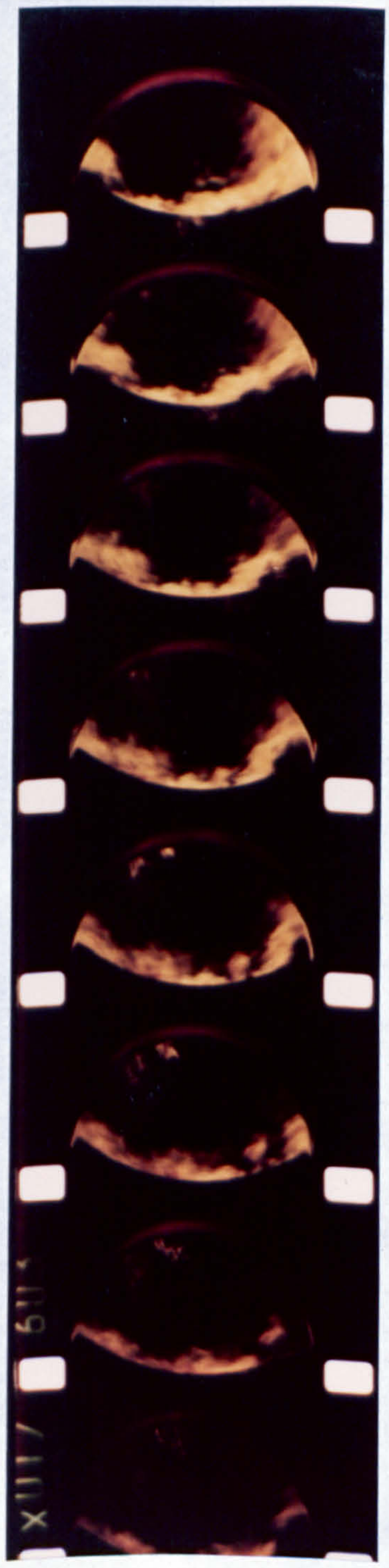

frame No.

[18]

— 20 atdc

[20]

[22]

— 25 atdc

[24]

— 28·3 atdc

Combustion Sequence for the (4 hole x 0·24 mm. dia.) Fuel Nozzle.

Fig. 7·16

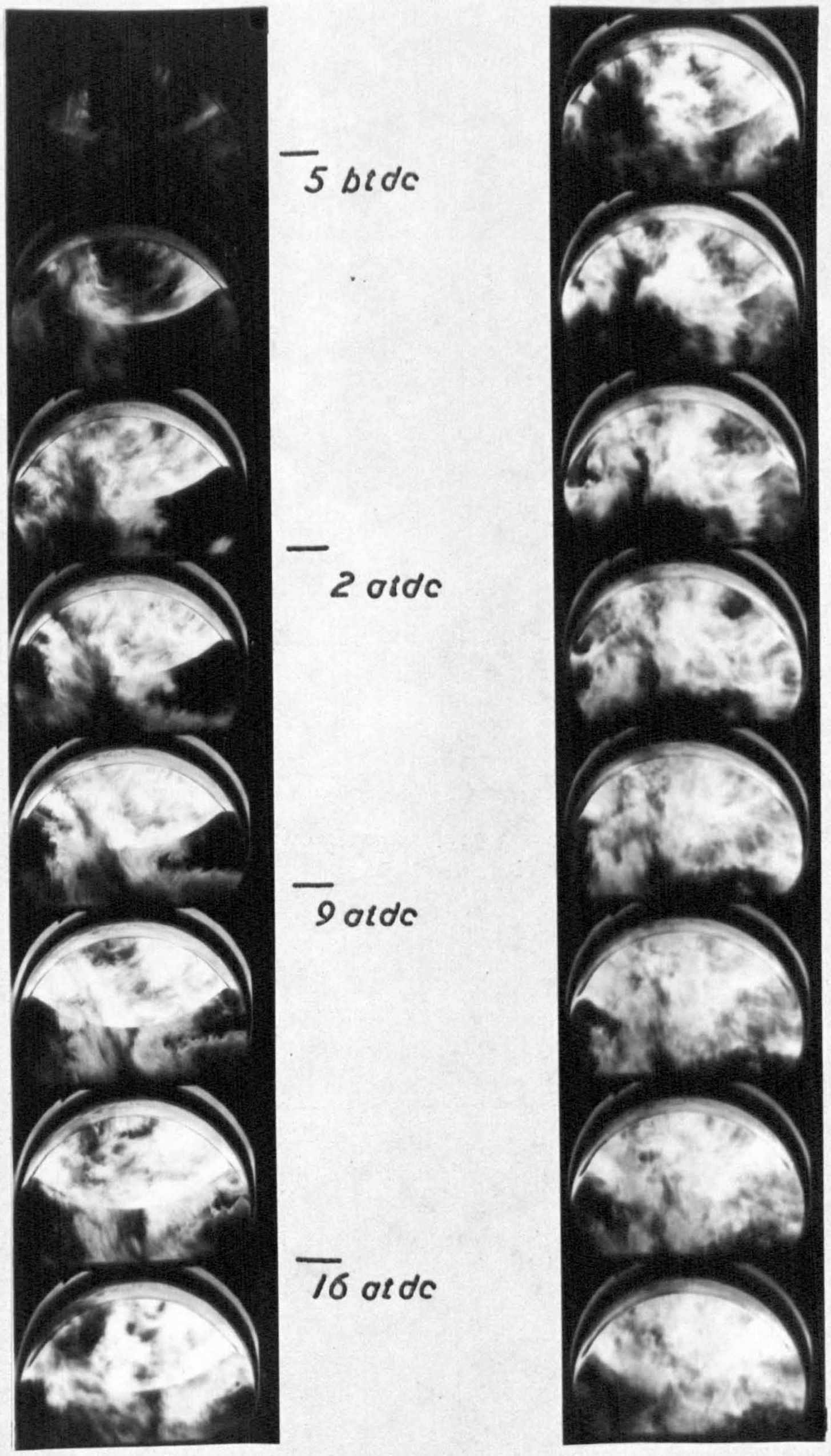

(comb. chamber II)

Combustion Sequence for the (1 hole x 0·35 mm. dia.) Fuel Nozzle.

Fig. 7·17

Test Engine and Anemometry Equipment.

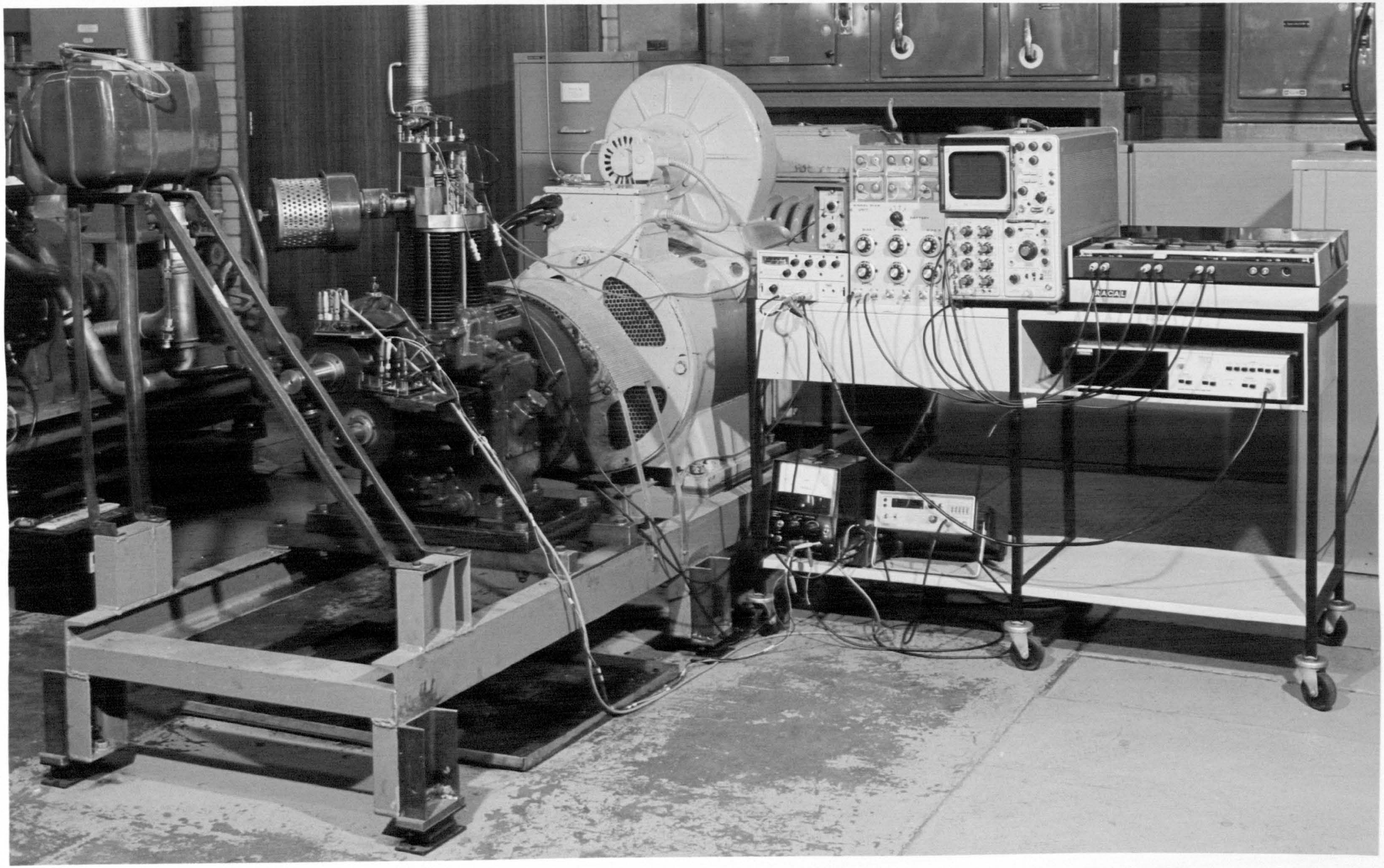

Fig. 7.18

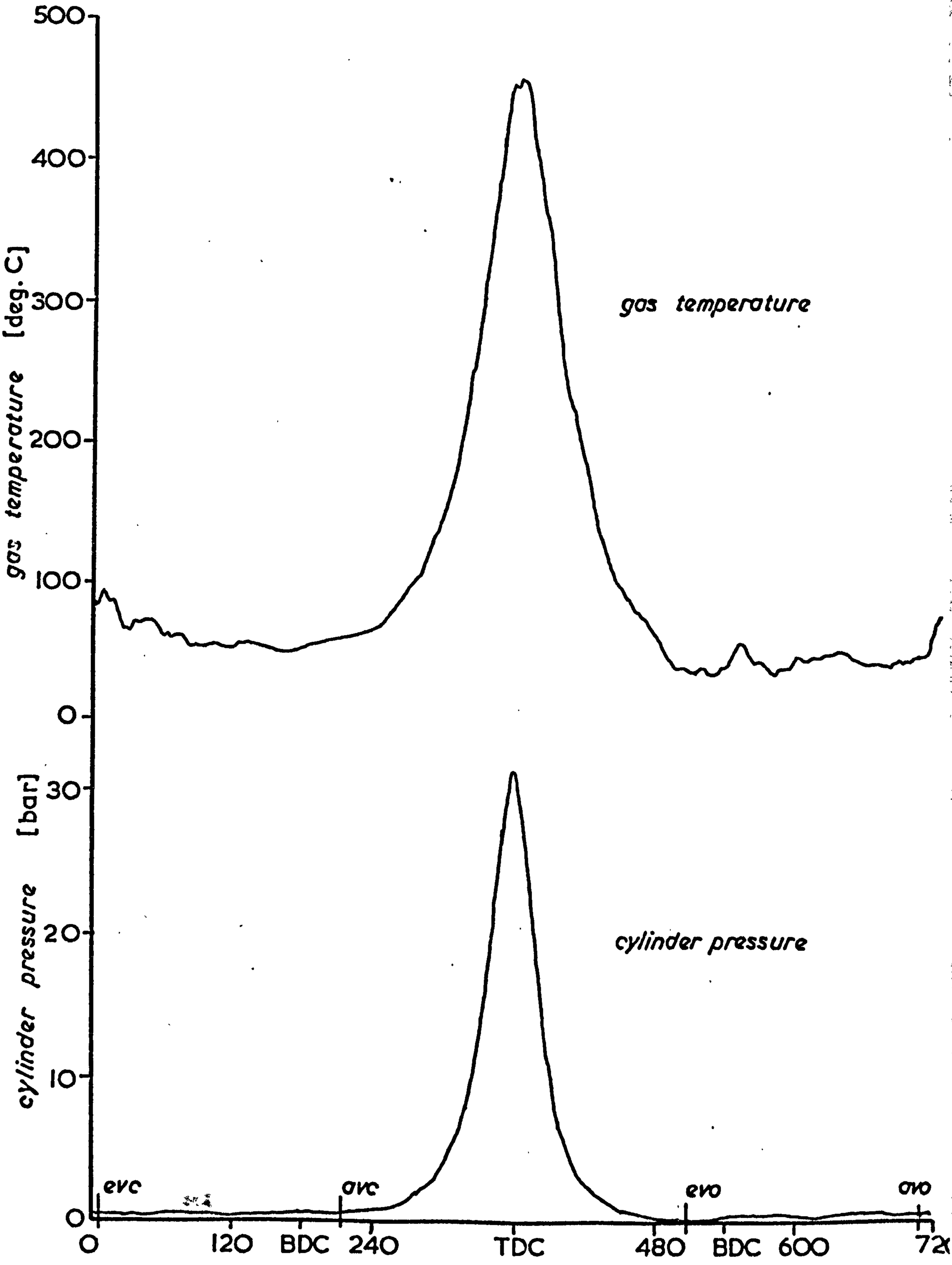

Motored Engine Temperature & Pressure Traces.
(at 1000 rev./min.)

Fig. 7·19

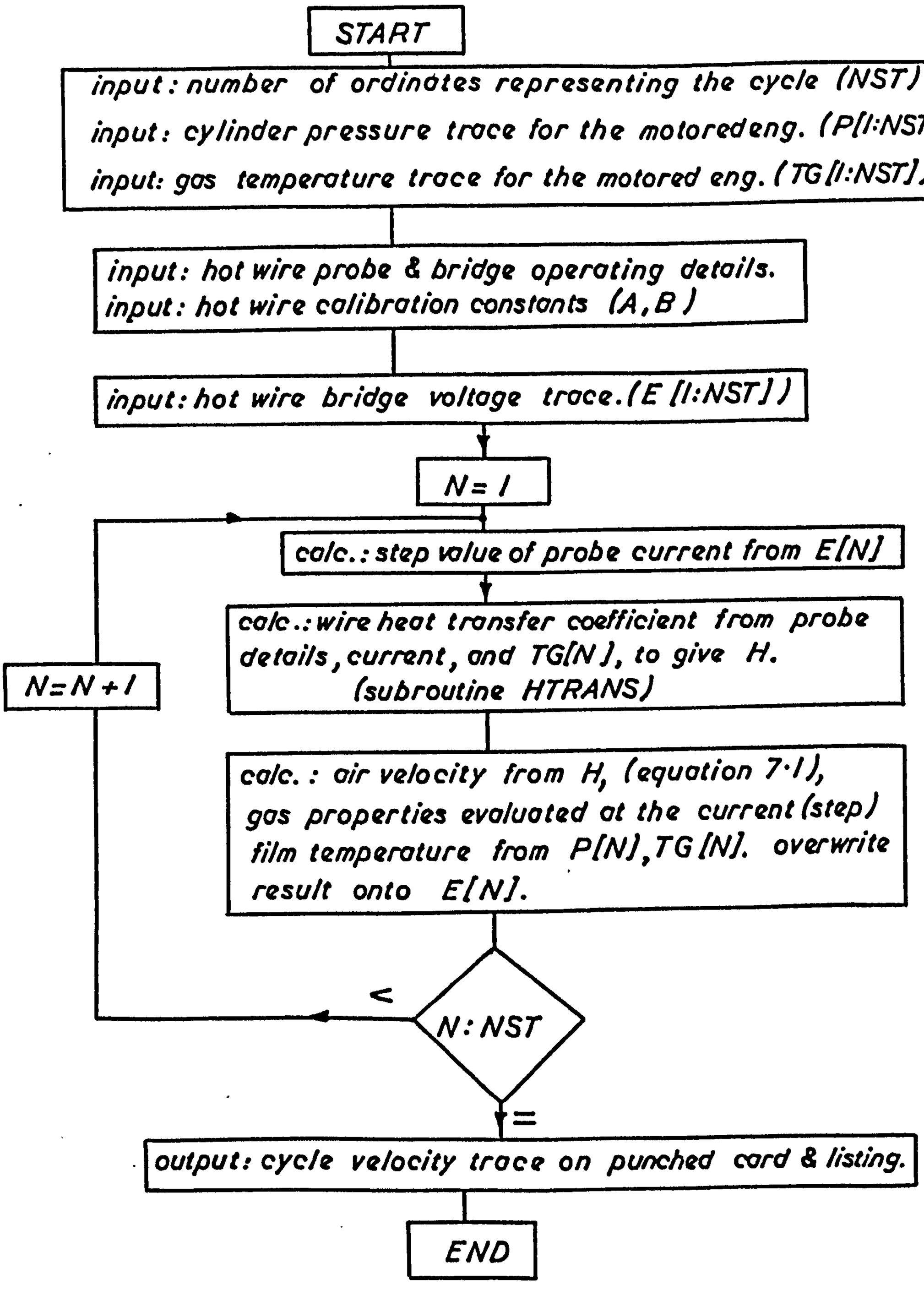

Schematic Flow Chart for the Computation of Motored Engine Air Velocity.

Fig. 7·20

Swirl Velocity at 5 mm Radius
(Combustion Chamber I)

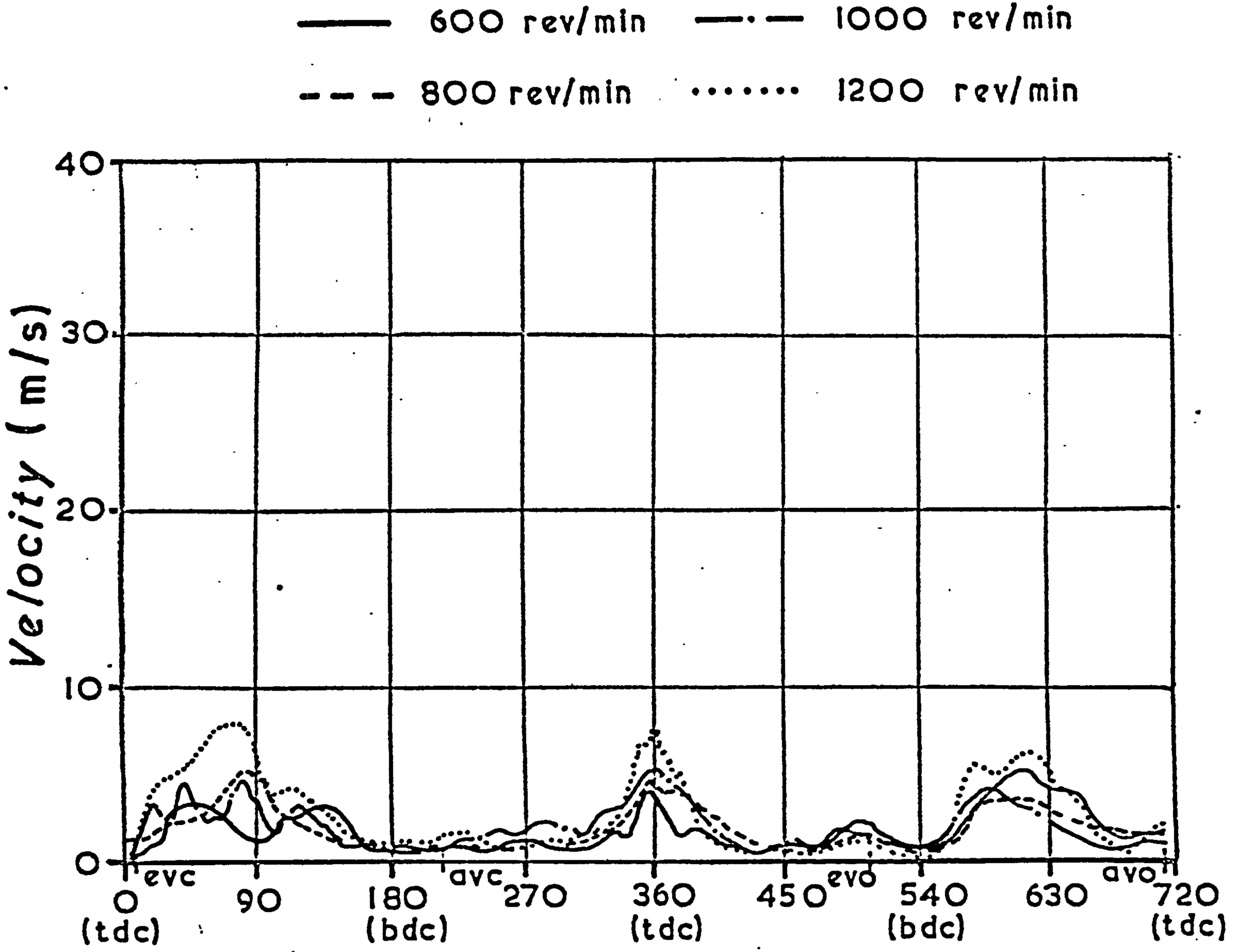

Fig. 7.21

Swirl Velocity at 10 mm Radius
(Combustion Chamber I)

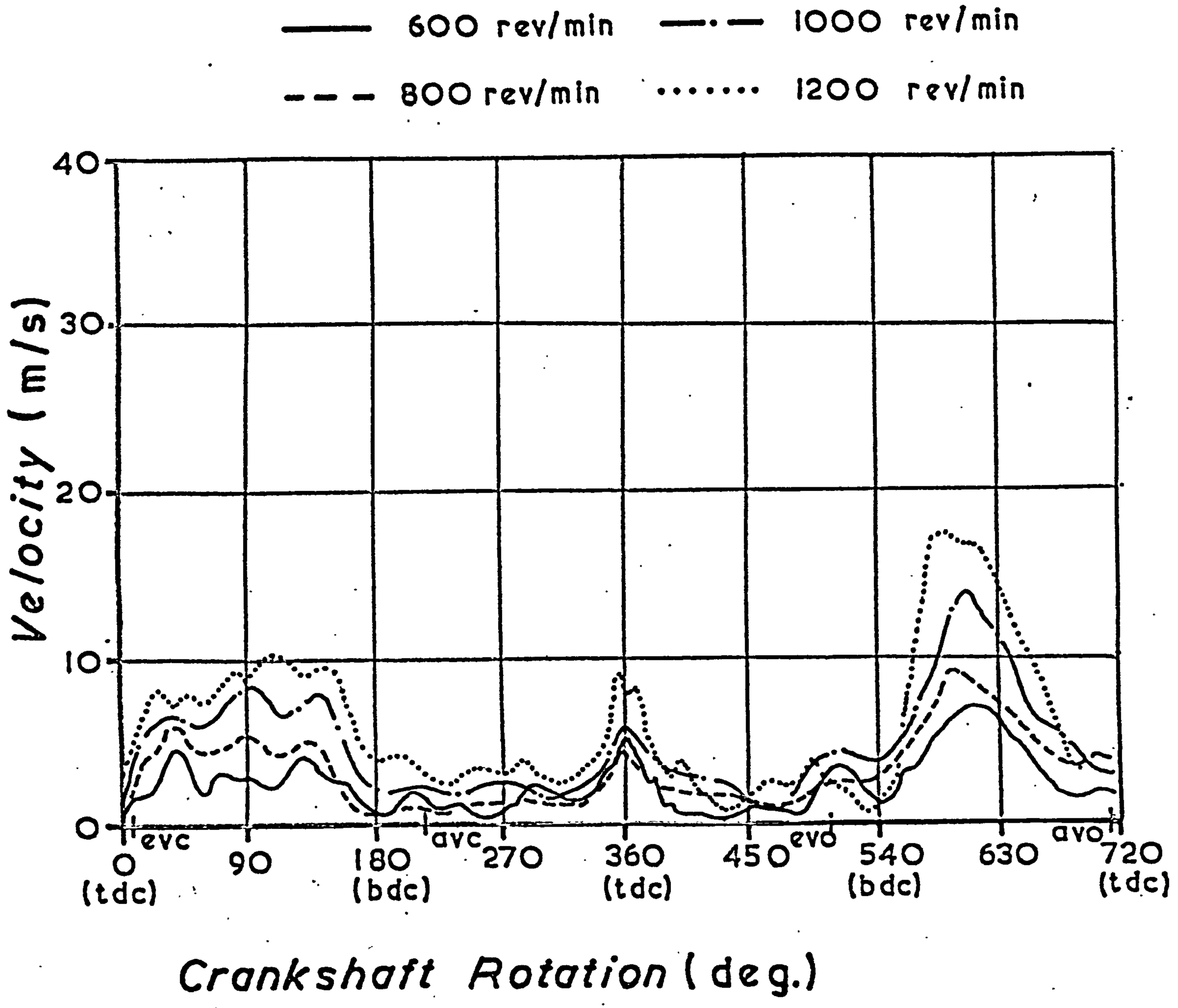

Fig. 7.22

Swirl Velocity at 17 mm Radius
(Combustion Chamber I)

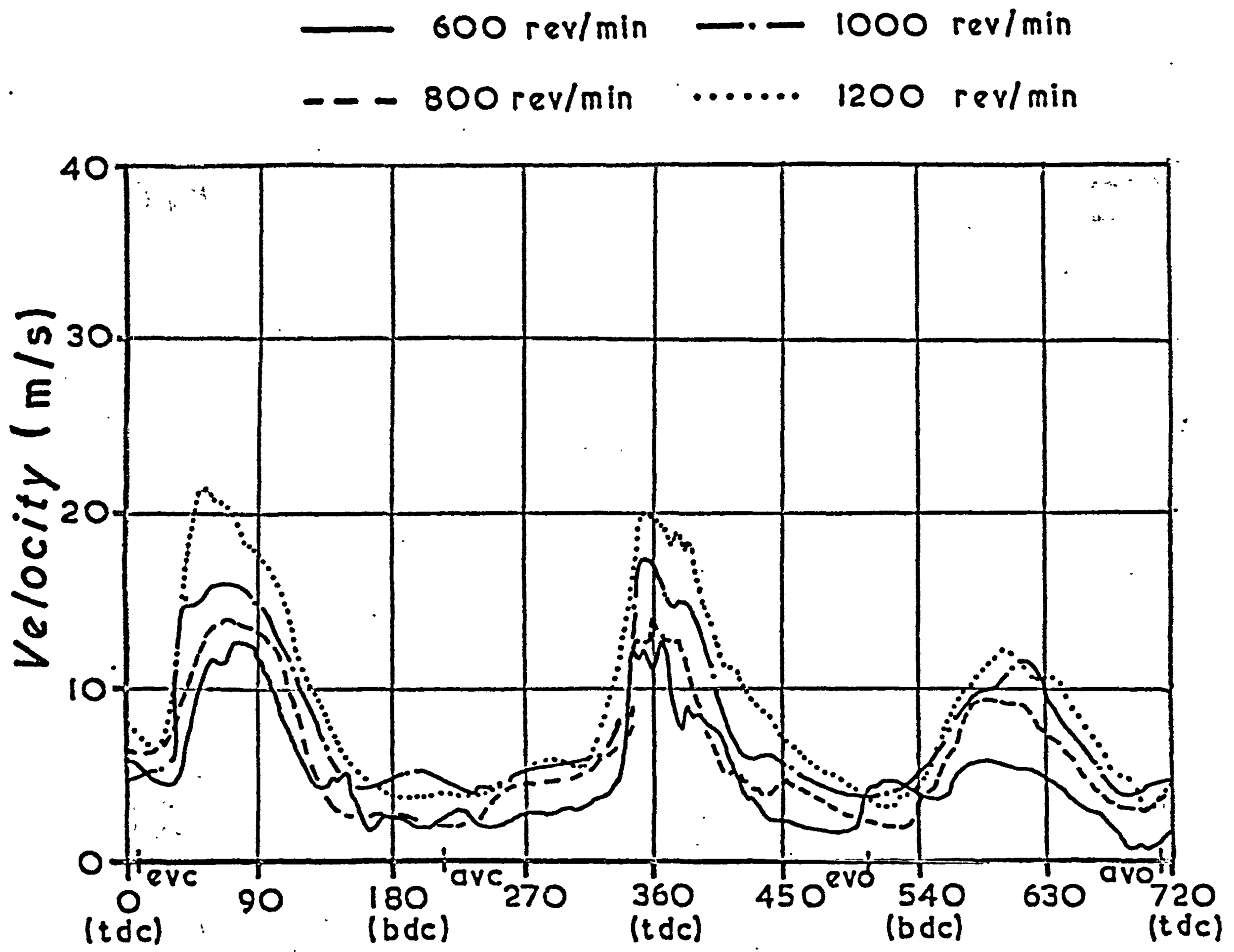

Fig. 7.23

Swirl Velocity at 21 mm Radius
(Combustion Chamber I)

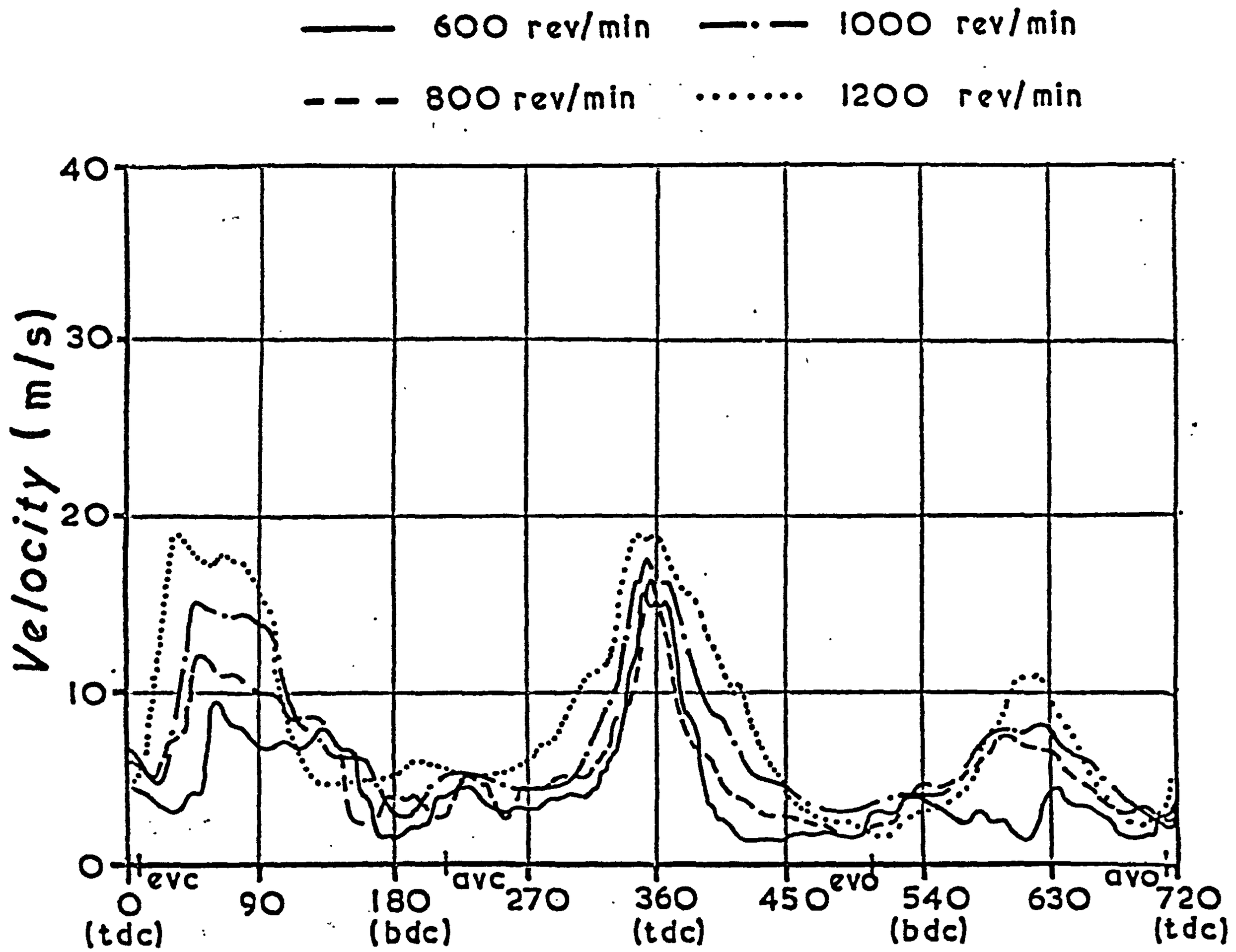

Fig. 7.24

Swirl Velocity at 27 mm Radius
(Combustion Chamber I)

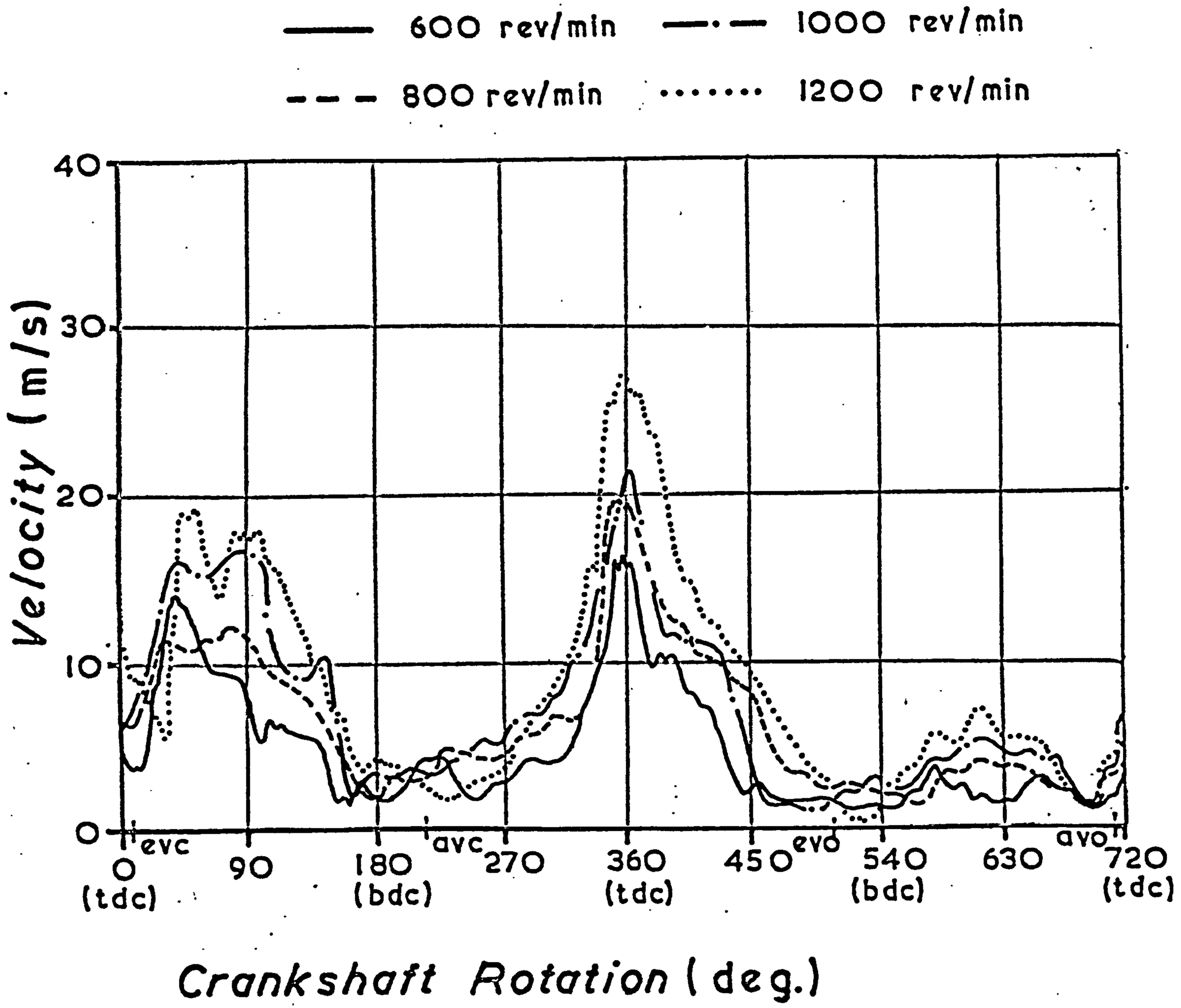

Fig. 7.25

Squish Velocity at 27 mm Radius
(Combustion Chamber I)

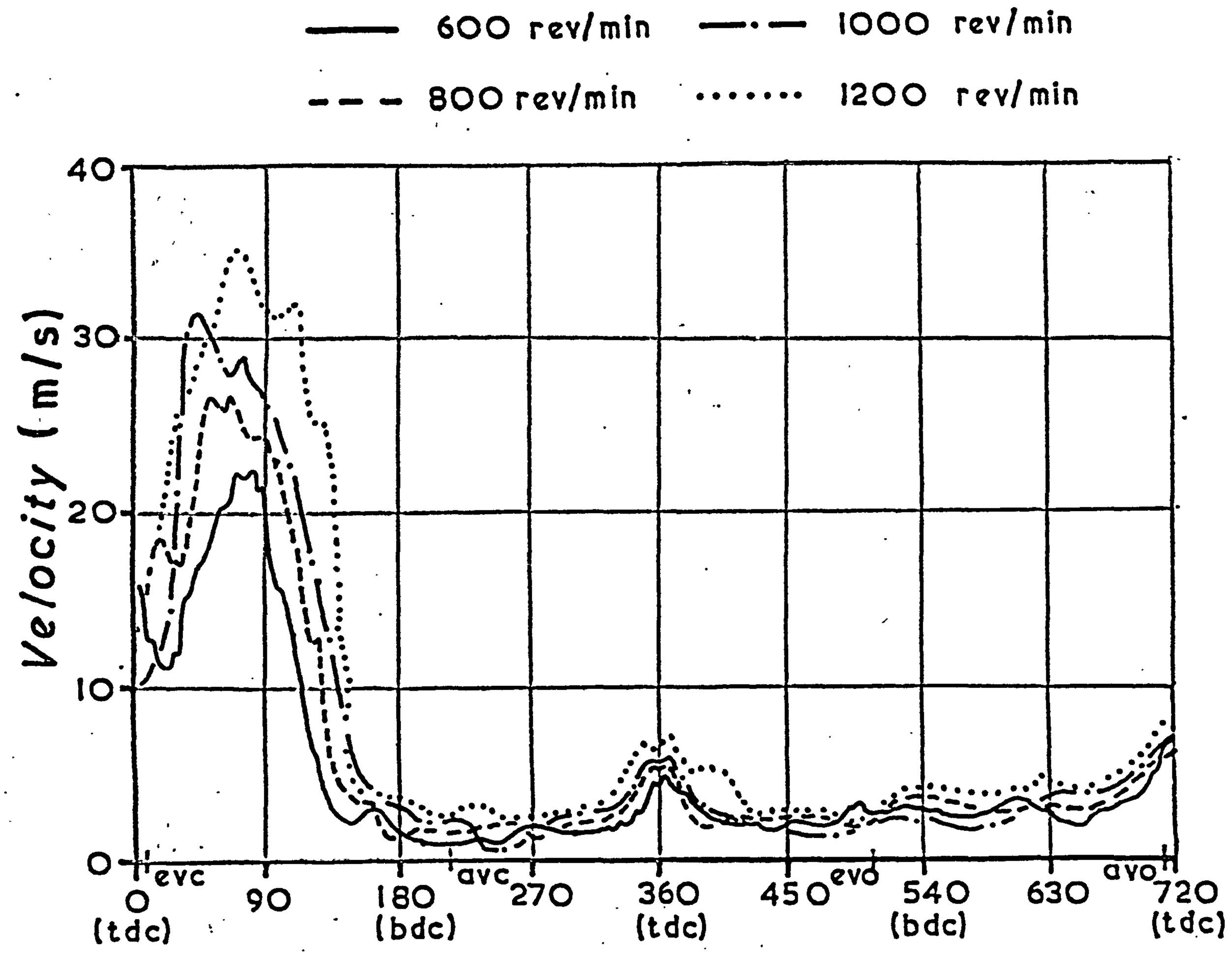

Fig. 7.26

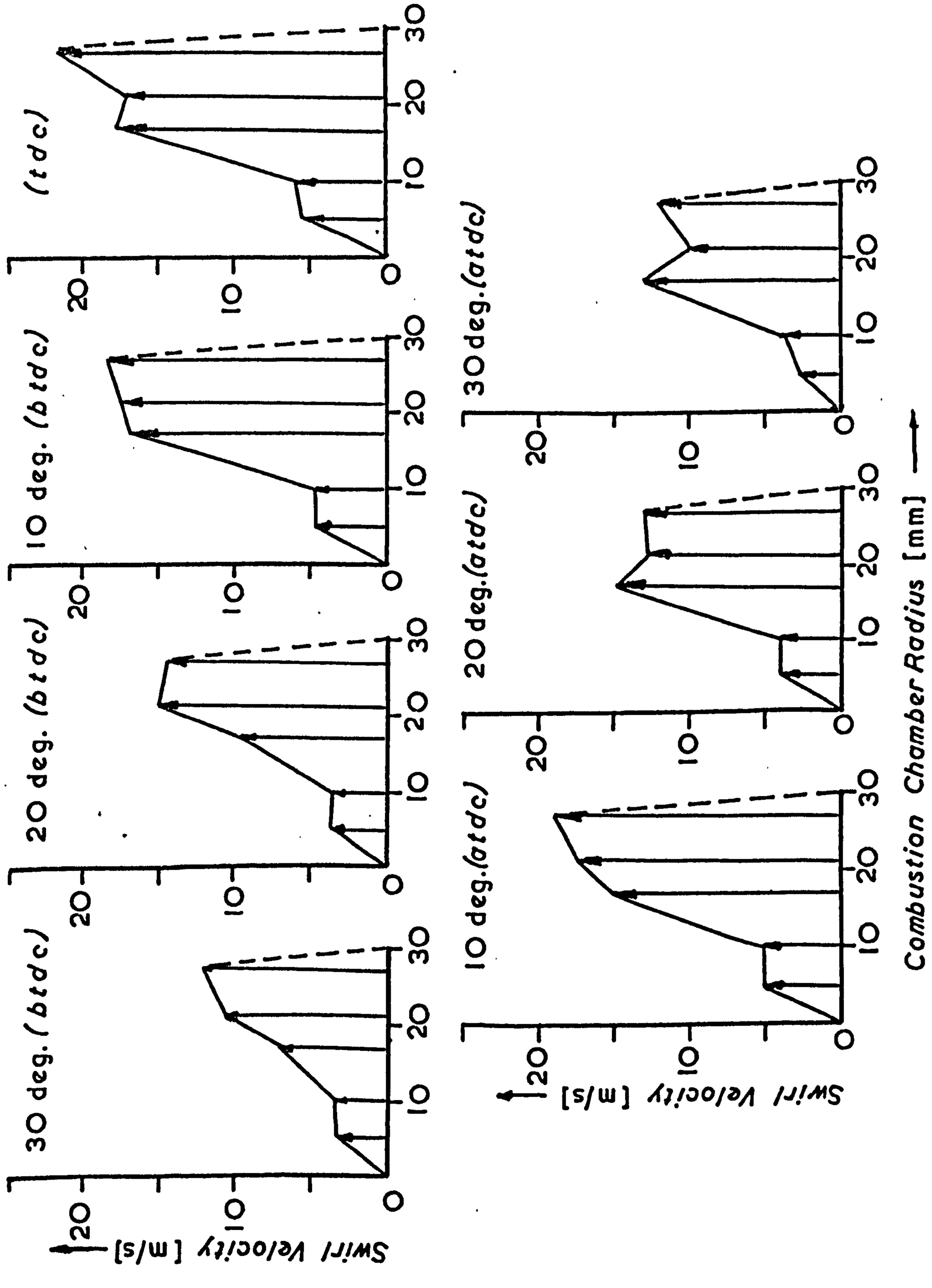

Measured Variation of Swirl Profile close to C.T.D.C. at 1000 rev/min.

Fig. 7·27

(• – comparison point for combustion chamber II)

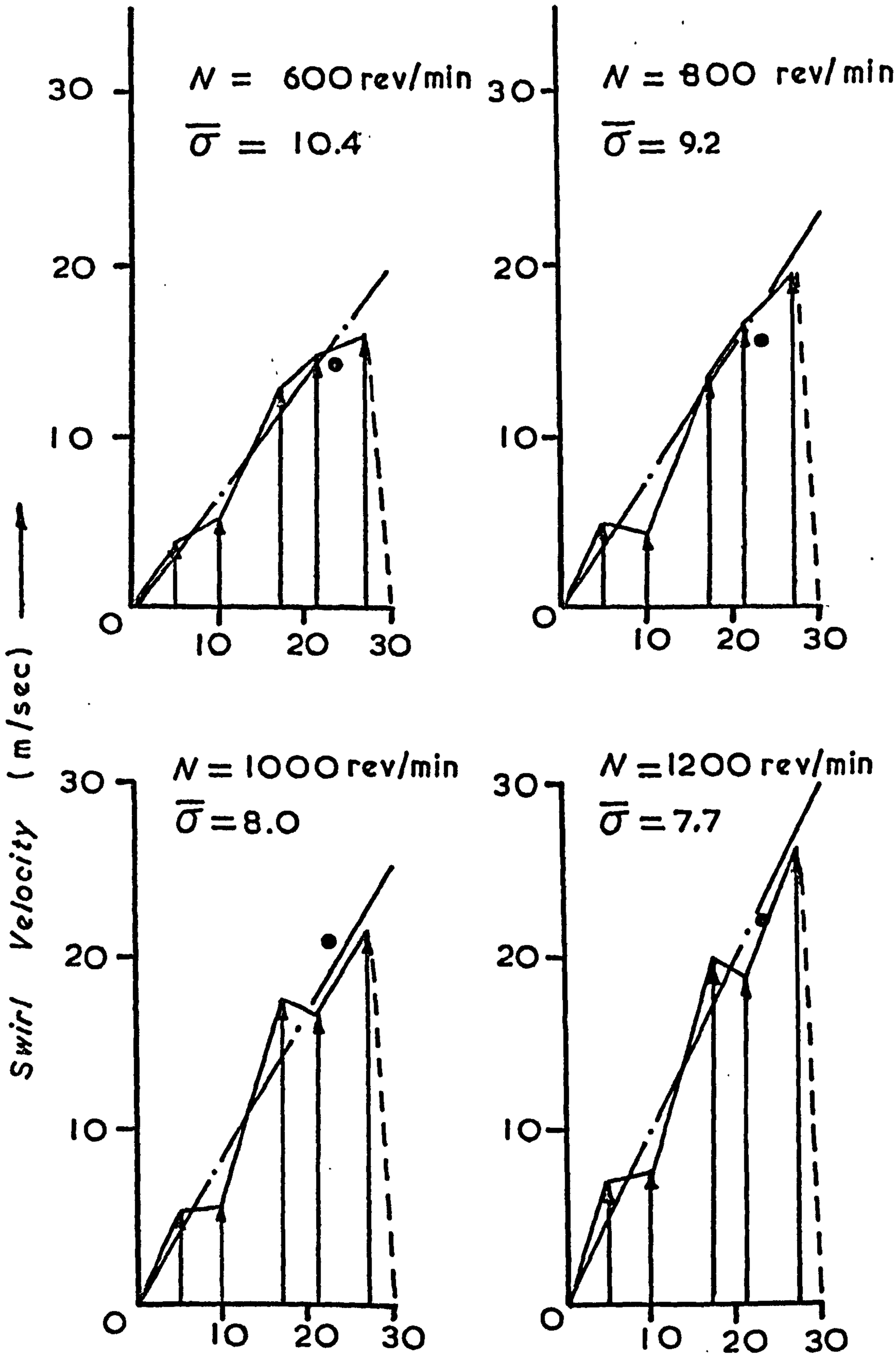

Radial Profiles of Swirl Velocity at Compression Top Dead Centre

Fig. 7·28

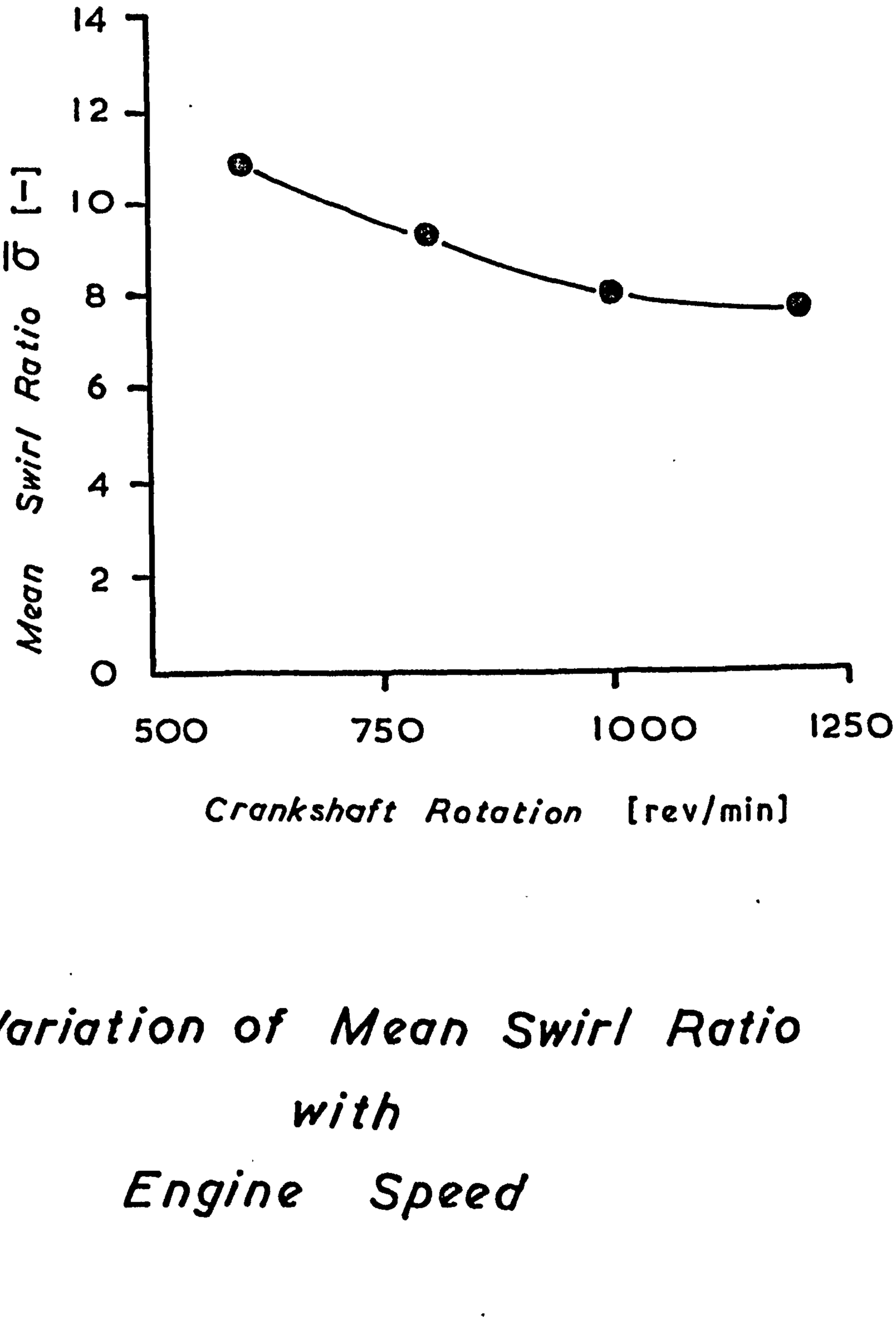

Variation of Mean Swirl Ratio
with
Engine Speed

Fig. 7·29

Swirl Velocity at 23 mm Radius
(Combustion Chamber II)

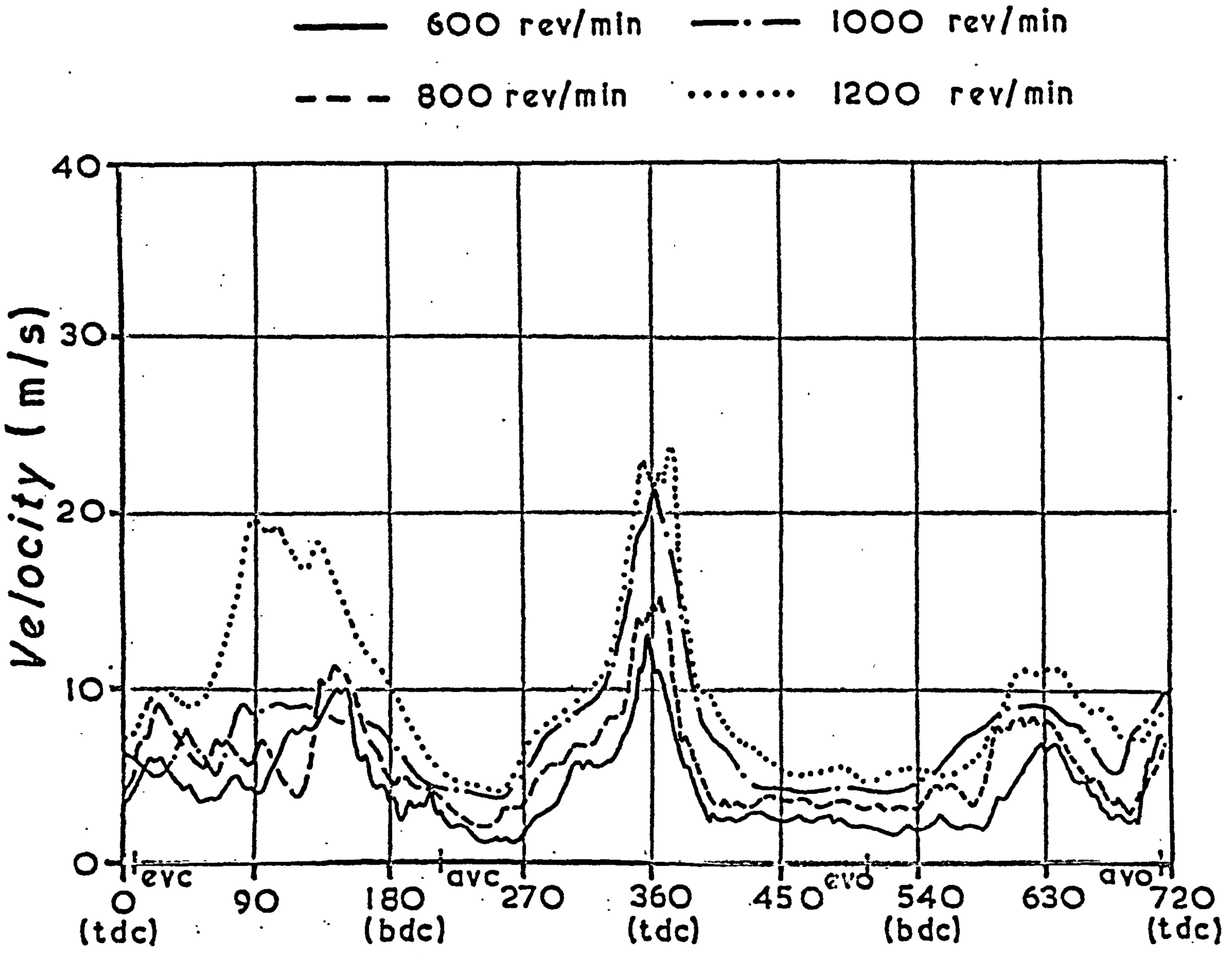

Fig. 7.30

Squish Velocity at 23 mm Radius
(Combustion Chamber II)

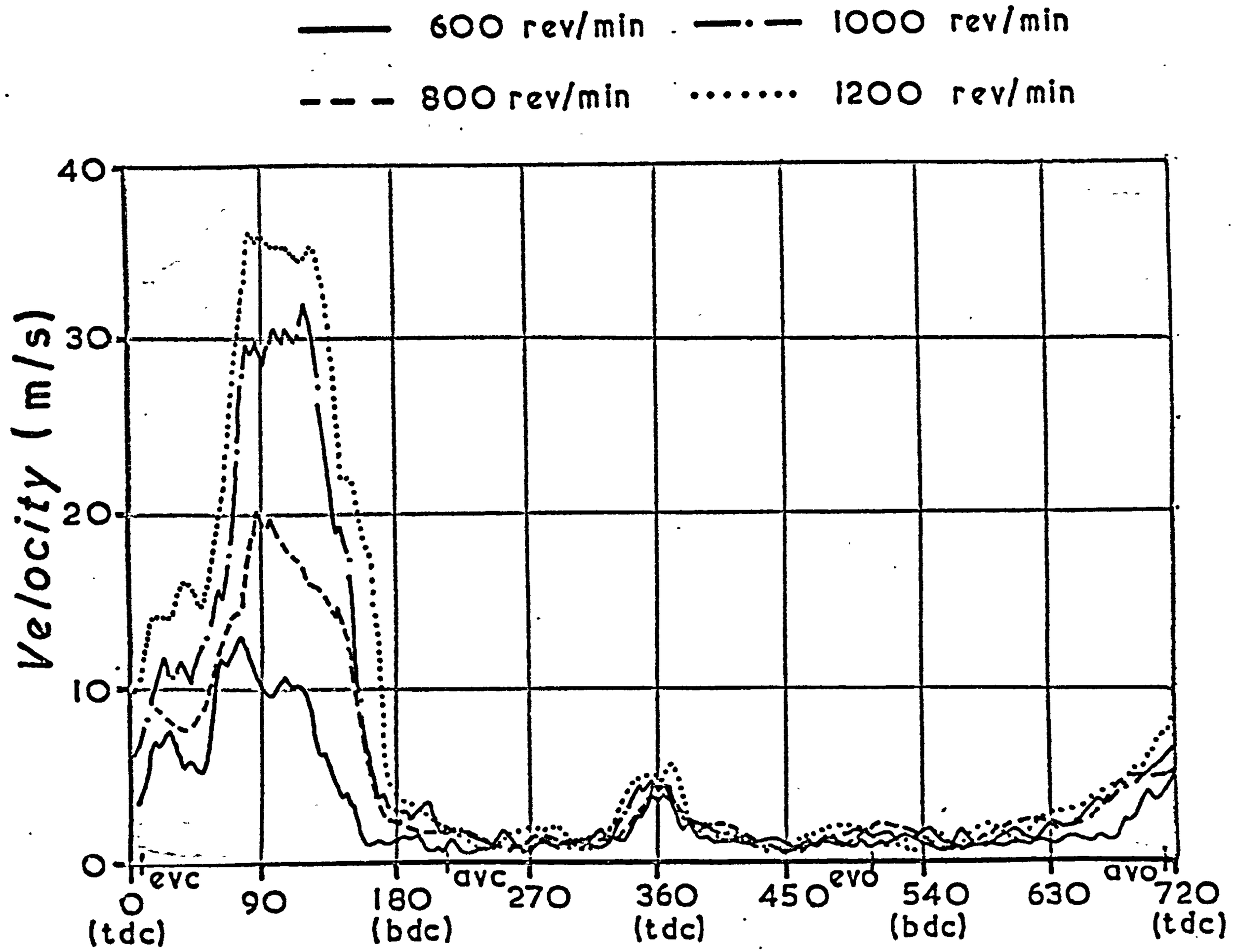

Fig. 7.31

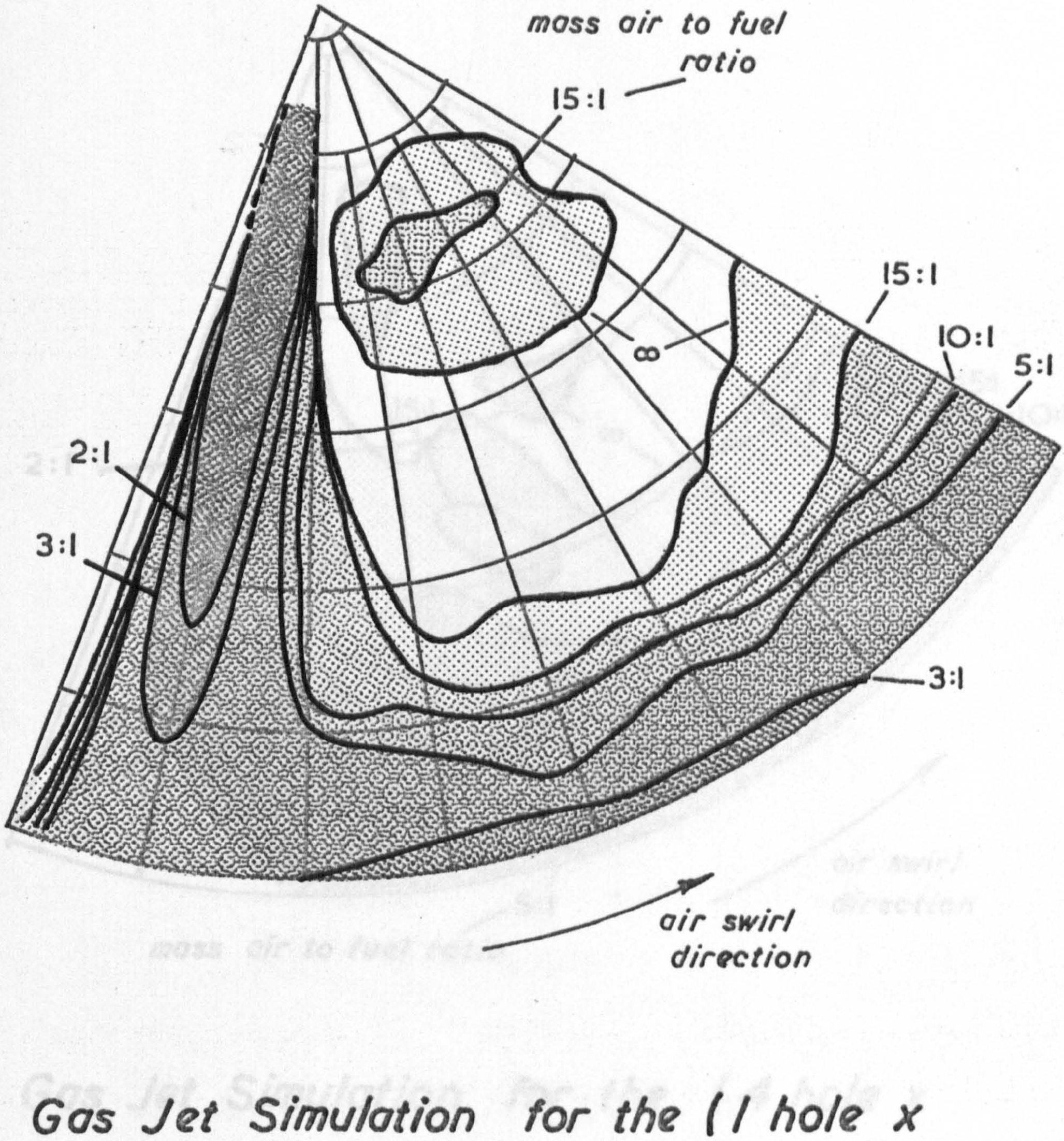

Gas Jet Simulation for the (1 hole x 0·35 mm. dia.) Fuel Nozzle.

Fig. 7·32

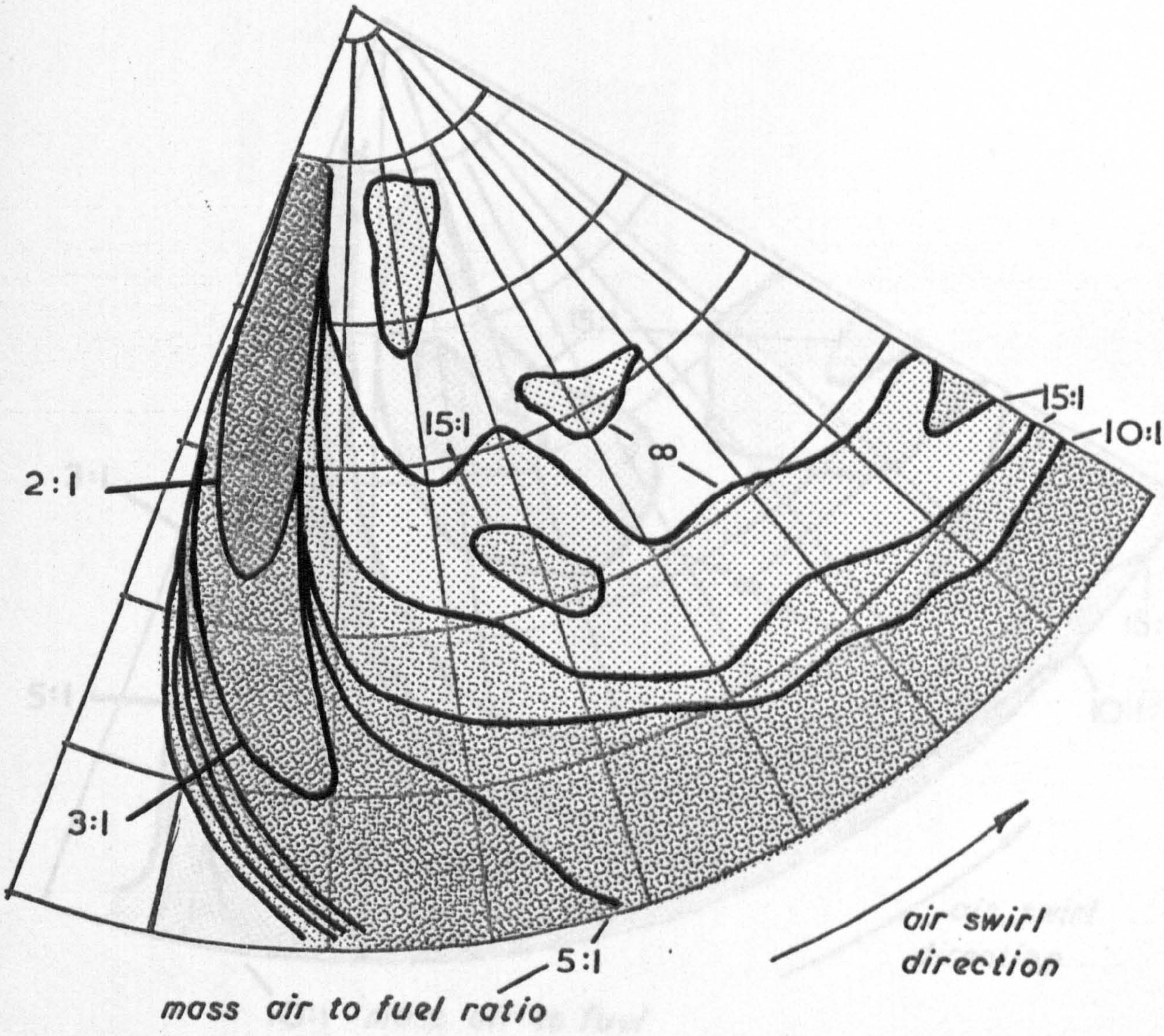

Gas Jet Simulation for the (4 hole x 0·30 mm. dia.) Fuel Nozzle.

Fig. 7·33

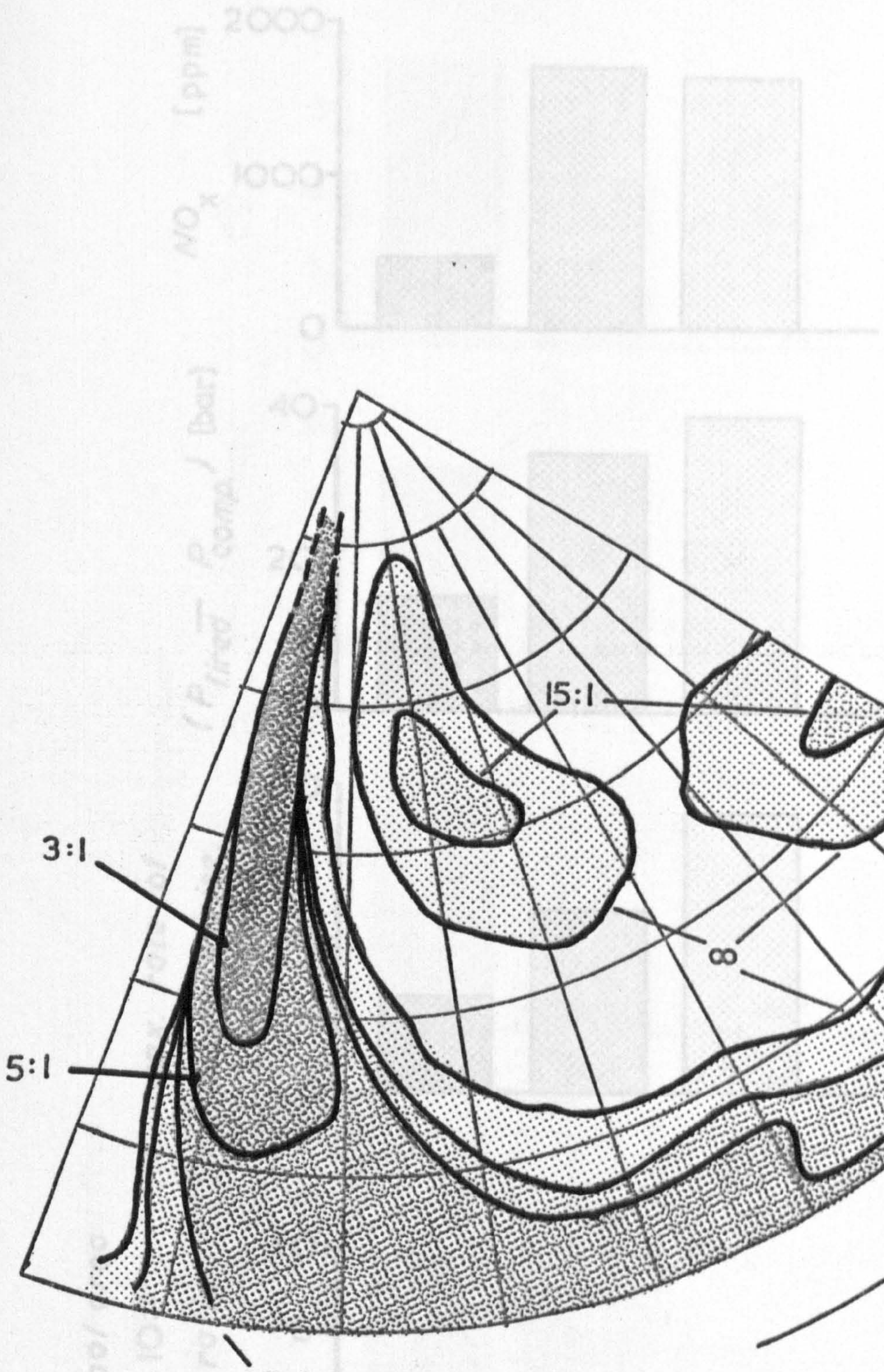

Gas Jet Simulation for the (4 hole x 0·24 mm. dia.) Fuel Nozzle.

Fig. 7·34

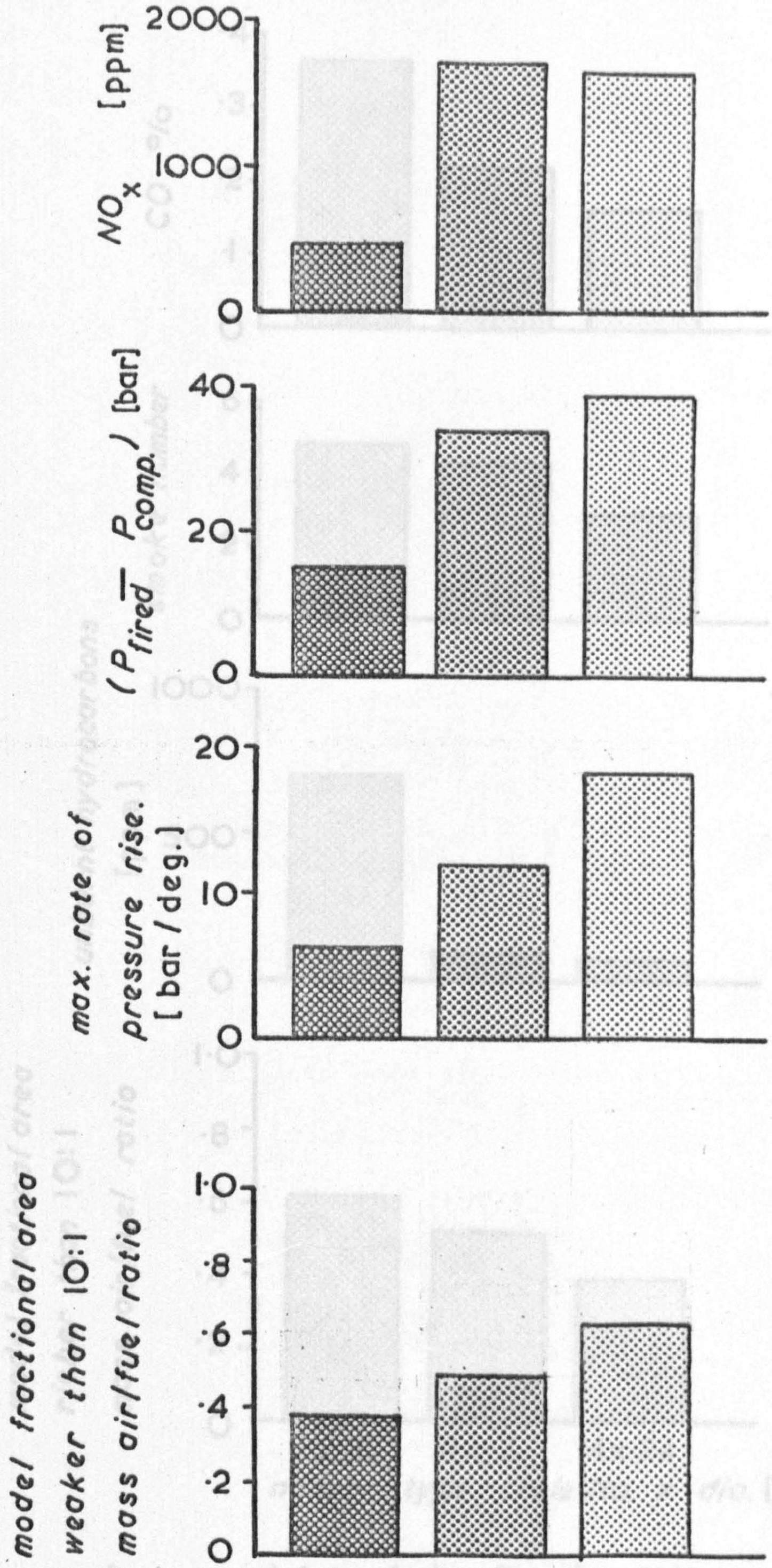

Comparison of Model Fuel Mixture Area Parameter with Engine Data.

Fig. 7·35

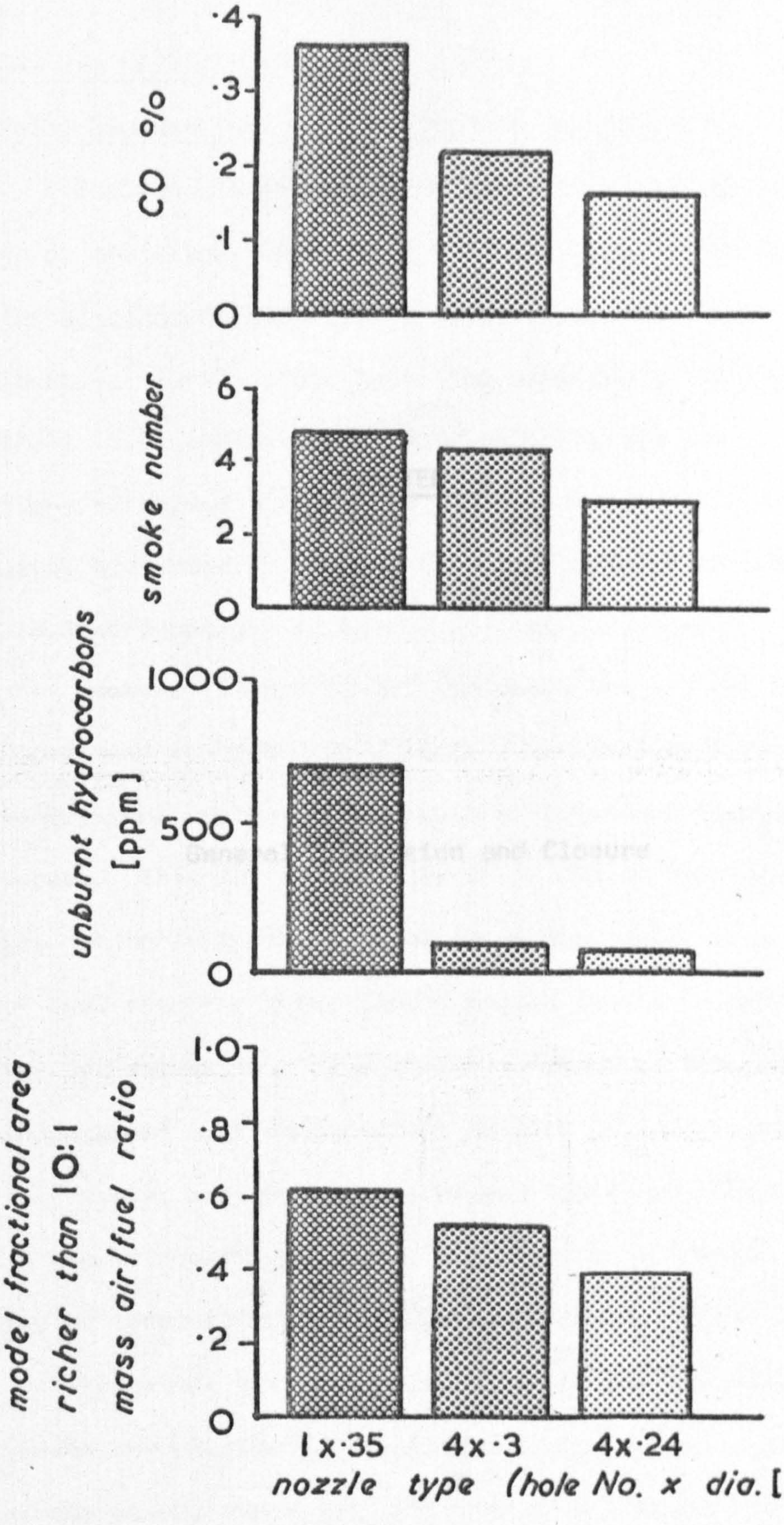

Comparison of Model Fuel Mixture Area Parameter with Engine Data.

Fig. 7·36

CHAPTER 8

General Discussion and Closure

8.1 Gas Jet Modelling Results

8.1.1 Model Representation of Trajectory and Spread

The results of chapter 6 illustrate that the engine fuel spray trajectory and spread are well represented by the gas jet simulation (see figures (6.9),(6.16),(6.19),(6.22),(6.23) (6.26)). Further, the modelling experiments of figures (6.6), (6.7) (6.8) indicate that substantially the same model predictions of spread, trajectory and fuel dispersion are created, using different tracer gas types and model mean swirl velocity, provided equations (2.19) (2.20) are satisfied.

However, figure (6.22) indicates the gas jet is slightly wider than the fuel spray in this particular instance where impingement of the spray onto the combustion chamber wall occurs. This may be reasoned to be due to the inability of the gas jet to 'wet' the combustion chamber wall, i.e. extraction of fuel from the spray in the engine cannot be represented by the jet simulation. The basic mechanism at the point of gas jet impingement must be different to that of the two phase liquid fuel spray, and the results of gas jet models should therefore be viewed accordingly, i.e. High gas concentration in the model may be taken to infer wall wetting in the engine.

Transient gas jet analysis (see figure (6.13)) was shown to produce successive jet envelopes propagating along the same path as the steady state jet, and therefore compliments the quasi-steady jet, and quasi-solid body assumptions as used by Adler and Lyn (24) in their mathematical analysis (see figure (1.30)). In relation to the modelling experiments the result indicates that in cases where ignition occurs in the established spray, (i.e. injection duration exceeds ignition

delay), a simpler steady state analysis will be indicative of the fuel dispersion at the instant of ignition. Saving on labour and time is therefore considerable.

8.1.2 Representation of Fuel Dispersion

Published experimental data on fuel dispersion, or local air to fuel ratio within the fuel spray, is rare. Consideration to obtaining such data on the experimental test engine used for the data of chapter 7, was given, but total time of the project prevented completion of this set of tests beyond preliminary work on the measurement technique using a gas chromatograph. Such an analysis would be a substantial piece of work and is discussed more fully in section (8.4).

However, the results of chapter 7, and figures (6.23) (6.25) provide evidence that the model jet fluid dispersion is indicative of engine fuel dispersion.

Auto-ignition has been seen to occur in regions predicted to be close to stoichiometric, and typically in the range 10:1 to 15:1 mass air to fuel ratio. Prediction of the exact location of the auto-ignition site from the gas jet simulation requires additional knowledge of temperature distribution in the spray, since auto-ignition will logically occur where suitable concentration and temperature coincide. This will receive further discussion in section (8.4).

The data of Rife and Heywood (figure (6.24)) indicates that initial flame propagation is along model predicted contours in the region of 15:1 to 10:1, with a more intense combustion at the chamber wall where impingement presented a model air to fuel ratio of 8:1, (figures (6.23) (6.25)). Similarly for the engine

data of chapter 7 the photographed combustion sequences show ignition to occur in model regions represented by bands of mixture between 10:1 and the outer boundary of the jet. In particular comparison of figures (7.13) and (7.33) indicates that large spread of the early ignition regions in the engine fuel spray is represented in the model by a wide trail down stream of the fuel jet.

Excessively rich regions predicted in the model (less than 5:1 air to fuel ratio) in figures (7.32) (7.33), occurring both in the spray core and along the wall, are reasoned to promote both smoke formation and considerable delay in combustion when related to the corresponding film sequences of figures (7.11) to (7.14). Conversely the leaner wall and spray core mixtures of the model of figure (7.34) correspond to rapid clean combustion in the engine fuel spray of figure (7.15).

The model area parameter, developed to quantify the model predicted fuel dispersion, shows a strong correlation with the engine produced data of figures (7.35) (7.36). Trend in the proportion of model lean mixture area is seen to be matched by trend in engine produced data related to lean region combustion (Henein (35) figure (1.15)). i.e. Increase in nitrous oxide emission, rate of pressure rise, and peak pressure is seen to correspond to increase in lean mixture proportion as predicted by the models. Additionally, increases in carbon monoxide, smoke, and unburnt hydrocarbon emission are shown to correspond to increase in rich mixture proportion as predicted by the models.

The lean mixture 'patches' produced close to the nozzle in the models of figures (7.34), (7.32), (6.23) are worthy of

discussion. Little evidence of such fuel accumulation is apparent in the engine fuel spray. However the regions are of lean mixture, typically less than stoichiometric, and unlikely to provide suitable auto-ignition sites. The possibility of their existence in the engine cannot be overruled therefore, but 'combustion evidence' of these fuel areas is scarce and only truly apparent in figure (7.15), frame (2), just after 10 deg. BTDC, when auto-ignition is seen to occur close to this region. Existence of these areas corresponds to the wake regions in the gas jet concept of figure (2.1), and explained as a low pressure region behind the almost 'solid' body cylinder representing the spray. It is of interest to note, therefore, that such regions do not occur in the models where deflection and spread is large, (figures (6.26) (7.33)), and occurrence of these regions therefore shows a relation to the jet momentum compared to the cross flow intensity.

8.2 Application of the Modelling Technique to Engine Development

Section (1.1) presented a survey of published engine performance data in relation to the fuel mixing process. The work of chapter 7 now compliments this and illustrates that variation in engine performance with nozzle configuration, such as those surveyed in figures (1.11) (1.8) (1.9) (1.6), may be explained by suitable gas jet models. The concept of 'thermal pinch' was proposed as a feasible explanation of the overswirled state resulting in increased smoke emission. (section 1.1.2). In particular, it was proposed that for figure (1.11) increased smoke emission with increased hole number, i.e. increased swirl effect, could be explained by thermal pinch where under penetration of the spray was suggested. Under penetration of the 4 x .33 mm nozzle of figure (1.11) was thought to be suggested due to the large hole area promoting a low nozzle injection velocity.

It is now of interest to note that the same argument could be applied to the low injection velocity, 4 x 0.3 mm nozzle, of chapter 7, if no modelling data was available. On this faulty train of logic, correction would be suggested by reducing swirl rate, the model of figure (7.33) clearly indicates that increased wall impingement and smoke generation would result.

The usefulness of the modelling technique is therefore apparent.

Section (1.1) showed that engine performance is a function of many variables such as nozzle hole size, injection velocity, spray path length, and swirl intensity. The marked similarity between engine data for the two combustion chamber shapes of chapter 7 illustrates that the major controlling factors are those listed above. Engine development by progression from one combination to the next by changing a single variable, such as nozzle size, may be misleading

since interpretation of the engine data is in itself an uncertain process.

The work of chapters (6) (7) illustrate that the gas jet modelling technique can represent the fuel mixing process with sufficient realism to allow selection of suitable injection rate, nozzle configuration, swirl rate and spray path length at the design stage. Subsequent development would then be restricted to fine variation of the generally correct combination.

In particular the universal correlation of engine produced data as a function of a spread parameter is desirable for the prediction of relative performance between various injection systems. It has already been shown that the proportion of model area weaker than 10:1 air to fuel ratio is indicative of the exhaust emission levels and pressure loadings created by combustion in the engine (figures (7.35) (7.36). From the work of chapter 2 it may be seen that increased penetration occurs with increase in the ratio of nozzle momentum flux to cross flow momentum flux (J), and increase in the ratio (d_f/R). Hence the parameter:

$$J.\ d_f/2R \qquad \ldots\ldots\ldots \quad (8.1)$$

may be anticipated to increase with jet penetration potential. However, spread of the fuel spray is not well represented by such a parameter since equal values of expression (8.1) may be obtained for cases of low J, high d_f/R, and, high J but low d_f/R. Further, as in the case of the data of Stock (86) (see figures (6.9) (6.17) (6.20)), jet inclination can be seen to produce variation in fuel dispersion. Hence, the model area parameter of figures (7.35) (7.36) may be included as a dispersion factor:-

$$\text{i.e.} \qquad J.\ d_f/(2R.\ A_p) \qquad \ldots\ldots\ldots \quad (8.2)$$

may be expected to increase with jet intensity and jet rich mixture proportion (where A_p is the area proportion of the gas jet model weaker

than 10:1 air to fuel ratio).

Available data to check the correlation of engine variables with the parameter (8.2) between different combustion chambers and fuel injection systems is not provided by the data of this project. It is to be recommended therefore that future modelling studies may include work to establish such a universal parameter.

Figure (8.1) shows engine data plotted against the parameter (8.2) for the three considered injection cases of chapter 7. The presented data is obviously limited in this respect, but tends to suggest an optimum value of the parameter for smoke and CO emissions which correspond to the maximum rate of pressure rise. More data from different engines and corresponding gas jet models, plotted on this basis would hopefully correlate to produce a universal guide for the optimum value of parameter (8.2).

8.3 Remarks on the Hot Wire Techniques

Development of the hot wire heat transfer correlating equation of Chapter 4 for probes with wires of sufficient strength for engine velocity measurement work, and over a sufficiently wide overheat ratio range, allowed the direct application of the derived relationship without the complication and uncertainty previously produced by amendment to published relationships (section 3.5.1). However, limitation on the general application of the correlating equation is imposed by the specially devised techniques of quartz coating and cold resistance measurement. Non-coated wires, and use of operating temperatures based on directly measured cold resistance values, may be expected not to provide correlation on the same equation form. Therefore, future application of equation (4.36) should also be accompanied by application of the quartz coating and cold resistance measurement techniques.

The binary concentration measurement technique has been a useful research tool in the present project, and the sensitivity predictions for various tracer gases (section 5.2) provide a realistic method of determining measurement accuracy. Application in other modelling experiments to describe mixing phenomena is clearly possible.

8.4 Recommendations for Further Work

Further validation of the model air to fuel ratio predictions may be made by direct sampling experiments on fuel spray in the engine cylinder. A high speed sampling valve would then be used to withdraw samples of air-fuel mixture from discrete locations in the spray. Suitable complete combustion of the withdrawn mixture could then be achieved on a continual flow basis. Measurement of the gaseous products after combustion, notably, carbon dioxide, carbon monoxide, oxygen and unburnt hydrocarbons, would allow computation of the original air to fuel ratio providing the injected fuel was a pure hydrocarbon such as n-heptane. Combustion of the spray in the engine cylinder would have to be avoided, possibly by reduction in compression ratio. Direct comparison with the corresponding gas jet model would then be possible.

The dependance of fuel spray auto-ignition site location on local temperature could be determined by temperature measurement in an additional non-isothermal model, created on the same basis as the gas mixing model. Local temperature could be readily measured using a hot wire probe as a resistance thermometer. Similarity criteria for air and jet fluid temperatures would require derivation, and in the case of impingement, the model wall temperature would also have to be controlled. Mapping of temperature profiles, superimposed on the gas concentration model map, would then indicate where stoichiometric mixture, and suitable ignition temperature coincide. Comparison with engine photographic data would then provide a test for validation.

The computation of exhaust emission levels and heat release from data on fuel injection rate and swirl intensity is a complex problem hampered by the pre-requisite of describing the mixing process. It is therefore logical to suggest that data on the fuel distribution,

generated by the gas jet modelling technique, could be used as input data to a combustion analysis to predict heat release and exhaust emission levels. The problem of predicting the combustion process through the hetrogeneous mixture is in itself a formidable task. However, it may be claimed that the ability to realistically represent the local fuel concentrations removes a major problem area.

8.5 Conclusion

Trajectory and spread of the gas jet models based on the theory of chapter (2) have been shown to closely represent those of the engine fuel spray, and a comparison of engine combustion data and model mixture prediction has been presented.

A good indication of combustion performance may be inferred from the model air to fuel ratio map and the likely performance of the combustion system thereby predicted. Therefore the technique has been proposed to have immediate application in engine development work and as a suitable means of presenting mixture data for input to computational combustion models.

Extension of the technique is recommended to provide data on the temperature dependence of auto-ignition sites, and further validation by mixture sampling on the engine is suggested.

The developed hot wire anemometer heat transfer correlation is of direct use in engine velocity measurement work, and the binary concentration measurement technique is generally applicable to modelling experiments of mixing phenomena.

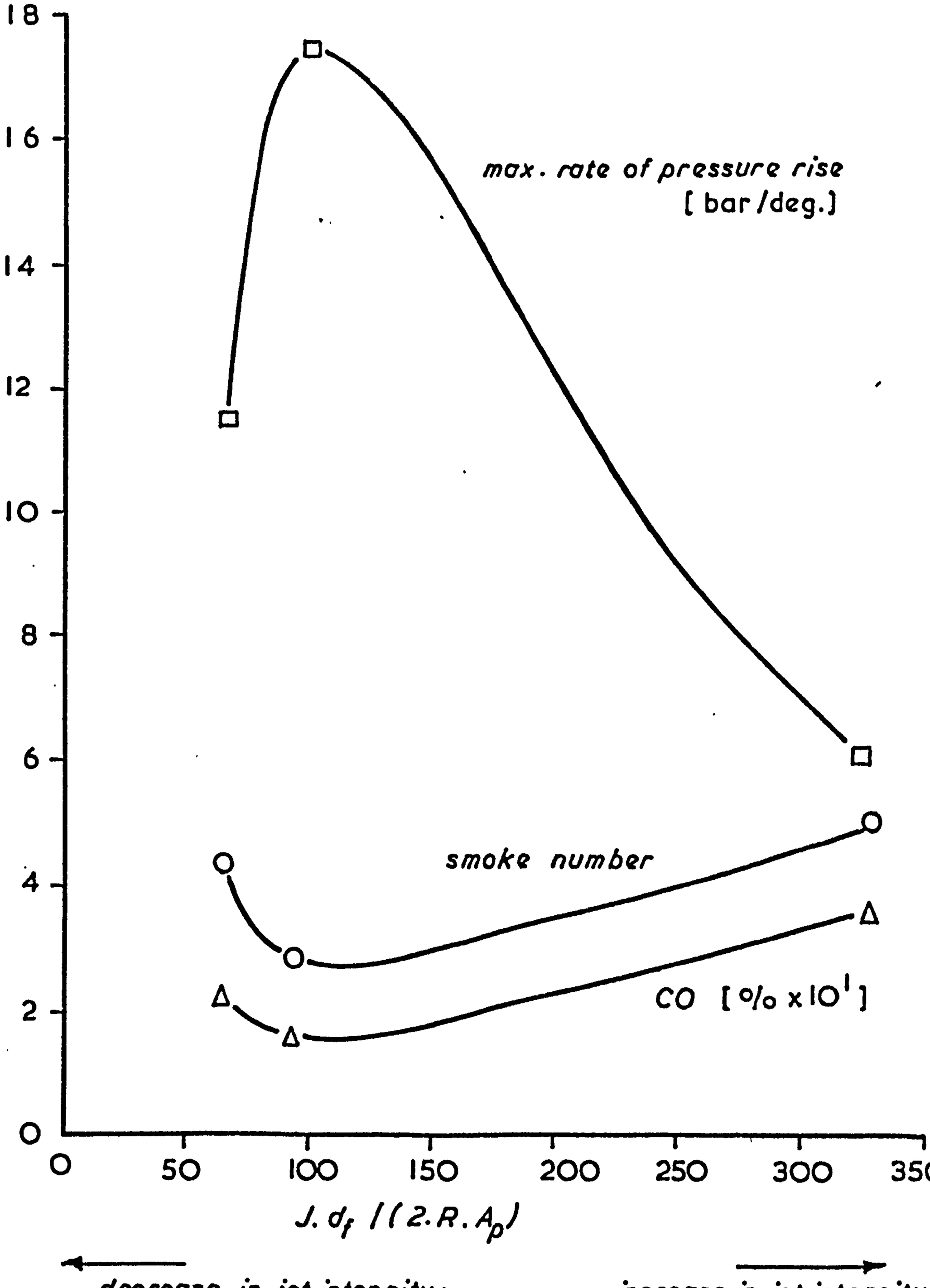

(A_p = gas jet proportion weaker than 10:1)

Engine Variables as a Function of the Spread Parameter.

Fig. 8·1

9.0 References and Appendices

REFERENCES

1. Urlaub, A. 'The Effect of Air Motion on Mixture Formation in Direct Injection Diesel Engines'. Translation No. 55/65. The Motor Industry Research Association, Lindley (Translation of Ref. 2)

2. Urlaub, A. 'Der Einfluss der Luftbewegung auf die Gemischbildung im Diesel motor mit Direkter Einspritzung'. VDl - Fortschritts-Berichte, Reihe 6, Nr. 6, 1965.

3. Melton R.B. Rogowski, A.R. 'The Interaction of Air Motion, Fuel Spray, and Combustion in the Diesel Combustion Process'. Trans A.S.M.E. Ser A. vol 94, No. 1, Jan. 1972. pp 11 - 16

4. Nagao, F. Ikegami M, Kujota Y., Mitsuda, T. Kawatei K. 'A Study on Combustion in Direct Injection Diesel Engines'. (lst report. In the case of shallow dish chamber). Bul. J.S.M.E. Vol. 16, No. 93, Mar. 1973, pp. 588 - 598.

5. Nagao, F. Ikegami, M. Mitsuda, T. Kawatei, K., Fujikawa, T. 'A study on Combustion in Direct Injection Diesel Engines' (2nd Report. In the case of deep bowl chamber). Bul. J.S.M.E. Vol. 16, No. 93, Mar. 1973, pp. 599 - 609.

6. Watts R. Scott, W.M. 'Air Motion and Fuel Distribution Requirements in High Speed Direct Injection Diesel Engines'. I. Mech. E., Symp. - Diesel Engine Comb., London April, 1970, paper 17, pp. 167 - 177.

7. Pischinger, A. Pischinger, F. 'Der Einfuss der Wand bei der Verbrennung eines Brennstoffstrahls im einem Luftwirbel.' MTZ Jahrg. 20 (1959), Nr. 1. S. 4/9.

8. Eisfeld, F. 'Beobachtung der Verdampfung eines Kraftstoffilms in stromender Luft.' D.F.L. - Bericht No.200 (1964).

9. Huber, E.W. Stock D. Pischinger, F. 'Investigation of Mixture Formation and Combustion in a Diesel Engine with the aid of the Schlieren Method'. 9th Int. Congress on Comb. Eng. C.I.M.A.C. A.14, Stockholm, Sweden, 1971.

10. Khan, I.M. Grigg, H.C. 'Progress of Diesel Combustion Research'. 9th Int. Cong. on Comb. Eng. C.I.M.A.C. A.18, Stockholm, Sweden, 1971.

11. Lyn, W.T. Valdmanis, E. 'The Effects of Physical Factors on Ignition Delay'. Proc. Mec. Eng. 1966-67 vol. 181, pt 2A, No. 1 pp. 34 - 59.

12. Godsave G.A.E. 'The Combustion of Drops in A Fuel Spray'. N.G.T.E. October, 1950. M 95.

13. Godsave, G.A.E 'Combustion of Droplets in a Fuel Spray.' Nature. Vol. 164, 1949, pp. 708-709.

14. Henein, N.A. 'A Mathematical Model for the Mass Transfer and Combustible Mixture Formation Around Fuel Droplets'. Paper 710221, S.A.E. Automotive Eng. Congress. Detroit, Jan. 1971.

15. Schweitzer, P.H. 'Penetration of Oil Sprays'. Penn. State College Engineering Experiment Station. Bulletin No. 46 (1937).

16. Schweitzer, P.H. 'Mathematical Supplement to the Penetration of Oil Sprays'. Pennsylvania State College. July 1937.

17. Melton, R.B. 'Diesel Engine Fuel Injection Viewed as a Jet Phenomenom'. S.A.E. Trans. 710132 1969.

18. Wakuri, Y. Fujii, M. Amitani, T. Tsuneya, R. 'Study on the Penetration of Fuel Spray in a Diesel Engine'. Bul. J.S.M.E., Vol. 3, No. 9, 1960. pp 123.130.

19. Thring, M.W. Newby, M.P. "Combustion Length of Enclosed Turbulent Jet Flames'. 4th Symp. on Combustion 1952. pp. 789-796.

20. Dent, J.C. 'A Basis for the Comparison of Various Methods for Studying Spray Penetration'. S.A.E. trans. 710571. 1971.

21. Forstall, W. Shapiro, A.H. 'Momentum and Mass Transfer in Co-Axial Gas Jets'. Jn. App. Mech., Vol. 17., 1950 pp. 399.

22. Bormann, G.L., Johnson, J.H. 'Unsteady Vaporisation Histories and Trajectories of Fuel Droplets Injected into Swirling Air! A.S.M.E. paper 598C. 1962.

23. Hussmann, A.W. Kahoun, F. Taylor, R.A. "Charge Stratification by Fuel Injection into Swirling Air'. S.A.E. Trans, Vol. 71, 1963, pp. 421-444.

24. Adler D. Lyn W.T. 'The Evaporation and Mixing of a Liquid Fuel Spray in a Diesel Air Swirl'. I. Mech. E. Symp. - Diesel Eng. Comb., London, April, 1970, paper 16, pp 157 - 166.

25. Sass, F. 'Compressorless Diesel Engines'. Berlin, Julius Springer, 1929.

26. Taylor, D.H.C. 'The Analysis of Fuel Spray Penetration and Distribution in a Medium Speed Diesel Engine Using Optical Techniques'. Ph.D. Thesis, Loughborough University of Technology, 1967.

27. Burt, R.
Troth, K.A.
'Penetration and Vaporisation of Diesel Fuel Sprays'.
I.Mech.Eng., Symp - Diesel Engine Comb. Paper 15, London, April, 1970.

28. Parks, M.V.
Polonski, C.
Toye, R.
'Penetration of Diesel Fuel Sprays in Gases'.
Pap. 660747, presented at S.A.E. Combined Power plant and Transportation Meeting, Chicago, October, 1966.

29. Gray, J.T.
Mecher, N.T.
Manheimer, R.J.
'Some observations on the Liquid Injection Technique as a Research Tool'.
S.A.E. Trans. Vol. 75. paper 660748.

30. Lee, D.W.
'A study of Air Flow in Air Engine Cylinders'.
N.A.C.A. Tr. No. 653 (1939).

31. Derham, J.A.
'Air Motion in a Four Stroke Direct Injection Diesel Engine'.
Ph.D. thesis - University of Loughborough 1972.

32. Horvatin, M.
'Beitrag Zur Awendung Des Hitzdraht - Anemometers Für Strömungs Und Turbulenzmessungen in Ver Brennungs motoren'.
Dr. Ing. Thesis, Technical University, Munich 1971.

33. Dlauhy T.
Garvin, W.H.
'Evaporation in Spray Drying'.
Can.J. Chem.Eng. 1960. p.38.

34. Abramovich, G.N.
'The Theory of Turbulent Jets'
M.I.T. Press 1963.

35. Henein, N.A.
'Combustion and Emission Formation in Fuel Sprays Injected into Swirling Air'.
Presented at Aut. Eng. Cong. Detroit Jan. 1971.
S.A.E. paper 710220.

36. Rife, J.
Heywood, J.B.
'Photographic and Performance Studies of Diesel Combustion with a Rapid Compression Machine'
Presented: Aut. Eng. Cong. Toronto, Canada.
October, 1974. S.A.E. paper 740948.

37. Ranz, W.E.
Marshall, W.R.
'Evaporation from Drops'.
Chem. Eng. Prog., Vol. 48, No. 3. (1952)
pp 141 - 148.

38. Spalding, D.B.
'Some Fundamentals of Combustion'.
Gas Turbine Series, Vol. 2., Butterworths, 1955.

39. Kumagi, S.
Isoda, H.
'Combustion of Fuel Droplets in a Falling Chamber'. 6th Symp. (Int.) on Comb., N.Y.
Reinhold Publishing Co. (1956) pp. 726-731.

40. Wegstein, J.H.
'Accelerating Convergence of Iterative Processes'.
Comm. Assoc., Comp. Mach. Vol.1, No. 6, 1968.

41. Hassan, H.
'Unsteady Heat Transfer in a Motored Internal Combustion Engine'.
Ph.D., Thesis, University of Loughorough.
September, 1968.

42. Weidenmüller, M.
'Geschwindigkeiten und Temperaturen in einem geschleppten Diesel motor mit Direkteinspritzung'.
Dissertation 1969 Fakutät für Maschinenwesen der Technischen Universität Berlin.

43. Corrsin, S.
'Extended Applications of the Hot Wire Anemometer'.
N.A.C.A. Tech. Note. No. 1864. 1949.

44. Way, J.
Libby, P.A.
'Hot Wire Probes for Measuring Velocity and Concentration in Helium Air Mixtures'.
A.I.A.A. Jn. Vol. 8, No. 5, 1970. pp. 976 - 978.

45. Devilliers, J.F.
Diep, G.B.
'Hot Wire Measurements of Gas Mixture Concentrations in a Supersonic Flow'.
DISA Information No. 14, March, 1973 pp 29-36.

46. Simpson, R.L.
Wyatt, W.G.
'The Behaviour of Hot Film Anemometers in Gas Mixtures'.
Jn. Phys. E. Vol.6, No. 10 1973, pp 981-986.

47. Baccaglini, G.
Kassoy, D.R.
Libby, P.A.
'Heat Transfer to Cylinders in Nitrogen-Helium and Nitrogen-Neon Mixtures'.
Phys. of Fluids, Vol.12, No. 7, 1969, pp. 1378-1381.

48. Wasan, D.T.
Baid K.M.
'Measurement of Velocity in Gas Mixtures: Hot-Wire and Hot Film Aneometry'.
A.I.Ch.E.Jn. Vol. 17, No. 3, 1971 pp. 729-731.

49. Wasan, D.T.
Davis, R.M.
Wilke, C.R.
'Measurement of the Velocity of Gases with Variable Fluid Properties'.
A.I.Ch.E.Jn., Vol. 14, No.2, 1971, pp 227-234.

50. Hassan, H.
Dent, J.C.
'Correction for Temperature Loading and High Gas Pressure Effects for the Constant-Temperature Hot Wire Anemometer'.
J.Phys., D., Appl. Phys. 2., 1969.

51. Dent, J.C.
Derham, J.A.
'A Method for Checking the Consistency of Velocity Computations from Hot Wire Anemometer Measurements in Variable Density Flows'.
J.Phys., E., Scientific Instruments, 1972, Vol.5.

52. King, L.V.
'On the Convective Heat Transfer from small cylinders in a stream of fluid. Determination of convective constants of small platinum wires with application to hot wire anemometry'.
Phil. Trans. R. Soc. 214A, pp 373-432 (1914).

53. Hilpert, R.
'Wärmeabgabe von geheizten Drähten und Rohren in Luftstrom'.
Forsch. Geb. Ing. 4, pp 215-224, (1933).

54. Collis, D.C.,
Williams M.J.
'Two-dimensional convection from heated wires at low Reynolds numbers'.
J.Fluid Mech. 6, pp 357-384 (1959).

55. Davies, P.O.A.L.
Fisher, M.J.
'Heat Transfer from electrically heated Cylinders'.
Proc. R. Soc., 280 A, pp 486-527 (1964)

56. Ahmed, A.M.
'Forced Convective Heat Transfer to Cooled Cylinders at Low Reynolds Numbers and with Large Temperature Differences'.
C.A.R.D.E. Tech.Rpt. 588/68., Project D46-95-51-10, Quebec, 1968.

57. Ahmed, A.M.
'Comments on Forced Convective Heat Transfer to Cooled Cylinders'.
Advances in Hot Wire Anemometry, pp 66-70.
Maryland Univ. (1968).

58. McAdams, W.H.
'Heat Transmission'.
Third edition., Chap. X., McGraw-Hill, New York (1954).

59. Kramer, H.
See Hinze J.O. 'Turbulence'
McGraw Hill Book Co., Inc., London pp 75-124.

60. Andrews, G.E.
Bradley, D.
Hundy, G.F.
'Hot Wire Anemometer Calibration for Measurements of Small Gas Velocities'.
Int. J. Heat Mass Transfer. Vol. 15 pp 1765-1786, 1972.

61. Parnas, A.L.
'Temperature Loading Influence on Heat Transfer from a cylinder in an air cross-flow'.
Inzh-Fiz. Zh. vol 7, pp 37-44, (1964).

62. Horvatin, M.
Hussmann, A.W.
'Measurement of Air Movements in Internal Combustion Engine Cylinders'.
DISA Information, No. 8, July, 1969, pp 13-22.

63. Grigull,
Erk,
Gröber
'Wärmeübertragung'.
Springer-Verlag, 3rd edition, 1963.

64. Tombach, I.H. 'Velocity Measurements with a New Probe in Inhomogeneous Turbulent Jets'. Thesis, California Institute of Technology, 1969.

65. Reid, R.C. Sherwood, T.K. 'The Properties of Gases and Liquids'. McGraw Hill Book Co., Inc., 1958.

66. Mason, E.A. Saxena, S.C. 'Approximate Formula for the Thermal Conductivity of Gas Mixtures'. Phys. Fluids. Vol. 1, No.5, 1958, pp. 361-39.

67. Lichtarowitcz, A. Duggins, R.K. Markland, E. 'Discharge Coefficients for Incompressible Non-Cavitating Flow through Long Orifices'. Jn. Mech.Eng.Sc., Vol 7., No. 2, 1965, pp 210-219.

68. Barratt, T. 'Thermal and Electrical Conductivities of Some of the Rarer Metals and Alloys'. Phys. Soc. of London. V.25-26, 1912-1914. pp 347-365

69. Darling, A.S. 'Iridium Platinum Alloys'. Johnson Mathey Ltd., Platinum Metals Review, Vol. 4, Jan., 1960, No. 1, pp 18-26.

70. Powell, R.W. Tye, R.P. Woodman, M.J. 'Thermal Conductivities and Electrical Resistivities of the Platinum Metals'. Johnson Mathey Ltd., Plat. Metals Rev. Vol.6. 1962. pp 138-143.

71. DISA DISA Probe Manual. Feb., 1973. DISA Elecktronik A/S DK-2730 Herlev, Denmark.

72. Bradley, D. Entwistle, A.G. 'Anomalous Electrical Resistance Effects in Small Diameter Platinum and Platinum-Rhodium Resistance Elements at Temperatures in Excess of 1000^{o}C in a Gaseous Environment'. 'Temperature, It's Measurement and Control'. Vol. 3, part 1, pp 319-325.

73. Irving, J.B.
Jamieson, D.T.
Paget, D.S.
'The Thermal Conductivity of Air at Atomospheric Pressure'.
Trans. Instn. Chem. Engrs., Vol. 51, 1973.
pp. 10-13.

74. Ehya, H.
Faubert, F.M.
Springer, G.S.
'Thermal Conductivity Measurements of Propane and N-Butane in the Range 300 to 1000 deg K'.
ASME. Ser. E. Vol.94, Aug., 1972 pp. 262-265.

75. Din, F.
'Thermodynamic Functions of Gases'.
Butterworths; Vol. 2, 1956; vol 3, 1961.

76. Rogers, G.F.C.
Mayhew, Y.R.
'Thermodynamic Properties of Fluids and Other Data'.
Oxford. Basil Blackwell 1964.

77. Kutateladze, S.S.
Borishanskii, V.M.
'A concise Encyclopedia of Heat Transfer!
Pergamon Press. 1966.

78. Spiers, H.M.
'Technical Data on Fuel'.
Sixth Edition, British National Committee, World Power Conference, 201, Grand Buildings, Trafalgar Square, London.

79. Dent, J.C.
'Estimation of Experimental Error'
Internal Circular, University of Loughborough, Department of Mechanical Engineering.

80. Kamotani, Y.
Greber, I.
'Experiments on a Turbulent Jet in a Cross-Flow'.
A.I.A.A. Jn. Vol. 10, No. 11, 1972, pp 1425-1429.

81. Margason, R.J.
'The Path of a Jet Directed at Large Angles to Subsonic Free Stream'.
TND-4919, 1968, NASA. RP.

82. Jordinson, R.
'Flow in a Jet Directed Normal to the Wind'.
Aero. Res. Council, 1956. R & M No. 3074.

83. Callaghan, E.E.
Ruggeri, R.S.
'Investigation of an Air Jet Directed Perpendicularly to an Air Stream'.
TN-1615, 1948, NACA.

84. Storms, K.R. 'Low Speed Wind Tunnel Investigation of a Jet Directed Normal to the Wind'. Rep. 885, Aeronaut. Lab., University of Washington, Nov., 1965.

85. Hestroni, G. Sokolov, M. 'Distribution of Mass, Velocity, and Intensity of Turbulence in a Two Phase Turbulent Jet'. Jn. App. Mech., Vol. 38., ser E., No. 2. pp 315-327, June, 1971.

86. Stock D. "Untersuchungen der Gemischbildungs, Zund- und Verbrennungsvorgange eines direkteinspritzenden Diesel motors'. Doktor-Ingenieur Dissertation: Fakultat fur Maschinenwesen der Technischen Universitat, Berlin - July, 1970.

87. Giffen, E. Muraszew, A. 'The Atomisation of Liquid Fuels'. Chapman and Hall, 1953.

Appendix A

One Dimensional Single Droplet Theory

A.1 Basic Assumptions

a. The life of the droplet is divided into two stages:-

   i. Unsteady 'heat up' period: the temperature of the droplet increases to that of the boiling point of the hydrocarbon.

   ii. Steady state evaporation period.

b. The considered droplet is not influenced by adjacent droplets.

c. Radiant heat transfer is negligible.

d. Infinite thermal conductivity of the droplet due to rapid circulation of fluid (Biot modulus <0.1).

e. The vapour pressure on the droplet surface is assumed equal to the saturation pressure corresponding to the liquid temperature.

f. The main driving force for the diffusion of vapour from the droplet surface is the mass concentration gradient.

g. 'Cracking' of the hydrocarbon fuel does not occur.

A.2 Governing Equations

A 2.1 Velocity Decay

Equating the inertia and drag forces of the droplet yields:-

$$\rho_f \cdot \frac{\pi D^3}{6} \cdot \frac{d\,U_f}{dt} = - C_d \cdot \frac{\rho_g}{2} \cdot (U_f - U_g)^2 \cdot \frac{\pi D^2}{4} \quad \ldots\ldots (A.1.1)$$

where:

C_d ..... drag coefficient

ρ_f, ρ_g ..... respective fuel and gas densities

U_f, U_g ..... respective fuel and gas velocities

The drag coefficient of a sphere may be represented as a function of Reynolds number from standard published data, and fitted by an 8th order polynomial.

A 2.2 Droplet Temperature

Equating the convective heat transfer to the droplet with the increase in internal energy and the heat lost due to evaporation yields:

$$\lambda \frac{dm}{dt} + m\,c \frac{d\theta}{dt} = h \frac{\pi D^2}{4} (\theta_g - \theta) \quad \ldots\ldots (A.1.2)$$

where:

θ ..... droplet temperature

λ ..... latent heat of evaporation

m ..... droplet mass

c ..... specific heat of the fuel oil

θ_g ..... gas temperature

The average surface heat transfer coefficient h can be calculated by the relation due to Froessling (37):

$$Nu = 2(1 + 0.276\, Re^{\frac{1}{2}}\, Pr^{1/3}) \quad \ldots\ldots (A.1.3)$$

where:-

Re ..... Reynolds number

Pr ..... Prandtl number

Nu ..... Nusselt number

A 2.3 Evaporation Rate

By mass transfer theory (38):

$$\frac{dm}{dt} = Ag\ B \qquad \ldots\ldots\ldots \text{(A 1.4)}$$

where:-

A ..... droplet surface area

B ..... mass transfer driving potential

g ..... is defined by:

$$g = \frac{h}{C_p} \quad \frac{\log_e (1 + B)}{B} \qquad \ldots\ldots \text{(A 1.5)}$$

The driving potential B may be defined as:

$$B = \frac{m_g - m_s}{m_s - m_t}$$

where m ..... mass of vapour per unit mass of mixture.

subscripts g ..... denotes the gaseous phase-removed from the droplet boundary layer.

s ..... denotes the surface condition.

t ..... denotes the transported property.

Considering the vapour to behave as a perfect gas, and applying Dalton's Law of partial pressure yields:

$$B = C \frac{(P_g - P_s)}{P_c} \qquad \ldots\ldots \text{(A 1.6)}$$

where:

P_s ..... saturated vapour pressure.

P_g ..... vapour pressure in the gaseous phase.

P_c ..... total cylinder pressure.

C = (mol. wt. of fuel/mol. wt. of air)

A.3 Solution and Computation of the Governing Equations

A 3.1 General

It has been shown that the four variables velocity, mass, temperature, and time are inter-related by equations (A 1.1, A 1.2, A 1.3, A 1.4, A 1.5, A 1.6), the relationship may be represented as below:

	mass	temp.	velocity	time
mass	-	I	I, II	I, II
temp.	I	-	I	I
velocity	I, II	-	-	I, II

where I, and II represent the stage of the droplets life over which they are dependent.

The process of solving the three basic sets of equations becomes that of a step-by-step iterative method. The iteration providing a suitable value of Reynolds number and evaporation rate for the time step currently considered.

A 3.2 Calculation of Velocity Decay

Rewriting equation A 1.1 yields:

$$\frac{d\,U_f}{(U_f - U_g)^2} = -\frac{C_d}{D} \cdot \frac{3}{4} \cdot \frac{\rho_g}{\rho_f} \cdot dt$$

If a change in velocity across a small time step is considered for which the iteration process provides a mean Re ($\bar{R}e$) based on a mean diameter $\bar{D}$, a mean value of C_d ($\bar{C}_d$) can be defined from the relationship of Reynolds number to drag coefficient. Thus, direct integration of the above equation is valid using these representative values as constants over the time increment:-

$$U_{f_{t+\Delta t}} = \frac{U_{ft} + U_g (U_{ft} - U_g)\ \beta .\ \Delta t}{1 + \beta\ (U_{ft} - U_g)\ .\ \Delta t} \qquad \ldots\ldots \text{(A 1.7)}$$

where $\beta = \frac{\overline{C}_d}{\overline{D}} \cdot \frac{3}{4} \cdot \frac{\rho_g}{\rho_f}$

U_{ft} ..... fuel droplet velocity at time t.

$U_{f_{t+\Delta t}}$ .... fuel droplet velocity at time $t+\Delta t$

A 3.3 Calculation of Droplet temperature and Mass change during Stage I

The droplet temperature and mass inter-relationship is specified by equation A(1.2), but the evaporation rate is also specified in equations (A 1.4, A 1.5, A 1.6 and A 1.3) where Pr is replaced by Schmidt number (Sc) in A 1.3. Godsave (12) and Kumagi and Isoda (39) showed that the droplet diameter changes little during the unsteady heat up period. Hence, during the small time step the droplet diameter will be taken as that calculated for the end of the last time interval. Hence given a representative value of Reynolds number (from the current iteration estimate) it can be shown that:

$$\dot{m} = \text{const. for } \Delta t.$$

This reduces the differential equation (A 1.2) to the form:

$$\frac{d\theta}{dt} + \propto\theta = \gamma$$

which has the solution:

$$\frac{\theta_{t+\Delta t} - \gamma/\propto}{\theta_t - \gamma/\propto} = e^{-\propto \Delta t}$$

or re-arranging:-

$$\theta_{t+\Delta t} = \frac{\gamma}{\propto} + \left(\theta_t - \frac{\gamma}{\propto}\right) e^{-\propto \Delta t} \qquad \ldots\ldots \text{(A 1.9)}$$

where:

$$\alpha = \frac{\bar{h}\, A}{\bar{m}\, C_p} \qquad \ldots\ldots\ldots \text{(A 1.9a)}$$

$$\gamma = \frac{\bar{h}\, A}{\bar{m}\, C_p}\ \theta_g - \frac{\lambda}{\bar{m}\, C_p} \cdot \dot{m} \qquad \ldots\ldots\ldots \text{(A 1.9b)}$$

and ' bar ' quantities represent the mean of initial and final step values by the iteration process.

A 3.4 Calculation of Droplet Mass during Stage II

By the assumption of a constant temperature during this stage, the mass variation may be calculated directly by equations A 1.3 to A 1.6, the only variable being the mean time step Reynolds number.

A 3.5 Suitable Iteration Procedure

The iteration process used is that due to Wegstein as described in reference (40).

Reynolds number has been used as the iteration variable since a stable end of step value will represent a convergence of both droplet diameter and velocity.

The program flow chart is shown in figure (A 1.1).

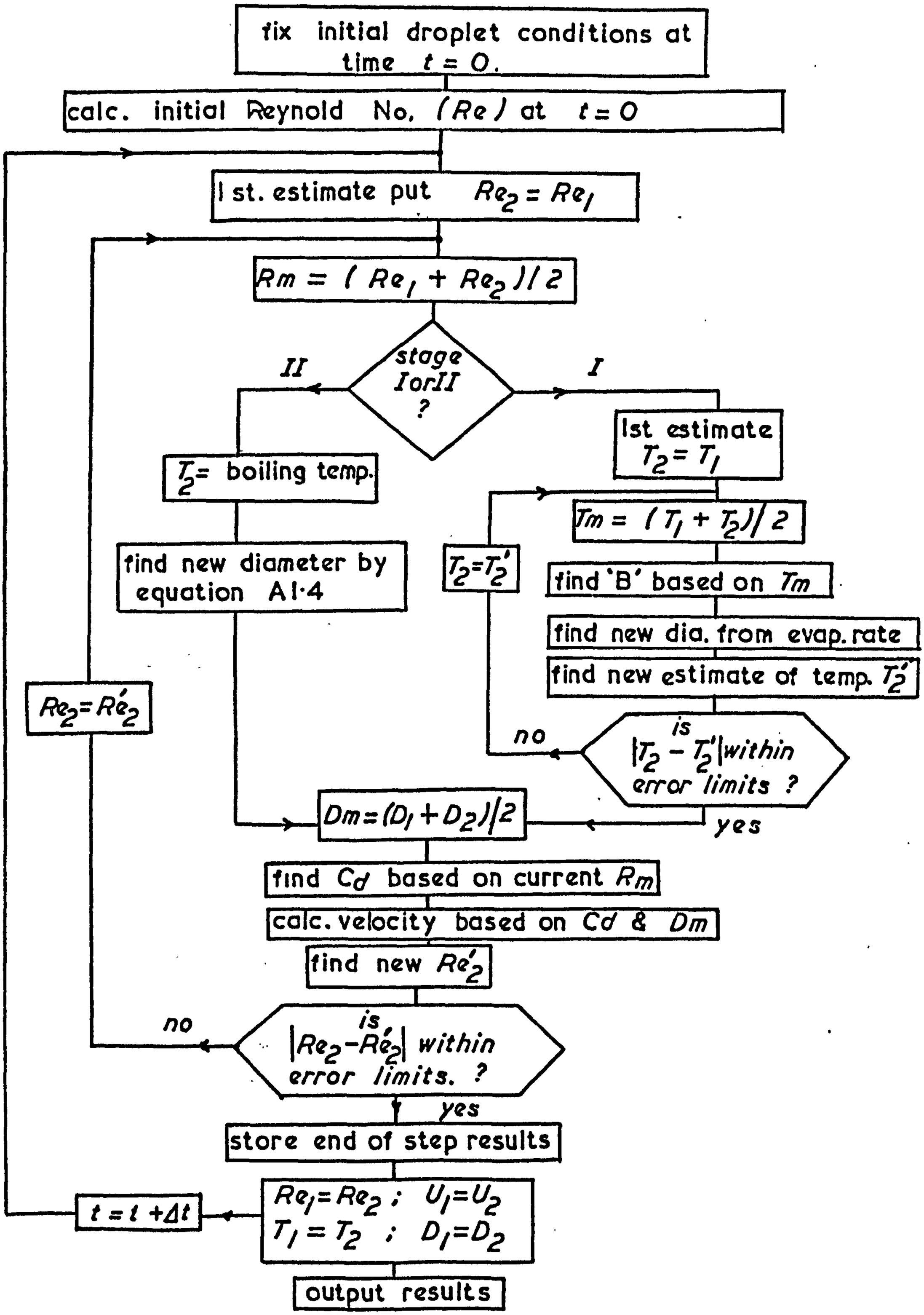

Schematic Flow Chart of Droplet Computation Sequence.

Fig. A·1

Appendix B

General Iteration Technique

The iteration method reported here is suitable for solving non-linear equations of the form F(X) = 0, and is based on an IBM software routine. It has been developed for application in this project to calculate the hot wire heat transfer coefficient, (hence requiring iteration to the value of K1 to yield zero value of equation 4.15), and also for the calculation of binary gas concentration (hence requiring iteration to the value of χ to yield zero value of equation (5.1) via equations (4.29), (4.30), (4.24), (4.25)).

In general an external function Fn(x) is required to define the function form and convergence will be achieved providing the root exists between the stipulated initial iteration bounds (XLI, XRI), and the derivative of Fn(x) at the root is not zero. The technique employed is Muellers iteration method and may be studied by reference to the following computer listing and the flow diagram of figure B.1. Application of the iteration subroutine may be seen in subroutines 'HTRANS' and 'CONXZ' of appendix (C).

Solution of the function Fn(x) = 0 is achieved by successive bisection and interpolation, which starts at the initial bounds XLI, XRI. Subsequent bisection and interpolation loops reduce the bounds until the function value Fn(x) at either bound or bisection midpoint becomes less than 100 x EPS, where EPS is the input argument representing the iteration tolerance. Alternatively, convergence is considered to exist if the separation of the two bounds, (maintained on opposite sides of the root), becomes less than EPS. For additional information see the reference of the comment section of the following program listing. The additional parameters A, B, C, D, contained in the function argument list are constants allowing flexibility in the

function definition, and not iteration variables.

```
      SUBROUTINE CJMIT(X,V1,V2,V3,V4,FN,XLI,XRI,EPS,IEND,IER,M)
C     SOLVES GENERAL NON-LINEAR EQUATIONS OF THE FORM FN(X,A,B,C,D)=0
C     BY MUELLERS ITERATION METHOD
C     PARAMETER FN CALLS AN EXTERNAL FUNCTION SUPPLIED BY THE USER
C     DESCRIPTION OF PARAMETERS
C          X=   RESULTANT ROOT OF EQUATION FN(X,A,B,C,D)=0
C          V1-V4 VALUES OF CONSTANTS A,B,C,D
C          FN= NAME OF EXTERNAL FUNCTION USED
C          XLI=INITIAL LEFT BOUND OF THE ROOT X.
C          XRI=INITIAL RIGHT BOUND OF THE ROOT X
C          EPS=UPPER BOUND OF THE ERROR OF RESULT X
C          IEND=MAX NUMBER OF ITERATION STEPS SPECIFIED
C          IER=RESULTANT ERROR PARAMETER
C               IER=1 NO CONVERGENCE AFTER IEND ITERATIONS FOLLOWED
C                     BY IEND SUCCESSIVE STEPS OF BISECTION.
C               IER=2 BASIC ASSUMPTION FN(XLI)*FN(XRI)LESS THAN ZER
C                     IS NOT SATISFIED.
C               IER=0 NO ERROR
C     SOLUTION OF EQUATION FN(X,A,B,C,D)=0 IS ACHIEVED BY MEANS OF
C     MUELLERS ITERATION METHOD OF SUCCESSIVE BISECTION AND INVERSE
C     PARABOLIC INTERPOLATION,WHICH STARTS AT THE INITIAL BOUNDS XLI
C     AND XRI. CONVERGENCE IS QUADRATIC IF THE DERIVATIVE OF FN AT THE
C     ROOT X IS NOT EQUAL TO ZERO. ONE ITERATION REQUIRES TWO
C     EVALUATIONS OF FN(X,A,B,C,D).
C     FOR REFERENCE SEE G.K.KRISTIANSEN,ZERO OF ARBITARY FUNCTIONS,BIT.
C     VOL 3(1963),PP205-206.
C
C     PREPARE ITERATION
      IER=0
      XL=XLI
      XR=XRI
      X=XL
      TOL= X
      F= FN(TOL,V1,V2,V3,V4)
      IF(F) 1,16,1
    1 FL=F
      X=XR
      TOL= X
      F= FN(TOL,V1,V2,V3,V4)
      IF(F) 2,16,2
    2 FR=F
      IF(SIGN(1.00,FL)+SIGN(1.00,FR)) 25,3,25
C     BASIC ASSUMPTION FL*FR LESS THAN 0 SATISFIED.
C     GENERATE TOLERANCE FOR FUNCTION VALUES.
    3 I=0
      TOL= 100.0*EPS
C     START ITERATION LOOP
    4 I=I+1
      M= I
C     START BISECTION LOOP
      DO 13 K=1,IEND
      X= 0.5*(XL+XR)
      TOL=X
      F= FN(TOL,V1,V2,V3,V4)
      IF(F) 5,16,5
    5 IF(SIGN(1.00,F)+SIGN(1.00,FR)) 7,6,7
C     INTERCHANGE XL AND XR IN ORDER TO GET SAME SIGN IN FL AND FR
    6 TOL= XL
      XL=XR
      XR= TOL
      TOL= FL
```

```
      FL=FR
      FR= TOL
    7 TOL= F-FL
      A= F*TOL
      A=A+A
      IF(A-FR*(FR-FL)) 8,9,9
    8 IF(I-IEND) 17,17,9
    9 XR=X
      FR=F
C     TEST ON SATISFACTORY ACCURACY IN BISECTION LOOP
      TOL= EPS
      A= ABS(XR)
      IF(A-1.00) 11,11,10
   10 TOL= TOL*A
   11 IF(ABS(XR-XL)-TOL) 12,12,13
   12 IF(ABS(FR-FL)-TOLF) 14,14,13
   13 CONTINUE
C     END BISECTION LOOP
C
C     NO CONVERGENCE AFTER IEND ITERATIONS AND BISECTIONS
C     SET IER=1 .ERROR RETURN.
      IER= 1
   14 IF(ABS(FR)-ABS(FL)) 16,16,15
   15 X=XL
      F=FL
   16 RETURN
C     COMPUTATION OF ITERATED X-VALUE BY INVERSE PARABOLIC INTERPOLATION
   17 A=FR-F
      DX=(X-XL)*FL*(1.00+F*(A-TOL)/(A*(FR-FL)))/TOL
      XM=X
      FM=F
      X=XL-DX
      TOL=X
      F= FN(TOL,V1,V2,V3,V4)
      IF(F) 18,16,18
C     TEST ON SATISFACTORY ACCURACY IN ITERATION LOOP
   18 TOL= EPS
      A=ABS(X)
      IF(A-1.00) 20,20,19
   19 TOL= TOL*A
   20 IF(ABS(DX)-TOL) 21,21,22
   21 IF(ABS(F)-TOLF) 16,16,22
C     PREPARATION OF NEXT BISECTION LOOP
   22 IF(SIGN(1.00,F)+SIGN(1.00,FL)) 24,23,24
   23 XR=X
      FR=F
      GOTO 6
   24 XL=X
      FL=F
      XR=XM
      FR=FM
C     END ITERATION
      GOTO 6
C     ERROR RETURN IN CASE OF WRONG INPUT DATA.
   25 IER= 2
      RETURN
      END
```

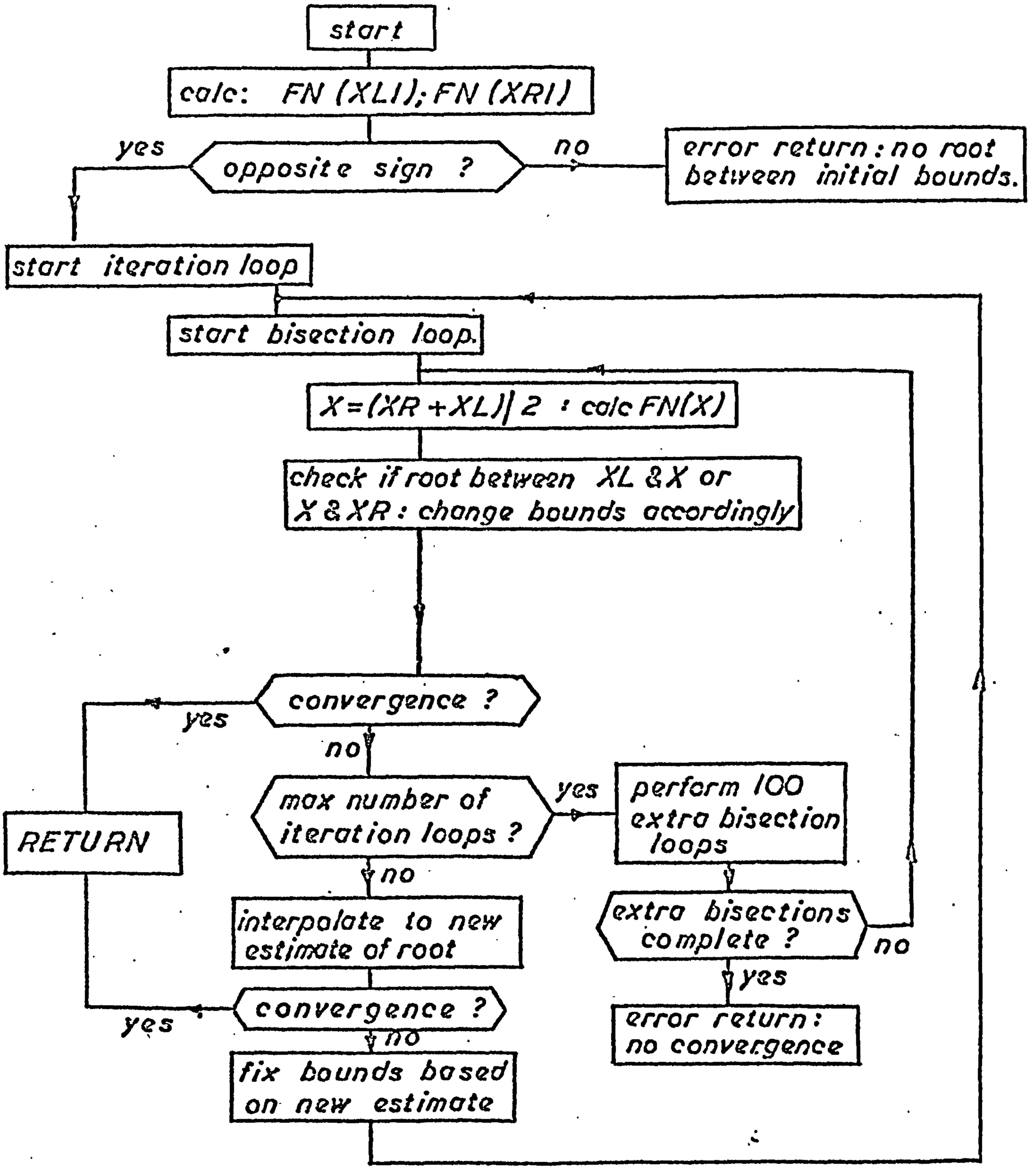

Schematic Flow Chart for the Iteration Subroutine.

Fig. B·1

Appendix C

Hot Wire Concentration Calibration and Heat Transfer Correlation Program

Master Segment 'CON2'

Purpose:-

a. To generate and least squared error fit the Nusselt-Reynold number data from the flow calibration rig test results, (fig. (4.5), section (4.1.3)), and hence provide the constants A, B in equation (4.36). (Input NV = 1).

b. Subsequently provide the concentration function plot data from the calibration constants as in figure (5.1). (Input NV = 1).

c. Provide the computational sequence to calculate experimental concentration values from bridge voltage outputs of calibrated wires. (Input NV = 0).

d. Provide the constants A, B in equation (4.36) for wires calibrated in air on equipment for which the velocity is directly known (such as the DISA wind tunnel). (Input NV = 2).

Arrangements of the program master segment is as in figure (5.23) and the required subroutines may now be discussed in relation to the program text and selected flow charts.

Subroutine 'HTRANS'

Purpose: To solve equation (4.15) for K1, hence define the heat transfer coefficient by equation (4.14).

Input Arguments: As defined in the program text. For high gas temperature data wire material resistivity and wire 'cold' resistance should be externally defined at the appropriate gas temperature.

Internal Call Statements: 'CJMIT' and 'FK1'

Notes: Failure on the iteration process is denoted by setting $H = 10^8$ and K1 = default coding.

i.e. K1 = 1 exceeded max. iteration loops.

K1 = 2 no root between initial bounds.

Further details in the flow chart of figure C.1 and the program text.

Subroutine 'CONX2'

Purpose:- To iterate to the value of gas molar concentration which satisfies equation (5.1).

Input Arguments: 'FX'; external function name which defines equation (5.1). 'H1, H2' the two experimental heat transfer coefficients.

Common Statements: 'PROP', arrays of gas properties at T_{m1}, T_{m2} for the two pure component gases. 'GEN', defining the gas and reference temperatures. 'PROBES' defining the two wire's details.

'OP', defining the wire operating details.

'TEST', to output check function values of 'FCX'.

Internal Subroutines: 'CJMIT'

External Function: 'FCX' defining equation (5.1), and additionally requiring functions 'VM', 'KM' (see miscellaneous segments).

For further details see the flow chart of figure C.2 and the program text.

Subroutine 'VELX2"

Purpose: To calculate the gas velocity predicted by each wire at known binary gas concentration (provided by 'CONX2').

Input Arguments: 'FVX', external velocity function name. XB, molar concentration level. H1, H2 heat transfer coefficients. 'PA, TP' ambient pressure and mean film temperature.

Common Statements: Previously defined (CONX2) except 'COEFS', contains the two wires intercept and slope constants for equation (4.36).

Internal Call Segments: 'KM', 'VM', 'CPM', 'FVX' (see miscellaneous segments).

Notes: Function 'FVX' defines the velocity by re-arrangement of equation (4.36). Separate velocity estimates from each wire will agree closely provided the concentration estimate is correct.

Further details from the flow chart of figure C.3 and the program test.

Subroutine 'ODATA'

Purpose: To read the flow calibration rig data, (orifice heads and temperatures etc.), and calculate the test section velocity and gas concentration. Subsequently to sort data to order of increasing velocity within concentration.

Input Arguments: 'NF', number of flows to consider. 'WM', array of molecular weights for the two gases. 'M', sorting reference array.

Common Statements: 'VELO' output of test section velocities and orifice predicted concentrations, and, test section gas temperature.

Internal Call Statements: 'ORIFLOW', used to calculate the mass flow through an orifice using the relationship for C_d defined by equation (4.2). 'SORTXY', used to sort the data after computation (see miscellaneous segments).

Subroutine 'NDATA'

Purpose: To generate Nusselt-Reynold co-ordinates from the calculated wire heat transfer coefficients and rig velocity data. Subsequently to least square fit the data to produce the constants A, B in equation (4.36).

Input Arguments: 'PRE', Reynolds number exponent, (0.4).
'PPR', Prandtl number exponent (redundant).
'PTC' film temperature correction exponent (-0.12).
'NF', number of flow cases. 'M', sorting reference array. 'H', two dimensional array of experimental heat transfer coefficients. PA, ambient pressure.

Common Statements: Previously defined except 'POL', contains the polynomial coefficients for the gas property temperature relationships.

Internal Call Statements: 'KM', 'VM', 'CPM', 'CJMLSF'. (see miscellaneous segments).

Further details from the flow chart of figure C.4 and the program text.

Miscellaneous Segments

'KM', 'VM' Calculate the mean mixture gas properties by equations (4.25) (4.24) respectively. An additional segment 'CPM' calculates the mean specific heat of the gas mixture and was originally used for Prandtl number evaluation early in the development of the correlating equation (4.36), but is now redundant.

'CJMLSF' Subroutine to produce the least squared error line through a set of data points.

'SORTXY' Subroutine to sort data to order of array 'Y' within order of array 'X' in increasing magnitude. Original data locations are stored in array 'M'.

'PROPTAB' Subroutine to tabulate binary gas mixture properties as calculated by equations (4.24, 4.25, 4.29, 4.30) at chosen temperature intervals and concentrations X = 0, to 1.0 in steps of 0.1.

'PROPVAL' Evaluates the pure gas component properties at the two wires respective film temperatures and stores in appropriate two dimensional arrays.

PROGRAM LISTING

```
      MASTER CON2
      DIMENSION BV(2,50),M(50),TP(2),BR(2),XB(50),A(10),VXW(2,50),VXO(2,
     150),XMW(50),Q(2,50)
      COMMON        /PROP/   CP(2,2),CN(2,2),VI(2,2),WM(2)
     1              /POL/   VPC(2,9),CPC(2,9),CNC(2,9)
     1              /GEN/   TA,TO
     1              /PROBES/   RC(2),BETO(2),ZW(2),DW(2),ALP(2),RL(2)
     4              /OP/      R(2),T(2)
     5              /TEST/   F(11)
     6              /VELO/   VTSO(50),VTSP(50),XMO(50),TS(50)
     7              /COEFS/   CI(5),CS(5)
      EXTERNAL FCX,FVX
      PI= 3.141592654

      READ(1,1050) NGAS
      DO 50 IG=1,NGAS
      READ(1,1050) NRUN
C     READ POLYNUMIAL COEFS FOR GAS PAIR
      READ(1,1010)((VPC(I,J),J=1,9),I=1,2),((CPC(I,J),J=1,9),I=1,2),
     1((CNC(I,J),J=1,9),I=1,2)

      DO 45 IR=1,NRUN

      READ(1,1000)(WM(I),I=1,2),TA,PATIO
      READ(1,1050) NP,NV,NF,NW
C     NP= 1  PROVIDE OUTPUT OF GAS PROPERTIES
C     NV=0  CONC RUN WITH CALIBRATED WIRES
C     NV=1  WIRE CALIBRATION IN GAS MIXTURES ON CONC. RIG
C     NV= 2  READ GAS VELOCITY BY DIRECT INPUT(DISA CAL TUNNEL)
C     NF  NUMBER OF FLOW CASES.
C     NW  NUMBER OF WIRES ON PROBE.

      WRITE(2,2000)

      READ(1,1030)(A(I),I=1,10)
      WRITE(2,1030)(A(I),I=1,10)
      WRITE(2,2010) NP,NV,NF,NTP,NW
      IF(NP.EQ.1) CALL PROPTAB(600.,25.,WM)

C     READ AND CALCULATE FLOW CONDITIONS.
      IF(NV.NE.0)              GOTO 4
      READ(1,1000)(TS(I),I=1,NF)
      DO 3      I=1,NF
      XMO(I)= 0.0
    3 M(I)= I
    4 CONTINUE
      IF(NV.EQ.1) CALL ODATA(NF,WM,M)
      IF(NV.NE.2) GOTO 10
      READ(1,1000)(VTSO(I),I=1,NF)
      DO 5 I=1,NF
      TS(I)= TA
      M(I)=I
    5 XMO(I)= 0.0
   10 CONTINUE

      READ(1,1020)((RC(I),RL(I),DW(I),ZW(I),ALP(I),BETO(I),BR(I)),I=1,2)
      WRITE(2,2020)((RC(I),RL(I),DW(I),ZW(I),ALP(I),BETO(I),
     1BR(I)),I=1,NW)
      IF(NV.EQ.0)      READ(1,1000)          ((CI(I),CS(I)),I=1,2)

      WR= WM(2)/WM(1)
      NNF= NINT(FLOAT(NF)/10.0)*10
      IF(NNF.LT.NF) NNF= NNF+10
      WRITE(2,2000)
      READ(1,1020) ((R(I),T(I)),I=1,2)
      WRITE(2,2030)((R(I),T(I)),I=1,2)
      READ(1,1000)((BV(I,J),J=1,NNF),I=1,2)
```

```
      DO 20       J=1,NF
      DO 15       I=1,2
      PC= BV(I,J)/(BR(I)+R(I)+RL(I))
      Q(I,J)=  PC*PC*R(I)
      RA=  RC(I)*(1+ALP(I)*(TS(J)-TO))
      BETA= BETO(I)*(1+ALP(I)*(TS(J)-TO))
      CALL HTRANS(BV(I,J),GA1,PC,R(I),RA,T(I),TS(J),BETA,ZW(I),DW(I),ALP
     1(I),MM)
   15 CONTINUE
   20 CONTINUE

      IF(NV.EQ.0)         GOTO 25
      CALL NDATA(0,4,0.555,0.12,NF,M,BV,PA,CI,CS,GR)
      AA= CI(5)
      BB= CS(5)
   25 CONTINUE

      DO 30          J=1,NF
      DO 27          I=1,2
      TP(I)= (T(I)+TS(J))/2
   27 VXO(I,J)= 0.0
      CALL PROPVAL(TP,CP,CN,VI,CPC,CNC,VPC)
      TA= TS(J)
      CALL CONX2(FCX,XB(J),BV(1,J),BV(2,J))
      CALL VELX2(FVX,XB(J),BV(1,J),BV(2,J),PA,TP,VXW(1,J),VXW(2,J))
      XMW(J)= XB(J)*WR/(1-XB(J)*(1-WR))

      IF(NV.EQ.0)       GOTO 30

      DO 28          K=1,NF
   28 IF(M(K).EQ.J)     XBO= XMO(K)/(WR+XMO(K)*(1-WR))
      CALL VELX2(FVX,XBO,BV(1,J),BV(2,J),PA,TP,VXO(1,J),VXO(2,J))
   30 CONTINUE

C     OUTPUT CONCENTRATION RESULTS IN ORDER OF ARRAY M
      WRITE(2,2050)
      DO 35 J=1,NF
      N= M(J)
      QE1= PI*DW(1)*ZW(1)*BV(1,N)*(T(1)-TS(N))
      QE2= PI*DW(2)*ZW(2)*BV(2,N)*(T(2)-TS(N))
      PC1= 100.0*(Q(1,N)-QE1)/Q(1,N)
      PC2= 100.0*(Q(2,N)-QE2)/Q(2,N)
      Q(1,N)= Q(1,N)*1000.0
      Q(2,N)= Q(2,N)*1000.0
   35 WRITE(2,2060) XMO(J),XMW(N),VTSO(J),VTSP(N),VXW(1,N),VXW(2,N),VXO(
     11,N),VXO(2,N),BV(1,N),BV(2,N),N,TS(N),Q(1,N),Q(2,N),PC1,PC2

   45 CONTINUE
   50 CONTINUE
 1000 FORMAT(10F0.0)
 1010 FORMAT(3E20.12)
 1020 FORMAT(7F0.0)
 1030 FORMAT(10A8)
 1040 FORMAT(2I3,3F0.0)
 1050 FORMAT(5I3)
 2000 FORMAT(1H1)
 2010 FORMAT(20X,' CONTROL INTEGERS ',3I3)
 2020 FORMAT(////,20X,' PROBE INFORMATION ',///,' COLD RES.   LEAD RESIST.
     :     WIRE DIA.    WIRE LENGTH  ALPHA          BETA          BRIDGE ',//
     2,7E12.4)
 2030 FORMAT(20X,'OPERATING CONDITIONS',///,20X,'RESISTANCE 1 = ',F0.2,
     1' WIRE TEMP. 1= ',F6.2,                                    //,20X,'RESISTANCE
     2 2 = ',F6.2,' WIRE TEMP. 2= ',F6.2)
 2040 FORMAT(///,' THERM COND  VISCOSITY   SPEC HEAT GAS TEMP',///,4(5E12
     1.4,2I5,/),///)
 2050 FORMAT(2X,'  XMO     XMW    VTSO     VTSP    VXW1    VXW2  VXO1     VXO2
     '   HTR1     HTR2    CASE     TG      MW1     MW2     PE1     PE2')
 2060 FORMAT(2X,6F7.2,2F7.1,I7,5F7.1)
      STOP
      END
```

```
      SUBROUTINE HTRANS(H,K1,CUR,RW,RO,TW,TO,BETO,Z,D,ELP,M)
C     CALCULATES THE HEAT TRANSFER COEFICIENT FOR A FINE WIRE IN A
C     CROSS FLOW OF GAS.
C     H=  HEAT TRANSFER COEFICIENT.
C     K1= FUNCTION VARIABLE.
C     CUR=WIRE CURRENT.
C     RW=  WIRE OPERATING RESISTANCE.
C     RO=  WIRE RESISTANCE AT TEMPERATURE TO
C     TW=  WIRE OPERATING TEMPERATURE.
C     TO=  REFERENCE AMBIENT TEMPERATURE.
C     BETO=RESISTIVITY OF WIRE MATERIAL AT TO.
C     Z=   TOTAL WIRE LENGTH.
C     D=  WIRE DIAMETER.
C     ELP= FIRST TEMPERATURE COEFICIENT OF RESISTANCE FOR WIRE MATERIAL.
C     M=  NO OF ITERATIONS EXECUTED IN CJMIT.
C     ADDITIONAL SUBROUTINES REQUIRED-- CJMIT,FK1.
C     FOR REFRENCE SEE INTERNAL REPORT.
      REAL K1
      DIMENSION FN(20)
      EXTERNAL FK1
      PI= 3.141592654
      A= PI*D*D/4
      CNWS= 2.23*(TO+273)/((10.**A)*BETO)
      CNWT= 2.23*(TW+273)/((10.**A)*BETO*(1+ELP*(TW-TO)))
      G1= CUR*CUR*RW/(A*CNWT*Z*(TW-TO))
      G2= 2*CNWS*RO/(Z*CNWT*RW)
      G3= (RW-RO)/RW
      G4= Z/2
      XL= 0.01
      XR= 10.**(12.)
      EPS= 10.**(-7)
      IFN0= 100
      CALL CJMIT(K1,G1,G2,G3,G4,F,FK1,XL,XR,EPS,IEND,IER,M)
      IF(IER.LT.1) GOTO 1
      H= 100000000.0
      CUR= F
      K1= IER
      RETURN
    1 CONTINUE
      K1= ABS(K1)
      H= (K1*CNWT*A*CUR*CUR*ELP*RO/Z)/(PI*D)
      RETURN
      END


      FUNCTION FK1(K1,G1,G2,G3,G4)
      REAL K1,KA,KSA
      KA= ABS(K1)
      KSA= SQRT(KA)
      FK1= G1-(1-G2*TANH(KSA*G4)/KSA-G3)-KA
      RETURN
      END
```

```
      SUBROUTINE CONX2 (FX,XB,H1,H2)
      DIMENSION H(2),RG(2),BETG(2)
      REAL K1
      COMMON        /PROP/ CP(2,2),CN(2,2),VI(2,2),WM(2)
     1              /GEN/ TA,TO
     2              /PROBES/ RC(2),BETO(2),Z(2),D(2),ALPHA(2)
     4              /OP/    HW(2),TW(2)
     5              /TEST/    F(11)

      H(1)= H1
      H(2)= H2
      DO 1        I=1,2
    1 IF( H(I).GT.99999999. ) GOTO 4
C     CALCULATE CHECK FUNCTION VALUES
      DO 2 I= 1,11
      XB=    FLOAT(I-1)*0.1
    2 F(I)= FX(XB,H(1), D(1),H(2), D(2))
      WRITE(2,22)(F(I),I=1,11)
C     CALCULATE GAS MOLAR CONCENTRATION
      CALL CJMIT( XB,H(1), D(1),H(2), D(2),FV,FX,1.U0,0.0,0.0,0.0000000001,10
     20,IER,M.
      IF(IER.GT.0) GOTO 3
      RETURN
    3 WRITE(2,20) IER
      IF((F(11).GT.0.0).AND.(TW(1).LT.TW(2)))        XB=1.0
      IF((F(11).LT.0.0).AND.(TW(1).GT.TW(2)))          XB=1.0
      RETURN
    4 WRITE(2,21) K1,I
      RETURN
   20 FORMAT(' ITERATION FAILURE IN CONX2 ON XB   IER= ',I3)
   21 FORMAT(' ITERATION FAILURE IN CONX2-HTRANS  IER= ',E12.4,'
     1WIRE NUMBER ',I2)
   22 FORMAT(2X,11E10.3)
      END
```

```
      FUNCTION FCX(XB,H1,DW1,H2,DW2)
      COMMON        /PROP/  CP(2,2),CN(2,2),VI(2,2),WM(2)
     1              /COEFS/ CI(5),CS(5)
     2              /GEN/  TA,TO
     3              /OP/ R(2),T12)
      DIMENSION H(2),DW(2),TM(2)
      REAL NU(2),MU(2),KM
      H(1)= H1
      H(2)= H2
      DW(1)= DW1
      DW(2)= DW2
      DO 1 I=1,2
      MU(I)= VM(XB,WM(2),WM(1),VI(2,I),VI(1,I))
      CNM= KM(XB,WM(2),WM(1),VI(2,I),VI(1,I),CN(2,I),CN(1,I))
      NU(I)= H(I)*DW(I)/CNM
      TM(I)= (TA+T(I))/2
      FTC= ((TA+273.)/(TM(I)+273.))**0.12
      NU(I)=NU(I)*FTC
    1 CONTINUE
      RE= ((TM(2)+273.)*DW1*MU(2))/((TM(1)+273.)*DW2*MU(1))
      RE= RE**0.4
      B1=   CS(1)
      B2= CS(2)
      RE=  RE*B1/B2
      FCX= (NU(2)-CI(2))*RE     -(NU(1)-CI(1))
      RETURN
      END
```

```
      SUBROUTINE VELX2(FVX,XB,H1,H2,PA,TP,V1,V2)
      REAL KM,NU
      COMMON          /PROP/ CP(2,2),CN(2,2),VI(2,2),WM(2)
     1                /PROBES/  RC(2),BETU(2),ZW(2),DW(2),ALP(2),RL(2)
     1                /COEFS/ CI(5),CS(5)
      DIMENSION H(2),V(2),TP(2)
      H(1)= H1
      H(2)= H2
      WR= WM(2)/WM(1)
      DO 1 I=1,2
      CNM=     XM(XB,WM(2),WM(1),VI(2,I),VI(1,I),CN(2,I),CN(1,I))
      CPMM=    CPM(XB,WM(2),WM(1),CP(2,I),CP(1,I))
      VIM=     VM(XB,WM(2),WM(1),VI(2,I),VI(1,I))
      NU= H(I)*DW(I)/CNM
      XM= XB*WR/(1+XB*(WR-1))
      XM= XM*8314.3/WM(2)+8314.3*(1.-XM)/WM(1)
      RO= PA/(XM*(TP(I)+273.))

      A= CI(I)
      B= CS(I)
    1 V(I)= FVX(NU,RO,CNM,CPMM,VIM,TP(I),DW(I),A,B)
      V1= V(1)
      V2= V(2)
      RETURN
      END



      FUNCTION FVX(NU,RHO,CN,CP,VI,TP,DW,A,B)
      REAL NU
      COMMON / GEN / TA,TO
      FTC=  ((TA+273.)/(TP+273.))**0.12
      NU=   NU*FTC
      IF(NU.LT.A)      NU = A
      C=  ((NU-A)/B)**2.5
      FVX=   VI*C/(RHO*DW)
      RETURN
      END
```

```
      SUBROUTINE ODATA(NF,WM,M)
      COMMON          /VELO/ VU(50),VP(50),XM(50),TSS(50)
                      /POL/ VPC(2,9),CPC(2,9),CNC(2,9)
      DIMENSION WM(2),M(NF),VC(9),FM(2),HO(2),TO(2),DHO(2),DX(2),ZX(2)
      READ(1,10)((DX(I),ZX(I)),I=1,2)
      READ(1,10) FDHP,FDHO,FHO,FTO,FTS,PTS,PA,DD,DTS
      R1= 8314.3/WM(1)
      R2= 8314.3/WM(2)
      ATS= 3.141592654*DTS*DTS/4
      DO 3 J=1,NF
      M(J)= J
      READ(1,10) HO(1),HO(2),DHO(1),DHO(2),TO(1),TO(2),DHP,TS
      DHP= DHP*FDHP
      TSS(J)= TS*FTS
      TS= TSS(J)
      DO 2 I=1,2
      HO(I)= HO(I)*FHO
      TO(I)= TO(I)*FTO
      DHO(I)= DHO(I)*FDHO
      FM(I)= 0.0
      DO 1 K=1,9
    1 VC(K)= VPC(I,K)
    2 CALL ORIFLOW(ZX(I),DX(I),DD,HO(I),PA,TO(I),WM(I),VC,DHO(I),RE,FM(I
     1),Q,CD)
      XM(J)= FM(2)/(FM(1)+FM(2))
      RM= XM(J)*R2+R1-XM(J)*R1
      RHO= PTS/(RM*(TS+273.))
      VO(J)=(FM(1)+FM(2))/(RHO*ATS)
      DGP= DHP*1000.0/RHO-DHP
      VP(J)= SQRT(2*9.81*DGP)
    3 CONTINUE
C     SORT TO VELOCITY WITHIN CONC. ORDER, ORIGINAL LOCATION IN ARRAY M
      CALL SORTXY(XM,VO,M,NP)
      RETURN
   10 FORMAT(10F0.0)
      END
```

```
      SUBROUTINE ORIFLOW(L,D,DD,HO,PA,TO,WM,VC,DH,RE,FMR,Q,CD)
      REAL L
      DIMENSION VC(9)
      IF(DH.LE.0.0000001)  GOTO 3
      PI= 3.141592654
      FM= D*D/(DD*DD)
      A= PI*D*D/4
      PO= HO*10300.0/10.29
      RHO= WM*(PO+PA)/((TO+273.)*8314.3)
      VTO= CPY(VC,TO,9)
      H= DH*1000.0/RHO-DH
      RE= SQRT(2*9.81*H)*RHO*D/VTO
      CDO= 0.827-0.0085*L/D
      IF(RE-20000.0) 1,2,2
    1 G1= 20.0*(1+2.25*L/D)/RE
      G2= ALOG(0.00015*RE)**2
      G3= 0.03*L/(D*(1+7.5*G2))
      RCD= 1/CDO+G1-G3
      CDO= 1/RCD
    2 CD=CDO
      Q= CD*A*SQRT(2*9.81*H/(1-FM*FM))
      FMR= RHO*Q
      RETURN
    3 CD= 0
      Q= 0
      RETURN
      FMR= 0
      END
```

```
      S'BROUTINE NDATA(PRE,PPR,PTC,NF,M,H,PA,A,B,GR)
      REAL KM,NU(2,50)
      DIMENSION H(2,50),PR(2,50),RE(2,50),TC(2,50),CM(2),CPMM(2),VIM(2),
     1RHO(2),X(50),Y(50),A(5),B(5),M(NF),TP(2),GR(2)
      COMMON          /PROP/  CP(2,2),CN(2,2),VI(2,2),WM(2)
     1                /VELO/  V(50),VP(50),XM(50),TS(50)
     2                /PROBES/  RC(2),BETO(2),ZW(2),DW(2),ALP(2),RL(2)
     3                /OP/  R(2),T(2)
     4                /POL/  VPC(2,9),CPC(2,9),CNC(2,9)
      WRITE(2,25) PRE,PPR,PTC
      WRITE(2,20)
      WR= WM(2)/WM(1)
      DO 2 J=1,NF
      N= M(J)
      TP(1)=  TS(N)+T(1))/2
      TP(2)=  TS(N)+T(2))/2
      CALL PROPVAL(TP,CP,CN,VI,CPC,CNC,VPC)
      XB= XM(J)/(WR+XM(J)*(1-WR))
      RM= XM(J)*8314.3/WM(2)+(1-XM(J))*8314.3/WM(1)
      DO 1 I=1,2
      RHO(I)= PA/(RM*(TP(I)+273.))
      CM(I)= XM(XB,WM(2),WM(1),VI(2,I),VI(1,I),CN(2,I),CN(1,I))
      CPMM(I)= CPM(XB,WM(2),WM(1),CP(2,I),CP(1,I))
      VIM(I)= VM(XB,WM(2),WM(1),VI(2,I),VI(1,I))
      TC(I,J)= ((TS(N)+273.)/(TP(I)+273.))**PTC
      NU(I,J)= H(I,N)*DW(I)/CM(I)
      RE(I,J)= RHO(I)*V(J)*DW(I)/VIM(I)
      PR(I,J)= VIM(I)*CPMM(I)/CM(I)
    1 CONTINUE
      WRITE(2,21) N,XM(J),XB,((CM(I),CPMM(I),VIM(I),NU(I,J),RE(I,J),PR(I
     1,J)),I=1,2)
    2 CONTINUE

      XC= 0.0
      DO 5 L=1,3,2
      DO 4 LL=1,2
      N= L+LL-1
      A(N)= 0.0
      B(N)= 0.0
      NN= 0
      DO 3 J=1,NF
      IF(XM(J).NE.XC)        GOTO 3
      NN= NN+1
      Y(NN)= NU(LL,J)*TC(LL,J)
      X(NN)= RE(LL,J)**PRE
    3 CONTINUE
      IF(NN.EQ.0) GOTO 4
      CALL LJMLSF(X,Y,A(N),B(N),NN)
    4 CONTINUE
      XC= 1.0
    5 CONTINUE
      WRITE(2,22)((A(I),B(I)),I=1,4)
      DO 6 J= 1,NF
      RR= (RE(1,J)/RE(2,J))**PRE
      Y(J)= (NU(2,J)*TC(2,J)-A(2))*RR*B(1)/B(2)
    6 X(J)= NU(1,J)*TC(1,J)-A(1)
      WRITE(2,27)
      WRITE(2,28)((X(J),Y(J)),J=1,NF)
      CALL LJMLSF(X,Y,A(5),B(5),NF)
      WRITE(2,26) A(5),B(5)
      WRITE(2,23)
      DO 10 J=1,NF
      DO 9 I=1,2
      NU(I,J)= NU(I,J)*TC(I,J)
      RE(I,J)= RE(I,J)**PRE
    9 PR(I,J)= PR(I,J)**PPR
   10 CONTINUE
      WRITE(2,24) (M(J),XM(J),((NU(I,J),RE(I,J),PR(I,J)),I=1,2)),J=1,NF
     1)
```

```
20 FORMAT(////,20X,' NUSSELT-REYNOLD DATA ',////,' SET  XMASS XMUL
  1 CM1   CPM1    VM1*E4  NU1     RE1     PR1     CM2     CPM2  VM2*E4  NU2
  2     RE2     PR2 ')
21 FORMAT(2X,I3,2F7.4,2(  F7.4,F7.1,4PF7.4,UPF7.4,2F7.4))
22 FORMAT(//,'            COEFS WIRE 1-IN AIR',F10.4,F10.4,//,
  1          '            COEFS WIRE 2 IN AIR',F10.4,F10.4,//,
  2          '          COEFS WIRE 1 IN GAS',F10.4,F10.4,//,
  3          '          COEFS WIRE 2 IN GAS',F10.4,F10.4,//)
23 FORMAT(///,'  SET XMASS    NUC1  RE1**E PR1**E    NUC2 RE2**E PR2**E
  1')
24 FORMAT(2X,I3,7F7.4)
25 FORMAT('  PRE = ',E12.4,'  PPRM ',E12.4,'  PTC = ',E12.4)
26 FORMAT(//,'     CONC FUNCTION LSF',F10.4,F10.4)
27 FORMAT(//,'                    CONC, FUNCTION PLOT',//)
28 FORMAT(2X,8F10.4)
   RETURN
   END
```

```
      REAL FUNCTION KM(XB,WB,WA,VIB,VIA,CNB,CNA)
      AB= ((1+SQRT(VIA/VIB)*((WB/WA)**0.25))**2.)/SQRT(8*(1+WA/WB))
      BA= ((1+SQRT(VIB/VIA)*((WA/WB)**0.25))**2.)/SQRT(8*(1+WB/WA))


      KM= XB*CNB/(XB+(1-XB)*BA)+(1-XB)*CNA/(XB*AB+(1-XB))
      RETURN
      END
```

```
      FUNCTION CPM(XB,WB,WA,CPB,CPA)
      XMB= XB*WB/(WA*(1+XB*(WB/WA-1)))
      CPM= XMB*CPB+(1-XMB)*CPA
      RETURN
      END
```

```
      FUNCTION VM(XB,WB,WA,VIB,VIA)
      AB= ((1+SQRT(VIA/VIB)*((WB/WA)**0.25))**2.)/SQRT(8*(1+WA/WB))
      BA= ((1+SQRT(VIB/VIA)*((WA/WB)**0.25))**2.)/SQRT(8*(1+WB/WA))
      VM= XB*VIB/(XB+(1-XB)*BA)+(1-XB)*VIA/(XB*AB+(1-XB))
      RETURN
      END
```

```
      SUBROUTINE CJMLSF(X,Y,A,B,N)
      DIMENSION X( N ),Y( N )

      Q= 0.0
      R= 0.0
      DO 1 I=1,N
      Q=Q+X(I)
    1 R=R+Y(I)
      XM= Q/N
      YM= R/N
      DO 2 I=1,N
      X(I)= X(I)-XM
    2 Y(I)= Y(I)-YM
      Q= 0.0
      R= 0.0
      DO 3 I=1,N
      S= Y(I)*X(I)
      T= X(I)*X(I)
      Q= Q+T
    3 R= R+S
      B= R/Q
      A= YM-B*XM
      RETURN
      END
```

```
      SUBROUTINE PROPVAL(T,CP,CN,VI,CPC,CNC,VPC)
      DIMENSION CP(2,2),CN(2,2),VI(2,2),CPC(2,9),CNC(2,9),VPC(2,9),T(2),
     1C(9),CC(9),CCC(9)
      DO 3 I=1,2
      DO 1 J=1,9
      C(J)= CPC(I,J)
      CC(J)= CNC(I,J)
    1 CCC(J)= VPC(I,J)

      DO 2      J=1,2
      CP(I,J)= CPT(C,T(J),9)
      CN(I,J)= CPT(CC,T(J),9)
      VI(I,J)= CPT(CCC,T(J),9)
    2 CONTINUE

    3 CONTINUE
      RETURN
      END


      FUNCTION CPT(AC,T,N)
      DIMENSION AC(9)
      IF(T.EQ.0.0) GOTO 2
      CPT= 0.0
      DO 1 I=1,N
      CPT= CPT+AC(I)*(T**(I-1))
    1 CONTINUE
      RETURN
    2 CPT=AC(1)
      RETURN
      END


      SUBROUTINE PROPTAB(TMAX,DT,WM)
      REAL KM
      COMMON/POL/ VPC(2,9),CPC(2,9),CNC(2,9)
      DIMENSION  T(2),CP(2,2),CN(2,2),VI(2,2),WM(2)
      WRITE (2,20)
      NT= NINT(TMAX/DT)+1
      T(2)= 0.0
      DO 2 J=1,NT
      T(1)= FLOAT(J-1)*DT
      WRITE(2,21) T(1)
      CALL PROPVAL(T,CP,CN,VI,CPC,CNC,VPC)
      DO 1 I=1,11
      XB= (I-1)*0.1
      CNM= KM(XB,WM(2),WM(1),VI(2,1),VI(1,1),CN(2,1),CN(1,1))
      CM= CPM(XB,WM(2),WM(1),CP(2,1),CP(1,1))
      VIM= VM(XB,WM(2),WM(1),VI(2,1),VI(1,1))
      PR= VIM*CM/CNM
      VIM= VIM*(10.**6)
      WRITE(2,22) XB,CNM,CM,VIM,PR
    1 CONTINUE
    2 CONTINUE
      RETURN
   20 FORMAT(20X,' PROPERTIES OF GASES ',///,2X,' GAS TEMP  MOL CONC  ME
     1AN K      MEAN CP  MEAN VISC*(E6) PRANDTL  ')
   21 FORMAT(2X,F10.3)
   22 FORMAT(' 2X,F10.3,F10.6,3F10.3)
      END
```

SUBROUTINE SUBTXY(X,Y,M,N)

```
      DIMENSION X(N ),Y(N ),M(N )
      L=N-1
      DO 4 K=1,N
      DO 3 J=1,L
      IF(X(J)-X(J+1)) 3,1,2
    1 IF(Y(J)-Y(J+1)) 3,3,2
    2 Z= X(J)
      X(J)= X(J+1)
      X(J+1)= Z
      Z= Y(J)
      Y(J)= Y(J+1)
      Y(J+1)= Z
      NN= M(J
      M(J)= M(J+1)
      M(J+1)= NN
    3 CONTINUE
    4 CONTINUE
      RETURN
      END
```

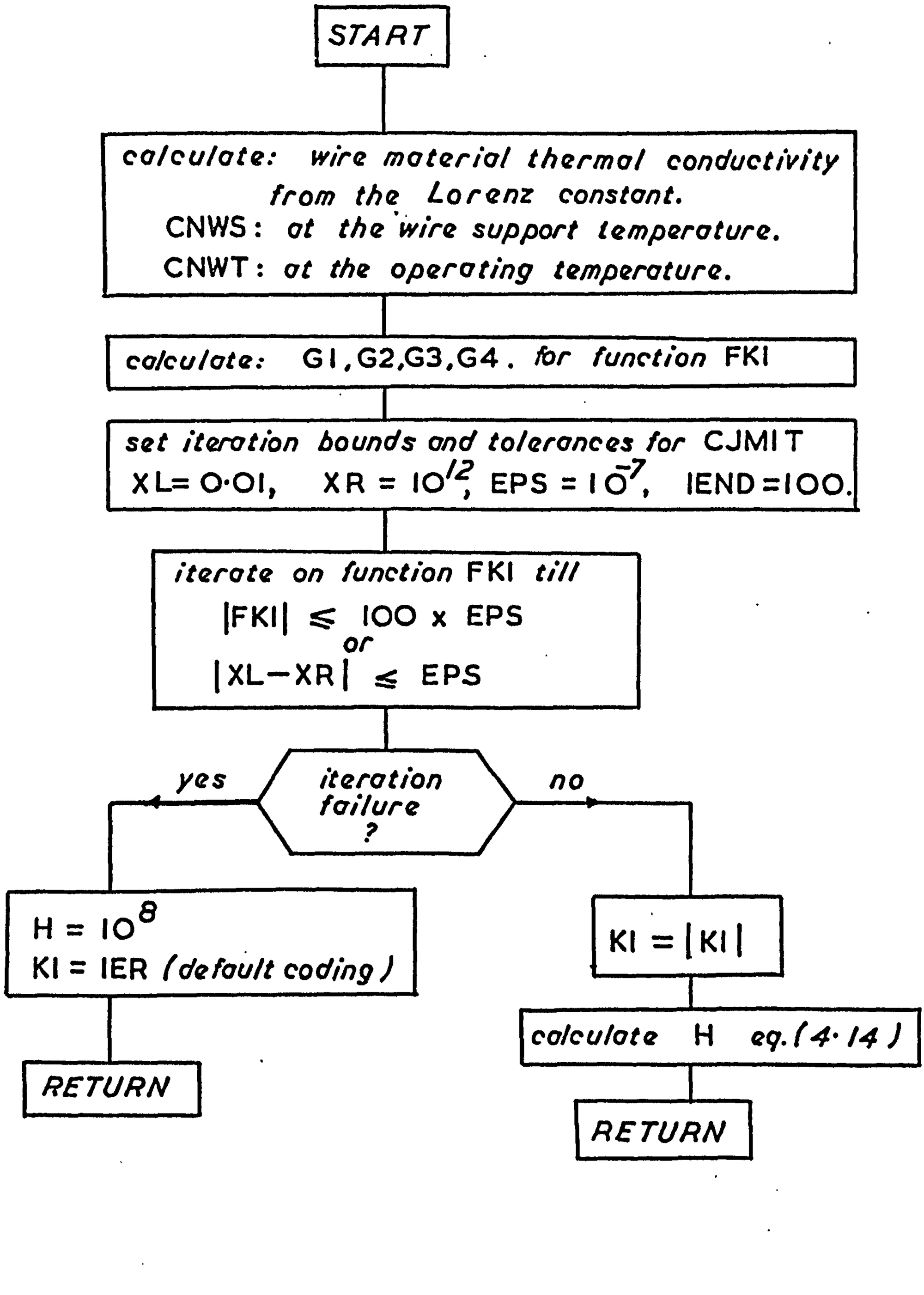

Schematic Flow Chart for Subroutine 'HTRANS'

Fig. C·1

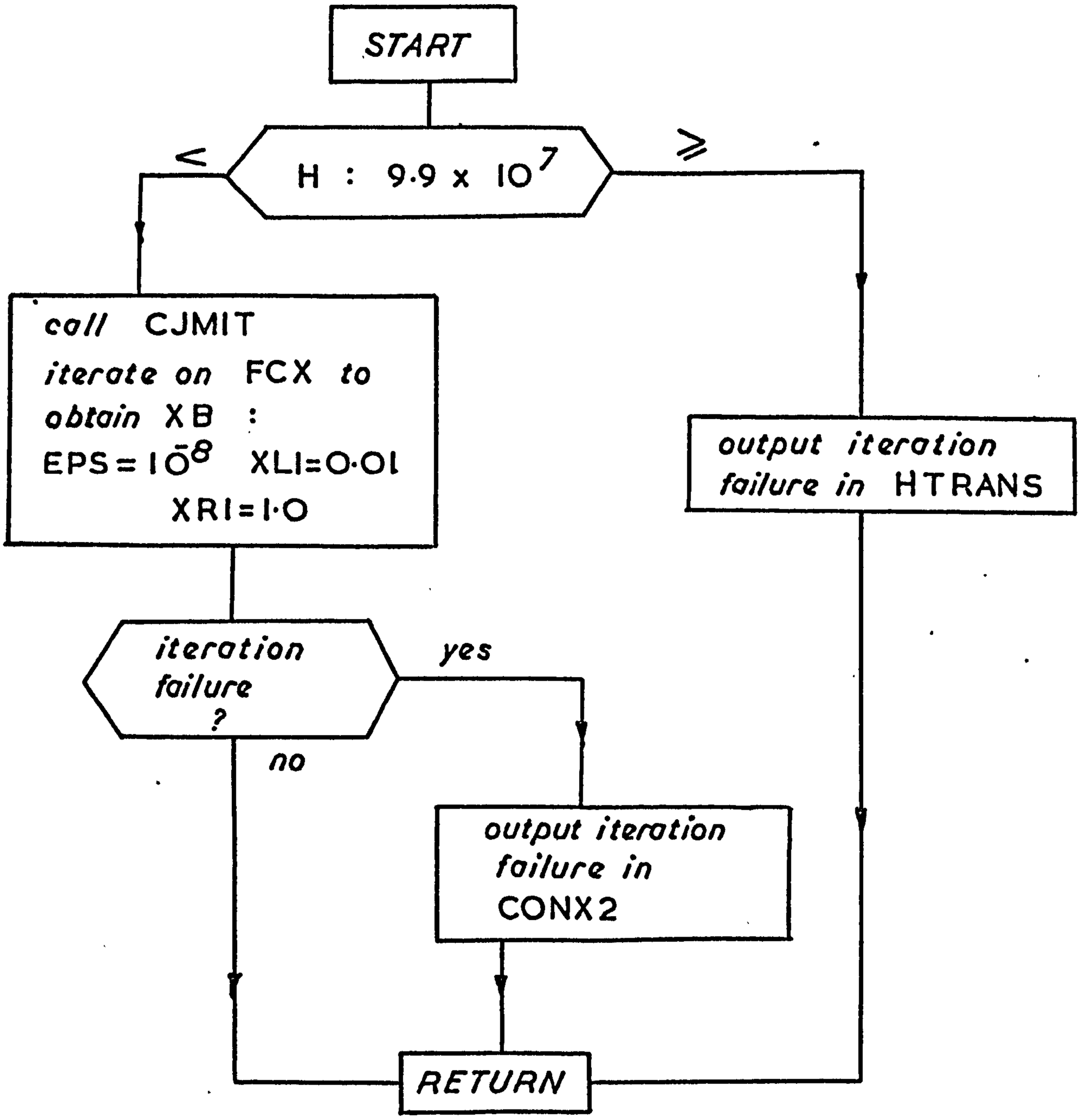

Schematic Flow Chart for Subroutine 'CONX2'

Fig. C·2

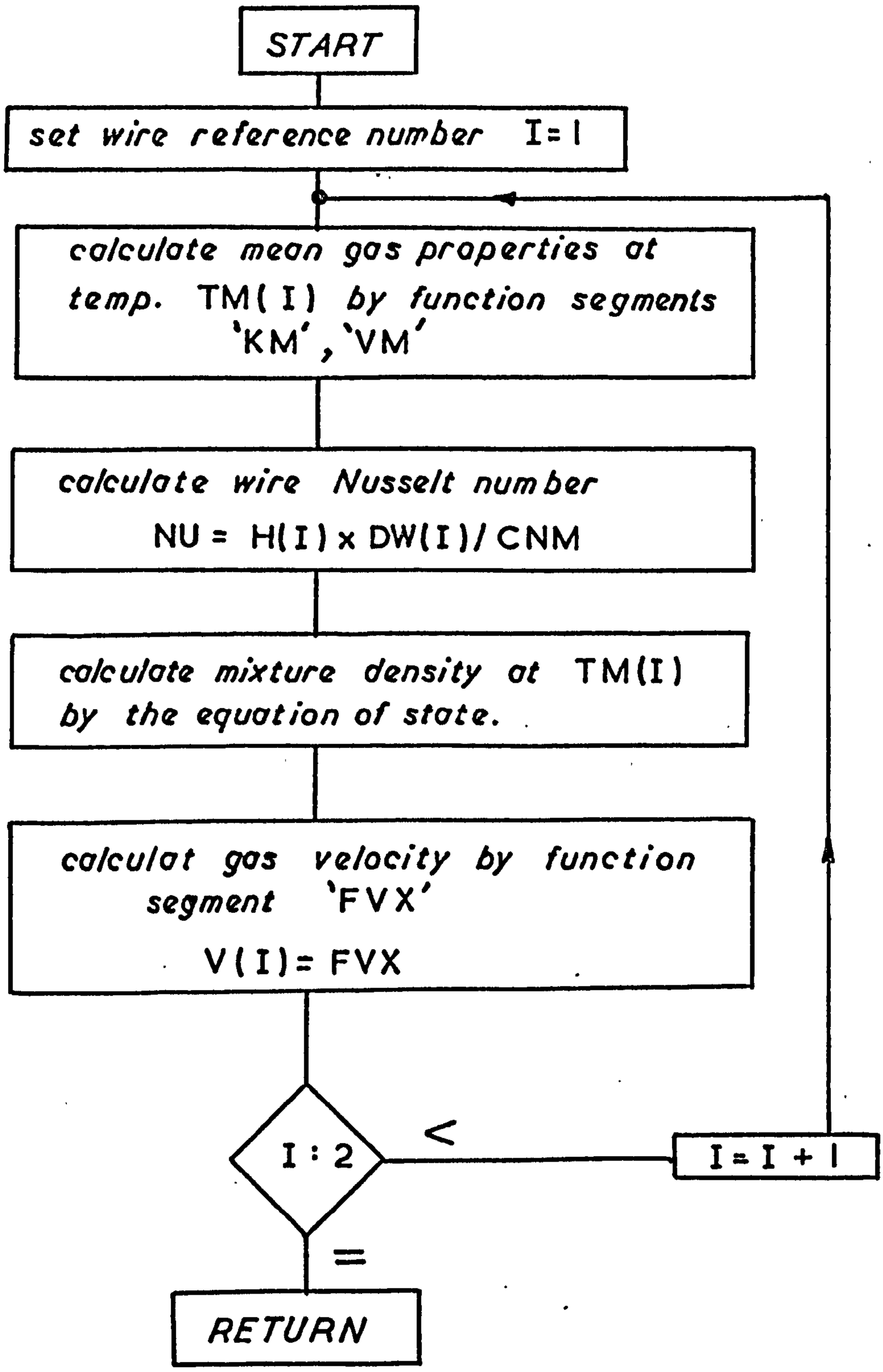

Schematic Flow Chart for Subroutine 'VELX2'

Fig. C·3

Schematic Flow Chart : 'NDATA'

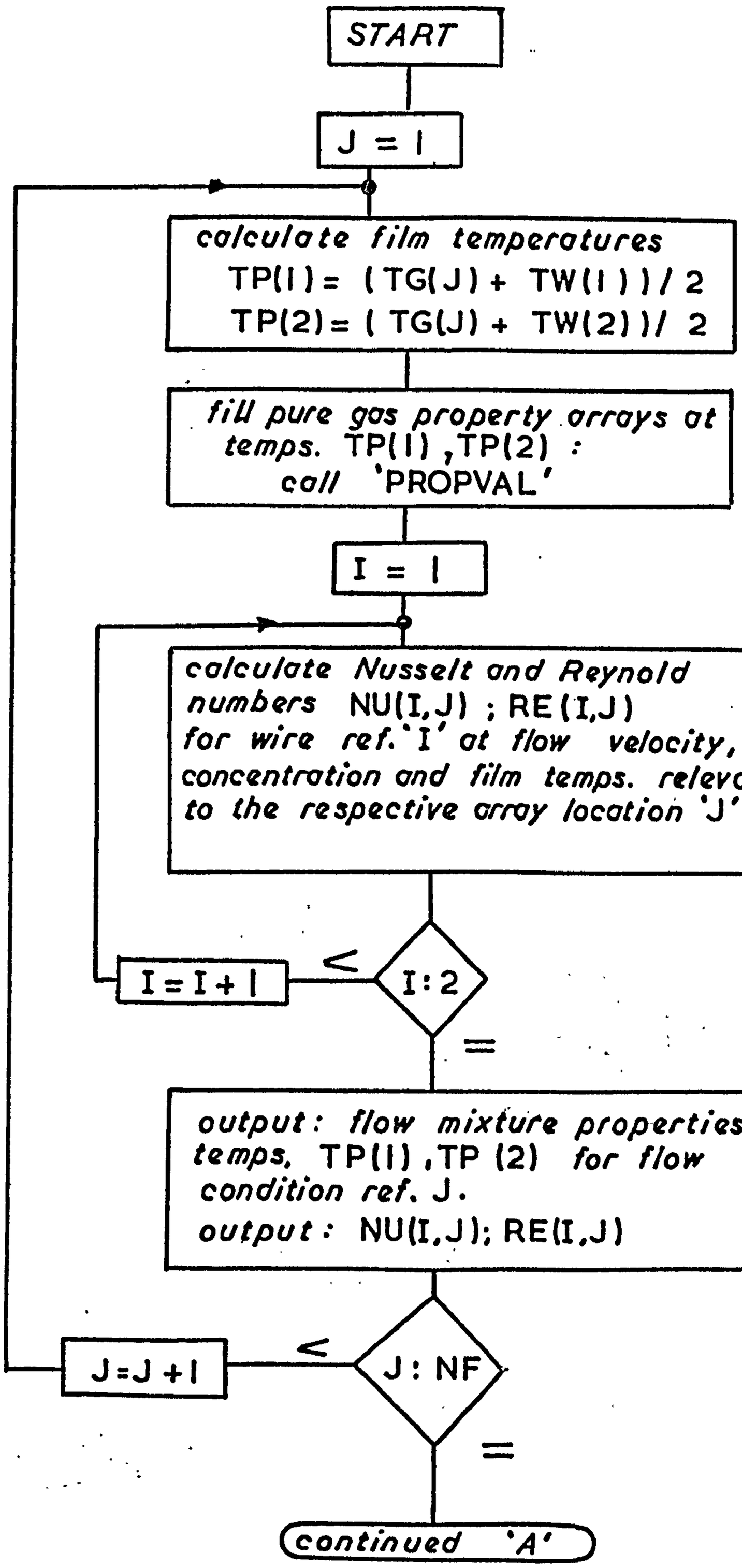

Fig. C·4

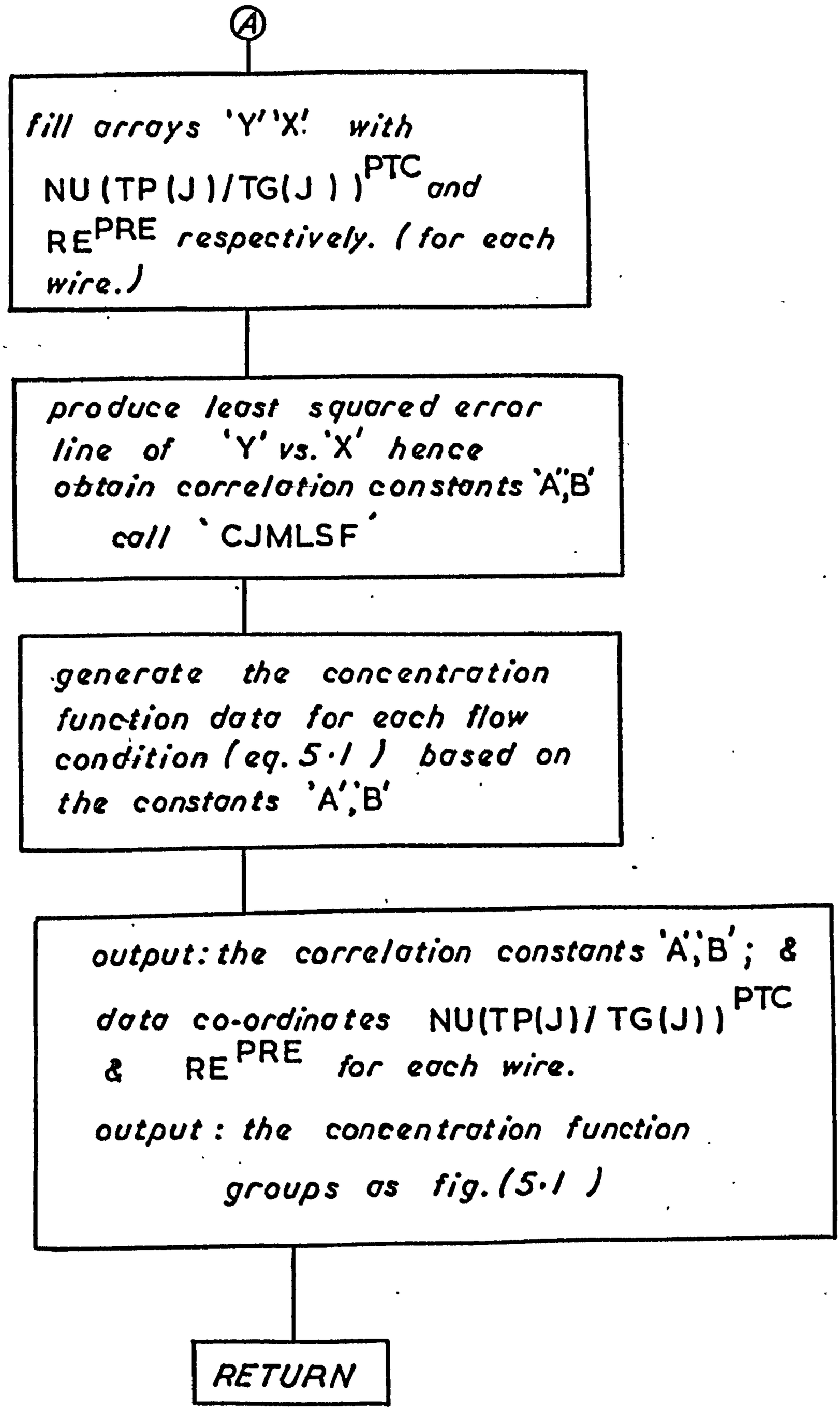
A
fill arrays 'Y' 'X' with NU(TP(J)/TG(J))^PTC and RE^PRE respectively. (for each wire.)
produce least squared error line of 'Y' vs. 'X' hence obtain correlation constants 'A','B' call 'CJMLSF'
generate the concentration function data for each flow condition (eq. 5·1) based on the constants 'A','B'
output: the correlation constants 'A','B'; & data co-ordinates NU(TP(J)/TG(J))^PTC & RE^PRE for each wire.
output: the concentration function groups as fig. (5·1)
RETURN

Fig. C·4 (CONTD.)

Appendix D

Petter PJ1 Test Engine Salient Details

Description: 4-stroke cycle, overhead valve, direct injection diesel engine.

Geometry:-

bore:	96.8 mm
stroke:	110 mm
connecting rod length:	231.9 mm

Valve timings (.18 mm tappet clearance (hot)):-

inlet valve opens	4.5 deg. BTDC
inlet valve closes	35.5 deg. ABDC
exhaust valve opens	35.5 deg. BBDC
exhaust valve closes	4.5 deg. ATDC

Modified Compression Ratio	16.9:1
Maximum Governed Speed (overspeed governor fuel 'cut-off')	1500 rev/min.
Recommended spill port timing	23 deg. BTDC.